WOODHEAD PUBLISHING SERIES IN CIVIL AND STRUCTURAL ENGINEERING



Advances in Asphalt Materials

Road and Pavement Construction

Edited by Shin-Che Huang
and Hervé Di Benedetto

WP

www.EngineeringEBooksPdf.com

Woodhead Publishing Series in Civil and Structural Engineering: Number 56

Advances in Asphalt Materials

Road and Pavement Construction

Edited by

Shin-Che Huang and Hervé Di Benedetto



AMSTERDAM • BOSTON • CAMBRIDGE • HEIDELBERG
LONDON • NEW YORK • OXFORD • PARIS • SAN DIEGO
SAN FRANCISCO • SINGAPORE • SYDNEY • TOKYO
Woodhead Publishing is an imprint of Elsevier



www.EngineeringEBooksPdf.com

Woodhead Publishing is an imprint of Elsevier
80 High Street, Sawston, Cambridge, CB22 3HJ, UK
225 Wyman Street, Waltham, MA 02451, USA
Langford Lane, Kidlington, OX5 1GB, UK

Copyright © 2015 Elsevier Ltd. All rights reserved.

No part of this publication may be reproduced, stored in a retrieval system or transmitted in any form or by any means electronic, mechanical, photocopying, recording or otherwise without the prior written permission of the publisher.

Permissions may be sought directly from Elsevier's Science & Technology Rights Department in Oxford, UK: phone (+44) (0) 1865 843830; fax (+44) (0) 1865 853333; email: permissions@elsevier.com. Alternatively you can submit your request online by visiting the Elsevier website at http://elsevier.com/locate/permissions, and selecting Obtaining permission to use Elsevier material.

Notice
No responsibility is assumed by the publisher for any injury and/or damage to persons or property as a matter of products liability, negligence or otherwise, or from any use or operation of any methods, products, instructions or ideas contained in the material herein. Because of rapid advances in the medical sciences, in particular, independent verification of diagnoses and drug dosages should be made.

British Library Cataloguing-in-Publication Data
A catalogue record for this book is available from the British Library

Library of Congress Control Number: 2014959675

ISBN 978-0-08-100269-8 (print)
ISBN 978-0-08-100271-1 (online)

For information on all Woodhead Publishing publications visit our website at http://store.elsevier.com/

Typeset by SPi Global
www.spi-global.com
Printed and bound in the United Kingdom



www.EngineeringEBooksPdf.com

List of contributors

M. Audo IFSTTAR, Centre de Nantes, Bouguenais, France

J. Beiswenger Western Research Institute, Laramie, WY, USA

A. Bhasin The University of Texas at Austin, Austin, TX, USA

J.F. Branthaver Chatham, IL, USA

D. Cebon University of Cambridge, Cambridge, UK

E. Chailleux IFSTTAR, Centre de Nantes, Bouguenais, France

C.Y. Cheung University of Cambridge, Cambridge, UK

A. Cookman Western Research Institute, Laramie, WY, USA

M.K. Darabi University of Kansas, Lawrence, KS, USA

H. Di Benedetto University of Lyon/ENTPE (Ecole Nationale des Travaux Publics de l'Etat), Vaulx en Velin, France

S. Goyer CEREMA, Saint-Brieuc, France

D. Hernando University of Florida, Gainesville, FL, USA

S.-C. Huang Western Research Institute, Laramie, WY, USA

A. James Akzo Nobel Surface Chemistry, Chicago, IL, USA

N. Kringos KTH Royal Institute of Technology, Stockholm, Sweden

D.N. Little Texas A&M University, College Station, TX, USA

R. Luo Texas A&M Transportation Institute, College Station, TX, USA

X. Luo Texas A&M Transportation Institute, College Station, TX, USA

R.L. Lytton Texas A&M University, College Station, TX, USA

www.EngineeringEBooksPdf.com

O. Marzouk CEREMA, Saint-Brieuc, France

M. Mohajeri Gebr. Van der Lee contractors, Lelystad, The Netherlands; Delft University of Technology, Delft, The Netherlands

A.A.A. Molenaar Delft University of Technology, Delft, The Netherlands

F. Olard Eiffage Travaux Publics R&D Department, Corbas, France

A.T. Pauli Western Research Institute, Laramie, WY, USA

S. Pouget Eiffage Travaux Publics R&D Department, Corbas, France

C. Queffelec CEISAM, Université de Nantes, Nantes, France

R. Roque University of Florida, Gainesville, FL, USA

C. Sauzeat University of Lyon/ENTPE (Ecole Nationale des Travaux Publics de l'Etat), Vaulx en Velin, France

M. Southern Eurobitume, Brussels, Belgium

K. Takamura University of California, Davis, CA, USA

B.S. Underwood Arizona State University, Tempe, AZ, USA

M.F.C. Van de Ven Delft University of Technology, Delft, The Netherlands

A. Varveri Delft University of Technology, Delft, The Netherlands

R. Will Grimes Western Research Institute, Laramie, WY, USA

Y. Zhang Texas A&M Transportation Institute, College Station, TX, USA

J. Zhu KTH Royal Institute of Technology, Stockholm, Sweden

J. Zou University of Florida, Gainesville, FL, USA

www.EngineeringEBooksPdf.com

Woodhead Publishing Series in Civil and Structural Engineering

1 **Finite element techniques in structural mechanics**
C. T. F. Ross
2 **Finite element programs in structural engineering and continuum mechanics**
C. T. F. Ross
3 **Macro-engineering**
F. P. Davidson, E. G. Frankl and C. L. Meador
4 **Macro-engineering and the earth**
U. W. Kitzinger and E. G. Frankel
5 **Strengthening of reinforced concrete structures**
Edited by L. C. Hollaway and M. Leeming
6 **Analysis of engineering structures**
B. Bedenik and C. B. Besant
7 **Mechanics of solids**
C. T. F. Ross
8 **Plasticity for engineers**
C. R. Calladine
9 **Elastic beams and frames**
J. D. Renton
10 **Introduction to structures**
W. R. Spillers
11 **Applied elasticity**
J. D. Renton
12 **Durability of engineering structures**
J. Bijen
13 **Advanced polymer composites for structural applications in construction**
Edited by L. C. Hollaway
14 **Corrosion in reinforced concrete structures**
Edited by H. Böhni
15 **The deformation and processing of structural materials**
Edited by Z. X. Guo
16 **Inspection and monitoring techniques for bridges and civil structures**
Edited by G. Fu
17 **Advanced civil infrastructure materials**
Edited by H. Wu
18 **Analysis and design of plated structures Volume 1: Stability**
Edited by E. Shanmugam and C. M. Wang
19 **Analysis and design of plated structures Volume 2: Dynamics**
Edited by E. Shanmugam and C. M. Wang
20 **Multiscale materials modelling**
Edited by Z. X. Guo

www.EngineeringEBooksPdf.com

21 **Durability of concrete and cement composites**
Edited by C. L. Page and M. M. Page
22 **Durability of composites for civil structural applications**
Edited by V. M. Karbhari
23 **Design and optimization of metal structures**
J. Farkas and K. Jarmai
24 **Developments in the formulation and reinforcement of concrete**
Edited by S. Mindess
25 **Strengthening and rehabilitation of civil infrastructures using fibre-reinforced polymer (FRP) composites**
Edited by L. C. Hollaway and J. C. Teng
26 **Condition assessment of aged structures**
Edited by J. K. Paik and R. M. Melchers
27 **Sustainability of construction materials**
J. Khatib
28 **Structural dynamics of earthquake engineering**
S. Rajasekaran
29 **Geopolymers: Structures, processing, properties and industrial applications**
Edited by J. L. Provis and J. S. J. van Deventer
30 **Structural health monitoring of civil infrastructure systems**
Edited by V. M. Karbhari and F. Ansari
31 **Architectural glass to resist seismic and extreme climatic events**
Edited by R. A. Behr
32 **Failure, distress and repair of concrete structures**
Edited by N. Delatte
33 **Blast protection of civil infrastructures and vehicles using composites**
Edited by N. Uddin
34 **Non-destructive evaluation of reinforced concrete structures Volume 1: Deterioration processes**
Edited by C. Maierhofer, H.-W. Reinhardt and G. Dobmann
35 **Non-destructive evaluation of reinforced concrete structures Volume 2: Non-destructive testing methods**
Edited by C. Maierhofer, H.-W. Reinhardt and G. Dobmann
36 **Service life estimation and extension of civil engineering structures**
Edited by V. M. Karbhari and L. S. Lee
37 **Building decorative materials**
Edited by Y. Li and S. Ren
38 **Building materials in civil engineering**
Edited by H. Zhang
39 **Polymer modified bitumen**
Edited by T. McNally
40 **Understanding the rheology of concrete**
Edited by N. Roussel
41 **Toxicity of building materials**
Edited by F. Pacheco-Torgal, S. Jalali and A. Fucic
42 **Eco-efficient concrete**
Edited by F. Pacheco-Torgal, S. Jalali, J. Labrincha and V. M. John
43 **Nanotechnology in eco-efficient construction**
Edited by F. Pacheco-Torgal, M. V.Diamanti, A. Nazari and C. Goran-Granqvist
44 **Handbook of seismic risk analysis and management of civil infrastructure systems**
Edited by F. Tesfamariam and K. Goda

www.EngineeringEBooksPdf.com

45 **Developments in fiber-reinforced polymer (FRP) composites for civil engineering**
Edited by N. Uddin
46 **Advanced fibre-reinforced polymer (FRP) composites for structural applications**
Edited by J. Bai
47 **Handbook of recycled concrete and demolition waste**
Edited by F. Pacheco-Torgal, V. W. Y. Tam, J. A. Labrincha, Y. Ding and J. de Brito
48 **Understanding the tensile properties of concrete**
Edited by J. Weerheijm
49 **Eco-efficient construction and building materials: Life cycle assessment (LCA), eco-labelling and case studies**
Edited by F. Pacheco-Torgal, L. F. Cabeza, J. Labrincha and A. de Magalhães
50 **Advanced composites in bridge construction and repair**
Edited by Y. J. Kim
51 **Rehabilitation of metallic civil infrastructure using fiber-reinforced polymer (FRP) composites**
Edited by V. Karbhari
52 **Rehabilitation of pipelines using fiber-reinforced polymer (FRP) composites**
Edited by V. Karbhari
53 **Transport properties of concrete: Measurement and applications**
P. A. Claisse
54 **Handbook of alkali-activated cements, mortars and concretes**
F. Pacheco-Torgal, J. A. Labrincha, C. Leonelli, A. Palomo and P. Chindaprasirt
55 **Eco-efficient masonry bricks and blocks: Design, properties and durability**
F. Pacheco-Torgal, P.B. Lourenço, J.A. Labrincha, S. Kumar and P. Chindaprasirt
56 **Advances in asphalt materials: Road and pavement construction**
Edited by S.-C. Huang and H. Di Benedetto
57 **Acoustic emission (AE) and related non-destructive evaluation (NDE) techniques in the fracture mechanics of concrete: Fundamentals and applications**
Edited by M. Ohtsu

www.EngineeringEBooksPdf.com

Preface

Because of the urgent need for infrastructure rehabilitation and maintenance, the introduction and application of sustainable and environmentally friendly bituminous materials will have a significant impact on the national economy as well as on energy sustainability. It is for this reason that more research is needed on understanding bituminous materials.

This book provides a comprehensive review of recent advances in research and technological developments in bituminous materials, from fundamental material properties in the microscale and macroscale to modeling techniques. It covers a wide range of subjects, including the perspective of bituminous binder specification; characterization and analysis of asphalt materials; pavement distresses such as thermal cracking, fatigue cracking, healing, permanent deformation, moisture damage, and oxidative aging; alternative binders; the blending issue of reclaimed asphalt pavement; asphalt emulsion; and aggregate gradation optimization. It also includes developments to understand the response behavior of bituminous material under various mechanical and environmental impacts for the selection criteria, so that longer lasting asphalt pavements can be achieved.

This book is essential for researchers, practitioners, and transportation engineers who need updated and valuable information in material characterization and field validation for both short- and long-term performance of asphalt pavements.

We would like to express our most sincere thanks to all the authors for their hard work. Without their efforts, we would not have had such high-quality content in this publication. Thanks are also extended to Gwen Jones and Josh Bennett of Woodhead Publishing for their skillful management of the revision and publication process, and to our colleagues, friends, and families for their forbearance and support during the long process leading to this book.

Shin-Che Huang
Hervé Di-Benedetto

www.EngineeringEBooksPdf.com

Introduction

S.-C. Huang[1], *H. Di Benedetto*[2]
[1]Western Research Institute, Laramie, WY, USA; [2]University of Lyon, Lyon, France

Asphalt materials (or bituminous materials) have been used for road construction and maintenance since the end of the nineteenth century. They are the most common materials for quality road surfaces and structures. The importance of these materials in road construction can be demonstrated by their extraordinary physical and chemical properties. However, their complex thermoviscoelastoplastic and chemical behavior are still not well understood, even after several decades of application, and are in need of new investigations, from nanoscale up to structure levels.

In light of growing concerns about environmental and health protection, the techniques and processes used for energy-saving and natural materials should be redesigned, and new materials should be invented. These evolutions are part of the natural process of "sustainable development" and need technological breakthroughs. All of these will be possible only if scientific locks are solved. They can be accomplished only if better knowledge of the complex behavior of asphalt materials is developed. This book provides updates of the most advanced developments in asphalt materials, including asphalts, mastics, and mixes, and aims to provide information and knowledge that help to solve the new challenges of road construction.

Asphalt, also known as bitumen, is the black glue that binds more than 90% of highway together. It is largely produced from the refining of crude oils. The chemical and physical properties of crude oils that are obtained from different oil fields (sources) are generally different. These differences have a significant effect on the properties of asphalts, especially when they come into contact with aggregates in the pavement engineering field. Asphalt binder is a mixture of a wide variety of hydrogen and carbon compounds. Some are aliphatic (waxy asphalts), some are aromatic (airblown asphalts), and some molecules include both aliphatic and aromatic carbon. These components appear to vary widely in molecular size, and it is the known tendency of polar molecules to form molecular associations. Such associations are usually held together by weak forces compared with the bonding forces that hold individual atoms together in molecules. Polars tend to associate strongly to form organized structures and cause stiffening, while nonpolars cause dissociation of polars and softening of the whole asphalt.

It is known that polar associations in asphalt are of great importance in influencing asphalt properties, and it is important to introduce a model of asphalt structure in which molecular associations are central. This model historically has been known as the colloidal model, and assumes that polar molecules in crude oil residua interact

www.EngineeringEBooksPdf.com

to form molecular associations. These molecular associations are believed to be dispersed in a bulk solvent, which consists of the saturated components, the aromatic compounds, and the less polar heteroatom-containing compounds. Unfortunately, current research does not provide sufficient information on how these microstructures influence the rheological properties of asphalt binders, or on pavement performance.

Several distresses are observed in road structures. It appears that a good knowledge of the composition of asphalt and asphalt aggregate interaction must be considered for a good description of these distresses. For example, cracking is one of the serious failure modes in pavement. If the molecular network becomes too stiff (rigid), the stability of an asphalt to deform elastically will be lost. Instead, the asphalt will fracture and likely will be separated sufficiently so that healing cannot occur.

Asphalts in pavements that exist as thin films exposed to aggregates, fillers, water, oxygen, and traffic are the real service conditions in which they should have predictable performance. However, the different classification systems, such as the current performance grade (PG) system, provide no assurance to the asphalts that like grades will have the same stiffness when water is present in pavement, nor are there any criteria to differentiate the oxidation effect. Oxidation very well may cause different embrittlements after a few years of pavement service. Oxidation imparts permanent hardening either in asphalt or in a mixture. When asphalt oxidizes, it stays stiffer at any given set of conditions of storage time, temperature, and shear. Asphalt suffers oxidative hardening continuously during its lifetime, and this type of hardening cannot be removed by heat alone. The intent of developing a new specification was to classify asphalts by their expected pavement performance, but the real-world environments are largely ignored in the current design methods. Even the current global aging system does not address photooxidation, nor does the current aging model include "fundamental" binder properties.

Healing is another important phenomenon in which asphalt concrete is observed to regain strength during a rest period after loss of strength during heavy traffic use. This phenomenon, which still needs to be defined correctly, has been studied extensively in recent years by many researchers. They envision a process wherein microcracks formed in asphalt concrete during heavy traffic loads fuse back together when allowed to rest. Clearly, this would require the asphalt to flow to refill the microcracks, and certainly would be accelerated by confining pressure. A critically important observation is that not all asphalt concretes heal at the same rate, nor to the same extent. Variations in asphalt composition cause major differences in healing propensity. Clearly, fast and complete healing are performance advantages, but currently there is no binder specification for healing rate or efficiency. No advantage is made of this knowledge that asphalts can be distinguished with respect to performance.

Moisture damage is another common problem in asphalt pavement. Moisture may invade pavement from rain, subgrade water, drainage, humidity, and so on. Water is a highly polar material that can be transported into the asphalt by virtue of attraction of polar water molecules to polar asphalt components. When water penetrates the asphalt concrete, the mechanical strength will be reduced. However, current methods, such as the Superpave system, do not provide guidelines on how water influences the strength of asphalt concrete.

www.EngineeringEBooksPdf.com

Permanent deformation (which induces rutting) and fatigue damage have been well recognized as two of the most important distresses, and they have been studied extensively over the years. However, these phenomena are not always modeled correctly. In addition, past research has always focused on these two phenomena separately. In a real pavement situation, these two phenomena occur simultaneously.

The use of reclaimed asphalt pavement (RAP) has become relatively common practice in most countries, as it is both an environmentally and economically attractive proposition. A survey conducted by the Federal Highway Administration's RAP expert task group shows that the average RAP content in hot mix is only 10–20% as used in the United States, even though specifications allow up to 30%. The primary reason for this limited use is the uncertainty of the long-term performance of RAP materials. Research is still needed for characterizing asphalt binders extracted from RAP and recycled hot-mix asphalts. Furthermore, the interaction between new and old asphalt binders in the mixtures containing RAP has not been studied extensively, and the physicochemical interaction is still not well understood. It is essential to understand the fundamental properties of recycled asphalt binder as well as the interaction between the old binder in the recycled asphalt and the fresh binder in the new mix.

With the development of cold and warm mix techniques, new additives and new processes appeared. The properties of these new asphaltic materials are different from those of classical hot mixes, and therefore raise new questions. Again, research is needed for better materials and structure design.

The strong demand for natural petroleum and the high cost of asphalt cement has encouraged the development of alternative binders to replace asphalt binders. The benefits of using alternative binders are that they can help save natural resources and reduce energy consumption, all while maintaining and in some cases improving pavement performance. Common alternative binders include fossil fuel, biobinder, soybean oil, palm oil, vegetable oil, engine oil residue, grape residue, swine waste, and pyrolized materials, among others. It has been observed that most, if not all, of these alternative binders contain chemical compositions somewhat similar to those of conventional asphalt binders (hydrocarbons, aromatics, saturates, asphaltenes, etc.). However, research results indicate significant variability in the properties of alternative binders. In addition, the modification mechanism (chemical) for asphalt with alternative binders depends on the base asphalt, and is therefore not well understood.

Achievement of consistent performance with asphalts requires accurate classification and better understanding of the causes of pavement distresses.

This introduction presented some key unsolved questions related to asphalt materials and road applications. This book presents the current advances in asphalt research that cause different distresses, and how they influence overall pavement performance. It is especially designed to cover everything from the microscale of fundamental chemical properties of asphalt binder, to the macroscale of mixture properties, how they influence each other, and pavement performance. Obviously, additional research is needed to better understand the relationship among age hardening, binder viscosity, healing, moisture, fatigue cracking, and so on in pavement using asphalt.

www.EngineeringEBooksPdf.com

This book consists of a total of 15 chapters, written by authors from international societies and separated into three parts: (1) Characterization and analysis of asphalt materials; (2) Damage mechanisms; and (3) Alternative asphalt materials. Following this introduction, Chapter 1, entitled "A perspective of bituminous binder specifications," provides the binder specification perspective of the past, present, and future. Chapter 2, entitled "Analytical separation methods in asphalt research," introduces the typical analytical techniques for characterizing the chemical properties of asphalt binder. Chapter 3, entitled "Tridimensional linear viscoelastic behavior of bituminous materials," provides a new way of thinking on how rheological models, via 3D linear viscoelastic theory, link to thermomechanical properties of asphalt mixtures, and provides a better simulation model for real pavement. Chapter 4, entitled "Characterization of asphalt materials by scanning probe microscopy," introduces how current atomic force microscopy (AFM) is used as a nanomechanical technique to measure mechanical properties of bituminous materials at micron and submicron scale. Chapter 5, entitled "Cracking mechanisms in asphalt pavements," introduces the cracking mechanisms in asphalt pavements and provides a top-down cracking performance prediction model to illustrate the full potential of the critical condition approach. Chapter 6, entitled "Deformation mechanisms of bituminous materials," provides insights on how the mechanical behavior of pure bitumen contributes to the deformation-mechanism maps. Chapter 7, entitled "Damage healing in asphalt pavements: theory, mechanisms, measurement, and modeling," treats healing phenomena and presents a methodology by which the intrinsic and the long-term healing properties can be measured and used in fatigue damage analysis. Chapter 8, entitled "The fatigue cracking of asphalt mixtures in tension and compression," summarizes the results of testing and analysis methods developed to provide the engineering properties of asphalt mixtures in tension and compression both in the undamaged and the damaged states. Chapter 9, entitled "Multiscale modeling approach for asphalt concrete and its implications on oxidative aging," provides a link from constituent binder behavior (mastic) to mixture in terms of oxidative aging models. Chapter 10, entitled "Moisture damage in asphaltic mixtures," introduces the mechanism of moisture damage and how the finite element method is used to simulate water flow induced by the moving wheel, and provides guidelines for mix design of moisture-resistant asphalt mixtures. Chapter 11, entitled "Advances in the development of alternative binders from biomass for the production of biosourced road binders," gives information on some new products that could replace asphalt in the future. Chapter 12, entitled "Blending of virgin bitumen and RA binder in mixtures with high amounts of RA," discusses if full blending occurred and how the blending influences the RAP mixture properties. Chapter 13, entitled "Paving with asphalt emulsions," provides information on emulsion production, emulsion properties, and curing mechanisms. Chapter 14, entitled "A new approach for aggregate grading optimization for mixtures," presents a new method to obtain aggregate gradation and packing, improving mix performance.

www.EngineeringEBooksPdf.com

A perspective of bituminous binder specifications

1

M. Southern
Eurobitume, Brussels, Belgium

1.1 Scope and terminology

This chapter will cover the concept and content of specifications for petroleum bitumen produced by the refining of crude oil. Although bitumen-like deposits occur naturally in natural asphalt, rock asphalt, lake asphalt, and oil sands, and such materials may be used in similar applications as refined bitumen, they are not considered within the scope of this chapter.

Bitumen is known by different names throughout the world. In most European countries, the term "bitumen," or "refined bitumen," is used predominantly and is synonymous with the term "asphalt," or "asphalt cement," used in the United States. Outside the United States, the term "asphalt" is often used to describe a mixture of bitumen with aggregate, sand, and filler. In this chapter, the term "bitumen," or "bituminous binder," will be used to refer to the liquid product.

Different types of binders exist, including paving-grade bitumens, polymer-modified binders, hard paving-grade binders, and multigrade binders, and these are used for numerous different applications. The predominant focus of the chapter will be specifications for binders for asphalt pavements, but it is recognized that in many regions there are large numbers of pavements that are either unbound, or paved using thin surfacings, or some form of surface treatment. The same principles of specifications apply to these products and processes, but the specific end use is not considered in detail in this chapter.

The chapter will cover the important aspects of specifications and test methods, what makes a good specification, and considerations for development of new specifications. It is not the intention to provide detailed listings of individual product specifications, although the concepts of different specifications will be discussed.

1.2 Introduction

Bitumen is an engineering material, and is produced to meet a variety of specifications in which the properties are defined based on physical properties. It is the residual product from the distillation of crude oil in petroleum refining. It is a viscoelastic waterproofing and construction material. It behaves like a Newtonian liquid at high temperatures (>100 °C), exhibits relatively complex rheological behavior at intermediate temperatures, and is an elastic solid at low temperatures (<0 °C). The main characteristics

Advances in Asphalt Materials. http://dx.doi.org/10.1016/B978-0-08-100269-8.00001-5
© 2015 Elsevier Ltd. All rights reserved.

www.EngineeringEBooksPdf.com

of bitumen that make it suitable as a binder for asphalt are that it is adhesive, waterproof, thermoplastic, durable, inexpensive, modifiable, and recyclable.

1.3 What is a specification?

A specification can be considered to be a detailed description of a given material, enabling parties on either side of a commercial transaction to understand what can be expected in performance terms at the point of transfer of ownership. In the context of bituminous binder specifications, the specification should address properties that are relevant to the end use for construction products in which they are used.

1.3.1 Characteristics, properties, test methods, and values

The starting point for development of a bituminous binder specification is the identification of the characteristics required for performance. The binder imbues certain characteristics important to the performance of the asphalt. For this reason, it is important that the role played by the binder in the asphalt mixture is understood so that a binder specification focuses on the relevant characteristics of the binder.

For asphalt mixtures, pertinent characteristics might include

- Mechanical properties and stability
- Durability
- Safety in use

Additional properties are often included in a specification relating to specific characteristics that might not be directly relevant to performance, but that provide important practical information relating to handling and application.

After the important characteristics of the end product have been defined, the properties of the binder that relate to these characteristics can be considered for inclusion in the specification. Once the properties have been defined, the properties can be measured using a defined test method under identified test conditions, which will then provide specific values that can be introduced to a product specification.

The importance of the above process is to define a range of values, tested under specified conditions so that important properties of the binder can be compared by different laboratories. For this reason, standardized test methods are required for use within specifications.

The above concepts can be illustrated as follows.

Stiffness of an asphalt mixture is an important property that relates to the load-bearing capability of the road pavement. The binder plays a role in providing stiffness to the mixture, and this is evident from the fact that a stiffer binder provides a stiffer asphalt mixture. Therefore, binder stiffness is a **characteristic** that is important to define within a specification. A binder **property** that relates to the stiffness might be the needle penetration value or the complex shear modulus G^*. Therefore, a specification that considers binder stiffness important should include a measurement

www.EngineeringEBooksPdf.com

relating to this property. Having identified the property, the next step is to identify a **test method** that measures the property; this might be carried out using a needle penetrometer, or a dynamic shear rheometer (DSR). Bitumen stiffness is highly temperature and loading-time dependent; therefore, the test method must include the conditions under which the property should be measured. These would include details of the test equipment geometry, test conditions, and temperature.

Having identified the property and test method to be used to measure a characteristic, it is necessary to include in the specification a **value** or range of values that are required in order for the binder to be considered fit for purpose.

A good specification will measure important properties of the binder that are relevant to the performance of the product in which it is being used. Furthermore, the properties will be measured using test methods that are relevant to the property, provide a reasonable precision of measurement, and establish appropriate limits for the measured property.

1.3.2 Attributes of a good specification

A well-written specification should be able to differentiate between a binder that will be suitable for purpose and one that will not, although it must be recognized that the binder is not the sole determinant of end-product performance.

Most binder specification systems evaluate the properties of binders to consider the predominant failure modes of the pavement, such as elevated service-temperature properties (to address permanent deformation), low service-temperature properties (to address low-temperature cracking), and intermediate service-temperature properties (to address pavement stiffness under "normal" service conditions, or to evaluate fatigue behavior on an aged binder).

Road pavements have a long life cycle; therefore, durability is important. Depending on the failure property under evaluation, the binder might be subjected to some form of aging/conditioning step prior to establishing the property of interest. In addition, a specification might include nonperformance-related requirements, such as information that is important for safety, handling, storage, or application of the material, such as viscosity, solubility, or storage stability.

1.3.3 Geographical considerations

Road pavements must be able to withstand geographic, seasonal, and diurnal (day–night) variations in temperature, which may be quite extreme. In some countries, such variations might exceed 70 °C, and range from extreme periods of heat or cold to frequent heavy precipitation. Many specifications are designed to cover the range of climatic conditions that can be reasonably anticipated during the service life of the pavement. In some regions, specifications are "imported" from other areas, or countries. In such cases, it is essential to consider whether the criteria used in the development of the original specifications remain valid for the new region in which the specification is to be used.

www.EngineeringEBooksPdf.com

Bituminous binders are used to build road pavements, which are engineering structures; therefore, the engineering properties used within specifications must be appropriate for the climatic and traffic conditions that the pavement will experience during its lifetime. For any sizable geographic region, it is unlikely that a single grade of bitumen will be suitable for the range of conditions likely to be encountered over the lifetime of a pavement. To that end, many specifications list not only a range of properties to be measured, but also a series of grades of bitumen that may be selected for the appropriate performance required.

Specifications can be national, regional, or local, depending on the contract in which they are being used. Generally, the specifying agency within a country will produce specifications that cover the predominant grades of bitumen applicable to the climatic and traffic conditions likely to be found within the region of use, and also covering the types of pavement construction used.

Two of the larger regions in the world, the United States and Europe, have approached binder specifications in a somewhat different manner from each other; these will be examined in further detail in this chapter. The majority of specifications used elsewhere in the world use one or the other of these concepts.

Most specifications focus on the main mechanical aspects of binder performance, which is rational, given that the pavement must withstand the traffic loads to be experienced.

1.4 Regulatory frameworks

In order that different people measuring the same product obtain the same or similar results, it is important that specifications and test methods are harmonized within a given regulatory area. To date, there are few standards that are fully international, and specifications are generally restricted to national or regional boundaries. Within these boundaries, there are national or regional bodies responsible for developing and maintaining the test methods and specifications that are used within their jurisdiction. Two of the larger geographical areas covered by specifications are Europe and the United States.

1.4.1 Europe

At the time of writing, the European Union (EU) comprises 28 countries, and the European Economic Area (EEA) includes a further four European Free Trade Association (EFTA) countries. A founding principle of the union is free trade between member states. A key to this is the ability to prevent barriers to trade that might prevent the movement of goods across national boundaries. The large number of countries and the wide spread of climatic conditions present a number of challenges in ensuring free trade, in particular due to historic differences in specifications. Such differences have been viewed in the past as technical barriers to trade, something forbidden within the union.

Common specifications are desirable, even necessary, in order to permit manufacturers to produce goods that can be sold throughout the region. This is achieved by the

www.EngineeringEBooksPdf.com

implementation into each member state's national legislation of a series of legal instruments covering broad areas of activity, such as construction products. The Construction Products Regulation (CPR)[1] is the most relevant for bituminous binders, and sets out criteria for products used within the EU by specifying a series of basic requirements. At the practical level, the requirements of the CPR mean that national standards for construction products, including bituminous binders, must be harmonized so that common specifications are used throughout the EU. These specifications must comply with the CPR and incorporate criteria to ensure that such binders are suitable for purpose by complying with the basic requirements. The body in Europe responsible for producing specifications is CEN.[2]

1.4.1.1 Comité Européen de Normalisation

Comité Européen de Normalisation (CEN), the European Committee for Standardization, was founded in 1961 by the national standardization bodies in the European Economic Community and EFTA countries. Currently, CEN has 33 national standardization body members.[3] In addition, there are associate members who participate in the standardization process but do not have a vote. Each full member has voting rights in the general assembly and administrative board of CEN and provides delegations to the technical board, which defines the work program.

CEN works closely with the European Committee for Electrotechnical Standardization (CENELEC), the European Telecommunications Standards Institute (ETSI), and the International Organization for Standardization (ISO). It also has close liaisons with European trade and professional organizations such as trade associations, as well as other national or regional standardization bodies. Work for various product categories covered by CEN is conducted by technical committees (TCs). Working groups (WGs) report to the TCs, and task groups (TGs) carry out the development of test methods and product standards. WGs and TGs are populated by experts in their fields, whereas formal voting and decision making is conducted by representatives of the national standardization bodies within the TC.

Bitumen specifications in Europe are based on broad categories of binder type. The main specifications for binders fall into binders for paving applications, surface treatments, and those used for roofing and industrial applications.

The TC responsible for producing the specifications for bituminous binders is CEN TC 336. WGs produce "harmonized" specifications and test methods for bituminous binders following the principles outlined above.

[1] Regulation (EU) No. 305/2011 of the European Parliament and of the Council laying down harmonized conditions for the marketing of construction products and repealing Council Directive 89/106/EEC.

[2] http://www.cen.eu/cen/pages/default.aspx.

[3] Austria, Belgium, Bulgaria, Croatia, Cyprus, Czech Republic, Denmark, Estonia, Finland, France, Germany, Greece, Hungary, Iceland, Ireland, Italy, Latvia, Lithuania, Luxembourg, Malta, The Netherlands, Norway, Poland, Portugal, Romania, Slovakia, Slovenia, Spain, Sweden, Switzerland, The Former Yugoslav Republic of Macedonia, Turkey, and United Kingdom.

www.EngineeringEBooksPdf.com

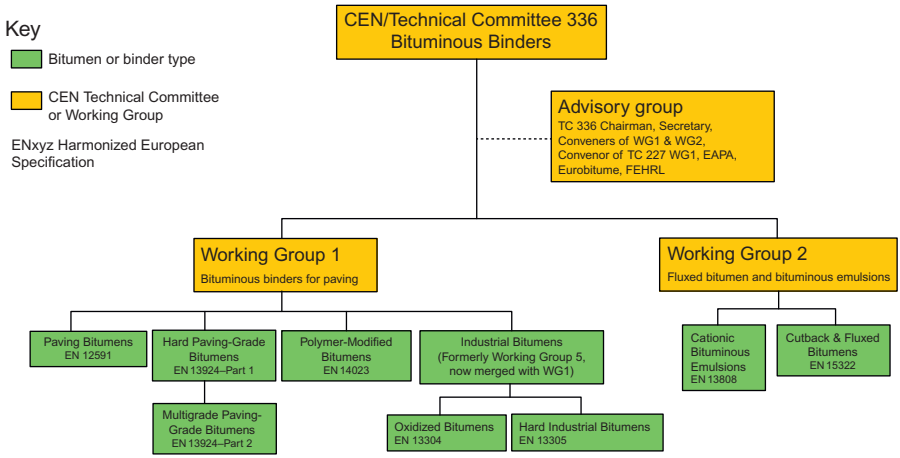


Figure 1.1 Schematic diagram of the structure of CEN/TC 336.

In addition to the national standardization bodies, TC 336 also includes several associate members who participate in the TC activity but do not vote. These associate members include the European bitumen association (Eurobitume), the European Asphalt Paving Association (EAPA), and the Forum of European Highway Research Laboratories (FEHRL). TC 336 works closely with CEN/TC 227 WG1—bituminous mixtures, responsible for the standardization of asphalt mixtures.

A schematic diagram of the structure of CEN/TC 336 is shown in Figure 1.1, together with the standards for bituminous binders.

For bituminous binders, a review of asphalt mixture and related binder properties was compiled by TC 336 WG1; parts of this list are shown in Table 1.1. The list was intended to cover most applications for paving bitumen performance, and it was recognized that for certain properties there was no test method currently available. Nevertheless, the list was considered reasonably comprehensive.

For several of the properties above, there are currently no harmonized test methods available; therefore, those properties cannot be included in binder specifications at present.

1.4.2 United States

In the United States, test methods and specifications are standardized by ASTM International and American Association of State Highway and Transportation Officials (AASHTO).

ASTM International was formerly known as the American Society for Testing and Materials (ASTM). It operates in a broadly similar way to CEN in the development and delivery of international standards. At the time of writing, some 12,000 ASTM standards are used around the world.

The AASHTO is a nonprofit, nonpartisan association representing highway and transportation departments in the United States. It represents all five transportation modes: air, highway, public transportation, rail, and water. Its primary goal is to foster

www.EngineeringEBooksPdf.com

Table 1.1 Relevant binder properties derived from asphalt performance characteristics

Asphalt mixture characteristic	Binder property relevant to that characteristic
Stripping	Adhesion
Hardening during mixing	Aging—Short-term
Resistance to aging in the road	Aging—Long-term
Resistance to fretting and cracking	Cohesion
Resistance to low-temperature cracking	Combination of rheological and failure properties (Fraass–BBR)
Resistance to fatigue cracking	Fatigue property
Explosion elimination	Flammability/flash point
Rutting resistance	Rheological property at high/elevated service temperature
Structural strength/bearing capacity	Complex modulus
Resistance to segregation	Shear viscosity after short-term aging
Asphalt stiffness	Stiffness
Production phase	Storage stability (of modified binders)
Resistance to stripping	Tackiness/stickiness
Structural strength	Tensile test
Resistance to reflective cracking	Toughness
Rutting resistance	Viscosity versus temperature
Recuperation of crack initiation	Viscous flow/binder viscosity
Explosion elimination	Volatility/loss of mass

Adapted from CEN/TC 336 WG1 TG 5.

the development, operation, and maintenance of an integrated national transportation system.

AASHTO serves as a liaison between state departments of transportation and the federal government and, alongside ASTM International, is involved in establishing technical standards for all phases of highway system development. Standards are issued for design, construction of highways and bridges, materials, and numerous other technical areas.[4]

Throughout the remainder of this chapter, references are provided, where appropriate, for test methods and specifications from CEN, ASTM International, and AASHTO.

[4] From http://www.transportation.org/Pages/Organization.aspx, Copyright 2014, by the American Association of State Highway and Transportation Officials, Washington, DC. Used by permission.

www.EngineeringEBooksPdf.com

1.4.2.1 The Strategic Highway Research Program and Superpave

The current specification for bituminous binders in the United States (US), Superpave, was the result of a major research program funded by the Federal Highway Administration (FHWA), known as the Strategic Highway Research Program (SHRP).

SHRP was a $150 million project funded by the US Congress to improve the highway infrastructure of the United States. The bituminous binder part of the project amounted to some $50 million. SHRP led to the development of numerous new test methods and culminated in the development of a novel type of binder specification known today as Superpave (AASHTO M320, ASTM D6373), the name of which derives from SUperior PERforming asphalt PAVEments (Kennedy et al., 1994). The Superpave specification differs from most other types of specifications in that the grade of binder to be selected for a given application is determined directly from a combination of the climatic conditions prevailing in a given area and the anticipated traffic levels.

A key part of the research was to determine the climatic conditions under which the binder would need to perform; therefore, temperature maps for the entire US geographical area were developed. Weather data for some 6000 weather stations across the United States were reviewed for a period of approximately 20 years, following which the highest sustained temperature (hottest 7-day period) was identified for each station. However, the climate data evaluated were air temperatures and not pavement temperatures; therefore, a correction was required to convert the air temperature to a pavement temperature. Furthermore, permanent deformation resulting from extended periods of hot weather is the result of a softening of the surface layer, and therefore a conversion was required to estimate the temperature of the pavement at a depth of 20 mm. This was conducted with corrections for heat flow, with energy balance assuming typical values for solar absorption. More detail on the modeling carried out can be found in report SHRP-A-410 (Kennedy et al., 1994). Following the modeling, this criterion became the high temperature limit for use in the specification.

The low service-temperature criterion was selected to be the lowest single temperature experienced at the pavement surface. Once again, this temperature was derived using a model that included parameters for air temperature, latitude, and the standard deviation of the mean low air temperature.

The Superpave binder specification (ASTM D6373, AASHTO M320) differs from most specifications insofar as it does not differentiate between different types of binders, such as modified or unmodified. Instead, it provides an elevated service temperature and a low service temperature "performance grade." Users of the specification must select the appropriate temperature range required for the region in which the binder is to be used, and this is the basis for selection of the performance grade of the binder. The performance grade can be increased if the anticipated traffic level is particularly high, using a technique known as "grade bumping."

The Superpave binder specification does not discriminate between modified and unmodified binders; instead, binders are selected on the upper and lower performance-grade requirement. The specification is based on stiffness of the aged binder for a specific combination of traffic loading and environmental conditions. Thus, binder grades are specified primarily with respect to pavement temperatures, allowing a binder to be selected for a specified design combination of high and low temperatures. The

www.EngineeringEBooksPdf.com

loading condition related to elevated service-temperature performance is modeled to represent a vehicle speed of 100 km/h and a traffic volume of less than 10^7 equivalent single-axle loads (ESALs).

The average 7-day maximum pavement-design temperature is the average of the highest daily pavement temperatures for the 7 hottest consecutive days in a year. The lowest annual pavement temperature is the single coldest temperature of the year.

The binder specification (ASTM D6373,[5] AASHTO M320[6]) uses the designation

$$\text{PG}\, x - y$$

where PG, performance graded; x, high pavement-design temperature; and y, low pavement-design temperature.

Details on the test methods used to determine the PG grading are provided later in this chapter.

1.4.3 Bitumen Test Method Validation

In order to take a systematic approach to the development of new binder specifications in Europe, the bitumen and asphalt industry made major efforts to define the "performance-related" (P-R) requirements for paving binders. It is recognized that binder properties alone do not determine pavement or even mixture performance; other parameters, such as aggregate characteristics, mixture design, manufacture, and laying, are also considered important. A process was followed to ensure that, for the next generation of standards, the performance relationships of a binder property are assessed before a specification is developed. The Bitumen Test Validation (BiTVal) project was developed to assist that process.

In 2004, the management of the FEHRL agreed that the first phase of the project should proceed. Many FEHRL members from around Europe, who had to arrange their own financing for the project, agreed to participate in phase 1, a literature study analyzing information gathered from all sources. Additional work needed was to be identified during this process. The BiTVal project was expected to:

- Deliver the appropriate answers for assessing the suitability of test methods for characterizing the relevant performance of related bitumen properties.
- Establish their relevance and correlation to the asphalt pavement performance.
- Give the required level of confidence in the future European specification system.

The key outputs of phase 1 of the BiTVal project were a database covering publications of the identified bitumen properties and their relationship to asphalt properties and/or road performance, and a FEHRL report (FEHRL, 2006) to CEN TC 336 WG1 summarizing the performance-related aspects for each test method, together with recommendations for their use in the next generation of standards.

Problems with funding meant that BiTVal phases 2 and 3 were never conducted.

[5] ASTM D6373 Standard Specification for Performance-Graded Asphalt Binder.

[6] AASHTO M320 Standard Specification for Performance-Graded Asphalt Binder.

www.EngineeringEBooksPdf.com

1.5 Test methods for use in binder specifications

Test methods are used to measure a specified property of binders. New test methods are continually under development, but binder specifications are often based on and evolve from historic, empirical test methods that have a track record of proven performance. However, empirically based specifications may not provide an accurate reflection of performance for new or rheologically different classes of binders. For this reason, it is necessary to review specifications from time to time and consider whether the existing test methods employed in the specifications are still applicable.

Many paving bitumen specifications are predominantly focused on the measurement of mechanical properties at elevated, intermediate, and low service temperature. The vast majority of bitumen that is manufactured is unmodified binder for asphalt paving applications. As such, this chapter will cover mainly those aspects of specifications relevant to asphalt mixture performance. A good specification should address the predominant failure modes of asphalt pavements. As previously mentioned, specifications typically measure binder properties relating to predominant failure modes in service; these are generally high temperature properties and low temperature properties. The properties of the binder at "normal," or intermediate, service conditions are also measured.

1.5.1 Elevated service-temperature test methods

Permanent deformation (rutting) is a phenomenon that results from nonrecoverable deformation of the pavement. This is related to pavement stiffness, and also to the rheological (flow) properties of the binder. Because bituminous binders become softer with increasing temperature, the tendency to permanent deformation also increases with increasing temperature. For this reason, the measurement of properties relating to rutting are typically conducted at elevated temperature. Most product specifications assess the tendency for permanent deformation using an elevated service temperature property. As the name suggests, permanent deformation is a nonrecoverable, dissipative phenomenon, and relates to viscous or plastic flow within the binder.

Examples of commonly used test methods for determination of permanent deformation include the following.

1.5.1.1 Ring-and-ball softening point (EN 1427, ASTM D36, AASHTO T53)

The ring-and-ball softening point (SPt) test is a widely used method for the determination of the SPt of bitumen and bituminous binders, in the range of 30–150 °C. Two horizontal disks of bituminous binder, cast in brass rings, are heated at a controlled rate (5 °C/min) in a liquid bath while each supports a steel ball. The SPt is reported as the mean of the temperatures at which the two discs soften enough to allow each ball, enveloped in bituminous binder, to fall a distance of 25 mm. There is a significant difference between the European and US test methods, in that the former method uses a stirrer in the water bath, whereas the latter does not. This is reported to lead to a

www.EngineeringEBooksPdf.com

systematic difference between the results of the two methods: the ASTM International method is believed to produce results that can be 1.5 °C higher than the EN apparatus, although it is not known if this difference applies to polymer-modified binders.

Heukelom (1969) reported that for most (unmodified) bitumens, the SPt equated to a needle penetration of approximately 800×0.1 mm^2.

SPt is used in many specifications to provide information about the elevated temperature performance of binders. However, the relevance of the SPt to indicate the behavior of polymer-modified binders is questionable, and therefore, alternative test methods for this property have been sought.

1.5.1.2 Dynamic viscosity using a capillary tube (EN 12596, ASTM D 2171, AS 2341.2)

A number of national specifications use dynamic viscosity as the elevated service-temperature parameter. The determination of dynamic viscosity by vacuum capillary of bituminous binders at 60 °C, in the range from 0.0036 to 580,000 Pa s, is usually used to determine viscosity of unmodified bitumen at 60 °C.

There is evidence that permanent deformation relates to some type of viscosity, as both processes are dissipative. However, although some relationships have been identified for unmodified bitumens (Prowell, 2001), no formal correlations are available due to a lack of data. However, the BiTVal final report noted that the dynamic viscosity at 60 °C measured with the capillary viscometer test to the Australian standard AS 2341.02[7] was correlated with other binder properties for multigrade binders (Alexander et al., 2000). A good correlation is reported with $G^*/\sin\delta$ at a frequency of 10 rad/s and 60 °C before and after rolling thin-film oven (RTFO)-aging. The correlation of dynamic viscosity with the ring-and-ball SPt was good after RTFO-aging, but not before.

No relationships have been demonstrated for polymer-modified bitumens using dynamic viscosity measured with a Brookfield viscometer (Khattak and Baladi, 2001).

1.5.1.3 G*/sin δ (inverse of the loss compliance) (ASTM D7175, AASHTO T315)

This rheological parameter was developed as a product of SHRP and is included in the Superpave binder specification as the elevated service-temperature property.[8] The property is measured using a DSR operated in oscillatory mode under specified temperature and frequency conditions. The value is derived as a function of the complex shear modulus (G^*) divided by the sine of the phase lag (phase angle), δ. Increased values of this parameter lead to a reduced tendency to permanent deformation.

[7] Standards Australia Limited. Methods of testing bitumen and related road making products, Part 2: Determination of dynamic (coefficient of shear) viscosity by flow through a capillary tube. AS 2341.02. Standards Australia Limited, Sydney.

[8] AASHTO T315-09, Standard method of test for determining the rheological properties of asphalt binder using a dynamic shear rheometer (DSR).

www.EngineeringEBooksPdf.com

The measured property is related to the viscous component of the binder, as measured by the sine of the phase lag, but also takes into account the binder stiffness by including the complex shear modulus.

$G^*/\sin\delta$ has been shown to correlate well with the tendency for permanent deformation in unmodified bitumens. However, for binders that contain significant amounts of polymers and some other modified binders, this parameter works less well (Carswell and Green, 2000; Chabert et al., 1999; Claxton et al., 1996; Proteau and Yvan, 2001). This is believed to be because modified binders exhibit nonlinear rheological behavior; in other words, an increase in the applied stress is not reflected by the resultant strain in a proportional manner.

For this reason, the Superpave binder expert task group (ETG) sought to identify an alternative property for the measurement of elevated service-temperature properties. The multiple stress creep recovery test (MSCRT) is proposed as a replacement for $G^*/\sin\delta$ in the Superpave specification.

1.5.1.4 Multiple stress creep recovery test (prEN 16659, ASTM D7405, AASHTO TP70)

The MSCRT is tested using a DSR in creep mode at a specified temperature. The measurement involves applying a consecutive series of static loads, followed by a period of recovery to a binder sample; the test method measures the nonrecoverable creep compliance. Stress sensitivity of the binder is measured by applying different stress levels: the test starts with the application of a low stress (0.1 kPa) for 10 creep/recovery cycles, and then the stress in increased to 3.2 kPa and repeated for an additional 10 cycles. The result of the test provides the percentage of recoverable and nonrecoverable creep compliance of bitumen and bituminous binders. The nonrecoverable creep compliance at multiple stress levels is intended as an indicator for the sensitivity to permanent deformation and stress dependence of bituminous binders. The stress application and typical resultant strain are shown in Figure 1.2.

The result of the testing is calculated using the relationship shown in Figure 1.3.

Unmodified binders do not exhibit significant stress/strain sensitivity under moderate conditions of stress/strain, nor do they exhibit significant recovery under creep conditions; therefore, MSCRT testing is not required for the testing of unmodified binders. However, it does show promise as a performance indicator for modified binders, and is being implemented into the Superpave binder specification and is likely to be used in European binder standards for polymer-modified binders.

1.5.1.5 Other test methods

A number of other tests have been considered as indicators for permanent deformation, but have not been implemented in specifications for various reasons, including practicality, or because they did not predict behavior better than existing tests. These include zero shear viscosity (CEN TS 15325) (Phillips and Robertus, 1996), low shear viscosity (CEN TS 15324), and coaxial cylinder viscosity test (EN 13702-2).[9] At the

[9] Bitumen and bituminous binders—determination of dynamic viscosity of modified bitumen—part 2: Coaxial cylinders method. EN 13702-2: 2003.

www.EngineeringEBooksPdf.com

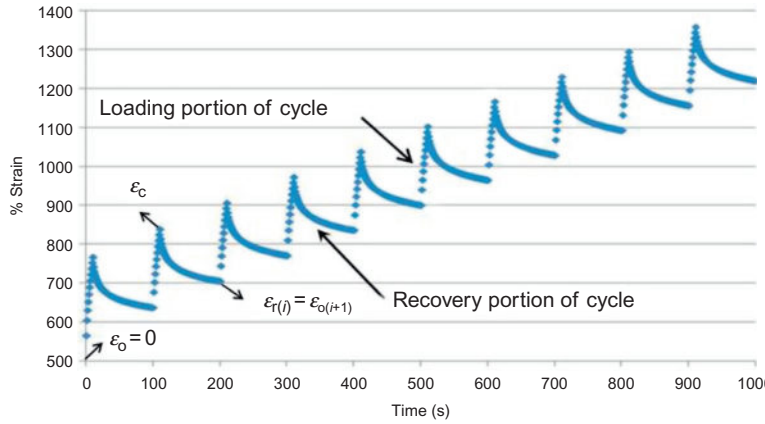


Figure 1.2 Typical creep–recovery curve after 10 consecutive cycles (Federal Highways Administration, 2011).

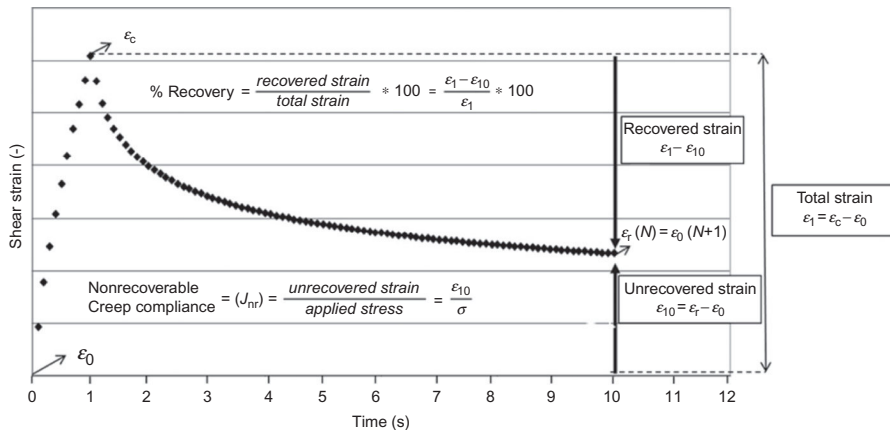


Figure 1.3 Typical creep and recovery cycle.

time of writing, these tests are not being implemented into binder specifications due to the tests not correlating well for all types of binders, or being impractical because of the time taken to conduct the tests.

1.5.2 Low service-temperature properties

Bituminous binders become stiffer as the temperature is reduced. While this would lead to higher mixture stiffness, which would ordinarily be a positive factor in respect to load-bearing capacity, the ability of the binder to dissipate stress diminishes as the temperature reaches the glass transition temperature. Low temperature properties are therefore associated with a cracking tendency. Bituminous binders also become stiffer as they react with atmospheric oxygen, and therefore, tests to measure low

www.EngineeringEBooksPdf.com

service-temperature properties are often conducted on binders that have been subjected to an aging or conditioning procedure.

Examples of binder tests used in specifications for low temperature cracking include the following.

1.5.2.1 Fraass breaking point (EN 12593)

The Fraass breaking point is used as the low service-temperature property in European specifications. It is tested on fresh binders, as there is no long-term aging (LTA)/conditioning step in the specifications at the time of writing. A sample of bituminous binder is applied to a metal plate at an even thickness. This plate is submitted to a constant cooling rate and flexed repeatedly until the binder layer breaks; the temperature at which the first crack appears is reported as the Fraass breaking point.

1.5.2.2 The bending beam rheometer test (Bahia et al., 1991) (EN 14771, ASTM D6816, AASHTO T313)

The bending beam rheometer (BBR) test applies a static stress to a beam of bitumen and measures the strain rate to derive the stiffness of the beam. The BBR test is conducted on binder that has been subjected to both short-term aging (STA) and LTA/conditioning. The test criterion is generally taken as the temperature at which the stiffness of the binder is 300 MPa. The BBR test is used in the Superpave specification as the low service-temperature criterion. An additional test criterion is the "m-value": this value is the tangent of the creep curve at 60 s load time, and was selected to provide an indication of the ability of a binder to dissipate stresses or relax. Although the BBR test does not involve failure of the binder, the properties measured have been correlated with asphalt failure tests, such as the thermal stress restrained specimen test (TSRST) (Hesp et al., 2000; Lecomte et al., 2000; Lu et al., 2003).

1.5.2.3 Fracture toughness (CEN TS 15963)

The fracture toughness test for bituminous binders is currently under evaluation in Europe as a candidate low service-temperature test, but has not yet been developed into a harmonized standard (Chailleux et al., 2012). It is based upon ASTM E399 (standard test method for linear-elastic plane-strain fracture toughness (KIC) of metallic materials) and ISO 13586 (plastics—determination of fracture toughness (GIC and KIC)—linear-elastic fracture mechanics (LEFM) approach).

In the test, a three-point monotonic bending stress is applied to a notched beam of binder at low temperature until the beam fractures. The binder fracture toughness (KIC) and fracture energy (GIC) are measured.

1.5.3 Fatigue testing

Fatigue of asphalt mixtures is an important failure mechanism in the later life of the pavement. Fatigue is the term given to the reduction of stiffness of the asphalt mixture following repeated loading by traffic. Fatigue of mixtures is believed to be due to the

www.EngineeringEBooksPdf.com

formation of microcracks in the binder or mortar of the mixture. This is supported by the fact that rest periods during fatigue testing appear to improve the fatigue life of mixtures, which is believed to be due to the healing of the microcracks. Therefore, it is unsurprising that testing of the binder alone is found to be unreliable (Boussad and Dony, 1996; Paez et al., 1999).

Typically, fatigue cracking is associated with aged binder, and therefore, testing for this property is generally conducted on binder or mixtures that have been subjected to an aging or conditioning procedure.

There are not very many standardized test methods for determination of the fatigue properties of bituminous binders, and the methods available are not universally agreed to measure this property accurately. Nevertheless, the following methods have been developed, some of which are in use in specifications today, while others are proposed as candidate test methods.

1.5.3.1 The loss modulus; G*/sin δ (ASTM D7175, AASHTO T315)

The loss modulus forms part of the Superpave binder specification and is based on the concept that part of the dissipated energy is spent in generating microscopic damage (cracks) that eventually leads to fatigue (Bahia et al., 2001). In Superpave, the fatigue parameter is tested on pressure aging vessel (PAV)-aged binder at a relatively low temperature, and a maximum value (5000 kPa) is set as the failure criterion.

1.5.3.2 RILEM binder fatigue method

The International Union of Laboratories and Experts in Construction Materials, Systems and Structures (RILEM)[10] is evaluating two possible methods for examining binder fatigue, using the DSR and a tension/compression tester.

In the DSR method, a sinusoidal stress is applied to a binder sample and the change in the complex shear modulus (G^*) is measured. After a period of time, the complex shear modulus starts to drop, and ultimately, if stress continues to be applied, the sample fractures. The test method is undergoing evaluation at the time of writing, but initial conclusions from round-robin testing suggest that although the test ranks binders in a similar way to fatigue tests carried out on asphalt mixtures, the test is difficult to perform, and the gain in testing time against mixture testing is limited. Furthermore, the deformation in the sample is different from that experienced by the binders in a mixture, and a suitable failure criterion has yet to be established for this test method.

The second method under evaluation exposes a ligament of binder to tensile and compressive strain in a controlled strain mode. Complex shear modulus and phase angle are measured during the test, and the test concludes when the binder sample fractures. The test appears to rank binders in a similar fashion to asphalt mixture testing in controlled strain fatigue tests, but at present, the results only demonstrate a trend, and results are not sufficiently strong to provide a correlation to mixture testing.

[10] www.rilem.org.

www.EngineeringEBooksPdf.com

This is likely due to the complexity of trying to predict such a complex phenomenon using only one component of a mixture.

1.5.3.3 The linear amplitude sweep test (AASHTO TP101)

The linear amplitude sweep test (LAST) uses a DSR to assess the fatigue behavior of bituminous binders by the application of systematically increasing load amplitudes under cyclic loading. The binder is subjected to a frequency sweep to determine a damage analysis parameter (α). A second test is then conducted in oscillatory shear, in strain-controlled mode, at a frequency of 10 Hz. Strain is increased linearly from 0.1% to 30% over the course of 3100 cycles of loading, for a total test time of 310 s. Peak shear strain and peak shear stress are recorded every 10 load cycles (1 s), along with phase angle [$|G^*|$, degrees] and complex shear modulus [$|G^*|$, Pa].

The fatigue behavior is calculated using a viscoelastic continuum damage (VECD) model.

At the time of writing, the LAST is not currently used in specifications, but is undergoing robustness testing to identify the precision of the test method.

1.5.4 Intermediate service temperature

Testing of binders at intermediate temperatures is used to provide information useful to mixture and pavement designers on the properties of the binder at average service conditions.

1.5.4.1 Needle penetration (EN 1426, ASTM D5, AASHTO T049)

The penetration value of a binder is determined as the depth, in 1/10ths of a millimeter, to which a standard needle penetrates in a given time. The test conditions generally used for determination of this value are 100 g, 5 s, and 25 °C.

Needle penetration has been used for decades to determine the stiffness of bituminous binders at intermediate temperature. For unmodified bitumens, the penetration test correlates well with the stiffness of the bitumen measured, using the DSR, at the same temperature (25 °C) and at a frequency of 0.4 Hz. In rheological terms, a good correlation has been identified between the logarithm of the complex shear modulus (G^*) and the logarithm of the penetration value (Gershkoff, 1995).

1.5.4.2 Complex shear modulus (G*) (EN 14770, ASTM D7175, AASHTO T315)

The European standard for the DSR test describes a procedure for the determination of the complex shear modulus and phase angle using a DSR. The test is performed in oscillatory shear, in stress or in strain-controlled mode, over a range of temperatures and frequencies. The rheometer is fitted with parallel plates, with a constant gap. Temperature control encompasses both plates. Parallel plates with a diameter between 8 and 25 mm and gap settings from 0.5 to 2.0 mm are recommended.

www.EngineeringEBooksPdf.com

1.5.5 Temperature sensitivity

Although current specifications generally test the performance of the binder at elevated, intermediate, and low service temperatures, some specification systems evaluate the change in properties with temperature.

1.5.5.1 Penetration index (Pen/Pen, Pen/SPt)

The penetration index (PI) (Pfeiffer and van Doormaal, 1936) is a measure of the temperature susceptibility of a bitumen that can be derived mathematically, either from the penetration values at two temperatures or from the standard penetration and SPt values, as given in the following equations.

$$PI = \frac{\log(pen@T_1) - \log(pen@T_2)}{T_1 - T_2}$$

$$PI = \frac{1950 - 500\log(pen) - 20SP}{50\log(pen) - SP - 120}$$

In the above example, the SPt is based on ASTM D36, which is an unstirred method. It is generally accepted that the European test method (EN 1427) provides results approximately 1.5 °C lower than the ASTM International method.

The values of PI for unmodified bitumens range from around −3 for highly temperature-susceptible bitumens to around +7 for highly oxidized bitumens with low temperature susceptibility. For paving-grade bitumens used for highways, the typical range is −1.5 to +1.0. Due to the different rheological nature of polymer-modified bitumens, the PI is meaningless for such binders.

1.5.6 Binder aging and conditioning regimes

Bitumen properties change over the lifetime of the pavement due to the combined action of heat during the manufacturing process, evaporation of volatile components within the bitumen, and reactions with atmospheric oxygen. The effect of these factors is that the physical properties of the bitumen change, generally leading to a hardening of the product. At a certain moment, the properties will change to the point where the pavement is unable to accommodate the stresses placed upon it, and a failure will occur. This phenomenon of hardening over time is known as aging. Aging of the binder in the pavement is a slow process, and there is a need for a laboratory aging and conditioning procedure. Several methods have been developed to simulate the aging process and provide a sample of aged binder that can be tested within a reasonable time period.

The reaction kinetics and thermodynamics of bitumen aging are complex and change with temperature (Claine Petersen, 2009; Choquet and Verhasselt, 1993); therefore, any conditioning procedures used should ideally provide a reasonable approximation to the type and degree of aging that can be expected in the field (Pfeiffer and van Doormaal, 1936; van Gooswilligen et al., 1985).

www.EngineeringEBooksPdf.com

Asphalt mixtures are generally produced at high temperatures, typically in the region of 150 °C (NAPA & EAPA, 2011). During the mixing, handling, and application stage of the asphalt mixture, a degree of aging occurs; therefore, the properties of the binder will change from the fresh condition to the point where the asphalt is placed into the pavement. Various aging and conditioning regimes are standardized for use in specifications, and are intended to be used to simulate STA and LTA, respectively. A review of the aging/conditioning methods used in Europe was conducted recently as part of the CEN TC 336 activity (Besamusca et al., 2012a).

1.5.6.1 *The rolling thin-film oven test (EN 12607-1, ASTM D 2872, AASHTO T240)*

The rolling thin-film oven test (RTFOT) is one of the most commonly used standardized tests to simulate the STA of binders. This test is used to measure the combined effects of heat and air on a thin film of bitumen or bituminous binder in permanent renewal. It aims to simulate the hardening that a bituminous binder undergoes during the mixing, transporting, and compacting processes, referred to as STA.

A moving film of bituminous binder is heated in an oven to a specified temperature, for a given period of time, with a constant supply of air.

The effects of heat and air are determined on the basis of the change in mass (expressed as a percentage) or the change in the bituminous binder's characteristics before and after the period in the oven.

The RTFOT is used as the conditioning regime in many binder specifications to provide a sample of binder representing the "as laid" properties. The standardized test conditions differ in different standards, but are typically 163 °C (325 °F) for 75 min (EN 12607-1) or 85 min (ASTM D2872, AASHTO T240). During the test, the binder sample may lose material due to evaporation of the lighter components, and may gain weight due to reaction with atmospheric oxygen; therefore, the test method reports a change in mass of the sample, rather than a gain or loss of mass. In some cases, particularly where highly polymer-modified bitumens are used, problems have been reported where the binder "climbs" out of the glass bottles used in the test. Moreover, different grades of bitumen have different viscosities at a given temperature and, because the RTFOT is conducted at a constant temperature, the film thickness of the bitumen in the flask will differ for different bitumens. This has led to the development of modified versions of the test, including the modified RTFOT (M-RTFOT).

The test is identical to the standard RTFOT, except that a set of steel rods is positioned inside the glass bottles during oven aging. The principle is that the steel rods create shearing forces to spread the binder into thin films, thereby overcoming the problem of aging high-viscosity binders. Initial trials of the M-RTFOT indicate that the rods do not have any significant effect on the aging of conventional penetration-grade bitumens. However, research work (Airey, 2002) has indicated that using the metal rods in the M-RTFOT does not always solve the problem of rollout of modified binder, and further validation work is required before the technique can be used in binder specifications.

www.EngineeringEBooksPdf.com

With the increasing use of warm mix asphalt, where the asphalt is manufactured at a lower temperature than usual, the relevance of RTFOT conducted at 163 °C has been questioned. Further research is needed to ascertain whether the degree of aging is accurately represented for such materials by the current standardized test conditions.

1.5.6.2 Thin-film oven test (EN 12607-2, ASTM D1754, AASHTO T179)

Another test to simulate the STA of binders is the TFOT. In the TFOT, a 50-ml sample of bitumen is placed in a flat 140 mm diameter container, resulting in a film thickness of 3.2 mm. Two or more of these containers are then positioned on a shelf, rotating at 5–6 rpm in an oven for 5 h at 163 °C. The TFOT was adopted by AASHTO in 1959 and by ASTM in 1969 (ASTM D1754) as a means of evaluating the hardening of bitumen during plant mixing. However, a potential problem with the TFOT is that the thick binder film results in relatively small surface-area-to-volume ratio of the binder. There is a concern that aging (primarily volatile loss) may be limited because the bitumen is not agitated or rotated during the test. Furthermore, some binders, particularly polymer-modified binders, can separate during the test, leading to problems with sample homogeneity during testing of the aged material.

1.5.6.3 Rotating cylinder aging test (EN 15323)

Rotating cylinder aging test (RCAT) is a device for aging/conditioning bituminous binders (Verhasselt, 2002). Simulation of STA and/or LTA of paving-grade or modified bitumen or of mastics (binder + filler) can be performed using the same piece of equipment.

The RCAT comprises a closed testing cylinder with a central opening that allows sampling of small portions at predetermined exposure times. During the conditioning, the opening is fitted with a Teflon plug, through which a stainless steel tube feeds the cylinder with a constant flow of oxygen (LTA) or air (STA). For temperature calibration purposes, a thermocouple can be fixed onto the tube. During the conditioning, the testing cylinder rotates at 1 revs/min (LTA) or 5 revs/min (STA) on two round drive bars in a ventilated oven. A grooved solid stainless steel roller is also introduced inside the rotating cylinder to distribute the binder in the cylinder into an even film against the inner wall of the cylinder. The conditioning procedure uses air at a temperature of 163 °C for 235 min; the LTA procedure uses oxygen at a temperature of 90 °C for 140 h. The STA procedure gives results that are comparable with the RTFOT.

Although the RCAT is not currently used in specifications, the unique aspect of this equipment is that both STA and LTA conditioning can be conducted in the same piece of equipment. Furthermore, the single stainless steel drum enables relatively large quantities of binder (525–550 g) to be prepared, which minimizes losses when transferring the conditioned binder into the test equipment. Safety concerns have been expressed over the use of pure oxygen in the LTA procedure, leading to the possibility of fire, but no incidents have been reported.

www.EngineeringEBooksPdf.com

1.5.6.4 The pressure aging vessel (EN 14769, ASTM D6521, AASHTO R28)

The PAV was developed as part of the SHRP project to simulate long-term, in-service oxidative aging of bitumen in the field. The procedure is carried out using bitumen that has already been subjected to STA, either by RTFOT or TFOT, followed by oxidation of the residue in a pressurized aging vessel. In the Superpave specification, the PAV procedure entails aging bitumen in 140 mm diameter steel trays (such as those used in the TFOT) within a heated vessel, pressurized with air to 2.07 MPa for 20 h at temperatures between 90 and 110 °C. The PAV has space for 10 trays, each holding 50 g of binder; therefore, the method can prepare relatively large quantities of binder. Other conditions have been used, such as reducing the temperature to 85 °C for 65 h in the United Kingdom, where the test is known as PAV85 or the high-pressure aging test (HiPAT) (Energy Institute, 2003).

The PAV is widely used to prepare binders for testing in the LTA state. However, there have been a number of criticisms about the method on the basis that the aging mechanism of the binder might not be fully representative of that which occurs in practice, due to the high pressures used during the procedure, which preclude any evaporative aging; the static nature of the procedure, which may permit separation of some polymer-modified binders; and the high temperature at which the aging is conducted, which might change the chemistry of the oxidation processes in comparison with aging at a lower temperature.

Comparisons between PAV aging and RCAT aging were conducted (Airey, 2002), and suggested that the results are broadly comparable. However, the results were dependent upon the duration and temperature of the conditioning.

1.5.7 Adhesion testing

It is generally accepted that adhesion is the property that characterizes the bond between two materials. In the case of asphalt mixtures, this is considered to be the interaction of the binder and the aggregate material and filler.

It is obvious that adhesion between the components of an asphalt mixture is important. However, the measurement of this property is difficult in practice. Most tests are directed toward measuring a lack of adhesion, or stripping, because adhesive failure is directly related to pavement distress or *in situ* damage (e.g., raveling). In the context of asphalt mixtures, one of the more important aspects of adhesion is the presence of water. Therefore, the susceptibility to moisture or the resistance toward debonding is considered a good indirect indicator of the power of a binder to adhere to aggregates. In this context, it is frequently referred to as a stripping phenomenon. This idea has already been taken up in standards EN 12697-11[11] and EN 13697-12,[12] which deal with the

[11] EN 12697-11; Bituminous mixtures. Test methods for hot mix asphalt—part 11. Determination of the affinity between aggregate and bitumen.

[12] EN 12697-12; Bituminous mixtures. Test methods for hot mix asphalt. Determination of the water sensitivity of bituminous specimens.

www.EngineeringEBooksPdf.com

assessment of the adhesion within asphalt mixtures. Rather than a direct measurement of a property, most test methods addressing adhesion report a ratio of a given mechanical property, for example mixture stiffness, before and after immersion in water.

Asphalt mixtures are composite mixtures, containing aggregates (which are themselves heterogeneous), sand, filler, and perhaps also modifiers. As such, adhesion within an asphalt mixture is extremely complex, and interpretation of results is made difficult by this complexity. In mixture tests, there is the added complication of trying to separate the adhesive contribution from the cohesive, that is, bitumen–bitumen, bond strength. However, because adhesion is an interfacial property, test procedures generally consider both the binder and the aggregate.

Many different test methods have been developed purporting to measure adhesion, but in a study conducted by members of CEN TC 227 WG1 and CEN TC 336 WG1 (Besamusca et al., 2012b), a series of six binders was tested, using nine readily available test methods purporting to measure adhesion. The study concluded that there was no easy-to-use test method available that could characterize the adhesion or stickiness of bitumen, and it was unlikely that one would emerge in the near future. The candidate tests evaluated did not measure binder adhesion, but in some cases measured moisture sensitivity of mixtures or temperature dependence.

Many of the tests purporting to measure adhesion in fact assess the kinetic aspects of disbonding, that is, how quickly the binder might strip from the aggregate surface, rather than the fundamental adhesion of the components. While this property is informative for identifying the mixture moisture sensitivity and when it may fail, it is important to understand that it is different from adhesion of bitumen to aggregate. At this time, tests that do measure properties related to adhesion, such as surface energy, are not suitable for inclusion in a specification, as they are either too complex and time consuming or require expensive and sensitive test equipment.

A number of tests have been standardized that are capable of measuring moisture sensitivity of binder/aggregate combinations, or mixtures. Some of these are listed below:

- Rolling bottle test and boiling-water stripping method; EN 12697-11, bituminous mixtures. Test methods for hot mix asphalt. Determination of the affinity between aggregate and bitumen.
- Boiling-water stripping test; ASTM D3625, standard practice for effect of water on bituminous coated aggregate using boiling water.
- Indirect tensile stiffness on saturated specimens; EN 12697-12, bituminous mixtures. Test methods for hot mix asphalt. Determination of the water sensitivity of bituminous specimens.
- Immersion–compression test; ASTM D1075, AASHTO T165, standard test method for effect of water on compressive strength of compacted bituminous mixtures.
- AASHTO T283, standard method of test for resistance of compacted asphalt mixtures to moisture-induced damage.

1.6 Precision of test methods

Specifications are used as the basis for many commercial transactions; it is therefore important to understand the reliability of a given test result. If different operators or

www.EngineeringEBooksPdf.com

different laboratories are testing the same product, it is clearly desirable that they achieve the same test results. The first step in ensuring that this occurs is to ensure that test methods are standardized and that operators have been trained in conducting the tests. Harmonized test methods generally contain a section on the precision that can be expected when conducting the test in accordance with the standard. This is generally given as a statement of repeatability and reproducibility. The precision of a measurement system, related to repeatability and reproducibility, is the degree to which repeated measurements under unchanged conditions show the same results.[13] The repeatability of a test method is defined as the single operator precision, or the closeness of results that is obtained when one individual tests the same product under the same conditions. It is referred to in EN standards as "r." The reproducibility of a given test method is the degree of agreement between measurements or observations conducted on replicate specimens in different locations by different people, or multi-operator precision, referred to in EN test methods as "R." In general, the reproducibility is a larger value than the repeatability because of the increased variables associated with different operators using different equipment. The precision of a given test method is generally determined by round-robin testing of binders.

Due to the potential for multiple operators to obtain different results, specifications should take into account the precision of a given test method when setting the limits for grade boundaries. According to EN ISO 4259,[14] the value chosen for a specification limit shall take into account the reproducibility of the test method adopted, as follows:

– For a double limit (A1 and A2), the specified range shall be not less than four times the reproducibility R, that is, $(A1–A2) \geq 4R$.

1.7 Future specifications: fundamental or empirical binder testing?

Roads are engineering structures, and therefore the components of asphalt mixtures used in roads and the pavement itself should be specified using engineering units and principles. There is an inevitability that future specifications will use test methods that provide results in engineering units. However, empirical specifications have been developed over many decades to provide some road materials with a track record of proven performance for unmodified binders. Empirical specifications still work well for conventional, unmodified binders, and the relationship between properties and performance is well understood, having been built up over a long period of time. However, such specifications have limitations when used for binders that have been modified or have different rheological performance to conventional materials. Therefore, specifications that are designed to be "blind" to the binder type should measure properties that are directly related to their performance.

[13] Joint Committee for Guides in Metrology 200:2008, International vocabulary of metrology—basic and general concepts and associated terms (VIM), Bureau International des Poids et Mesures, www.bipm.org.

[14] EN ISO 4259:2006 Petroleum products. Determination and application of precision data in relation to methods of test.

www.EngineeringEBooksPdf.com

1.7.1 Performance-related specifications

Defining relationships between binder properties and field pavement performance is technically challenging and, with our current understanding, cannot be conclusively established. However, certain properties of bituminous binders are known to be related to mixture properties, and therefore, test methods that relate to those properties can be considered as candidates for inclusion in a performance-related specification.

The aim of performance-based standards is to measure/predict/declare the performance of the binder, how the properties will change over time, and how the binder properties will influence the performance of the asphalt mixture. A performance-related bitumen standard does not guarantee the functional performance of the asphalt mixture or the final pavement, as there are numerous other factors that can influence performance. A performance test or a series of performance tests on bitumen, each relating to a specific functional property, is needed to predict the important characteristics according to the essential requirements outlined in the specification.

A major problem that has held back the development of truly functional specifications is the complexity of behavior for bituminous binders. Because the properties are both time and temperature dependent, the ability of a test method to adequately determine the behavior at a different loading time/temperature, or over a range of loading times/temperatures, is limited.

The main criterion for developing future specifications should be to maintain the confidence of all parties (i.e., binder producers, asphalt producers, road users, and authorities) to permit the specification of bituminous materials that are suitable to construct a high standard of road pavements.

1.7.2 Purchase specifications

Performance-related test methods and aging procedures may not necessarily be suitable or practical to ensure the constancy of binder properties produced or supplied on a day-to-day basis. Some of the more complex testing required for performance-related specifications might be too time consuming to conduct on a daily basis. For example, aging procedures for simulation of LTA might take several days to complete, which is impractical for routine production. Therefore, purchase or supply specifications might be based upon simpler surrogate tests designed to demonstrate consistency of production.

1.7.3 The CEN data collection program

In 2006, CEN published TR15352,[15] which reported on the work carried out to develop the next generation of performance-related standards. The report recommended that data be collected on a range of "new" test methods to measure binder properties relevant to asphalt mixture properties. Data comparing properties measured using traditional and new rheologically based test methods have been collected, and the outcome of that

[15] CEN TR 15352: Bitumen and bituminous binders—development of performance-related specifications: status report, 2005.

www.EngineeringEBooksPdf.com

process has been reviewed. Eurobitume, the European bitumen association, collated and analyzed 146 data sets, the results of which were published in 2009.[16]

At the time of writing, paving-grade bitumens are specified in Europe using empirical test methods, such as penetration and ring-and-ball SPt. The binder characteristics in the paving bitumen specification relate to the performance of these binders in asphalt mixtures, and the relationship between each property measured and asphalt performance is well understood, having been developed over many years. The CEN data collection database has been shown to provide good correlations between the empirical properties specified in EN 12591 and other test results on fresh binder, as well as on binders that have been subjected to both STA and LTA. Therefore, the main binder properties can be considered to be adequately described using empirical test methods, and new test methods should be considered only if they add information that is not provided by the existing ones.

The behavior of polymer-modified binders and binders used in special applications is more complex/specific than that of (unmodified) paving-grade bitumens. For these binders, empirical test methods do not necessarily relate to performance of the asphalt mixture in the same way as for paving-grade bitumen. The CEN data collection project showed that fundamental test methods can add extra information about the behavior of the binder. Therefore, new test methods are necessary to determine properties relating to performance for binders with complex rheology.

Specifications for these more complex/specific binders should be based on the measurement of fundamental binder properties that have a demonstrable relationship with asphalt properties. The CEN data collection project evaluated a number of candidate test methods to measure properties of binders used in Europe, and the development of performance-related standards for complex binders should incorporate the knowledge derived from the results.

1.8 Summary

Specifications offer a means of providing an agreed-upon set of properties that enable the purchaser to select the product appropriate for a given use. However, a specification does not, by itself, mean that the product specified is necessarily fit for a given purpose. The end user of a product should consider the choice of available materials, specify the correct one, and use it correctly.

Specifications should address the important characteristics of a product, and might also include characteristics important for handling and application, as well as for safe use. Properties of the product that relate to the important characteristics should be measured using robust, relevant, and standardized test methods. Limits within specifications should be selected that take into account the precision of the test method and that do not conflict with other elements of the specification.

[16] Eurobitume TF Data Collection Position Paper on Test Methods used during the Data Collection, May 2009. Published by the European Bitumen Association, ISBN 2-930160-11-X, D/2009/7512/12, May 2009.

www.EngineeringEBooksPdf.com

Defining relationships between binder properties and field pavement performance is technically challenging and, with our current understanding, cannot be conclusively established. However, certain properties of bituminous binders are known to be related to mixture properties; therefore, test methods that relate to those properties can be used in specifications.

A satisfactory specification enables the measurement of the performance of the binder and evaluates how the performance will change over time and how the binder performance will influence the characteristics of the asphalt mixture. A specification does not guarantee the functional performance of the asphalt mixture or the final pavement. A specification provides a test value or a series of values for a binder, each relating to a specific functional property that is needed to predict the important characteristics.

Many current specifications use empirically based test methods, that is, test methods that have been developed using experience. More recently developed test methods provide measurements in functional engineering units, which can make them more attractive for use within specifications. Many empirical test methods also address properties relating to performance, and the relationship to field performance is well understood. The CEN data collection project (see Section 1.7.1) demonstrated good correlations between empirical properties specified for unmodified bitumens and more recently developed test methods. The use of empirically based test methods is therefore justified for such binders, and new, fundamental specifications are not justified for such materials unless that added information is not otherwise addressed by the specification.

The material properties of polymer-modified binders are more complex than those of unmodified binders, and empirically based test methods do not necessarily relate to performance for these binders in the same way as for the more rheologically simple unmodified binders. For these binders, fundamental test methods providing properties in engineering units are justified, and newer test methods provide information that the empirical test methods do not. Specifications for these more complex/specific binders should be based on the measurement of fundamental binder properties that have a demonstrable relationship with asphalt properties.

Because of the long product life cycle, specifications should include conditioning regimes that address STA and/or LTA conditions when necessary, combined with testing of properties that are likely to be performance-limiting on the aged material.

Acknowledgments

I would like to thank Eurobitume for providing me with support in my work on this chapter. I would specifically like to thank the Technical Committee of Eurobitume for their help and assistance in providing information and for taking the time to review and comment on the chapter in its draft form.

References

Airey, G.D., 2002. Optimising the returns from long life roads. In: Durability Review. In: Review of Durability Test Methods, vol. III. Scott Wilson Pavement Engineering Limited, Nottingham.

www.EngineeringEBooksPdf.com

Alexander, C.F., Budija, M., Cornelius, P.D.M., Parry, M.A., Stannard, P.G., 2000. Multigrade binders—new high performance bitumens. In: 1st International Conference, World of Asphalt Pavements, Sydney, Australia, February 20–24.

Bahia, H.U., Anderson, D.A., Christensen, D.W., 1991. The bending Beam Rheometer: a simple device for measuring low-temperature rheology of asphalt binders. J. Assoc. Asphalt Paving Tech. 61, 117–135, AAPT, Seattle.

Bahia, H.U., Zhai, H., Zeng, M., Hu, Y., Turner, P., 2001. Development of binder specification parameters based on characterization of damage behaviour. J. Assoc. Asphalt Paving Tech. 70, 442–470. (AAPT, Seattle).

Besamusca, J., Sörensen, A., Southwell, C., 2012a. Addressing ageing characteristics of bituminous binders in Europe. In: Proceedings of the 5th Eurasphalt & Eurobitume Congress, Istanbul.

Besamusca, J., van Rooijen, R., Robertus, C., Beuving, E., 2012b. The search for simple tests to assess the complex properties of adhesion and durability of adhesion. In: Proceedings of the Eurasphalt & Eurobitume Congress.

Boussad, N., Dony, A., 1996. Polymer modified bitumen: relationship between binder and mix rheology. In: Eurasphalt & Eurobitume Congress.

Carswell, J., Green, P.J., 2000. Prediction of rutting resistance in hot rolled asphalt using rheological parameters. In: 1st International Conference, World of Asphalt Pavements, Sydney, Australia, February 20–24.

Chabert, D., Triquigneaux, J.-P., Vaniscote, J.-C., 1999. Rheology of elastomer binders and rutting resistance of bituminous mixes. In: Performance Related Properties for Bituminous Binders, Eurobitume Workshop, Luxemburg.

Chailleux, E., Le Guern, M., Farcas, F., Dreessen, S., 2012. Interpreting a three-point bending test on pre-notched bitumen beam to determine cracking behavior at low temperature. In: Proceedings of the 5th Eurasphalt & Eurobitume Congress, Istanbul.

Choquet, F., Verhasselt, F.A., 1993. Ageing of bitumen: from the road to the laboratory and vice versa. In: Proceedings of the Conference on the SHRP and Traffic Safety on Two Continents, The Hague, Netherlands, September 22–24.

Claine Petersen, J., 2009. In: A Review of the Fundamentals of Asphalt Oxidation Chemical, Physicochemical, Physical Property, and Durability Relationships, Transportation Research Circular E-C140, October.

Claxton, M., Lesage, J., Planque, L., 1996. When can bitumen rheological properties be used successfully to predict asphalt mix performance? In: 1st Eurasphalt & Eurobitume Congress, Strasburg.

Energy Institute, 2003. Assessment of the reproducibility of a long term ageing test for bituminous binders. Report No. STE-01/2004, Scott Wilson Pavement Engineering Ltd.

Federal Highways Administration, 2011. The Multiple Stress Creep Recovery (MSCR) Procedure, April. FHWA-HIF-11-038.

FEHRL, 2006. BitVal—analysis of available data for validation of bitumen tests. Report on Phase 1 of the BiTVal Project, http://bitval.fehrl.org/.

Gershkoff, D., 1995. Polymer modified bitumens—performance in empirical and rheological tests. In: First European Workshop on the Rheology of Bituminous Binders, April, Paper 34.

Hesp, S.A.M., Terlouw, T., Vonk, W.C., 2000. Low Temperature Performance of SBS-Modified Asphalt Mixes. Association of Asphalt Paving Technologists, Reno.

Heukelom, W., 1969. A bitumen test data chart for showing the effect of temperature on the mechanical behaviour of asphaltic bitumens. J. Inst. Pet. Technol. 55, 404–417.

www.EngineeringEBooksPdf.com

Kennedy, T., Huber, G., Harrigan, E., Cominsky, R., Hughes, C., Von Quintus, H., Moulthrop, J., 1994. Superior performing asphalt pavements, (Superpave), The Product of the SHRP Asphalt Research Program, Report SHRP-A-410.

Khattak, M.J., Baladi, G.Y., 2001. Fatigue and permanent deformation models for polymer-modified asphalt mixtures. In: 80th Annual Meeting. Transportation Research Board, Washington.

Lecomte, M.J., Durand, G., Robert, M., Phillips, M.C., 2000. Examination of the capability of SUPERPAVE tests to predict the low-temperature performance of polymer modified binders. In: 2nd Eurobitume & Eurasphalt Congress, Barcelona.

Lu, X., Isacsson, U., Ekblad, J., 2003. Influence of polymer modification on low temperature behaviour of bituminous binders and mixtures. In: 6th International RILEM Symposium.

NAPA & EAPA, 2011. Production, Use, Properties, and Occupational Exposure Reduction Technologies and Trends, second ed. NAPA & EAPA, The Asphalt Paving Industry: A Global Perspective. ISBN 0-914313-06-1.

Paez, D.A., Sanchez, C.J., Unzueta, E.E., Juarez, A.F., 1999. Relationships between rheology of mix and binder. In: Application to High Modulus Mixes Eurobitume Workshop 99—Performance Related Properties for Bituminous Binders, Paper No. 097.

Pfeiffer, J.P., van Doormaal, P.M., 1936. The rheological properties of asphaltic bitumens. J. Inst. Pet. Technol. 22, 414–440.

Phillips, M., Robertus, C., 1996. Binder rheology and asphaltic pavement permanent deformation; the zero-shear viscosity. In: Proceedings of the 1st Eurasphalt & Eurobitume Congress, Paper 5.134.

Proteau, M., Yvan, P., 2001. Contribution de différents bitumes purs et bitumes modifies par ajout de polymères à la résistance à l'orniérage. In: International Road Federation World Road Congress, Paris, France, 10–15 June.

Prowell, B.D., 2001. Design, construction, and early performance of Virginia's hot-mix asphalt stabilizer and modifier test sections. In: 80th Annual Meeting. Transportation Research Board, Washington.

van Gooswilligen, G., Berger, H., de Bats, F.Th., 1985. Oxidation of bitumens in various tests. In: 3rd Eurobitume Symposium, The Hague, September.

Verhasselt, A., 2002. Long-Term Ageing—Simulation by RCAT Ageing Tests. In: 9th International Conference on Asphalt Pavements. ISAP, Copenhagen. Lanham, MD/Brussels, Belgium: NAPA/EAPA.

www.EngineeringEBooksPdf.com

Analytical separation methods in asphalt research

2

J.F. Branthaver[1], *S.-C. Huang*[2]
[1]Chatham, IL, USA; [2]Western Research Institute, Laramie, WY, USA

2.1 Introduction

Most asphalts of commerce are products of the refining of crude oils. The properties of these asphalts are determined by the chemical composition of their parent crude oils and the methods used to refine them.

It is important to be able to predict the performance behavior of asphalts derived from the wide variety of crude oils available to refiners. In order to do this, a number of tests have been in use over the years. Many of these tests measure global chemical and physical properties of whole asphalts. Examples of global chemical analyses are elemental composition—carbon, hydrogen, nitrogen, oxygen, and sulfur contents; functional group analysis by infrared (IR) spectroscopy; acidity and basicity by potentiometric titration; and nuclear magnetic resonance (NMR) measurement of carbon and hydrogen type. The information obtained from these tests contributes to the understanding of the nature of asphalts. However, the important physical properties that determine pavement performance appear to depend on more subtle variables than those mentioned above. Therefore, in order to gain a better understanding of the relationship of chemical compositional factors to performance-related physical properties of asphalts, it was found to be necessary to separate asphalts into fractions and study the influence of the various fractions on properties of interest.

The objective of this chapter is to provide historical background to some of the separation methods that have been used in the study of asphalts and the influence of some of these methods on the development of a model of asphalt microstructure.

2.2 Separations of asphalts based on solvent precipitation and extraction

2.2.1 Precipitation of asphaltenes

One of the simplest separations applied to asphalts is the precipitation of asphaltenes. Asphaltenes are that portion of an asphalt that is insoluble in low molecular weight (MW)-saturated alkanes. Asphaltenes are black, friable solids. The solvents used to precipitate asphaltenes usually are straight-chain alkanes ranging in carbon number from 3 (propane) to 10 (*n*-decane). The branched-chain alkane *iso*-octane also may be used. In most investigations, *n*-pentane and *n*-heptane are the precipitants.

Advances in Asphalt Materials. http://dx.doi.org/10.1016/B978-0-08-100269-8.00002-7
© 2015 Elsevier Ltd. All rights reserved.

www.EngineeringEBooksPdf.com

The yield of asphaltenes is a function of the precipitant (Girdler, 1965). Yields decrease with increasing chain length of the alkane used. This is because the solubility parameters (a measure of solvent power) of alkanes increase from propane to *n*-decane. Asphaltenes are more aromatic than their parent asphalts and contain higher concentrations of nitrogen, oxygen, and sulfur. Therefore, asphaltenes are more polar than their parent asphalts.

Typical asphaltene yields (mass %) of neat asphalts using *n*-heptane as solvent range from 4% to 25%. Yields are higher for oxidatively aged asphalts. In addition to the precipitating solvent selected, asphaltene yields are a function of experimental variables. These variables include the amount of solvent used for each gram of asphalt, temperature, contact time, and the method used to wash the precipitated asphaltenes. Speight (1987) recommends 40 mL solvent per gram of asphalt. After asphaltenes are precipitated, they are collected by filtration. Solvent is removed from filtrates by distillation. The residue from this process is known as maltenes, petrolenes, or deasphaltened oils. Some volatile materials indigenous to asphalts are lost in the maltene recovery process. For this reason, solvents with higher boiling points than *n*-heptane are not commonly employed.

The asphaltene content of an asphalt provides important information about the nature of an asphalt. Asphalts with high asphaltene contents almost always are high in sulfur content and may be expected to readily undergo oxidative age hardening. Asphaltenes are the viscosity-building component of asphalts, although it is not necessarily true that asphaltene content will correlate directly with viscosity when various asphalts are compared.

Asphaltene contents provide a basis for classification of asphalts into sol-or-gel types. An asphalt high in asphaltene content will have properties characteristic of gel-type asphalts. Among these properties are high degree of complex flow, relatively low change of viscosity with temperature, low ductility, and susceptibility to oxidative age hardening (Traxler, 1961). Asphalts with low asphaltene contents will have properties characteristic of sol-type asphalts. Such asphalts are frequently observed to yield "tender" pavements. Sol-type asphalts are ductile, have low degrees of complex flow, and exhibit large changes of viscosity with temperature. Asphalts with intermediate asphaltene contents will have properties intermediate between the extremes of sol- and gel-type behavior.

The sol–gel description of asphalt structure views asphalts as dispersions of asphaltenes in a maltene solvent phase. Based on this simple model, relative viscosities of asphalts may be calculated by measuring viscosities of an asphalt and its maltene fraction under identical conditions. The relative viscosity (η_{rel}) of an asphalt is a number obtained by dividing the viscosity of the asphalt by that of its maltene fraction. For sol-type asphalts, η_{rel} values are fairly low. For gel-type asphalts, η_{rel} values are high. Thus, the simple fractionation of an asphalt into two fractions provides important information about an asphalt that is not obtained from global properties.

Heithaus (1962) developed a method that distinguishes between sol- and gel-type asphalts. Although it is not strictly a separation method, it is based on the flocculation behavior of asphaltenes. In the Heithaus procedure, several solutions of asphalts in toluene of varying concentrations are prepared. A precipitating solvent, such as

www.EngineeringEBooksPdf.com

n-heptane, is then added to each of the solutions until flocculation is observed. The amount of *n*-heptane required will vary depending on the concentrations of the toluene solutions. The amounts of *n*-heptane required to effect precipitation are then plotted on a graph versus concentrations of the solutions. The resulting straight line is used to calculate Heithaus parameters. One of these parameters, the *P* value, is a quantitative measurement of the overall compatibility of maltenes and asphaltenes in an asphalt or an asphalt blend. The *P* value distinguishes between gel- and sol-type asphalts in that the former are incompatible and the latter are compatible. The Heithaus method also measures the solubility characteristics of maltenes and asphaltenes by the parameters p_0 and p_a. The p_0 values measure maltene solvent power and the p_a values measure the ease by which asphaltenes are solvated.

The Heithaus method is useful in predicting properties of asphalt blends and emulsion behavior. Recently, the Heithaus method has been fully automated, removing operator dependence on identifying the onset of flocculation (Pauli, 1996). In the automated method, *iso*-octane replaces *n*-heptane as the precipitating solvent. This method has been published as an ASTM International procedure (2009).

When applied to asphalt, the terms gel-type and sol-type assume that asphalts are not pure solutions, but have elements of internal structure. This hypothesis was termed the colloidal model and was discussed at length by Petersen to rationalize the relationships between asphalt composition and pavement performance (Pfeiffer and Saal, 1940; Petersen, 1984).

Asphalts are highly complex mixtures of compound types, varying widely in molecular size and polarity. The most abundant compounds are hydrocarbons, composed of the two elements carbon and hydrogen. Asphalt hydrocarbons vary widely in molecular size and aromaticity. A considerable number of asphalt hydrocarbons are saturated alkanes, some of which are long-chain compounds of high carbon number. These are the waxes, discussed subsequently. Saturated alkanes are nonpolar, and do not interact with one another or with other compounds. Other hydrocarbons contain one or more aromatic rings and are said to be unsaturated. Aromatic compounds are slightly polar and interact weakly with one another and with other compounds. Thus they are slightly polar—polarity being a crude measure of the capability of a molecule to engage in interactions with other polar molecules.

The nonhydrocarbon constituents of asphalts are heteroatom-containing compounds, those that contain one or more nitrogen, oxygen, or sulfur atoms. These compounds are the most polar components of asphalts and interact with one another, in some cases fairly strongly. Among the common polar compounds in asphalts are carboxylic acids, various nitrogen bases, and thiophenes. Oxidative aging results in the formation of polar sulfoxides from nonpolar aliphatic sulfides, and polar ketones from weakly polar aromatic hydrocarbons.

In the colloidal model of asphalt structure, it is assumed that the more polar molecules of asphalt interact to form molecular associations. These associations are dispersed in a bulk solvent, consisting of the saturated hydrocarbons, most aromatic hydrocarbons, and some of the less polar heteroatom-containing compounds. The size of the molecular associations, which are held together by forces varying in strength, is a function of the nature of the polar compounds, temperature, rate of shear, and the

www.EngineeringEBooksPdf.com

effectiveness by which the associations are solvated. Within the associations, it is speculated there is a polarity gradient going from the centers to the peripheries. The forces holding the associations together are not nearly as strong as the covalent chemical bonds, which are not broken at asphalt service temperatures and by shear. The strongest forces in the molecular associations would be carboxylic acid hydrogen bonds. Weaker polar interactions are broken up by heating and shear, whose variables reduce the sizes of the molecular associations and increase the bulk solvent. According to the model, interactions involving molecular associations explain some of the rheological properties of asphalts, the large temperature variation of asphalt viscosities, and the property changes observed as a result of oxidative aging. Assuming the validity of the above model, information obtained by such tests as the Heithaus and its modifications should be useful in predicting pavement performance.

Redelius (2000) developed a method to separately measure hydrogen-bonding and other polar interactions in aged asphalts and asphalt-flux mixtures. This method supplements the standard Heithaus test. Redelius titrated toluene solutions of the subject materials with 2-methyl-1-hexanol (*iso*-octanol) to measure hydrogen-bonding interactions. The solutions were titrated with 2-butanone (methylethyl ketone) to measure polar interactions that are not as strong as hydrogen bonds.

2.2.2 Other solvent precipitation and solvent extraction methods

Solvent precipitation methods that separate asphalts into more than two fractions have been proposed in the past. Traxler and Schweyer developed a method based on treating asphalts with 1-butanol, which partly dissolves asphalts. The undissolved solids, designated as asphaltics (and not identical with asphaltenes obtained by precipitation using *n*-alkanes), are obtained by filtration and weighed. Butanol is evaporated from the filtrate, and the residue treated with hot acetone. The acetone solution then is chilled to −23 °C (10 °F), resulting in precipitation of a saturate fraction. The saturates are obtained by decanting the acetone solution. Materials termed cyclics are obtained by evaporation of the acetone. The masses of the asphaltics, saturates, and cyclics are plotted on a triangular chart. It was claimed that asphalts of different types may be distinguished (Traxler and Schweyer, 1953). The asphaltic fraction may be further treated with *n*-pentane to yield insoluble asphaltenes and soluble resins. Traxler used mass fraction data from all four fractions to calculate a coefficient of dispersion (Traxler, 1960). This parameter is the ratio of the cyclics plus resins divided by saturates plus asphaltenes. An asphalt having a high coefficient of dispersion would be expected to have properties different from an asphalt having a low coefficient of dispersion.

Marvillet (1975) proposed a separation method consisting of two successive solvent precipitation steps. Asphalt is first treated with propane, yielding soluble maltenes and asphaltenes. The propane asphaltenes are then treated with *n*-heptane, which partially dissolves them. The three fractions obtained are weighed and the mass fractions are plotted on a triangular chart. Asphalts are classified according to data-point positions on the chart. An advantage of this procedure is that some lower-boiling components that might be present in asphalt are not lost due to the ease of removal of propane.

www.EngineeringEBooksPdf.com

Waxes in petroleum are hydrocarbons that are solids or semisolids at ambient temperatures. Straight-chain (normal) alkanes of carbon number greater than 20 are a major component of petroleum waxes. Some other hydrocarbon types also may be part of the wax component of crude oils, namely, branched alkanes. Waxes consisting mainly of normal alkanes are known as paraffin waxes. Waxes will become concentrated in asphalts made from crude oils that contain these hydrocarbons. Gupta and Agrawal studied a variety of petroleum waxes that had been separated from their parent crudes. The waxes were of the paraffin-type and were characterized by melting points in the 50 °C (122 °F) to 70 °C (158 °F) range. Average carbon numbers ranged from 28 to 33, determined by X-ray diffraction (Gupta and Agrawal, 2000). These investigators determined the proportion of waxes existing in the crystalline state at ambient temperatures. Of those studied, crystallinity values varied from 78% to 90%, the remainder being amorphous. The amorphous waxes were assumed to be branched-chain or cyclic alkanes, or aromatic hydrocarbons having long side-chains. Based on these observations, it is likely that waxes in asphalts will form separate crystalline phases at low temperatures. Wax crystals occupy less volume than their molten phases. These crystals and their accompanying voids may be centers of weakness in pavements. Bahia and Anderson have shown that there is a relationship between wax content and low-temperature hardening of asphalt (Bahia and Anderson, 1995). Claudy et al. (1992) also have studied the effect of time and temperature on wax crystal formation in asphalts.

Several procedures to recover waxes from crude oils have been developed, and some of them have been modified to apply to asphalts. The methods are based on the observation that waxes are relatively insoluble in common solvents and are the least polar constituents of asphalts. In the reported separation schemes, at least two steps are required. Usually, one of the steps will involve a chromatographic technique, some of which are discussed subsequently.

The existence of paraffinic and microcrystalline waxes in crude oils has long been known. Paraffin waxes are a homologous series of normal alkanes ranging in carbon number from 20 to 60 in many crude oils. However, in some crudes, the homologous series extends far beyond this range, and these compounds will be incorporated into asphalts (Boduszynski et al., 1981). Microcrystalline waxes also contain molecules of substantial size. Asphaltene fractions thus may not consist entirely of polar molecules. The high carbon number alkanes in asphaltenes thus are not part of the dispersed molecular associations of polar molecules that the colloidal model assumes to exist in neat asphalts.

Recently, Schabron et al. (2012) formed a method called the Waxphaltene Determinator. A 2-butanone (methylethyl ketone) solution of asphalts is cooled to −24 °C, which results in the precipitation of waxes and asphaltenes. These solids then are redissolved in a series of solvents: *n*-heptane at −24 °C (−11.2 °F); *n*-heptane at 60 °C (140 °F); toluene at 30 °C (86 °F); and dichloromethane-methanol, 98:2 v/v, at 30 °C (86 °F). This method allows for the isolation of waxes, polar materials, and pericondensed aromatics in a few minutes.

www.EngineeringEBooksPdf.com

Solvent precipitation methods are useful techniques for the isolation of fractions of interest from asphalts. The fractions are defined by solubility behavior. Relative masses of the fractions serve to classify asphalts. The fractions may be studied by various analytical methods and be subjected to other separation procedures. An advantage of the solvent precipitation methods is that they are simple and not overly time-consuming. However, they usually involve handling large volumes of solvents, which may be a problem in some laboratories.

2.3 Separation methods based on adsorption chromatography

2.3.1 Methods of Marcusson, Corbett, and others

Early in the investigation of asphalt composition, it was found to be necessary to generate more fractions than maltenes and asphaltenes if useful characterization of an asphalt was to be achieved. The pioneering work of Marcusson early in the twentieth century is described by Traxler (1961) and by Barth (1962). Marcusson precipitated asphaltenes from asphalts using light petroleum naphtha, a mixture of low-boiling normal and branched alkanes. After filtering the asphaltenes, the maltene filtrate was contacted with fuller's earth, an adsorbent clay. Polar materials in the maltene solution were absorbed on the clay. The naphtha solution was decanted from the clay, which was then immersed in carbon disulfide to desorb the polar materials. Solvents were evaporated and the residues were weighed. Marcusson designated the portion of the maltenes unabsorbed by fuller's earth as oils, and the materials adsorbed on the clay were termed resins. Subsequent separation schemes involving solvent precipitation of asphaltenes followed by maltene fractionation have not differed greatly from Marcusson's approach. Hubbard and Stanfield (1948) modified the procedure by replacing petroleum naphtha with *n*-pentane in the solvent precipitation step and replacing fuller's earth with anhydrous alumina.

The most widely used separation method derived from Marcusson's research is the one developed by Corbett. Corbett tried a number of different separation schemes before settling on a procedure that separates asphalts into four fractions. He chose four fractions because he did not believe that two or three provided enough information to effectively characterize asphalts. More than four fractions introduced complications.

In the standard Corbett procedure, asphalts are first contacted with a designated volume of *n*-heptane. After asphaltene precipitation is complete, the solids are recovered by filtration. The maltene solution then is poured onto a bed of alumina in a chromatography column. Elution is continued with *n*-heptane, followed by a calculated amount of benzene to yield a saturate fraction. Elution is continued with more benzene, followed by a mixture of benzene and methanol to yield a naphthene aromatic fraction. A polar aromatic fraction then is eluted with trichloroethylene. After solvent removal, the fractions are weighed (Corbett, 1970). Recent restrictions on the use of benzene in laboratories require that toluene replace benzene in the Corbett and other procedures.

The Corbett procedure has been scaled up to provide larger amounts of the four fractions (Peterson et al., 1994).

www.EngineeringEBooksPdf.com

Assuming that the model of asphalt structure discussed earlier is valid, the relative amounts of the Corbett fractions should provide a measure of whether an asphalt is of the gel, sol, or intermediate type. Gaestel et al. (1971) divided the sum of the mass fractions of asphaltenes and saturates by the sum of the mass fractions of naphthene aromatics and polar aromatics to obtain a value known as the Gaestel index. Saturates and asphalenes are polar opposites. Naphthene aromatics and polar aromatics are compatible with one another. Presumably, the saturates comprise most of the solvent component of an asphalt and the asphaltenes comprise most of the dispersed component. The naphthene aromatics and polar aromatics improve the solvent's ability to disperse asphaltenes. Thus, the more of the saturate and asphaltene fractions in an asphalt compared with the other two fractions, the less compatible, or gel-like, the asphalt will be. Alternatively, sol-type, or compatible asphalts, will have larger amounts of naphthene aromatics and polar aromatics. Relative compatibilities will be reflected in physical properties.

The Corbett procedure was found to be useful in forensic studies of asphalts at a time when embrittlement caused by oxidative aging was a pavement failure mode of major concern. There exists a substantial database of results. Notable among these results are data from extracts of cores obtained in the Michigan road test (Corbett and Merz, 1975). In this well-known investigation, sections of road six miles in length were laid down using six different binders available in Michigan. Aggregate gradations and construction procedures were carefully controlled so that the single variable among the test sections was the nature of the binder. After several years, the test sections were examined by highway engineers and rated according to performance. Extracts were obtained from top and bottom layers of cores drilled from each of the sections. The extracts then were separated into fractions using the Corbett procedure. The four mass fractions were compared with similar data from the original binders. It was found that oxidative aging was more extensive in the top layers than in the bottom layers, as would be expected. During the process of oxidation, the saturate fractions were found to be relatively unchanged, whereas naphthene aromatics became converted to polar aromatics. Asphaltene yields also increased.

2.3.2 Modern chromatographic separations and methods of analysis

The separation methods described earlier were developed before the advent of high-performance chromatographic techniques. In the earlier separations, asphaltenes were isolated in a preliminary step, and no subsequent separations were performed on these highly polar materials. Asphaltenes are composed of materials that bind irreversibly to chromatographic absorbents such as alumina, clays (fuller's earth), and silica gel. Chromatographic separations are performed only on maltenes.

There have been some attempts to fractionate asphaltenes into subfractions. Selucky et al. eluted asphaltene-coated silica gel using solvents ranging in polarity from *n*-pentane to a mixture of tetrahydrofuran (THF) and 2-amino-propane (*iso*-propylamine) (Selucky et al., 1981). Almost all of the asphaltenes were recovered from the silica gel column in several fractions. They reported that MWs of the

www.EngineeringEBooksPdf.com

fractions determined by vapor phase osmometry (VPO) decreased with increasing polarity of the solvent used to generate the fraction.

A refinement of absorption chromatographic separation of asphalts for the purpose of rapid "fingerprinting" is the iatroscan method. This is a thin-layer chromatographic procedure. Solutions of asphalts in carbon disulfide are "spotted" on specially prepared glass rods coated with silica (Wan et al., 1992). The spotted rods are then "developed" by partial elution with a series of three solvents, *n*-heptane, toluene, and THF. Each of the solvents causes different compound types to move along the rods from the original spot. After development, the rods are moved along a hydrogen flame, which burns off the organic material on the rod. A flame ionization detector (FID) quantifies the ions generated. The FID responses over time are correlated with the organic material eluted to various positions on the rods by the three solvents. Saturates, naphthene aromatics, and polar aromatics are eluted by *n*-heptane, toluene, and THF, respectively. Asphaltenes remain at the point of the original spot. Iatroscan can provide rapid results similar to those obtained in Corbett analyses. Iatroscan is a method of analysis rather than a physical separation of asphalt fractions, so handling substantial quantities of solvents is not required.

In the above separation methods, the objective is to correlate chemical compositional data with various asphalt properties, such as rheological behavior and hardening tendencies. Corbett (1970) lists the effects of each of the fractions generated in the separation method bearing his name on asphalt physical properties. He claims that ductility is largely a function of the polar aromatic fraction, and that this same fraction has a deleterious effect on temperature susceptibility. Various combinations of fractions influence hardness, softening point, shear susceptibility, and other properties. If the objective of predicting asphalt properties from chemical composition data can be met, then binders conforming to desired criteria may, in theory, be designed and manufactured in refineries.

The success of some of these methods, as well as others discussed below, in achieving the above objective has been evaluated by Goodrich et al. (1986) and by Dukatz et al. (1984). These investigators claim that physical tests are more reliable guides to asphalt performance. Goodrich et al. (1986) contend that two of the most important performance-related properties, age hardening and temperature susceptibility, are not readily predicted by the classical separation methods described above.

2.4 Methods for separation of asphalts into chemically distinct fractions by affinity chromatography

The methods of asphalt fractionation described previously are based on solubility and absorption behavior, and usually involve an asphaltene precipitation step. Many of the important rheological properties of asphalts are dominated by the asphaltene fraction. If the model of asphalt structure proposed earlier is valid, asphaltene-like polar molecular associations exist in asphalts, and asphaltenes are not mere artifacts of precipitation. If so, separation methods that fractionate asphalts into components according to chemical similarity or molecular size, without a preliminary precipitation of asphaltenes, should provide fractions similar to asphaltenes in properties.

www.EngineeringEBooksPdf.com

One method used to separate crude oils, tar and bitumens, shale oils, and other organic complex mixtures into neutral, acidic, and basic fractions is ion-exchange chromatography (IEC). This method was used in the study of the "heavy ends" of petroleum in American Petroleum Institute (API) Project 60 (McKay et al., 1978). Solutions of materials to be separated pass through (either by gravity or by pumping) columns filled with either activated anion resins or activated cation resins. Resins as they are obtained from manufacturers cannot be used. They must be treated with a series of solvents in order to activate them. The activated anion resins contain functional groups that react with acidic molecules and separate them from solutions of materials that contact the resins. The activated cation resins contain functional groups that react with basic materials. Compounds containing neither acidic nor basic functional groups do not interact with the resins and pass through them unabsorbed. The compounds absorbed on the resins are recovered by desorption with acidic or basic reagents. Thus, it is possible to separate bituminous materials such as asphalts into specifically defined chemical fractions. In IEC separations of asphalts, a disadvantage is that material recoveries are less than 100% because some highly polar materials are irreversibly absorbed on the resins.

Green et al. (1984) developed an IEC separation method for a variety of petroleum-derived materials into five fractions: neutrals, weak acids, strong acids, weak bases, and strong bases. In this procedure, the sample to be separated is dissolved in a polar solvent, and the solution is pumped through a column of activated anion resins. The solution emerging from this column then is pumped through a column of activated cation resins. Strong acids are absorbed on the anion resins, and strong bases are absorbed on the cation resins. The solution passing through both columns unabsorbed are divested of solvent, and the residue is redissolved in cyclohexane. This solution is then pumped through two columns containing freshly activated anion and cation resins. Weak acids are absorbed in the second anion resin column, and weak bases are absorbed in the second cation resin column. Neutral materials pass through all four columns unabsorbed.

One of the earliest separations of asphalts by IEC was reported by Boduszynski et al. (1977a,b) using Romashkino asphalt. These workers separated solutions of Romashkino maltenes and asphaltenes into various acidic, basic, and neutral fractions.

In the late 1980s, the Strategic Highway Research Program (SHRP) was launched. One objective of SHRP was the development of methods that would lead to better correlations between the chemical composition of asphalts and their performance-related physical properties. The rationale for this research was to identify, by correlation with chemical compositional variables, which physical properties were fundamental to asphalt performance (and which were not) and therefore would serve as the basis for asphalt selection criteria. Except for the development of oxidative aging tests, which must predict the course of chemical changes in binders, it was not the objective of SHRP to develop chemical methods as asphalt selection guides. Because it is known that physical properties of all organic materials are strongly influenced by polarity and molecular size, the SHRP Binder Characterization and Evaluation project employed separation methods that fractionated asphalts based on these two compositional variables. The method selected to separate asphalts according to polarity was IEC.

Two complementary preparative IEC methods were used in the SHRP Binder Characterization and Evaluation study (1993). One was identical to that of

www.EngineeringEBooksPdf.com

Green et al. (1984). An alternative procedure was employed to separate asphalts into four fractions of interest rather than five. In this procedure, a cyclohexane solution of an asphalt was pumped into a column of activated cation resins, and the eluates from this column then were pumped through a column of activated anion resins. The column sequence is opposite to that of Green et al. (1984). The polar materials absorbed on the two columns were desorbed and divested of solvent. The polar materials absorbed on the cation resins were redissolved in cyclohexane, and this solution was pumped through a second anion resin column. The eluates from this procedure were divested of solvent, yielding the base fraction. Eluates from the first step that interacted with neither column comprise the neutral fraction. Materials absorbed on the first anion resins are the acid fraction. Those materials absorbed on the cation resins and also on the second anion resins are the amphoteric fraction. Details of this procedure have been published (SHRP-A-368, 1993). Flow sheets for the two IEC procedures are illustrated in Figures 2.1 and 2.2.

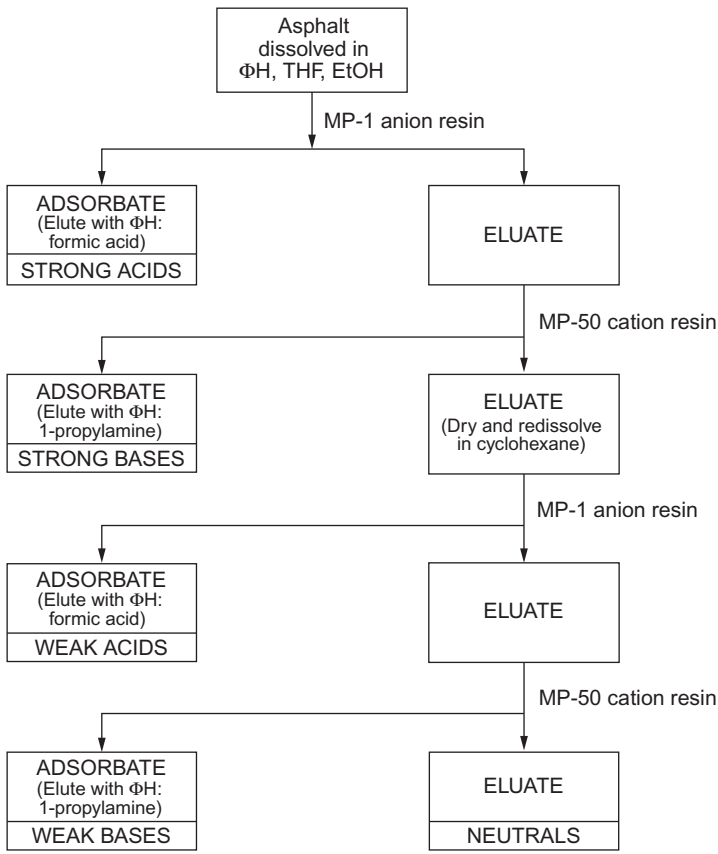


Figure 2.1 Flow sheet for separation of asphalts into five fractions by ion-exchange chromatography (IEC) (SHRP-A-368, 1993).

www.EngineeringEBooksPdf.com

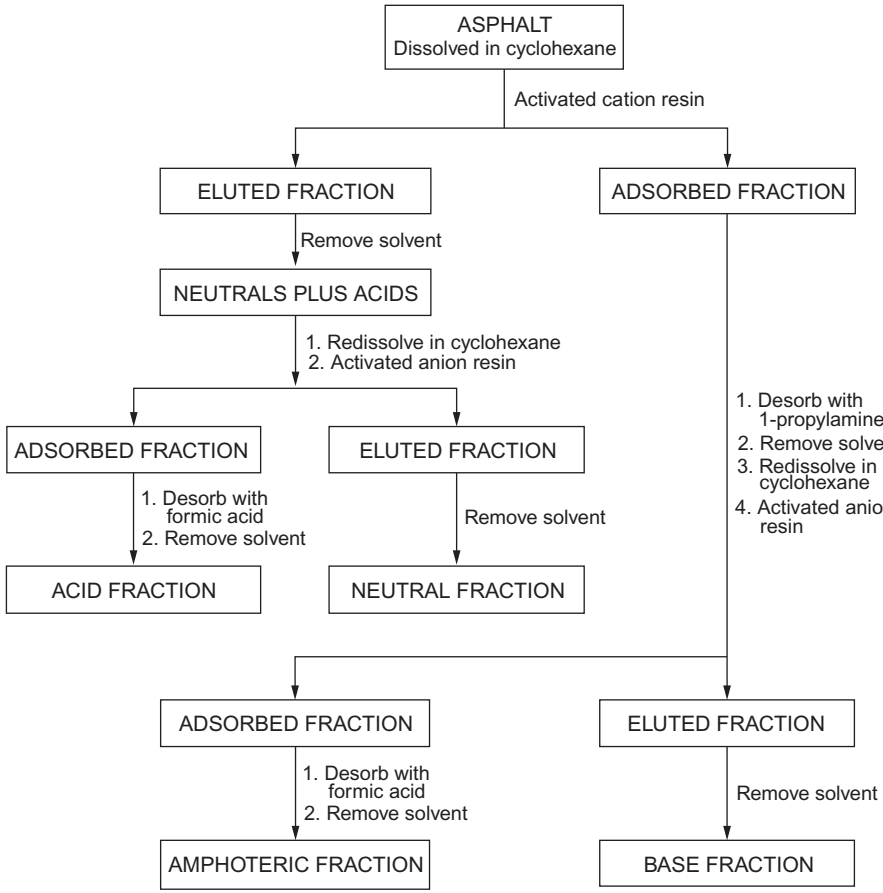


Figure 2.2 Flow sheet for isolation of amphoterics by IEC (SHRP-A-368, 1993).

Amphoteric molecules contain at least one acidic and one basic functional group. Such molecules would be expected to be highly polar and interact with one another to form molecular associations. They would likely be major components of asphaltene fractions of asphalts. Also contained in the amphoteric fraction would be molecules that strongly absorb to ion-exchange resins for any reason (e.g., polyaromatic molecules).

Several selected SHRP asphalts were separated into four fractions using the above procedure. As expected, neutral fractions comprised the bulk of all asphalts tested, ranging from 52 to 61 mass %. These neutral fractions were liquids, with viscosity orders of magnitude lower than those of the parent asphalts. For example, the viscosity of asphalt AAD-1, one of the eight SHRP "core" asphalts, was found to be 39,440 Pa s at 25 °C (77 °F) and 1.0 rad/s. Under the same conditions of measurement, the IEC neutral fraction of AAD-1 was found to be 20 Pa s. Number-average MWs of the whole asphalt AAD-1 and its IEC neutral fraction were found to be 700 and 510 Da, respectively. Obviously, the three polar fractions, acid, base, and amphoteric, must be the viscosity-building components of asphalts.

www.EngineeringEBooksPdf.com

The IEC neutral fractions appear to largely determine asphalt low-temperature properties, such as the glass transition temperature (Turner et al., 1995). This is because the waxes and any other crystallizable materials are found in the neutral fractions of asphalts (Robertson et al., 2001a,b). On average, glass transition temperatures (T_g) of the neutral fractions are 10 °C (18 °F) lower than T_g values of parent asphalts. The absence of polar materials in the neutral fractions allows for more refined investigation by such techniques as differential scanning calorimetry than is possible with whole asphalts.

IEC neutral fractions have been treated to isolate waxes (McKay et al., 1995). The neutral fractions were dissolved in toluene, and then a calculated amount of 2-butanone (methylethylketone) was added to the solution. The mixture then was chilled, and the precipitated waxes were recovered by filtration. The waxes then were weighed. Of the eight SHRP core asphalts, wax contents varied from less than 2–25%, the latter value being an outlier. Of the other seven core asphalts, the highest wax content was 8%. When the isolated wax fractions were studied by IR spectrometry, substantial 723 cm^{-1} peaks were observed, characteristic of long-chain saturated hydrocarbons. Most of the waxes were hard, brittle solids at ambient temperatures. The exception was asphalt AAM-1, the outlier containing 25 mass % wax content. These waxes were observed to be gelatinous, and were microcrystalline waxes, distinct from the paraffin waxes in the other SHRP core asphalts.

Neutral fractions of asphalts obtained by the IEC method have been separated to isolate compound types other than waxes. Green et al. (1989) fractionated IEC neutral fractions of a Cerro Gordo resin using high-performance liquid chromatographic (HPLC) techniques. Aliphatic sulfides were isolated using a column doped with palladium. The remaining neutral materials were separated into saturate, monoaromatic, diaromatic, triaromatic, and polyaromatic fractions using other HPLC methods.

The results of Green, Reynolds, and Yu demonstrate that IEC neutral fractions of asphalts are a highly complex mixture of a variety of compound types. Although IEC neutral materials are lower in MW than whole asphalts, the MW range of IEC neutral components is substantial. MW values of mixtures of compounds determined by VPO are averages. Salmans et al. (1998) reported results from the separation of the IEC neutral fraction of SHRP core asphalt AAB-1 into subfractions of various molecular sizes using the size-exclusion chromatographic (SEC) method, described in more detail subsequently (Robertson et al., 2001a,b). The highest MW subfraction, comprising 5% of the mass of the IEC neutral fraction, was found to have a MW of 2760 Da. This is a much larger value than that of the IEC neutral fraction as a whole, and corresponds to hydrocarbons having carbon numbers of approximately 200. These are true MWs, as polar molecular associations cannot exist in the IEC neutral fractions. Other investigators also have reported the existence of fairly high MW molecules in crude oils (Thanh et al., 1999; Carbognani et al., 2000; Carbognani and Orea, 1999).

The solvent strengths of the IEC neutral fractions have been measured and were found to be equivalent to that of 2,2,4-trimethyl pentane (*iso*-octane). This solvent precipitates asphaltenes, so if IEC neutral fractions are the bulk of asphalt solvent phases, other agents must be present if asphaltene-like materials are to be stabilized in whole asphalts. It is believed that stabilizing materials correspond roughly with the

www.EngineeringEBooksPdf.com

IEC base and acid fractions, which readily dissolve in the IEC neutral fractions but also are sufficiently polar to assist in the solubilization of IEC amphoterics, which comprise most of the asphaltene fraction of asphalts. Thus, the traditional model of asphalt structure, in which asphaltenes are dispersed in maltenes by means of resins, is supported by the IEC data.

The amphoteric fractions of those asphalts subjected to IEC were the next most abundant fraction, ranging from 18 to 25 mass % of the eight SHRP core asphalts. Amphoterics are the most aromatic of the four IEC fractions studied, and also are high in nitrogen-containing compounds. Number-average MW values of the amphoteric materials, determined at 60 °C (140 °F) by VPO in toluene, range from two to four times the values of parent asphalts. Amphoteric materials are the viscosity-building components of asphalts. Mixtures of IEC neutrals, acids, and bases (i.e., asphalts minus amphoterics) are much less viscous than whole asphalts measured under identical conditions (SHRP-A-368, 1993). These findings provide further support for the model of asphalt structure proposed earlier.

Carboxylic acids are a significant component of some asphalts. These compounds might be expected to react chemically with basic sites on aggregates, and thus be contributors to stripping. If it is necessary to isolate a carboxylic acid rich fraction from asphalts for study, a procedure for doing so has been reported (Ramljak et al., 1977). A modification of the procedure allows the isolation of two quinolones, amphoteric molecules that contain an acidic group comparable in acidity to carboxylic acids (Preece et al., 1992).

The IEC methods are expensive and tedious, but provide detailed compound-type analyses of asphalts. Such time-consuming methods are not suitable for most studies of asphalts. The various IEC separation methods do provide substantial amounts of distinct components that can be used in other studies. The IEC method can process large quantities of an asphalt in one experiment.

Environmental concerns involving fossil fuels and products derived from them tend to focus on polyaromatic, heteroatom-containing compounds, which are major components of asphalts. Some asphalts, particularly those derived from heavier crudes, are rich in such metals as vanadium and nickel. These metals are components of organic complexes and are not entrained inorganic salts (Filby and Branthaver, 1987). In the future, it may be necessary to have more detailed information about the abovementioned compound types, and IEC is one method that might prove useful.

2.5 Size-exclusion chromatography separation of asphalts

The separation methods discussed so far depend on solubility behavior or chemical affinity. Separation methods exist that enable larger molecules, or associations of smaller molecules, to be separated from smaller molecules. Among these methods are centrifugation, ultrafiltration, and SEC. Only the latter method is practical for asphalts, due to their high viscosities.

www.EngineeringEBooksPdf.com

The SEC method, often referred to as gel-permeation chromatography, has been used for many years to separate asphalts into fractions of varying molecular sizes. In their review of SEC in asphalt studies, Davison et al. claim that "asphalt is probably the most complex material routinely studied by SEC" (Davison et al., 1995). In SEC, solutions of asphalts are pumped through columns filled with particles of polymeric gels that are swelled in a solvent. The swelled gel particles are highly porous, and the pores are of varying sizes. The distribution of pore sizes is controlled during the manufacture of the gels. A typical gel used in SEC is a polystyrene cross-linked with divinyl benzene. When an asphalt solution is introduced into the gel bed, the largest molecules (or the largest stable molecular associations) do not enter the throats of the gel pores, but percolate through the gel bed in the carrier solvent between gel particles. Therefore, the largest molecular entities elute first in SEC separations. Smaller molecules (or smaller molecular associations) spend more time inside the gel pore structure (during which time they are immobilized), and the time spent is in inverse proportion to their hydrodynamic volume, which is a function of molecular size. The smallest molecules freely enter almost all of the gel pore structure, and are last to elute. A mixture of molecules having approximately the same molecular size will not be separated by SEC. Neither will a mixture containing only molecules or molecular associations that are larger than the maximum pore size of the gel used in the separation. If chemical differences among constituents of a mixture vary according to molecular size, then SEC will effect a chemical-type separation as well as one based on molecular size. Unlike ion-exchange and absorption chromatographic separations, recoveries in SEC separations usually are nearly quantitative.

The SEC technique should be able to separate those constituents in asphalts that form stable molecular associations from those constituents that do not. In order to accomplish this goal, it is necessary to dissolve asphalt in a solvent in which the stronger molecular associations are not broken up by dilution. Moreover, if the so-called colloidal model of asphalt structure is correct, the first eluates in an SEC separation should resemble the most polar materials obtained by IEC. The later SEC eluates should be similar in properties to the low MW neutral, acid, and base fractions obtained by IEC. Failure to effect separation by SEC into fractions with substantially different properties would refute the colloidal model or any similar model. A successful SEC separation of asphalts into distinct fractions does not necessarily prove the model, because it is conceivable that the largest size entities in asphalts might be macromolecules derived from biopolymers. The SEC method will separate asphalt components according to absolute molecular size in such a case. A large molecule cannot behave as a small molecule, although smaller molecules might interact to form molecular associations and behave as large entities in SEC. However, the investigations of Boduszynski (1988), and that of Groenzin and Mullins (2000), among other studies, argue against macromolecules being present in petroleum in substantial quantities.

The use of the SEC technique for separation of heavy ends of petroleum was pioneered by Altgelt (1965) and Altgelt and Hirsh (1970). SEC was extensively used in API Project 60, which emphasized research on petroleum residua (Sugihara et al., 1970). Early work separating asphalts by SEC was predominantly directed toward differentiating among various asphalts by "fingerprinting" apparent molecular size distributions. The initial experiments using SEC to profile asphalts were methods

www.EngineeringEBooksPdf.com

of analysis rather than actual separations. Small amounts of asphalts were dissolved in a solvent, usually THF, which is highly polar and breaks up all but the strongest asphalt polar associations. The solutions then were injected into columns of various pore size distributions. Refractive index (RI) or ultraviolet–visible (UV–vis) detectors were used to monitor fractionation patterns. Molecular size distributions were established by measuring elution behaviors of model compounds of known molecular size (Otocka, 1973). The SEC method soon came into widespread use among asphalt researchers. Breen and Stephens determined molecular size distributions of 50 different asphalts using a combination of three gel columns, each having different pore size distributions (Breen and Stephens, 1969). The solvent used was THF, and the detector was a differential refractometer. These investigators observed that most asphalts exhibited bimodal molecular size distributions. An initial peak, or bulge of material of apparently large molecular size (LMS) was observed, followed by a valley, and then a second higher peak consisting of lower molecular size material.

Bynum and Traxler (1970) used SEC to analyze bitumens extracted from pavement cores. They compared results with SEC chromatograms of samples of the original asphalts used in the pavements. They found that the SEC chromatograms of the asphalts that showed poor resistance to oxidative age hardening differed noticeably from SEC chromatograms of the original asphalts. A bimodal distribution of molecular sizes was observed in the nine asphalts investigated. Bynum and Traxler noticed that size of the peak (determined by RI) corresponding to the higher molecular size entities increased with extent of oxidative age hardening, and that the size of the second peak decreased. It also was reported that the SEC chromatograms of asphalts of a given specification grade from the same supplier changed with time.

Haley (1975) separated air-blown asphalts and their parent residues by SEC and analyzed the fractions by NMR. He observed that the LMS material increases as a result of air blowing.

Reerink and Lijzenga (1975) analyzed asphaltenes from heavy crudes and various fractions from a Kuwait asphalt by SEC. They demonstrated that SEC calibration curves based on polystyrenes could not be used as universal calibration curves for the asphaltenes. This is because hydrodynamic volumes of polystyrenes differ greatly from hydrodynamic volumes of asphaltene components, and SEC separates according to hydrodynamic volume. Usually, hydrodynamic volume correlates with molecular size. However, an alkane and an aromatic compound of identical MW may be separated by SEC because of the larger hydrodynamic volume of the alkane.

Altgelt and Harle (1975) separated asphalts with different rheological properties by preparative SEC. They measured MWs of each of seven fractions by VPO, asphaltene contents of each of the fractions, and intrinsic viscosities of the fractions. This latter property should vary directly with MW. They found that, for Boscan (a heavy Venezuelan crude) asphalt SEC fractions, MW values varied from 25,000 to 960 Da. The earliest eluted fractions, which are of largest molecular size, consisted entirely of asphaltenes. The latest eluted fractions contained few asphaltenes. Intrinsic viscosities of the fractions, measured in benzene, decreased by a factor of two from the first to the last of the seven eluates. These results confirmed that SEC does effect a separation of asphalt solutions by molecular size, and that the asphaltene fraction

www.EngineeringEBooksPdf.com

of Boscan asphalt contains either predominantly materials of relatively LMS or materials that tend to form fairly strong molecular associations.

Brule (1979, 1980) and Brule et al. (1986, 1994) in the Laboratoire Central des Ponts et Chaussées in France separated many asphalts by analytical SEC in order to elucidate chemical composition-physical property relationships. They developed a rapid SEC separation of THF solution of asphalts through dual columns using UV detection. In theory, the fast separation should not allow molecular associations' time to break up completely into constituent molecules so that some of the presumed colloidal structure of the materials should be preserved. The SEC chromatograms of straight-run asphalts almost always were observed to be bimodal. The SEC chromatograms of aged asphalts exhibited three peaks, the third corresponding to entities larger than those found in straight-run asphalts. In Brule's interpretation, these peaks correspond (in reverse order of elution) to an intermicellar solvent phase, a dispersed phase, and a phase corresponding to micellar aggregations, which occurs only in aged materials. The third peak becomes larger with longer aging time and higher aging temperatures. It is speculated that buildup of these large aggregations is responsible for embrittlement of aged pavements.

Jennings et al. (1988) and Jennings and Pribanic (1989) have published a number of reports in which SEC chromatograms of asphalts are correlated with pavement performance. One study of Montana pavements manufactured from asphalts obtained from refineries in the state indicates that SEC chromatographic data of original asphalts can predict cracking tendencies in pavements. These researchers arbitrarily divide the chromatograms into three areas: LMS, medium molecular size (MMS), and small molecular size (SMS). Jennings and Pribanic claim that asphalt behavior in pavements is predicted by the shape of the SEC chromatograms, which are measures of molecular size distributions. They claim that SEC chromatograms demonstrate differences among asphalts that are not detected by other methods, particularly standard physical grading methods. In the Montana road study, it was found that pavements made with an optimum LMS content ($\sim$18%) as measured by SEC exhibited few cracks after 4 years of service. Pavements made from asphalts having higher LMS contents were observed to undergo cracking. In this study, Corbett's analyses also were performed on the asphalts studied. Pavements made from asphalts low in asphaltene content were observed to undergo rutting (Jennings and Pribanic, 1989).

In a study of pavements from localities outside Montana, Jennings and Pribanic (1989) showed that optimum LMS content, with regard to cracking, varied with climate. In warmer areas, pavements made from asphalts with higher LMS content exhibited less cracking than pavements made from similar asphalts in cold climates.

Jennings et al. (1992) and Pribanic et al. (1989) experimented with the use of diode array detectors in SEC separations. Eluates can be monitored from 200 to 600 nm instead of only one preset wavelength, which allows for the construction of three-dimensional SEC chromatograms. Highly aromatic species tend to absorb at higher wavelengths in the UV–vis range. Molecular size distributions of a wide variety of aromatic species can be obtained by this method. For example, metalloporphyrins, chlorophyll-derived components of many crude oils, have strong absorbance at 570 nm, where few other species interfere. By setting a detector at 570 nm, metalloporphyrin distributions in asphalts over a wide MW range can be measured.

www.EngineeringEBooksPdf.com

Plummer and Zimmerman (1984) reported molecular size distributions of asphalts recovered from pavement cores in Michigan and Indiana. Some of the pavements in both states exhibited extensive cracking problems, while others did not. The asphalts extracted from the more distressed pavements contained more high MW materials than did the less distressed pavements. The presence of greater amounts of high MW materials was directly correlated with hardness. Harder asphalts were utilized in the Indiana roads than were used in the Michigan roads, reflecting the warmer climate of Indiana. Without there ever having been quantitative measurements of molecular size distributions, asphalts selected for use in warmer climates tended to be harder than those used in colder climates. This was the result of trial and error in the construction of pavements over time.

Glover et al. (1988) obtained SEC chromatograms for many asphalts used in Texas and for recovered materials from pavement test sections. Solvents used in the SEC separations were THF or toluene. The chromatograms were distinctly different for the two solvents, partly because only one column was used in the toluene separations, while two columns were used in the THF separations. The SEC chromatograms were divided into LMS, MMS, and SMS sections. Asphalts exhibited unique SEC chromatograms depending on the crude oils (sources) from which they were derived, as would be expected. Different viscosity grades from identical sources are characterized by similar, but distinguishable, SEC chromatograms. In a related study, Glover et al. (1987) also showed that SEC could be used to monitor seasonal changes in asphalts obtained from various suppliers in Texas. The authors emphasize that asphalts from various sources having identical viscosity grades may exhibit widely different SEC chromatograms, demonstrating that there is little correlation between asphalt viscosity (which is a made-to-order property depending on the method of manufacture) and composition as measured by SEC.

Davison et al. (1995) have done extensive research on changes in SEC chromatograms as asphalts oxidatively age. They found that LMS increase in the chromatograms correlates with degree of oxidation and also is asphalt dependent.

Along with other researchers, Glover et al. (1988) found good correlations between relative amounts of LMS in SEC chromatograms of neat asphalts with the physical parameter viscosity–temperature susceptibility (VTS). This parameter measures the rate of change of viscosity as a function of temperature, and is an important predictor of pavement performance. The same correlation was not observed in asphalts recovered from pavement cores. Asphalts having small amounts of LMS, as determined by SEC, often were found to be prone to "tenderness" in mixes. The tendency toward tenderness could also be measured by the Heithaus test (see Section 2.2.1). Asphalts low in apshaltene content usually, but not always, exhibit low LMS peaks in their SEC chromatograms.

Bishara and McReynolds (1990, 1992), and Bishara et al. (1991) at the Kansas Department of Transportation utilized SEC to study molecular size distributions of neat and aged asphalts, and samples of asphalts obtained from pavement cores. Instead of using data obtained from UV and RI detectors, they developed a technique utilizing a gravimetric finish to calculate molecular size distributions. Asphalts contain molecules that do not absorb in the UV–vis range, so this fact limits the accuracy by which UV detectors can monitor MW distributions. Even those compounds that are UV-active will have different molar absorptivities. It has been alleged that MW data

www.EngineeringEBooksPdf.com

obtained from RI data have reproducibility problems, and refractive indices vary with MW. Bishara and McReynolds dissolved small (<5 mg) samples of asphalts in THF and injected the solutions into an SEC column. A mixture of THF with a small amount of pyridine (to prevent tailing) was the carrier solvent. Various fractions were collected, solvent was removed, and the separate fractions were weighed on a microbalance. Cut points were determined from retention times of polystyrene standards. Bishara et al. (1991) and Bishara and McReynolds (1992, 1993) claim that the adoption of a gravimetric finish resolves those difficulties encountered in comparing results from different SEC columns.

Following the practice of Jennings, Bishara and McReynolds divided asphalt SEC chromatograms into molecular size regions of LMS, MMS, and SMS. The SMS regions of the asphalts studied were minor compared with the other two regions. Molecular size distributions were calculated based on relative amounts of LMS and MMS in the SEC chromatograms. Bishara, McReynolds, and Lewis correlated the molecular size distributions with various physical and chemical properties of 20 neat asphalts. Good correlations were observed with VTS and penetration viscosity number (PVN) at 135 °C (275 °F), but not with PVN at 60 °C (140 °F). They also found relationships between the molecular size distributions and two compositional parameters, asphaltene content and the Gaestel index. When the asphalts were treated by the thin-film oven (TFO) aging test, LMS-to-MMS ratios increased. The authors summarize their results in the statement that good field performance should be correlated with low VTS and high resistance to oxidative aging. The asphalts they examined that had relatively high LMS/MMS ratios were desirable on both counts. Their results indicate that SEC should be a good method for screening asphalts for acceptable values of these properties.

Burati and co-workers have studied the correlation of asphalt physical properties with SEC molecular size distributions by dividing the chromatograms into a large number of fractions (Kim and Burati, 1993; Kim et al., 1993, 1995; Churchill et al., 1995). Price and Burati (1989) claim that for binders alone, physical tests in current use are not particularly good predictors of long-term pavement performance. This statement appears to contradict previous assertions that VTS is a good performance predictor, but the authors emphasize long-term performance, which is strongly influenced by oxidative age hardening of binders. They also claim that most chemical fractionation data are not useful for mix designs. The SEC method, however, differentiates among asphalts of the same viscosity grade and should be useful in performance prediction. Price and Burati (1989) showed that molecular size distributions determined from SEC profiles of several asphalts were related to penetration, PVN, VTS, and other physical parameters. Kim et al. (1993) found that too much LMS material resulted in lower tensile strengths of binders. In other work, Kim et al. (1995) observed that those components corresponding to the first 17% of the SEC chromatograms have the most significant correlation with selected physical properties. They claim that this initial fraction, as determined by RI, should be designated the LMS fraction rather than LMS fractions designated by other researchers. Their SEC chromatograms were subdivided into 30 slices, the first 11 of which comprise the LMS fraction. Interestingly, it is claimed that a particular subfraction of the

www.EngineeringEBooksPdf.com

LMS fraction proved to be better correlated with physical properties than the subfraction containing the largest molecules. Kim and Burati (1993) and Churchill et al. (1995) studied molecular size distribution profiles of aged asphalts by the methods described above. They found, as have other researchers, that asphalts having similar initial physical properties exhibit differences in aging behavior.

The significance of the above results is that a molecular size distribution profile obtained by SEC can be a surrogate for a variety of physical measurements. Even if the particular physical measurements are not good predictors of pavement performance, the SEC method would be no worse.

Noureldin and Wood (1989) reported the use of SEC to evaluate the effect of recycling agents on molecular size distributions of aged asphalts. The subjects of their experiments were asphalts that were artificially aged in the laboratory or were field aged and recovered from pavements. The SEC chromatograms of the materials were divided into LMS, MMS, and SMS portions in accordance with the precedent established by Jennings. It was observed that the relative amount of LMS in the chromatograms increased with aging severity. Adding recycling agents to the aged binders did not always restore the original molecular size distribution of parent-unaged binders, although some physical properties were restored to those of the original materials. Some recycling agents caused reduced amounts of LMS materials in the SEC chromatograms of the age-hardened binders, but also increased the amounts of the SMS materials. The MMS fractions of the aged binders treated with recycling agents were observed to be low compared with original materials. Noureldin and Wood point out that, in sufficient amounts, most recycling agents can restore the original consistency to aged binders. However, the important property VTS might not be restored to its original value. They advise that recycling agents be chosen so that the molecular size distributions of aged asphalts are restored as closely as possible to original values.

Garrick and Wood (1986) and Garrick and Biskur (1990) investigated the relationship between selected asphalt physical properties and SEC profiles. Three physical properties were of particular interest in their studies: (1) rheological type, measured by PVN and VTS; (2) durability, measured by the ratio of viscosities at 60 °C (140 °F) before and after a TFO test; and (3) consistency, measured by viscosity at 60 °C (140 °F). In order to relate the SEC data with the physical properties, the SEC chromatograms were divided into several areas. Garrick showed that there exists a good relationship between SEC profiles and asphalt rheological type. Asphalts with broad molecular size distributions tend not to be temperature susceptible, based on VTS, the opposite being true of asphalts with narrower molecular size distributions. The latter are more durable (Garrick, 1992, 1994). Garrick extended his analysis to analytical SEC data reported by Duvall for SHRP asphalts (1993). Physical properties of the SHRP asphalts were used to predict shapes of SEC profiles using Garrick's method. Good correlations with the actual results of Duvall, who used a different method to obtain SEC data, were observed.

In the Binder Characterization and Evaluation Project of SHRP, preparative SEC was extensively employed (Duvall et al., 1993). In a typical separation, a toluene solution of a 16 g asphalt sample was introduced into a large jacketed glass column (which allowed the progress of the separation to be monitored visually) filled with a

www.EngineeringEBooksPdf.com

polystyrene-divinyl benzene gel swelled in toluene. The column was maintained at 40 °C (104 °F). After breakthrough of colored material from the column, the initial cut point was based on fluorescence. Many years ago, Dr George Wu observed that the initial eluates in preparative SEC separations of heavy crudes, tar sand bitumens, and asphaltenes derived from these materials do not fluoresce when irradiated with 350 nm light. At a certain point in the preparative SEC separations, eluates suddenly exhibit fluorescence to 350 nm light. In some of the preparative SEC separations, this was the only cut point, so asphalts were only separated into two fractions, designated SEC fraction-I and SEC fraction-II. In other preparative SEC separations, the materials collected after the onset of fluorescence were collected as eight subfractions. Upon completion of each separation, the various fractions were dried, weighed, and subjected to various analyses. The SEC chromatograms of eight SHRP core asphalts are illustrated in Figure 2.3. Mass fraction data are plotted versus percentages of bed volume. The clear division of the SEC fraction-I materials from the remaining SEC fractions is evident for all but one of the asphalts.

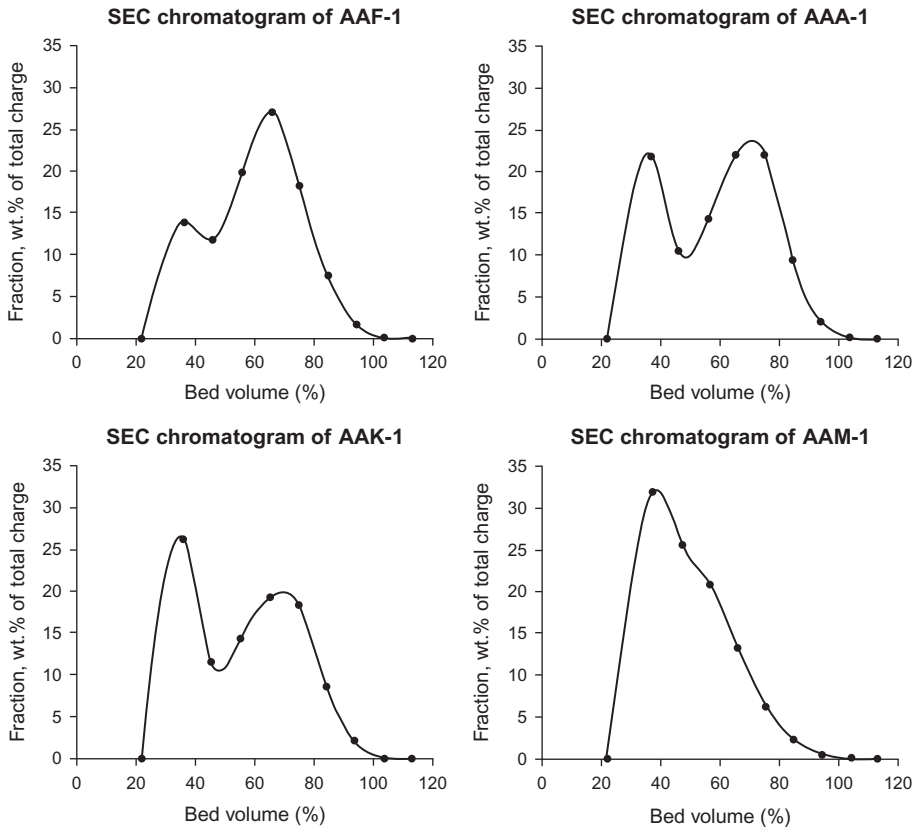


Figure 2.3 SEC chromatograms of core asphalts (SHRP-A-368, 1993).

www.EngineeringEBooksPdf.com

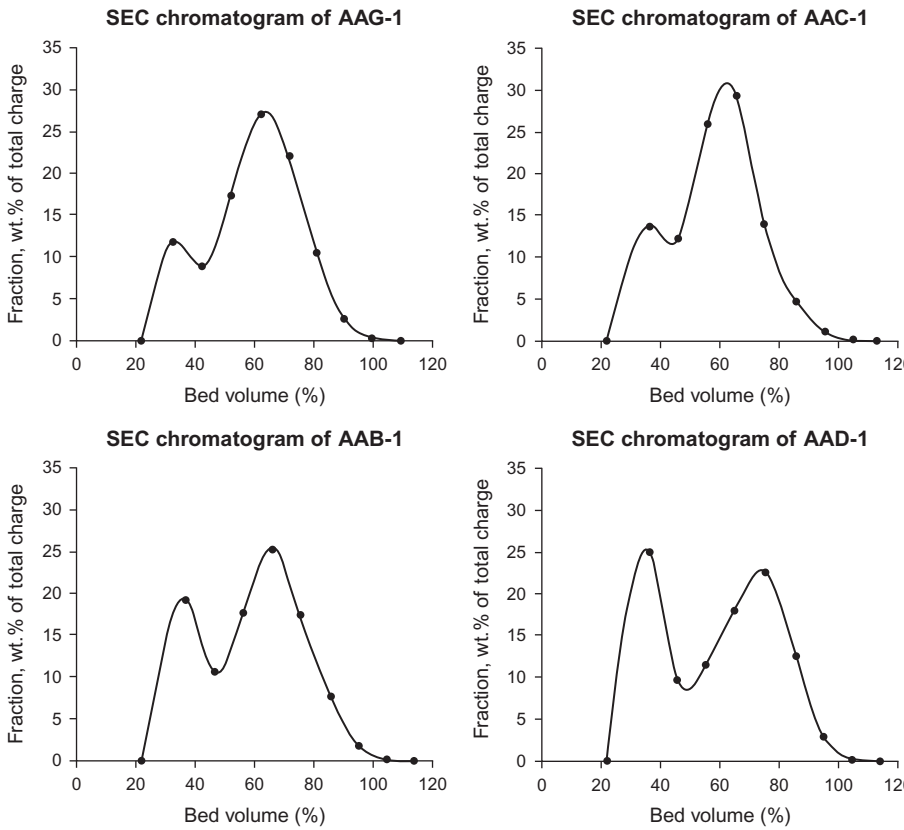


Figure 2.3. Continued.

It is speculated that the nonfluorescent SEC fraction-I materials correspond to the dispersed component of an asphalt. Those materials contain those asphalt components of highest MW and the most aromatic constituents. Individually, the aromatic molecules would be expected to be fluorescent, but molecular association tends to suppress fluorescence. Thus, the molecules comprising the SEC fraction-I materials are involved in associative interactions, in accord with the colloidal model. Buisine et al. (1993) reported similar observations.

In the preparative SEC separations of the eight SHRP core asphalts, the amount of the initial SEC fraction-I materials varied considerably among the asphalts. In those separations in which eight subfractions of SEC fraction-II were collected, the middle subfractions contained the most amount of material. The last two subfractions contained minor amounts of material. The preparative SEC method thus results in separation of asphalts into bimodal distributions, in accordance with what was observed by the analytical separations.

www.EngineeringEBooksPdf.com

MW values of the preparative SEC fractions, determined by VPO, decreased from the initial fraction to the last subfraction. For one of the SHRP asphalts, AAK-1, SEC fractions-I had a MW value of 10,000 Da, while the final measured subfraction had a MW value of 340 Da. Turner et al. (1995) reported a relationship between elution order of the preparative SEC fractions and glass transition temperature. Other chemical and physical properties of the preparative SEC fractions have been reported. The SEC fraction-I materials are black, friable solids. The SEC fraction-II materials are viscous liquids that are much lower in viscosity than their parent asphalts (SHRP-A-368, 1993).

In theory, the SEC fraction-I materials might be considered the dispersed phase of an asphalt, and SEC fraction-II materials the solvent phase. If so, the question arises as to whether the nature of the dispersed and solvent phases (as represented by the two SEC fractions) is as important in influencing rheological properties of asphalts as the relative amounts of the two phases. To test this theory, cross-blended mixtures of SEC fractions of four SHRP asphalts were prepared. For each cross-blended mixture, the variables considered were the source of each of the two SEC fractions and their relative abundances. For a given asphalt, there is a specific natural abundance level of the two SEC fractions. For each set of cross-blends of two asphalts, eight mixtures were prepared. Four of the mixtures contain the SEC fraction-II materials of one asphalt, and four mixtures contain SEC fraction-II materials of the other asphalt. Each set of four cross-blends is combined with one or the other SEC fraction-I materials at one of the two natural abundance levels. Two of the eight cross-blends reconstitute the original asphalts. Rheological data on the cross-blends were obtained (Robertson et al., 2001a,b). Cross-blends of some asphalts did not differ greatly from one another with respect to rheological properties, while other cross-blends exhibited great differences. These differences could not be accounted for solely by relative amounts of the two fractions. Rheological properties of those cross-blends must be determined by the nature of the components and their mutual compatibility, a finding that must be taken into account when fundamentally different asphalt types are blended.

2.6 Summary

Asphalts are highly complex mixtures of a wide variety of chemical compounds. Before the advent of chromatographic techniques, chemical separation methods yielded limited information about relationships between asphalt composition and performance-related physical properties. Eventually, the chromatographic techniques allowed for rapid profiling of asphalts and their separation into defined fractions were based on chemical-type or molecular size. The fractions so obtained then could be studied by other methods. As a result of these efforts, a model of asphalt microstructure was developed over the years, which rationalizes many of the interesting properties of binders.

This chapter has focused on the development of classical methods of asphalt analysis and separation. Contemporary refinements of these methods hopefully will prove to be even more valuable techniques applied to asphalt science.

www.EngineeringEBooksPdf.com

Disclaimer

The contents of this chapter reflect the views of the authors and others cited herein. The contents do not necessarily reflect the official views or policy of any government agency.

Acknowledgments

The authors thank the Strategic Highway Research Program and the Federal Highway Administration for support of some of the research reported herein. Thanks are expressed to Miss Rachel Huang and Miss Caitlin Huang for their help in the preparation of this manuscript.

References

Altgelt, K.H., 1965. Fractionation of asphaltenes by gel permeation chromatography. J. Appl. Polym. Sci. 9, 3389.

Altgelt, K.H., Harle, O.L., 1975. The effect of asphaltenes on asphalt viscosity. Ind. Eng. Chem. Prod. Res. Dev. 14, 240.

Altgelt, K.H., Hirsh, E., 1970. GPC separation and integrated structural analysis of petroleum heavy ends. Sep. Sci. 5, 855.

ASTM D4124-09, 2009. Standard Test Method for Separation of Asphalt into Four Fractions. ASTM International, West Conshohocken, PA.

Bahia, H.U., Anderson, D.A., 1995. Strategic Highway Program binder rheological parameters: background and comparison with conventional properties. Transportation Research Record, TRB, National Research Council, No. 1488, pp. 32–39.

Barth, E.J., 1962. Asphalt. Gordon and Breach, New York.

Bishara, S.W., McReynolds, R.L., 1990. Use of HPGPC with UV detection for determination of molecular size distribution of asphalt cement after quantitative correction for molar absorptivity variation and saturated oils. Transportation Research Record, TRB, National Research Council, No. 1296, pp. 40–47.

Bishara, S.W., McReynolds, R.L., 1992. A new approach for the determination of MSD of asphalt cement using HPGPC. Fuel Sci. Technol. Int. 10, 433.

Bishara, S.W., McReynolds, R.L., 1993. Gravimetric determination of molecular size distribution of asphalt using HPGPC. Overcoming problems associated with column source. In: Presented at Petersen Conference, Laramie, WY, July.

Bishara, S.W., McReynolds, R.L., Lewis, E.R., 1991. Interrelationship between performance-related properties of asphalt cement and their correlation with molecular size distribution. Transportation Research Record, TRB, National Research Council, No. 1323, pp. 1–9.

Boduszynski, M., 1988. Composition of heavy petroleums, 2, molecular characterization. Energy Fuel. 2, 597.

Boduszynski, M., Chadha, B.R., Pineles, H., 1977a. Investigations on Romashkino asphaltic bitumen, 1, use of ion-exchange and adsorption chromatography for the separation of maltenes. Fuel 56, 145.

Boduszynski, M., Chadha, B.R., Szkuta-Pochopien, T., 1977b. Investigations on Romashkino asphaltic bitumen, 3, fractionation of asphaltenes using ion-exchange chromatography. Fuel 56, 432.

www.EngineeringEBooksPdf.com

Boduszynski, M., McKay, J.F., Latham, D., 1981. Composition of heavy ends of a Russian petroleum. Prepr. Div. Fuel Chem. Am. Chem. Soc. 26 (4), 865.

Breen, J.J., Stephens, J.E., 1969. The interrelationship between the glass transition temperature and molecular characteristics of asphalt. In: Proceedings, Association of Asphalt Paving Technologists, vol. 38, pp. 706–712.

Brule, B., 1979. Characterization of bituminous compounds by gel permeation chromatography (GPC). J. Liq. Chromatogr. 2, 165.

Brule, B., 1980. Contribution of gel permeation chromatography (GPC) to the characterization of asphalts. In: Cazes, J., Delamare, X. (Eds.), Liquid Chromatography of Polymers and Related Materials. Marcel Dekker, New York, pp. 215–248.

Brule, B., Ramond, G., Such, C., 1986. Relationships between composition, structure, and properties of road asphalts: state of research at the French Public Works Central Laboratory. Transportation Research Record, TRB, National Research Council, No. 1096, pp. 22–34.

Brule, B., Ramond, G., Such, C., 1994. Relationships among the composition, structure, and properties of road asphalts. In: Yen, T.F., Chilingarian, G.V. (Eds.), In: Asphaltenes and Asphalts, vol. 1. Elsevier, New York, pp. 427–449.

Buisine, J.M., Joly, G., Eladlani, A., Such, C., Farcas, F., Ramond, G., Claudy, P., Letoffe, J.M., King, G.N., Planche, J.P., Germanaud, L., 1993. Thermodynamic behavior and physico-chemical analysis of eight SHRP bitumens. Transportation Research Record, TRB, National Research Council, No. 1386, pp. 1–9.

Bynum, D., Traxler, R.N., 1970. Gel permeation chromatography data on asphalts before and after service in pavements. In: Proceedings, Association of Asphalt Paving Technologists, vol. 39, pp. 683–702.

Carbognani, L., Orea, M., 1999. Studies on large crude oil alkanes. I. High temperature liquid chromatography. Petrol. Sci. Technol. 17, 165.

Carbognani, L., De Lima, L., Orea, M., Ehrmann, U., 2000. Studies on large crude oil alkanes. II. Isolation and characterization of aromatic waxes and waxy alkanes. Petrol. Sci. Technol. 18, 607.

Churchill, E.V., Amirkhanian, S.N., Burati, J.L., 1995. HP-GPC characterization of asphalt aging and selected properties. J. Mater. Civil Eng. 7, 41.

Claudy, P., Letoffe, J.M., King, G.N., Planche, J.P., 1992. Characterization of asphalt cements by thermomicroscopy and differential scanning calorimetry: correlation to classic physical properties. Fuel Sci. Technol. Int. 10, 735.

Corbett, L.W., 1970. Relationship between composition and physical properties of asphalt. In: Proceedings, Association of Asphalt Paving Technologists, vol. 39, pp. 481–491.

Corbett, L.W., Merz, R.E., 1975. Asphalt binder hardening in the Michigan Test Road after 18 years of service. Transportation Research Record, TRB, National Research Council, No. 544, pp. 27–34.

Davison, R.R., Glover, C.J., Burr, B.L., Bullin, J.A., 1995. SEC of asphalts. In: Wu, C.-s. (Ed.), Handbook of Size Exclusion Chromatography. Marcel Dekker, New York, pp. 211–247.

Dukatz, E.L., Anderson, D.A., Rosenberger, J.L., 1984. Relationship between asphalt flow properties and asphalt composition. In: Proceedings, Association of Asphalt Paving Technologists, vol. 53, pp. 160–185.

Duvall, J.J., Miyake, G., Catalfomo, M.W., Kim, S.S., Colgin, D.C., Branthaver, J.F., 1993. Size exclusion chromatography and ion exchange chromatography separations of asphalts. Strategic Highway Research Program, SHRP-A-663, National Research Council, Washington, DC.

Filby, R.A., & Branthaver, J.F. (Eds.), 1987. Metal Complexes in Fossil Fuels. ACS Symposium Series, vol. 344. American Chemical Society, Washington, DC.

www.EngineeringEBooksPdf.com

Gaestel, C., Smadja, R., Lamminan, K.A., 1971. Contribution a la connaissance des proprietes des bitumesroutiers. Rev. Gen. Routes Aerodr. 466, 85.

Garrick, N.W., 1992. Modeling the effects of temperature and shear rate on the viscosity of asphalt cements. In: Proceedings, Association of Asphalt Paving Technologists, vol. 61, pp. 1–26.

Garrick, N.W., 1994. Use of gel-permeation chromatography in predicting properties of asphalt. J. Mater. Civil Eng. 6, 376.

Garrick, N.W., Biskur, R.R., 1990. A classification system for interpreting GPC profiles of asphalts. In: Proceedings, Association of Asphalt Paving Technologists, vol. 59, pp. 33–53.

Garrick, N.W., Wood, L.E., 1986. Relationship between high-pressure and gel permeation chromatography data and the rheological properties of asphalts. Transportation Research Record, TRB, National Research Council, No. 1096, pp. 35–41.

Girdler, R.B., 1965. Constitution of asphaltenes and related studies. In: Proceedings, Association of Asphalt Paving Technologists, vol. 34, pp. 45–79.

Glover, C.J., Bullin, J.A., Button, J.W., Davison, R.R., Donaldson, G.R., Hlavinka, M.W., Philip, C.V., 1987. Characterization of asphalts using gel permeation chromatography and other methods. Research Report 419-1 F, Study 2-9-84-419 State Department of Highways and Public Transportation, Austin, TX, May 1987.

Glover, C.J., Davison, R.R., Bullin, J.A., Button, J.W., Donaldson, G.R., 1988. Chemical characterization of asphalt cement and performance-related properties. Transportation Research Record, TRB, National Research Council, No. 1171, pp. 71–81.

Goodrich, J. L., Goodrich, J.E., Kari, W.J., 1986. Asphalt composition tests: their application and relation to field performance. Transportation Research Record, TRB, National Research Council, No. 1096, pp. 146–167.

Green, J.B., Hoff, R.J., Woodward, P.W., Stevens, L.L., 1984. Separation of liquid fossil fuels into acid, base, and neutral concentrates, 1. An improved nonaqueous ion exchange method. Fuel 63, 1290.

Green, J.B., Reynolds, J.W., Yu, S.K., 1989. Liquid chromatographic separations as a basis for improving asphalt composition-physical property correlations. Fuel Sci. Technol. Int. 7, 1327.

Groenzin, H., Mullins, O., 2000. Molecular size and structure of asphaltenes from various sources. Energy Fuel. 14, 677.

Gupta, A., Agrawal, K., 2000. Crystallinity and average carbon number of petroleum waxes by X-ray diffraction. Petrol. Sci. Technol. 18, 141.

Haley, G., 1975. Changes in chemical composition of a Kuwait short residue during air blowing. Anal. Chem. 47, 2432.

Heithaus, J.J., 1962. Measurement and significance of asphaltenepeptization. J. Inst. Petrol. 48, 45.

Hubbard, R.L., Stanfield, K.E., 1948. Determination of asphaltenes, oils, and resins in asphalt. Anal. Chem. 20, 460.

Jennings, P.W., Pribanic, J.A.S., 1989. A perspective on asphalt chemistry research and the use of HP-GPC analysis. Fuel Sci. Technol. Int. 7, 1269.

Jennings, P.W., Pribanic, J.A.S., Smith, J., Mendes, T.M., 1988. Predicting the performance of Montana test sections by physical and chemical testing. Transportation Research Record, TRB, National Research Council, No. 1171, pp. 59–65.

Jennings, P.W., Pribanic, J.A.S., Mendes, T.M., Smith, J.A., 1992. High performance gel permeation chromatography in the characterization of self-assemblies in asphalt. I. Fuel Sci. Technol. Int. 10, 809.

www.EngineeringEBooksPdf.com

Kim, K.W., Burati, J.L., 1993. Use of GPC chromatograms to characterize aged asphalt cements. J. Mater. Civil Eng. 5, 41.

Kim, K.W., Burati, J.L., Amirkhanian, S.N., 1993. Relation of HP-GPC profile with mechanical properties of AC mixtures. J. Mater. Civil Eng. 5, 447.

Kim, K.W., Burati, J.L., Park, J.S., 1995. Methodology for defining LMS portion in asphalt chromatogram. J. Mater. Civil Eng. 7, 31.

Marvillet, J., 1975. Influence of asphalt composition on its rheological behavior. In: Proceedings, Association of Asphalt Paving Technologists, vol. 44, pp. 416–443.

McKay, J.F., Amend, P.J., Cogswell, T.E., Harnsberger, P.M., Erickson, R.B., & Latham, D.R., 1978. Petroleum asphaltenes: chemistry and composition. In: Uden, P., Siggia, S., Jensen, H. (Eds.), Analytical Chemistry of Liquid Fuel Sources. In: Advances in Chemistry Series, vol. 170. American Chemical Society, Washington, DC, pp. 128–142.

McKay, J.F., Branthaver, J.F., Robertson, R.E., 1995. Isolation of waxes from asphalts and the influence of waxes on asphalt rheological properties. Prepr. Div. Fuel Chem. Am. Chem. Soc. 40, 794.

Noureldin, A.S., Wood, L.E., 1989. Variations in molecular size distribution of virgin and recycled asphalt binders associated with aging. Transportation Research Record, TRB, National Research Council, No. 1228, pp. 191–197.

Otocka, E.P., 1973. Modern gel permeation chromatography. Acc. Chem. Res. 6, 348–354.

Pauli, A.T., 1996. Asphalt compatibility testing using the automated Heithaus titration test. Prepr. Div. Fuel Chem. Am. Chem. Soc. 41, 1276.

Petersen, J.C., 1984. Chemical composition of asphalt as related to asphalt durability: state of the art. Transportation Research Record, TRB, National Research Council, No. 999, pp. 13–30.

Peterson, G.D., Davison, R.R., Glover, C.J., Bullin, J.A., 1994. Effect of composition on asphalt recycling agent performance. Transportation Research Record, TRB, National Research Council, No. 1436, pp. 38–53.

Pfeiffer, J.P., Saal, R.N.J., 1940. Asphaltic bitumen as a colloidal system. J. Phys. Chem. 44, 139.

Plummer, M.A., Zimmerman, C.C., 1984. Asphalt quality and yield predictions from crude oil analyses. In: Proceedings, Association of Asphalt Paving Technologists, vol. 53, pp. 138–159.

Preece, S.C., Branthaver, J.F., Kim, S.S., 1992. Separation of a quinoline-enriched fraction from SHRP asphalts. Prepr. Div. Fuel Chem. Am. Chem. Soc. 37, 1342.

Pribanic, J.A.S., Emmelin, M., King, G.N., 1989. Use of a multiwavelength UV–VIS detector with HP-GPC to give a three-dimensional view of bituminous materials. Transportation Research Record, TRB, National Research Council, No. 1228, pp. 168–176.

Price, R.P., Burati, J.L., 1989. A quantitative method using HP-GPC to predict laboratory results of asphalt cement tests. In: Proceedings, Association of Asphalt Paving Technologists, vol. 58, pp. 182–219.

Ramljak, Z., Solc, A., Arpino, P., Schmitter, J., Guiochon, G., 1977. Separation of acids from asphalts. Anal. Chem. 49, 1222.

Redelius, P., 2000. Solubility parameters and bitumen. Fuel 79, 27.

Reerink, H., Lijzenga, J., 1975. Gel-permeation chromatography calibration curve for asphaltene and bituminous resins. Anal. Chem. 47, 2160.

Robertson, R.E., Branthaver, J.F., Harnsberger, P.M., Petersen, J.C., Dorrence, S.M., McKay, J.F., Turner, T.F., Pauli, A.T., Huang, S.C., Huh, J.D., Tauer, J.E., Thomas, K.P., Netzel, D.A., Miknis, F.P., Williams, T., Duvall, J.J., Barbour, F.A., Wright, C., 2001a. Fundamental

www.EngineeringEBooksPdf.com

properties of asphalts and modified asphalts, volume I, interpretive report. Final Report for Federal Highway Administration Contract No. DTFH61-92C-00170, October, 2001.

Robertson, R.E., Branthaver, J.F., Harnsberger, P.M., Petersen, J.C., Dorrence, S.M., McKay, J.F., Turner, T.F., Pauli, A.T., Huang, S.C., Huh, J.D., Tauer, J.E., Thomas, K.P., Netzel, D.A., Miknis, F.P., Williams, T., Duvall, J.J., Barbour, F.A., Wright, C., Salmans, S.L., Hansert, A.F., 2001b. Fundamental properties of asphalts and modified asphalts, volume II, new methods. Final Report for Federal Highway Administration Contract No. DTFH61-92C-00170, October, 2001.

Salmans, S.L., Pauli, A.T., Branthaver, J.F., Robertson, R.E., Gardner, G.W., 1998. Properties of asphalt neutral fractions. In: Presented at the 35th Annual Petersen Asphalt Research Conference, Laramie, Wyoming, July 13, 1998.

Schabron, J.F., Rovani, J.F., Sanderson, M.M., Loveridge, J.L., McKenna, A.M., Marshall, A. G., 2012. Waxphaltene determinator method for automated precipitation and redissoluion of wax and asphaltene components. Energy Fuel 26, 2256–2268.

Selucky, M.L., Kim, S.S., Skinner, F., Strausz, O.P., 1981. Structure-related properties of Athabaskaasphaltenes and resins as indicated by chromatographic separation. In: Bunger, J.W., Li, N.C. (Eds.), Chemistry of Asphaltenes. In: Advances in Chemistry Series, vol. 195. American Chemical Society, Washington, DC, pp. 83–118.

SHRP-A-368, 1993. In: Binder Characterization and Evaluation. In: Chemistry, Strategic Highway Research Program, vol. 2. National Research Council, Washington, DC.

Speight, J.G., 1987. Initial reactions in the coking of residua. Prepr. Div. Fuel Chem. Am. Chem. Soc. 32, 413.

Sugihara, J.M., Branthaver, J.F., Wu, G.Y., Weatherbee, C., 1970. Research on metal compounds in petroleum-present and future. Prepr. Div. Fuel Chem. Am. Chem. Soc. 15, C5.

Thanh, N., Hsieh, M., Philp, R., 1999. Waxes and asphaltenes in crude oils. Org. Geochem. 30, 119.

Traxler, R.N., 1960. Relation between hardening and composition of asphalt. Prepr. Div. Fuel Chem. Am. Chem. Soc. 5, A-71.

Traxler, R.N., 1961. Asphalt. Reinhold Publishing Co., New York.

Traxler, R.N., Schweyer, H.E., 1953. Separating asphalt materials-butanol acetone method. Oil Gas J. 52, 158.

Turner, T.F., Kim, S.S., Branthaver, J.F., McKay, J.F., 1995. Chemical compositional effects on glass transition phenomena in asphalt. In: Symposium on Chemistry and Technology of Asphalt-Containing Materials, 210th Meeting of the American Chemical Society, Chicago, IL, August 22, 1995.

Wan, C.C., Waters, T.H., Wolever, R.D., 1992. Development of a reproducible iatroscan method to chemically characterize asphalt. Prepr. Div. Fuel Chem. Am. Chem. Soc. 37, 1350.

www.EngineeringEBooksPdf.com

Tridimensional linear viscoelastic behavior of bituminous materials

3

C. Sauzeat, H. Di Benedetto
University of Lyon/ENTPE (Ecole Nationale des Travaux Publics de l'Etat), Vaulx en Velin, France

3.1 Introduction

In order to analyze the structural behavior of pavements and its evolution with time, thermomechanical properties of bituminous mixtures must be investigated with regard to the following aspects:

- Stiffness and stiffness change with time in the linear domain.
- Fatigue and damage law evolution.
- Permanent deformation and accumulation of this deformation.
- Crack and crack propagation, particularly at low temperature.

These four properties are of main interest when analyzing pavement behavior. The first one is observed for very small strain amplitudes and corresponds to linear viscoelastic (LVE) behavior of mixtures. The other three aspects are at the origin of major distresses, respectively: degradation by fatigue, rutting, and crack propagation. Each of these properties or distresses appears for a given domain of loading and corresponds to a specific type of behavior for the mixtures.

When considering the plot of Figure 3.1, proposed by Di Benedetto (1990), it is possible to identify the domains corresponding to the different aspects previously introduced and the corresponding "typical" type of behavior of mixtures. Of course, this figure is schematic, and the boundaries of the different domains should be considered as a general indication. In reality, the transition from one domain to another is made in a smooth and continuous way.

In order to cope with the complexity of the observed problems, as well as the appearance of new types of structures, new innovative materials, and increasing durability concerns, the use of rational methods is needed. Work has already been done in this direction, such as the developments of the French method (SETRA-LCPC, 1997; NF P98-086, AFNOR, 2011), applied since the 1970s, and more recently, efforts engaged in the United States within the framework of the Strategic Highway Research Program (1988–93, continued after 1996), which allowed the development of the Superpave method and the American Association of State Highway and Transportation Officials (AASHTO, 1993) pavement design guide.

In this chapter, we will focus on the 3D LVE behavior of bituminous materials. LVE behavior has been widely studied in the one-dimensional case. Nevertheless, considering the complex stress and strain state occurring in the pavement under traffic,

Advances in Asphalt Materials. http://dx.doi.org/10.1016/B978-0-08-100269-8.00003-9
© 2015 Elsevier Ltd. All rights reserved.

www.EngineeringEBooksPdf.com

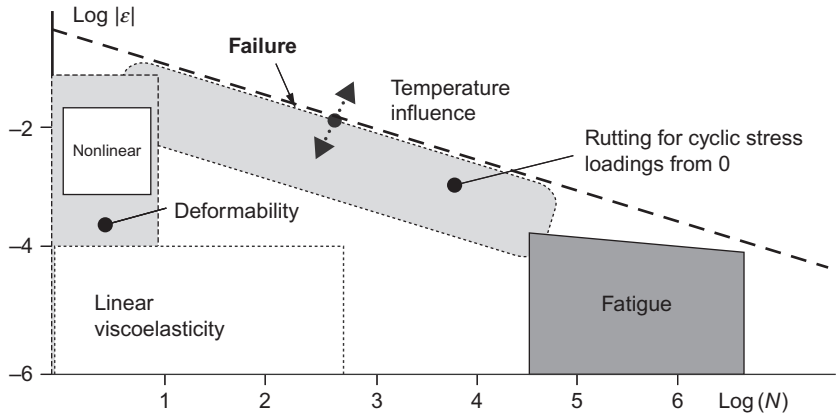


Figure 3.1 Domains of behavior for bituminous mixtures (ε, strain amplitude; N, number of cycles).
From Di Benedetto (1990).

it is of outmost importance to obtain a complete 3D characterization of bituminous materials. Although a gap still exists between the results obtained from research and the introduction of this knowledge in design methods, computation and calculation methods (such as finite element methods) are nowadays sufficiently powerful to implement 3D models for more realistic simulation of bituminous pavements.

In the following, experimental tools developed to investigate 3D behavior are presented. Then, observed 3D LVE behavior is shown for different bituminous materials. Some characteristics are specifically analyzed, such as the validity of the time–temperature superposition principle in 3D, the anisotropy, and the influence of loading history.

The rheological 2S2P1D model, capable of describing the observed 3D LVE behavior of bituminous materials, is also introduced. Then, the proposed method to obtain the LVE properties of mixtures from bitumen (and vice versa) is described.

The developments presented hereafter are based on many works corresponding mainly to PhD studies performed in the laboratory of the University of Lyon/ENTPE (Ecole Nationale des Travaux Publics de L'Etat) approximately in the last decade.

3.2 Complex modulus and complex Poisson's ratio tests

A complex modulus can be obtained from different types of tests, using different specimen geometries and loading configurations. Several existing tests are nonhomogeneous and are based on back analysis of obtained measurements. First, the behavior of the tested material must be assumed, and then the parameters of constitutive equations are deduced from measurements. In order to obtain directly the behavior of the studied materials without the need for hypotheses, homogeneous tests should be carried out.

www.EngineeringEBooksPdf.com

This is the approach chosen by the University of Lyon/ENTPE laboratory to study bituminous materials. Tension/compression tests are performed with different specimen sizes and geometries (Di Benedetto et al., 2007a, 2011; Mangiafico et al., 2013; Nguyen et al., 2009, 2013; Pouget et al., 2010; Tapsoba et al., 2014).

3.2.1 Testing devices and specimens

Tension/compression tests are carried out using a hydraulic press, equipped with a load cell, used to monitor axial stress. The electronic control system allows one to perform axial stress-controlled or axial strain-controlled tests.

A thermal chamber is used for thermal conditioning of specimens during tests. Temperature is measured using a thermal sensor (e.g., a PT100 temperature probe) fixed on the surface of the specimen.

A general view of the equipment is shown in Figure 3.2.

Different devices can be used to measure locally the strain at the surface of the specimen, depending on specimen size and shape.

Usually, a cylindrical specimen is used, with a height ranging from 120 to 160 mm, and a diameter from 75 to 80 mm. Several studies were carried out using three axial extensometers located at 120° around the specimen to measure axial strain (Figure 3.3). Axial strain is considered the mean of the three measurements. Radial strain can be obtained from two noncontact displacement transducers (with a 500 μm range) that measure diameter changes at mid-height of the specimen. In order to study the potential anisotropy of the materials, four noncontact displacement transducers have also been used to measure specifically the radial strains in two orthogonal directions.

In some other studies (Clec'h et al., 2009, 2010), in order to measure axial and lateral strain, 50 mm long-strain gauges have been used. For cylindrical samples, four strain gauges were placed diametrically: two to measure axial strain and two to measure orthoradial strain. For parallelepiped samples, six gauges have been used (two for axial and four for radial strain).

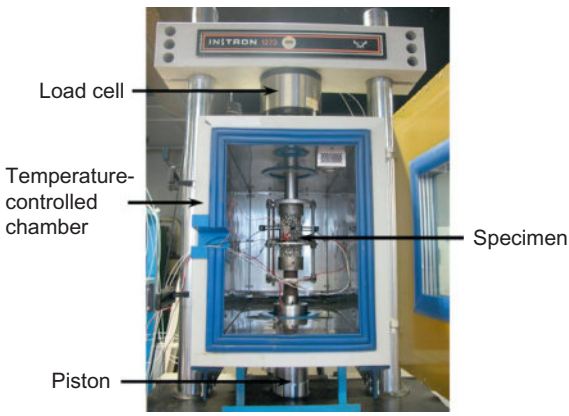


Figure 3.2 General view of the test equipment at the University of Lyon/ENTPE.

www.EngineeringEBooksPdf.com

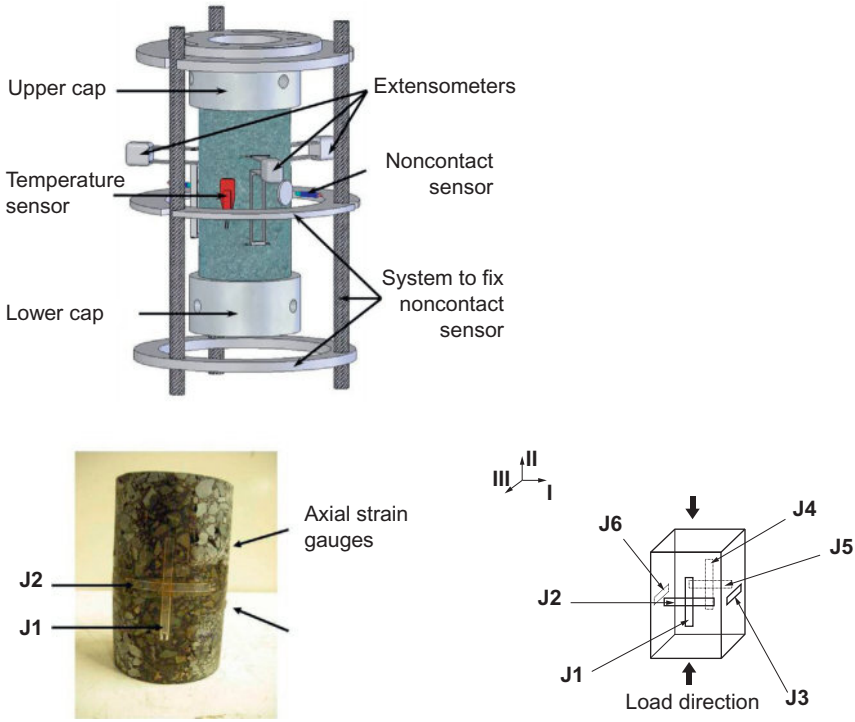


Figure 3.3 Two different strain measurement systems developed at the University of Lyon/ENTPE to measure axial strain and radial strain with extensometers, noncontact transducers, and strain gauges.

3.2.2 Test principle

Advanced complex modulus tests have been carried out using the described equipment. Sinusoidal tension/compression axial loading is applied at different loading frequencies, ranging from 0.001 to 10 Hz, and different temperatures, ranging from −30.0 to 60.0 °C, in order to determine the viscoelastic properties of tested materials on a range as wide as possible. Axial strain amplitude is chosen so that the behavior remains in the linear domain, namely small-strain amplitude domain. As it is intended to measure complex Poisson's ratio, axial amplitude has to be high enough to ensure sufficient accuracy. For bituminous mixtures, the strain amplitude is generally chosen equal to 50 μm/m. The number of applied loading cycles varies according to frequencies (from one or two cycles at 0.001 Hz up to ∼100 cycles at 10 Hz). A rest period (about 5 min) is also applied between two successive cyclic loading periods (i.e., at each frequency change) to avoid self-heating effects. For each temperature, the procedure involves a test duration of one hour. A conditioning period of 4 h is also considered when the temperature is changed, to ensure a homogeneous temperature inside the specimen. During this period, the load applied on the specimen is null.

www.EngineeringEBooksPdf.com

When applying a sinusoidal axial strain (ε_{ax}), a sinusoidal axial stress (σ_{ax}), and a sinusoidal radial strain (ε_{rad}) are obtained. The following equations are used:

$$\varepsilon_{ax}(t) = \varepsilon_{Aax}\sin(\omega t) \tag{3.1}$$

$$\sigma_{ax}(t) = \sigma_{Aax}\sin(\omega t + \varphi_E) \tag{3.2}$$

$$\varepsilon_{rad}(t) = \varepsilon_{Arad}\sin(\omega t + \pi + \varphi_\nu) = -\varepsilon_{Arad}\sin(\omega t + \varphi_\nu) \tag{3.3}$$

where φ_E is the phase angle between the axial strain and the axial stress; φ_ν is the phase angle between the axial strain and the opposite radial strain; and ε_{Aax}, ε_{Arad}, and σ_{Aax} are axial strain amplitude, radial strain amplitude, and axial stress amplitude, respectively (Figure 3.4).

When applying Equations (3.1)–(3.3), the complex modulus (E^*) and complex Poisson's ratio (ν^*) are calculated as follows:

$$E^* = \frac{\sigma_{Aax}}{\varepsilon_{Aax}} e^{j\varphi_E} = |E^*| e^{j\varphi_E} \tag{3.4}$$

$$\nu^* = -\frac{\varepsilon_{Arad}}{\varepsilon_{Aax}} e^{j\varphi_\nu} = |\nu^*| e^{j\varphi_\nu} \tag{3.5}$$

where $|E^*|$ is the norm of complex modulus, $|\nu^*|$ is the norm of Poisson's ratio, and j is the complex number defined by $j^2 = -1$.

Depending on the performed analysis and available measurements, complex modulus E^* and complex Poisson's ratio ν^* may be obtained in different directions.

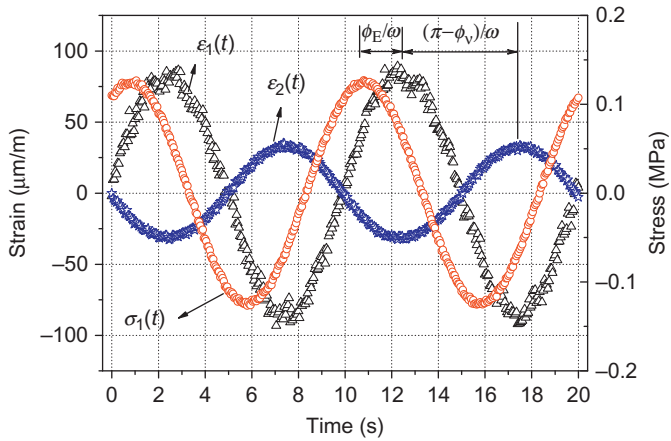


Figure 3.4 Example of measured axial stress (σ_1), axial strain (ε_1), and radial strain (ε_2) (two cycles at 0.1 Hz) on a bituminous mixture (BBSG, "Béton Bitumineux Semi-Grenu," according to the French classification with 5.7% pure 50/70 bitumen) (Nguyen et al., 2012).

www.EngineeringEBooksPdf.com

3.3 Example of 3D linear viscoelastic (LVE) experimental results on bituminous mixtures

Different bituminous materials have been tested with the equipment presented in Section 3.2, produced with or without recycled asphalt pavement, recycled asphalt shingles, and additives (e.g., polyphosphoric acids, polymers), and with different manufacture processes (e.g., hot, warm, half-warm).

In this section, no exhaustive results for the different materials are exposed. Some examples are given in order to describe general common observed tendencies. Other results with different bituminous materials are also shown in following sections.

Hereafter, complex modulus test results are presented for a classic bituminous mixture made with 15% reclaimed asphalt pavement (RAP), and performance-grade (PG) 58-28 added bitumen, for a 5.02% total bitumen content (Tapsoba, 2012; Tapsoba et al., 2014). These results show the influence of temperature and frequency on complex Young's modulus $|E^*|$ and complex Poisson's ratio $|\nu^*|$, as well as their respective phase angles φ_E and φ_ν.

Figures 3.5 and 3.6 show, respectively, isothermal curves of the norm of complex Young's modulus E^* and complex Poisson's ratio ν^* and isothermal curves of their phase angles.

E^* results are classic. It may be seen that the norm of the Poisson's ratio $|\nu^*|$ is not a constant, as generally admitted in the literature. $|\nu^*|$ varies between about 0.10 for high frequencies and/or low temperatures and 0.36 for low frequencies and/or high temperatures. It decreases when temperature decreases and when frequency increases.

In addition, the phase angle of Poisson's ratio φ_ν varies between about 0° and −7°. This phase angle is very small and negative but not nil, as it is generally supposed in the literature. The obtained negative values indicate that the radial strain is slightly late compared with axial strain. This result appears as physically acceptable.

Figure 3.7 shows complex modulus results in Black and Cole–Cole diagrams. These representations are classic for a complex Young's modulus. They are extended to the results of the complex Poisson's ratio in Figure 3.8. The fact that a unique curve

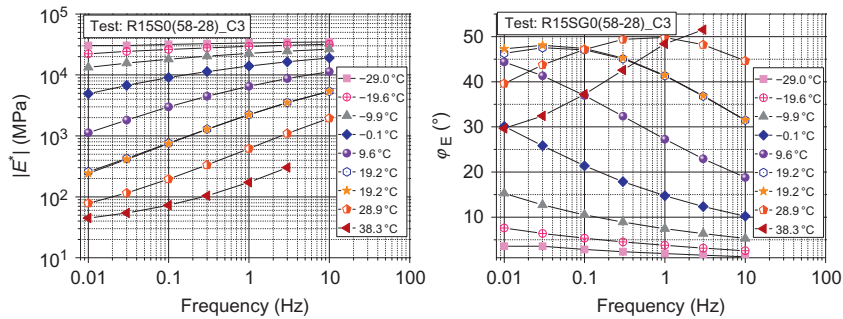


Figure 3.5 Isothermal curves of norm and phase angle of complex Young's modulus for a bituminous mixture (Test R15S0(58-28)_C3) (Tapsoba, 2012; Tapsoba et al., 2014).

www.EngineeringEBooksPdf.com

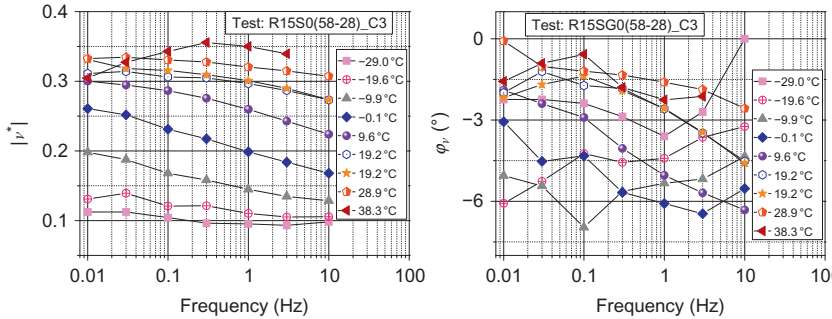


Figure 3.6 Isothermal curves of norm and phase angle of complex Poisson's ratio for a bituminous mixture (Test R15S0(58-28)_C3) (Tapsoba, 2012; Tapsoba et al., 2014).

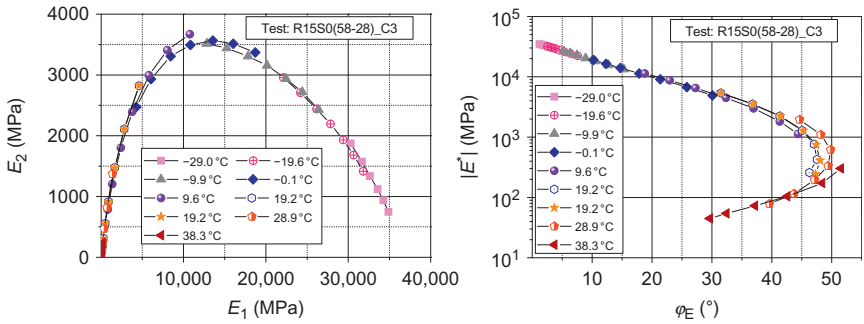


Figure 3.7 Complex Young's modulus for a bituminous mixture in Cole–Cole and Black spaces (Test R15S0(58-28)_C3) (Tapsoba, 2012; Tapsoba et al., 2014).

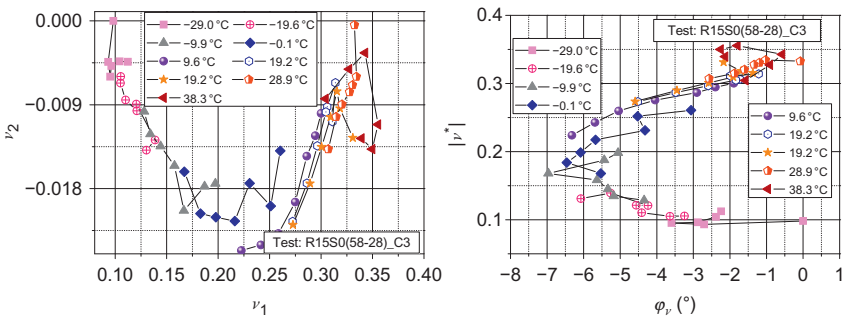


Figure 3.8 Complex Poisson's ratio for a bituminous mixture in Cole–Cole and Black spaces (Test R15S0(58-28)_C3) (Tapsoba, 2012; Tapsoba et al., 2014).

www.EngineeringEBooksPdf.com

could be defined in these axes shows that the time–temperature superposition principle is verified. Many studies confirm that the unidirectional LVE behavior (complex Young's modulus E^* or complex shear modulus G^*) of bituminous materials is thermorheologically simple (i.e., the time–temperature superposition principle (TTSP) is verified) as a good approximation (Di Benedetto et al., 2004, 2007a, 2011; Di Benedetto and Corté, 2005; Airey et al., 2003; Delaporte et al., 2007). For a complex Young's modulus, it is therefore possible to obtain

$$E^*(T_1, f_1) = E^*(T_2, f_2) \tag{3.6}$$

with two different couples of temperature and frequency.

As shown in Figure 3.8, and also in recent studies carried out at the University of Lyon/ENTPE laboratory, the TTSP can be extended to the tridimensional case:

$$v^*(T_1', f_1') = v^*(T_2', f_2') \tag{3.7}$$

The TTSP allows one to plot a unique master curve for the norm as well as the phase angle of the complex modulus at any chosen reference temperature (T_{ref}). The following relationship can be written:

$$E^*(T, a_{TE} f) = E^*(T_{ref}, f) \tag{3.8}$$

with $a_{TE,}$ called the shift factor, depending only on the temperature ($a_{TE} = 1$ for $T = T_{ref}$). The shift factor a_{TE} corresponds to the shifting value along the frequency axis. The complex modulus master curves (norm and phase angle) obtained are plotted in Figure 3.9 (considering a_{TE} shift factors) for $T_{ref} = 9.6$ °C.

It is worth noting that, as already explained, results of the unidirectional case can be extended to the 3D case. Figure 3.10 shows that a master curve can also be plotted for a complex Poisson's ratio:

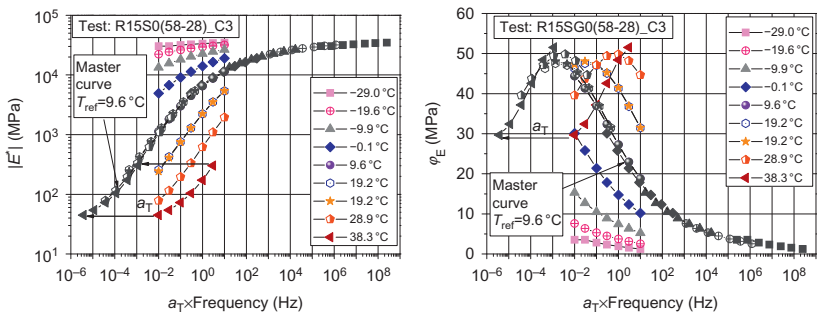


Figure 3.9 Experimental values of E^* and master curves plotted at the reference temperature of 9.6 °C (Test R15S0(58-28)_C3) (Tapsoba, 2012; Tapsoba et al., 2014).

www.EngineeringEBooksPdf.com

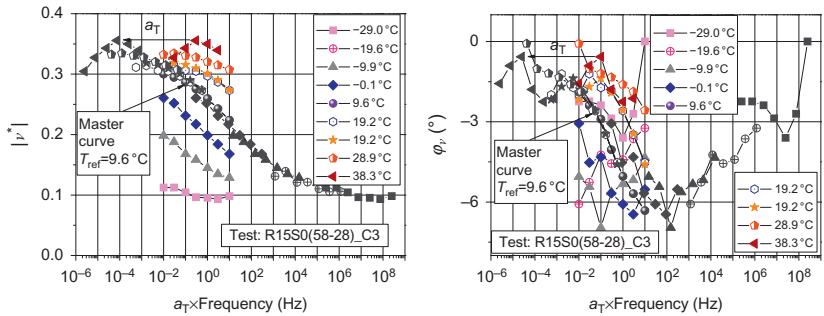


Figure 3.10 Experimental values of v^* and master curves plotted at the reference temperature of 9.6 °C (Test R15S0(58-28)_C3) (Tapsoba, 2012; Tapsoba et al., 2014).

$$v^*(T, a_{Tv}f) = v^*(T_{ref}, f) \tag{3.9}$$

Furthermore, the obtained shift factors for Poisson's ratio (a_{Tv}) can be considered identical to shift factors (a_{TE}) obtained for the complex Young's modulus (E^*):

$$a_T = a_{Tv} = a_{TE} \tag{3.10}$$

Shift factor a_T values are plotted in Figure 3.11 and fitted with the classic William, Landel, and Ferry (WLF) equation (Ferry, 1980).

3.4 3D LVE modeling: two springs, two parabolic elements, one dashpot (2S2P1D) model

3.4.1 *Description of tridimensional 2S2P1D model*

Extensive works performed at the University of Lyon/ENTPE laboratory on the LVE properties of bituminous binders and mixes (Di Benedetto and Yan, 1994; Di Benedetto and Neifar, 2002; Di Benedetto et al., 2004, 2007b; Neifar and Di

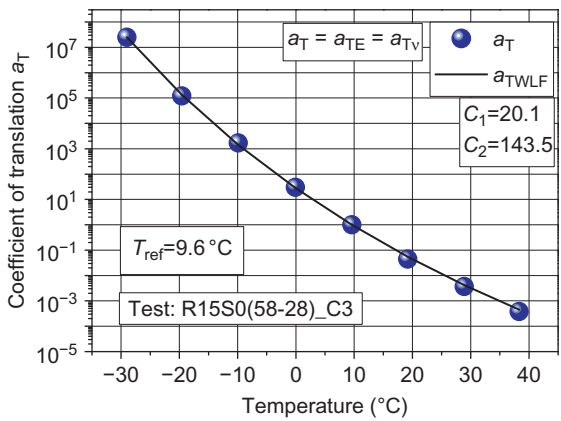


Figure 3.11 Shift factor a_T (complex Young's modulus and complex Poisson's ratio) and fitted WLF equation (Test R15S0 (58-28)_C3) (Tapsoba, 2012; Tapsoba et al., 2014).

www.EngineeringEBooksPdf.com

Benedetto, 2001; Olard and Di Benedetto, 2003; Olard et al., 2003; Olard and Di Benedetto, 2005; Tiouajni et al., 2011; among others) allowed the formulating of a general unidirectional (1D) LVE model with a continuum spectrum called 2S2P1D. This model, based on a combination of simple physical elements, is presented in Figure 3.12a. From measured complex Poisson's ratio data, a tridimensional generalization of the two springs, two parabolic elements, one dashpot (2S2P1D) model is presented hereafter.

The 2S2P1D model consists of a generalization of the Huet–Sayegh model (Huet, 1963). It has been shown in several previous publications (Di Benedetto et al., 2004; Delaporte et al., 2007; Olard and Di Benedetto, 2003, Olard et al., 2003) that the model is capable of simulating the LVE behavior (in the small-strain domain) of bituminous binders, mastics, and mixes, over a very wide range of frequencies and temperatures.

The complex modulus expression of the 2S2P1D model is given in Equation (3.11). It requires only seven constants ($E_{00}, E_0, \delta, k, h, \eta, \tau$) at a given temperature. The influence of some parameters on the 2S2P1D model is represented in Figure 3.13.

$$E^*_{2S2P1D}(j\omega t) = E_{00} + \frac{E_0 - E_{00}}{1 + \delta(j\omega\tau)^{-k} + (j\omega\tau)^{-h} + (j\omega\beta\tau)^{-1}} \tag{3.11}$$

where

- j is the complex number defined by $j^2 = -1$;
- ω is the pulsation, so that $\omega = 2\pi f$ (f is the frequency);
- k, h are constants with $0 \le k \le h \le 1$;
- δ is a constant;
- E_{00} is the static modulus, which is the value of E^* when ω tends toward 0 ($\omega \to 0$);

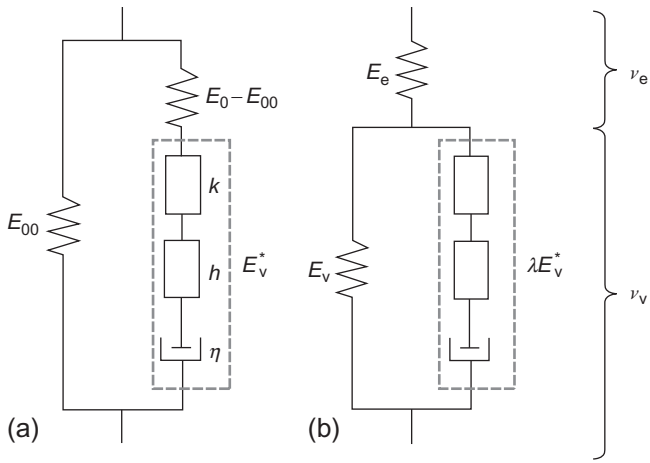


Figure 3.12 (a) Analogical scheme of 2S2P1D model (k and h represent parabolic elements) and (b) equivalent analogical scheme of 2S2P1D model with possible extension to 3D modeling (Pouget, 2011).

www.EngineeringEBooksPdf.com

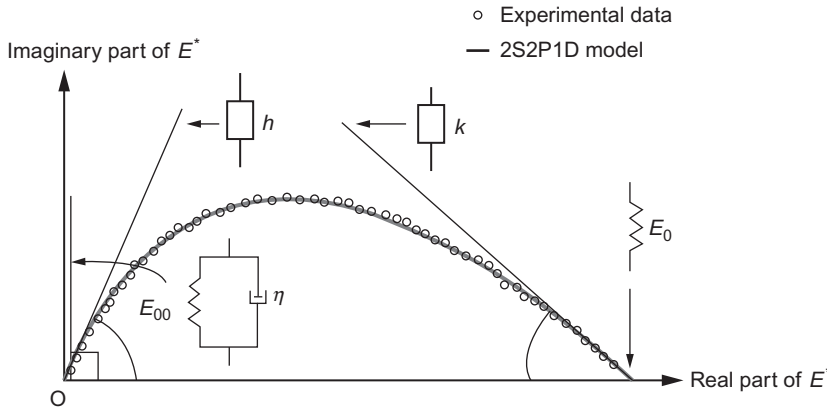


Figure 3.13 Influence of 2S2P1D model parameters on a complex modulus in Cole–Cole space (Di Benedetto et al., 2004).

- E_0 is the glassy modulus, which is the value of E^* when ω tends toward infinity ($\omega \to \infty$);
- η is Newtonian viscosity, defined as $\eta = (E_0 - E_{00})\beta\tau$;
- τ is the characteristic time, whose value varies only with temperature. τ evolution may be approximated by a WLF-type law in the range of considered temperatures. It accounts for the time–temperature superposition principle: $\tau(T) = a_T(T)\tau_0$, where $a_T(T)$ is the shift factor at temperature T. $\tau_0 = \tau(T_{ref})$ is determined at T_{ref}.

The shift factor at temperature T, $a_T(T)$, can be determined by means of the WLF Equation (3.12) for bituminous materials.

$$\log(a_T) = -\frac{C_1(T - T_{ref})}{C_2 + T - T_{ref}} \tag{3.12}$$

It has to be emphasized that only seven constants (E_{00}, E_0, δ, k, h, η, τ) are needed to entirely determine the LVE behavior of the considered material at a given temperature. If the hypothesis of a LVE thermorheologically simple behavior can be applied to the considered materials (which means the time–temperature superposition principle is validated), only parameter τ depends on temperature. If the TTSP holds, the two additional constants C_1 and C_2 (calculated at the reference temperature T_{ref} with the WLF equation) are needed. Then, the total number of constants of the unidirectional expression of the model amounts to nine.

A generalization of the 2S2P1D model for the three-dimensional case (3D 2S2P1D) is proposed in Figure 3.12b and Equation (3.19).

The analogical representation of the 3D 2S2P1D model is given in Figure 3.12b, assuming an isotropic behavior. For isotropic LVE materials, only the expression of complex Poisson's ratio ν^* is needed. The representation in Figure 3.12b is equivalent to the classic one presented in Figure 3.12a, if the following relationships between parameters are verified:

www.EngineeringEBooksPdf.com

$$E_e = E_0 \tag{3.13}$$

$$E_v = \frac{E_0 E_{00}}{E_0 - E_{00}} \tag{3.14}$$

$$\lambda = \left(\frac{E_0}{E_0 - E_{00}}\right)^2 \tag{3.15}$$

In Figure 3.12b, ν_e and ν_v are, respectively, the values of Poisson's ratio (real number) for the upper part (purely elastic) and the lower part (viscoelastic) of the model.

Complex Poisson's ratio is then expressed by

$$\nu^*_{2S2P1D}(\omega) = \nu_v + (\nu_e - \nu_v)\frac{E^*_{2S2P1D}(\omega)}{E_0} \tag{3.16}$$

with the following adequate values:

$$\nu_e = \nu_0 \tag{3.17}$$

$$\nu_v = \frac{\nu_{00} E_0 - \nu_0 E_{00}}{E_0 - E_{00}} \tag{3.18}$$

Thus, the proposed expression for complex Poisson's ratio ν^* is given in Equation (3.19).

$$\frac{\nu^*_{2S2P1D} - \nu_0}{\nu_{00} - \nu_0} = \frac{1}{1 + \delta(j\omega\tau)^{-k} + (j\omega\tau)^{-h} + (j\omega\beta\tau)^{-1}} \tag{3.19}$$

where only two new constants are added:

- ν_{00}, which is the value of ν^* when ω tends toward 0 ($\omega \to 0$);
- ν_0, which is the value of ν^* when ω tends toward infinity ($\omega \to \infty$).

The other constants are the same as in Equation (3.14).

From Equations (3.14) and (3.16), it can be checked that the global expression of the 2S2P1D model in the 3D case for isotropic LVE material requires 11 constants. This model allows the simulating of any loading conditions, including temperature changes.

3.4.2 Examples of modeling for different bituminous materials

The 2S2P1D model has been widely used and has shown its ability to model the LVE behavior of several bituminous materials. Some examples are given here.

In the framework of a research project supported by the French National Research Agency, roller-compacted concrete (material with hydraulic binder) with and without RAP was studied (Bilodeau, 2012). Results of five different materials are presented

www.EngineeringEBooksPdf.com

and modeled with the 2S2P1D model. The first is a classic high-modulus mixture ("Enrobé à Module Elevé" (EME)). The second is RAP-extracted binder. The third and fourth materials are roller-compacted concretes containing, respectively, about 40% and about 80% of RAP. Their hydraulic binder content is equal to 12% and their bitumen content (coming from RAP) is, respectively, equal to 1.4% and 3%. The fifth material (called ERTALH as a company product) is also a material treated with hydraulic binder, containing about 80% RAP. Its hydraulic binder content is only 5%.

In Figure 3.14, a measured complex Young's modulus and 2S2P1D fitting curves in Cole–Cole space are presented. In Figure 3.15, corresponding master curves are shown. Parameters of the 2S2P1D model are given in Table 3.1 for each material.

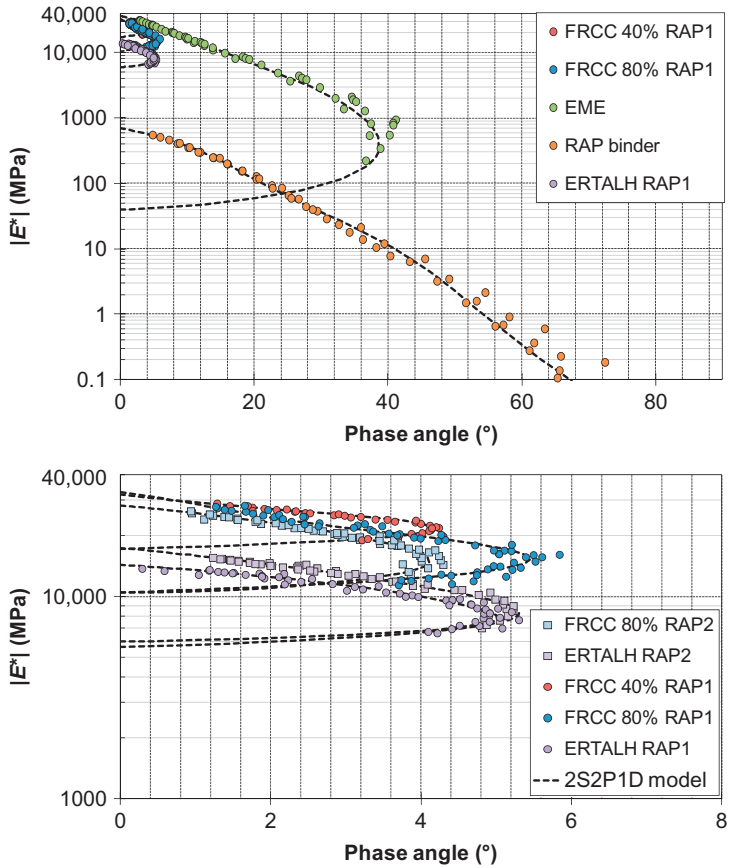


Figure 3.14 Complex modulus data and 2S2P1D modeling in Cole–Cole space for different bituminous materials: high-modulus mixture (EME); RAP1-extracted binder; roller-compacted concrete with 0%, 40%, and 80% RAP (named, respectively, FRCC 0% RAP, FRCC 40% RAP, and FRRC 80% RAP); and ERTALH® with two different RAP (RAP1 and RAP2) (Bilodeau et al., 2010, 2012).

www.EngineeringEBooksPdf.com

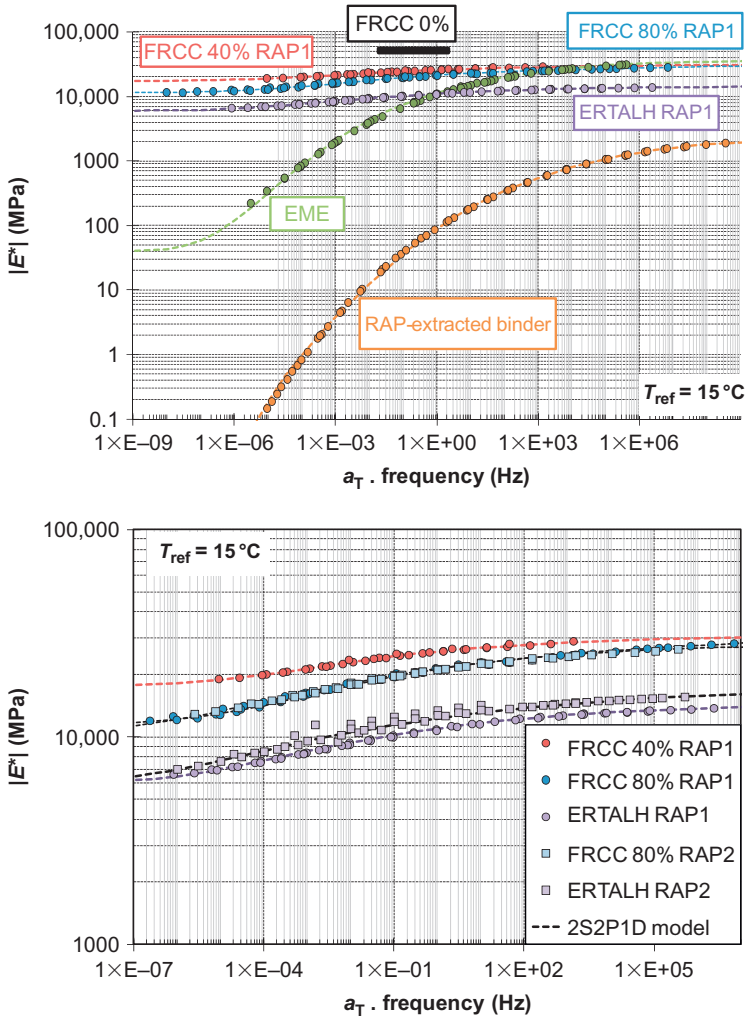


Figure 3.15 Complex modulus data and 2S2P1D modeling master curves for different bituminous materials: high-modulus mixture (EME); RAP1-extracted binder; roller-compacted concrete with 40% and 80% RAP (named, respectively, FRCC 40% RAP and FRRC 80% RAP); and ERTALH® with two different RAP (RAP1 and RAP2) (Bilodeau et al., 2010, 2012).

It is remarkable that the 2S2P1D model simulates very well all these very different types of materials.

As explained before, the 2S2P1D model could also be used for complex Poisson's ratio simulation. As an example, some results obtained for materials studied in a research project (also supported by the French National Research Agency) dealing with bituminous materials for orthotropic bridge deck surfacing are presented (Pouget, 2011). Three different types of bituminous materials were studied, along with

www.EngineeringEBooksPdf.com

Table 3.1 2S2P1D model parameters for bituminous materials presented in Figures 3.14 and 3.15: high-modulus mixture (EME), RAP1 extracted binder, roller-compacted concrete with 40% and 80% RAP (FRCC 40% RAP and FRRC 80% RAP), and ERTALH® (with two different RAP materials (RAP1 and RAP2))

Materials	E_{00} (MPa)	E_0 (MPa)	k	h	δ	Tau	Beta	C_1	C_2
RAP1-extracted binder	0	2625	0.13	0.35	1.5	0.00002	100,000	25.8	187.3
F40% RAP1	15,000	35,000	0.13	0.35	1.5	300	100,000	29.3	250.5
F80% RAP1	11,000	27,500	0.13	0.35	1.5	175	100,000	28.8	243.1
ERTALH RAP1	5250	15,150	0.13	0.35	1.5	135	100,000	27	246
F80% RAP2	11,250	27,500	0.165	0.43	2.6	1122.6	10,000	472	3656
ERTALH RAP2	5700	16,750	0.165	0.43	2.6	2230	10,000	472	3656

Bilodeau et al. (2010, 2012)

www.EngineeringEBooksPdf.com

two binders (a polymer-modified binder Orthoprene® and a pure 50/70 penetration-grade bitumen, B5070); two mixtures made with these binders, respectively, called Orthochape® (used for the Millau Viaduct in France, the highest bridge in the world at its opening in 2006) and E5070; and a bituminous mastic of Paraforpont® sealing sheet (to be used between the steel deck and the bituminous surfacing). The complex Poisson's ratio was measured for both mixtures.

Master curves for the complex modulus and complex Poisson's ratio are presented in Figures 3.16 and 3.17, respectively, as well as 2S2P1D modeling, for the studied materials. As shown before, the 2S2P1D model gives very good results for the complex modulus. It is also able to model very well the complex Poisson's ratio. Some scattering appears for the phase angle of materials containing polymer (Orthoprène® binder, Orthochape® mixture, and also Paraforpont®). Because of the presence of polymer, TTSP is not valid at high temperature. As TTSP is assumed valid for modeling, 2S2P1D simulations are not correct in this domain.

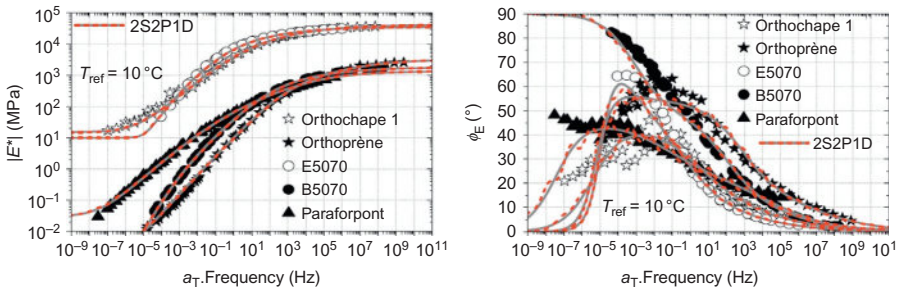


Figure 3.16 Complex modulus measured data and 2S2P1D modeling master curves for different bituminous materials: two binders (B5070 and Orthoprène®), two corresponding mixtures (E5070 and Orthochape®), and bituminous mastic of sealing sheet (Paraforpont®) (Pouget et al., 2010; Pouget, 2011).

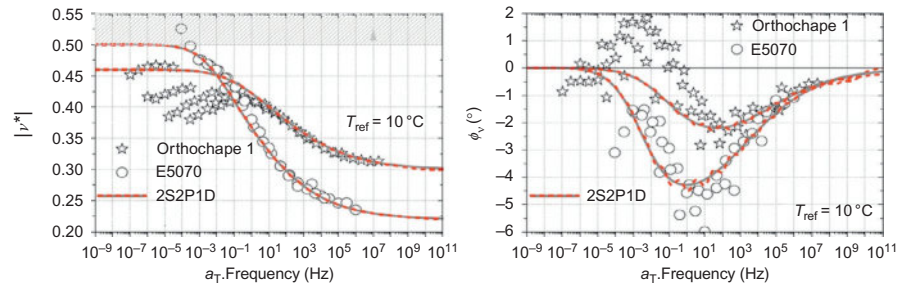


Figure 3.17 Complex Poisson's ratio measured data and 2S2P1D modeling master curves for two different bituminous mixtures (E5070 and Orthochape®) (Pouget et al., 2010; Pouget, 2011).

www.EngineeringEBooksPdf.com

Presented results give some convincing examples of the ability of the 2S2P1D model to simulate the 3D LVE behavior of bituminous materials. They also show that some parameters of the model (k, h, δ) for mixtures are directly inherited from the binder. The next section deals with this subject.

3.5 Determining 3D LVE bituminous mixture properties from LVE binder properties

Many researchers have focused on the prediction of a mixture–complex modulus from binder properties. For practitioners, this would be a very useful tool to spare testing time. This is also an interesting topic for researchers in order to better understand the complex behavior of mixes. A considerable amount of work has already been done and presented in the literature to relate binder and mix moduli for a given mix design (Lytton et al., 1993; Franken and Vanelstraete, 1995; Zeng et al., 2001; Olard and Di Benedetto, 2003; Di Benedetto et al., 2004; among others). However, the relationships between binder and mixture moduli are often valid over a narrow range of frequencies and temperatures, or even only for one type of given mixture. For very different conditions of temperature and frequency, or different mixes, these relationships are no longer valid.

In this section, a method to determine 3D LVE bituminous mixtures from LVE binder properties is presented. The obtained relationship is based on the developments made by Di Benedetto and Olard for both phase angle and norm of the complex modulus (Di Benedetto et al., 2004). An extension is proposed to the tridimensional behavior of mixtures. Even though this relationship was developed with the help of the 2S2P1D model, presented in Section 3.4, it is independent of any rheological model.

3.5.1 Normalized LVE parameters from complex modulus tests

From complex modulus tests, it is possible to determine LVE parameters, complex Young's modulus E^*, and complex Poisson's ratio ν^*. One might normalize these parameters with the following expressions:

$$E^*_{\text{norm}} = \frac{E^* - E_{00}}{E_0 - E_{00}} \tag{3.20}$$

$$\nu^*_{\text{norm}} = \frac{\nu^* - \nu_{00}}{\nu_0 - \nu_{00}} \tag{3.21}$$

With the same notation used in Section 3.4, parameters E_{00}, ν_{00} correspond to the asymptotic values (when ω tends toward 0), and the parameters E_0, ν_0 correspond to the asymptotic values (when ω tends toward infinity) of, respectively, E^* and ν^*.

An example of these normalized parameters is given in Figure 3.18. E^*_{norm} is represented in Cole–Cole space, namely the imaginary part of E^*_{norm} in a function of the real part of E^*_{norm} for four different materials already presented in Section 3.4.

www.EngineeringEBooksPdf.com

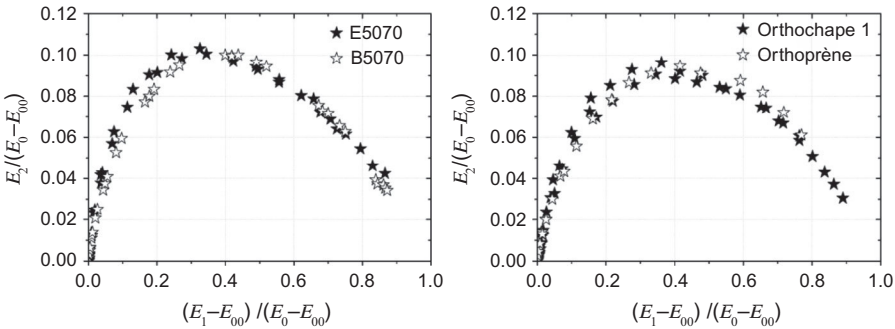


Figure 3.18 Normalized complex Young's moduli for two different bituminous mixtures (E5070 and Orthochape®) and their corresponding binders (B5070 and Orthoprène®) (see Section 3.4) (Pouget et al., 2010; Pouget, 2011).

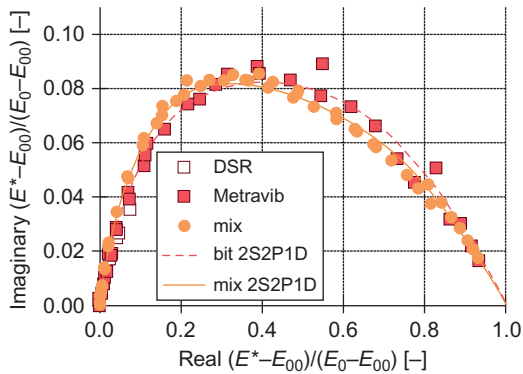


Figure 3.19 Cole–Cole plot of normalized complex Young's moduli for a mixture made with 20% RAP and 35–50 penetration fresh-added bitumen and its corresponding binder (DSR and Metravib tests) (Mangiafico, 2014; Mangiafico et al., 2013).

The same observation has been made by Mangiafico et al. (2013) on bituminous mixtures containing 20% RAP and their corresponding binders (blend of RAP-extracted binder and fresh binder mixed in the laboratory). Some results are presented in Figure 3.19. Binders were tested using dynamic shear rheometer (DSR) at high temperature ($\geq$10 °C) and Metravib tension/compression tests at low temperature ($\leq$10 °C).

From such results, it has been concluded that when plotted in a Cole–Cole diagram, normalized moduli of materials produced with the same binder generate curves that superpose with each other. This confirms that time and temperature dependency of these materials originates from binder behavior, regardless of the aggregate skeleton. This is the basis of the method developed by Olard and Di Benedetto (2003) to deduce a mixture–complex modulus from binder one. An extension to complex Poisson's ratio of mixtures was proposed by Pouget et al. (2010).

www.EngineeringEBooksPdf.com

3.5.2 ENTPE transformation, SHStS: from binder to mixture properties

The following relationships among mixture–complex modulus (E^*_{mix}), mixture–complex Poisson's ratio (ν^*_{mix}), and binder–complex modulus (E^*_{binder}) are proposed:

$$E^*_{mix}(\omega,T) = E_{00_mix} + \left[E^*_{binder}(10^{\alpha}\omega,T) - E_{00_binder}\right]\frac{E_{0_mix} - E_{00_mix}}{E_{0_binder} - E_{00_binder}} \quad (3.22)$$

$$\nu^*_{mix}(\omega,T) = \nu_{00_mix} + \left[E^*_{binder}(10^{\alpha}\omega,T) - E_{00_binder}\right]\frac{\nu_{0_mix} - \nu_{00_mix}}{E_{0_binder} - E_{00_binder}} \quad (3.23)$$

Only five constants are required when binder characteristics (E_{0_binder}, E_{00_binder}) are known:

- E_{00_mix} and ν_{00_mix}, which correspond to the asymptotic values (when ω tends toward 0) of E^* and ν^* of the bituminous mixture.
- E_{0_mix}, ν_{0_mix}, which correspond to the asymptotic values (when ω tends toward infinity) of E^* and ν^* of the bituminous mixture.
- α, which is a parameter depending on the considered mix design and binder aging occurring during mixing.

It should be underlined that both Equations (3.22) and (3.23) are very simple and cover the whole range of frequency (or pulsation ω) and temperature (T).

Because E_{00_binder} is nil for pure binders, and in most cases negligible compared to E_{0_binder}, the following simplified formulae can be considered:

$$E^*_{mix}(\omega,T) = E_{00_mix} + E^*_{binder}(10^{\alpha}\omega,T)\frac{E_{0_mix} - E_{00_mix}}{E_{0_binder}} \quad (3.24)$$

$$\nu^*_{mix}(\omega,T) = \nu_{00_mix} + E^*_{binder}(10^{\alpha}\omega,T)\frac{\nu_{0_mix} - \nu_{00_mix}}{E_{0_binder}} \quad (3.25)$$

As a matter of fact, these equations correspond to a simple geometric transformation of the binder curve in the Cole–Cole plane. Figure 3.20 explains how to obtain a practically complex modulus and complex Poisson's ratio of the mix from a binder-complex modulus. Starting from binder–complex modulus $E^*_{binder}(\omega, T)$ at any given pulsation ω and temperature T, three steps have to be carried out to obtain mix modulus $E^*_{mix}(10^{-\alpha}\omega, T)$ (respectively $\nu^*_{mix}(10^{-\alpha}\omega, T)$) at a pulsation equal to $10^{-\alpha}\omega$ and at the same temperature T:

(i) A negative translation along the real axis of value E_{00_binder} (we also can consider $E_{00_binder} \approx 0$ and skip this step if the frequency is not too low).

(ii) A homothetic expansion from the origin with a ratio of $\frac{E_{0_mix} - E_{00_mix}}{E_{0_binder} - E_{00_binder}}$ for the complex modulus (respectively, $\frac{\nu_{0_mix} - \nu_{00_mix}}{E_{0_binder} - E_{00_binder}}$ for Poisson's ratio).

(iii) A positive translation along the real axis of value E_{00_mix} (respectively, ν_{00_mix}).

www.EngineeringEBooksPdf.com

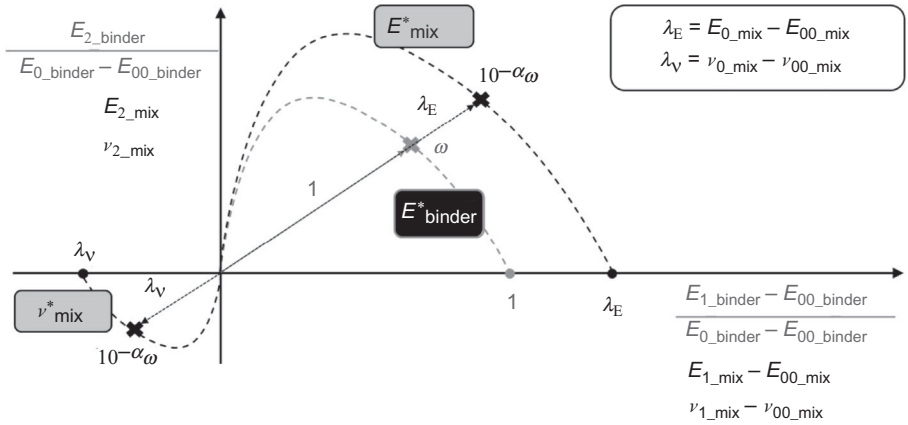


Figure 3.20 Schematic representation of the SHStS transformation, to obtain mixture properties from binder in Cole–Cole space (Pouget et al., 2010; Pouget, 2011).

In summary, on a common Cole–Cole plan, the relationship corresponds to the sequence of a shift along the horizontal axis, a homothetic transformation, a shift of characteristic time, and a second shift along the horizontal axis. For this reason, it is called SHStS (Shift-Homothety-Shift and time-Shift) transformation.

The complex modulus of any bitumen is therefore sufficient to predict the LVE properties of the corresponding mix.

Some examples of simulation using SHStS transformation and E^* data of bitumen or bitumen blend contained in the mixtures are presented in Figures 3.21–3.23, respectively, for mixture E5070 made with B5070 pure bitumen, mixture Orthochape® made with the polymer-modified bitumen Orthoprène®, and a mixture made with 20% RAP and a 35–50 penetration fresh-added bitumen.

For mixture E5070 (Figure 3.21), the simulation gives remarkably good results for E^* as well as for ν^*, with a relative error lower than 10% for both norms of these parameters.

In Figure 3.21, it can be observed that Orthochape® mix and Orthoprène® bitumen do not conform very well to TTSP at high temperatures. This is a classic result explained by the high content of polymer. However, the predicted curves describe quite well the evolution of the complex modulus and of complex Poisson's ratio. The relative difference between predicted and experimental values of the norms $|E^*|$ and $|\nu^*|$ for Orthochape® mix, on the wide considered frequency–temperature range, remains for most of the data below 30%.

Figure 3.23 shows that SHStS transformation is also valid for a mixture with 20% RAP, provided that data from the blend of RAP-extracted bitumen and fresh bitumen are used for simulation. This also indicates a good blending between bitumen inside the mixture.

www.EngineeringEBooksPdf.com

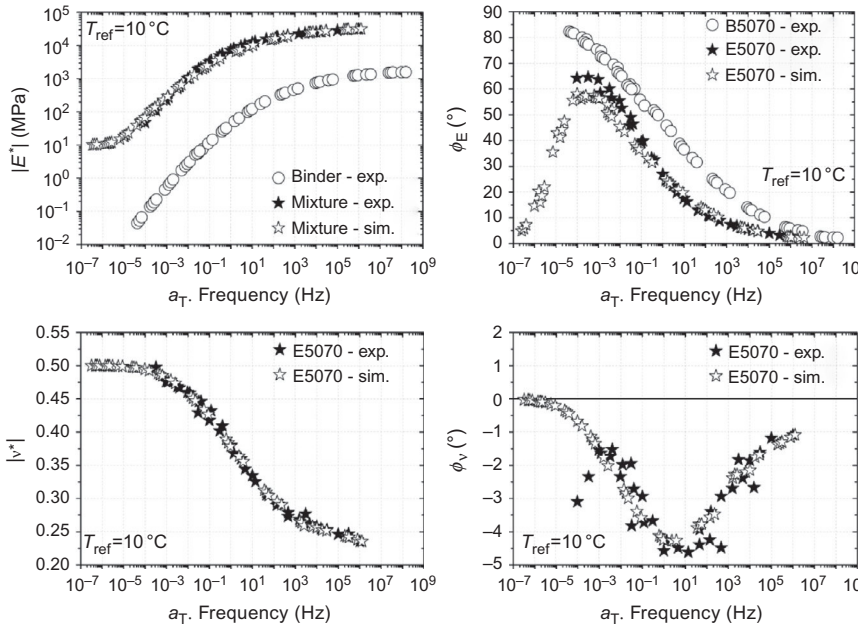


Figure 3.21 LVE properties of E5070 mixture at the reference temperature $T_{ref} = 10$ °C: experimental data and prediction from SHStS transformation using the experimental data of B5070 bitumen (Pouget et al., 2010; Pouget, 2011).

3.6 Determination of 3D LVE properties with acoustic wave propagation

Ultrasonic (US) wave propagation has been widely studied with various geomaterials like concretes and sands, but not developed as much for bituminous mixtures. Even though some studies have been proposed on the subject (Di Benedetto et al., 2009; Hochuli et al., 2001; Kweon and Kim, 2006; Mounier et al., 2012; Norambuena-Contreras et al., 2010), further developments are still needed to interpret the data, in particular considering the viscous properties of such materials. US wave propagation methods have the advantage of being nondestructive. Moreover, the equipment used for these tests is much cheaper than traditional machines used to characterize mechanical behavior of bituminous mixtures. The tests are quite simple and quick to carry out. All these aspects make the methods very interesting and justify their development, which could be eventually adapted for pavement investigations.

Two methods are presented in this chapter. The first is called "Direct measurement of flying time," and can be used with compression "*P*" waves and shear "*S*" waves. The second method, called "Impact Resonance (IR) test," is applied to compression waves and is based on the phenomenon of resonance. Some authors used this method for bituminous mixtures (Kweon and Kim, 2006; Lacroix et al., 2009).

www.EngineeringEBooksPdf.com

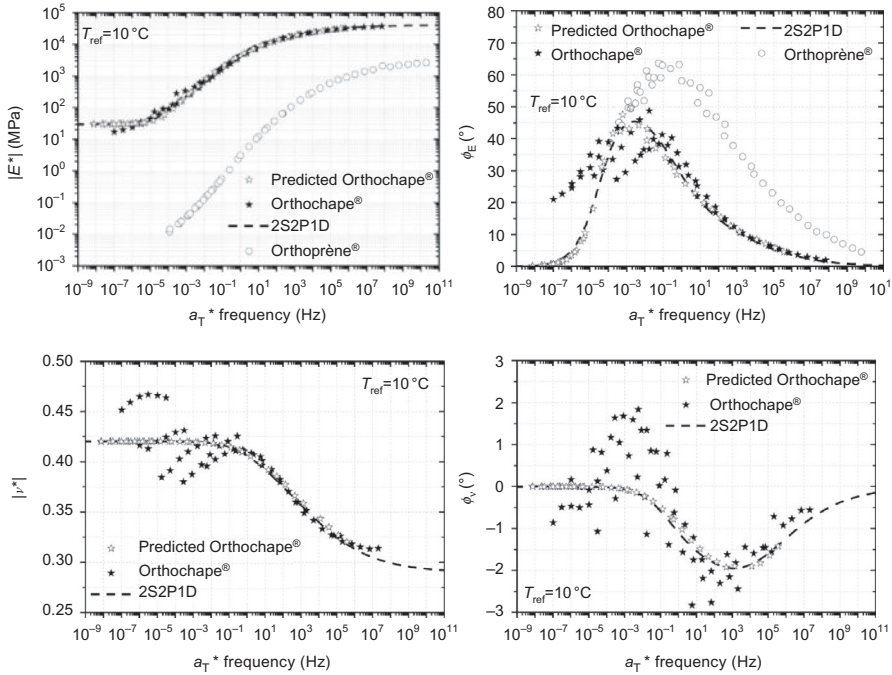


Figure 3.22 LVE properties of Orthochape® mixture at the reference temperature $T_{ref} = 10$ °C: experimental data and prediction from SHStS transformation using the experimental data of Orthoprène® bitumen (Pouget et al., 2010; Pouget, 2011).

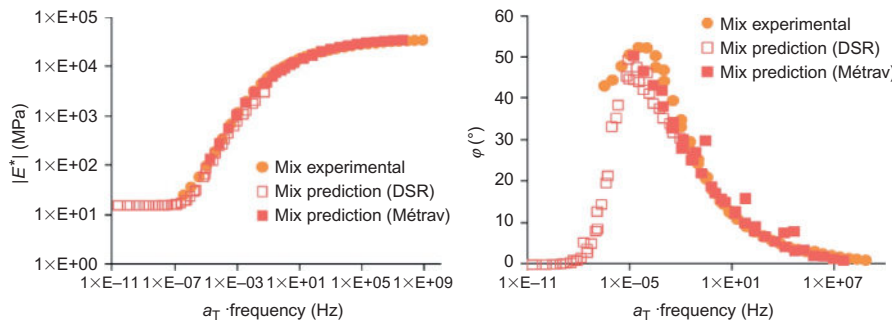


Figure 3.23 Complex modulus of mixture made with 20% RAP and 35–50 penetration fresh-added bitumen ($T_{ref} = 14.2$ °C): experimental data and prediction from SHStS transformation using experimental data obtained for the corresponding binder blend (DSR and Metravib tests) (Mangiafico, 2014; Mangiafico et al., 2013).

www.EngineeringEBooksPdf.com

3.6.1 Direct-measurement flying-time method

As an introduction, the theoretical study of plane wave propagation in isotropic LVE materials is introduced and related to the rheological parameters of bituminous mixtures.

Several sorts of waves may exist within or at the surface of a specimen, depending on their type (e.g., compression, torsion, bending). Only volumetric plane waves are considered, which can be either compression "P" waves, or shear "S" waves.

As the amplitude of the strains created by the waves is less than 10^{-6} m/m, it can be considered that the bituminous mixtures behave like viscoelastic materials (Di Benedetto et al., 2011).

The two types of sinusoidal plane waves that propagate in a linear isotropic viscoelastic material match Equation (3.26) for "P" waves and Equation (3.28) for "S" waves.

$$\underline{u_P}\left(\underline{x},t\right)=\underline{u_{P_0}}\,e^{-\omega\frac{\underline{x}\cdot\underline{p}\tan\left(\frac{\varphi}{2}\right)}{C_P}}e^{i\omega\left(t-\frac{\underline{x}\cdot\underline{p}}{C_P}\right)} \tag{3.26}$$

$\underline{u_P}$ is the particle displacement, $\underline{u_{P_0}}$ the initial particle displacement, $\underline{x}$ the position vector, $\underline{p}$ the propagation vector of the wave, and t the time. The velocity of the compression waves C_P is given by Equation (3.27):

$$C_P=\frac{1}{\cos\left(\frac{\varphi}{2}\right)}\sqrt{\frac{(1-\nu)|E^*|}{(1+\nu)(1-2\nu)\rho}} \tag{3.27}$$

For shear waves "S," it is

$$\underline{u_S}\left(\underline{x},t\right)=\underline{u_{S_0}}\,e^{-\omega\frac{\underline{x}\cdot\underline{p}\tan\left(\frac{\varphi}{2}\right)}{C_S}}e^{i\omega\left(t-\frac{\underline{x}\cdot\underline{p}}{C_S}\right)} \tag{3.28}$$

with $\underline{u_S}$ the particle displacement, $\underline{u_{S_0}}$ the initial particle displacement, and C_S the velocity of the shear waves given by Equation (3.29):

$$C_S=\frac{1}{\cos\left(\frac{\varphi}{2}\right)}\sqrt{\frac{|E^*|}{2(1+\nu)\rho}} \tag{3.29}$$

The value of Poisson's ratio ν is considered constant in Equations (3.27) and (3.29). The two velocities (C_P and C_S) are the physical properties that are experimentally measured.

In order to evaluate the velocity C_P or C_S of the waves, two piezoelectric compression sensors are placed on opposite sides of samples (Figure 3.24). Tested samples are placed on a soft material (polystyrene) to prevent unexpected waves from reflecting.

www.EngineeringEBooksPdf.com

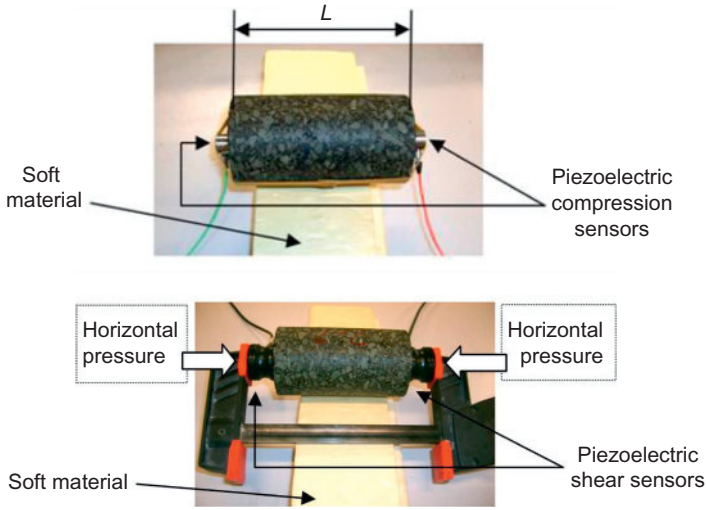


Figure 3.24 Positioning of the sample and sensors for the direct measurement of flying-time method for compression waves (top) and shear waves (bottom) (Di Benedetto et al., 2009; Mounier et al., 2012).

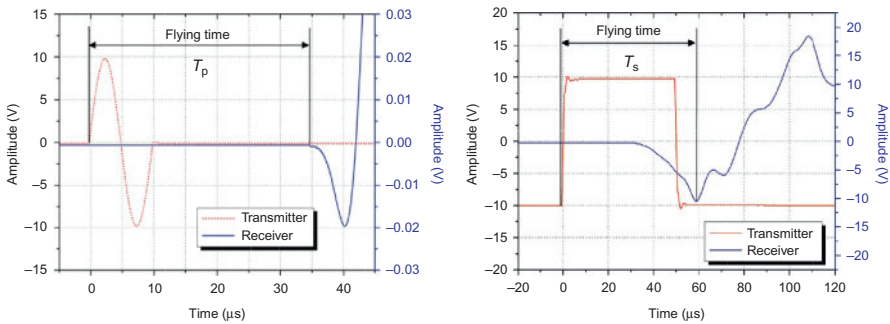


Figure 3.25 Example of emitted and received recorded signals (received signal is the average of 256 pulses) and determination of propagation time for compression and shear waves (Mounier et al., 2012).

An electric signal is sent to one sensor (called "transmitter"), which creates a compression or shear wave within the sample. This wave propagates and is received by the second sensor (called "receiver"). Examples of sent and received electric signals to and from piezoelectric sensors are shown in Figure 3.25.

Signals recorded by both sensors are monitored to determine the wave flying time T_P or T_S (Figure 3.25) necessary to cover the distance L within the sample. For compression waves, the very first deviation of both signals is considered to determine T_P.

www.EngineeringEBooksPdf.com

For a shear wave, the arrival of the wave is considered at the first minimum of the signal. The velocity of waves is then computed as $C_P = L/T_P$ and $C_S = L/T_S$.

Regarding frequency, a Fourier transformation of the receiver sensor signal gives a peak frequency considered for the analysis. For the used sensors, the value is about 137 kHz for compression waves and 12 kHz for shear waves (Figure 3.26).

3.6.2 Impact resonance method

This method uses the phenomenon of resonance of the compression waves. The principle of this test is simply to induce an excitation at one end of the specimen with a shock, and to monitor the amplified response captured by a piezoelectric sensor placed at the opposite side. A Fourier transformation of the output signal is performed to determine the resonant frequency f_r, which is required to characterize material behavior. Different types of waves actually propagate within the sample, but only compression plane waves, which are the fastest ones, are considered. A great number of waves of different wavelengths exist in the sample after the impact. Resonance is created by waves having a wavelength of $L = \lambda/2$ that amplify at each reflection on the boundaries of the sample.

The theoretical analysis of resonant waves in LVE materials is based on the equations developed for elastic materials, and introduces correction coefficients that are calculated following the types of sample and material. As a first approximation, these coefficients could be neglected because the correction is very small. The resonant compression wave velocity is calculated as

$$V_c = f_r \lambda \tag{3.30}$$

where f_r is the resonant frequency and λ the considered wavelength, equal to $2L$.

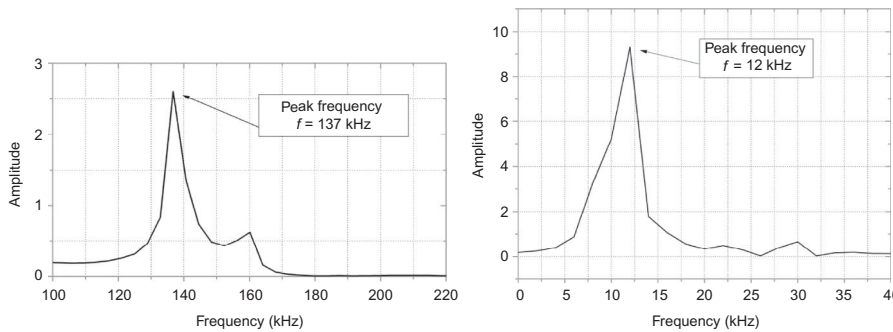


Figure 3.26 Fourier analysis of the receiver sensor signal for compression (left) and shear (right) waves (same tests as Figure 3.25) (Mounier et al., 2012).

www.EngineeringEBooksPdf.com

The norm of the complex modulus is calculated as

$$|E^*| = \rho V_c^2 \tag{3.31}$$

As the material is viscoelastic, the wave is damped all along its propagation. The phase angle can then be calculated from the logarithmic decrement δ measured between two peaks of the recorded signal (Figure 3.28).

$$\varphi = 2.\arctan\frac{\delta}{2\pi} \tag{3.32}$$

The experimental device used by Mounier et al. (2012) consists in exciting the sample with the impact of a stiff ball (made of glass, having a 16-mm diameter and 5.5-g mass). A piezoelectric compression sensor placed on the other side of the sample receives the wave. The experimental setup is presented in Figure 3.27. An example of a recorded signal during the IR test and the associated Fourier transform are presented in Figure 3.28.

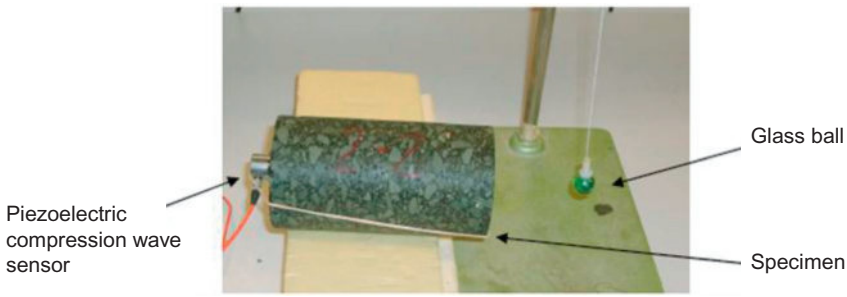


Figure 3.27 Experimental device for the IR test (compression waves) (Mounier et al., 2012).

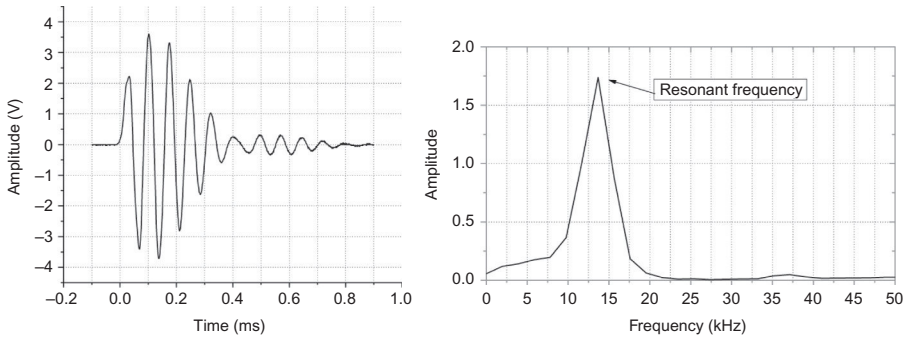


Figure 3.28 Example of the recorded signal during the IR test at 20 °C and Fourier transformation of the signal (Mounier et al., 2012).

www.EngineeringEBooksPdf.com

3.6.3 Results: TTSP validity at high frequency and 3D LVE parameters

Results of an experimental campaign are exposed as an example of more generally obtained results on bituminous mixtures (Di Benedetto et al., 2009). The tested material is a classic French mixture ("Béton Bitumineux Semi-Grenu" (BBSG) type), with 6% of bitumen by weight of aggregates and 96% compacity. Tested samples are cylindrical, with a length (L) of about 120 mm and a diameter (D) of 75 mm.

One sample was used to carry out the classic complex modulus test (in the quasi-static regime), and data were fitted with the 2S2P1D model. A second sample was used to perform US wave propagation, with both presented methods at the temperatures of −19, 0, 20, and 40 °C.

A complex modulus master curve is presented in Figure 3.29 in order to compare graphically the results obtained with both methods to the tension/compression complex modulus test results performed on the duplicate specimen and to the rheological 2S2P1D model. The chosen reference temperature is 0 °C.

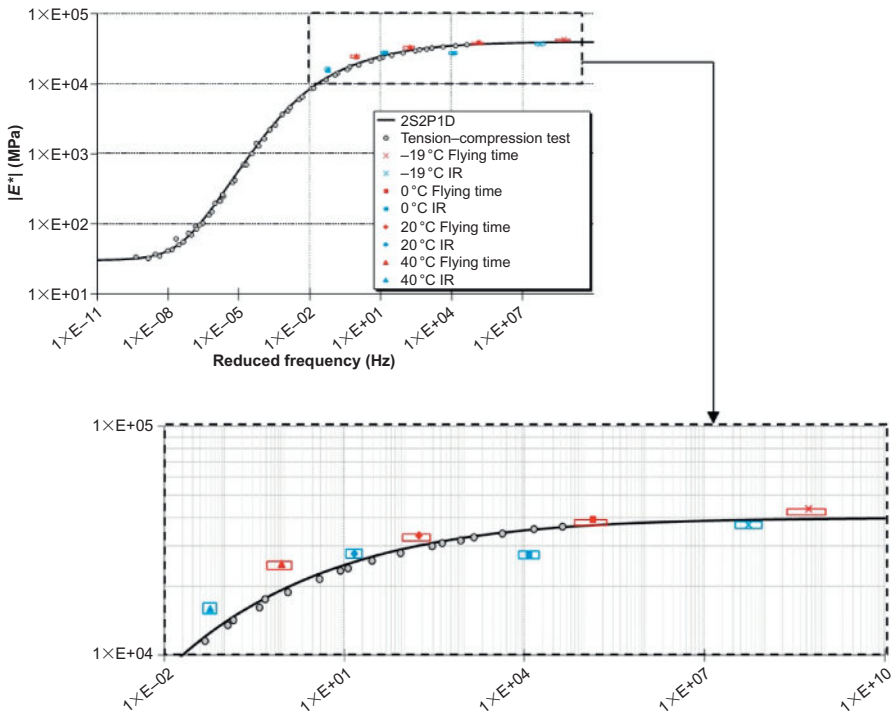


Figure 3.29 Complex modulus master curve for bituminous mixture at a reference temperature of 0 °C with values from the Tension–compression test performed on the duplicate specimen, 2S2P1D modeling, direct measurement of flying time (in red), and impact resonance test (in blue) (Di Benedetto et al., 2009).

www.EngineeringEBooksPdf.com

Two parameters (phase angle of complex modulus and Poisson's ratio) are needed to calculate a complex modulus value from measured flying time. In this example, they were estimated with a fitted 2S2P1D model. On the contrary, interpretation of the IR test does not require such parameters.

Both direct measurement of flying time and the IR test provide good values of the complex modulus for a wide range of equivalent frequencies, with a relative error globally lower than 20% in relative value. The shift factors used to plot the master curves for both methods are those obtained experimentally during complex modulus tests. This shows that the time–temperature superposition principle is valid at high frequencies.

Furthermore, propagation of US shear waves was also used in this campaign to determine experimentally the Poisson's ratio of the mixtures. Considering the theoretical relations that link compression and shear wave velocities with the material parameters (Equations (3.27) and (3.29)) for isotropic materials, the following relationship can be found for a fixed temperature:

$$\frac{C_P(f)}{C_S(f)} = \frac{t_S(f)}{t_P(f)} = \sqrt{\frac{2(1-\nu)}{(1-2\nu)}} \tag{3.33}$$

where t_S and t_P are the flying times of shear and compression waves, respectively, at a frequency f.

The measurements of the compression wave flying time are performed at a frequency of 137 kHz, which is different from the shear wave one (12 kHz). These frequencies are imposed by the characteristics of the "P" wave and "S" wave sensors. However, Equation (3.33) requires measurements of compression and shear wave flying times at the same frequency "*f*" in order to obtain the Poisson's ratio for this frequency "*f*."

A first calculation was considered without taking into account the frequency difference between "P" and "S" waves (137 and 12 kHz, respectively). The obtained results have shown that complex Poisson's ratio could be estimated with relative errors lower than 30%. If the 2S2P1D model is used to determine the value of T_P at the frequency of 12 kHz (to coincide with the frequency of shear waves), the relative errors become lower than 10%.

3.7 Anisotropy

A classic hypothesis of isotropic behavior is made for the bituminous mixtures. This enables one to describe their LVE behavior with only two parameters: the complex modulus and the Poisson's ratio (which is also usually considered a constant real number). This simplification should be verified, and is not obvious or commonsensical when considering the classic compaction method for pavement. With the presented developed testing method, isotropy hypothesis has been investigated, first by

www.EngineeringEBooksPdf.com

measuring the complex modulus and second by measuring the complex Poisson's ratio, both in different directions.

3.7.1 Complex modulus anisotropy

In order to investigate anisotropy of bituminous mixtures, wave propagation tests can be performed in different directions. First, this method was used on parallelepipedic specimens sawn into plate ($60 \times 40 \times 15$ cm^3) made using the French LPC wheel compactor (according to European standard EN12697-33:2003+A1:2007, AFNOR, 2007b). Orientation of the sample relative to the compactor wheel displacement is indicated in Figure 3.30. X direction corresponds to the displacement of the wheel, Z is the vertical direction, and Y is perpendicular to X and Z. The dimensions of the specimen are indicated in Table 3.2.

Wave propagation tests and interpretation using the back analysis presented in Section 3.6 were done for specimens in directions X, Y, and Z at a temperature of 26 °C. As the obtained anisotropy is less than 15% (see results below), the hypothesis of isotropy could still be considered with a good approximation for the dynamic back analysis. The Poisson's ratio and the phase angle of parallelepipedic samples, which are unknown, were evaluated to $\phi = 10°$ and $\nu = 0.3$. From these values and the dynamic tests, the complex modulus can be determined using previously presented methods. Values of propagation times, velocities of the P waves, and the obtained complex modulus are given in Table 3.2.

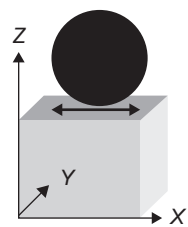


Figure 3.30 Parallelepipedic specimen sawn into plate made with the French LPC compactor. X, Y, and Z orientations are given from vertical direction and wheel displacement (Di Benedetto et al., 2009).

Table 3.2 Values of propagation time, velocity of P waves, and obtained complex modulus for the parallelepipedic specimen ($T = 26$ °C)

Direction of wave propagation	T_p (μs)	L (cm)	C_P (m/s)	$\lvert E^* \rvert$ (MPa)
X	20.8	7.5	3625.3	23,750
Y	18.3	6.5	3581.6	23,200
Z	21.5	7.1	3284.8	19,500

Di Benedetto et al. (2009).

www.EngineeringEBooksPdf.com

It can be seen from Table 3.3 that the complex moduli in directions X and Y are very close, while the modulus in direction Z is about 10% smaller. It is

$$|E^*(X)| \approx |E^*(Y)| \geq |E^*(Z)| \tag{3.34}$$

This last observation reveals that, of the specimens made with the plate compactor, Z direction is the softest. Other wave propagation tests were also made on specimens obtained from a gyratory compactor (according to European standard NF EN 12697-31, AFNOR, 2007a), which is also slightly anisotropic, with a stiffer vertical direction Z. In both cases, this is explained by a different geometrical organization of the granular skeleton, whose effects are far from negligible.

3.7.2 Poisson's ratio in different directions

Tension–compression complex modulus tests were performed on parallelepipedic specimens with the device developed at the University of Lyon/ENTPE (Clec'h et al., 2009, 2010). Sinusoidal axial and lateral strain were measured with strain gauges as well as sinusoidal axial stress on specimens obtained from the French wheel compactor (Figure 3.31a).

Two cases were considered (Figure 3.31b):

- Axial loading applied in the direction of compactor wheel displacement (direction I).
- Axial loading applied in the direction of compaction (direction II).

The bituminous specimens were loaded for different temperatures (from −26.3 to 56.6 °C) at different frequencies (0.01, 0.03, 0.1, 0.3, 1, 3, and 10 Hz for each temperature). The relation between stress and strain inside the parallelepipedic specimen is defined by the following equation, expressed in axes I, II, and III:

$$\underline{\varepsilon^*} = \underline{\underline{M^*}}\,\underline{\sigma^*} \text{ with } \underline{\underline{M^*}} = \begin{pmatrix} \frac{1}{E_{\mathrm{I}}^*} & -\frac{\nu_{\mathrm{III}}^*}{E_{\mathrm{II}}^*} & -\frac{\nu_{\mathrm{IIII}}^*}{E_{\mathrm{III}}^*} \\ -\frac{\nu_{\mathrm{III}}^*}{E_{\mathrm{I}}^*} & \frac{1}{E_{\mathrm{II}}^*} & -\frac{\nu_{\mathrm{IIIII}}^*}{E_{\mathrm{III}}^*} \\ -\frac{\nu_{\mathrm{III}}^*}{E_{\mathrm{I}}^*} & -\frac{\nu_{\mathrm{IIIII}}^*}{E_{\mathrm{II}}^*} & \frac{1}{E_{\mathrm{III}}^*} \end{pmatrix}, \quad \underline{\varepsilon^*} = \begin{pmatrix} \varepsilon_{\mathrm{I}}^* \\ \varepsilon_{\mathrm{II}}^* \\ \varepsilon_{\mathrm{III}}^* \end{pmatrix} \text{ and } \underline{\sigma^*} = \begin{pmatrix} \sigma_{\mathrm{I}}^* \\ \sigma_{\mathrm{II}}^* \\ \sigma_{\mathrm{III}}^* \end{pmatrix} \tag{3.35}$$

Complex modulus E_{I}^* and complex Poisson's ratios $\nu_{\mathrm{II\,I}}^*$ and $\nu_{\mathrm{III\,I}}^*$ were obtained from the complex modulus test with specimens loaded in direction I. Comparatively, when the complex modulus test was performed in direction II, it was possible to obtain complex modulus E_{II}^* and complex Poisson's ratios $\nu_{\mathrm{I\,II}}^*$ and $\nu_{\mathrm{III\,II}}^*$.

Figure 3.32 shows $|E_{\mathrm{I}}^*|$ and $|E_{\mathrm{II}}^*|$ experimental master curves obtained at the reference temperature of 10 °C and the corresponding master curves obtained with the 2S2P1D model. On Figure 3.32, $|E_{\mathrm{I}}^*|$ and $|E_{\mathrm{II}}^*|$ values (23,750 and 19,500 MPa) obtained from wave propagation tests presented previously on the same bituminous

www.EngineeringEBooksPdf.com

Table 3.3 2S2P1D model parameters for bituminous materials presented in Figures 3.16 and 3.17: two binders (B5070 and Orthoprène®), two corresponding mixtures (E5070 and Orthochape®), and bituminous mastic of sealing sheet (Paraforpont®)

Materials	E_{00} (MPa)	E_0 (MPa)	k	h	δ	Tau (s)	Beta	ν_{00}	ν_0	C_1	C_2
Binder B5070	0	1800	0.20	0.55	1.9	0.0002	500	–	–	25	170
Mixture E5070	10	36,000	0.20	0.55	1.9	0.04	100	0.50	0.22	25	170
Binder Orthoprène®	0	3250	0.22	0.60	3.2	1.2e−5	6000	–	–	35	218
Mixture Orthochape®	15	41,500	0.22	0.60	3.2	0.005	6000	0.46	0.30	35	218
Sealing sheet Paraforpont®	0.03	1350	0.25	0.52	6	0.005	1e10	–	–	17	132

Pouget et al. (2010) and Pouget (2011).

www.EngineeringEBooksPdf.com

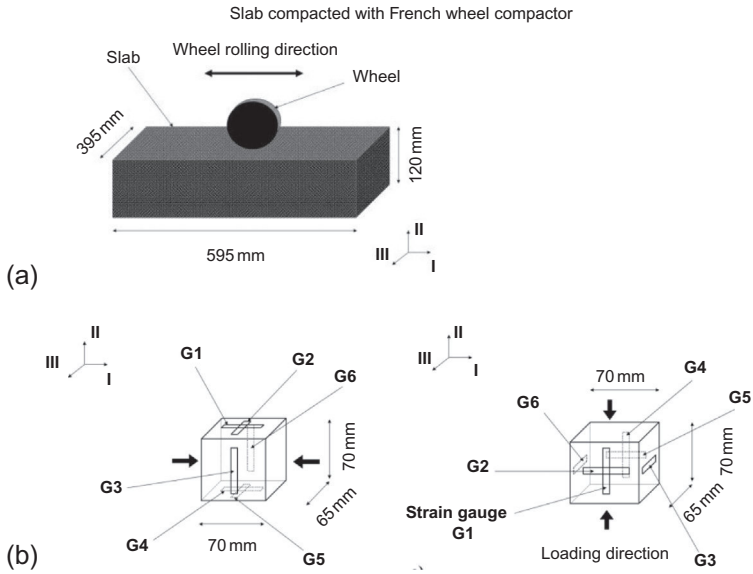


Figure 3.31 (a) Direction of compacting method and (b) tested specimen with loading directions (direction I for first specimen and direction II for second specimen) and strain-gauge positions (G1 to G6) (Clec'h et al., 2009, 2010).

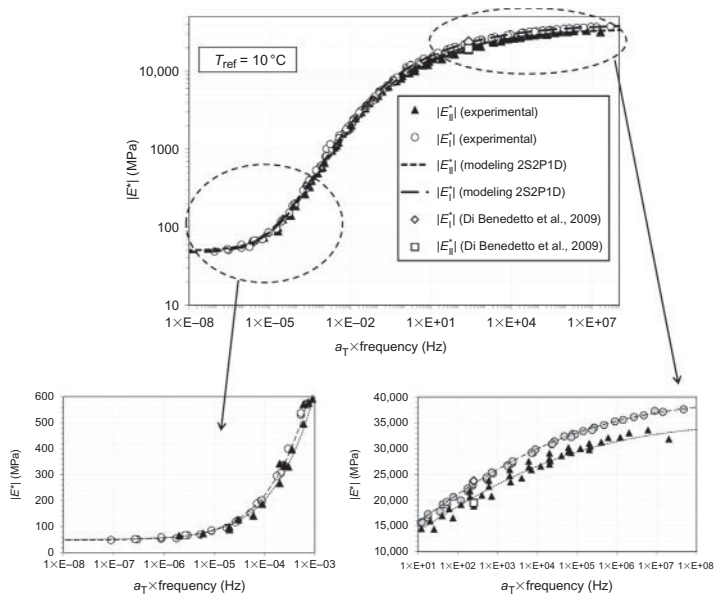


Figure 3.32 Master curves of $|E_I^*|$ and $|E_{II}^*|$ plotted at a reference temperature of 10 °C and 2S2P1D models (Clec'h et al., 2009, 2010).

www.EngineeringEBooksPdf.com

mixture at a temperature of 26 °C and a frequency of about 30,000 kHz are also plotted. The results presented here fit well with wave propagation tests results.

It can be seen that $|E_{\mathrm{I}}^*|$ and $|E_{\mathrm{II}}^*|$ are very close for low frequencies, while for high frequencies, $|E_{\mathrm{II}}^*|$ is about 10% smaller, which confirms results found with wave propagation:

$$\begin{cases} |E_{\mathrm{I}}^*| \approx |E_{\mathrm{II}}^*| \text{for low frequencies} \\ |E_{\mathrm{I}}^*| \geq |E_{\mathrm{II}}^*| \text{for high frequencies} \end{cases} \tag{3.36}$$

For high frequencies, the vertical direction appears softer than the other one. The anisotropy of the specimens appears more significantly for high frequencies.

With tension–compression complex modulus tests, it was possible to investigate other LVE parameters such as phase angle and complex Poisson's ratio.

Figure 3.33 shows $\phi(E_{\mathrm{I}})$ and $\phi(E_{\mathrm{II}})$ experimental master curves obtained at a reference temperature of 10 °C, and the corresponding master curves obtained with the 2S2P1D model. $\phi(E_{\mathrm{I}})$ and $\phi(E_{\mathrm{II}})$ are very close, like shift factors $a_{\mathrm{TE\,I}}$ and $a_{\mathrm{TE\,II}}$. There are very few differences between the two directions I and II for parameters concerning viscous effects.

Figure 3.34 shows $|\nu_{\mathrm{I\,II}}^*|$, $|\nu_{\mathrm{III\,II}}^*|$, $|\nu_{\mathrm{II\,I}}^*|$, and $|\nu_{\mathrm{III\,I}}^*|$ master curves at 10 °C and the corresponding master curves obtained with the 2S2P1D model. $|\nu_{\mathrm{II\,I}}^*|$ and $|\nu_{\mathrm{I\,II}}^*|$ are very close. $|\nu_{\mathrm{III\,I}}^*|$ is definitely smaller. It must be noticed that this result was also obtained with another test. $|\nu_{\mathrm{III\,II}}^*|$ is close to $|\nu_{\mathrm{II\,I}}^*|$ and $|\nu_{\mathrm{I\,II}}^*|$ for the highest frequencies (or the lowest temperatures) and is higher than the other three for the lowest frequencies (or the highest temperatures). When the material is not isotropic, it is possible to obtain Poisson's ratios higher than 0.5. By analogy with elasticity, to respect physical considerations about energy conservation, a necessary condition is

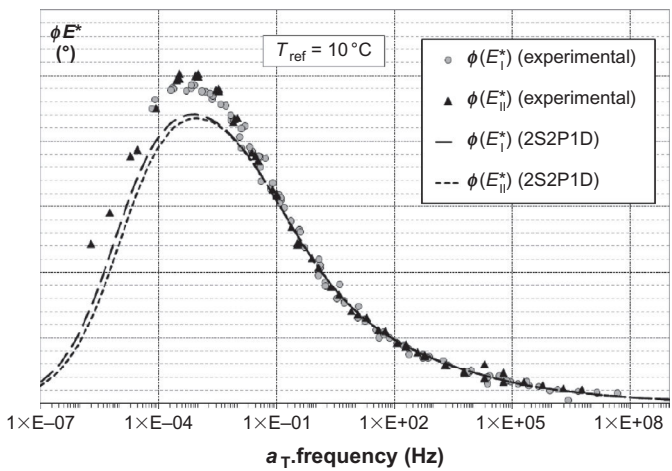


Figure 3.33 Master curves of $\phi(E_{\mathrm{I}})$ and $\phi(E_{\mathrm{II}})$ plotted at a reference temperature of 10 °C and 2S2P1D models (Clec'h et al., 2009, 2010).

www.EngineeringEBooksPdf.com

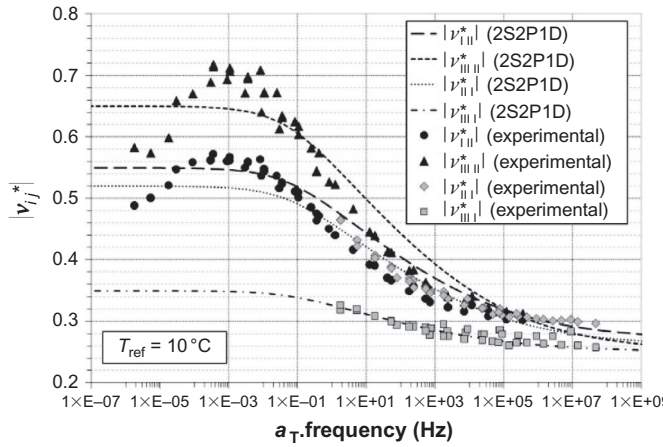


Figure 3.34 Master curves of $|\nu^*_{I\,II}|$, $|\nu^*_{III\,II}|$, $|\nu^*_{II\,I}|$, and $|\nu^*_{III\,I}|$ plotted at a reference temperature of 10 °C and 2S2P1D models (Clec'h et al., 2009, 2010).

$$1-|\nu^*_{I\,II}||\nu^*_{II\,I}|-|\nu^*_{I\,III}||\nu^*_{III\,I}|-|\nu^*_{III\,II}||\nu^*_{II\,III}|-2|\nu^*_{II\,I}||\nu^*_{III\,II}||\nu^*_{I\,III}|>0 \tag{3.37}$$

From this equation, it is quite easy to verify that Poisson's ratio could become higher than 0.5 for anisotropic materials.

3.8 Future developments

Some developments have been described about the LVE behavior of bituminous materials. As shown, several findings are based on the development of new accurate experimental devices, which allow the investigation of the 3D behavior of materials and their anisotropy. It is therefore possible to develop new models or improve existing models to take the observed behavior into account. The next step is to introduce these models in calculation tools in order to have better insight into real pavement response.

Some phenomena need to be further studied to get a more comprehensive 3D description of material behavior, such as 3D loading history and stress axes rotation, for instance. Triaxial tests able to apply confining pressure cycles reaching 10 Hz (as for axial loading) will be required, as well as some hollow cylinder apparatus with torsional loading capability or similar tests able to apply loading with stress axes rotation. Concerning experimental advances, some new techniques based on wave propagation are expected to develop in order to describe material behavior on a whole range of temperatures and frequencies, not only at some specific high frequencies. For example, it is possible to refer to Gudmarsson et al. (2014), where a promising spectroscopy analysis method is described. Such advances will enable the development of even more accurate modeling in the future.

www.EngineeringEBooksPdf.com

References

AASHTO, 1993. Guide For Design of Pavement Structures. American Association of State Highway and Transportation Officials, Washington, DC.

AFNOR, 2007a. Mélanges bitumineux—Méthodes d'essai pour mélange hydrocarboné à chaud —Partie 31: Confection d'éprouvettes à la presse à compactage giratoire (Bituminous mixtures—test methods for hot mix asphalt—part 31: specimen preparation by gyratory compactor). NF EN 12697-31, aout.

AFNOR, 2007b. Mélange bitumineux—Méthodes d'essai pour mélange hydrocarboné à chaud —Partie 33: confection d'éprouvettes au compacteur de plaque (Bituminous mixtures—test methods for hot mix asphalt—part 33: specimen prepared by roller compactor). NF EN 12697-33+A1, septembre.

AFNOR, 2011. Dimensionnement structurel des chaussées routières—Application aux chaussées neuves. NF P98-086, octobre.

Airey, G.D., Rahimzadeh, B., Collop, A.C., 2003. Linear Viscoelastic Performance of Asphaltic Materials. Road Mater. Pave. Des. 4 (3), 269–292.

Bilodeau, K., 2012. Comportement thermomécanique des matériaux traités au liant hydraulique et des bétons compactés routiers incluant des fraisâts bitumineux et des fibres métalliques. PhD thesis, University of Lyon/ENTPE, Lyon, France.

Bilodeau, K., Sauzeat, C., Di Benedetto, H., Olard, F., Bonneau, D., 2010. Mechanical Behavior of Fiber Reinforced Compacted Concrete with Incorporation of Reclaimed Asphalt Pavement. ISAP, Nagoya.

Bilodeau, K., Sauzeat, C., Di Benedetto, H., Olard, F., 2012. Roller compacted concrete for road base layer with RAP and steel fibers: viscous properties and fatigue behavior. In: International Conference on Concrete Pavement, Quebec, 16 p.

Clec'h, P., Sauzeat, C., Di Benedetto, H., 2009. Multidirectional behavior of bituminous mixture. In: Tutumluer, E., Al Qadi, I.L. (Eds.), 8th International Conference on the Bearing Capacity of Roads, Railways and Airfields. Urbana Champaign, IL, pp. 377–386.

Clec'h, P., Sauzéat, C., Di Benedetto, H., 2010. Multidirectional linear visco-elastic behavior and anisotropy of bituminous mixtures. In: GeoShanghai International Conference – Paving Materials and Pavement Analysis, Shanghaipp. 103–115.

Delaporte, B., Di Benedetto, H., Chaverot, P., Gauthier, G., 2007. Linear viscoelastic properties of bituminous materials: from binders to mastics. J. Assoc. Asphalt Paving Technol. 76, 455–494.

Di Benedetto, H., 1990. Nouvelle approche du comportement des enrobés bitumineux: résultats expérimentaux et formulation rhéologique. In: Eustacchio, E., Fritz, H.W. (Eds.), Mechanical Tests for Bituminous Mixes, Characterization, Design and Quality Control : Proceedings of the Fourth RILEM Symposium. CRC Press, USA.

Di Benedetto, H., Corté, J.-F., 2005. Matériaux routiers bitumineux, Vol. 2. Hermes-Lavoisier, Paris, 283 p. (in French).

Di Benedetto, H., Neifar, M., 2002. Experimental characterisation and modelling of thermo-visco-plastic behaviour of bituminous mixtures. International Conference on Bearing Capacity of Roads and Airfields, Lisbon, pp. 41–50.

Di Benedetto, H., Yan, X., 1994. Comportement mécanique des enrobés bitumineux et modélisation de la contrainte maximale. Mater. Struc. 21, 539–547 (in French).

Di Benedetto, H., Olard, F., Sauzéat, C., Delaporte, B., 2004. Linear viscoelastic behavior of bituminous materials: from binders to mixes. Road Mater. Pave. Des. 5 (SI), 163–202.

Di Benedetto, H., Delaporte, B., Sauzeat, C., 2007a. Three-dimensional linear behavior of bituminous materials: experiments and modeling. Int. J. Geomech. ASCE 7 (2), 149–157.

www.EngineeringEBooksPdf.com

Di Benedetto, H., Neifar, M., Sauzeat, C., Olard, F., 2007b. Three-dimensional thermo-viscoplastic behaviour of bituminous materials: the DBN model. Road Mater. Pave. Des. 8 (2), 285–316.

Di Benedetto, H., Sauzéat, C., Sohm, J., 2009. Stiffness of Bituminous mixtures using ultrasonic waves propagation. Road Mater. Pave. Des. 10 (4), 789–814.

Di Benedetto, H., Nguyen, Q.T., Sauzeat, C., 2011. Nonlinearity, heating, fatigue and thixotropy during cyclic loading of asphalt mixtures. Road Mater. Pave. Des. 12 (1), 129–158.

Ferry, J.D., 1980. Viscoelastic Properties of Polymers, 3rd ed. John Wiley & Sons, New York, 672 p.

Franken, L., Vanelstraete, A., 1995. Relation between mix stiffness and binder complex modulus. In: The Rheology of Bituminous Binders, European Workshop, Brussels, 5–7 April 1995.

Gudmarsson, A., Ryden, N., Di Benedetto, H., Sauzeat, C., Tapsoba, N., Birgisson, B., 2014. Comparing linear viscoelastic properties of asphalt concrete measured by laboratory seismic and tension–compression tests. J. Nondestruct. Eval. 33, 571–582.

Hochuli, A.S., Sayir, M.B., Poulikakos, L.D., Part, L.M.N., 2001. Measuring the complex modulus of asphalt mixtures by structural wave propagation. J. Assoc. Asphalt Paving Technol. 70, 546–574.

Huet, C., 1963. Etude par une méthode d'impédance du comportement viscoélastique des matériaux hydrocarbonés. Faculté des sciences de Paris, Paris, 69 p. (in French).

Kweon, G., Kim, Y.R., 2006. Determination of Asphalt Concrete Complex Modulus with Impact Resonance Test. Transport. Research Record, No 1970, pp. 151–160.

Lacroix, A., Kim, Y.R., Far, M.S., 2009. Constructing the dynamic modulus mastercurve using impact resonance testing. J. Assoc. Asphalt Paving Technol. 78, 67–95.

Lytton, R.L., Uzan, J., Fernando, E.G., Roque, R., Hiltunen, D., Stoffels, S.M., 1993. Development and validation of performance prediction models and specifications for asphalt binders and paving mixes. SHRP-A-357, Strategic Highway Research Program, National Research Council, Washington, DC.

Mangiafico, S., 2014. Linear viscoelastic properties and fatigue of bituminous mixtures produced with Reclaimed Asphalt Pavement and corresponding binder blends. PhD thesis, University of Lyon/ENTPE, Lyon, France.

Mangiafico, S., Di Benedetto, H., Sauzeat, C., Olard, F., Pouget, S., Planque, L., 2013. Influence of reclaimed asphalt pavement content on complex modulus of asphalt binder blends and corresponding mixes: experimental results and modelling. Road Mater. Pave. Des. 14 (SI), 132–148.

Mounier, D., Di Benedetto, H., Sauzeat, C., 2012. Determination of bituminous mixtures linear properties using ultrasonic wave propagation. Construct. Build Mater. 36, 638–647.

Neifar, M., Di Benedetto, H., 2001. Thermo-viscoplastic law for bituminous mixes. Road Mater. Pave. Des. 2 (1), 71–96.

Nguyen, H.M., Pouget, S., Di Benedetto, H., Sauzeat, C., 2009. Time-temperature superposition principle for bituminous mixtures. Euro. J. Environ. Civil Eng. 13 (9), 1095–1107.

Nguyen, Q.T., Di Benedetto, H., Sauzeat, C., 2012. Behavior of asphalt mixture under large amplitude cyclic loading. In: 2nd International Conference on Transportation Geotechnics, Hokkaido, Japan, pp. 388–393.

Nguyen, Q.T., Di Benedetto, H., Sauzeat, C., Tapsoba, N., 2013. Time temperature superposition principle for bituminous mixes in the linear and nonlinear domains. J. Mater. Civil. Eng. 25 (9), 1181–1188.

Norambuena-Contreras, J., Castro-Fresno, D., Vega-Zamanillo, A., Celaya, M., Lombillo-Vozmediano, I., 2010. Dynamic modulus of asphalt mixture by ultrasonic direct test. NDT&E Int. 43 (7), 629–634.

www.EngineeringEBooksPdf.com

Olard, F., Di Benedetto, H., 2003. General "2S2P1D" model and relation between the linear viscoelastic behaviors of bituminous binders and mixes. Road Mater. Pave. Des. 4 (2), 185–224.

Olard, F., Di Benedetto, H., 2005. Experimental characterization and constitutive modeling of the thermo-visco-elasto-plastic behavior of bituminous mixes : the "DBN" law. J. Assoc. Asphalt Paving Technol. 74. AAPT, Lino Lakes, MN, USA.

Olard, F., Di Benedetto, H., Eckmann, B., Triquigneaux, J.-P., 2003. Linear viscoelastic properties of bituminous binders and mixtures at low and intermediate temperatures. Road Mater. Pave. Des. 4 (1), 77–108.

Pouget, S., 2011. Influence des propriétés élastiques ou viscoélastiques des revêtements sur le comportement des ponts à dalle orthotrope. PhD thesis, University of Lyon/ENTPE, Lyon France.

Pouget, S., Sauzeat, C., Di Benedetto, H., Olard, F., 2010. From the behavior of constituent materials to the calculation and design of orthotropic bridge structures. Road Mater. Pave. Des. 11 (SI), 111–144.

Setra-Lcpc, 1997. Guide technique. In: French Design Manual for Pavement Structures. LCPC et SETRA, Paris.

Tapsoba, N., 2012. Comportement des enrobés bitumineux à base de matériaux recyclés et/ou fabriqués à température réduite. PhD thesis, University of Lyon/ENTPE, Lyon, France.

Tapsoba, N., Sauzeat, C., Di Benedetto, H., Baaj, H., Ech, M., 2014. Behavior of asphalt mixtures containing RAP and shingles. Road Mater. Pave. Des. 15 (2), 330–347.

Tiouajni, S., Di Benedetto, H., Sauzeat, C., Pouget, S., 2011. Approximation of linear viscoelastic model in the 3 dimensional case with mechanical analogues of finite size application to bituminous materials. Road Mater. Pave. Des. 12 (4), 897–930.

Zeng, M., Bahia, H.U., Zhai, H., Anderson, M.R., Turner, P., 2001. Rheological modeling of modified asphalt binders and mixtures. In: Annual Meeting of the Association of Asphalt paving Technologists.

www.EngineeringEBooksPdf.com

Characterization of asphalt materials by scanning probe microscopy

4

A.T. Pauli, R. Will Grimes, A. Cookman, J. Beiswenger
Western Research Institute, Laramie, WY, USA

4.1 Introduction

4.1.1 Review of scanning probe microscopy imaging investigations of bituminous materials

Asphalt binders used in the construction of pavements exhibit unique compositional properties at the micron and nanometer scale. Lesueur (2009) gives both historical and modern accounts of progress made toward explaining the relationships between chemical (compositional) and rheological (physical) material properties of asphalt as related to pavement longevity. Asphalt binders are generally defined as the residuum from the distillation of petroleum crude stocks. Molecular species that comprise these materials vary in chemical structure from that of nonpolar waxy and oily type hydrocarbon molecules to heteroatom-containing condensed polyaromatic ring molecules (Tissot and Welte, 1984; Yen and Chilingarian, 1994). The chemical composition of asphalts varies significantly from one crude source to the next (Branthaver et al., 1993).

The Strategic Highway Research Program (SHRP) applied research to address the problem of the deteriorating condition of US highways. SHRP research directed toward developing a better understanding of how asphalt chemistry influences performance resulted in a microstructure model that related asphalt chemistry to physical properties. The model predicts a variety of intermolecular associations as largely responsible for the physical properties of asphalt. This microstructure is assumed to be a three-dimensional association of polar constituents variously distributed in a less-polar liquid phase (Halladay, 2007).

The limited usefulness of optical microscopy techniques led some researchers to try scanning probe microscopy (SPM) techniques in an attempt to characterize asphalt microstructure. Loeber et al. (1996, 1998) were among the first researchers to investigate asphalt bitumen with atomic force microscopy (AFM). In this work, asphalt films prepared on stainless-steel substrates were imaged with AFM and scanning tunneling microscopy. Force-mode (contact) AFM imaging revealed the development of small oblong-shaped structures with a rippled interior several micrometers in diameter and tens of nanometers in height. The structures were present in greater number in gel-type (i.e., higher asphaltene content) asphalts. The authors coined the term "bumble bees" to describe the structures, which resembled the yellow and black

Advances in Asphalt Materials. http://dx.doi.org/10.1016/B978-0-08-100269-8.00004-0
© 2015 Elsevier Ltd. All rights reserved.

www.EngineeringEBooksPdf.com

stripes of a bumble bee. Other shapes and textures, including networks and spherical clusters, were also observed. Loeber et al. (1998) also investigated emulsions, describing the structures in the wet samples as micelle-like, and the dry samples as a network composed of the residue of surfactant left behind after breaking the emulsion and removing the water.

Pauli et al. (2001, 2003a,b) used AFM to study the SHRP asphalts (Jones, 1993) prepared as solutions and cast on glass microscope slides. Both lateral-scanning friction-force AFM and tapping-mode AFM revealed "bumble bee" structures identical to the type reported by Loeber et al. (1996). The authors also observed patchy or spotty phases in some asphalts, and the disappearance of structures in certain other cases. Pauli and Grimes (2003) also observed that structures would appear to dissolve or melt away with repetitive scanning over the same area.

Masson et al. (2006) reported using a phase-contrast AFM technique, where images are produced based on the time delay between the drive and response signals of an oscillating tip to study phases in asphalt. These authors considered the "catanaphase" (the ripples), "periphase" (football silhouette), "paraphase" (solvent regions), and "salphase" (high-phase contrast spots, very small in size). Masson et al. (2007) also reported using cryogenic phase-detection AFM to study asphalt films' heat cast onto glass slides. Samples were imaged in intermittent-contact mode at −10, −20, and −50 °C. In the temperature range of −10 to −20 °C (specified as being above the glass transition temperature), the authors reported observing material phase contraction (shrinkage). Below −55 °C (well below the glass transition temperature of most asphalts), additional liquid-like phases were observed.

Wu et al. (2009) studied neat and styrene–butadiene–styrene (SBS) polymer-modified asphalts prior to aging, and after aging. The images presented by Wu show bees in both neat and polymer-modified materials after aging. The authors concluded that bee structures increased in both neat and polymer-modified materials after aging. Carrera et al. (2009, 2010) considered variations in morphology of chemically treated bitumen by AFM. Isocyanate-based polymer-modified bitumen and bitumen after chemical foaming, respectively, were considered in these studies. Bee structures were observed to develop with the addition of the modifier when samples were heated to 50 °C. AFM imaging of chemically foamed bitumen revealed that modified materials, as compared to their parent neat-material binder, showed more extensive and larger structuring of the familiar "bee" type.

Studies reported by De Moraes et al. (2010), Schmets et al. (2010), and Pauli et al. (2011) indicate that "bee" structuring is likely attributed to wax crystallization. AFM imaging of thermally conditioned samples demonstrates that bee structures change at temperatures that coincide with melting/recrystallization of wax in asphalt. Pauli et al. (2011, 2014) further show that bitumen commonly observed to be void of bee structures, once blended with model paraffin wax in the 1–3 wt.% range, will show bee structuring. In later publications, Soenen et al. (2014), Qin et al. (2014), Fischer et al. (2013), and Fischer and Dillingh (2014) report additional studies involving blending of bitumen with wax, followed by AFM analysis and/or differential scanning calorimetric approaches, all of which indicate that bee structuring is most likely related to wax crystallization.

www.EngineeringEBooksPdf.com

Pauli et al. (2011) point out several important factors that influence the interpretation of AFM images generated for bituminous materials: "Image is of the sample surface, it is necessarily related to, but may or may not be representative of bulk constituents. Hysteresis effects, particularly with respect to thermal cycling, can significantly change the appearance of the sample surface. Asphalt surfaces tend to be inhomogeneous at several length scales so that the area imaged may not be representative of the overall surface characteristics. Experimental/instrumental factors including contamination of the cantilever or probe tip, changes in set point, and incorrectly set gains in the feedback loop can result in dramatic changes in the image. Anomalies such as apparent phase inversion and changes in resolution are often the result of these factors (Bhushan and Qi, 2003). Sample variables, such as film thickness, solvent selection, and solution concentration can strongly influence what is seen in the image." Fischer and Dillingh (2014) recently demonstrated differences in bulk relative to surface structuring in freeze-fractured bitumen specimens imaged with AFM. Their findings now suggest that different ordering occurs in the bulk relative to the surface in many bituminous materials.

Very recent publications discuss AFM imaging of new and more novel modified bitumen, including aging of organo-montmorillonite-modified bitumen (Zhang et al., 2011), vermiculite-modified bitumen (Zhang et al., 2013), bio-oil-derived polyurethane-modified bitumen (Cuadri et al., 2014), and asphalt clay nanocomposites (Nazzal et al., 2013).

4.1.2 SPM nanomechanic techniques

Nanomechanical approaches have been employed to differentiate relative hardness of features observed in AFM images of asphalt surfaces. Indentation testing with hard tips of known shape and size, pressed into a surface, constitute one method for determining material hardness. Nanoindentation applies at much smaller scale to measure stiffness and creep relaxation properties of thin films (Bhushan, 2005; Fisher-Cripps, 2004; Geng et al., 2005; Huang and Lu, 2006; Liu et al., 2006; Zhou and Komvopoulos, 2006).

AFM-nanomechanical approaches have been applied to study the mechanical and compositional properties of asphalts. Jäger et al. (2004) reported that noncontact and pulsed-force mode AFM offer both surface topographical and near-surface mechanical property identification, respectively, of bitumen microphases. This type of investigation measures contact stiffness of "bee" structures. The authors suggest that a material secant stiffness,

$$K_{\mathrm{T}} = \Delta F/_{s}\Delta z \tag{4.1}$$

determined from a measure of the force increment

$$\Delta F_s = \xi_s k V_s \tag{4.2}$$

is a function of a force increment "history" signal V_s, given the cantilever force constant k, the cantilever penetration depth into the surface Δz, and a parameter ξ_s that is a

www.EngineeringEBooksPdf.com

function of the cantilever oscillation amplitude and detection sensitivity of the AFM. Likewise, the force of adhesion

$$F_{ad} = \xi_{ad} k V_{ad} \tag{4.3}$$

is measured based on a minimum cantilever deflection signal V_{ad}, given the instrument settings parameter ξ_{ad}. These investigators showed that bee structures and surrounding matrix "domains" exhibit both harder and softer regions and that the bee structures are of lower adhesion compared to the surrounding matrix domains.

Tarefder and Zaman (2010, 2011) reported using AFM noncontact mode imaging and chemically functionalized tip force-distance adhesion measurements, in addition to nanoindentation, to study changes in mechanical and adhesive properties of asphalt materials before and after moisture conditioning (Section 4.2.1). The Oliver and Pharr model (Oliver and Pharr, 1992) was used to interpret test results for mastic sample studies where hardness decreased more for "wet" compared to "dry" unconditioned samples.

Allen et al. (2012, 2013) used AFM nanoindentation to calculate moduli for virgin and aged asphalts derived from different crude sources. The authors noted both an increase in the elastic modulus with aging and differences in the elastic modulus for different surface phases. This work provides an analytical expression for calculating the viscoelastic modulus based on the Galin–Sneddon solution, suggesting that the indent depth of elastic material

$$h(t) = \sqrt{\left(\frac{\pi}{2\tan\theta}\right)\left(\frac{P(t)(1-v^2)}{E}\right)} \tag{4.4}$$

given the indentation load force $P(t)$, material elastic modulus E, Poisson's ratio v, and indenter geometric angle θ may be transformed from the t-domain to the s-domain, which applies to viscoelastic material as

$$\widetilde{h}(s) = \sqrt{\left(\frac{\pi}{2\tan\theta}\right)\left(\frac{\widetilde{P}(s)\left(1-\widetilde{v}^2(s)\right)}{\widetilde{E}(s)}\right)} \tag{4.5}$$

given the transform variables $\widetilde{P}(s) = P/s$, $\widetilde{v}(s) = v$, and $\widetilde{E}(s)^{-1} = s^2\widetilde{D}(s)$. This contribution should prove extremely useful for future asphalt material research.

While a powerful tool, application of nanoindentation and interpretation of results for viscoelastic materials is necessarily complex. Frequently, the same tip to indent a sample is also used to image and quantify the indent area. However, tip size and shape are rarely known with precision. Tips are often rounded, truncated cones with a nominal radius of ~10-nm, but vary in dimension. Tip geometry can be obtained by imaging with a scanning electron microscope. Furthermore, asphalt tends to wet and coat the tip so that the actual tip geometry, after first use, is unknown. At nanoscale, asphalt surfaces are far from smooth. Surface irregularities can be as large as the area of the

www.EngineeringEBooksPdf.com

indentation, leading to inconclusive tip-area values. The response of a viscoelastic material to indenting is sensitive to test temperature, rate of loading, and plastic flow; thus, material can "pile up" around indentation "holes." Thus, it is not a simple matter to define indent geometry. These factors should be carefully considered in the interpretation of AFM nanoindentation results.

4.1.3 SPM nanochemical and nanoadhesive techniques

Nanochemical and nano-adhesive techniques are strongly influenced by inter- and intra-molecular forces and tip-sample mechanical response. Pauli et al. (2003) used AFM force–displacement and friction scanning to study adhesive properties of asphalt. Asphalt films (1-μm) were subjected to force–displacement testing using cantilevers (spring constants of $k = 7$ and 14-N/m) fitted with 5- or 10-μm diameter glass microbead "colloidal" tips. Asphalt surface tensions at ~22 °C ranged from 40 to 50-dyn/cm based on measures of work of adhesion, interpreted in terms of the "pull-off" force required to break contact between the "colloidal" tip and sample surface.

Yu et al. (2013) conducted pull-off force measurements with standard cantilevers reporting adhesion in nanonewtons (nN). In most samples, two phases were observed, one of which was of higher profile. The authors noted that higher profile domains were of higher adhesion compared to lower profile domains.

Lyne et al. (2013a) used PeakForce QNM (Quantitative Nanomechanical Property Mapping), or AFM-QNM, a force-mapping technique that produces images relative to differences in adhesive and compliance properties, to characterize adhesion and stiffness of asphalt binders of the same 70/100 binder grade. The authors reported that catanaphase (the ripples) and periphase (surrounding area) domains were of lower adhesion but higher Young's modulus compared to paraphase (solvent regions).

Rebelo et al. (2014) characterized low-wax-content asphalt binders of neat and aged asphalt samples employing several different AFM techniques, including phase and lateral imaging and force–displacement measurements. Topography phase images of unaged, rolling thin-film oven test aged, and pressure aging vessel aged sample materials showed two phases. Force–displacement analysis was utilized to determine elastic modulus, apparent viscosity, and work of adhesion, concluding that the domains observed related to asphaltene micelles.

Nanochemical techniques use cantilever tips functionalized with colloidal particles and/or chemical moieties such as methyl groups (—CH_3), hydroxyl groups (—OH), carboxyl groups (—COOH), and amine groups (—NH_3). The technique is referred to as chemical force microscopy (CFM). CFM involves scanning the surface with functionalized tips or a series of pull-off force measurements. As with all types of SPM, CFM, which measures the interaction of the tip with various surface features, simultaneously detects variations in topography and mechanical properties, resulting in complex contrast in CFM images; thus, image interpretation is difficult.

Tarefder and Zaman (2010, 2011) used CFM to evaluate moisture damage propensities among bitumen derived from different crude sources, polymer and antistrip chemical modification, and aged asphalt. Differences in adhesive character,

www.EngineeringEBooksPdf.com

particularly between polymer-modified compared to unmodified binders, were reported for dry and wet conditioned samples.

Allen et al. (2014) report force–displacement measurements using "standard tip size" silicon cantilevers functionalized with methyl (—CH_3), and carboxyl groups (—COOH) to study asphalts doped with their own chromatograph fractions. Two bitumen samples were separated as saturates, aromatics, resins, and asphaltenes, and then separately blended back into their respective parent bitumen. This study demonstrated that bee structuring increased with the addition of saturate materials, which is assumed to contain paraffin waxes, supporting the hypothesis that bees may be closely related to wax.

4.2 Sample preparation methods

There is currently no universal consensus of best practices for sample preparation to study asphalt microstructure. Sample preparation methods commonly used for AFM are generally described as either heat casting or solvent casting. Thus, an understanding of how sample preparation influences image quality is needed to realize the full potential of AFM in studies of asphalt.

4.2.1 Heat and solvent casting techniques

Loeber et al. (1998) prepared samples for AFM by heating asphalt to 99 °C, then dropping it onto stainless-steel substrates and cooling to −5 °C. Masson et al. (2006, 2007) prepared samples by pouring asphalt onto small heated steel disks and spreading with a blade, followed by an additional minute of heating. Zhang et al. (2013) and Rebelo et al. (2014) followed a procedure similar to that used by Masson, except that the asphalt was heated and poured at higher temperatures. Lyne et al. (2013a) used a variation of the heat casting technique, in which the asphalt was heated to 150 °C and poured into 1-cm square aluminum molds, generating 10-mm-thick samples.

Tarefder and Zaman (2010, 2011) used a glass slide wrapped with high-temperature tape, forming a small gap into which heated polymer-modified asphalt was poured. The coated glass substrate was placed in an oven to distribute the asphalt evenly. After preparation, wet conditioned samples were stored under water. Both dry and wet conditioned samples were dried overnight in a draft oven at 40 °C, prior to AFM analyses.

Nazzal and Abu-Qtaish (2013) evaluated warm-mix asphalts using the Tarefder and Zaman (2010, 2011) approach, and a second method in which asphalt was sandwiched between two glass slides under the pressure of a 100-g weight in an oven at 120 °C. The sandwich was separated by sliding the cover slide off and then placed back into the oven for 15 min.

Pauli et al. (2001, 2003) used a solvent casting technique where 20 μL of a 0.20 g/mL solution of asphalt dissolved in dichloromethane was deposited toward the center of a glass slide using a pipette. The solution was slowly swirled to distribute the asphalt film to the edges of the slide as the casting solvent evaporated. For films

www.EngineeringEBooksPdf.com

observed to be nonuniform, two or three drops of toluene were deposited onto thicker regions of the film and swirled to achieve uniformity. Samples were stored in a vacuum desiccator for a minimum of 48 h, allowing for evaporation of casting solvent prior to AFM analysis.

4.2.2 Spin casting techniques

Spin casting techniques adopted from polymer science (Hall et al., 1998) often produce more uniform sample films in the thickness range of nanometers to micrometers. With this technique, a bitumen sample is dissolved in solvent or heated, and then dispensed onto a spinning substrate (e.g., glass microscope slide, silicon wafer, polished salt crystal). The angular velocity of the spinning substrate generates a centrifugal force, driving the "liquid" sample over the substrate to produce uniform films.

Allen et al. (2012, 2013, 2014) placed solvent spin-cast asphalt films, prepared as 1.5-g bitumen/11-mL HPLC-grade toluene, onto ethanol-cleaned (precleaned) glass microscope slides. Films were spin cast at 1000 rpm for 15 s, resulting in a film thickness of 1000 $\pm$ 200 nm. In this procedure, solution is "liberally" dispensed over the surface of the glass slide with a pipette prior to spin casting. Films are dried by heating under dry nitrogen in a vacuum desiccator for 2 h to remove residual solvent. Dry films are annealed for 1 h at 50 °C under nitrogen gas purge to eliminate artifacts, and then stored in an airtight chamber prior to analysis to prevent film oxidation.

Pauli et al. (2011, 2013, 2014) worked on a confined film translational deposition spin-coating procedure. Pauli et al. describe an International Crystal Laboratories (ICL) rotational casting Roto-Film™ apparatus fitted with a custom fabricated robotic arm with a precision digital syringe pump (Harvard Apparatus). With this system, a droplet of solution is confined in a small gap between the tip of the dispensing syringe needle and the rotating substrate. A robotic arm moves the depositing confined droplet at a controlled rate laterally across the surface of the substrate from center to edge, depositing asphalt solution at a controlled rate. Sample solutions are spin cast at angular velocities of 400–1000 rpm to fine-control film thickness. Films are stored in an inert-gas-purged (argon or nitrogen) drying box for no less than 24 h prior to AFM analysis. The apparatus generates uniform films of $<$10 to $>$5000 nm in thickness.

Nazzal et al. (2013) employed spin coating without solvent. Asphalt is heated to 165 °C, and then deposited onto precleaned glass slides and spin cast at speeds of 5000–8000 rpm.

4.2.3 Sample conditioning

A majority of researchers now report conditioning sample films to make surfaces smooth and even prior to AFM imaging (Soenen et al., 2014). Conditioning generally entails thermal treatment at elevated temperatures to liquefy in order to smooth and even out film surfaces.

Pauli et al. (2011, 2013, 2014) report heating sample films to 60–80 °C under nitrogen in a vacuum oven for 30 min, followed by cooling (under nitrogen) to ambient temperature for at least 24 h. Sample films are stored under nitrogen purge to ensure

www.EngineeringEBooksPdf.com

complete evaporation of solvent. Allen et al. (2013) utilize ultra-high purity dry nitrogen in a heated vacuum desiccator to eliminate residual solvent prior to annealing films, for 1 h at 50 °C under nitrogen gas purge. Some authors also report storing samples for longer periods of time. McCarron et al. (2012) report covering samples, left to air-dry for a week, prior to imaging.

Tarefder and Zaman (2010, 2011), employing specialized methods of sample conditioning, prepare wet conditioned films by saturation with water for 30 min in a vacuum, then submersion for 72 h. Dry and wet conditioned samples are dried overnight in a draft oven at 40 °C. Fischer and Dillingh (2014) employ a cold mechanical extraction and freeze fracturing procedure to prepare samples for AFM imaging. Fischer et al. (2013) also report preparing small "bead" amounts of asphalt applied to mineral surfaces. Asphalt is deposited on a flat region of a mineral substrate, heated (1–2 min, 125 °C), then tilted to establish advancing and receding angles to the drop to image the contact line where the asphalt drop contacts and wets the mineral substrate.

4.2.4 Advantages and disadvantages in current approaches

Very different AFM images can be obtained depending on sample preparation technique and conditions. Use of solvent, temperature, presence of oxygen, annealing rates, thermal history, and sample thickness, as well as other factors, all influence structuring on asphalt film surfaces (Pauli et al., 2011; Soenen et al., 2014). Some researchers now claim that annealing is beneficial for repeatable structure identification, while conflicting interpretations of the nature of the structures commonly observed remain.

Heat casting is a quick and easy method for film preparation that eliminates the variability associated with the addition of solvent, but at the expense of control over "film" thickness. Temperature conditioning necessarily needs to be uniformly controlled between sample sets for legitimate image interpretation. Solvent casting methods also have advantages and disadvantages. McCarron et al. (2012) speculate that solvent casting affects the chemical bonds within the binder. Thermal techniques have thus been preferred by researchers who believe that structuring may change with the presence of solvent. But solution cast methods allow multiple samples to be prepared quickly, with high repeatability in film thickness. Thermal annealing is then commonly used to dry and condition the sample. Soenen et al. (2014) recently reported finding no evidence that microstructures observed for solvent spin-cast asphalt films varied significantly after thermal annealing compared to heat-cast films. Thus, solvent casting techniques coupled with thermal annealing, which provides control of film thickness, may be exploited for some purposes, while heat casting may be preferred when solvent effect is a concern.

Sample preparation techniques coordinated with experimental objectives should lead to a better understanding of material composition. To date, there is no universally accepted technique for preparation of asphalt for AFM imaging. As with all microscopy techniques, what is observed or detected depends to a large extent on how the sample is prepared. An appropriate sample preparation technique should be chosen in accord with experimental objectives. A variety of preparation techniques work adequately to observe "bee structures" on asphalt films. However, when trying to establish quantitative

www.EngineeringEBooksPdf.com

measures of surface structure based on AFM images, the relationship between sample preparation and what is seen in the image must be carefully considered.

4.3 Atomic force microscopy (AFM) analysis of surface structuring in asphalt thin films

4.3.1 Surface characteristics of wax-containing asphalts

Several research groups now hypothesize that waxes are responsible for, or are associated with, "bee" structures observed in asphalt thin-film samples via AFM, although the asphaltene–resin micelle hypothesis is still considered. The appearance of surface structuring has been shown to relate to wax type, wax concentration, crystallizing conditions, and crude source (Pauli et al., 2011). Cooling rate also affects changes in morphology of the film. The effects of temperature and cooling rate on asphalt surface morphology have prompted some researchers to conduct AFM imaging as a function of temperature (Pauli and Grimes, 2003; Masson et al., 2007; Fischer et al., 2013; Soenen et al., 2014; Nahar et al., 2013; Pauli, 2014). Variable-temperature AFM images of sample films heated and cooled in stepwise increments reveal a metamorphosis in surface structuring, as depicted in Figures 4.1 and 4.2.

In these two figures, a spin-cast 1-μm thick film of SHRP asphalt (AAK-1), prepared in toluene solution followed by drying several days under inert gas, was imaged while heated/cooled on a Peltier temperature stage in 5 °C increments. After each temperature change, the film was thermally stabilized for 20 min and then imaged in AFM tapping mode. These two figures effectively show melting/recrystallization of the familiar "bee" microstructures (Figure 4.2e and f).

4.3.2 Surface freezing crystallization of wax in asphalt: theory

It is casually noted that despite the fact that surface structuring in bituminous materials, otherwise referred to as "bee" microstructures, have been reported in the literature since the mid-1990s, few publications offer a plausible mechanism for their formation. Among these publications, Lyne et al. (2013b) report a plausible mechanism for bee formation involving differential expansion–contraction of a biphase system. In this model, Lyne et al. (2013b) consider the bees to be stiffer laminate structures in contact with a softer matrix surface. With cooling, the laminate contracts and wrinkles relative to the matrix surface on which it is in contact. The authors argue that surface wetting of the lower surface free-energy paraffin molecules on the higher surface free-energy matrix surface accounts for the phenomena of bee structuring at the surface interface.

Comparatively, Pauli et al. (2011) report in a recent study on the phenomena of wax structure formation in bituminous asphalt binders. These authors adopt a mechanism based on surface freezing of paraffin wax in model paraffin solvents to describe the structuring of wax on asphalt thin-film surfaces. Wu et al. (1993a,b), Ocko et al. (1997, 2001), and Sloutskin et al. (2001, 2003) originally considered the formation of surface crystallized wax lamella, which requires the elimination of a liquid–vapor

www.EngineeringEBooksPdf.com

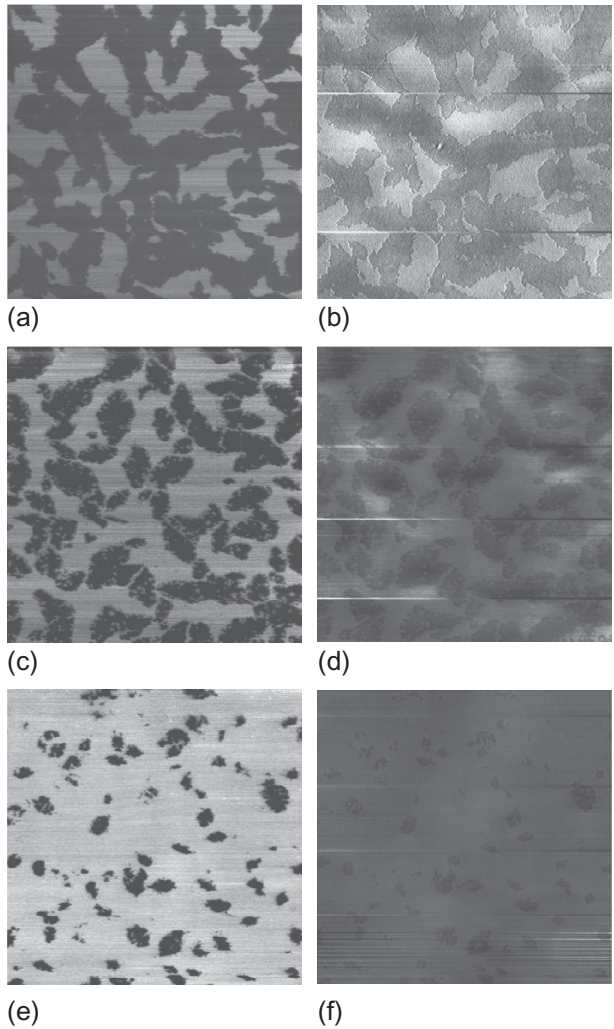


Figure 4.1 AFM phase (a, c, e) and topography (b, d, f) scans (20×20-μm area) of a Boscan crude asphalt designated SHRP AAK-1 imaged during heating on a thermal stage, depicted at 25 °C (a, b), 30 °C (c, d), and 35 °C (e, f).

interface with an accompanying free-energy gain of γ_{lv}, followed by the creation of two crystal interfaces—a solid–vapor interface and a solid–liquid interface—with accompanying free-energy loss of $\gamma_{sv} + \gamma_{sl}$. Thus, the criteria for surface freezing is defined as

$$\gamma_{lv} > (\gamma_{sv} + \gamma_{sl}) \tag{4.6}$$

Pauli et al. (2014) report that surface free-energy measurements of asphalts and their fractions, including maltenes and chromatographically separated oil fractions, satisfy this

www.EngineeringEBooksPdf.com

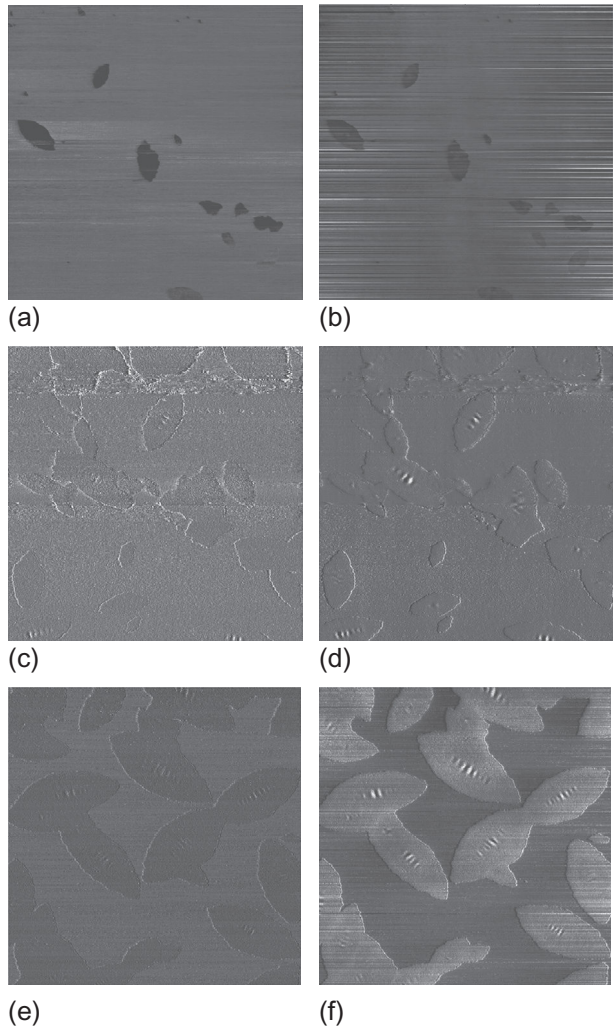


Figure 4.2 AFM phase (a, c, e) and topography (b, d, f) scans (20×20-μm area) of a Boscan crude asphalt designated SHRP AAK-1 imaged during cooling on a thermal stage after heating to 40 °C, depicted at 35 °C (a, b), 30 °C (c, d), and 25 °C (e, f).

criterion. They further propose a rippling mechanism theory for the formation of bee structures based on crystallization thermodynamics, for which they attribute the phenomena of rippling to curvature elastic strain in a sectorized crystal (Dorset et al., 1990, 1993; Bassett et al., 1988; Loveinger et al., 1994; Tsukruk and Reneker, 1995; Zhou et al., 2000; Guenthner and Kyu, 2000; Kyu et al., 2000; Mehta et al., 2004a,b; Xu et al., 2005).

Assuming that bee formation is a result of surface freezing crystallization of wax on a bitumen film surface, bulk-to-surface phase transformation thermodynamics in model paraffin systems are considered (Sloutskin et al., 2001, 2003). Sloutskin

www.EngineeringEBooksPdf.com

et al. (2001, 2003) developed a thermodynamic model for the demixing of paraffins in a bulk solution (or melt) and the corresponding surface crystallization (or surface freezing) with cooling. Accordingly, the free energy of a mixture of N-number of type-n paraffins dissolved in M-number of type-m paraffins (solvent) is defined by

$$\mathcal{F}^{lb} = Nf_n^{lb} + Mf_m^{lb} + k_B T[N \ln \varphi_N + M \ln \varphi_M] \tag{4.7}$$

given the number fractions $\varphi_N = N/N+M$ and $\varphi_M = M/N+M$, the Boltzmann constant k_B, and the free-energy expressions in each material type $f_{i:n,m} = \epsilon_{i:n,m} - TS_{i:n,m}$ ($\epsilon_{i:n,m}$: enthalpies and $S_{i:n,m}$: entropies).

The chemical potentials that define these species in the bulk-b and liquid-l states are expressed by

$$\frac{\partial \mathcal{F}_n^{lb}}{\partial N} = \mu_n^{lb} \tag{4.8}$$

and

$$\frac{\partial \mathcal{F}_m^{lb}}{\partial M} = \mu_m^{lb} \tag{4.9}$$

where the free energy of surface freezing is expressed by

$$\mathcal{F}^{s\sigma} = Nf_n^{s\sigma} + Mf_m^{l\sigma} + k_B T[N \ln \varphi_N + M \ln \varphi_M] \tag{4.10}$$

The corresponding chemical potentials for these same species at the surface-σ, in the liquid-l and solid-s state, are expressed by

$$\frac{\partial \mathcal{F}_n^{s\sigma}}{\partial N} = \mu_n^{s\sigma} \tag{4.11}$$

and

$$\frac{\partial \mathcal{F}_m^{l\sigma}}{\partial M} = \mu_m^{l\sigma} \tag{4.12}$$

Performing four derivatives while assuming the equilibrium condition $\mu_i^{lb} = \mu_i^{s\sigma}$, followed by substitution into the surface excess free-energy expression

$$\gamma_i A_i = f_i^{\sigma} - f_i^{b} = \epsilon_i^{\sigma} - \epsilon_i^{b} - T\left(S_i^{\sigma} - S_i^{b}\right) \tag{4.13}$$

results in the expression

$$\gamma_m A_m - \gamma_n A_n = \left(f_m^{l\sigma} - f_m^{lb}\right) - \left(f_n^{s\sigma} - f_n^{lb}\right) = k_B T \ln\left[\frac{\varphi_M^{lb}}{\varphi_M^{l\sigma}}\right] - k_B T \ln\left[\frac{\varphi_N^{lb}}{\varphi_N^{s\sigma}}\right] \tag{4.14}$$

www.EngineeringEBooksPdf.com

Sloutskin et al. (2001, 2003) noted that this expression leads immediately to the extended Langmuir isotherm expression (Piñeiro et al., 2004; Brocos et al., 2007)

$$\Gamma \equiv \frac{\varphi_N^{s\sigma}\varphi_M^{lb}}{\varphi_N^{lb}\varphi_M^{l\sigma}} = e^{(\gamma_m A_m - \gamma_n A_n)/k_B T} \tag{4.15}$$

Thus, assuming the transfer of type-n species from the bulk (with number fraction φ) to the surface φ^σ, the relative surface excess adsorption Γ is defined by

$$\frac{\varphi_N^{s\sigma}\varphi_M^{lb}}{\varphi_N^{lb}\varphi_M^{l\sigma}} \equiv \frac{\varphi^\sigma(1-\varphi)}{\varphi(1-\varphi^\sigma)} = \frac{\varphi^\sigma(\varphi-1)}{\varphi(\varphi^\sigma-1)} = \Gamma \tag{4.16}$$

Solving for the number fraction of solidified surface species leads to what is referred to here as the Wu–Ocko–Sloutskin (WOS) extended Langmuir model:

$$\varphi^\sigma = \frac{\varphi\Gamma}{1-\varphi+\varphi\Gamma} \tag{4.17}$$

Progressively thinner bitumen films can thus provide depleted quantity of wax in the bulk φ that is available to crystallize at the surface of a film φ^σ. Thus, given a critical film thickness h_c and critical number fraction of wax in the bulk,

$$\varphi_c = \frac{(N_{C_nH_{2n+2}})_c}{N_{\text{total}}} \tag{4.18}$$

the total number of paraffins plus all other asphalt particles in the critical film volume is defined by

$$N_{\text{total}} = \frac{\pi(r_c)^2 h_c}{\langle \overline{V}_{\text{particles}} \rangle} N_0 = \frac{\pi(r_c)^2 h_c}{\left\langle (\mathcal{M}/\rho)_{\text{particles}} \right\rangle} N_0 \tag{4.19}$$

given the mean mass per density $\left\langle (\mathcal{M}/\rho)_{\text{particles}} \right\rangle$ of the particle and Avogadro's number N_0. The resultant paraffin number fraction, as a function of film thickness, is expressed by

$$\varphi = \varphi_c(h/h_c) \tag{4.20}$$

The input variables of a model to predict the variation in surface coverage of solidifying paraffins, with variation in film thickness in an asphalt thin film, may be expressed by

$$\varphi^\sigma(h) = \frac{(\varphi_c/h_c)he^{(\gamma_m A_m - \gamma_n A_n)/k_B T}}{(1-(\varphi_c/h_c)h + (\varphi_c/h_c)he^{(\gamma_m A_m - \gamma_n A_n)/k_B T})} \tag{4.21}$$

Recent studies of molecular weight distribution in heavy oil residual suggest that the average molecular weight is in the order of 200–700 Da (Liu et al., 2010). Thus, a

www.EngineeringEBooksPdf.com

paraffin $\mathcal{M}_{C_{31}H_{64}}(g/mol) = 437$ with a surface free energy of $\gamma_n(Jm^2) = 0.031$ (Sloutskin et al., 2001, 2003) was selected as a solute. In regard to the effective surface area of paraffin species in the surface crystallized state, a value of $\mathcal{A}_n(m^2) = 2.0014 \times 10^{-19}$ constitutes an effective radius of $r_n(nm) = 0.2524$ (Sloutskin et al., 2001, 2003). These values may be rationalized if it is assumed that paraffins are stacked in columns in a solidified state. By contrast, the remaining asphalt molecules are likely arranged in a more random manner at a surface when assumed to be in a liquid state.

Pauli (2014) suggests that the average surface free energy of asphalt is $\gamma_m(Jm^2) = 0.045$. Assuming the average molecular mass and density of asphalt, namely, $\mathcal{M}_{asphalt} = 450\,Da$ and $\rho_{asphalt} = 1\,g/cm^3$, the effective radius of an asphalt molecule is $r = \sqrt[3]{3\mathcal{M}_{asphalt}/4\pi N_0 \rho_{asphalt}}$, or $r_n(nm) = 0.56$, which corresponds to an effective surface area of $\mathcal{A}_m(m^2) = 9.852 \times 10^{-19}$. Then, given the constants $k_B = 1.3806488 \times 10^{-23}\left(m^2\,kg\,s^{-2}\,K^{-1}\right)$, $T = 298.15\,K$, and $N_0 = 6.02205 \times 10^{23}\left(mol^{-1}\right)$, plots of $\varphi^\sigma(h)$ may be constructed (Figure 4.3) showing both the influence of

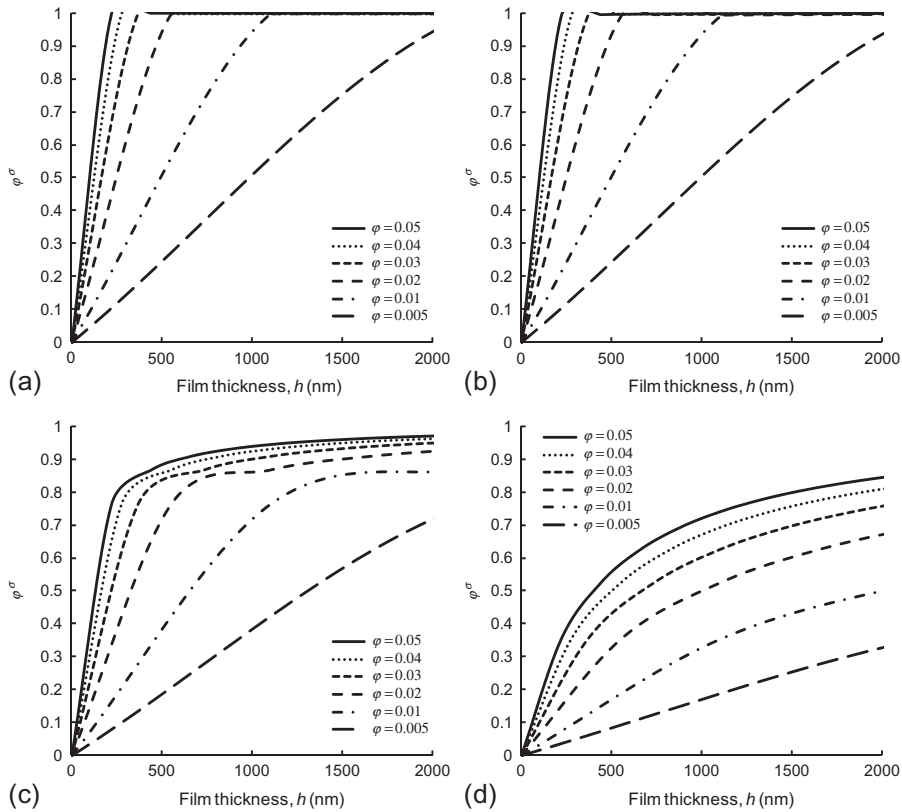


Figure 4.3 Plots of $\varphi^\sigma(h)$ at different φ for paraffin $\mathcal{M}_{C_{31}H_{64}}(g/mol) = 437$, $\mathcal{A}_n(m^2) = 0.20\,nm$ with a surface free energy of $\gamma_n(Jm^2) = 0.031$ and asphalt with $\gamma_m(Jm^2) = 0.045$ where (a) $\mathcal{A}_m(m^2) = 0.66\,nm$ ($\mathcal{M}_{asphalt} \sim 750$ Da), (b) $\mathcal{A}_m(m^2) = 0.56\,nm$ ($\mathcal{M}_{asphalt} \sim 450$ Da), (c) $\mathcal{A}_m(m^2) = 0.46\,nm$ ($\mathcal{M}_{asphalt} \sim 250$ Da), and (d) $\mathcal{A}_m(m^2) = 0.40\,nm$ ($\mathcal{M}_{asphalt} \sim 150$ Da).

www.EngineeringEBooksPdf.com

the effective asphalt molecular radius r_n(nm) = 0.66, 0.56, 0.46, and 0.40, and the initial concentration (partial number fraction) of paraffin φ in the bulk film on plots of $\varphi^{\sigma}(h)$.

4.3.3 Surface freezing crystallization of wax in asphalt: determination of wax concentration in a bulk film

Utilizing the WOS extended Langmuir model for paraffin surface freezing in asphalt films, experiments were carried out to test the model's validity. Asphalt binders derived from different crude sources known to contain different wax concentrations were selected (Branthaver et al., 1993). Asphalt solutions were prepared in toluene solvent (HPLC-grade) at 1–10% by mass-to-volume ratio and spin cast as thin films at 600 rpm. Sample films were dried for several days in a nitrogen-gas-purged drying box. Average film thicknesses $\langle h_{\text{film}} \rangle$ were calculated based on knowledge of the solution concentration C_{sl}(g/mL), the volume of the drop originally deposited on a spinning slide (1 or 2 μL) V_{drop}(μL), and the measured area of the film A_{film} determined with Image-Pro version 6.2 (2005), assuming an average density of asphalt $\rho_{\text{asphalt}} = 1\,\text{g/cm}^3$, as

$$\langle h_{\text{film}} \rangle \approx \frac{V_{\text{drop}} C_{\text{sl}}}{\rho_{\text{asphalt}} A_{\text{film}}} \tag{4.22}$$

Figure 4.4 depicts two sets of AFM phase and (black-and-white) area contrast images of films of different thickness for unannealed SHRP AAK-1 dried under nitrogen gas for 24 h, and thermally annealed SHRP AAB-1 annealed for 30 min under nitrogen gas purged at 115 °C. All films were imaged near the film's center. Unannealed films have the appearance of two phases with different contrast, which appear patchy or spotty, and "bee" structures are not present or are very thin when compared to thermally annealed sample films (Figure 4.4a). On the other hand, sample films that are thermally annealed exhibit "bee" structuring. Thermally annealed samples also exhibit larger, more clumped together structuring compared to unannealed samples (Figure 4.4b).

To quantify the fraction of the area covered by surface structures, image analysis software was utilized (Image-Pro version 6.2, 2005) to "mask" structured areas as white and remaining areas as black. The sum or cumulative white areas A_{spots} per total scan area A_{scan} constitutes a measure of the surface coverage Θ. Table 4.1 lists solution concentrations C_{sl}(g/mL), Θ-values determined for asphalt binders SHRP AAB-1 (prior to and after thermal annealing), and calculated "average" film thicknesses $\langle h_{\text{film}}(\mu\text{m}) \rangle$. Figure 4.5 depicts plots of "wax" area fraction (i.e., surface coverage Θ) as a function of average film thickness $\langle h_{\text{film}} \rangle$

$$\frac{A_{\text{spots}}}{A_{\text{scan}}} \equiv \Theta = \alpha \langle h_{\text{film}} \rangle + \Theta_0 \tag{4.23}$$

for four SHRP asphalts where Θ_0 is the surface coverage at infinitesimally thin film thickness.

www.EngineeringEBooksPdf.com

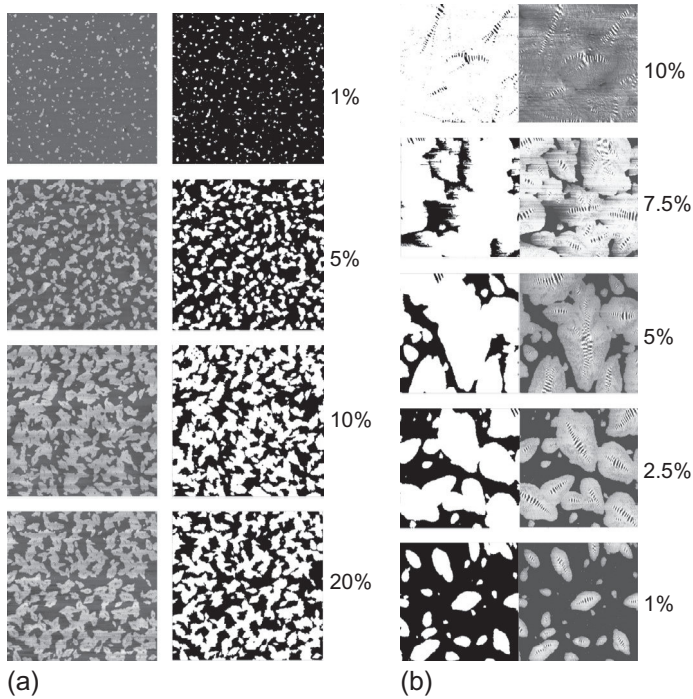


Figure 4.4 AFM phase and (black and white) area contrast images of (a) SHRP AAK-1 (80 × 80-μm area) dried under Nitrogen gas for 24 h (not annealed), and (b) SHRP AAB-1 (20 × 20-μm area) annealed 30 min, Nitrogen gas purged at 115 °C.

Table 4.1 Example data, solution concentrations, average film thickness, and surface coverage for SHRP asphalt AAB-1, for annealed and unannealed films

Sample	Solution concentration C_{sl}(g/mL)	Average film thickness $\langle h_{film}(\mu m)\rangle \approx \frac{V_{drop}C_{sl}}{\rho_{asphalt}A_{film}}$	Surface coverage $A_{spots}/A_{scan} \equiv \Theta$
AAB-1 unannealed	0.010	0.122	0.186
	0.025	0.308	0.317
	0.050	0.664	0.586
	0.075	1.065	0.406
	0.100	1.193	0.343
AAB-1 annealed (30 min, 115 °C)	0.010	0.122	0.254
	0.025	0.308	0.620
	0.050	0.664	0.768
	0.075	1.065	0.820
	0.100	1.193	0.990

www.EngineeringEBooksPdf.com

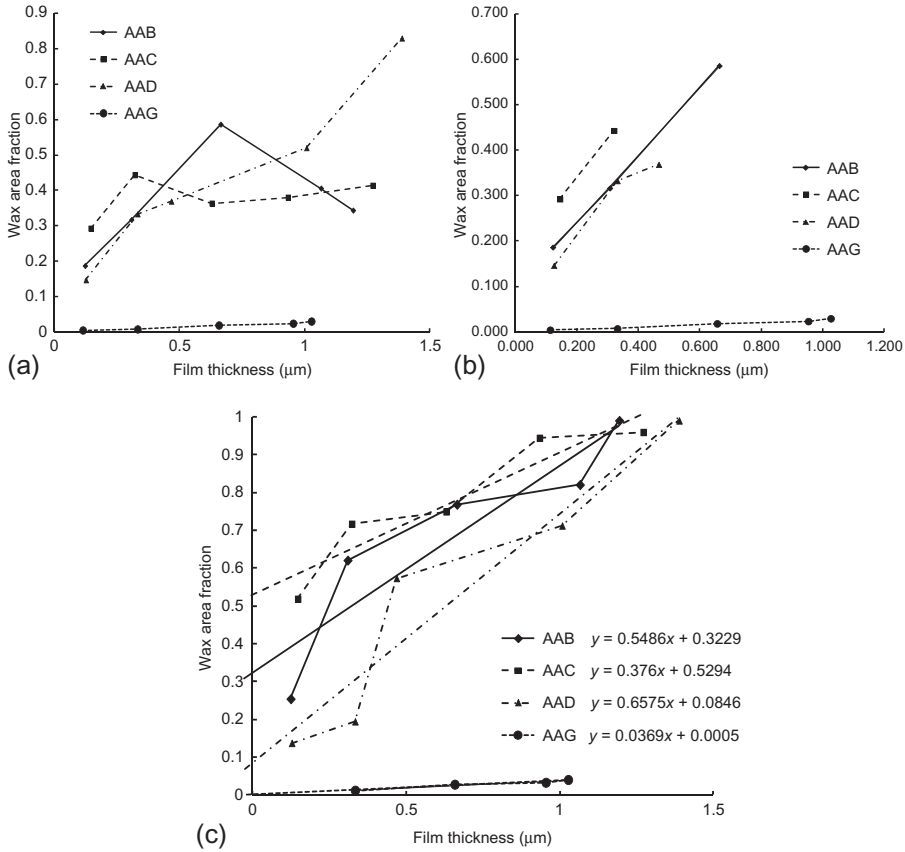


Figure 4.5 Plots of wax area fraction Θ as a function of average film thickness $\langle h_{\text{film}} \rangle$ representing films prepared from four SHRP asphalt for (a) unannealed inert gas dried films, (b) truncated data plot unannealed inert gas dried films, and of (c) thermally annealed films (30 min at 115 °C under nitrogen).

Regarding unannealed films (Figure 4.5a), some data points decrease with increasing film thickness. These data sets were truncated for values of $\langle h_{\text{film}} \rangle > 0.5\,\mu\text{m}$ (Figure 4.5b).

Films were then thermally annealed for 30 min at 115 °C under nitrogen, cooled to room temperature, and reevaluated in terms of surface coverage Θ_0 measurements (Figure 4.5c), where thermal annealing is observed to improve the trend in data. Correlation plots were constructed relating surface coverage Θ_0 to established measures of bulk wax concentration (Table 4.2), as depicted in Figure 4.6. The best regression fits were observed for thermally annealed samples. Direct correlation of $(\Theta)_i$ and $(\langle h_{\text{film}} \rangle)_i$ data (Table 4.2) were also fit to the functional form of the model

www.EngineeringEBooksPdf.com

Table 4.2 Asphalt binder wax content reported in a Branthaver et al. (1993), and wax area fraction values determined from AFM thin-film imaging experiments

Asphalt	% Wax/asphalt extracted from IEC neutrals[a]	% Crystalline material (DSC)[a]	Wax area fraction Θ_0 at $h = 0$	Wax area fraction Θ_0 at $h = 0$	Γ
			Unannealed	Annealed film	
AAB-1	4.7	2.3	0.09	0.36	3.02
AAC-1	7.0	2.7	0.17	0.55	5.35
AAD-1	1.9	0.6	0.08	0.09	1.53
AAG-1	1.2	0.0	0.00	0.00	0.21

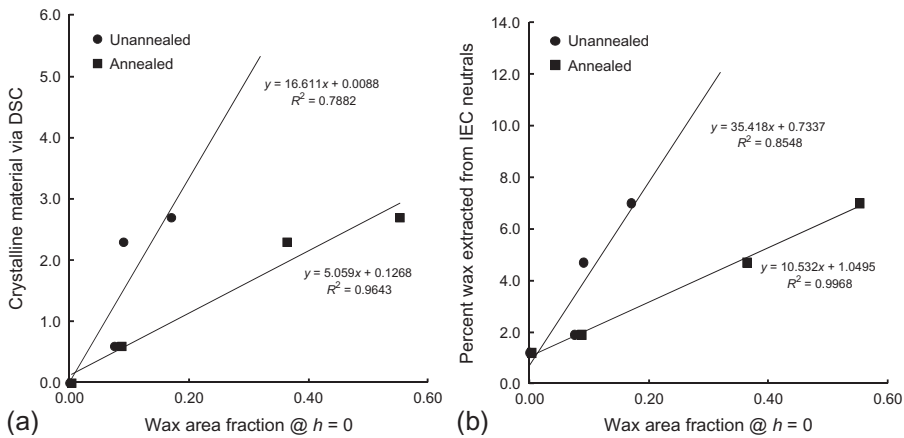


Figure 4.6 Correlation plots relating surface coverage Θ_0 to accepted measures of wax concentration, including (a) percent crystalline material as determined by differential scanning calorimetry (DSC), and (b) weight percent wax extracted for ion exchange chromatography (IEC neutrals fractions).

$$(\Theta)_i = \frac{(\langle h_{\text{film}} \rangle)_i \Gamma}{\left(1 - (\langle h_{\text{film}} \rangle)_i + (\langle h_{\text{film}} \rangle)_i \Gamma\right)} \tag{4.24}$$

where Γ represents the regression coefficient of the analysis. Figure 4.7 depicts regression analysis plots of the function $\Theta(\langle h_{\text{film}} \rangle)$ for annealed sample data sets (Table 4.2). Figure 4.8 depicts the correlation plots relating the Γ regression coefficient to accepted measures of wax concentration (percent crystalline material as determined by differential scanning calorimetry (DSC) and weight percent wax extracted for ion-exchange chromatography (IEC) neutral fractions).

www.EngineeringEBooksPdf.com

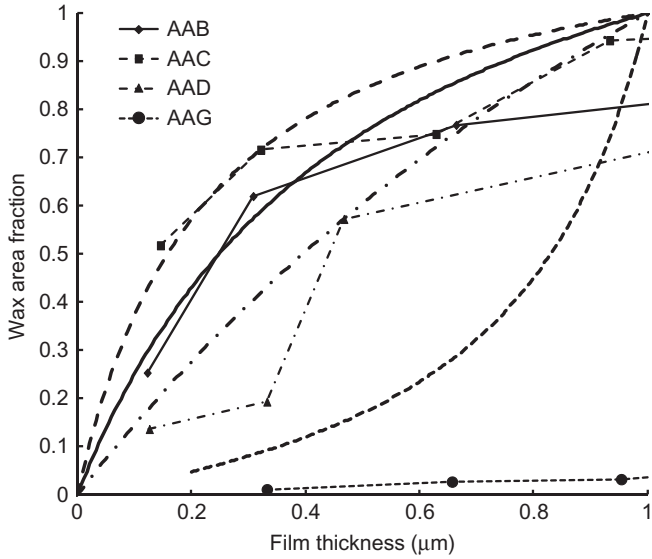


Figure 4.7 Regression analysis plots of the function $\Theta_0(\langle h_{\text{film}} \rangle)$ for annealed sample data sets.

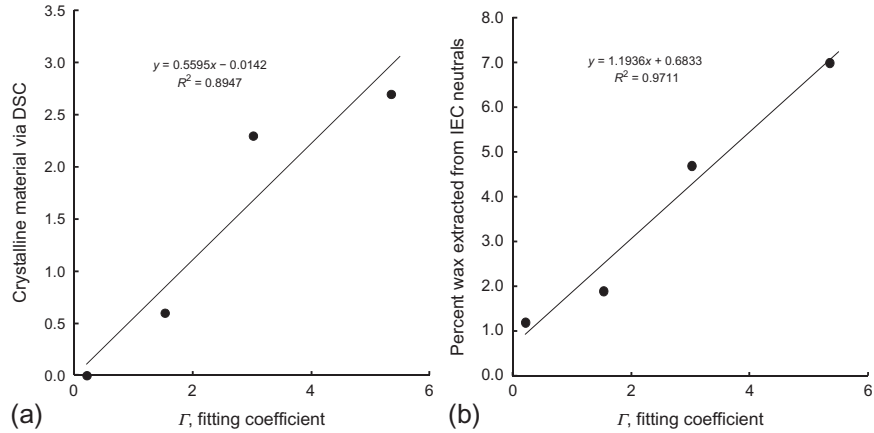


Figure 4.8 Correlation plots relating the Γ regression coefficient to accepted measures of wax concentration, (a) percent crystalline material as determined by differential scanning calorimetry (DSC) and (b) weight percent wax extracted for ion exchange chromatography (IEC neutrals fractions).

The utility of controlling film thickness when employing solvent spin-cast film preparation techniques, followed by the practice of thermal annealing conditioning of films, effectively leads to more physically representative conclusions as to the compositional nature of the structuring observed by AFM in bituminous materials. It is again cautioned that standardized methods of sample preparation may produce

www.EngineeringEBooksPdf.com

misleading conclusions regarding surface and bulk compositional properties when asphalt film thicknesses greater than 1 μm are investigated.

4.3.4 Imaging of specimens via novel sample preparation techniques

Over the 15-plus years in which AFM has been applied to the study of asphalt, some agreement, though certainly not universal, has emerged regarding the "bee structures" that have been commonly observed on the surface of asphalt films. Many researchers (De Moraes et al., 2010; Schmets et al., 2010; Pauli et al., 2011) currently agree that these structures are wax crystals, and while there is certainly strong evidence to support this theory, there is still disagreement.

It is possible that whatever their exact composition, bee microstructures form preferentially at the air/asphalt interface and, therefore, may not be representative of the asphalt microstructure within the bulk. Considering the relevant differences in physical properties (density, interfacial tension, heat capacity, etc.) associated with an asphalt/air interface, compared to internal interfaces, it is unlikely that the microstructure observed on an asphalt surface would be the same as the microstructure in the interior of the film.

Commonly observed surface microstructures may be indicative of important compositional characteristics that drive mechanical response, and, as such, a better understanding of this structuring may lead to a viable performance indicator. However, useful relationships between this type of structuring and pavement performance constitute ongoing research. While this type of surface structuring remains of scientific interest, microstructuring more likely to be relevant to the material's bulk mechanical properties is the microstructure that exists within the interior of thin films (of, say, 8–15-μm thickness; Kandhal and Chakaraborty, 1996). It is this type of structuring that is more commonly believed to bond filler and aggregate particles in an asphalt pavement.

If the surface structuring observed by AFM in fact relates to wax, as many researchers now contend, then an "unseen" underlying structure still exists related to associations among polar constituents, as predicted by Petersen et al. (1994). Given the discussion in previous sections, one would hypothesize that structuring among polar constituents could be revealed after rinsing an asphalt surface with a low-polarity solvent in order to selectively remove the surface structures to expose the underlying microstructure.

Four sample asphalts, derived from a pavement performance site constructed in Minnesota where differentiation in pavement performance for asphalts of the same performance grade but from different crude sources may be compared, were spin cast from toluene solution and then thermally annealed at 95 °C for 30 min. Figures 4.9 through 4.12 depict AFM topography images of these four asphalts before and after rinsing the film with a drop of *n*-heptane. After initial imaging, the sample slides were each stood on edge. A drop of *n*-heptane was then dispensed so that it would run quickly down and across the surface of the film. These figures clearly show that a very different structure is revealed after this type of treatment.

www.EngineeringEBooksPdf.com

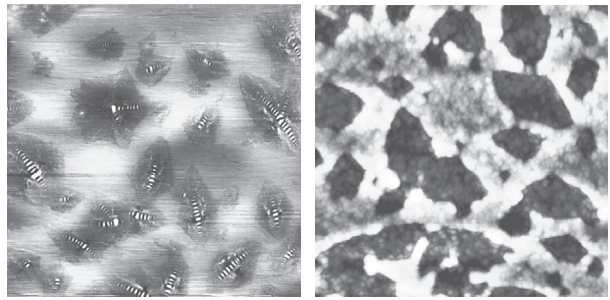


Figure 4.9 AFM topography height of (a) CPPA-MN1-thermally annealed ($l \times w \times h = 40 \times 40 \times 0.18$ μm) and (b) CPPA-MN1-thermally annealed-rinse with *n*-heptane ($40 \times 40 \times 0.86$ μm).

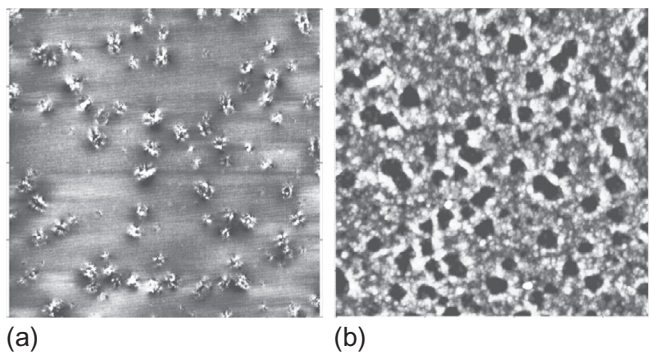


Figure 4.10 AFM topography height of (a) CPPA-MN2-thermally annealed ($l \times w \times h = 40 \times 40 \times 0.09$ μm) and (b) CPPA-MN2-thermally annealed-rinse with *n*-heptane ($40 \times 40 \times 0.64$ μm).

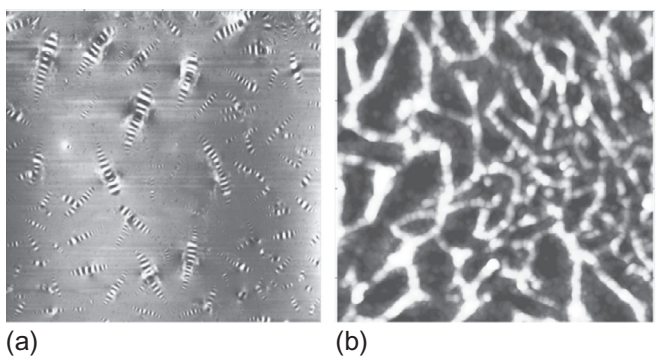


Figure 4.11 AFM topography height of (a) CPPA-MN3-thermally annealed ($l \times w \times h = 40 \times 40 \times 0.20$ μm) and (b) CPPA-MN3-thermally annealed-rinse with *n*-heptane ($40 \times 40 \times 1.11$ μm).

www.EngineeringEBooksPdf.com

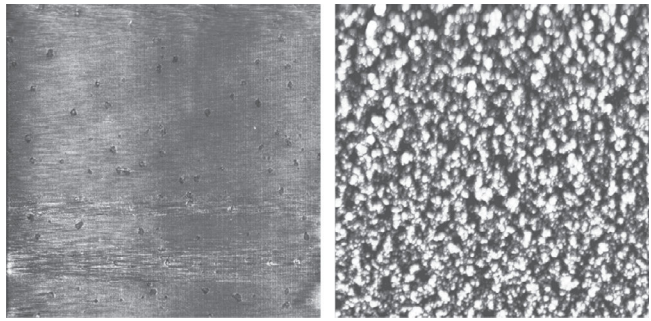


Figure 4.12 AFM topography height of (a) CPPA-MN4-thermally annealed ($l \times w \times h = 40 \times 40 \times 0.04$ μm) and (b) CPPA-MN4-thermally annealed-rinse with *n*-heptane ($40 \times 40 \times 0.77$ μm).

Relative to the expected selectivity of the solvent (*n*-heptane), it is expected that the revealed structure is related to polar constituents in the asphalt, commonly associated with asphaltenes.

While there is no obvious similarity between the bee surface microstructures and microstructures revealed after *n*-heptane rinsing, the relative "amount" of darker areas (i.e., lower topography) in the rinsed samples tends to correlate with the relative areas of original bee structures. It is difficult to say in such preliminary studies that the two structures (i.e., crystalline wax or associated polar constituents) are spatially and volumetrically interrelated. This work is new, and still open to interpretation. However, these images reveal an underlying microstructure, presumed to be composed mainly of polar constituents, which exists simultaneously with the bee surface microstructures.

At present, the composition and nature of the microstructures revealed by *n*-heptane rinse is speculative. It should be kept in mind that after 15-plus years, there is still no universal consensus as to the compositional nature of the surface microstructures first reported by Loeber et al. (1996, 1998). Suffice to say that this underlying structuring is differentiated from surface structuring, and that what one sees in an AFM image of an asphalt film can be dramatically affected by how the sample is prepared. Again, it is advantageous to overemphasize the point, negating the various imaging techniques that are commonly available with AFM, that what one observes in AFM scans strongly depends upon how the sample is prepared and that sample preparation must be coordinated with experimental objectives if useful and meaningful data are to be obtained.

4.4 Force–displacement AFM

AFM is now commonly used to measure and map the adhesive forces between an AFM tip and a test substrate like asphalt. Adhesive measurements are made with AFM by pressing the probe tip into the surface of a sample, followed by pulling the tip loose from

www.EngineeringEBooksPdf.com

the surface while recording the deflection of the cantilever. The record of the tip displacement (via cantilever deflection) associated with the pressing and pulling of the tip is typically referred to as a force–displacement curve (FDC). In a typical FDC, the relative change in the distance between the tip mount (bimorph) and the substrate surface is plotted on the x-axis, with the corresponding cantilever deflection plotted on the y-axis. Analysis of FDCs can reveal important mechanical information such as the yield strength and linear elastic–plastic response of contact/fracture, as these properties relate to the contact between the probe tip and sample surface.

4.4.1 Force–displacement AFM: theory

Fracture processes based on Griffith's criterion (Griffith, 1921; Shull, 2002) relate the release of stored strain energy $\mathcal{U}$ to the fracture energy absorbed $\mathcal{G}$. An extending crack of length $2a$, for example, is related to the applied stress σ in terms of the strain or fracture energy

$$\frac{-\mathrm{d}\mathcal{U}}{\mathrm{d}a} = \mathcal{G} = \frac{\pi a \sigma^2}{E} \tag{4.25}$$

where E is the Young's modulus of the material undergoing fracture. Extending this criterion to the rupture of adhesive bonds, where the adhesive exhibits viscoelastic character, $\mathcal{G}$ is referred to as the adherence fracture energy. Adherence energy is defined in terms of the equilibrium work of adhesion $\mathcal{G}_0$ and energy lost due to dissipative processes $\mathcal{G}_{\mathrm{diss}}$ (Packham, 1996),

$$\mathcal{G} = \mathcal{G}_0 + \mathcal{G}_{\mathrm{diss}} \tag{4.26}$$

Rate υ and temperature T dependence of $\mathcal{G} \equiv \mathcal{G}(\upsilon, T)$ are accounted for by expressing $\mathcal{G}$ as

$$\mathcal{G}_{\mathrm{diss}} = \mathcal{G}_0 \Psi(\upsilon/\upsilon^*, a_T), \tag{4.27}$$

defined in terms of a viscoelastic loss function Ψ, given a characteristic crack speed υ^* and a rate-temperature dependent shift factor a_T (Ahn and Shull, 1996; Crosby and Shull, 1999; Shull, 2002).

4.4.2 Force–displacement AFM: methodology

The potential energy experienced by the cantilever is measured by the "work to break contact" $\mathcal{U}$ derived by numerical integration of FDCs evaluated using a trapezoidal technique

$$U_{\mathrm{tot}}(\mathrm{test}) \approx \mathcal{U} = \int_{Z_0}^{Z_1} F\mathrm{d}Z = \int_{Z_0}^{Z_1} (F_c + F_s)\mathrm{d}Z \approx \frac{(\Delta Z = Z_1 - Z_0)}{2N} \sum_{i=1}^{n} [F(Z_{i+1}) + F(Z_i)] \tag{4.28}$$

www.EngineeringEBooksPdf.com

Work to break contact potential energy for a given temperature is plotted as a function of reduced rate (i.e., stage velocity υ, per critical crack speed, υ^*), where the critical crack speed in the present analysis is the slowest stage velocity for a given set of measurements.

Experimentally, the change in displacement of the piezo scanner-cantilever assembly at increasing rate $\Delta Z(\upsilon)$ becomes much greater than the average in the cantilever deflection $\delta_c(\upsilon)$, suggesting that the material is being stretched or elongated to a greater extent with increasing separation rate.

To determine the adherence energy $\mathcal{G}$, work to break contact potential energy versus reduced rate data is fit to the energy dissipation function

$$\mathcal{U} = \mathcal{U}_0[1 + (\upsilon/\upsilon^*)^n] \tag{4.29}$$

where $\mathcal{U}_0$ and n are regression coefficients. Equilibrium work of adhesion $\mathcal{G}_0$, in turn, is calculated as

$$\mathcal{G}_0 = \frac{P_{\mathrm{DMT}}}{2\pi R} = \frac{k_c \delta_c}{2\pi R} \tag{4.30}$$

The adherence energy $\mathcal{G}$ is thus derived as

$$\mathcal{G} = \langle \mathcal{G}_0 \rangle [1 + (\upsilon/\upsilon^*)^n] \tag{4.31}$$

given the regression coefficient n and average value in $\langle \mathcal{G}_0 \rangle$.

A commercial AFM was modified to perform force–displacement atomic force microscopy (FD-AFM) measurements. The components of the system include a Quesant Q-Scope 250 AFM, a nanopositioning stage (Mad City Labs, Inc.) with a Peltier thermal stage heater/cooler, and an environmental chamber (Kringos et al., 2013). The cantilevers used for FD-AFM measurements are custom fabricated by Novascan Technologies to have a nominal spring constant of 14 N/m and a nominally spherical glass microbead tip with radius of approximately 5000 nm.

To conduct FD-AFM measurements, an AFM controller provides voltage to a piezo scanner to initially establish contact between the cantilever tip and sample surface. A laser and quad photodetector monitor the deflection signal of the cantilever. The AFM electronics and feedback loop establish a controlled preloading of an adhesive contact. A nanopositioning stage controller and software package (NanoRoute®3D) are used to retract the sample from the cantilever at a controlled rate, thus rupturing the contact. A National Instruments data acquisition module programmed with LabVIEW and an associated PC are used to monitor signals for the stage position, feedback loop, and cantilever deflection as a function of time.

Calibration of this system entails initially engaging the probe with a glass surface, followed by locking the AFM feedback loop, moving the nanostage at a specified distance, and recording the cantilever deflection as a voltage signal. The stage motion divided by the cantilever deflection voltage gives the cantilever calibration factor. Values of stage and cantilever offset hold time and rate of stage motion, and voltage-versus-time slopes $\xi_s = \Delta V_s/\Delta t_s$ and $\xi_c = \Delta V_c/\Delta t_c$, respectively, are used

www.EngineeringEBooksPdf.com

to convert raw signal data to force curves. Specifically, voltage signals for cantilever and stage, and time data, defined as

$$\mathbf{V}^{c,s} = \begin{bmatrix} V_1^{c,s} \\ \vdots \end{bmatrix} \text{ and } \mathbf{t} = \begin{bmatrix} t_1 \\ \vdots \end{bmatrix}, \text{ are used to calculate the total } (z\text{-axis}) \text{ distance}$$

$$\mathbf{Z} = \upsilon_s \mathbf{t} = \begin{bmatrix} \upsilon_s(t_1 - t_h) \\ \vdots \end{bmatrix} = \begin{bmatrix} Z_1 \\ \vdots \end{bmatrix} \tag{4.32}$$

Cantilever and stage deflections, accounting for offsets and hold time, are calculated as

$$\boldsymbol{\delta}_c = \begin{bmatrix} V_1^c + \Delta_c \\ \vdots \end{bmatrix} (1/\xi_c) = \begin{bmatrix} \delta_1^c \\ \vdots \end{bmatrix} \tag{4.33}$$

and

$$\boldsymbol{\delta}_s = \begin{bmatrix} V_1^s - \Delta_s \\ \vdots \end{bmatrix} (1/\xi_s) = \begin{bmatrix} \delta_1^s \\ \vdots \end{bmatrix} \tag{4.34}$$

Distance-versus-deflection ($\mathbf{Z}$ vs. $\boldsymbol{\delta}_c$) curves are plotted to isolate the adhesive contact region (Pauli et al., 2014).

4.4.3 Work of adhesion and viscoelastic response to temperature and rate

Adherence energy determined from FD-AFM experiments defines the adhesive and viscoelastic properties of test samples (asphalt thin films). Viscoelastic materials exhibit rate- and temperature-dependent behavior in terms of stress/strain response in fracture. As a representative class of materials, asphalt binders were examined by FD-AFM in terms of temperature- and rate-dependent fracture behavior.

In FD-AFM experiments, work to break contact potential energy $\mathcal{U} = \mathcal{U}_0[1 + (\upsilon/\upsilon^*)^n]$ determined at a given reduced temperature (T/T^*), where T^* represents the lowest test temperature, is initially plotted as a function of reduced rate (υ/υ^*), where the critical crack speed is the slowest stage velocity. Tables 4.3 and 4.4 report representative data measured for SHRP asphalt AAG-1. For this particular data set, five force–displacement measurements were obtained at three different rates (1, 5, and 10-μm/s), at five different temperatures (−5, 0, 5, 10, and 15 °C), for a total of 75 deflection-distance curves. The average in five data points represents an average work to break contact potential energy $\overline{\mathcal{U}}$ at a given rate and temperature. An average work of adhesion value of $\langle \mathcal{G}_0 \rangle = 86 \pm 3 \text{mJ/m}^2$ is determined from an average of 75 deflection-distance curves by virtue of pull-off deflection-distance measurements (Equation (4.30)). Figure 4.13 depicts work to break contact potential energy and adherence energy versus reduced rate curves, respectively, for data listed in Tables 4.3 and 4.4.

Regression analyses are then conducted to fit $\mathcal{U}$ and (υ/υ^*) data to the cantilever work function (Equation (4.29)). The average work of adhesion $\langle \mathcal{G}_0 \rangle$ and regression coefficient n can then be used to determine adherence energy as

www.EngineeringEBooksPdf.com

Table 4.3 Work to break contact data determined at three different rates and five different temperatures

$v/v^* = v$, $v^* = 1$ μm/s	$\mathcal{U}(@T/T^* = 1.00)$ (μN · μm), $T^* = 263$ K	$\mathcal{U}(@T/T^* = 1.02)$ (μN · μm), $T^* = 263$ K	$\mathcal{U}(@T/T^* = 1.04)$ (μN · μm), $T^* = 263$ K	$\mathcal{U}(@T/T^* = 1.06)$ (μN · μm), $T^* = 263$ K	$\mathcal{U}(@T/T^* = 1.075)$ (μN · μm), $T^* = 263$ K
1	2.36	2.58	3.13	3.41	3.41
5	2.82	2.95	3.14	3.37	3.50
10	2.95	3.04	3.14	3.40	3.57

Table 4.4 Adherence energy data determined at three different rates and five different temperatures

T (K)	$\mathcal{G}(@v/v^* = 1)$ (mJ/m^2)	$\mathcal{G}(@v/v^* = 5)$ (mJ/m^2)	$\mathcal{G}(@v/v^* = 10)$ (mJ/m^2)
268	203	243	254
273	222	253	261
278	270	270	270
283	293	290	292
288	293	301	307

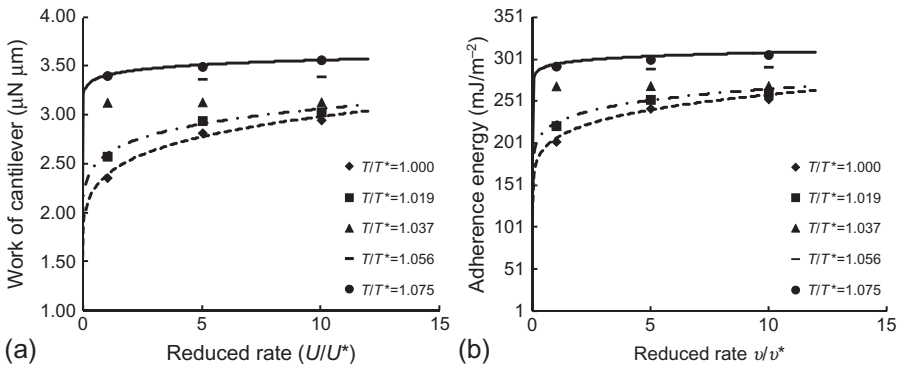


Figure 4.13 (a) Work to break contact and (b) adherence energy versus reduces rate plots derived from FD-AFM measurements of a 1-μm thick film of SHRP AAG-1 asphalt sample.

$$\mathcal{G}(v, a_T) = \langle \mathcal{G}_0 \rangle \left[1 + (v/v^*)^{n(T/T^*)} \right] = \langle \mathcal{G}_0 \rangle \left[1 + (v/v^*)^{\xi_2 (T/T^*)^2 + \xi_1 (T/T^*) + \xi_0} \right] \quad (4.35)$$

The adherence energy function expressed in Equation (4.35) represents a phenomenological model of the time–temperature response of adhesive contact in a viscoelastic thin film of asphalt and, as such, is limited to the rate and temperature regimes in which measurements are obtained.

www.EngineeringEBooksPdf.com

4.4.4 Adherence energy and ductile–brittle transition temperature

To show the relationship between $\mathcal{G}(\upsilon, a_T)$ and reduced temperature regression coefficients, n-values are plotted versus (T/T^*), as depicted in Figure 4.14. In the present case, good data fits were found for $\mathcal{G}(\upsilon/\upsilon^*)$ data at $(T/T^*) = 1.000, 1.019,$ and 1.075, with corresponding n-values of 0.178, 0.133, and 0.038, respectively.

Potentially of interest to asphalt technologists, $\mathcal{G}(\upsilon, a_T)$ may be used to determine the ductile–brittle transition temperature T_{d-b}, as this relates to fatigue performance. The ductile–brittle transition temperature represents an inflection in the response of adherence energy as a function of temperature, where at higher temperatures, pull-off force measurements tend to become independent of rate and simply correspond to a measure of the surface tension of the material, while at lower temperatures, ductile flow of the material, which manifests as necking of the material, diminishes and the material simply responds as an elastic solid with corresponding surface energy. Thus, to calculate T_{d-b}, plots of $\mathcal{G}$ as a function of temperature are fit to an appropriate function to determine the ductile–brittle inflection point. Figure 4.15 depicts plots of adherence energy versus temperature at different reduced rates.

Although a sigmoidal function is a logical choice for initial data fits, $\mathcal{G}$ versus T data are conveniently fit with a third-order polynomial function

$$\mathcal{G}(T) = \zeta_3 T^3 + \zeta_2 T^2 + \zeta_1 T + \zeta_0 \tag{4.36}$$

The inflection of this function is determined as

$$0 = \frac{d^2}{dT^2}\mathcal{G}(T) = 6\zeta_3 T + 2\zeta_2 \tag{4.37}$$

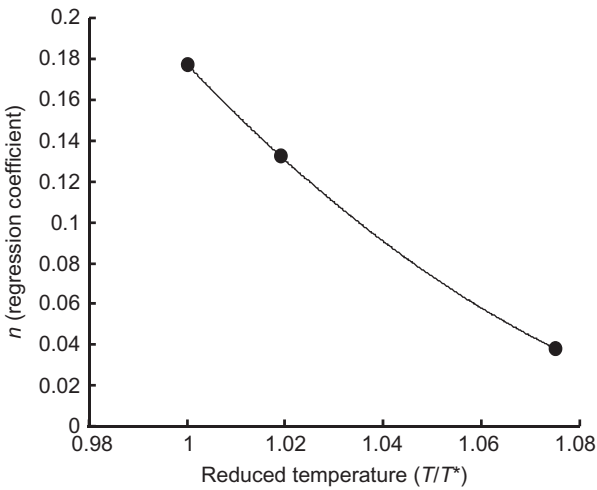


Figure 4.14 Functional relationship between regression coefficients, n-values, and reduced temperatures (T/T^*).

www.EngineeringEBooksPdf.com

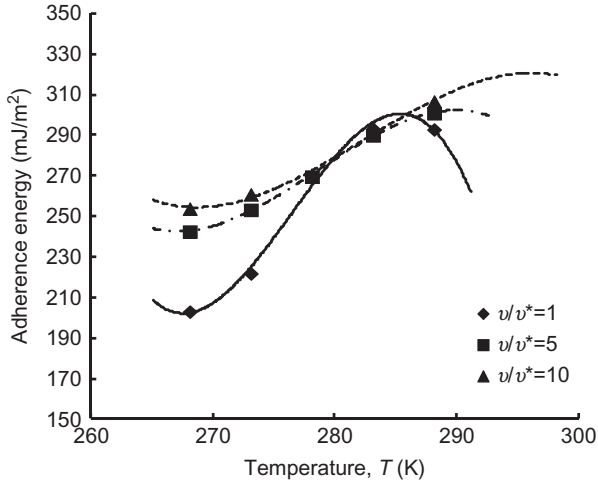


Figure 4.15 Functional relationship between adherence energy and temperature at different reduced rates.

where the ductile–brittle transition temperature T_{d-b} is determined by

$$T_{d-b} = \frac{-\zeta_2}{3\zeta_3} \tag{4.38}$$

Table 4.5 lists regression coefficient data (ζ_2 and ζ_3) and corresponding ductile–brittle transition temperatures determined at three different reduced rates of adhesive failure for samples prepared from SHRP AAG-1. Figure 4.16 depicts a plot of the functional relationship between ductile–brittle transition temperature and reduced rate. This figure shows that ductile–brittle transition temperatures decrease with decreasing rate. These findings are consistent with linear viscoelastic theories, which contend that materials respond with higher elasticity at lower temperatures or with faster rates of displacement.

Table 4.5 Regression data (ζ_3 and ζ_2) corresponding ductile–brittle transition temperatures at three different reduced rates of adhesive failure

v/v^*	ζ_3	ζ_2	T_{d-b}(K)
1	−0.0355	0.3543	276
5	−0.0101	0.1643	279
10	−0.0065	0.1804	282

www.EngineeringEBooksPdf.com

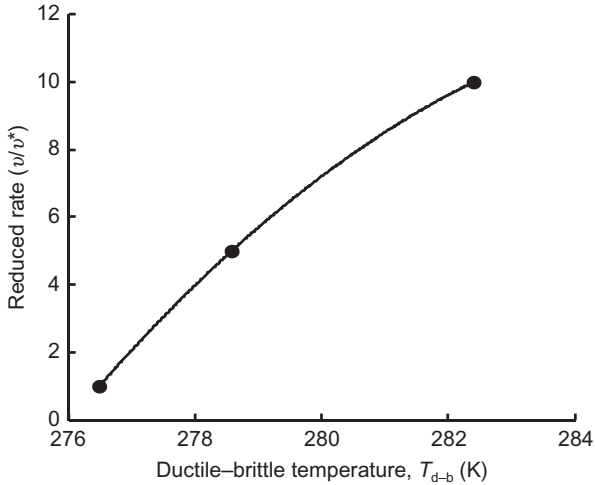


Figure 4.16 Functional relationship between ductile–brittle transition temperature and reduced rate.

4.5 Future trends

4.5.1 Nanorheological methodologies

In simple terms, rheology is the study of the flow characteristics of matter. Thus, it follows that nanorheology is the study of the flow of matter at a very small scale. Rheology is typically used to describe the mechanical properties of liquids and semisolids that exhibit strain-rate dependent viscosity (i.e., viscoelastic materials), such as asphalts. For this type of material, the "hardness" is a function of both temperature and shear rate. Materials are typically characterized in terms of a storage modulus, a loss modulus, and a phase angle. Moduli values are reported in terms of force per unit area (i.e., as pressure). The phase angle is then the lag between the applied pressure of the storage modulus and the loss modulus, reported in degrees or radians. For a purely elastic material, there is no lag in response, and the phase angle is then 0.

Rheological measurements based on dynamic shear are made by confining the material in a known geometry at a controlled temperature, applying a sinusoidal oscillating force, and measuring the transmission of force through the material. In theory, this type of measurement can be made at nanoscale using an AFM. An AFM generates an image of a surface by applying a small force and measuring the response; thus, it is potentially capable of making rheological-type measurements. As reported in this chapter, good progress has already been made utilizing nanoindentation and FD-AFM in the field of bitumen nanorheology (Jäger et al., 2004; Tarefder and Zaman, 2010, 2011; Allen et al., 2012, 2013; Pauli et al. (2013, 2014). But, one of the greatest difficulties still remaining is in adequately defining the geometry of the system so that modulus values can be determined accurately. As the development of AFM nanomechanic techniques continue, better methods to define the geometry, perhaps based on interferometer or piezo-electromechanical sensors, will and have

www.EngineeringEBooksPdf.com

emerged. Once the difficult problem of defining geometry is solved, the use of AFM to make reliable nanomechanical measurements should become routine.

4.5.2 Nano-infrared

Nano-infrared (nano-IR) incorporates infrared spectroscopy with SPM to determine the chemical composition of species present on a sample surface at nanoscale (Dazzi et al., 2010, 2012; Kjoller et al., 2010). The technique involves illuminating a sample plated on a ZnSe crystal substrate with a tunable IR-laser at wavelengths where the molecules in the sample absorb IR-light, inducing a photothermal response in the sample. The absorbed light, once converted to the form of heat, results in a rapid thermal expansion pulse that is detected by the cantilever probe tip in contact with the surface. Nano-IR then provides an infrared spectrum of specific image features with micron and nanometer spatial resolution in the *x*–*y* plane, well in excess of the capabilities of optical IR-microscopes. This method has been successfully applied to the chemical identification of polymer microdomains, cellular structures, and fullerene and fiber nanomaterials. As experience in applying this relatively new technique to asphalt materials accumulates, a better understanding of its potential utility will develop. Combined with nanomechanical techniques, nanoscale IR measurements can potentially show a great deal about the link between chemistry and mechanical properties for asphalt materials.

4.5.3 Scanning thermal imaging

Scanning thermal probe imaging encompasses a variety of techniques devised to provide thermal response information at very small scale (Duvigneau et al., 2010). These AFM instruments are commonly equipped with special cantilevers that serve as a tiny thermocouple incorporated with a heating stage. Variants of this system could potentially provide nanoscale information with respect to properties such as thermal conductivity, heat capacity, and melting point. Scanning thermal AFM data can be useful for differentiating between structural phases, for example in terms of melting point (or other thermal characteristics), which, in turn, can potentially be used to correlate chemical composition to mechanical properties.

4.5.4 Sources of further information and advice

AFM provides a powerful tool with which to visualize surfaces at very small scale. For some types of surfaces, subnanometer size features can easily be resolved in the *x*–*y* plane. AFM creates a false-color image relative to the interaction (a combination of attractive and repulsive forces) between the tip and the sample surface beneath the probe tip. It is this complex interaction of forces that is recorded in the AFM image, and while these "images" are necessarily related to the characteristics of the surface, the exact nature of the surface–force interaction with the probe remains difficult to resolve in bitumen research. The relative force felt by the tip is affected by the composition and charge distribution in the sample and the intervening media (i.e., air, liquid, and vapor), as well as the relative distance between the tip and the surface. The

www.EngineeringEBooksPdf.com

complex nature of the forces acting between the tip and the surface provide room for a variety of interpretations of the resulting images.

Multiple image types (e.g., topography, phase, and lateral friction) are often considered to provide clues as to how an image may best be interpreted. Nonetheless, interpretation of the images can still be difficult, as evidenced by the variety of hypotheses that have been presented to explain the "bee structures" that are commonly observed on asphalt surfaces. Over the course of some 15-plus years, numerous hypotheses relating these microstructures to a variety of chemical constituents have been advanced. As the volume and quality of experimental evidence increased, current hypotheses were adjusted. Many of the researchers currently using AFM to study asphalt now agree that the bee structures are related to waxy materials crystallizing on the surface, but this interpretation, even after 15-plus years of study, is still of debate.

Practical guidelines for the interpretation of AFM images of complex media such as bitumen are emerging. For example, if a feature is present in the phase image, but not in the topography image, it can be concluded that the contrast in the phase image is probably due to the composition, rather than the relative height of the sample surface, and vice versa. Imaging at more than one set point (i.e., magnitude of the tip-sample interaction as controlled by the instrument) can provide additional clues as to the nature of the interaction that has resulted in some area of contrast in the image. Combining different AFM techniques (e.g., phase with friction, nanomechanics with imaging) with other techniques (e.g., optical and environmental scanning electron microscopes) can help with image interpretation.

In general, for a complex material such as asphalt, the interpretation of AFM images will not be a simple matter. Accurate interpretation will likely require integration of experimental techniques. To further aid image interpretation, there is a variety of image analysis software that provides qualitative and quantitative information to help interpret images, typically relative to a prescribed contrast range, which may in turn be correlated with some particular characteristic of the sample. These types of software can be particularly useful for combining image information from different techniques to develop a multifaceted picture of the sample surface.

Finally, sample preparation may be the most critical aspect of any imaging technique. What one sees often depends to a very large extent upon how the sample was prepared prior to imaging. Most researchers have noted that the appearance of an asphalt surface, as imaged by AFM, can change dramatically when the sample is heated and cooled. AFM imaging provides no way to determine which image is best representative of the actual microstructure. AFM can only image a surface, so the method used to prepare a sample surface becomes extremely important. There is significant disagreement among researchers as to whether the microstructures frequently imaged on asphalt surfaces are representative of the structural arrangement in the bulk material. This is an important question, because it is likely that the bulk structure is as relevant as surface structuring in terms of influencing the mechanical properties, and hence the performance, of bituminous materials.

As mentioned previously in this chapter, various sample preparation techniques that are designed to expose an interior surface to the AFM probe, without significantly altering that surface, are currently being explored. These new techniques should allow researchers to better look "beneath the surface" to reveal the internal microstructure of

www.EngineeringEBooksPdf.com

asphalt materials. Using these new techniques, combined with traditionally utilized test methods, the thus far elusive connection between asphalt performance and asphalt microstructure as "seen" in AFM images may better be realized.

References

Ahn, D., Shull, K.R., 1996. JKR studies of acrylic elastomer adhesion to glassy polymer substrates. Macromolecules 29 (12), 4381–4390.

Allen, R.G., Little, D.N., Bhasin, A., 2012. Structural characterization of micromechanical properties in asphalt using atomic force microscopy. J. Mater. Civ. Eng. 24, 1317–1327.

Allen, R.G., Little, D.N., Bhasin, A., Lytton, R.L., 2013. Identification of the composite relaxation modulus of asphalt binder using AFM nanoindentation. J. Mater. Civ. Eng. 25, 530–539.

Allen, R.G., Little, D.N., Bhasin, A., Glover, C.J., 2014. The effects of chemical composition on asphalt microstructure and their association to pavement performance. Int. J. Pavement Eng. 15 (1), 9–22.

Bassett, D.C., Olley, R.H., Al Raheil, A.M., 1988. On isolated lamellae of melt-crystallized polyethylene. Polymer 29, 1539–1543.

Bhushan, B., 2005. Nanotribology and Nanomechanics: An Introduction. Springer-Verlag, Germany.

Bhushan, B., Qi, J., 2003. Phase contrast imaging of nanocomposites and molecularly thick lubricant films in magnetic media. Nanotechnology 14, 886–895.

Branthaver, J.F., Petersen, J.C., Robertson, R.E., Duvall, J.J., Kim, S.S., Harnsberger, P.M., Mill, T., Ensley, E.K., Barbour, F.A., Schabron, J.F., 1993. Binder Characterization and Evaluation, Volume 2: Chemistry. National Research Council, Washington, DC, Report SHRP-A-368, Strategic Highway Research Program.

Brocos, P., Piñeiro, Á., Amigo, A., Garcia-Fadrique, J., 2007. A proposal for the estimation of binary mixture activity coefficients from surface tension measurements throughout the entire concentration range. Fluid Phase Equilib. 260, 343–353.

Carrera, V., Partal, P., Garcia-Morales, M., Gallegos, C., Paez, A., 2009. Influence of bitumen colloidal nature on the design of isocyanate-based bituminous products with enhanced rheological properties. Ind. Eng. Chem. Res. 48, 8464–8470.

Carrera, V., Garcia-Morales, M., Navarro, F.J., Partal, P., Gallegos, C., 2010. Bitumen chemical foaming for asphalt paving applications. Ind. Eng. Chem. Res. 49, 8538–8543.

Crosby, A.J., Shull, K.R., 1999. Adhesive failure analysis of pressure-sensitive adhesives. J. Polym. Sci. B-Polym. Phys. 37, 3455–3472.

Cuadri, A.A., Garcia-Morales, M., Navarro, F.J., Partal, P., 2014. Processing of bitumens modified by a bio-oil-derived polyurethane. Fuel 118, 83–90.

Dazzi, A., Glotin, F., Carminati, R., 2010. Theory of infrared nanospectroscopy by photo thermal induced resonance. Appl. Spectrosc. 66 (12), 1365–1384.

Dazzi, A., Prater, C.B., Hu, Q., Chase, D.B., Rabolt, J.F., Marcott, C., 2012. AFM-IR: combining atomic force microscopy and infrared spectroscopy for nanoscale chemical characterization. J. Appl. Phys. 107,124519, 1–7.

De Moraes, M.B., Pereira, R.B., Simão, R.A., Leite, L.F.M., 2010. High temperature AFM study of CAP 30/45 pen grade bitumen. J. Microsc. 239 (1), 46–53.

Dorset, D.L., Hanlon, J., McConnell, C.H., Fryer, J.R., Lotz, B., Wittmann, J.C., Beckmann, E., Zemlin, F., 1990. Why do polyethylene crystals have sectors. Proc. Natl. Acad. Sci. U.S.A. 87, 1696–1700.

www.EngineeringEBooksPdf.com

Dorset, D.L., Alamo, R.G., Mandelkern, L., 1993. Surface order and sectorization of polyethylene lamellae. Macromolecules 26, 3143–3146.

Duvigneau, J., Schönherr, H., Vancso, G.J., 2010. Nanoscale thermal AFM of polymers: transient heat flow effects. ACS Nano 4 (11), 6932–6940.

Fischer, H.R., Dillingh, E.C., 2014. On the investigation of the bulk microstructure of bitumen – introducing two new techniques. Fuel 118, 365–368.

Fischer, H., Poulikakos, L.D., Planche, J.-P., Das, P., Grenfell, J., 2013. Challenges while performing AFM on Bitumen. In: Kringos, N., Birgisson, B., Frost, D., Wang, L. (Eds.), RILEM Book Series Volume 8, Multi-Scale Modeling & Characterization of Infrastructure Materials. Proceedings of the International RILEM Symposium Stockholm. Springer, Dordrecht, Heidelberg, New York, London. June, pp. 89–98.

Fisher-Cripps, A.C., 2004. A phenomenological approach to nanoindentation creep. Mater. Sci. Eng. A 385, 74–82.

Geng, K., Yang, F., Druffel, T., Grulke, E.A., 2005. Nanoindentation behavior of ultrathin polymeric films. Polymer 46, 11768–11772.

Griffith, A.A., 1921. The phenomena of rupture and flow in solids. Philos. Trans. R. Soc. Lond. A 221, 163–198.

Guenthner, A.J., Kyu, T., 2000. Formation of banded textures in liquid crystalline polymers with extended curvature elasticity. Macromolecules 33, 4463–4471.

Hall, D.B., Underhill, P., Torkelson, J.M., 1998. Spin coating of thin and ultrathin polymer films. Polym. Eng. Sci. 38 (12), 2039–2045.

Halladay, M., 2007. The Strategic Highway Research Program: An Investment That Has Paid Off, http://www.tfhrc.gov/pubrds/marapr98/shrp.htm, December.

Huang, G., Lu, H., 2006. Measurements of young's relaxation modulus using nanoindentation. Mech. Time-Depend. Mater. 10, 229–243.

Image-Pro Version 6.2, 2005. Media Cybernetics, Inc., Rockville, MD, USA.

Jäger, A., Lackner, R., Eisenmenger-Sittner, C., Blad, R., 2004. Identification of four material phases in bitumen by atomic force microscopy. Road Mater. Pavement Des. 5, 9–24.

Jones, D.R., 1993. Asphalt Cements: A Concise Data Compilation. National Research Council, Washington, DC, SHRP Materials Reference Library, SHRP-A-645, Strategic Highway Research Program.

Kandhal, P.S., Chakaraborty, S., 1996. Effect of asphalt film thickness on short and long term aging of asphalt paving mixtures. NCAT Report No. 96-01.

Kjoller, K., Felts, J.R., Cook, D., Prater, C.B., King, W.P., 2010. High-sensitivity nanometer-scale infrared spectroscopy using a contact mode microcantilever with an internal resonator paddle. Nanotechnology. 21,185705, 1–6.

Kringos, N., Birgisson, B., Frost, D., Wang, L., 2013. Multi-scale modeling and characterization of infrastructure materials. In: Pauli, T., Grimes, W., Wang, M., Lu, P., Huang, S.-C. (Eds.), Development of an Adherence Energy Test via Force–Displacement Atomic Force Microscopy (FD-AFM). Proceedings, 2013 International RILEM Symposium, Stockholm, June, pp. 273–284.

Kyu, T., Mehta, R., Chin, H.-W., 2000. Spatiotemporal growth of faceted and curved single crystals. Phys. Rev. E 61 (4), 4161–4170.

Lesueur, D., 2009. The colloidal structure of bitumen: consequences on the rheology and on the mechanics of bitumen modification. Adv. Colloid. Interface Sci. 145, 42–82.

Liu, C.-K., Lee, S., Sung, L.-P., Nguyen, T., 2006. Load–displacement relations for nanoindentation of viscoelastic materials. J. Appl. Phys. 100, 033503, 1–9.

Liu, P., Shi, Q., Chung, K.H., Zhang, Y., Pan, N., Zhao, N., Xu, C., 2010. Molecular characterization of sulfur compounds in Venezuela crude oil and its SARA fractions by

www.EngineeringEBooksPdf.com

electrospray ionization Fourier transform ion cyclotron resonance mass spectrometry. Energy Fuels 24, 5089–5096.
Loeber, L., Sutton, O., Morel, J., Valleton, J.-M., Muller, G., 1996. New direct observation of asphalts and asphalt binders by scanning electron microscopy and atomic force microscopy. J. Microsc. 182 (1), 32–39.
Loeber, L., Muller, G., Morel, J., Sutton, O., 1998. Bitumen in colloid science: a chemical, structural and rheological approach. Fuel 77 (13), 1443–1450.
Loveinger, A.J., Lotz, B., David, D.D., Schumacher, M., 1994. Morphology and thermal properties of fully syndiotactic polypropylene. Macromolecules 27, 6603–6611.
Lyne, L.Å., Wallqvist, V., Birgisson, B., 2013a. Adhesive surface characteristics of bitumen binders investigated by atomic force microscopy. Fuel 113, 248–256.
Lyne, L.Å., Wallqvist, V., Rutland, M.W., Claesson, P., Birgisson, B., 2013b. Surface wrinkling: the phenomenon causing bees in bitumen. J. Mater. Sci. 48, 6970–6976.
Masson, J.-F., Leblond, V., Margeson, J., Bundale-Perc, J., 2006. Low-temperature bitumen stiffness and viscous paraffinic nano- and micro-domains by cryogenic AFM and PDM. J. Microsc. 227 (3), 191–202.
Masson, J.-F., Leblond, V., Margeson, J., 2007. Bitumen morphologies by phase-detection atomic force microscopy. J. Microsc. 221 (1), 17–29.
McCarron, B., Yu, X., Tao, M., Burnham, N., 2012. The Investigation of 'Bee Structures' in Asphalt Binders. Department of Physics, Worcester Polytechnic Institute and the Department of Civil and Environmental Engineering, Worcester Polytechnic Institute. http://www.wpi.edu/Pubs/E-project/Available/E-project-042512-054125/unrestricted/FINAL_Draft_1.pdf, A Major Qualifying Project 2011–2012.
Mehta, R., Keawwattana, W., Kyu, T., 2004a. Growth dynamics of isotactic polypropylene single crystals during isothermal crystallization from a miscible polymeric solvent. J. Chem. Phys. 120 (8), 4024–4031.
Mehta, R., Keawwattana, W., Guenthner, A.L., Kyu, T., 2004b. Role of curvature elasticity in sectorization and ripple formation during melt crystallization of polymer single crystals. Phys. Rev. E 69, 061802.
Nahar, S.N., Schmets, A.J.M., Scarpas, A., Schitter, G., 2013. Temperature and thermal history dependence of the microstructure in bituminous materials. Eur. Polym. J. 49, 1964–1974.
Nazzal, M.D., Abu-Qtaish, L., 2013. The use of atomic force microscopy to evaluate warm mix asphalt. Report for the Ohio DOT and FHWA, State Job number 134626. http://www.dot.state.oh.us/Divisions/Planning/SPR/Research/reportsandplans/Reports/2012/Materials/134626_FR.pdf.
Nazzal, M.D., Kaya, S., Gunay, T., Ahmedzade, P., 2013. Fundamental characterization of asphalt clay nanocomposites. J. Nanomech. Micromech. 3, 1–8.
Ocko, B.M., Wu, X.Z., Sirota, E.B., Sinha, S.K., Gang, O., Deutsch, M., 1997. Surface freezing in chain molecules: normal alkanes. Phys. Rev. E 55 (3), 3164–3182.
Ocko, B.M., Sirota, E.B., Deutsch, M., DiMasi, E., Coburn, S., Strzalka, J., Zheng, S., Tronin, A., Gog, T., Venkataraman, C., 2001. Positional order and thermal expansion of surface crystalline N-alkane monolayers. Phys. Rev. E 63, 032602.
Oliver, W.C., Pharr, G.M., 1992. An improved technique for determining hardness and elastic modulus using load and displacement sensing indentation experiments. J. Mater. Res. 7 (6), 1564–1583.
Packham, D.E., 1996. Work of adhesion: contact angles and contact mechanics. Int. J. Adhes. Adhes. 16, 121–128.
Pauli, A.T., 2014. Chemomechanics of damage accumulation and damage recovery self-healing in bituminous asphalt binders. Dissertation, Sieca Repro, Delft, The Netherlands, 2014.

www.EngineeringEBooksPdf.com

Pauli, A.T., Grimes, W., 2003. Surface morphological stability modeling of SHRP asphalts. Am. Chem. Soc. Div. Fuel Chem. Prepr. 48 (1), 19–23.
Pauli, A.T., Branthaver, J.F., Robertson, R.E., Grimes, W., Eggleston, C.M., 2001. Atomic force microscopy investigation of SHRP asphalts. Am. Chem. Soc. Div. Fuel Chem. Prepr. 46 (2), 104–110.
Pauli, A.T., Grimes, W., Huang, S.C., Robertson, R.E., 2003. Surface energy studies of SHRP asphalts by AFM. Am. Chem. Soc. Div. Fuel Chem. Prepr. 48 (1), 14–18.
Pauli, A.T., Grimes, R.W., Beemer, A.G., Turner, T.F., Branthaver, J.F., 2011. Morphology of asphalts, asphalt fractions, and model wax-doped asphalts studied by atomic force microscopy. Int. J. Pavement Eng. 12 (4), 291–309.
Pauli, T., Grimes, W., Cookman, A., Huang, S.-C., 2013. Adherence energy of asphalt thin-films measured by force–displacement atomic force microscopy (FD-AFM). J. Mater. Civ. Eng. 26 (12), 04014089 (1–11).
Pauli, T., Grimes, W., Beiswenger, J., Schmets, A.J.M., 2014. Surface structuring of wax in complex media. J. Mater. Civ. Eng. http://dx.doi.org/10.1061/(ASCE)MT.1943-5533.0001023, C4014001.
Petersen, J.C., Robertson, R.E., Branthaver, J.F., Harnsberger, P.M., Duvall, J.J., Kim, S.S., Anderson, D.A., Christensen, D.W., Bahia, H.U., 1994. Binder Characterization and Evaluation, Volume 1. National Research Council, Washington, DC, Report SHRP-A-367, Strategic Highway Research Program.
Piñeiro, Á., Brocos, P., Amigo, A., Garcia-Fadrique, J., 2004. The standard Gibbs energy of adsorption from the bulk at the surface of liquid mixtures: reinterpretation of Traube's rule analysis of the dadsG0 contributions under the expended Langmuir model. Fluid Phase Equilib. 255, 343–353.
Qin, Q., Farrar, M.J., Pauli, A.T., Adams, J.J., 2014. Morphology, thermal analysis and rheology of sasobit modified warm mix asphalt binders. Fuel 115, 416–425.
Rebelo, L.M., Sousa, J.S., Abreu, A.S., Baroni, M.P.M.A., Alencar, A.E.V., Soares, S.A., Mendes Filho, J., Soares, J.B., 2014. Aging of asphaltic binders investigated with atomic force microscopy. Fuel 117, 15–25.
Schmets, A., Kringos, N., Pauli, T., Redelius, P., Scarpas, A., 2010. On the existence of wax induced phase separation in bitumen. Int. J. Pavement Eng. 11 (6), 555–563.
Shull, K.R., 2002. Contact mechanics and the adhesion of soft solids. Mater. Sci. Eng. R 36, 1–45.
Sloutskin, E., Sirota, E.B., Kraack, H., Ocko, B.M., Deutsch, M., 2001. Surface freezing in n-alkane solutions: the relation to bulk phases. Phys. Rev. E 64, 031708.
Sloutskin, E., Wu, X.Z., Peterson, T.B., Gang, O., Ocko, B.M., Sirota, E.B., Deutsch, M., 2003. Surface freezing in binary mixtures of chain molecules I: alkane mixtures. Phys. Rev. E 68, 031605.
Soenen, H., Besamusca, J., Fischer, H.R., Poulikakos, L.D., Planche, J.P., Das, P.K., Kringos, N., Grenfell, J.R.A., Lu, X., Chailleux, E., 2014. Laboratory investigation of bitumen based on round robin DSC and AFM tests. Mater. Sturct. 47 (7), 1205–1220.
Tarefder, R.A., Zaman, A.M., 2010. Nanoscale evaluation of moisture damage in polymer modified asphalts. J. Mater. Civ. Eng. 22, 714–725.
Tarefder, R.A., Zaman, A., 2011. Characterization of asphalt materials for moisture damage using atomic force microscopy and nanoindentation. In: Gopalakrishnan, K. (Ed.), Nanotechnology in Civil Infrastructure. Springer-Verlag Publishing, Berlin, pp. 237–256.
Tissot, B.P., Welte, D.H., 1984. Petroleum Formation and Occurrence. Springer Verlag Publishers, Berlin/Heidelberg, Germany.
Tsukruk, V.V., Reneker, D.H., 1995. Surface morphology of syndiotactic polypropylene single crystals observed by atomic force microscopy. Macromolecules 28, 1370–1376.

www.EngineeringEBooksPdf.com

Wu, X.Z., Ocko, B.M., Sirota, E.B., Sinha, S.K., Deutsch, M., Cao, B.H., Kim, M.W., 1993a. Surface tension measurements of surface freezing in liquid normal alkanes. Science 261, 1018–1020.

Wu, X.Z., Sirota, E.B., Sinha, S.K., Ocko, B.M., Deutsch, M., 1993b. Surface crystallization of liquid normal-alkanes. Phys. Rev. Lett. 70 (7), 958–961.

Wu, S.-P., Pang, L., Mo, L.-T., Chan, Y.-C., Zhu, G.-J., 2009. Influence of aging on the evolution of structure, morphology and rheology of base and SBS modified bitumen. Constr. Build. Mater. 23, 1005–1010.

Xu, H., Matkar, R., Kyu, T., 2005. Phase-field modeling on morphological landscape of isotactic polystyrene single crystals. Phys. Rev. E 72, 011804.

Yen, T.F., Chilingarian, G.V., 1994. Asphaltenes and Asphalts 1. Developments in Petroleum Science, vol. 40A Elsevier Science B.V., Amsterdam, The Netherlands.

Yu, X., Burnham, N.A., Mallick, R.B., Tao, M., 2013. A systematic AFM-based method to measure adhesion differences between micron-sized domains in asphalt binders. Fuel 113, 443–447.

Zhang, H.L., Wang, H.C., Yu, J.Y., 2011. Effect of aging on morphology of organo-montmorillonite modified bitumen by atomic force microscopy. J. Microsc. 242 (1), 37–45.

Zhang, H., Xu, H., Wang, X., Yu, J., 2013. Microstructures and thermal aging mechanism of expanded vermiculite modified bitumen. Constr. Build. Mater. 47, 919–926.

Zhou, J., Komvopoulos, K., 2006. Surface and interface viscoelastic behaviors of thin polymer films investigated by nanoindentation. J. Appl. Phys.. 100,114329, 1–8.

Zhou, W., Cheng, S.Z.D., Putthanarat, S., Eby, R.K., Reneker, D.H., Lotz, B., Magonov, S., Hsieh, E.T., Geerts, R.G., Palackal, S.J., Hawley, G.R., Welch, M.B., 2000. Crystallization, melting and morphology of syndiotactic polypropylene fractions. 4. In situ lamellar single crystal growth and melting in different sectors. Macromolecules 33 (18), 6861–6868.

www.EngineeringEBooksPdf.com

Cracking mechanisms in asphalt mixtures

5

R. Roque, J. Zou, D. Hernando
University of Florida, Gainesville, FL, USA

5.1 Introduction

A clear understanding of the mechanisms of pavement cracking is the cornerstone of effective mitigation of premature failure and evaluation of how introduction of new materials and technology will affect cracking performance. Traditionally, the asphalt pavement community has based most of its mixture and pavement design systems on the hypothesis that cracking, especially load-induced cracking, primarily results from a continuous accumulation of distress caused by repeated application of wheel loads from the time the pavement is open to traffic (traditional fatigue approach). Although it is undeniable that progression of pavement cracking involves repeated load applications, it does not necessarily follow that fatigue is the primary mechanism that leads to cracking in asphalt mixture and pavement.

An alternate explanation for the initiation and progression of pavement cracking is based on the hypothesis that all forms of pavement cracking, including load-induced cracking, are a result of relatively few critical loading conditions that induce permanent damage and development of cracks (critical condition approach). This approach implies that the majority of wheel load applications, especially during the early life of the pavement, do not contribute to cracking. Instead, changes in mixture properties throughout the life of the pavement that make the mixture stiffer, more brittle, and less able to heal may be one of the primary determinants of cracking performance. Furthermore, mixture failure limits defined on the basis of number of repeated load applications to failure (fatigue tests) may not be very effective for evaluating mixture performance.

Clearly, determination of which approach most accurately represents the actual mechanisms of pavement cracking is of great importance to the pavement community because it affects almost every aspect of asphalt pavement engineering, from material selection, testing, and specification, to pavement structural design. This chapter attempts to address this important issue by interpreting results of recent experiments, advanced modeling efforts, and evaluation of field performance in terms of their implications regarding mechanisms of pavement cracking. A thorough analysis of these results in Section 5.2 reveals that consideration of the critical condition approach is needed for better evaluation and prediction of cracking performance in asphalt pavements. Section 5.3 provides a comprehensive framework for implementation of the critical condition approach into a prediction model, hot mix

Advances in Asphalt Materials. http://dx.doi.org/10.1016/B978-0-08-100269-8.00005-2
© 2015 Elsevier Ltd. All rights reserved.

www.EngineeringEBooksPdf.com

asphalt-fracture mechanics (HMA-FM). Section 5.4 shows how the HMA-FM framework was integrated into a top-down cracking (TDC) prediction system. Example simulations are presented for two in-service pavement sections. Summary and conclusions are included in Section 5.5. The chapter concludes with some final thoughts regarding implications for research and practice related to asphalt pavement engineering.

5.2 Key observations on cracking

The summary presented in Table 5.1 shows that, in general terms, the causes and mitigating factors associated with three predominant types of cracking in flexible pavement systems are well understood. This understanding provides excellent insight as to how relative changes in material properties or pavement structural characteristics affect cracking. However, development of more effective material specifications and structural design systems requires a much higher level of understanding of the specific mechanisms describing the sequence of events and interrelationships among the different factors that lead to initiation and growth of cracks in actual pavement.

Table 5.1 Causes and mitigating factors of cracking in flexible pavements

Type	Primary causes	Secondary causes	Primary mitigating factors
Traditional fatigue cracking (bottom-up)	Structural: – Bending	Asphalt mixture: – Fracture and aging resistance	– Stiffer base (lower E_1/E_2 ratio) – Thicker asphalt layer
Top-down cracking	Asphalt mixture: – Fracture and aging resistance	Structural: – Bending Thermal: – Thermal stress	Higher fracture and aging resistance: – Modifier/binder – Gradation
Thermal cracking	Asphalt mixture: – Stiffness – Fracture and aging resistance	Structural: – Base/subgrade	– Softer binder – Gradation for less aging and thermal contraction

www.EngineeringEBooksPdf.com

The following sections attempt to extract greater clarity regarding cracking mechanisms by exploring key observations made on this subject over the last several decades. More specifically, emphasis is placed on determining whether the traditional fatigue approach or the critical condition approach is more closely aligned with observations made based on both experimental methods and advanced modeling regarding cracking performance of asphalt mixture and pavement. This is accomplished by examining whether observations made are consistent with the fundamental assumptions of the two approaches. Consequently, a brief overview of the approaches is helpful in putting observations into proper context.

Traditional fatigue is based on the hypothesis that progressive cumulative damage caused by repeated wheel load applications leads to pavement distress in the form of cracking in the wheel paths. Furthermore, implementation of this hypothesis assumes that results of laboratory fatigue tests are directly related to cracking distress in field pavement. A general form of a traditional fatigue relationship is shown in Equation (5.1) and further developed in Figure 5.1:

$$N_f = C \cdot \left(\frac{1}{E}\right)^{f_1} \cdot \left(\frac{1}{\varepsilon_t}\right)^{f_2} \tag{5.1}$$

where number of cycles to failure (N_f) is a function of laboratory fatigue test coefficients (f_1 and f_2), tensile strain at the bottom of the asphalt layer (ε_t), modulus of mixture (E), and a field calibration coefficient (C). Note that failure in traditional fatigue is usually associated with some percentage of pavement surface area cracked. Miner's (1945) hypothesis is employed to accumulate damage associated with changes in pavement temperature, which affect mixture stiffness (E), and moisture, which may affect stiffness of subgrade and other structural layers. Effects of load type (single axle, tandem axle, etc.) and magnitude are typically dealt with by using an equivalent load concept (e.g., ESAL). An examination of the elements associated with the traditional fatigue approach reveal the following inherent assumptions:

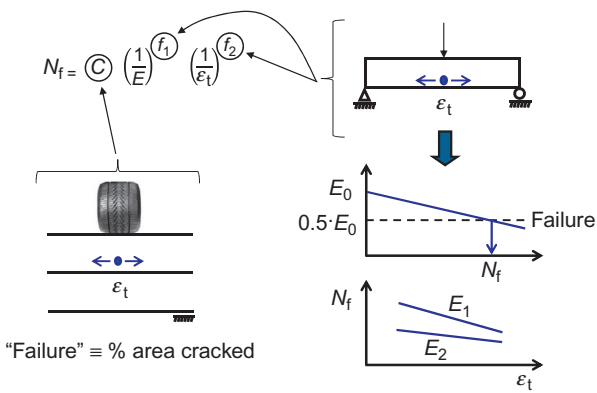


Figure 5.1 Development of a fatigue relationship for traditional fatigue approach.

www.EngineeringEBooksPdf.com

- Changes in pavement condition, particularly stress concentrations/intensities associated with initiation and progression of cracks, are not considered.
- Mixture failure, which is typically defined as the state when effective beam stiffness is reduced by 50%, is not fundamentally tied to fracture, so there is no direct relationship between rate of damage in the laboratory and rate of damage in the field.
- Healing is not considered, although its effect is probably lumped into calibration coefficients.
- Because of the enormous number of load applications and changing conditions during the service life of a pavement, implementation requires selection of a few representative temperature profiles and moisture conditions, which in effect precludes consideration of critical conditions that may result in damage rates far greater than those included in fatigue experiments.

Implications of these assumptions are shown in Figure 5.2, which conceptually illustrates characteristic differences in accumulation of distress for traditional fatigue and critical condition approaches. Both approaches begin with zero distress/cracking and end with a predefined threshold of distress/cracking considered to be failure. However, the path between these two points is clearly different.

Distress accumulates in a continuous manner in traditional fatigue, whereas accumulation of distress in critical condition is stepwise discontinuous. Furthermore, although some nonlinearity in distress accumulation may exist in traditional fatigue, the critical condition approach is by definition highly nonlinear, going from zero distress accumulation in early life to very rapid accumulation near end of life. This observation indicates that the critical condition approach appears to be more consistent with field observations, where cracking is typically not observed before pavement is several years in service. Reasons for the cited differences in distress accumulation are associated with the differences in fundamental assumptions between the two approaches. In contrast to traditional fatigue, the critical condition approach assumes the following:

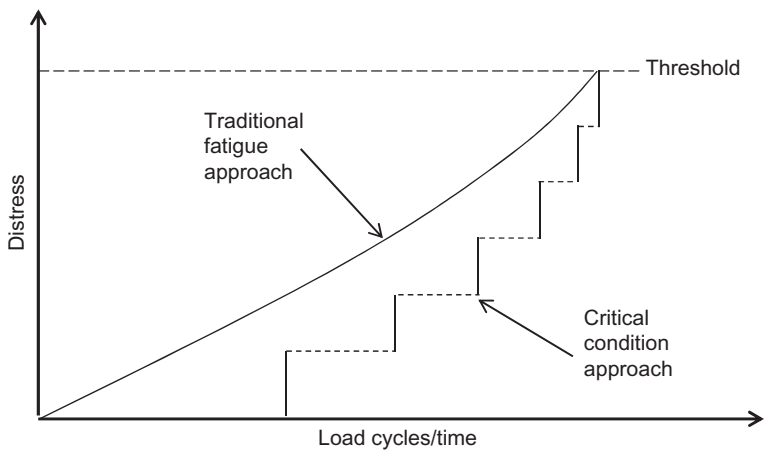


Figure 5.2 Differences in distress accumulation for traditional fatigue and critical condition approaches.

www.EngineeringEBooksPdf.com

- Changes in pavement condition caused by stress concentrations/intensities associated with initiation and progression of cracks are considered a very important factor in damage accumulation and must be dealt with explicitly.
- A threshold exists below which neither permanent damage accumulation nor crack propagation occurs, even though many load repetitions are applied. Consequently, pavement distress is a stepwise discontinuous process in that only critical combinations of loads, material properties, and pavement structure characteristics result in accumulation of distress or crack propagation.
- Mixture failure is fundamentally defined as initiation or advancement of a crack, so there is a direct relationship between rate of damage in the laboratory and rate of damage in the field.
- Healing is considered a very important factor in damage accumulation and must be dealt with explicitly.

In the following subsections, differences in assumptions between traditional fatigue and critical condition approaches are examined based on results of experiments and advanced model studies. Particular emphasis is placed on the following key questions:

- Is there a threshold below which damage does not accumulate?
- Does 50% reduction in stiffness define failure clearly enough for asphalt mixture?
- Is healing real and, if so, how important a role does it play in cracking performance?
- Is it likely that critical loading conditions commonly occur that induce permanent damage with few load applications?

5.2.1 Experimental observations

Implications of extensive experimental research findings associated with cracking mechanisms of asphalt mixture are examined in this section. Three general areas of research are examined: fatigue, microdamage healing, and failure limits (damage and fracture threshold).

5.2.1.1 Fatigue results

A summary of asphalt mixture fatigue coefficients reported by different institutions is presented in Table 5.2. The large variation in each of the coefficients reported indicates that traditional fatigue relationships are not fundamental enough to capture important differences in fatigue behavior for the range of binders and mixtures evaluated. The relative importance of stiffness and strain level, which is reflected in parameters f_1 and f_2, is enormous. Furthermore, field calibration coefficients not only vary greatly but also are far from a value of 1, indicating a large departure between failure as measured in the laboratory and that observed in field pavement. Although some variability and need for calibration is expected for a problem as complex as cracking in asphalt pavement, the lack of agreement or consistency in results legitimately raises the question of the validity of traditional fatigue.

Figure 5.3 (Lundstrom et al., 2004) illustrates the fact that fatigue test results can vary not only with mode of loading (controlled stress or controlled strain) but also with specimen geometry and strain (or stress) amplitude. The fact that mixtures do not

www.EngineeringEBooksPdf.com

Table 5.2 Summary of asphalt mixture fatigue coefficients reported by different institutions

Institution	C	f_1	f_2
Asphalt Institute (1982)	0.0796	0.854	3.291
Shell (1978)	0.0685	2.363	5.671
Transport and Road Research Laboratory (Powell et al., 1984)	1.66×10^{-10}	0	4.32
Belgian Road Research Center (Verstraeten et al., 1977)	4.92×10^{-14}	0	4.76

Coefficients for the general fatigue relationship $N_f = C \cdot \left(\frac{1}{E}\right)^{f_1} \cdot \left(\frac{1}{\varepsilon_t}\right)^{f_2}$.

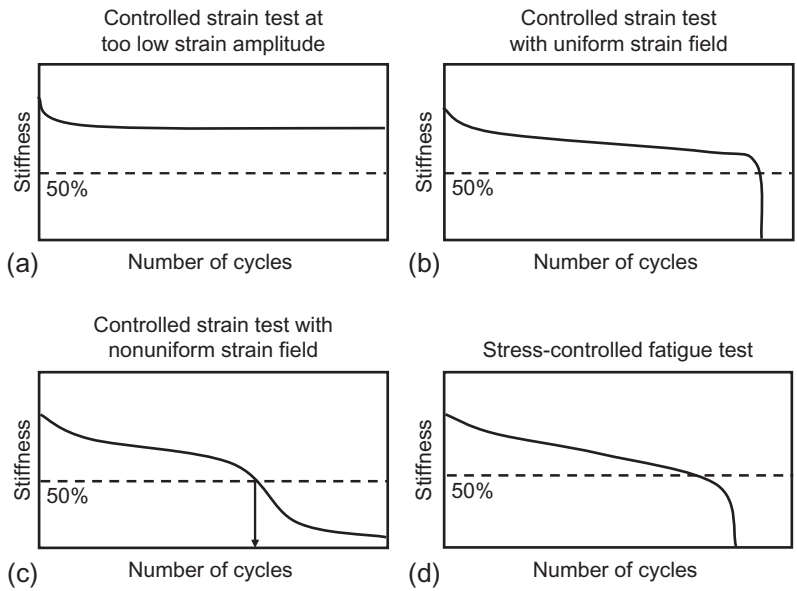


Figure 5.3 (a–d) Typical fatigue paths for asphalt mixtures from uniaxial testing and sinusoidal loading.
After Lundstrom et al. (2004).

appear to accumulate damage below a certain strain amplitude (controlled strain test at too low strain amplitude in Figure 5.3a) supports the existence of an endurance limit. More specific evidence of this phenomenon is presented in Section 5.2.1.3. Figure 5.3 also shows that identification of failure in fatigue can be affected by specimen geometry, even when failure is defined as 50% reduction in stiffness.

Figure 5.4 (adapted from Lundstrom et al., 2004) clearly shows that stiffness at failure increases (percent reduction in stiffness decreases) as the mixture gets stiffer and more brittle. Stiffer and more brittle mixtures typically yield a small reduction in stiffness at failure. It is interesting to note that stiffer and more brittle mixtures

www.EngineeringEBooksPdf.com

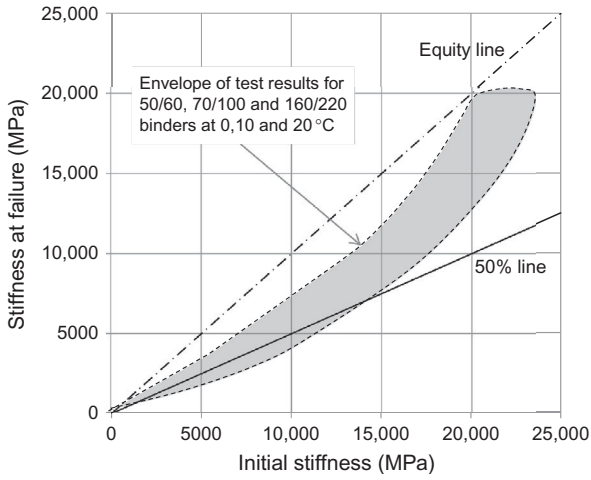


Figure 5.4 Stiffness at failure versus initial stiffness for controlled strain tests on dense-graded mixtures. Adapted from Lundstrom et al. (2004).

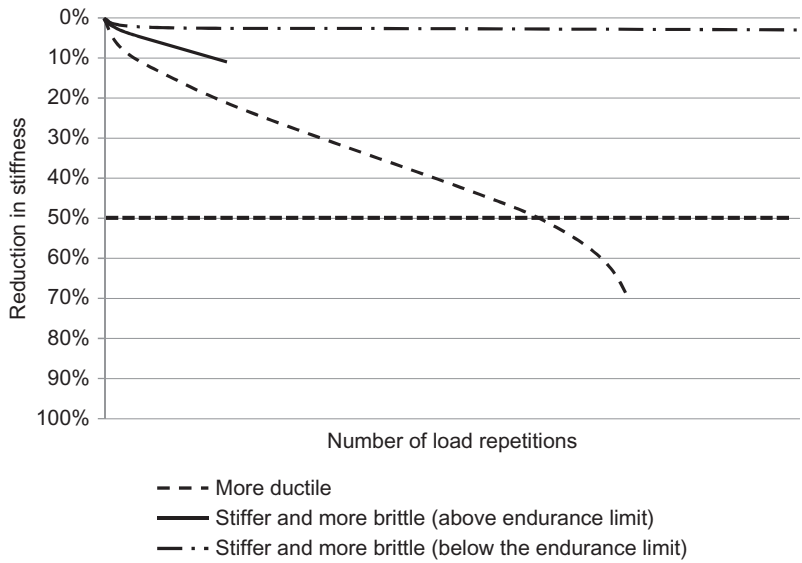


Figure 5.5 Mixture and strain level effects on reduction in stiffness at failure.

subjected to low strain levels (below the endurance limit) may withstand an indefinite number of cycles in a fatigue test (Figure 5.5). On the other hand, reduction in stiffness at failure for a more ductile asphalt mixture can exceed the 50% criterion used in traditional fatigue. These observations are clear evidence that 50% reduction in stiffness is not fundamentally tied to fracture. The other important implication of this observation, which is not explicitly shown in the previous figures, is that stresses closer to the absolute tensile strength of the mixture determined in monotonic loading are required to induce damage for a stiffer, more brittle mixture. This also means that it is much

www.EngineeringEBooksPdf.com

more difficult to select an appropriate strain amplitude for testing of a stiffer, more brittle mixture (i.e., the likelihood of getting a result similar to the one in Figure 5.3a increases). Consequently, fatigue tests can easily produce counterintuitive results for stiffer, more brittle materials. For example, a highly oxidized mixture, which most asphalt pavement engineers would agree will result in very poor cracking performance, may easily yield excellent fatigue results.

It should be noted that more advanced fatigue models developed more recently, such as the viscoelastic continuum damage (VECD) approach (Daniel and Kim, 2002) or DBN model (Di Benedetto et al., 2007), are more fundamental in nature and yield results that are independent of mode of loading. These models can effectively isolate microdamage from other effects, such as time dependency and temperature, that can also reduce the apparent stiffness during repeated load fatigue tests. However, even for these more advanced models, identifying a fundamental definition of failure (i.e., other than 50% reduction in stiffness) during repeated loading, and obtaining relevant test results for stiffer, more brittle mixtures, remain a challenge.

5.2.1.2 Microdamage healing

For more than 25 years, researchers have been reporting evidence of microdamage healing, initially on asphalt binders, and later on asphalt mixtures (Little et al., 1987, 1997; Kim and Little, 1989; Little and Prapnnachari, 1991). Figure 5.6 presents evidence of healing in asphalt mixtures reported by Daniel and Kim (2001). As shown in the figure, rest periods during repeated load fatigue tests resulted in nearly complete

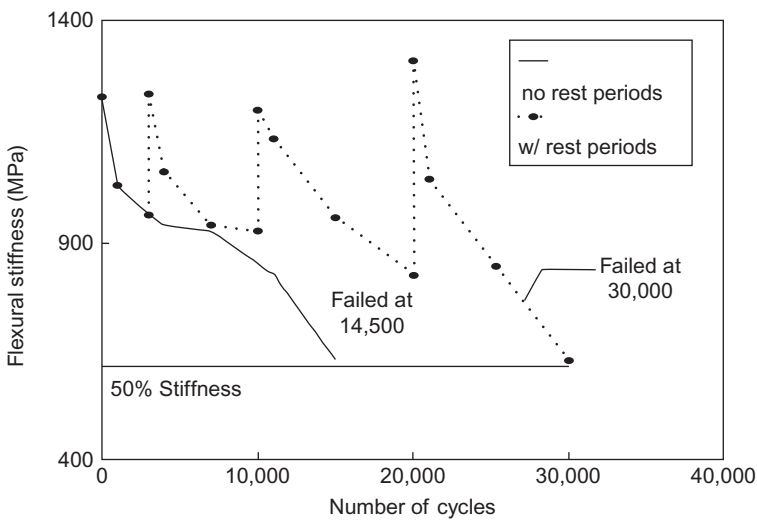


Figure 5.6 Effect of rest periods on number of cycles to failure at 20 °C.
After Daniel and Kim (2001).

www.EngineeringEBooksPdf.com

recovery of mixture stiffness. Tests clearly indicated that rest periods extended fatigue life. Their work also showed that healing was faster at 60 °C than at 20 °C.

Kim and Roque (2006) also presented clear evidence of healing in asphalt mixtures. Figure 5.7 shows nearly complete recovery of mixture stiffness (expressed as reduction in resilient horizontal deformation in the figure), which resulted in a manner of minutes after loading was stopped. Kim and Roque (2006) also showed that healing rate increased with temperature (Figure 5.8), and that rate of healing increased with level of damage (Figure 5.9). The latter result is particularly interesting because it indicates that about the same amount of time is required for full healing, regardless of damage level.

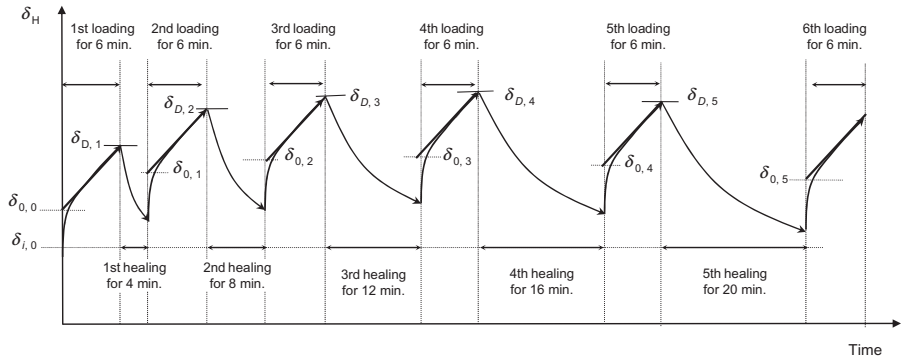


Figure 5.7 Recovery of stiffness (expressed as reduction in resilient deformation) for an asphalt mixture subjected to loading-healing cycles (Kim and Roque, 2006).

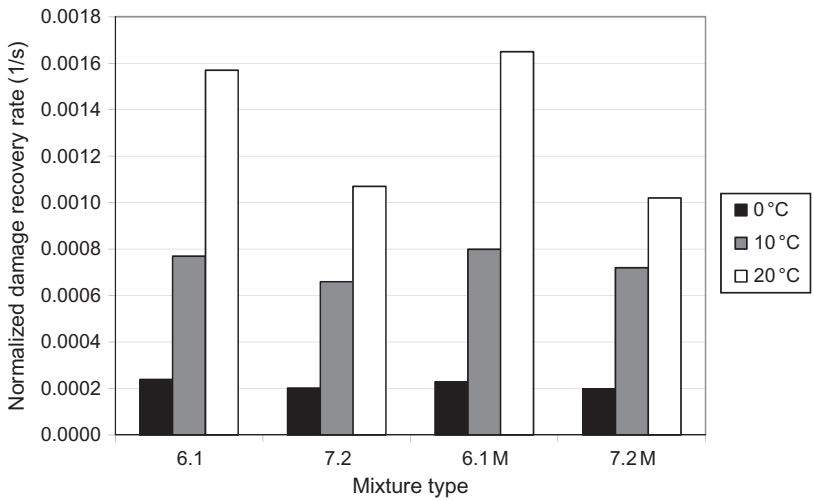


Figure 5.8 Normalized damage recovery rate for different mixtures as a function of temperature (Kim and Roque, 2006).

www.EngineeringEBooksPdf.com

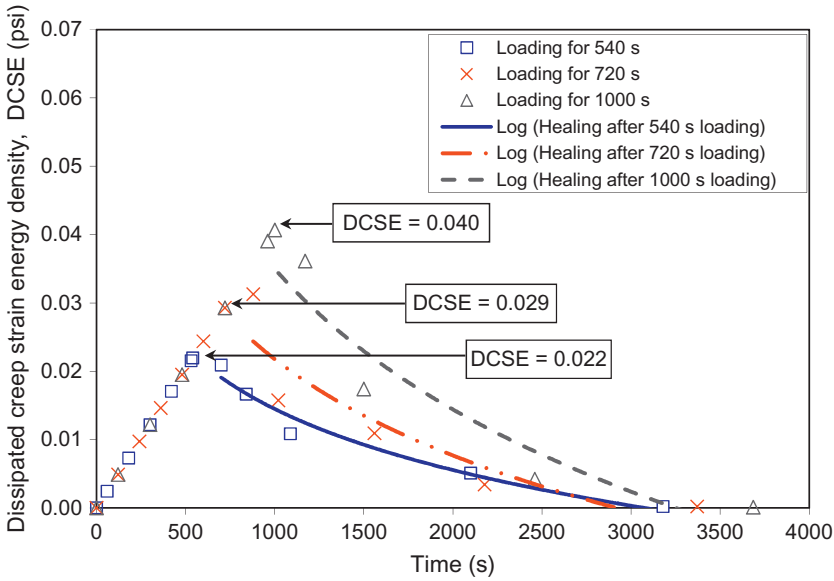


Figure 5.9 Healing rate (expressed as recovery in dissipated creep strain energy density) for different loading times (level of induced damage) at a constant temperature of 20 ºC (1 psi = 6.89 kJ/m^3) (Kim and Roque, 2006).

Given that even for the most heavily trafficked pavement, several minutes may pass between applications of heavy wheel loads in actual in-service conditions, these results imply that accumulation of damage is unlikely in the field. In addition, except in very cold climates, in-service pavement reaches temperatures well in excess of 20 °C on a daily basis, so even if some damage accumulated during the cooler part of the day, it is likely completely healed during the warmer part of the day.

5.2.1.3 *Damage and fracture threshold*

Ample evidence exists of a threshold below which neither permanent damage accumulation nor crack propagation occurs, even when many load repetitions are applied. Carpenter et al. (2003) reported identification of an endurance limit in asphalt mixtures, which is a strain threshold below which damage does not accumulate under repeated loading. Typical results of repeated load tests performed using strain levels below the endurance limit are presented in Figure 5.10 (Carpenter et al., 2003), which shows that after an initial loss of stiffness, which can be attributed to internal temperature changes and thixotropy effects, mixture stiffness remained constant as additional repeated loads were applied. Note the similarity between Figures 5.10 and 5.3a (controlled strain test at too low strain amplitude), which is in fact a fatigue test performed below the endurance limit. Figure 5.10 also shows that change in dissipated energy (ΔDE/DE) between load cycles remained constant while stiffness remained constant. This was interpreted as further evidence of no damage accumulation,

www.EngineeringEBooksPdf.com

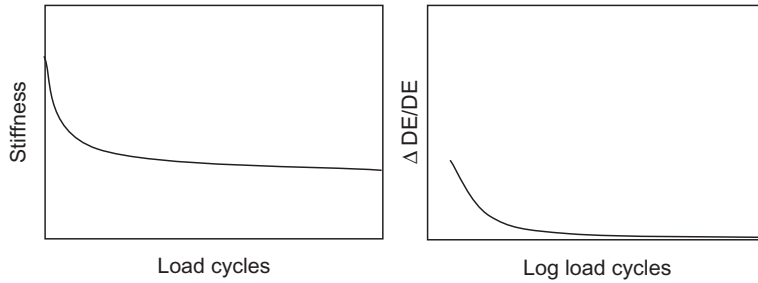


Figure 5.10 Evolution of stiffness and dissipated energy (ΔDE/DE) with number of load cycles for a mixture at 70 microstrain in flexure fatigue testing.
After Carpenter et al. (2003).

because accumulation of damage should lead to an increase in dissipated energy and reduction in stiffness. Existence of an endurance limit implies one of two possibilities: (1) no damage accumulates at strain levels below the endurance limit or (2) the rate of healing is equal to damage accumulation rate at these strain levels. Their findings indicated this threshold to be about 70–90 microstrain.

Roque et al. (2002) reported identification of a fracture energy threshold, below which microdamage is healable and above which macrocrack initiation and growth occur. In other words, this is the maximum energy that an asphalt mixture can absorb without fracturing. Figure 5.11 shows results of two repeated load tests. In the first case (Figure 5.11a), repeated loads were applied such that accumulated energy was maintained below the threshold. Repeated loading was then stopped, and the mixture was allowed to rest for 12 h at 30 °C. Repeated load applications commenced after the rest period, and the mixture was found to have fully recovered its original stiffness (as reflected by resilient deformation), indicating that damage had fully healed. In the second case (Figure 5.11b), the specimen was subjected to repeated loading such that accumulated energy exceeded the threshold. As before, repeated loading was then stopped, and the mixture was allowed to rest for 12 h at 30 °C. However, when repeated load applications commenced after the rest period, the mixture was found to not have recovered any of the stiffness lost, indicating that no healing had occurred. Furthermore, the rate of damage, as measured by rate of stiffness reduction, was found to be greater than it was during original loading. These results provide clear evidence that macrocracking had developed, which not only did not allow healing to occur but also resulted in stress intensities that accelerated the rate of damage accumulation. Additional evidence that microdamage is fully healable below the threshold was presented in Figures 5.6 and 5.7, which show that full healing occurred in repeated load tests where repeated load applications did not result in failure (i.e., fracture).

5.2.2 Advanced modeling observations

Implications of advanced modeling efforts associated with factors affecting stress distributions in pavement systems, particularly those that illustrate a significant departure from stresses typically used to evaluate mixture and pavement cracking performance,

www.EngineeringEBooksPdf.com

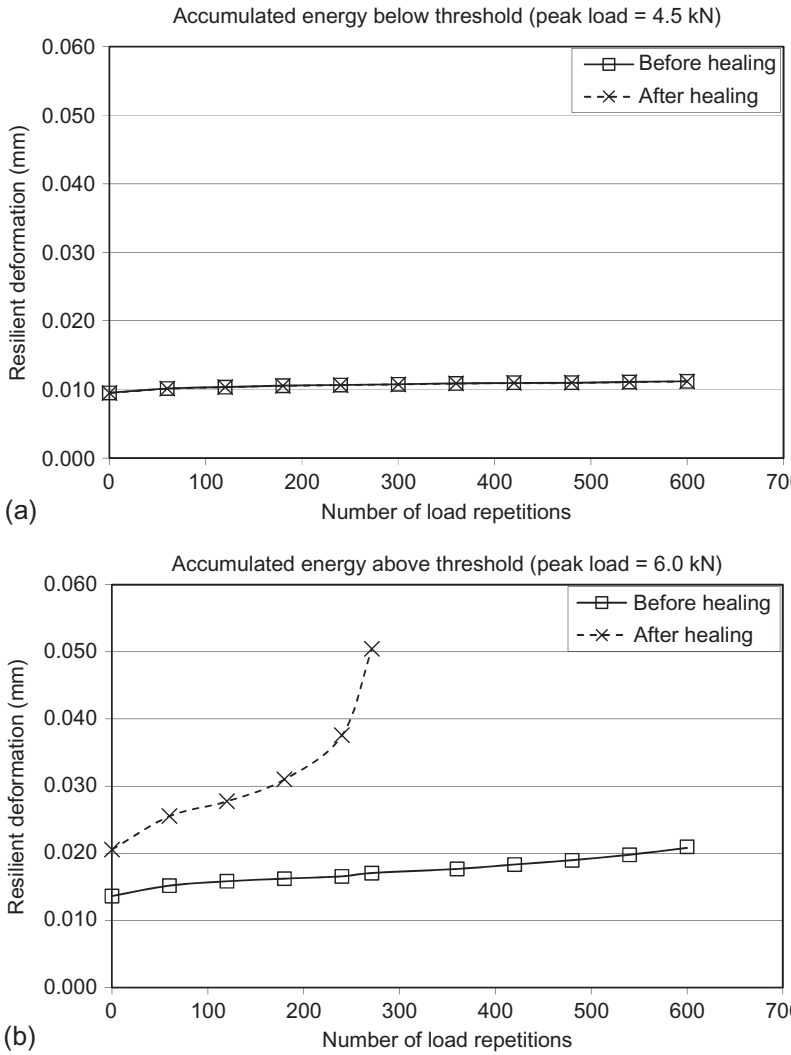


Figure 5.11 (a and b) Results of repeated load tests on dense-graded mixture subjected to two different load peak magnitudes (Roque et al., 2002).

are examined in this section. Three general areas are examined: radial tire contact stresses, presence of damage zones, and presence of cracks and mixture stiffness gradients.

5.2.2.1 Radial tire contact stresses

Based on measured contact stress distributions under radial truck tires, Myers et al. (1999) showed that resulting near-surface stress distributions could explain initiation of longitudinal surface cracks. Figure 5.12 shows the general effect associated with

www.EngineeringEBooksPdf.com

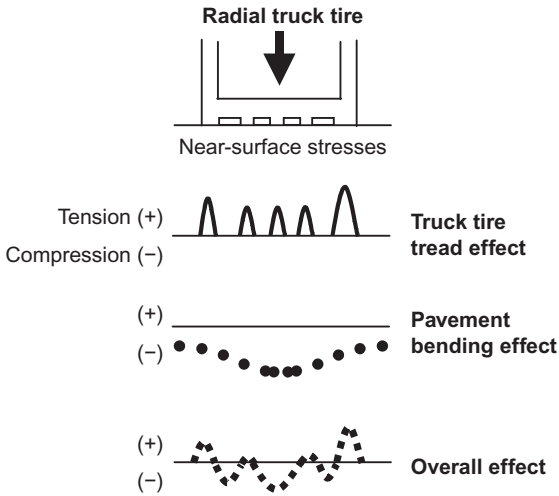


Figure 5.12 Contribution of radial tires and pavement bending to near-surface transverse stress distribution (Myers et al., 1999).

transverse tensile stress measured immediately under each tire rib. Even though pavement bending stresses are compressive in this zone, the overall effect is transverse tensile stress on the pavement surface, particularly under the outer rib of tire. Predicted stresses at the surface of the pavement based on measured tire contact stresses illustrate this point (Figure 5.13); the tire load resulted in high tensile stress immediately beneath rib 1 of this tire. As shown in Figure 5.14, the idea that these stresses can explain the initiation of longitudinal surface cracks, and more generally the incidence of TDC, becomes even more plausible when one considers the fact that the mixture near the surface is subjected to the highest level of oxidation and ultraviolet radiation, which makes the mixture stiffer and more brittle. The very significant effect of stress distribution of mixture stiffness gradients in the surface layer associated with greater aging and temperature differentials will be illustrated later in this section.

Molenaar (2004) came to a similar conclusion based on his observations, indicating that longitudinal cracks can develop at the pavement surface because of complex tire contact stresses, which result in sharp, clearly visible cracks due to localized stresses. He also indicated that bottom damage more likely develops as a zone of degradation, and he seriously doubted that it appears as a visible crack.

5.2.2.2 *Presence of damage zones*

If permanent microdamage can accumulate, which is an underlying premise of fatigue cracking, damage zones will develop at different locations in the asphalt layer. Mun et al. (2004) used VECD analysis to illustrate the potential development of damage zones in a pavement. Results are summarized in Figure 5.15, which indicates that location of the zones where the greatest damage occurs is dependent on pavement structural characteristics (e.g., stiffer, thicker surface layers combined with lower stiffness base exhibit greater propensity for surface damage).

www.EngineeringEBooksPdf.com

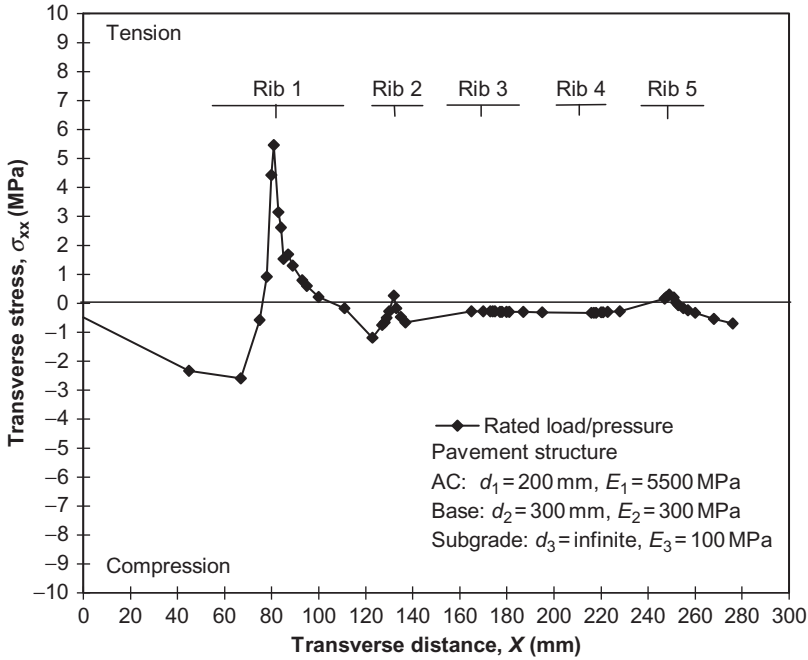


Figure 5.13 Predicted transverse stress distribution induced by radial truck tire near pavement surface (Myers et al., 1999).

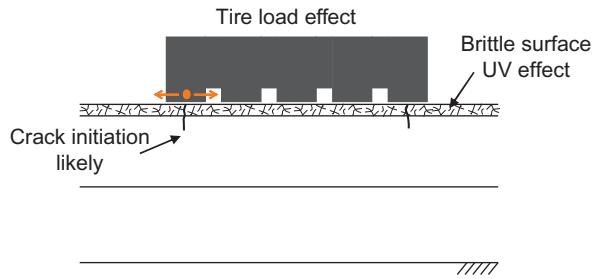


Figure 5.14 Combined effect of tensile stresses induced by radial tires and oxidation plus UV radiation on top-down cracking initiation.

One important effect of these zones is conceptually illustrated in Figure 5.16. Reduced mixture stiffness in these damage zones essentially results in a weakening of the structure and can significantly alter the stress distribution. Consequently, damage zones may accelerate progression of damage and cracking or even alter the mechanism of failure.

5.2.2.3 *Presence of cracks and stiffness gradients*

It is well known that the presence of cracks causes stress intensities, which can potentially result in localized stresses that approach the tensile strength of the material, even for modest load applications. Therefore, the need to account for the effects of cracks

www.EngineeringEBooksPdf.com

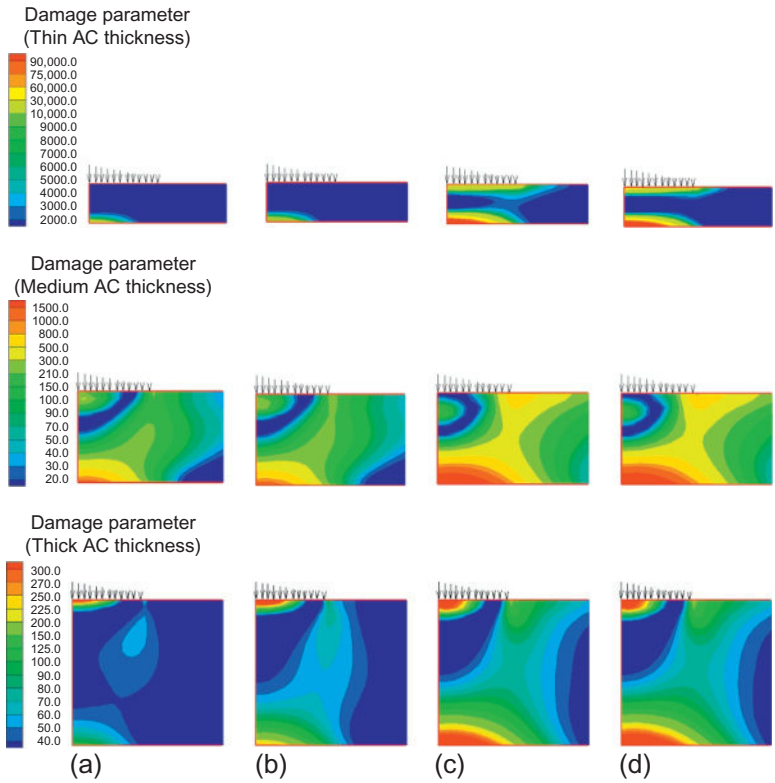


Figure 5.15 Damage contours for different asphalt layer thicknesses (from thin to thick) under nonuniform 40 kN load and different pavement structural characteristics: (a) stiff base and stiff subgrade; (b) stiff base and weak subgrade; (c) weak base and stiff subgrade and (d) weak base and weak subgrade.
After Mun et al. (2004).

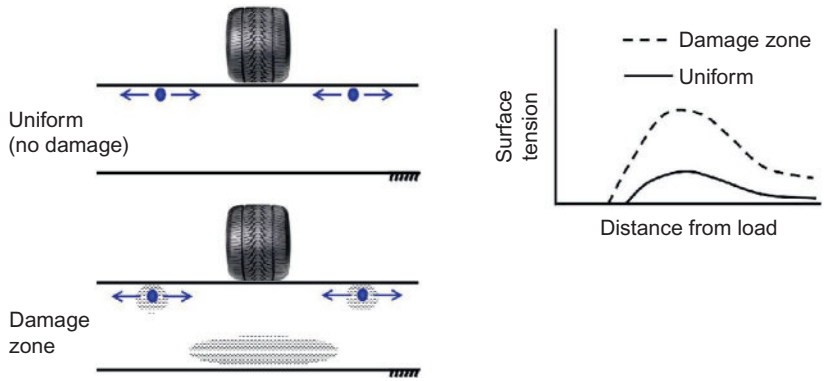


Figure 5.16 Effect of presence of damage zones on near-surface tensile stress distribution.

www.EngineeringEBooksPdf.com

on stress distribution seems undeniable. Myers and Roque (2002) showed that the effects of cracks are magnified when stiffness gradients in the asphalt layer, which are caused by significant variation in oxidative aging and temperature along the depth of the layer, are considered. They examined changes in stress intensity factor (K_I), for different stages of crack length (from 5 to 40 mm) and various positions of loading relative to crack location (20–75 cm distance), induced by different stiffness gradient combinations associated with differences in oxidative aging and temperature along the depth of the asphalt layer.

Results of the analyses presented in Figure 5.17 indicate that the combined presence of stiffness gradient and crack had an enormous impact on tensile stress ahead of the crack tip. In fact, resulting stress intensities were anywhere from 2 to 10 times greater than those predicted for a typical analysis performed with no stiffness gradient.

5.2.3 Concluding remarks

Results of experimental observations support the hypothesis that progression of pavement cracking is highly nonlinear, going from zero distress accumulation in early life to more rapid accumulation near end of life, which is consistent with the progression associated with the critical condition approach presented in Figure 5.2. This is also more consistent with field observations, where cracking is typically not observed before pavement is several years in service. The existence of a threshold indicates that microdamage is permanent only if the threshold is exceeded or if the mixture is no longer capable of microdamage healing. In addition, research on microdamage healing indicates that accumulation of damage is unlikely in the field, particularly early in

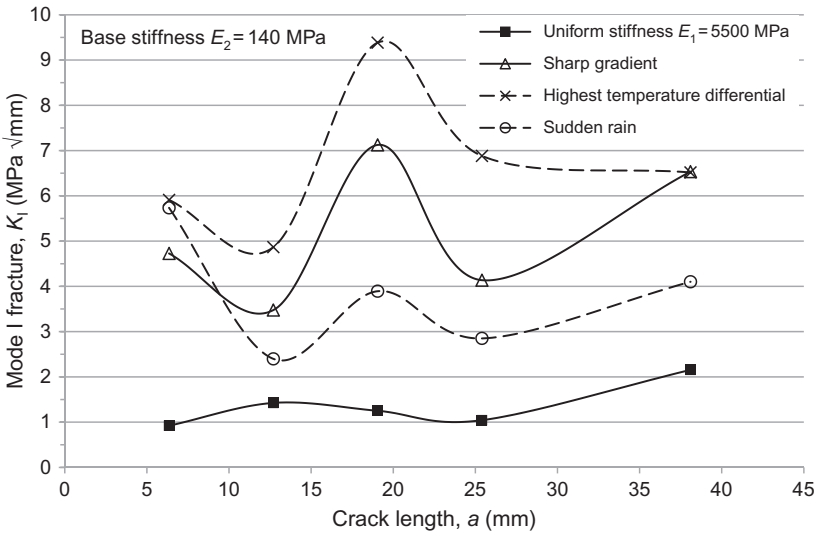


Figure 5.17 Effect of stiffness gradients on stress intensity factor K_I predicted at the crack tip for a 20-cm asphalt layer (load centered 64 cm from crack) (Myers and Roque, 2002).

www.EngineeringEBooksPdf.com

the life of a pavement. This appears to support the hypothesis that damage is only permanent when a critical combination of loading conditions, temperature, and material property changes (i.e., oxidative aging and moisture damage that stiffen and embrittle the mixture, reducing its fracture energy threshold and its healing potential) occur. Furthermore, one can logically conclude that these critical combinations are far more likely to occur later in the life of the pavement, after aging and moisture damage have occurred, and highly unlikely to occur early in its life, when the mixture strain tolerance is greatest and healing potential is at its peak (Figure 5.18). This all implies that progression of pavement cracking is highly nonlinear, going from zero distress accumulation in early life to more rapid accumulation near end of life, which is consistent with the progression associated with the critical condition approach presented in Figure 5.2. As mentioned earlier, this is also more consistent with field observations, where cracking is typically not observed before pavement is several years in service.

Results of advanced modeling efforts clearly indicate the need to consider conditions other than those typically used to determine pavement response in the traditional fatigue approach. There is significant evidence that discontinuities develop during a pavement service life, which result in magnification of stresses. Near-surface stresses under radial truck tires, damage zones, cracks, and stiffness gradients can significantly alter stress distribution in the pavement. This implies that the initiation and progression of cracks is likely greatly influenced by local stress concentrations caused by a combination of factors.

5.3 Implementation of the critical condition approach using hot mix asphalt-fracture mechanics (HMA-FM)

The thorough analysis of experimental observations and advanced modeling conducted in the previous section reveals that the critical condition approach better represents the mechanisms of cracking observed in asphalt pavements in the field. This section describes the development of a viscoelastic fracture mechanics-based

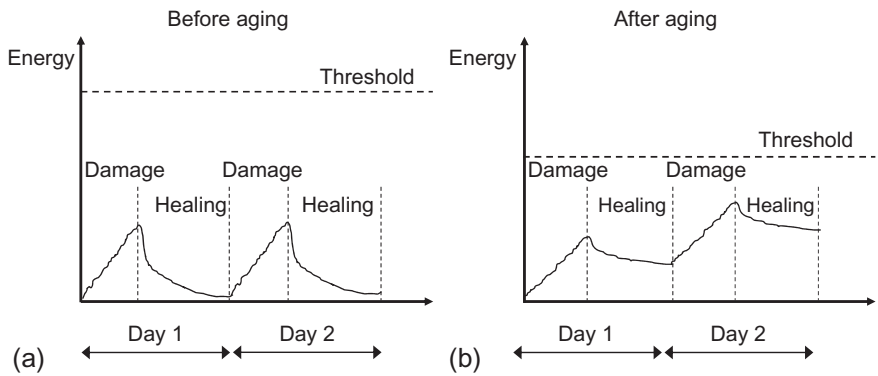


Figure 5.18 (a and b) Effect of aging on energy threshold and damage accumulation/healing.

www.EngineeringEBooksPdf.com

model, HMA-FM, which provides a comprehensive framework for practical implementation of the critical condition approach into an evaluation and prediction model.

The key features of HMA-FM are summarized as follows:

- The asphalt mixture is modeled as a viscoelastic material; damage is associated with its viscous response (creep).
- The verified threshold concept is introduced as a key element in the cracking process: if the threshold is not exceeded, only healable microdamage develops in the material; however, nonhealable macrodamage (crack initiation or growth) results once the threshold is exceeded.
- Asphalt mixture failure is fundamentally defined as the initiation or propagation of a crack.
- The model considers both fundamental failure limits and rate of damage to identify the onset of crack initiation and crack propagation.
- The effects of healing can be inherently dealt with in the crack growth law.
- Crack propagation is defined as a stepwise discontinuous process, which agrees with propagation observed in the field.
- The model accounts for the effects of pavement structural characteristics and material properties on cracking performance.
- The parameters required can be obtained from relatively simple and well-established Superpave Indirect Tension (IDT) tests.

HMA-FM appears to provide a powerful tool for mixture design and optimization. The model can also be used as the foundation for the prediction of pavement cracking performance for the purposes of specification development and mixture design. The following subsections further develop the basic principles of HMA-FM, its stepwise discontinuous crack growth law, and an energy-based performance parameter derived from field investigations.

5.3.1 Basic principles of HMA-FM

5.3.1.1 Threshold concept

The threshold concept is based on the observation that microdamage in asphalt mixtures (i.e., damage that may potentially lead to crack initiation or crack propagation) appears to be fully healable, whereas macrodamage (i.e., damage associated with crack initiation or propagation) does not appear to be healable (Zhang, 2000; Zhang et al., 2001a,b; Roque et al., 2002). This implies that a damage threshold exists below which damage is fully healable. Once the threshold is exceeded, the developed macrodamage is no longer healable. Therefore, the threshold defines the development of macrocracks (macrodamage), at any time during either crack initiation or propagation, at any point in the mixture. If loading and healing conditions are such that the induced energy does not exceed the mixture threshold, then the mixture may never crack, regardless of the number of load repetitions applied.

5.3.1.2 Failure limits

As discussed by Zhang (2000) and Roque et al. (2002), fracture (crack initiation or crack propagation) can develop in asphalt mixtures in two distinct ways: repeated load applications or a single load excursion. An energy threshold or failure limit has then

www.EngineeringEBooksPdf.com

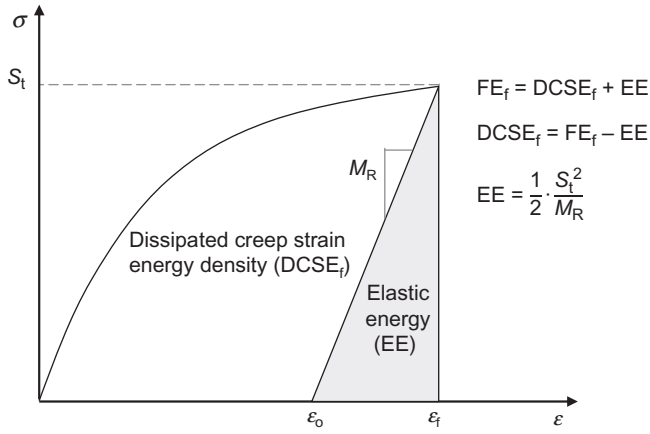


Figure 5.19 Determination of failure limits in asphalt mixtures from a stress (σ)–strain (ε) diagram: fracture energy density limit (FE_f) and dissipated creep strain energy density limit ($DCSE_f$).
Notes: Failure limits defined in terms of energy density should be reported in units of energy per unit volume (e.g., kJ/m^3).

been defined for each distinct fracture mode: dissipated creep strain energy density limit ($DCSE_f$) and fracture energy density limit (FE_f), respectively.

Failure limits can be easily determined from the stress–strain response of an asphalt mixture under a fracture test (Figure 5.19). The fracture energy density limit (FE_f) is determined as the area under the stress–strain curve, while the dissipated creep strain energy density limit ($DCSE_f$) is the fracture energy density limit minus the elastic energy (EE) at the time of fracture. A predicted or measured modulus, e.g., resilient modulus (M_R), and tensile strength (S_t) are used to define EE. It is important to point out that these two energy failure limits ($DCSE_f$ and FE_f) have been identified as fundamental material properties of asphalt mixtures, independent of mode of loading, rate of loading, and specimen geometry (Birgisson et al., 2007).

The lower energy threshold ($DCSE_f$) is selected as the failure criterion under repeated load applications (Figure 5.20a). When repeated stresses significantly below the tensile strength occur, cracking will eventually take place if the rate of damage

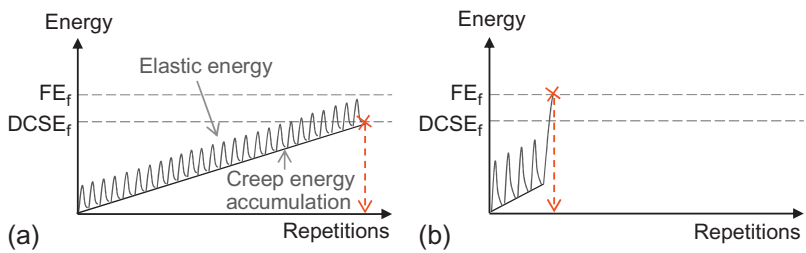


Figure 5.20 Potential failure modes under continuous loading: (a) repeated load applications and (b) single load excursion.

www.EngineeringEBooksPdf.com

accumulation exceeds the rate of healing during the loading period. In contrast, the upper energy threshold (FE_f) corresponds to the failure criterion under a single load excursion (Figure 5.20b). In this case, cracking will occur if any single load applied during the loading cycle exceeds the threshold required to fracture the mixture.

5.3.1.3 Rate of damage

One unique feature of the HMA-FM model is the consideration of both failure limit and rate of damage to predict fracture. The rate of damage of an asphalt mixture under repeated load applications is defined as the dissipated creep strain energy density accumulated per load cycle (DCSE/cycle). Therefore, there is an inherent assumption that damage can be quantified in terms of the viscous response (creep) of an asphalt mixture.

For a haversine load consisting of a 0.1-s loading period followed by a 0.9-s rest period (Figure 5.21), which represents a moving wheel in the field, DCSE/cycle is defined as the integral of the stress $\sigma(t)$ multiplied by the creep strain rate $\dot{\varepsilon}_{cr}(t)$:

$$\text{DCSE/cycle} = \int_0^{0.1} \sigma(t) \cdot \dot{\varepsilon}_{cr}(t) \cdot dt = \int_0^{0.1} \underbrace{\sigma_{ave} \cdot \sin(10\pi t)}_{\sigma(t)} \cdot \underbrace{\dot{\varepsilon}_{cr,max} \cdot \sin(10\pi t)}_{\dot{\varepsilon}_{cr}(t)} \cdot dt \tag{5.2}$$

where σ_{ave} represents the average peak stress in the zone of interest, and $\dot{\varepsilon}_{cr,max}$ is the maximum creep strain rate, which occurs at the peak stress. Note that according to the definition of viscosity (viscosity = stress/strain rate), creep strain rate follows the same sinusoidal function of the applied stress.

The maximum creep strain rate for a haversine load can be estimated from a creep test based on the relationship between strain $\varepsilon(t)$ and compliance $D(t)$:

$$\varepsilon(t) = \sigma \cdot D(t) \tag{5.3}$$

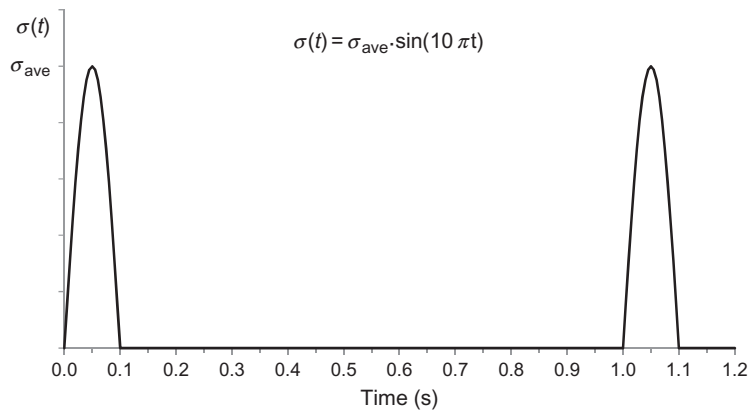


Figure 5.21 Haversine load representing a moving wheel in the field.

www.EngineeringEBooksPdf.com

A convenient way to express the compliance curve obtained from a creep test is the use of a power law fitting function (Equation 5.4). Note that D_0, D_1, and m are simply fitting parameters (they do not necessarily have a physical meaning):

$$D(t) = D_0 + D_1 \cdot (t)^m \tag{5.4}$$

Compliance rate $\dot{D}(t)$ can be derived from Equation (5.4):

$$\dot{D}(t) = \frac{dD(t)}{dt} = \frac{d}{dt}[D_0 + D_1 \cdot (t)^m] = m \cdot D_1 \cdot (t)^{m-1} \tag{5.5}$$

Typically, a 1000-s creep test has been considered to be enough to isolate the viscous response of asphalt mixture for intermediate temperatures associated with fatigue cracking ($0-25$ °C). Therefore, maximum creep strain rate can be estimated from compliance rate at $t = 1000$ s:

$$\dot{\varepsilon}_{\text{cr,max}} \approx \sigma_{\text{ave}} \cdot \dot{D}(t)\big|\text{t} = 1000\text{s} = \sigma_{\text{ave}} \cdot m \cdot D_1 \cdot (1000)^{m-1} \tag{5.6}$$

Substituting Equation (5.6) into Equation (5.2) and solving the integral in time for the sinusoidal function, the rate of damage (DCSE/cycle) is finally obtained:

$$\text{DCSE/cycle} = \frac{1}{20} \cdot (\sigma_{\text{ave}})^2 \cdot m \cdot D_1 \cdot (1000)^{m-1} \tag{5.7}$$

It should be pointed out that healing, which can be described in terms of recovered DCSE per cycle (Kim and Roque, 2006), should be determined and used to adjust the rate of damage.

5.3.1.4 Material parameters

Table 5.3 summarizes the material parameters considered in the model. All these parameters can be accurately determined using Superpave IDT tests, following the procedure described by Roque and Buttlar (1992), Buttlar and Roque (1994), and Kim and Roque (2006).

Not only can these parameters be used to predict damage and crack growth in mixtures subjected to generalized loading conditions, but they are also suitable for use in mixture design and optimization. For example, it is clear that fracture tolerance improves as the DCSE_f limit increases. Similarly, a lower creep rate, which is a function of D_1 and m-value, will result in a lower rate of damage accumulation. However, lower rate of damage does not necessarily ensure improved cracking performance, because failure limit and healing rate are also involved in the cracking mechanism.

5.3.2 Crack growth law

The HMA-FM model considers a stepwise discontinuous crack growth law, as shown in Figure 5.22. When DCSE accumulated in the zone with the highest average tensile stress equals the DCSE_f limit of the mixture, a crack initiates. After a damage

www.EngineeringEBooksPdf.com

Table 5.3 Asphalt mixture parameters considered in the HMA-FM model

Test	Temperature	Parameters	Application
Fracture	10 °C[a]	Fracture energy density (FE_f)	Failure limit
		Dissipated creep strain energy density ($DCSE_f$)	Failure limit
		Tensile strength (S_t)	Failure limit and Stress distribution
Resilient modulus test	10 °C[a]	Resilient modulus (M_R)	Failure limit
Creep test	10 °C[a]	Creep compliance rate: m, D_0, D_1	Rate of damage
Healing test	20 °C	Healing rate (h)	Rate of damage

[a]A temperature of 10 °C was found to be representative of the intermediate service temperatures associated with conditions that are conducive to cracking of asphalt mixtures in the field (Roque et al., 2004).

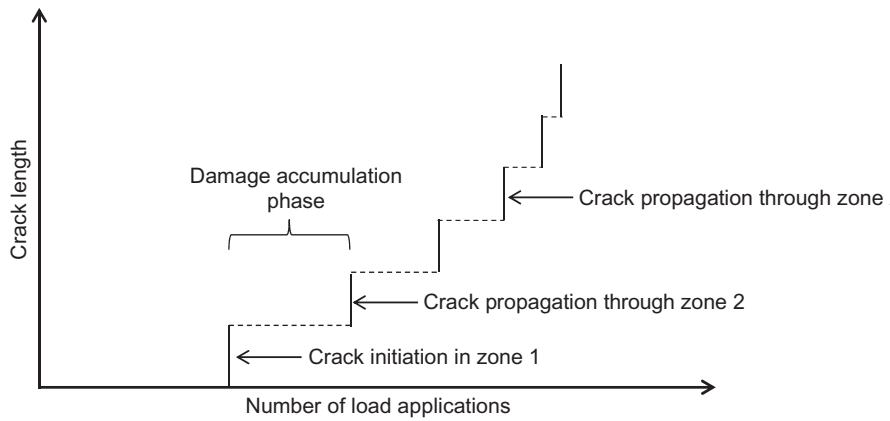


Figure 5.22 Stepwise discontinuous crack growth law used in HMA-FM model.

accumulation phase, the crack will propagate through the contiguous zone when the DCSE accumulated in that zone equals the $DCSE_f$ limit of the mixture, and so on. Note that the model keeps track of the DCSE induced in all zones where crack growth may be of interest, every step of the way.

The basic analysis framework of the model can be summarized as follows:

1. Divide potential crack path(s) into zones. Previous analysis showed that zone size had little effect on the predicted rate of crack propagation (Sangpetngam, 2003), so zones of fixed size are considered appropriate for the analysis. Typically, a zone size of 5 mm is used, which

www.EngineeringEBooksPdf.com

is assumed to capture the effect of stress concentration near the contact points between aggregates within the asphalt mixture.

2. Determine the stress distribution and compute the average tensile stress in each zone i during condition 1, $(\sigma_{ave})_{i,1}$.
3. Calculate the rate of damage in each zone for condition 1, $(DCSE/cycle)_{i,1}$, according to Equation (5.7) and the average tensile stresses calculated in step 2.
4. Compute the number of cycles for crack initiation in zone 1, $N_{f,1}$:

$$N_{f,1}(\text{initiation}) = \frac{DCSE_f}{(DCSE/cycle)_{1,1}} \tag{5.8}$$

in which $DCSE_f$ is the failure limit of the asphalt mixture and $(DCSE/cycle)_{1,1}$ is the rate of damage for zone 1 during condition 1.

5. Determine the new stress distribution as a result of crack growth. Once the crack initiates, the stress distribution ahead of the crack tip $\sigma(r)$ can be estimated as:

$$\sigma(r) = \sigma_{FA}\frac{a+r}{\sqrt{r}\cdot\sqrt{2a+r}} \tag{5.9}$$

where r is the distance measured from the crack tip, a is half the crack length, and σ_{FA} represents the faraway stress. As shown in Figure 5.23, tensile stress has an upper bound equal to the tensile strength of the asphalt mixture (S_t) and a lower bound equal to the faraway stress (σ_{FA}).

6. Compute the average tensile stress in each zone during condition 2, $(\sigma_{ave})_{i,2}$.
7. Calculate the rate of damage in each zone for condition 2, $(DCSE/cycle)_{i,2}$, according to Equation (5.7), and $(\sigma_{ave})_{i,2}$ obtained in step 6.
8. Compute the number of cycles for crack propagation through zone 2, $N_{f,2}$:

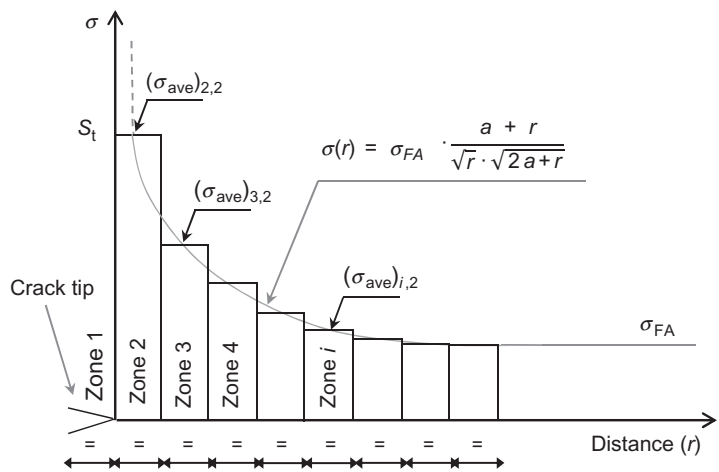


Figure 5.23 Stress distribution ahead of the crack tip after crack initiation (condition 2). *Note:* "a" is half the crack length.

www.EngineeringEBooksPdf.com

$$N_{f,2}(\text{propagation}) = \frac{\text{DCSE}_f - \overbrace{(\text{DCSE/cycle})_{2,1} \cdot N_{f,1}}^{\text{Accumulated from previous condition}}}{(\text{DCSE/cycle})_{2,2}} \tag{5.10}$$

where $(\text{DCSE/cycle})_{2,1}$ is the rate of damage for zone 2 during condition 1, $(\text{DCSE/cycle})_{2,2}$ is the rate of damage for zone 2 during condition 2, and $N_{f,1}$ is the number of cycles to fail zone 1.

9. Repeat steps 5 through 8 to determine crack propagation through contiguous zones. Note that the fracture energy density limit (FE_f) also has to be checked for every condition.

It should be pointed out that crack propagation predicted by the model (crack length vs. number of load repetitions) agreed closely with crack growth measured in laboratory tests (Zhang, 2000; Zhang et al., 2001b; Roque et al., 2002). These results support that the HMA-FM model appears to rationally and reliably predict cracking performance of asphalt mixtures.

5.3.3 Energy-based parameter to evaluate cracking performance

A detailed analysis and evaluation of 22 field test sections throughout the state of Florida resulted in the development and verification of energy-based criteria for cracking evaluation in asphalt mixtures (Roque et al., 2004). The work clearly indicated that there is no single mixture property or characteristic (volumetrics, viscosity of recovered binder, resilient modulus, tensile strength, creep compliance, etc.) that can reliably predict cracking performance of asphalt mixtures. A parameter named energy ratio (ER), which was derived using the HMA-FM model, was determined to accurately distinguish between pavements that exhibited cracking and those that did not, except for mixtures with excessively low or unusually high dissipated creep strain energy thresholds.

The ER is defined as the dissipated creep strain energy density limit of the mixture ($DCSE_f$) divided by a minimum dissipated creep strain energy ($DCSE_{min}$) for satisfactory performance:

$$ER = \frac{\text{DCSE}_f}{\text{DCSE}_{min}} = \frac{\text{DCSE}_f}{\frac{m^{2.98} \cdot D_1}{A}} \tag{5.11}$$

where m and D_1 are the creep compliance power-law fitting parameters and A is an empirical parameter that depends on the tensile stress in the pavement section (σ_t) and the tensile strength of the mixture (S_t). For σ_t and S_t expressed in MPa, and D_1 in GPa^{-1} A can be calculated as:

$$A = 8.64 \cdot 10^{-4} \cdot \frac{(6.36 - S_t)}{\sigma_t^{3.1}} + 3.57 \cdot 10^{-3} \tag{5.12}$$

The ER accounts for the effects of pavement structural characteristics (σ_t) and material properties ($DCSE_f$, S_t, m, D_1) on cracking performance: the higher the value of the

www.EngineeringEBooksPdf.com

ER, the better the expected cracking performance of the section. Therefore, ER can be used to integrate asphalt mixture properties in the pavement design process as well as to predict the performance of in-service pavement sections.

It is important to note that mixture properties for determination of ER should be obtained from mixtures conditioned to simulate field-aged materials. Roque et al. (2012) have determined that oxidative aging using the long-term oven aging (LTOA) procedure alone does not satisfactorily simulate long-term field aging as reflected by mixture failure limits. This work showed that cyclic pore pressure conditioning (CPPC) of mixtures is required after LTOA to more properly simulate field aging. In addition, ER should not be used to evaluate brittle mixtures as reflected by a fracture energy density limit lower than 0.75 kJ/m^3 (Roque et al., 2004).

5.4 Top-down cracking (TDC) performance model based on the critical condition approach

5.4.1 General framework

The HMA-FM-based enhanced cracking performance model (HMA-FM-E) developed as part of NCHRP Project 01-42A (Roque et al., 2010) was the result of continuous multiyear efforts of the University of Florida Pavement Research Group (Zhang et al., 2001b; Roque et al., 2002, 2004; Myers and Roque, 2002; Sangpetngam et al., 2004; Kim and Roque, 2006; Wang et al., 2007; Kim et al., 2008). The enhanced model maintained fundamental elements of the HMA-FM system. Major enhancements included the development and introduction of submodels that account for two key factors: aging and healing, which are shown to have significant influence on TDC performance (Zou et al., 2012).

As shown in the general model framework presented in Figure 5.24, the HMA-FM-E has four major components: (1) the mixture property submodels to account

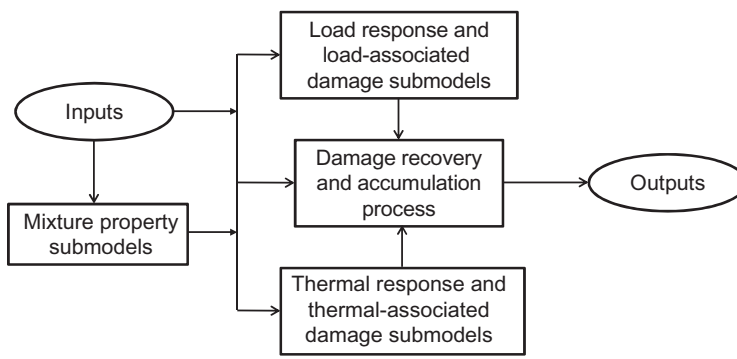


Figure 5.24 General framework of the hot mix asphalt-fracture mechanics enhanced cracking performance (HMA-FM-E) model.

www.EngineeringEBooksPdf.com

for changes in damage, fracture, and healing properties of the mixture due to oxidative aging, including aging submodels for asphalt concrete (AC) stiffness, tensile strength, and fracture energy density limit, as well as a healing submodel; (2) the load response and load-associated damage submodels to predict load-induced damage; (3) the thermal response and thermal-associated damage submodels to predict thermally induced damage; and (4) the damage recovery and accumulation process to accumulate damage after taking healing effects into account. Once the accumulated damage reaches an energy-based threshold, a crack will initiate or propagate. Details for these major components can be found in Zou and Roque (2011). The HMA-FM-E is capable of predicting the entire process of TDC, from the onset of cracking until pavement failure. Example simulations will be presented in Section 5.4.3 to illustrate the full capability of the enhanced performance model.

5.4.2 Model calibration and validation

The HMA-FM-E was calibrated and validated using data from Florida field sections (Zou and Roque, 2014). The model calibration process involved three phases: (1) field evaluation, which helped determine cracking performance of field sections and finalize the coring plan; (2) laboratory testing on field cores, which provided mixture properties for use in performance prediction utilizing the enhanced model; and (3) model calibration, which determined the calibration factor in the model by matching as closely as possible TDC predictions with observed cracking performance in the field.

For the calibration and validation efforts, 10 field sections were selected. These were composed of interstate highways and state roads covering a broad range of mixtures, traffic levels, and pavement structures, as shown in Table 5.4. Also presented in the table is cracking performance, including status of cracking at the time of field evaluation and crack initiation times, based on the following two sources:

- Crack rating data collected and maintained by the Florida Department of Transportation (FDOT) during its annually conducted pavement condition survey (PCS) (FDOT, 2009).
- Results of an independent visual inspection of all pavement sections conducted by the UF research team in 2003 to obtain information on pavement condition and identify specific distress patterns.

Model calibration was completed to determine the aging parameter k_1 (the only calibration factor of the performance model) by matching as closely as possible predicted with observed TDC performance in the field, that is, crack initiation time in this study. Parameter k_1 had a strong effect on fracture energy density limit FE_f over time, as shown in Equation (5.13):

$$FE_f(t) = FE_i - (FE_i - FE_{min})[S_n(t)]^{k_1} \tag{5.13}$$

where FE_i is the initial fracture energy density of the AC, FE_{min} is the minimum value of the FE after a sufficiently long aging period, and $S_n(t)$ is the normalized change in stiffness at the surface of the AC layer (Roque et al., 2010). It was found that the value of 3, among all eight k_1 values from 0.5 to 5 evaluated in the study, resulted in the best

www.EngineeringEBooksPdf.com

Table 5.4 Field sections with traffic information and cracking performance

Section ID	Section name	County	Traffic/year (kESALs)	Age (year)	Cracking performance	
					Status	t_i (year)
1	I-75 S1A	Charlotte	573	15	C	10
2	I-75 S1B	Charlotte	558	14	C	12
3	I-75 S3	Lee	674	15	C	11
4	I-75 S2	Lee	576	14	U	17
6	SR-80 S2	Lee	207	19	U	22
7	I-10 S1A	Suwannee	392	7	C	<7
8	I-10 S1B	Suwannee	392	7	U	8
9	SR-471	Sumter	26	3	C	2
10	SR-19	Lake	51	3	C	1
11	SR-997	Dade	89	40	C	38

kESALs denotes thousands of ESALs, C denotes cracked status, and U denotes uncracked status.

match between the predicted and observed crack initiation times, as indicated by the highest R^2 value of 0.933.

The prediction sum of squares (PRESS) method (Lytton et al., 1993) was used to conduct model validation. In the PRESS procedure, $n-1$ out of all n data sets/sections ($n=10$) were used at each time to determine the aging parameter k_1 (i.e., a new model was calibrated with nine sections at each time), and then one independent prediction was made for the remaining section using the calibrated model. The model calibration and subsequent independent prediction were conducted 10 times following the same procedure. Figure 5.25 presents the comparison between independent predictions using PRESS and the observations, where the PRESS R^2 was determined to be 0.932, indicating the strong predictive capability of the full model.

5.4.3 Example simulations

Example simulations of TDC in two pavement sections (namely P1 and P2) are presented to illustrate the full capability of the enhanced cracking performance model.

5.4.3.1 Input module

The inputs required for the HMA-FM-E included five categories: pavement structure, modulus of unbound materials and AC, fracture and healing property of AC, temperature of AC, and traffic. Details regarding input data for each category are described as follows:

www.EngineeringEBooksPdf.com

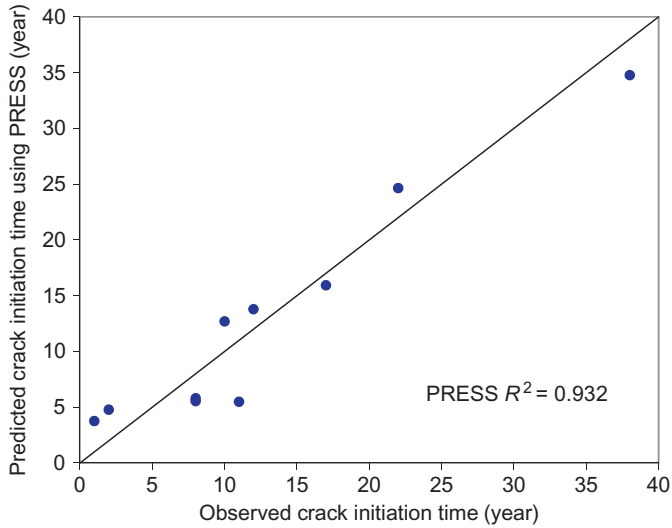


Figure 5.25 Predicted crack initiation time using prediction sum of squares (PRESS) procedure versus observed crack initiation time.

Table 5.5 Pavement structure, material properties, and traffic data used for example simulation

Section ID	Layer thickness (cm)		Layer modulus (MPa)		Traffic/ year (kESALs)
	AC	Base/subbase	Base/subbase	Subgrade	
1	18.9	55.0	348.3	355.3	480
2	18.8	56.7	591.2	280.6	1040

- Pavement structure: a three-layer pavement structure was selected for the simulations (Table 5.5). Thicknesses for AC and unbound base were obtained from design information.
- Modulus of unbound materials: base and subgrade moduli were determined based on back-calculation from falling weight deflectometer (FWD) tests conducted at the time of field evaluation (Table 5.5).
- Modulus of AC: the variation of AC modulus due to aging was predicted using the AC stiffness aging submodel, which requires gradation, binder type, and volumetric properties, as provided in Table 5.6.
- AC fracture and healing properties: variations of AC fracture property and healing potential over time/age were predicted using the FE limit aging submodel and the healing submodel. As shown in Table 5.7, these two submodels require the following properties measured on field cores using Superpave IDT tests (Roque et al., 1997): resilient modulus (M_R), tensile strength (S_t), fracture energy density limit (FE_f), creep compliance at 1000 s

www.EngineeringEBooksPdf.com

Table 5.6 Mixture gradation and volumetric properties used as input for AC stiffness aging submodel

Section ID	Percent passing by weight				V_{beff} (%)	V_a (%)	MAAT (°C)
	19 (mm)	9.5 (mm)	4.75 (mm)	0.075 (mm)			
1	100.0	99.0	64.0	5.1	10.1	5.4	20.6
2	100.0	89.0	45.0	4.9	10.0	4.2	20.0

V_{beff} is effective binder content (percent by volume), V_a is percent air voids, and MAAT denotes mean annual air temperature.

Table 5.7 Mixture fracture and damage properties used as input for the fracture energy limit aging submodel and healing submodel

Section ID	Age of cores (year)	$T = 10$ °C				$T = 20$ °C	Master curve	
		M_R (GPa)	S_t (MPa)	FE_f (kJ/m^3)	D_{1000} (1/GPa)	D_{1000} (1/GPa)	m	D_1 (1/GPa)
1	11	12.93	2.38	1.90	1.618	3.906	0.564	0.042
2	11	8.16	1.76	2.97	4.515	19.059	0.720	0.045

M_R is resilient modulus, S_t is tensile strength, FE_f is fracture energy density limit, D_{1000} denotes creep compliance at 1000 s, and m and D_1 are power-law fitting parameters determined for the creep compliance master curve.

(D_{1000}), and m and D_1 power-law fitting parameters determined for the creep compliance master curve (Buttlar et al., 1998).

- AC temperature: a nonfreeze climate in Melrose, Florida, was selected for the simulations. Based on the climatic condition and typical pavement material and structural properties of this area, hourly temperature variations at different depths in the AC layers were obtained using the enhanced integrated climatic model (Larson and Dempsey, 2003).
- Traffic: traffic data obtained for the year of field evaluation were used in the simulations (Table 5.5).

5.4.3.2 Predicted results

Predicted cracking performance was presented in terms of normalized crack amount (CA/CA_{max}) versus time, where CA denotes crack amount and CA_{max} is the maximum level of cracking considered to be pavement failure (Roque et al., 2010). Figure 5.26 shows the predicted cracking performance for pavement sections P1 and P2.

As can be seen, the crack amount increased over time in a stepwise discontinuous manner for both sections. The moment of the first increase in crack amount (i.e., the first step) corresponds to the onset of cracking, and the slope of the straight line connecting the point for onset of cracking and the point for maximum crack amount represent the overall rate of crack growth. It can be seen that P1 was predicted to have better performance than

www.EngineeringEBooksPdf.com

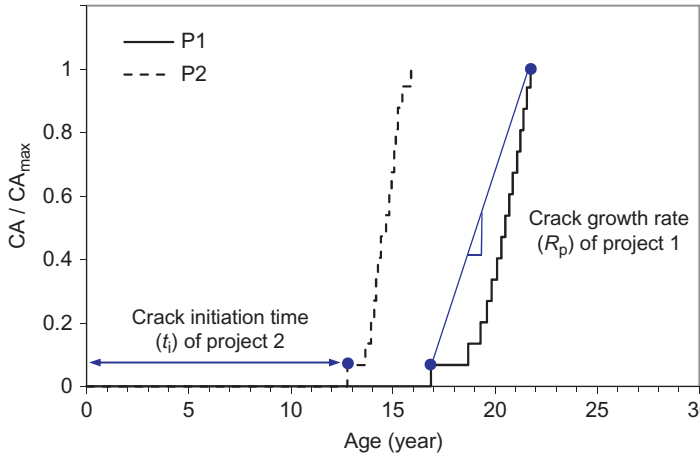


Figure 5.26 Predicted cracking performance for sections P1 and P2 using HMA-FM-E.

P2, in terms of both a longer time to crack initiation (16.9 vs. 12.8 years) and a slower rate of crack growth per year (0.2 vs. 0.3). It is important to note that the predicted crack initiation times were consistent with field observations, which were 16 and 10 years for sections P1 and P2, respectively. This example simulation showed that the performance model developed based on the critical condition approach appears to have excellent potential for accurately predicting TDC in field sections.

5.5 Summary and conclusions

A thorough comparison of the traditional fatigue approach and the critical condition approach was conducted to determine which is more representative of cracking mechanisms in asphalt pavement. This was accomplished by examining whether observations made were consistent with fundamental assumptions of the two approaches. Results of recent experiments, advanced modeling efforts, and field performance evaluation appeared to support that cracking is a stepwise discontinuous process in that only critical conditions result in crack initiation or propagation. Therefore, it appears that the critical condition approach most accurately represents the actual mechanisms of pavement cracking. Key findings are summarized below:

- Observations from laboratory experiments showed that most damage induced in pavements is healable; permanent damage and cracking occur only when critical conditions are reached, that is, when the energy threshold and healing potential of a mixture are diminished due to aging and the induced damage is sufficient to exceed the threshold.
- Observations from advanced modeling showed that changes in pavement condition (e.g., stiffness gradients due to aging, damage zones due to loads, stress concentrations/intensities) result in critical stresses that are likely to induce damage exceeding the mixture energy threshold. Clearly, there is a need to consider critical conditions other than those typically assumed for the traditional fatigue approach.

www.EngineeringEBooksPdf.com

- Evaluation of field performance revealed that cracking is typically not observed until pavement is in service for several years, and once it initiates, more rapid accumulation of permanent damage leads to pavement failure in less time than is required for crack initiation.

Implementation of the critical condition approach was illustrated using the HMA-FM model developed at the University of Florida to predict initiation and propagation of cracks in asphalt mixtures. The model accounts for microdamage, healing, and macrodamage (cracking) for specified loading conditions, temperatures, and rest periods. A TDC performance prediction model developed based on HMA-FM was used to show the full potential of the critical condition approach.

In conclusion, a paradigm shift from the traditional fatigue approach to the critical condition approach should be seriously considered for pavement cracking analysis and design. This should result in less "black box" effect (i.e., enhanced understanding of mechanisms), reduced number of calculations, and more accurate predictions.

5.6 Future research

The critical condition approach implies that changes in mixture properties throughout the life of the pavement that make the mixture stiffer, more brittle, and less able to heal are a dominant player for accurately predicting pavement cracking. There are two major challenges regarding successful implementation of the critical condition approach. One is accurately addressing and simulating, in both experimental and advanced modeling efforts, the changes in mixture properties over time due to aging, including damage properties, failure limits, and healing potential. Most efforts to date have focused on the development of relationships for simulating the effect of oxidation on mixture stiffness. There is a clear need for a better understanding of all aspects of aging in order to further improve our ability to predict changes in key material properties. The other challenge is to clearly identify and validate critical design conditions for various types of cracking distress.

References

Asphalt Institute, 1982. Research and Development of the Asphalt Institute's Thickness Design Manual (MS-1), ninth ed., Asphalt Institute, College Park.

Birgisson, B., Montepara, A., Romeo, E., Roque, R., Roncella, R., Tebaldi, G., 2007. Determination of fundamental tensile failure limits of mixtures. J. Assoc. Asphalt Paving Technol. 76, 303–344.

Buttlar, W.G., Roque, R., 1994. Development and evaluation of the Strategic Highway Research Program measurement and analysis system for indirect tensile testing at low temperatures. Transport. Res. Rec. 1454, 163–171.

Buttlar, W.G., Roque, R., Reid, B., 1998. Automated procedure for generation of creep compliance master curve for asphalt mixtures. Transport. Res. Rec. 1630, 28–36.

Carpenter, S.H., Ghuzlan, K.A., Shen, S., 2003. Fatigue endurance limit for highway and airport pavements. Transport. Res. Rec. 1832, 131–138.

www.EngineeringEBooksPdf.com

Daniel, J.S., Kim, Y.R., 2001. Laboratory evaluation of fatigue damage and healing of asphalt mixtures. J. Mater. Civil Eng. 13 (6), 434–440.

Daniel, J.S., Kim, Y.R., 2002. Development of a simplified fatigue test and analysis procedure using a viscoelastic continuum damage model. J. Assoc. Asphalt Paving Technol. 71, 619–650.

Di Benedetto, H., Heifar, M., Sauzeat, C., Olard, F., 2007. Three-dimensional thermo-viscoplastic behavior of bituminous materials: the DBN model. Int. J. Road Mat. Pavement Design 8 (2), 258–316.

Florida Department of Transportation (FDOT), 2009. Flexible Pavement Condition Survey Handbook. FDOT, Tallahassee.

Kim, Y.R., Little, D.N., 1989. Evaluation of healing in asphalt concrete by means of the theory of nonlinear viscoelasticity. Transport. Res. Rec. 1228, 198–210.

Kim, B., Roque, R., 2006. Evaluation of healing property of asphalt mixtures. Transport. Res. Rec. 1970, 84–91.

Kim, J., Roque, R., Birgisson, B., 2008. Integration of thermal fracture in the HMA fracture model. J. Assoc. Asphalt Paving Technol. 77, 631–662.

Larson, G., Dempsey, B., 2003. Enhanced Integrated Climatic Model: User's Guide Version 3.0. Applied Research Associates-ERES Division, Champaign.

Little, D.N., Prapnnachari, S., 1991. Investigation of the Microstructural Mechanisms of Relaxation and Fracture Healing in Asphalt: Annual Report to the Air Force Office of Scientific Research. Texas A&M University, College Station.

Little, D.N., Kim, Y.R., Benson, F.C., 1987. Investigation of the Mechanism of Healing in Asphalt: Report to the National Science Foundation. Texas A&M University, College Station.

Little, D.N., Lytton, R.L., Williams, D., Chen, C.W., Kim, Y.R., 1997. Healing of Microdamage in Asphalt and Asphalt Concrete: Draft Final Report Project 7229. Texas A&M University, College Station.

Lundstrom, R., Di Benedetto, H., Isacsson, U., 2004. Influence of asphalt mixture stiffness of fatigue failure. J. Mater. Civil Eng. 613 (6), 516–525.

Lytton, R.L., Uzan, J., Fernando, E.G., Roque, R., Hiltunen, D., Stoffels, S.M., 1993. Development and Validation of Performance Prediction Models and Specifications for Asphalt Binders and Paving Mixes: SHRP-A-357. Strategic Highway Research Program, National Research Council, Washington, DC.

Miner, M.A., 1945. Cumulative damage in fatigue. Trans. Am. Soc. Mech. Eng. 67, A159–A164.

Molenaar, A.A.A., 2004. Bottom-up fatigue cracking: myth or reality? In: Petit, C., Al-Qadi, I.L., Millien, A. (Eds.), Proceedings of the 5th International RILEM Conference. Cracking in Pavements: Mitigation, Risk Assessment and Prevention. RILEM Publications SARL, Limoges, pp. 275–282.

Mun, S., Guddati, M.N., Kim, Y.R., 2004. Fatigue cracking mechanisms in asphalt pavements with viscoelastic continuum damage finite element program. Transport. Res. Rec. 1896, 96–106.

Myers, L.A., Roque, R., 2002. Top-down crack propagation in bituminous pavements and implications for pavement management. J. Assoc. Asphalt Paving Technol. 71, 651–670.

Myers, L.A., Roque, R., Ruth, B., Drakos, C., 1999. Measurement of contact stresses for different truck tire types to evaluate their influence on near-surface cracking and rutting. Transport. Res. Rec. 1655, 175–184.

Powell, W.D., Potter, J.F., Mayhew, H.C., Nunn, N.E., 1984. The Structural Design of Bituminous Roads: TRRL Laboratory Report 1132. Transport and Road Research Laboratory, Crowthorne.

www.EngineeringEBooksPdf.com

Roque, R., Buttlar, W.G., 1992. The development of a measurement and analysis system to accurately determine asphalt concrete properties using the indirect tensile mode. J. Assoc. Asphalt Paving Technol. 61, 304–332.

Roque, R., Buttlar, W.G., Ruth, B.E., Tia, M., Dickson, S.W., Reid, B., 1997. Evaluation of SHRP Indirect Tension Tester to Mitigate Cracking in Asphalt Pavements and Overlays: Final Report of Florida Department of Transportation. University of Florida, Gainesville.

Roque, R., Birgisson, B., Sangpetngam, B., Zhang, Z., 2002. Hot mix asphalt fracture mechanics: a fundamental crack growth law for asphalt mixtures. J. Assoc. Asphalt Paving Technol. 71, 816–827.

Roque, R., Birgisson, B., Drakos, C., Dietrich, B., 2004. Development and field evaluation of energy-based criteria for top-down cracking performance of hot mix asphalt. J. Assoc. Asphalt Paving Technol. 73, 229–260.

Roque, R., Zou, J., Kim, Y.R., Beak, C., Thirunavukkarasu, S., Underwood, B.S., and Guddati, M. N., 2010. Top-down cracking of HMA layers: models for initiation and propagation, NCHRP Web-Only Document 162, National Cooperative Highway Research Program, Transportation Research Board of the National Academies. Available from: onlinepubs.trb.org/onlinepubs/nchrp/nchrp_w162.pdf (accessed September 2013).

Roque, R., Isola, M., Chun, S., Zou, J., Koh, C., Lopp, G., 2012. Effects of Laboratory Heating, Cyclic Pore Pressure, and Cyclic Loading on Fracture Properties of Asphalt Mixture: Final Report of the Florida Department of Transportation. University of Florida, Gainesville.

Sangpetngam, B., 2003. Development and evaluation of a viscoelastic boundary element method to predict asphalt pavement cracking. PhD dissertation. University of Florida, Gainesville.

Sangpetngam, B., Birgisson, B., Roque, R., 2004. Multilayer boundary-element method for evaluating top-down cracking in hot-mix asphalt pavements. Transport. Res. Rec. 1896, 129–137.

Shell, 1978. Shell Pavement Design Manual: Asphalt Pavements and Overlays for Road Traffic. Shell International Petroleum, London.

Verstraeten, J., Romain, J.E., Veverka, V., 1977. The Belgian Road Research Center's overall approach to asphalt pavement structural design. In: Proceedings of the Fourth International Conference on Structural Design of Asphalt Pavements, Ann Arbor, vol. 1. pp. 298–324.

Wang, J., Birgisson, B., Roque, R., 2007. Development of a Windows-based top-down cracking design tool for Florida based on the energy ratio concept. Transport. Res. Rec. 2037, 86–96.

Zhang, Z., 2000. Identification of suitable crack growth law for asphalt mixtures using the Superpave indirect tensile test (IDT). PhD dissertation. University of Florida, Gainesville.

Zhang, Z., Roque, R., Birgisson, B., 2001a. Evaluation of laboratory measured crack growth rate for asphalt mixtures. Transport. Res. Rec. 1767, 67–75.

Zhang, Z., Roque, R., Birgisson, B., Sangpetngam, B., 2001b. Identification and verification of a suitable crack growth law. J. Assoc. Asphalt Paving Technol. 70, 206–241.

Zou, J., Roque, R., 2011. Top-down cracking: enhanced performance model and improved understanding of mechanisms. J. Assoc. Asphalt Paving Technol. 80, 255–287.

Zou, J., Roque, R., 2014. Calibration and validation of an HMA fracture mechanics based enhanced cracking performance model. Int. J. Pavement Res. Technol. 7 (2), 93–100.

Zou, J., Roque, R., Byron, T., 2012. Effect of HMA aging and potential healing on top-down cracking using HVS. Int. J. Road Mat. Pavement Design 13 (3), 518–533.

www.EngineeringEBooksPdf.com

Deformation mechanisms of bituminous materials

6

D. Cebon, C.Y. Cheung
University of Cambridge, Cambridge, UK

6.1 Introduction

Pure bitumens are complex polymeric materials. They have been employed for years in the construction of flexible pavements. It is well known that the composition of pure bitumens has primary influence on their mechanical behavior, which is in turn very sensitive to stress, strain rate, and temperature. This chapter describes a framework by which the mechanical behavior of pure bitumens can be understood, in terms of simplified deformation models, over a wide range of stresses, strain rates, and temperatures.

6.1.1 The composition of pure bitumens

Given below is a brief review of the previous research on the composition of pure bitumens from which a simplified picture regarding their molecular structure will be established.

6.1.1.1 The molecular structure of pure bitumens

Prior to 1960, the molecular composition of pure bitumens was defined by the different fractions obtained by various fractionation schemes. One of the most popular schemes separated the fractions by polarity into asphaltenes, resins, aromatics, and saturates (see chemical definitions by Petersen, 1984). The resins, aromatics, and saturates were collectively called maltenes. The main characteristics of these fractions are discussed by Whiteoak et al. (2003). Subsequent research using more sophisticated analytical tools has revealed certain aspects of the chemistry of bitumens in greater depth. Some of the results that have strong implications on the mechanical behavior of pure bitumens will be reviewed in the following sections.

Glass transition of pure bitumens

The observation of the glass transition phenomenon and the measurement of the glass transition temperature T_g for pure bitumens began in the early 1960s. The main driving force behind the research efforts was the publication of the Williams–Landel–Ferry (WLF) equation (Williams et al., 1955) in 1955 and its subsequent success and wide acceptance in describing the flow behavior of a wide range of liquids above their glass transition temperatures. Volume dilatometry was commonly employed for measuring

Advances in Asphalt Materials. http://dx.doi.org/10.1016/B978-0-08-100269-8.00006-4
© 2015 Elsevier Ltd. All rights reserved.

www.EngineeringEBooksPdf.com

glass transition (Wada and Hirose, 1960; Schmidt and Santucci, 1966; Schweyer, 1974) by which a 50% increase in the thermal expansion coefficient was observed when the bitumens changed from glassy to liquid state. In later years, volume dilatometry was gradually replaced by differential thermal analysis (DTA) (Schmidt and Barrall, 1965), and subsequently by differential scanning calorimetry (DSC), in which the thermal response to a controlled heating or cooling program is measured (Noel and Corbett, 1970; Huynh et al., 1978; Claudy et al., 1991).

The research established that the usual range of T_g for bitumens is −40 to 0 °C. The value of T_g was shown to increase with increasing asphaltene content for bitumens derived from the same source (Wada and Hirose, 1960; Hirose et al., 1963; Schmidt and Barrall, 1965). Moreover, by DSC analysis of the various fractions of the bitumen, it was found that the glass transition of the overall bitumen can be attributed entirely to the transition of the aromatics and saturates (Noel and Corbett, 1970; Claudy et al., 1991). While the asphaltenes and the resins display no thermal effects within the commonly employed temperature ranges, their quantities and interactions with the other fractions can have strong effects on the glass transition of the overall bitumen (Noel and Corbett, 1970; Claudy et al., 1991). It is the composition of a given bitumen fraction that controls the value of T_g for that particular fraction, and not its molecular weight (Huynh et al., 1978). In addition, the value of T_g was found to be sensitive to pressure (Schweyer, 1974).

Due to limited success in correlating flow behavior to glass transition temperature, however, the measurement of T_g has never been employed for specification of pure bitumens.

Thermal behavior of pure bitumens

More recent emphasis of DSC measurements has shifted to broader investigations of the thermal behavior of pure bitumens. In addition to the increase in heat capacity upon heating, corresponding to the glass transition of the hydrocarbon matrix at low temperatures, a number of endothermal effects have been observed at higher temperatures. These are due to the dissolution of crystallized molecules present in the saturates (Claudy et al., 1991). In fact, the crystallizable material as measured by DSC was found to be different from the wax contents as measured by precipitation (Noel and Corbett, 1970), and its quantification provided a consistent means of estimating the real weight percentage of the crystallized fractions, which was superior to the traditional precipitation method. Attempts to estimate the values of T_g for individual fractions from the molar glass transition values of their various functional groups and the value of T_g for the overall bitumen based on the T_g values of its fractions were also reported (Huynh et al., 1978).

Importance of asphaltenes

The proportion of asphaltenes present in any particular bitumen, or the asphaltene content (by mass), remains the most useful parameter for describing the compositional characteristics of the bitumen. The asphaltene content has been shown to be related to a number of physical parameters, such as glass transition temperature (Wada and Hirose, 1960; Schmidt and Barrall, 1965) and viscosity (Mack, 1932;

www.EngineeringEBooksPdf.com

Altegelt and Harle, 1975). It also reflects the compositional changes that occur in a number of physical processes, such as aging of bitumens (Petersen, 1984).

It is well established in the literature that the state of the association and the peptization of asphaltenes is one of the most important factors in determining the different properties of various bitumens. As early as 1932, Mack (1932) analyzed solutions of various proportions of asphaltenes in maltenes at various temperatures, employing a number of hypotheses for describing the physical chemistry of these bituminous solutions. He concluded that the significant increase in viscosity with asphaltene content is more likely the result of association of the solute rather than a result of solvation. Winniford (1960, 1963) provided further evidence for the association of asphaltenes, even in diluted solution in good solvents. Because the state of aggregation of asphaltenes into clusters is reduced by agitation, the molecular weights of asphaltenes measured by methods involving "quiet" systems (e.g., ultracentrifuge) were significantly higher than those determined by agitated systems (e.g., viscosity) (Winniford, 1960, 1963).

Dickie and Yen (1967) subsequently summarized the results from various molecular weight studies of asphaltenes into a hypothesis regarding the molecular structure of bitumens in general. They proposed that the divergent results of molecular weight measurements could be explained by the fact that some measurements might correspond to the weight of the unit sheet, while others correspond to the weight of the stacked sheets or the micelle weight resulting from the association of two or more unit cells. More recently, Lian et al. (1994) suggested that an aggregate of asphaltene micelles with absorbed resins could form a supermicelle (10–20 nm), which in turn could coalesce into giant supermicelles (200–2000 nm) or flocs (~20 μm) and could even gradually grow into a liquid crystal (~0.1 mm). In addition to the quantity of asphaltenes and the extent of their aggregation, the chemical composition as well as the size (e.g., Winniford, 1960; Dickie and Yen, 1967; Reerink, 1973; Ferworn et al., 1993; Storm et al., 1993) and shape (e.g., Reerink, 1973; Ferworn et al., 1993; Storm et al., 1993) of the asphaltene particles were believed to be essential factors in determining the properties of the overall bitumen.

Significance of functional groups

The presence of certain functional groups in bitumens is known to have disproportionately large effects on various properties of the material (Petersen, 1984). Experimental methods for studying functional groups in bitumens include selective chemical reactions (Petersen, 1986), potentiometric titration (Nakajima and Tanobe, 1973), and infrared spectrometry (Brule et al., 1986; Petersen, 1986; Bukka et al., 1991, 1994). The benefits of functional group analysis were demonstrated by Bukka et al. (1991, 1994), who were able to show that the differences in viscosity among a number of bitumens were explained not by the asphaltene content, but by the amount of carboxylic acid present.

6.1.1.2 Compositional models for pure bitumens

In order to explain the mechanical behavior of pure bitumens in terms of their chemical composition, models describing the structural arrangement at the molecular level are required. Among the various efforts to summarize the wide range of observations

www.EngineeringEBooksPdf.com

into a molecular picture, the *colloidal* model remains the most successful. It was first proposed by Nellensteyn (1924), and then developed by Pfeiffer (1950) and refined by many other researchers. In its simplest form, the model suggests that pure bitumen is a colloidal system made up of a suspension of asphaltene micelles peptized by resins in an oily medium (Brule et al., 1986). Pfeiffer (1950) proposed three different models of colloidal structure: the solution SOL, the elastic SOL, and the gelatinous GEL. They used these models to explain the differences in the experimentally observed mechanical behavior of different types of bitumens.

Dickie and Yen (1967) proposed a more explicit picture, based on the colloidal model, for the molecular structure of the material. The picture consisted of various combinations of unit sheets of molecules to form particles, micelles, and clusters of micelles with different mechanisms of molecular interactions. Altegelt and Harle (1975) treated bitumens as a suspension of asphaltenes in maltenes as the solvent, and yet they considered the system to be a molecular solution rather than a suspension of small particles. Petersen (1984) stressed the importance of the molecular interaction of various components of bitumens with each other in order to form a balanced or compatible system. This approach to explaining the chemical and physical properties of bitumens by the sum total of the composition and interactions of their individual molecules is sometimes known as the Petersen model (Christensen and Anderson, 1992).

A direct challenge to the colloidal model and an explicit proposal of an alternative compositional model were reported by Anderson et al. (1991). Their model is called the dispersed polar fluid model, in which bitumen is pictured as a fluid consisting of a continuous distribution of molecules of varying size and polar functionality. The interactions among these molecules is due to van der Waals-type bonding, such as hydrogen bonding, pi–pi bonding, and polar–polar electrostatic interactions. This model emanated from the linear viscoelastic behavior observed in small-strain dynamic tests of the material. Its general acceptance as an alternative to the colloidal model is still to be established.

6.1.1.3 Summary of the current understanding

The current understanding of pure bitumen as a chemical compound can be summarized as follows. Bitumen is a complex polymeric system that can be characterized by:

(i) The properties of the asphaltenes, including physical properties such as quantities, sizes, and shapes, as well as chemical properties such as composition, presence of functional groups or heterocompounds, and reactivity. At the present time, only the quantity of asphaltenes can be quantified uniquely, provided that the solvent is specified. Understanding of the importance of the other elements is still limited.

(ii) The chemical nature of the maltenes. This includes a collection of characteristics that includes the peptizing power of the resins; the prominent functional groups present in the bitumen; the nature of the aromatics and saturates, which in turn determines the glass transition; the crystallization behavior of the bitumen; and the intrinsic properties of the oily medium in which the asphaltenes are dispersed. While understanding of individual elements varies, the overall quantification of the effects of individual elements or the collective effects of a combination of elements is not well understood.

www.EngineeringEBooksPdf.com

Ultimately, it will be desirable to quantify the relationships between the chemical composition and mechanical behavior of pure bitumens. The primary objective of this chapter is to quantify the mechanical behavior of pure bitumens by physical models explaining the deformation mechanisms over a wide range of stresses, temperatures, and strain rates. In order to demonstrate the advantages of employing these physical models, some quantitative correlation with the chemical composition (asphaltene content) is attempted. It will be seen that encouraging results can be obtained if correlations by the asphaltene contents are made for bitumens derived from the same source so that similar chemical nature of the maltenes can reasonably be expected.

6.1.2 Deformation mechanisms of engineering polymers

In amorphous polymers, the glass transition temperature T_g roughly divides the low temperature behavior from the high (Gilbert et al., 1986). In the glassy regime at temperatures well below T_g, bond stretching and bending control the modulus of the polymers, which directly reflects the stiffness of the van der Waals bonds binding one molecular chain to another. When the temperature increases, thermal expansion increases the molecular separation and lowers the van der Waals restoring forces, leading to a slow decrease in the modulus with increasing temperature. As the temperature is raised further to about $0.9T_g$, the van der Waals bonds start to melt. Segments of the previously elastically bonded chains can slide relative to each other, and the material behaves in a viscoelastic way. Finally, at sufficiently high temperature ($T > 1.2T_g$), the van der Waals bonds melt completely, and amorphous polymers deform by viscous flow. Brittle fracture is the dominant failure mechanism at low temperatures ($T < 0.8T_g$), while plasticity usually starts at around $0.8T_g$ in tension, but extends to much lower temperatures in compression (Bin Ahmad and Ashby, 1988). Many of these characteristics are displayed by bitumens (Harvey and Cebon, 2005).

The deformation mechanisms of crystalline materials are much better understood than those of amorphous materials. Deformation-mechanism maps have been constructed in which the kinetic processes of plastic flow of various crystalline materials are summarized into a comprehensive form (Frost and Ashby, 1982). Not only can maps for individual materials be used in material selection, but they can also allow various materials to be classified into isomechanical groups, from which insights into the physics of materials can be generated.

Deformation-mechanism maps (Bin Ahmad and Ashby, 1988) and modulus maps (Gilbert et al., 1986) have been developed for a number of commonly employed amorphous engineering polymers. The maps summarize the inelastic response of the materials to stress, over wide ranges of temperatures and strain rates in both tension and compression, into a number of mechanisms relevant to amorphous materials. Understanding of the mechanical behavior of particular materials is greatly enhanced, and many similarities are found for polymers having similar structures.

This chapter describes deformation-mechanism maps for a particular pure bitumen commonly employed for pavement construction in the UK. The behavior of pure bitumens can then be compared with that of a number of engineering polymers. This framework yields a set of simple phenomenological models and associated parameter

www.EngineeringEBooksPdf.com

values that fully characterize the material. It can also enable investigation of the variations in the behavior of bitumens as a function of their molecular structures.

6.2 High-temperature deformation

6.2.1 Free-volume model

At temperatures well above the glass transition, polymeric materials deform by viscous flow. Within this regime, the strain rate $\dot{\varepsilon}$ is related to the stress σ by

$$\dot{\varepsilon} = \frac{\sigma}{\eta} \tag{6.1}$$

where η is the tensile viscosity (three times the shear viscosity). The temperature dependence of the viscosity in this regime is normally described by the WLF equation (Williams et al., 1955). This model is based on the concept that the molecular mobility at any temperature depends primarily on the *free volume*. The WLF equation is given by

$$\eta = \eta_o \exp \frac{-2.303\ c_1^o (T - T_o)}{c_2^o + (T - T_o)} \tag{6.2}$$

where η_o is the reference viscosity at a reference temperature T_o, and c_1^o and c_2^o are constants. A particular form of Equation (6.2) was also suggested by Ferry (1980), which is applicable to a wide range of liquids above their glass transition. It is given by

$$\log_{10} a_T = \log_{10} \frac{\eta}{\eta_s} = \frac{-c_1^s (T - T_s)}{c_2^s + (T - T_s)} \tag{6.3}$$

where a_T is the shift factor, η_s is the reference viscosity at a reference temperature T_s, and c_1^s and c_2^s are "universal" constants that are equal to 8.86 and 101.6, respectively.

In the literature concerning bitumens, various researchers have used Equation (6.2) in different ways. For instance, Sisko and Brunstrum (1968) proposed the values of c_1^o and c_2^o to be 28.6 and 292 universally for more than 20 bitumens. They used a different T_o for each bitumen. Dickinson and Witt (1969) suggested c_1^o and c_2^o to be 10.86 and 133.2. Jongepier and Kuilman (1969) chose T_o to be an equiviscous temperature, and used different values of c_1^o and c_2^o for different bitumens. Heukelom (1973) used a constant value of 8.5 for c_1^o and a variable value of c_2^o, which depended on the *penetration index*. Schmidt and Santucci (1966) calculated optimum values of c_1^o and c_2^o, which were the same for more than 50 kinds of bitumens but were different for data at different strain rates. Khong et al. (1978a,b) suggested various values of c_1^o and c_2^o that were different for different bitumens and strain rates. Finally, Dobson (1969, 1972) and Vinogradov et al. (1977) retained the use of Equation (6.3) for temperatures higher than T_s, and yet proposed different values of c_1^o and c_2^o for lower temperatures.

The applicability of Equation (6.3) was also confirmed by a number of studies (Brodnyan, 1958; Brodnyan et al., 1960; Wada and Hirose, 1960; Sakanone, 1963a,b; Schmidt and Barrall, 1965), and the lower temperature limit was observed to be from

www.EngineeringEBooksPdf.com

$T_s - 20°C$ to $T_s - 50°C$. It was also suggested in Wada and Hirose (1960), Sakanone (1963a,b), and Schmidt and Barrall (1965) that $T_s - T_g \approx 50 \pm 5°C$, where T_g is the glass transition temperature.

The lack of consensus in the use of the WLF equation, and the wide range of values of the "universal" constants adopted previously, indicate that the temperature dependence of bitumens in the high-temperature region is not well understood.

In the present study, high-temperature deformation data for bitumens reported previously in the literature were reanalyzed. It was assumed that η_s and T_s are material parameters that characterize each particular bitumen. It was then found that Equation (6.3) can be used to describe almost all previously reported data, at temperatures well above the glass transition, using the values of the "universal" constants c_1^s and c_2^s proposed by Ferry (1980).

An example of this approach is shown in Figures 6.1 and 6.2. Figure 6.1 shows the raw viscosity data from Saal (1950a,b) for four bitumens, and from Mehrotra and Svrcek (1986, 1987) for two bitumens. Equation (6.3) was fitted to the data of each of the bitumens so as to characterize each by a value of η_s and a value of T_s. All of the results were then plotted as $\log_{10} a_T$ against $(T - T_s)$, as shown in Figure 6.2. All data points were brought onto a single line, reflecting the validity of Equation (6.3) with

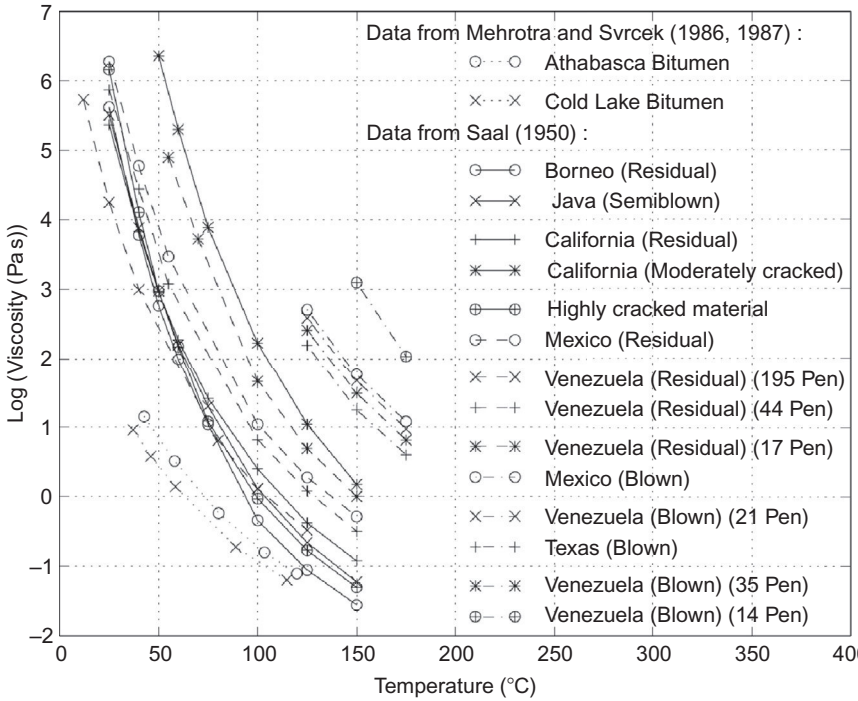


Figure 6.1 The dependence of viscosity on temperature, from Saal (1950a, 1950b) and Mehrotra and Svrcek (1986, 1987).
From Cheung (1995).

www.EngineeringEBooksPdf.com

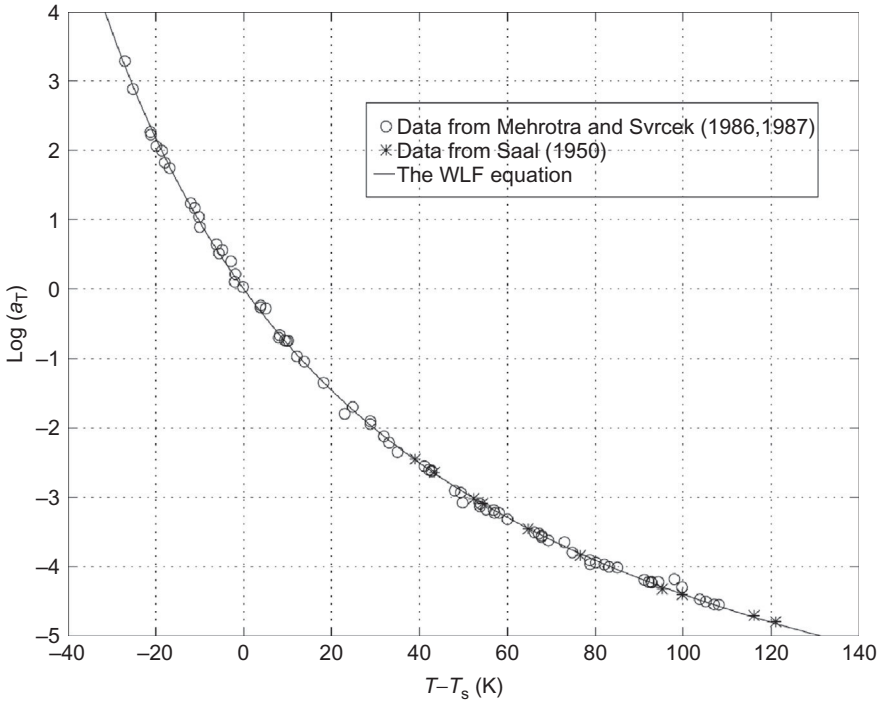


Figure 6.2 The general applicability of the "universal" WLF equation (Equation 6.3). From Cheung (1995).

c_1^s and c_2^s. Similar results were obtained for experimental data from several other sources; see Cheung (1995) for details.

Equation (6.3) implies that the magnitude of the free volume and its dependence on temperature is the same for all bitumens, if compared at the same values $(T - T_s)$. It also implies that the value of the free-volume expansion coefficient deduced from Equation (6.3), which is calculated to be 4.8×10^{-4}, is the same for all bitumens (see Cheung, 1995 for details).

Directly measured values of the *total* volume expansion coefficient α for a number of bitumens were reported by Saal (1950a,b). In all cases, α was found to be about 6×10^{-4}, and was quite insensitive to the type of bitumen. These results agree well with the observations of polymers in general that about two-thirds of the total thermal expansion is due to increase in the free volume (Ferry, 1980).

6.2.2 Dependence on composition

Studying the dependence of free-volume model parameters on the chemical composition of pure bitumens requires the availability of mechanical and compositional test data on the same bitumens. For this purpose, data from the U.S. Bureau of Public

www.EngineeringEBooksPdf.com

Roads (BPR) study (1959–1966) (Welborn and Halstead, 1959; Welborn et al., 1960; Rostler and White, 1962) were used. In the later stage of the study, 50 additional samples of viscosity-graded bitumens, collected by the coordinated effort of the Asphalt Institute and the BPR from 16 different sources, were included. Data collected for this group of bitumens included composition (Halstead et al., 1966), glass transition temperatures (Schmidt and Santucci, 1966), and rheological information (Welborn et al., 1966). This information constitutes one of the most comprehensive databases of the relationships among the physical and chemical properties of bitumens. Another source of data was Saal (1950a,b), who reported compositional data in addition to the viscosity data for the 14 bitumens, which were modeled in the previous section.

The WLF equation (Equation 6.3) was fitted to the high-temperature viscosity data from Welborn et al. (1966), and values of T_s and η_s were obtained for each of the 50 bitumens, from 16 sources (A–P). The values of T_s are compared with those of the directly measured T_g in Figure 6.3. For most of the bitumens, $T_s - T_g$ is between 50 and 70 K, which stays roughly the same among bitumens from the same source (the data for each source lie approximately on a line of slope l). For some of the sources (e.g., sources F, I, and J), however, the changes in T_s are poorly reflected by the changes in T_g (the data for these sources lie on a vertical line); that is, the differences in rheological behavior are not accompanied by different T_g values.

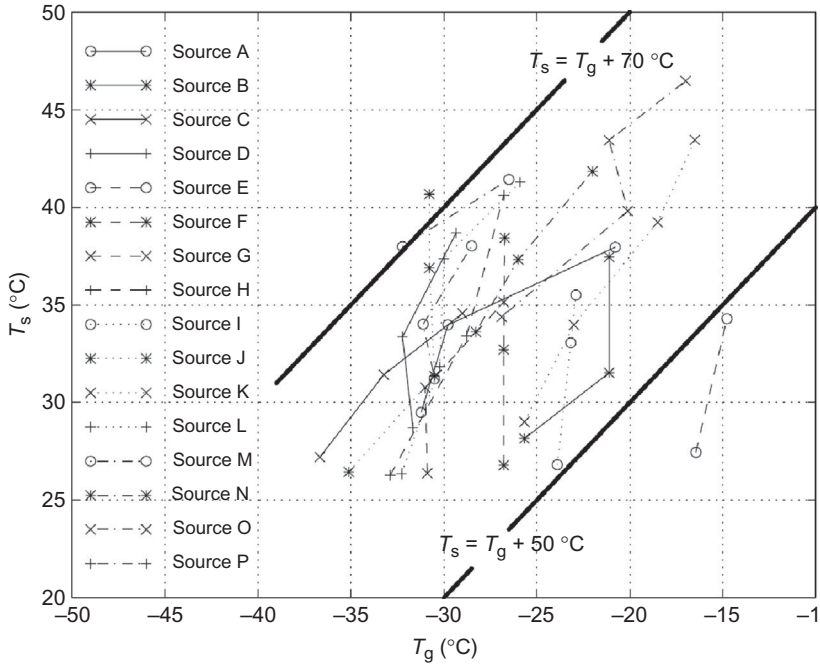


Figure 6.3 Comparison of the values of T_s deduced from the "universal" WLF equation and the values of T_g directly measured by volume dilatometry for the bitumens, reported by Welborn et al. (1966).

www.EngineeringEBooksPdf.com

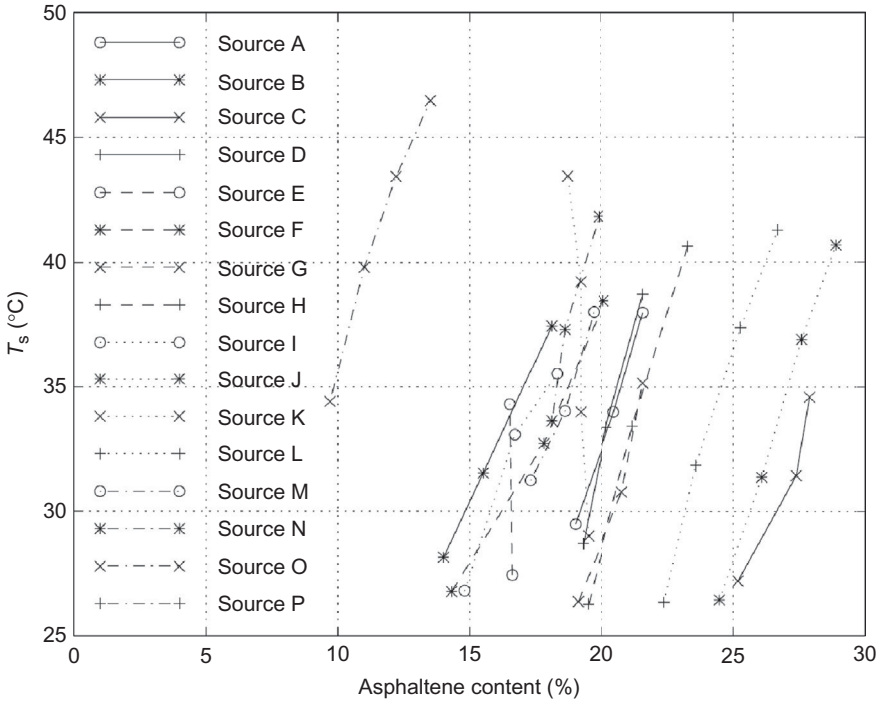


Figure 6.4 The effects of the asphaltene content on the values of T_s for the bitumens, reported by Welborn et al. (1966).

T_s is well correlated with the asphaltene content A_c, as shown in Figure 6.4, and T_s increases with A_c for bitumens from the same source. The poor correlation between T_g and A_c (implied from combining Figures 6.3 and 6.4) suggests that the glass transition phenomenon may depend on additional competing factors (other than A_c) that are related to the chemical properties of the maltenes. These results are in line with other previously reported conclusions (e.g., Schmidt and Santucci, 1966; Sisko and Brunstrum, 1968) that the high-temperature flow behavior is poorly correlated with the glass transition temperature. The present results indicate that T_s is a better parameter for characterizing the flow behavior at high temperatures. The failure of the WLF equation in the vicinity of the glass transition will be discussed later.

Although the value of A_c alone cannot determine the magnitude of T_s for each individual bitumen, the change in A_c does characterize the change in T_s among most bitumens from the same source. Moreover, the slopes of the changes are remarkably similar for most of the bitumen sources, and also agree with the T_g versus A_c relationship obtained by Schmidt and Barrall (1965). For those bitumens reported by Welborn et al. (1966), the only exceptions are the bitumens from sources E and K, for which the increase in T_s is not due to an increase in A_c, but to a decrease in the paraffin content. By plotting T_s against the asphaltene-to-paraffin ratio, the characteristics of bitumens from these two sources are brought into a form very similar to those from other sources

www.EngineeringEBooksPdf.com

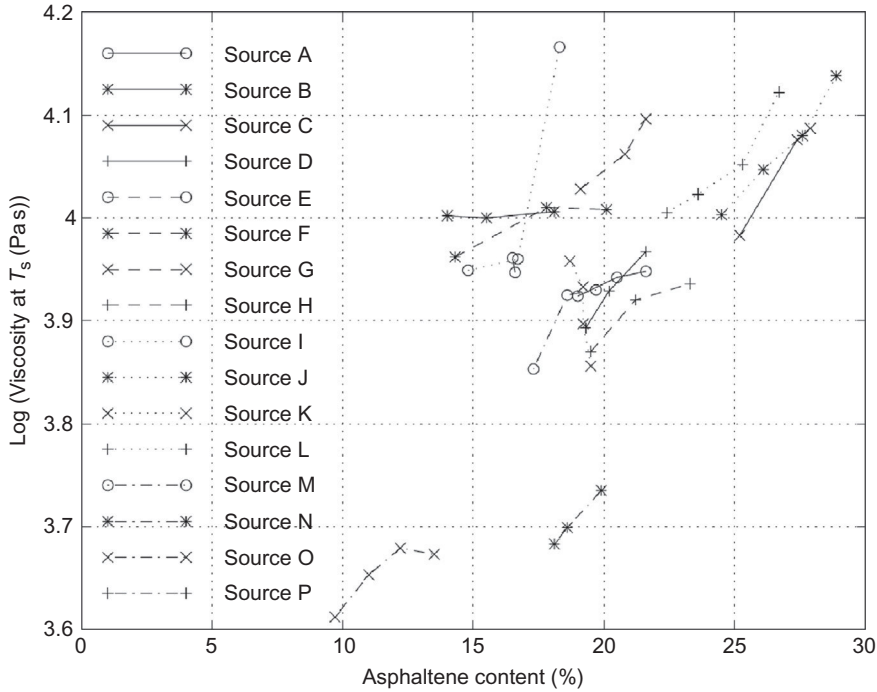


Figure 6.5 The effects of the asphaltene content on the values of η_s for the bitumens, reported by Welborn et al. (1966).

(Cheung, 1995). It can therefore be argued that although the use of A_c in most cases is sufficient to reflect the changes in rheological behavior, the more fundamental controlling parameter is really the relative quantity of asphaltenes in relation to some particular fractions of the maltenes.

Figure 6.5 shows that η_s also increases with increasing A_c for most of the bitumen sources. Combining the results shown in Figures 6.4 and 6.5, it can be concluded that for bitumens having maltenes of similar chemical nature, the high-temperature flow behavior (T_s and η_s) is largely determined by the amount of asphaltenes. However, for bitumens from different sources having the same asphaltene content but different viscosities, the differences in the high-temperature flow behavior can only be explained in terms of the chemical nature of the maltenes. Nevertheless, the effects of the chemical nature of maltenes upon viscosities are still poorly quantified and understood.

Another source of combined mechanical and compositional data is from Saal (1950a,b) for 14 bitumens, which were modeled in the previous section. The effects of A_c on T_s and η_s are shown in Figure 6.6. The slope of the T_s versus A_c relationship is very similar to that of Figure 6.4. The exception was the California bitumens, for which the T_s versus A_c graph had a smaller gradient than those of the other bitumens (see Cheung, 1995). The reason may lie in the fact that the California

www.EngineeringEBooksPdf.com

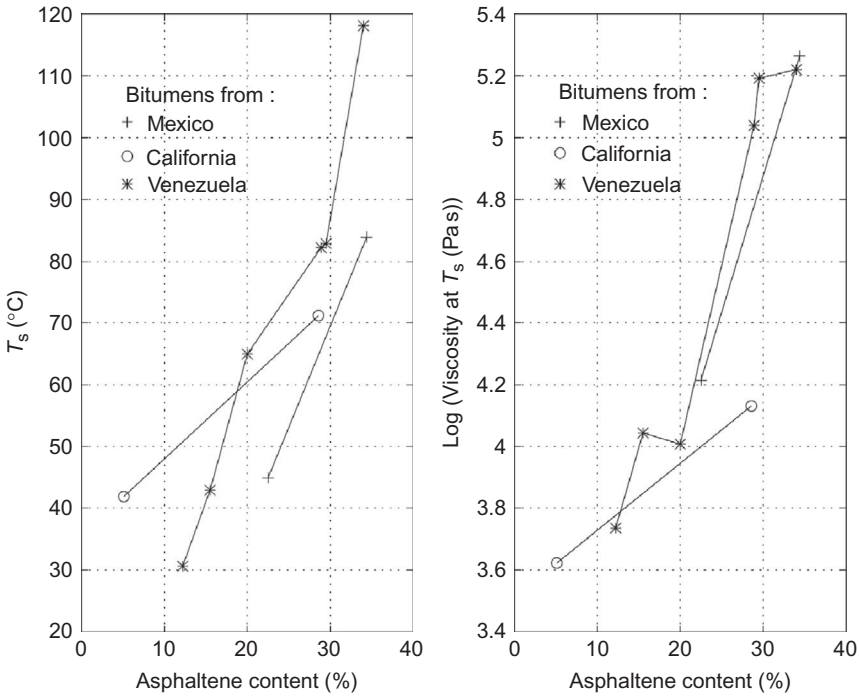


Figure 6.6 The effects of the asphaltene content on T_s and η_s for the bitumens, reported by Saal (1950a, 1950b).

bitumens were obtained by cracking rather the usual process of blowing. In this way, it may be speculated that the process of cracking may generate significant changes in the chemical nature of the maltenes, while the process of blowing primarily increases the asphaltene content. Such a speculation is in line with the results of the peptization study by Heithaus (1962), suggesting that the processes of oxidation and vacuum reduction are different from the process of cracking in terms of their effects on the bitumens. While oxidation and vacuum reduction produced only minor changes in the peptizability of the asphaltenes but might cause large changes in the peptizing power of the maltenes, cracking imposed major changes in the characteristics of both asphaltenes and maltenes.

6.2.3 Effects of aging

Experimental data for the 50 aged bitumens from the BPR study (Welborn et al., 1966) (aged by thin-film oven treatment) were also analyzed using the WLF equation. For the high-temperature viscosity data, the WLF equation was again fitted to obtain values of T_s and η_s. Results are shown in Figure 6.7, in which the values of T_s and η_s are compared for the unaged and aged bitumens. For most of the bitumens, the effect of aging is reflected mainly by a change in T_s, although bitumens from sources J and N display a more noticeable increase in η_s. While the change in T_s is associated with the change

www.EngineeringEBooksPdf.com

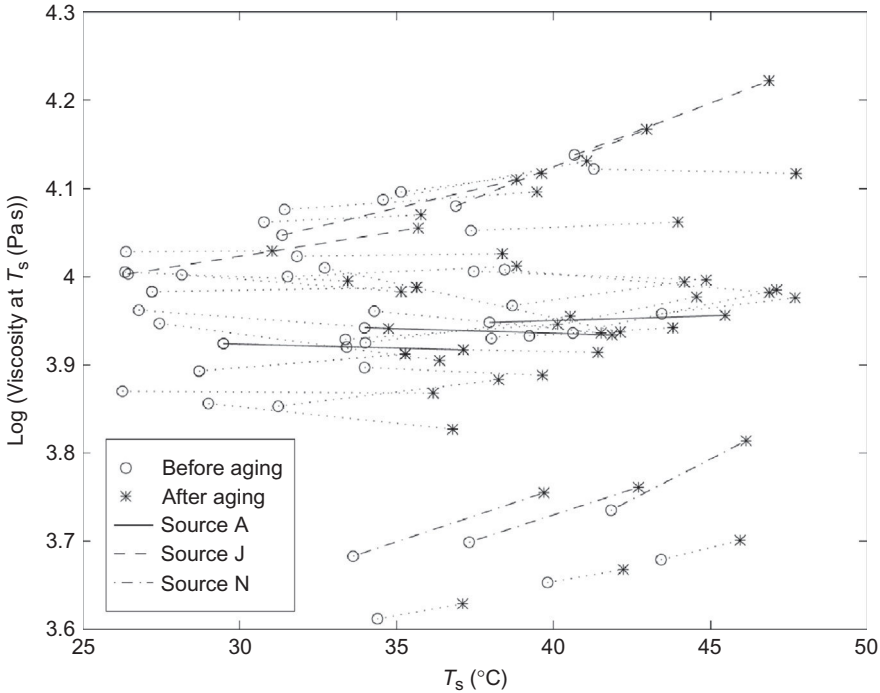


Figure 6.7 Effects of aging on the values of T_s and η_s for the bitumens, reported by Welborn et al. (1966).

in free volume as a function of temperature, the change in η_s is related to the change in the value of the intrinsic viscosity at any particular value of free volume. Nevertheless, because of the mathematical form of the WLF equation, the viscosity is much more sensitive to changes in T_s than changes in η_s for all of the bitumens. As a result, T_s can be used as a general material parameter to quantify the effects of aging on high-temperature viscosities.

Another interesting result from the analysis is that the effects of aging, as revealed by changes in T_s and η_s, are similar for bitumens from the same source, which is particularly demonstrated in Figure 6.7 by data from sources A, J, and N. Yet no correlation between the aging effects and the asphaltene content can be established. These observations are in line with the general view of aging—that it is the overall chemistry of the bitumen, rather than the quantity of asphaltenes alone, that determines the extent of aging (Petersen, 1984).

6.2.4 The dependence on pressure

The dependence of viscoelastic behavior on pressure can also be understood in terms of the fractional free volume on which molecular mobility depends (Ferry, 1980). The free volume decreases with increasing pressure, just as it does with decreasing

www.EngineeringEBooksPdf.com

temperature. By considering different forms of dependence of the free-volume compressibility β_f on pressure, models describing the dependence of the viscosity on pressure can be established (Ferry, 1980).

Cheung (1995) modeled the pressure-dependent viscosity data reported by Saal (1950a,b), Mehrotra and Svrcek (1986, 1987), and Puttagunta et al. (1993) using two forms of dependence of β_f on pressure. Values of β_f deduced from the models agreed well with the total volume compressibility β measured directly for some of the bitumens. Moreover, the compressibility of the total volume and the compressibility of the free volume were found to be dependent on both temperature and pressure. The dependence on pressure varies for different kinds of bitumens. The success of interpreting the pressure-dependent viscosity data in terms of the free-volume model strongly indicates that the dominant deformation mechanism for pure bitumens at temperatures well above their glass transition is controlled by the free volume present in the material.

6.3 Ambient temperature deformation

6.3.1 The power-law model

6.3.1.1 Stress dependence

Although linear behavior is observed in the dynamic properties of pure bitumens for relatively small strains, nonlinear behavior has long been recognized in quasistatic tests of the material at larger strains. Many early researchers like Saal (1950a,b), Lethersich (1942), and Brown and Sparks (1958) observed linear behavior for stress levels at or below 2 kPa, which they modeled successfully by the theories of linear viscoelasticity. However, some of these researchers stated that nonlinearities would become more significant at higher stress levels (e.g., Lethersich,, 1942). This was later confirmed by numerous experimental studies (Gaskins et al., 1960; Sisko, 1965; Welborn et al., 1966; Moavenzadeh and Stander, 1967; Khong et al., 1978a,b) at stress levels of 100 kPa to 1 MPa, where bitumen was found to behave nonlinearly.

Tensile tests were conducted on two nominal 50 pen bitumens (denoted B1 and B2) at ambient temperatures from −10 to 30 °C. Typical results for bitumen B1 are shown in Figure 6.8, which shows the steady-state strain rate plotted against the steady-state stress. Details of these tests can be found in Cheung (1995). From this figure, it can be seen that within the range of testing conditions, at any particular temperature, the bitumen behaves nonlinearly. The steady-state response can be represented by the power-law equation

$$\frac{\dot{\varepsilon}}{\dot{\varepsilon}_p} = \left(\frac{\sigma}{\sigma_{op}}\right)^{n_p} \tag{6.4}$$

where n_p is the creep exponent, and $\dot{\varepsilon}_p$ is the strain rate at a reference stress σ_{op}. The value of the creep exponent n_p shown in the fitted curves is 2.3. Although this value is

www.EngineeringEBooksPdf.com

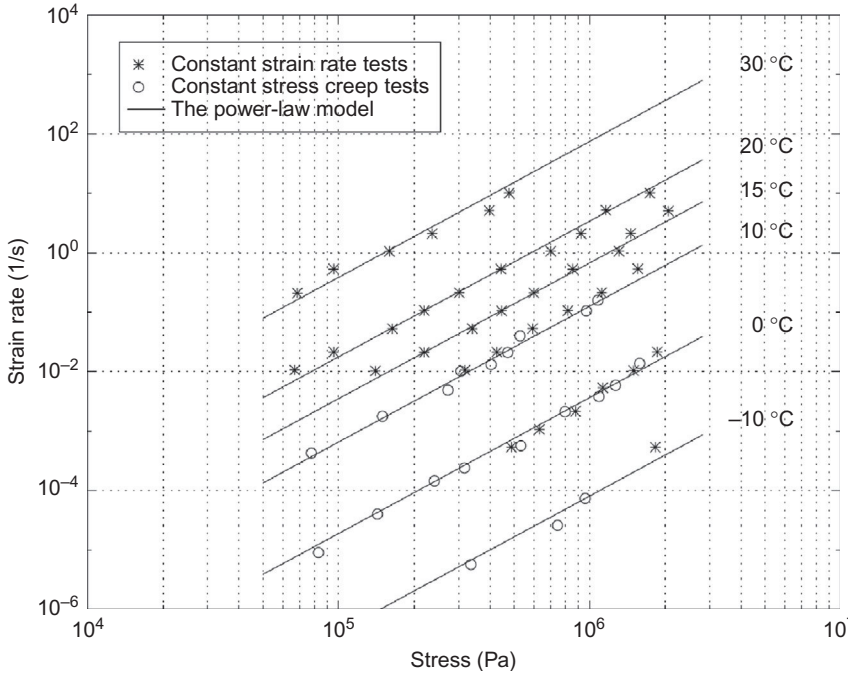


Figure 6.8 Steady-state creep behavior for bitumen B1, reported by Cheung (1995).

small compared with the usual range of 3–10 in crystalline materials (Frost and Ashby, 1982), it is sufficiently large to render the nonlinear behavior important at these stress levels.

Ambient temperature test data for the 16 sources of bitumen from the BPR study were reported by Welborn et al. (1966). All of these tests were conducted within a relatively narrow range of applied strain rates (0.001–0.1 /s). Equation (6.4) was fitted to the data at each temperature, and values of n_p were obtained for each temperature for all of the bitumens. Results of the n_p values plotted against the temperature $T-T_s$ are shown in Figure 6.9. It can clearly be seen that within the range of applied strain rates, linear behavior ($n_p=1$) is observed above a certain temperature. Below this temperature, nonlinear behavior becomes more significant.

Use of a power-law relationship, similar to Equation (6.4), was also discussed by Lee and Warren (1940), Moavenzadeh and Stander (1967), Schweyer et al. (1977), Ruth and Schweyer (1981), and Sybilski (1993). Observed values of the creep exponent n_p usually ranged from 1 to 2, although higher values were occasionally reported.

6.3.1.2 Temperature dependence

The time-temperature equivalence in crystalline solids for the rate of diffusion, for creep, and for other thermally activated processes can be understood by the transition state theory, which follows from the kinetic theory of simple thermally activated

www.EngineeringEBooksPdf.com

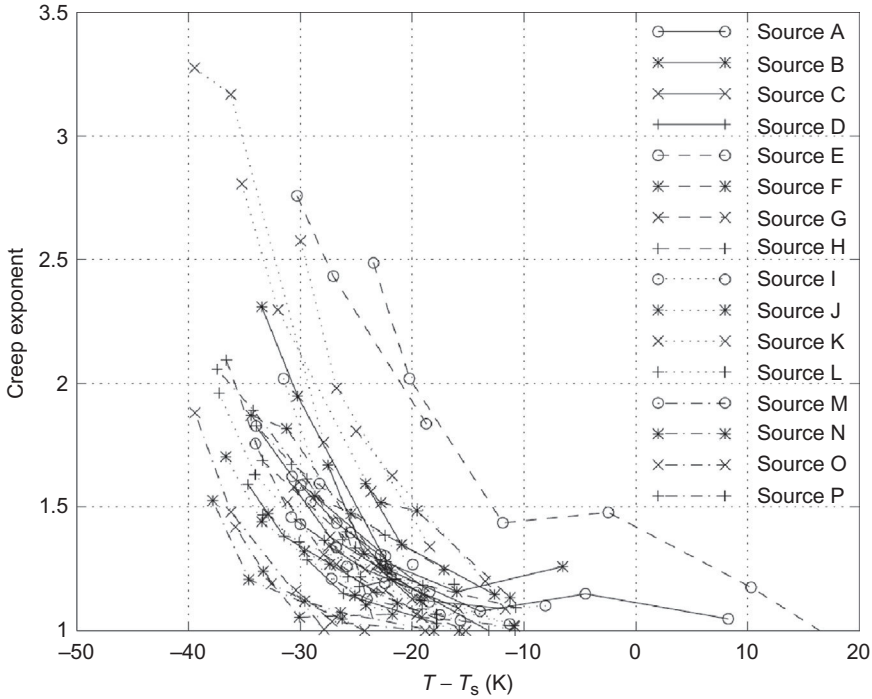


Figure 6.9 The general dependence of the creep exponent on $T-T_s$ for the bitumens, reported by Welborn et al. (1966).

processes (Ward, 1983; Gilbert et al., 1986). The frequency of diffusive molecular jumps w_1 at one temperature T_1 is related to frequency w_2 at another temperature T_2 by

$$\log_{10}\left(\frac{w_1}{w_2}\right) = \log_{10} a_T = \frac{Q}{2.303R}\left(\frac{1}{T_2}-\frac{1}{T_1}\right) \tag{6.5}$$

where Q is the activation energy for diffusion (Ward, 1983; Gilbert et al., 1986) and R is the universal gas constant.

Equation (6.5) is usually known as the Arrhenius equation, because it was first shown by Arrhenius that it describes the influence of temperature on the rate of chemical reactions (Ward, 1983).

If the dependence of the creep constant $\log_e\left(\dot{\varepsilon}_p/\sigma_{op}^{n_p}\right)$ in Equation (6.4), obtained from the data in Figure 6.8, is plotted against the reciprocal of the absolute temperature, a linear relationship is obtained, as shown in Figure 6.10. This indicates that the temperature dependence of the ambient temperature deformation behavior is described well by the Arrhenius equation (rather than the WLF equation). Including this temperature dependence in Equation (6.4) gives

www.EngineeringEBooksPdf.com

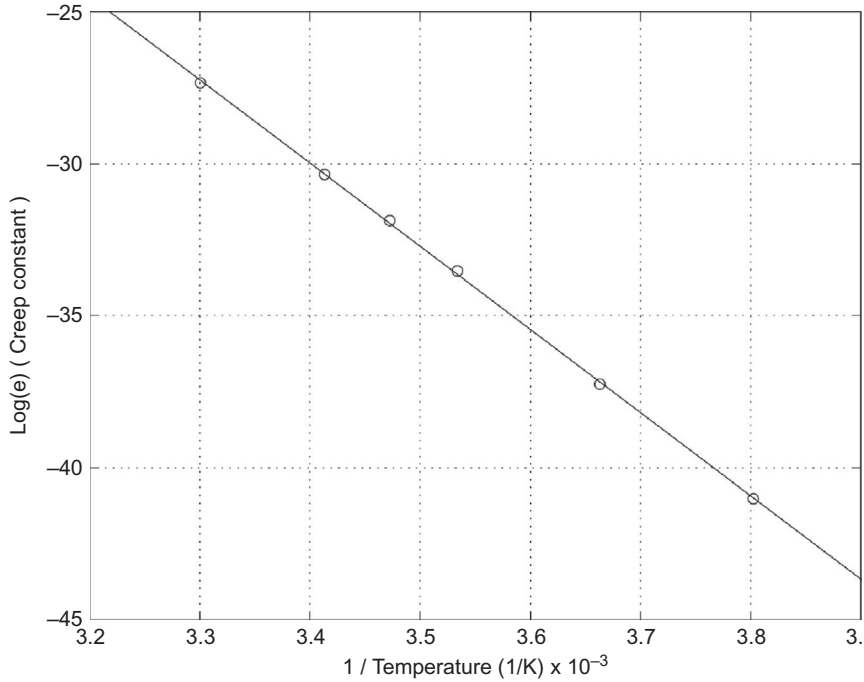


Figure 6.10 Change of creep constant with temperature for bitumen B1, reported by Cheung (1995).

$$\frac{\dot{\varepsilon}}{\dot{\varepsilon}_{op}} = \left(\frac{\sigma}{\sigma_{op}}\right)^{n_p} \exp\left(\frac{-Q_p}{RT}\right) \tag{6.6}$$

where $\dot{\varepsilon}_{op}$ is a reference strain rate and Q_p is the thermal activation energy.

Equation (6.6) is referred to as the power-law model (PLM). It is included in Figure 6.8 with $n_p = 2.3$ and a single value of $Q_p = 229$ kJ/mol, which is comparable to that of diffusional flow.

Another example of using the Arrhenius equation for ambient temperature deformation was reported by Anderson and coworkers (Anderson, et al., 1991; Christensen and Anderson, 1992; Anon, 1994). They suggested that $Q_p = 261$ kJ/mol for all bitumens involved in their experiments.

The change in the temperature dependence of the deformation properties from the WLF equation (Equation 6.3) at high temperature to the Arrhenius equation (Equation 6.5) at ambient temperature is best demonstrated by data generated from the van der Poel nomograph (van der Poel, 1954). The shift factor a_T is plotted against temperature for a nominal 50 pen bitumen in Figure 6.11. The fitted WLF equation and Arrhenius equation are also shown in the figure, indicating their applicability over different temperature ranges.

www.EngineeringEBooksPdf.com

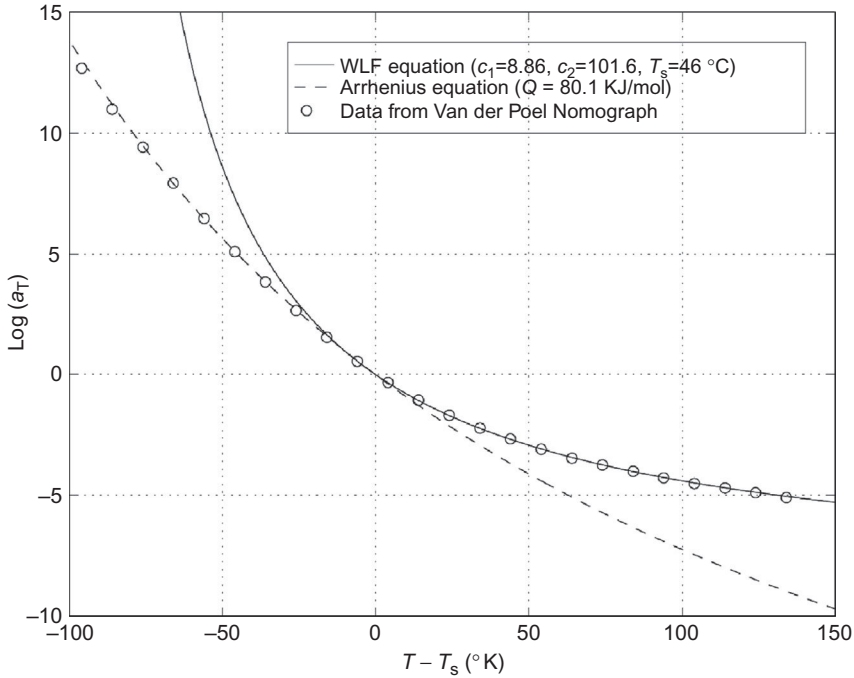


Figure 6.11 Modeling the (log a_T vs. T) master curve from the van der Poel nomograph by the "universal" WLF equation (Equation 6.3) and the Arrhenius equation (Equation 6.5). From Cheung (1995).

This change of deformation mechanism explains the reported failure of the "universal" WLF equation (Equation 6.3) in the vicinity of the glass transition in other studies (Brodnyan et al., 1960; Sakanone, 1963a,b; Dobson, 1969; Jongepier and Kuilman, 1969). Due to the nature of Equation (6.2), the wide ranges of log a_T and temperature involved, and the existence of experimental uncertainties, a reasonable fit to most experimental data can be attained by choosing a set of c_1^o and c_2^o suitably, or by retaining c_1^s and c_2^s for higher temperatures and using another set of c_1^o and c_2^o for lower temperatures. This explains why there are so many WLF models for bitumens reported in the literature, all of which fit their experimental data acceptably well (Cheung, 1995). A very similar breakdown of the free-volume model for a number of glass-forming liquids at temperatures in the vicinity of the glass transition was reported by Uhlmann and coworkers (Laughlin and Uhlmann, 1972; Cukierman et al., 1973).

6.3.1.3 Dependence on composition

Equation (6.6) was fitted to the ambient temperature test data for the 16 sources of bitumen from the BPR study reported by Welborn et al. (1966). An average value of the creep exponent n_p was obtained within the experimental ranges of temperatures and strain rates for each bitumen. The results are plotted against asphaltene content in Figure 6.12. For bitumens from the same source, the creep exponent generally

www.EngineeringEBooksPdf.com

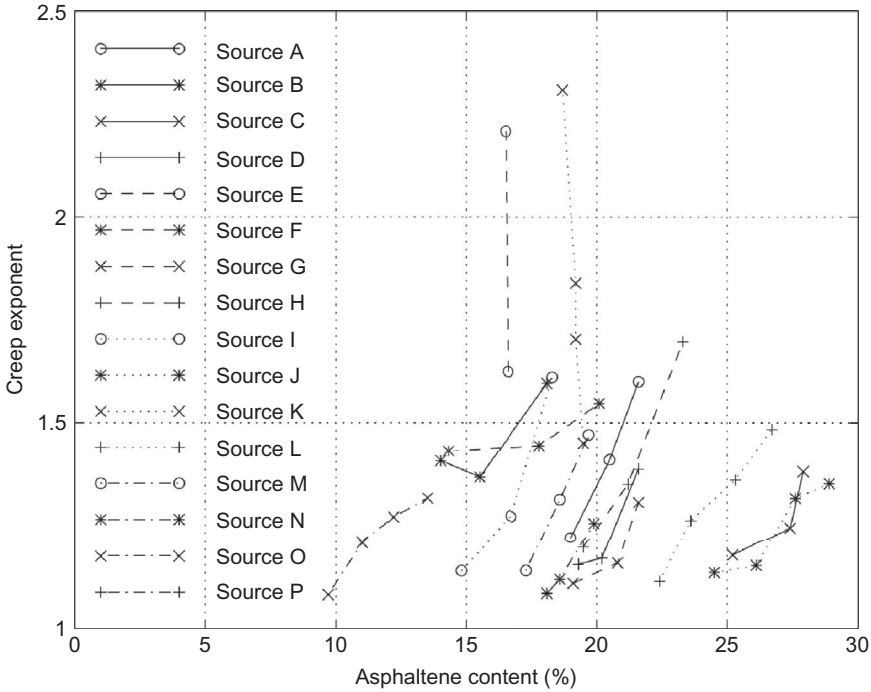


Figure 6.12 The effects of the asphaltene content on the values of the creep exponent for the bitumens, reported by Welborn et al. (1966).

increases with increasing asphaltene content. Nevertheless, the asphaltene content alone does not uniquely determine the creep exponent, and the chemical nature of the maltenes also affects the extent of nonlinear behavior within certain ranges of temperatures and strain rates.

Values of Q_p were also obtained for each bitumen, and these ranged from 160 to 250 kJ/mol (Cheung, 1995). However, due to the small ranges of temperatures associated with the data (4–25 °C), these values were not reliable, and they did not correlate well with the asphaltene content (see Cheung, 1995).

In general, the PLM satisfactorily describes the behavior of bitumens over limited ranges of temperatures and stresses, but does not describe well the deformation behavior in the presence of more significant changes in the creep exponent and the temperature dependence.

6.3.2 The modified cross model

6.3.2.1 Overall ambient temperature deformation behavior

The tensile test results on bitumen B2 from Cheung (1995) are shown in Figure 6.13. Although the temperature range of the tests was the same as for the bitumen B1, the stress range extended further into the low stress region. It can be seen that although the

www.EngineeringEBooksPdf.com

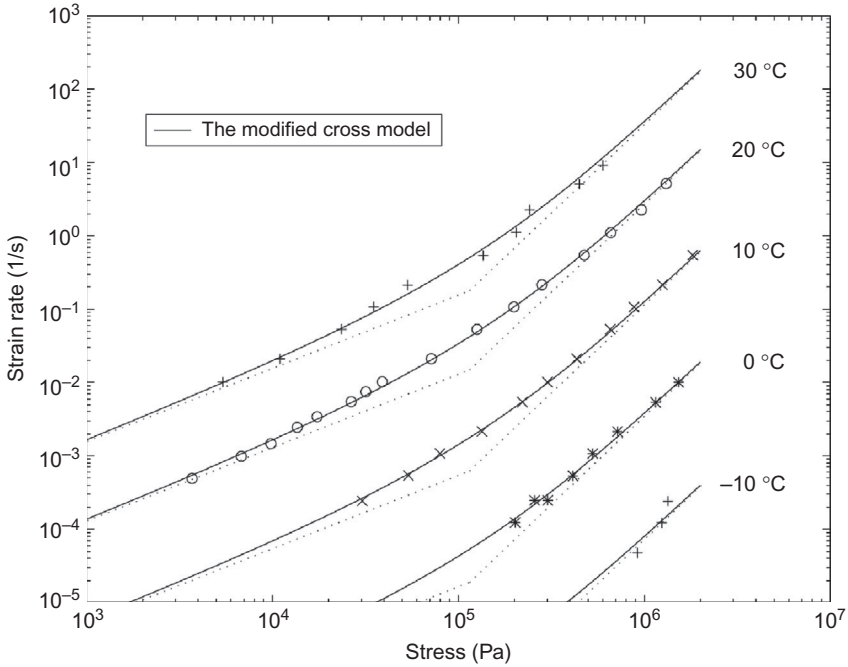


Figure 6.13 Steady-state creep behavior of bitumen B1, reported by Cheung (1995).

behavior follows a power law in the higher half of the stress range, it changes gradually to linear behavior (slope of 1) toward the lower half of the stress range. Moreover, the transition appears to take place at the same value of stress throughout the entire temperature range of interests. One of the interesting consequences of such behavior is that for any narrow range of stress, the stress/strain-rate relationship can always be fitted by a power law, the creep exponent of which can vary from unity at low stress to the maximum value at the highest stress levels before fracture intervenes. It is only by examining the behavior over a wide range of stress that the transition behavior can be seen.

Cheung (1995) proposed the use of the modified cross model (MCM) to summarize the deformation behavior of pure bitumens at temperatures immediately above the glass transition. The model originated from the pseudoplastic flow equation developed by Cross (1965) from considerations of the formation and rupture of structural linkages. The equation was modified by Cheung (1995) to include the temperature dependence of bitumens. The MCM summarizes the change from linear to power-law behavior with stress, and the change from free-volume dependent deformation (described by the WLF equation) to "diffusional" deformation (described by the Arrhenius equation) with temperature. The model is given by

$$\eta = \frac{\eta_{0T}}{1 + \left(\frac{\eta_{0T}\dot{\varepsilon}}{\sigma_{oc}}\right)^{n_c}} \tag{6.7}$$

www.EngineeringEBooksPdf.com

where

$$\eta_{oT} = \eta_{oc} \exp\left(\frac{Q_c}{RT}\right), \quad T > T_g \tag{6.8}$$

and

$$\eta_{oT} = \eta_s \exp\left(-\frac{2.303 c_1^s (T - T_s)}{c_2^s + (T - T_s)}\right), \quad T \gg T_g \tag{6.9}$$

In these equations,

σ_{oc} is the failure strength of structural linkages
n_c is a constant
η_{oc} is the preexponential for viscosity
Q_c is the thermal activation energy

The transition temperature distinguishing the two types of behavior can be obtained by solving Equations (6.8) and (6.9) simultaneously.

Cheung (1995) proposed that the change to nonlinear deformation behavior at high stresses is due to the rupture of the molecular network formed by the association of asphaltenes. A single value of σ_{oc} reflects the level of stress at which this change occurs for all temperatures. The change to Arrhenius behavior at temperatures immediately above the glass transition depends on factors related to the change of molecular structures with decreasing temperatures. The exact mechanisms are not yet understood.

The MCM is fitted to the two bitumens reported by Cheung (1995) in Figure 6.14, with one set of the parameters n_c, η_c, and Q_c chosen for each bitumen. Equation (6.7) is found to be in good agreement with the data for both bitumens, though the fitting to the data of bitumen B1 involves some extrapolation at low stress levels. The value of σ_{oc} for bitumen B2 is 115 kPa, while the estimated value for bitumen B1 is 68.6 kPa. It can be seen that the differences between the two nominally identical bitumens are well represented by the MCM (Cheung, 1995).

6.3.2.2 Dependence on composition

The MCM provides a consistent framework to characterize deformation behavior of pure bitumens in the linear (Newtonian) regime (at stress levels considerably lower than σ_{oc}), the transition regime (at stress levels in the vicinity of σ_{oc}), and the power-law regime (at stress levels considerably higher than σ_{oc}) through the use of the three material parameters η_{oc}, σ_{oc}, and n_c. Individual parameters can be established precisely if data for the corresponding regimes are available. Otherwise, extrapolated estimates for each regime can serve as useful bounds for comparison purposes. Conversely, the temperature dependence can always be deduced from the data using the MCM, without being constrained by the stress levels in the data. The MCM is especially useful when investigating the temperature dependence of the zero-strain-rate viscosity at low temperatures, the extrapolation of which was achieved rather arbitrarily in the past.

www.EngineeringEBooksPdf.com

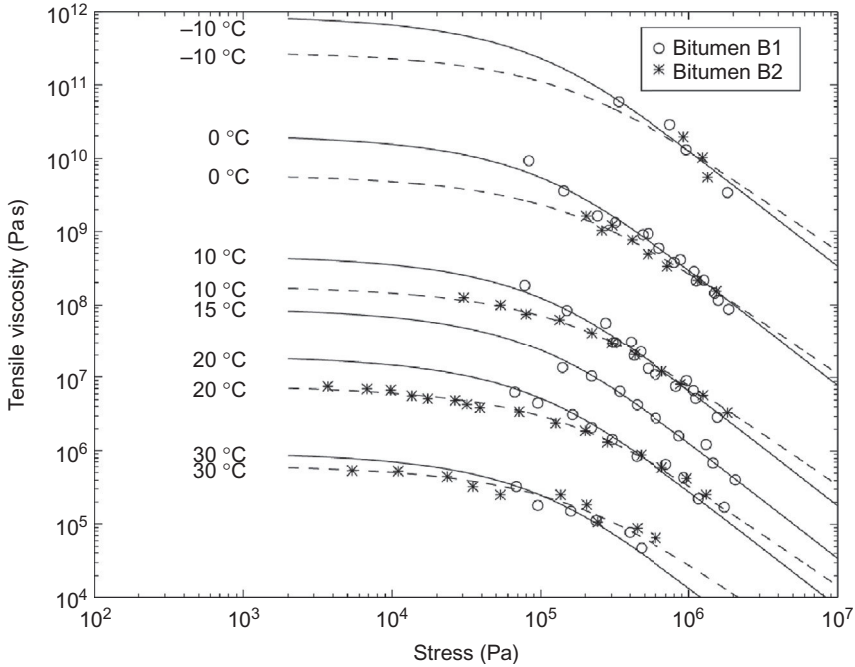


Figure 6.14 Steady-state creep behavior of the two batches of bitumens, reported by Cheung (1995).

The most comprehensive sources of viscosity data for a wide range of stresses and temperatures are from Sisko (1965) (3 bitumens) and Khong et al. (1978a,b) (8 bitumens). The MCM was applied to the data for all of these bitumens, and good agreements were achieved (see Cheung, 1995). An example of the model fitting to data for "bitumen C," reported by Sisko (1965), is given in Figure 6.15. The data support the assumption of the MCM that the stress level at which significant nonlinear deformation behavior occurs is constant for all temperatures ($\sigma_{oc} \approx 1.5$ kPa in this case).

The MCM was also applied to the 50 bitumens reported by Welborn et al. (1966). An example is given for the bitumen "E-5" in Figure 6.16. The majority of data for the 50 bitumens was in the linear and transition regimes, due to the more limited ranges of stresses and temperatures involved. As a result, the values of σ_{oc} and n_c obtained for these data were only extrapolated estimates. By combining the fitted parameters for the 50 bitumens from Welborn et al. (1966) with those from Sisko (1965) and Khong et al. (1978a, 1978b), it was found that values of σ_{oc} usually lie between 0.1 and 0.5 MPa, while values of n_c usually result in creep exponents between 2 and 2.5 in the power-law regime. This explains why previous viscoelastic models for data at stress levels less than about 0.1 MPa have always been linear.

www.EngineeringEBooksPdf.com

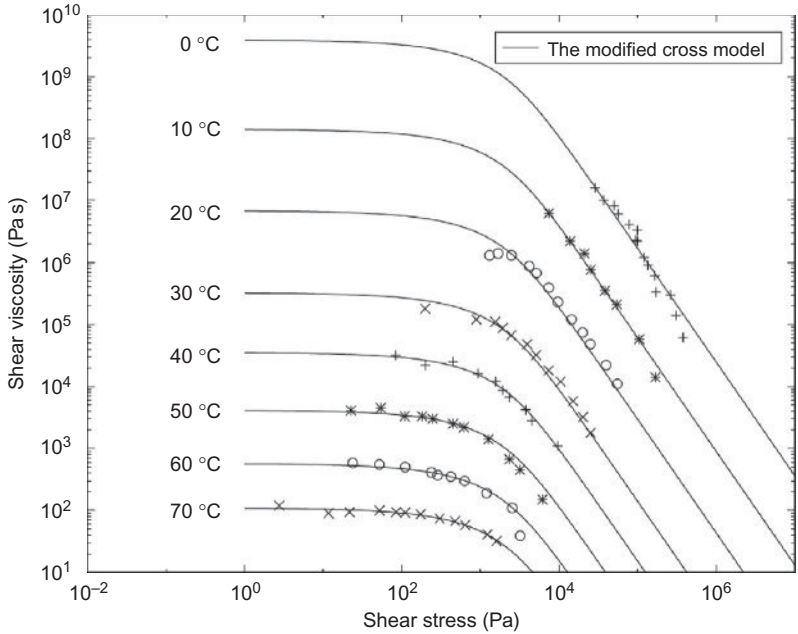


Figure 6.15 Application of the modified cross model to the viscosity data of bitumen C, reported by Sisko (1965).

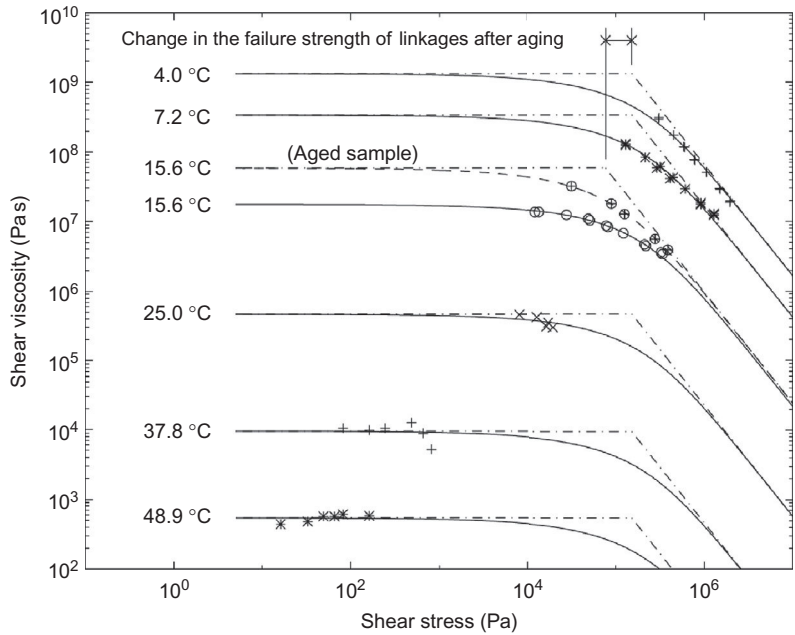


Figure 6.16 Application of the modified cross model to the viscosity data of bitumen E-5, reported by Welborn et al. (1966).

www.EngineeringEBooksPdf.com

6.3.2.3 Effects of aging

The aged data at 15.6 °C reported by Welborn et al. (1966) were also analyzed using the MCM. By assuming that the value of n_c is not affected by aging, values of η_{oT} and σ_{oc} after aging can be obtained. An example of modeling the aged data is included in Figure 6.16 for the bitumen "E-5." Although not all of the values of σ_{oc} deduced from the data of the 50 BPR bitumens are reliable estimates, there are sufficient consistent results to suggest that the value of σ_{oc} decreases as a result of aging. This is consistent with the observation previously discussed that the creep exponent increases upon aging for the same range of strain rates. The evidence is further enhanced by the fact that for "bitumen C" reported by Sisko (1965) (which was subjected to extra oxidation after reduction), σ_{oc} is particularly small (1.5 kPa; see Figure 6.15) compared with the usual range of the other bitumens. On the other hand, the value of η_{oT} always increases upon aging, but no data are available that enable the change of n_c as a result of aging to be studied.

Physically, the MCM suggests that the process of aging increases the proportion of molecules that are capable of forming linkages so that the limiting viscosity is increased as a result of the additional stiffening. However, the overall linkage structure thereby produced is more susceptible to strained ruptures than is the unaged one.

In the extreme case when a small increase in η_{oT} is accompanied by a large decrease in σ_{oc}, the aging process has a stiffening effect at small strain rates and a softening effect at higher strain rates.

6.4 Low-temperature deformation

6.4.1 Previous research at low temperatures

The majority of previous research on bitumens has been concerned with the viscoelastic and viscous flow regimes above T_g. The difficulties of experimenting with glassy bitumen at low temperatures have left its plastic behavior poorly understood. In most of the previous investigations that involved subzero testing temperatures, the low-temperature rheology of bitumens was usually studied by dynamic shear tests (Brodnyan, 1958; Brodnyan et al., 1960; Sisko and Brunstrum, 1968; Dobson, 1969; Jongepier and Kuilman, 1969; Christensen and Anderson, 1992), and data were always combined with those at higher temperatures into a master curve for the modulus.

Only a few constant stress creep tests on bitumens at subzero temperatures have been reported. Khong et al. (1979) studied the creep behavior of eight kinds of bitumens by sliding plate shear viscometry for temperatures down to −20 °C and time durations up to 2400 s. Only one stress level was employed, and the glass transition temperatures of all eight bitumens (obtained elsewhere: Khong et al., 1978a,b) appeared to be considerably lower than −20 °C. Majidzadeh and Schweyer (1967) conducted creep tests in compression on cylindrical specimens of four kinds of bitumens at two or three stress levels and at temperatures down to −9 °C. No glass transition data was given, and the time durations for the tests were 600 s. In the SHRP

www.EngineeringEBooksPdf.com

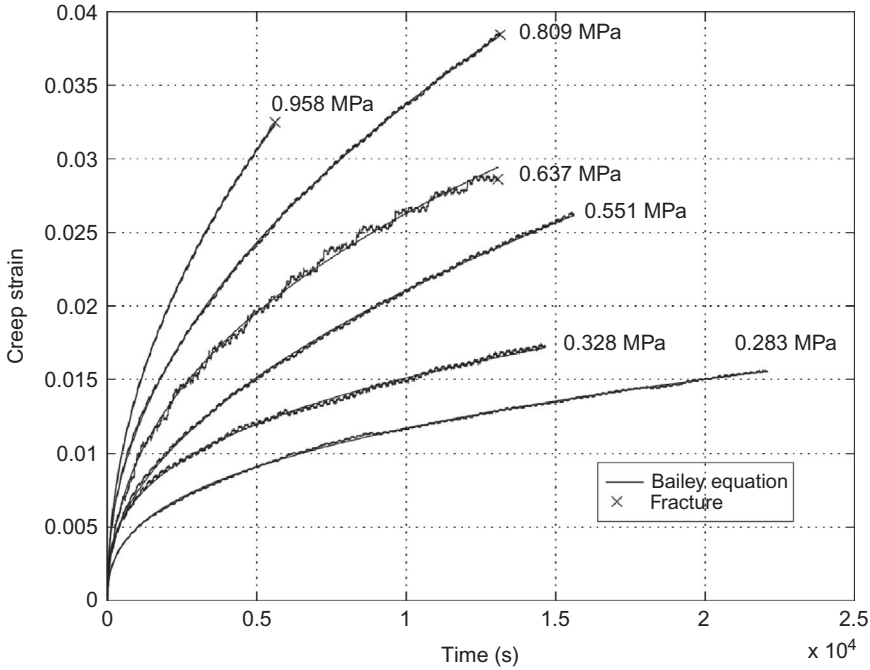


Figure 6.17 Constant stress creep tests in tension at −20 °C for bitumen B2, reported by Cheung (1995).

project (Anon, 1994), creep tests in bending were conducted at temperatures ranging from −35 to −15 °C. The durations of these tests were as short as 240 s, and the dependence on stress was assumed to be linear.

Cheung (1995) conducted creep tests in tension and in compression at temperatures from −35 to −20 °C on a 50 pen bitumen. The durations of the tests were up to about 20,000 s. Typical results of the tensile creep tests are shown in Figure 6.17. The strain rates at $t = 2000$ s deduced from individual creep curves are plotted against the applied stress in Figure 6.18.

6.4.2 The Eyring plasticity model

Based on the experimental data and the similarities of pure bitumens to other polymers, Cheung (1995) proposed the use of Eyring's viscosity equation (described in Ward, 1983) together with Bailey's time-hardening equation (described in Penny and Marriott, 1971) to describe the behavior of pure bitumens in the vicinity of and below the glass transition temperature. The proposed Eyring plasticity model (EPM) is given by

$$\frac{\dot{\varepsilon}}{\dot{\varepsilon}_e} = 2\exp\left(-\frac{Q_e}{RT}\right)\sinh\left(\frac{\tau v_s - P v_p}{RT}\right)\left(\frac{t}{t_o}\right)^{m_e} \tag{6.10}$$

www.EngineeringEBooksPdf.com

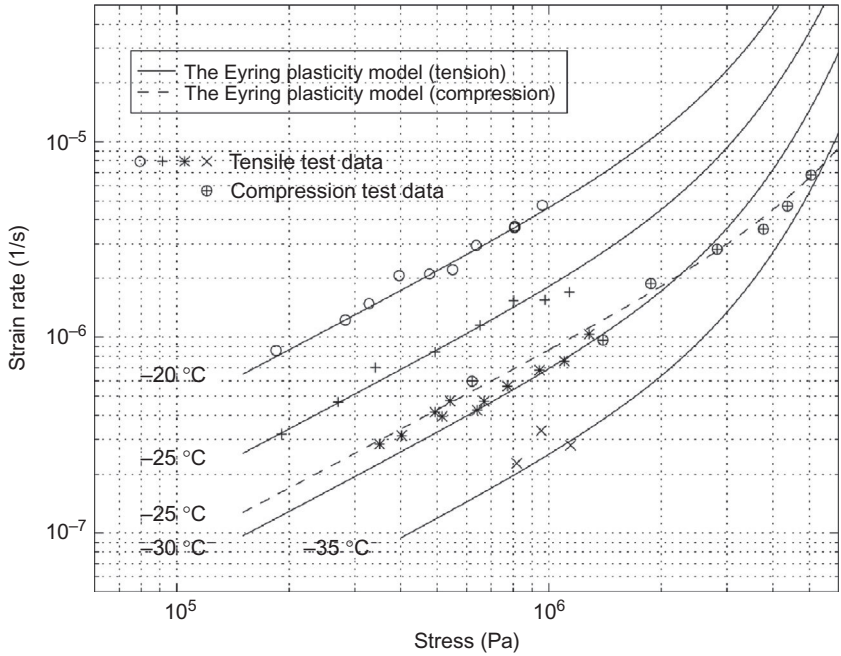


Figure 6.18 Low-temperature creep behavior at $t = 2000$ s for bitumen B2, reported by Cheung (1995).

where

$\dot{\varepsilon}$ is the strain rate
τ is the shear stress
P is the pressure
$\dot{\varepsilon}_e$ is a preexponential constant
Q_e is the activation energy for the flow process
v_s is the shear activation volume
v_p is the pressure activation volume
t_o is a reference time
m_e is the time-hardening constant

The EPM is fitted to the experimental data and is included in Figure 6.18.

It is interesting to see that the value of Q_e obtained in this case is 99 kJ/mol, which is considerably smaller than the value of Q_p (or Q_c) obtained at temperatures higher than the glass transition temperature. To explain this change in activation energy would require a deeper knowledge of the microstructure of bitumens than presently available. Nevertheless, there has to be a difference in the microstructure above and below the glass transition. While the value of Q_e represents the energy barrier imposed by the glassy structure, the value of Q_p (or Q_c) represents some intermediate structure that is not fully characterizable by the amount of free volume.

It can be seen from Equation (6.10) that $(\partial\tau/\partial P)_{\dot{\varepsilon},T} = v_p/v_s$. The value of $v_p/v_s = 0.5$, obtained for bitumen B2, is large when compared with a value of less than

www.EngineeringEBooksPdf.com

0.2 for the polymer polymethylmethacrylate (Ward, 1971). This suggests a particular sensitivity to pressure of the plastic behavior of glassy bitumens. According to Lian et al. (1994), such magnitudes of the activation volume are a result of the monomeric sheets or the micelle systems formed by association of unit cells. The Eyring theory of viscous flow therefore suggests that the flow process involves the movement of a relatively small number of unit sheets associated together. Although the existence of much larger supermicelles or giant supermicelles has been observed, usually at room temperature, it is the movement of the fundamental unit cell or small number of unit cells that appears to control the flow behavior of glassy bitumens at low temperatures.

More experimental studies of different bitumens at low temperatures are required to validate the general application of the EPM. In view of the brittleness of glassy bitumens, such studies should involve creep tests in tension, compression, and possibly under triaxial stress states as well.

6.5 Deformation-mechanism maps

Experimental findings for the deformation of pure bitumens have been accumulating for many years. The recognition of bitumen as a polymeric system has also been well established. As a result, it will be attempted in this section to summarize most of the understanding of the mechanical behavior of pure bitumens in relation to their microscopic structures in the form of deformation-mechanism maps (Frost and Ashby, 1982; Gilbert et al., 1986; Bin Ahmad and Ashby, 1988). It is intended, by the use of deformation-mechanism maps, not only to arrange the existing knowledge into a more global perspective, but also to shed new light on the particular behavior of bitumens by comparing these maps with those for other crystalline and amorphous materials. As has been discussed in earlier sections, the correlation of the mechanical behavior to the microstructure of bitumens is still in its infancy. Therefore, these maps only represent initial attempts to propose a framework by which bitumens can be better understood.

6.5.1 Construction of the deformation-mechanism map

The deformation-mechanism maps for a 50 pen bitumen (B2) were constructed using the experimental results from Cheung (1995) described previously in this chapter. The maps followed similar concepts to the construction of failure-mechanism diagrams for engineering polymers (Bin Ahmad and Ashby, 1988), except that fracture was assumed to be suppressed so that only steady-state deformation was considered. The material parameters for bitumen B2 are summarized in Table 6.1.

One form of the map with axes of strain rate and normalized stress (σ/E_o) is shown in Figure 6.19, and the contours are those of temperature. E_o is the modulus at 0 K, and is taken to be l GPa (estimated from initial modulus measurements at low temperatures). Also shown in Figure 6.19 are the measured isothermal data from which parameter values were obtained.

Another more conventional form of the map is shown in Figure 6.20, with axes of normalized stress σ/E_o and normalized temperature T/T_g, where T_g is the glass transition temperature, measured to be 248 K (Cheung, 1995). Contours of constant strain

www.EngineeringEBooksPdf.com

Table 6.1 Summary of the material parameters for bitumen B2

General material parameters
$E_o = 1 \times 10^9$ Pa
$T_g = 248$ K
$R = 8.314$ J mol^{-1} K^{-1}
EPM parameters
$\dot{\varepsilon}_e = 1.68 \times 10^{17}$ s^{-1}
$Q_e = 99 \times 10^3$ J mol^{-1}
$v_s = 3.45 \times 10^{-27}$ m^3
$v_p = 1.73 \times 10^{-27}$ m^3
$t_o = 1$ s
$m_e = -2/3$
MCM parameters
$\sigma_{oc} = 115 \times 10^3$ Pa
$n_c = 0.585$
$\eta_{oc} = 5.66 \times 10^{-34}$ Pa s
$Q_c = 228 \times 10^3$ J mol^{-1}
$c_1^s = 8.86$
$c_2^s = 101.6$
$T_s = 35.2\,^\circ$C
$\eta_s = 214 \times 10^3$ Pa s
PLM parameters
$\dot{\varepsilon}_{op} = 3.73 \times 10^{40}$ s^{-1}
$\sigma_{op} = 1 \times 10^6$ Pa
$n_p = 2.4$
$Q_p = 228 \times 10^3$ J mol^{-1}

From Cheung (1995).

rate $\dot{\varepsilon}$ are superimposed on the map. Because the first kind of map (Figure 6.19) does not extend to 0 K, it contains less information than the second kind of map (Figure 6.20) (Frost and Ashby, 1982).

The maps are divided into fields, within which a single deformation mechanism is dominant. The field boundaries are shown in heavy lines that are the loci of points at which two mechanisms have equal rates of deformation. The boundary between the elastic region and the Eyring plasticity regime in Figure 6.20 is chosen to be the contour at a strain rate of 10^{-12}/s, because in general it is difficult to make measurements at strain rates lower than this (Bin Ahmad and Ashby, 1988).

Two other forms of the map were constructed, shown in Figures 6.21 and 6.22, in which the viscosity is employed as one of the axes. In view of the concept of viscosity being frequently used in the study of bitumen rheology, such maps would have particular relevance in expressing the current understanding of the overall behavior of pure bitumens.

www.EngineeringEBooksPdf.com

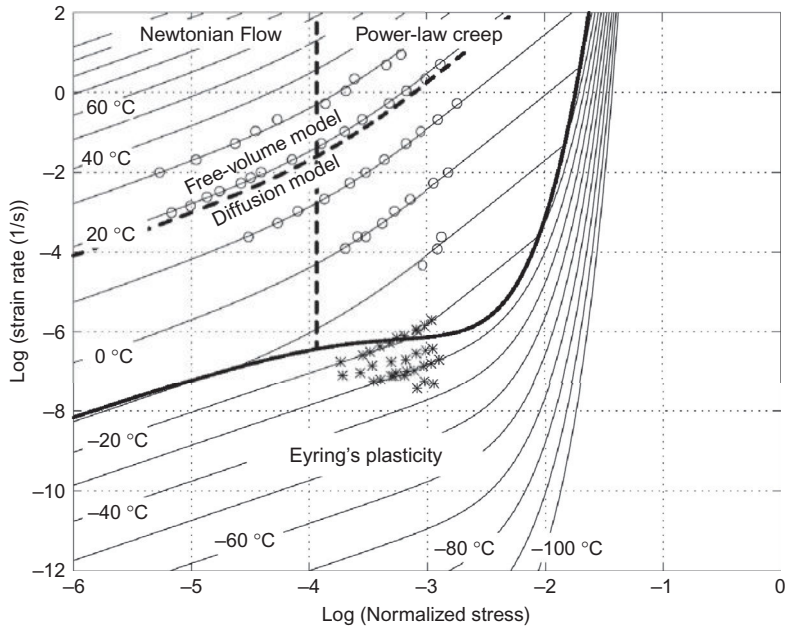


Figure 6.19 A strain-rate/stress deformation-mechanism map in tension for bitumen B2, reported by Cheung (1995).

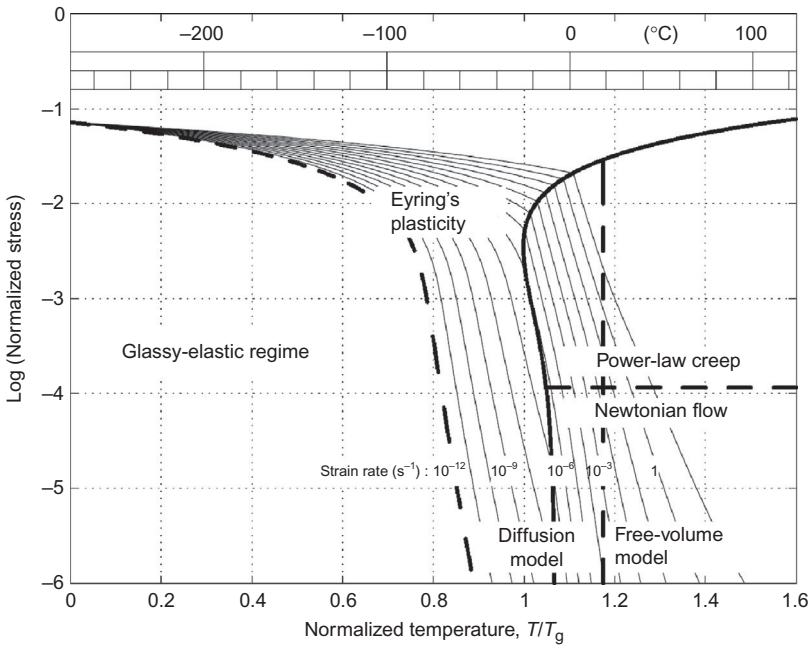


Figure 6.20 A stress/temperature deformation-mechanism map in tension for bitumen B2, reported by Cheung (1995).

www.EngineeringEBooksPdf.com

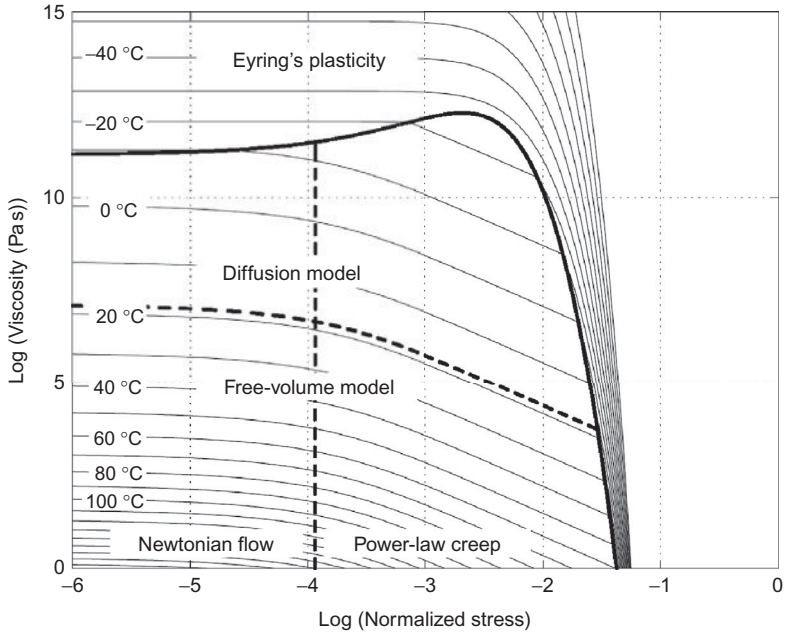


Figure 6.21 A viscosity/stress deformation-mechanism map in tension for bitumen B2, reported by Cheung (1995).

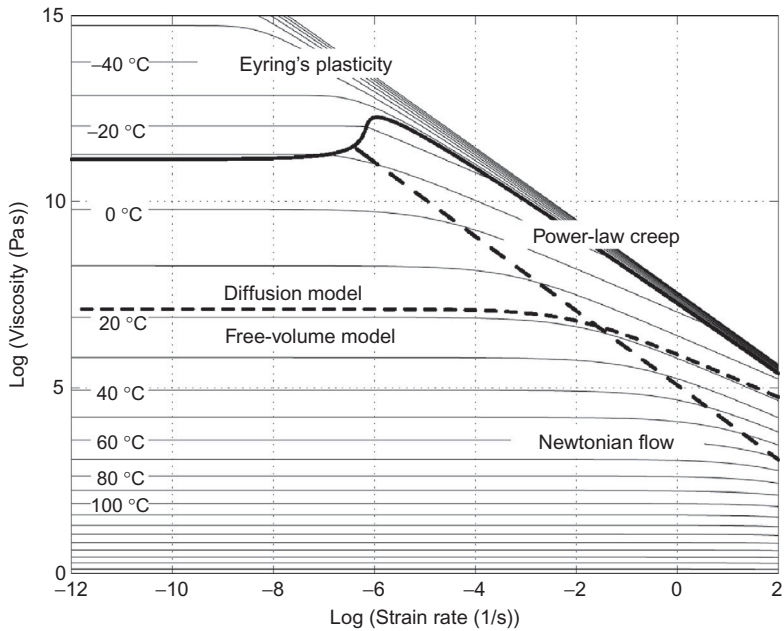


Figure 6.22 A viscosity/strain-rate deformation-mechanism map in tension for bitumen B2, reported by Cheung (1995).

www.EngineeringEBooksPdf.com

6.5.2 Features of the deformation-mechanism map

As can be seen in Figure 6.20, six regimes have been identified. At temperatures well below T_g, pure bitumen responds in a linear-elastic manner. Plastic behavior starts at roughly $0.8T_g$, which gives rise to linear behavior at low stresses. At temperatures beyond the glass transition, the complex colloidal nature of pure bitumen becomes important in affecting the viscous flow. At high stresses, it creeps in a power-law manner, whereas at low stresses, it is a Newtonian liquid. On the other hand, deformation is likely to be diffusion-controlled at temperatures in the vicinity of the glass transition, while at higher temperatures, it is controlled by the fractional free volume present in the molecular structure of the viscous liquid. No significant chemical changes occur up to $1.6T_g$.

When compared in this normalized form, the deformation-mechanism map for pure bitumen B2 is very similar to those for typical linear polymers (e.g., polymethylmethacrylate and polycarbonate) (Bin Ahmad and Ashby, 1988). The main differences are due to the ability of pure bitumen to develop a structural linkage, leading to a nonlinear flow region as well as the partial crystallization of fractions, which then leads to a diffusion-controlled region just beyond the glass transition.

Given specifications of the operating conditions under which a bitumen is to operate, the appropriate constitutive equation can easily be obtained from these deformation-mechanism maps. It is expected that similar deformation-mechanism maps would be obtained for other bitumens, with the main differences being due to variations in the 10 material parameters for the EPM and MCM listed in Table 6.1.

6.6 Conclusions

(i) Pure bitumens are complex polymeric materials, the molecular structure of which can be understood in terms of the colloidal model. The quantity of asphaltenes and the chemical nature of the maltenes are the two principal compositional aspects that influence the mechanical behavior of the bitumens.

(ii) The mechanical behavior of pure bitumens has been clarified and presented in the form of deformation-mechanism maps. Six regimes of deformation have been identified, all of which are described by physical models that are based on the current understanding of the molecular structure of pure bitumens. The behavior of the many varieties of pure bitumens encountered in practice are expected to be described by the same set of deformation mechanisms, with different values for the material parameters.

(iii) At temperatures above the glass transition, the deformation behavior of the test bitumens is linear viscous at low stress levels and power-law creep at high stress levels. The transition stress from linear to power-law behavior is a measure of the failure strength of the structural linkages in a bitumen. At temperatures in the vicinity of the glass transition, the temperature dependence of the deformation is described by the diffusion model. At temperatures well above the glass transition, it is described by the free-volume model. The steady-state behavior of bitumens above the glass transition is summarized by the MCM.

(iv) The MCM was found to apply accurately for 61 bitumens from a wide range of sources in the literature. The transition stress ranges from 0.1 to 0.5 MPa, and the creep exponent in the power-law regime ranges from 2 to 2.5. Over limited ranges of temperature and stress, the MCM is approximated satisfactorily by the PLM.

www.EngineeringEBooksPdf.com

(v) The asphaltene content, together with the chemical nature of the maltenes, has primary influence in determining the material parameters in the physical models of deformation. For those parameters that do not correlate with the asphaltene content, some other physical quantities that are representative of the microscopic structure of the material (for that particular deformation mechanism) are yet to be found.

(vi) The effects of aging upon the mechanical behavior of bitumens can be represented quantitatively in terms of the MCM. Aging increases the value of the limiting viscosity at small strain rate, and reduces the failure strength of the structural linkages, leading to an increase in the stress nonlinearities.

(vii) At temperatures below the glass transition, the steady-state and transient behavior of bitumen B2 are described by the EPM. The deformation behavior is pressure dependent in this regime, and the activation energy for the deformation is smaller than that for the deformation above the glass transition. However, more data for other bitumens below their glass transition is required for confirming the general applicability of the EPM.

References

Altegelt, K.H., Harle, O.L., 1975. The effect of asphaltenes on asphalt viscosity. Ind. Eng. Chem. Prod. Res. Dev. 14, 240–246.

Anderson, D.A., Christensen, D.W., et al., 1991. Physical properties of asphalt cement and the development of performance-related specifications. J. Assoc. Asphalt Paving Technol. 60, 437–532.

Anon, 1994. Binder Characterization and Evaluation, Volume 2, Physical Characterization. Strategic Highway Research Program, National Research Council, National Academy of Sciences, Washington DC, SHRP-A-369.

Bin Ahmad, Z., Ashby, M.F., 1988. Failure-mechanism maps for engineering polymers. J. Mater. Sci. 23, 2037–2050.

Brodnyan, J.G., 1958. Use of rheological and other data in asphalt engineering problems. Highw. Res. Bull. 192, 1–19.

Brodnyan, J.G., Gaskins, F.H., et al., 1960. The rheology of asphalt III. Dynamic mechanical properties of asphalt. Trans. Soc. Rheol. 4, 279–296.

Brown, A.B., Sparks, J.W., 1958. Viscoelastic properties of a penetration grade paving asphalt at winter temperature. J. Assoc. Asphalt Paving Technol. 27, 35–51.

Brule, B., Ramond, G., et al., 1986. Relationships between composition, structure and properties of road asphalts: state of research at the French Public Works Central Laboratory. Transport. Res. Rec. (TRB) 1096, 22–34.

Bukka, K., Miller, J.D., et al., 1991. Fractionation and characterization of Utah tar sand bitumens: influence of chemical composition on bitumen viscosity. Energy Fuels 5, 333–340.

Bukka, K., Miller, J.D., et al., 1994. The influence of carboxylic acid content on bitumen viscosity. Fuel 73, 257–268.

Cheung, C.Y., 1995. Mechanical behaviour of bitumens and bituminous mixes, PhD dissertation. Cambridge University Engineering Department.

Christensen, D.W., Anderson, D.A., 1992. Interpretation of dynamic mechanical test data for paving grade asphalt. J. Assoc. Asphalt Paving Technol. 61, 67–116.

Claudy, P., Letoffe, J.M., et al., 1991. Characterization of paving asphalts by differential scanning calorimetry. Fuel Sci. Technol. Int. 9 (1), 71–92.

www.EngineeringEBooksPdf.com

Cross, M.M., 1965. Rheology of non-Newtonian fluids: a new flow equation for pseudoplastic systems. J. Colloid Sci. 20, 417–437.
Cukierman, M., Lane, J.W., et al., 1973. High-temperature flow behaviour of glass-forming liquids: a free-volume interpretation. J. Chem. Phys. 59, 3639–3644.
Dickie, J.P., Yen, T.F., 1967. Macrostructures of the asphaltic fractions by various instrumental methods. Anal. Chem. 39 (14), 1847–1852.
Dickinson, E.J., Witt, H.P., 1969. The viscoelastic behaviour of confined thin films of bitumens in tension compression. Trans. Soc. Rheol. 13 (4), 485–511.
Dobson, G.R., 1969. The dynamic mechanical properties of bitumen. J. Assoc. Asphalt Paving Technol. 38, 123–139.
Dobson, G.R., 1972. On the development of rational specifcations for the rheological properties of bitumens. J. Inst. Pet. 58 (559), 14–24.
Ferry, J.D., 1980. Viscoelastic Properties of Polymers, 3rd ed. John Wiley and Sons, New York.
Ferworn, K.A., Mehrotra, A.K., et al., 1993. Measurement of asphaltene agglomeration from Cold Lake bitumen diluted with n-alkanes. Can. J. Chem. Eng. 71, 699–703.
Frost, H.J., Ashby, M.F., 1982. Deformation-Mechanism Maps: The Plasticity and Creep of Metals and Ceramics. Pergamon, Oxford.
Gaskins, F.H., Brodnyan, J.G., et al., 1960. The rheology of asphalt, II. Flow characteristics of asphalt. Trans. Soc. Rheol. 4 (435), 265–278.
Gilbert, D.G., Ashby, M.F., et al., 1986. Modulus maps for amorphous polymers. J. Mater. Sci. 21, 3194–3210.
Halstead, W.J., Rostler, F.S., et al., 1966. Properties of highway asphalts—part III, influence of chemical composition. J. Assoc. Asphalt Paving Technol. 35, 91–138.
Harvey, J.A.F., Cebon, D., 2005. Fracture tests on bitumen films. ASCE J. Mater. Civil Eng. 17 (1), 99–106.
Heithaus, J.J., 1962. Measurement and significance of asphaltene peptization. J. Inst. Pet. 48 (458), 45–53.
Heukelom, W., 1973. An improved method of characterizing asphaltic bitumens with the aid of their mechanical properties. J. Assoc. Asphalt Paving Technol. 42, 67–98.
Hirose, H., Tsuyuki, U., et al., 1963. Physical properties of asphalt at different stages of blowing process. Oyobutsur 32, 29–36.
Huynh, H.K., Khong, T.D., et al., 1978. Effect of molecular weight and composition on the glass transition temperatures of asphalts. Anal. Chem. 50 (7), 976–979.
Jongepier, R., Kuilman, B., 1969. Characteristics of the rheology of bitumens. J. Assoc. Asphalt Paving Technol. 38, 98–122.
Khong, T.D., Malhotra, S.L., et al., 1978a. Effect of shear rate, penetration and temperature on the viscosity of asphalts. J. Inst. Pet. Technol. Technical Report IP78-001.
Khong, T.D., Malhotra, S.L., et al., 1978b. A study of the glass transition temperature of asphalts and their viscosity. Rheol. Acta 17, 654–662.
Khong, T.D., Malhotra, S.L., et al., 1979. Rheological behaviour of asphalts. Rheol. Acta 18, 382–391.
Laughlin, W.T., Uhlmann, D.R., 1972. Viscous flow in simple organic liquids. J. Phys. Chem. 76 (16), 2317–2325.
Lee, A.R., Warren, J.B., 1940. The flow properties of asphaltic bitumens with reference to road behavior. J. Assoc. Asphalt Paving Technol. 11, 340–364.
Lethersich, W., 1942. The mechanical behaviour of bitumen. J. Soc. Chem. Ind., Trans. Commun. 61, 101–108.
Lian, H., Lin, J.R., et al., 1994. Peptization studies of asphaltene and solubility parameter spectra. Fuel 73, 423–428.

www.EngineeringEBooksPdf.com

Mack, C.J., 1932. Colloid chemistry of asphalts. J. Phys. Chem. 36, 2901–2914.
Majidzadeh, K., Schweyer, H.E., 1967. Viscoelastic response of asphalts in the vicinity of the glass transition point. J. Assoc. Asphalt Paving Technol. 36, 80–105.
Mehrotra, A.K., Svrcek, W.Y., 1986. Viscosity of compressed Athabasca bitumen. Can. J. Chem. Eng. 64, 844–847.
Mehrotra, A.K., Svrcek, W.Y., 1987. Viscosity of compressed Cold Lake bitumen. Can. J. Chem. Eng. 65, 672–675.
Moavenzadeh, F., Stander , Jr. R.R., 1967. Effect of aging on flow properties of asphalts. Highw. Res. Rec. 178, 1–29.
Nakajima, T., Tanobe, C., 1973. Determination of weak and very weak acids in bitumen and similar materials. J. Inst. Pet. 59 (569), 32–39.
Nellensteyn, F.J., 1924. The constitution of asphalt. J. Inst. Pet. Technol. 10, 311–325.
Noel, F., Corbett, L.W., 1970. A study of the crystalline phases in asphalts. J. Inst. Pet. 56 (551), 261–268.
Penny, R.K., Marriott, D.L., 1971. Design for Creep. Chapter 2, McGraw-Hill, New York.
Petersen, J.C., 1984. Chemical composition of asphalt as related to asphalt durability: state of the art. Transport. Res. Rec. 999, 13–30.
Petersen, J.C., 1986. Quantitative functional group analysis of asphalts using differential infrared spectrometry and selective chemical reactions—theory and application. Transport. Res. Rec. 1096, 1–11.
Pfeiffer, J.P., 1950. The Properties of Asphaltic Bitumen. Elsevier Publishing Company, Inc., New York, N.Y.
Puttagunta, V.R., Singh, B., et al., 1993. Correlation of bitumen viscosity with temperature and pressure. Can. J. Chem. Eng. 71, 447–450.
Reerink, H., 1973. Size and shape of asphaltene particles in relationship to high-temperature viscosity. Ind. Eng. Chem. Prod. Res. Dev. 12 (1), 82–88.
Rostler, F.S., White, R.M., 1962. Composition and changes in composition of highway asphalts 85–100 penetration grade. J. Assoc. Asphalt Paving Technol. 31, 271–327.
Ruth, B.E., Schweyer, H.E., 1981. Asphalt and mixture rheology as related to cracking of asphalt concrete pavements. In: Martinez, J.E. (Ed.), Proceedings of the Eighteenth Paving Conference. University of New Mexico, Albuquerque, pp. 44–82.
Saal, R.N.J., 1950a. Physical Properties of Asphaltic Bitumen. 1. Rheological Properties. Elsevier Publishing Company, Inc., New York.
Saal, R.N.J., 1950b. Physical Properties of Asphaltic Bitumen. 2. Surface Phenomena, Thermal and Electrical Properties. Elsevier Publishing Company, Inc., New York
Sakanone, S., 1963a. Nippon Kagaku Zasshi (Journal of Chemical Society of Japan) 84 (5), 384–392.
Sakanone, S., 1963b. Nippon Kagaku Zasshi (Journal of Chemical Society of Japan) 84 (6), 474–480.
Schmidt, R.J., Barrall, E.M., 1965. Asphalt transitions. J. Inst. Pet. 51 (497), 162–168.
Schmidt, J., Santucci, L.E., 1966. A practical method for determining the glass transition temperature of asphalts and calculation of their low temperature viscosities. J. Assoc. Asphalt Paving Technol. 35, 61–90.
Schweyer, H.E., 1974. Glass transition of asphalts under pressure. J. Test. Eval. 2 (1), 50–56.
Schweyer, H.E., Baxley, R.L., et al., 1977. Low-temperature rheology of asphalt cements—rheological background. Special technical publication 628: low-temperature properties of bituminous materials and compacted bituminous paving mixtures, American Society for Testing and Materials.

www.EngineeringEBooksPdf.com

Sisko, A.W., 1965. Determination and treatment of asphalt viscosity data. Highw. Res. Rec. 67, 27–37.
Sisko, A.W., Brunstrum, L.C., 1968. The rheology properties of asphalts in relation to durability and pavement performance. J. Assoc. Asphalt Paving Technol. 37, 448–475.
Storm, D.A., Sheu, E.Y., et al., 1993. Macrostructure of asphaltenes in vacuum residue by small-angle X-ray scattering. Fuel 72, 977–981.
Sybilski, D., 1993. Non-newtonian viscosity of polymer-modified bitumens. Mater. Struct. 26, 15–23.
van der Poel, C., 1954. A general system describing the visco-elastic properties of bitumens and its relation to routine test data. J. Appl. Chem. 4, 221–236.
Vinogradov, G.V., Isayev, A.I., et al., 1977. Rheological properties of road bitumens. Rheol. Acta 16, 266–281.
Wada, W., Hirose, H., 1960. Glass transition phenomena and rheological properties of petroleum asphalt. J. Phys. Soc. Jpn. 15 (10), 1885–1894.
Ward, I.M., 1971. Review: the yield behaviour of polymers. J. Mater. Sci. 6, 1397–1417.
Ward, I.M., 1983. Mechanical Properties of Solid Polymers. John Wiley and Sons, New York.
Welborn, J.Y., Halstead, W.J., 1959. Properties of highway asphaltsm. Part I, 85–100 penetration grade. J. Assoc. Asphalt Paving Technol. 28, 242–279.
Welborn, J.Y., Halstead, W.J., et al., 1960. Properties of highway asphalts. Part II, various grades. J. Assoc. Asphalt Paving Technol. 29, 216–245.
Welborn, J.Y., Oglio, E.R., et al., 1966. A study of viscosity-graded asphalt cements. J. Assoc. Asphalt Paving Technol. 35, 19–60.
Whiteoak, D., Read, J., et al., 2003. The Shell Bitumen Handbook, 5th ed., Shell Bitumen, UK.
Williams, M.L., Landel, R.F., et al., 1955. The temperature dependence of relaxation mechanisms in amorphous polymers and other glass-forming liquids. J. Am. Chem. Soc. 77, 3701–3707.
Winniford, R.S., 1960. The influence of asphalt composition on its rheology. Papers on road and paving materials (bituminous). American Society for Testing and Materials. Special technical publication 294.
Winniford, R.S., 1963. The evidence for association of asphaltenes in dilute solutions. J. Inst. Pet. 49 (475), 215–221.

www.EngineeringEBooksPdf.com

Damage healing in asphalt pavements: theory, mechanisms, measurement, and modeling

7

D.N. Little[1], *A. Bhasin*[2], *M.K. Darabi*[3]
[1]Texas A&M University, College Station, TX, USA; [2]The University of Texas at Austin, Austin, TX, USA; [3]University of Kansas, Lawrence, KS, USA

7.1 Introduction

This chapter presents the authors' ideas culminating from several decades of combined effort in the investigation of microdamage healing in asphaltic materials. The focus of this chapter is on the mechanisms responsible for healing in asphalt materials and, because the process of healing must focus on the component that provides the ability to heal, the major focus is placed on the binder and mastic. This chapter focuses on recent methods of characterizing the healing process in asphalt binders, mastics, and full mixtures. The chapter also addresses the importance of considering the impact of healing during cyclic loading with short rest periods as well as longer rest periods.

This chapter is presented in six sections. Following this introduction, Section 7.2 provides a succinct overview of the evidence of healing in asphaltic materials, including experiments, laboratory work, and field studies. Section 7.3 describes the authors' views regarding the mechanisms of microcrack healing and the influence of molecular morphology, with some validation from molecular dynamics computational modeling. Section 7.4 presents the authors' most recent work in measuring the intrinsic healing properties of asphalt binders, their relationship to fundamental surface properties of the binder (i.e., surface free energy), and the correlation between intrinsic healing and this fundamental property. Section 7.5 continues the description of methods to measure healing properties, this time for mastics and fine aggregate mixtures, using a continuum damage approach. Section 7.6 addresses important aspects regarding the impact of viscoelasticity in the healing process during cyclic loading and of the thermodynamics associated with the damage and microdamage healing processes, which must be understood in order to appreciate and grasp the mechanism and processes associated with healing. Section 7.6 also demonstrates how a healing evolution function in a continuum damage constitutive model of pavement behavior is necessary to predict damage.

Advances in Asphalt Materials. http://dx.doi.org/10.1016/B978-0-08-100269-8.00007-6
© 2015 Elsevier Ltd. All rights reserved.

www.EngineeringEBooksPdf.com

7.2 Evidence of healing in asphalt materials and in asphalt pavements

7.2.1 Laboratory studies

Experimental evidence of healing in asphalt mixtures dates back as far as 1967, when Bazin and Saunier developed automated test equipment to measure dynamic modulus and fatigue cracking. In their experiments, they also recognized that in addition to fatigue, healing was taking place, and that rest periods were prolonging life. Practitioners have understood the implications of healing as part of the fatigue damage process for decades, as evidenced by the inclusion of a healing shift factor along with the traffic wander factor in fatigue damage calculations in the Shell Pavement Design Manual (1978). Lytton et al. (1993) proposed a healing shift factor used to increase the dissipated energy of a load cycle after rest periods.

Little et al. (1987) found that healing was directly proportional to the number of longer-chained aliphatic molecules in saturates, and aliphatic side chains in the napthene aromatics and asphaltene generic fractions. They attempted to relate this morphology to molecular mobility and binder flow properties across fracture faces. Their findings seemed to be in keeping with Petersen's (1984) view, or peptization on the flow properties of asphalt.

Prapnnachari (1992) found evidence that the healing index—defined as the difference in pseudo dissipated energy before and after a rest period compared to that before the rest period—and relaxation spectra were related. Little and Prapnnachari (1991) discovered that the same methylene-to-methyl ratio (ratio of the number of methylene to methyl carbon atoms in independent aliphatic molecules or aliphatic chains attached to cycloalkanes or aromatic centers) that was determined by Kim et al. (1990) to be a significant indicator of healing index, was also indicative of the relaxation properties of the asphalt binders they evaluated. This is discussed further in Section 7.3.2. Prapnnachari used the Fourier transform infrared (FTIR) spectrometer to evaluate the response of different asphalt cement binders under tensile loading, and found aliphatic appendages or "side chains" to significantly influence the relaxation properties of the binders tested (Little et al., 1987).

Kim et al. (1990) used the elastic-viscoelastic correspondence principle to evaluate the hysteretic behavior of asphalt concrete. This principle states that one can reduce a viscoelastic (time-dependent) problem to an elastic (time-independent) problem merely by working in an approximately transformed domain and substituting elastic moduli. Using this approach, Kim et al. (1990) were able to evaluate fracture healing by increasing the amplitude of load until a significant level of damage was evident, as defined by the stress versus pseudostrain plots. Following rest periods, a significant change in the dissipated pseudostrain energy was noted as a result of "healing." The essence of the Kim et al. (1990) constitutive model is that it demonstrates that it is imperative to account for the effects of microdamage healing in order to predict fatigue damage. In addition, this constitutive model for fatigue damage illustrated an important response when the pseudostiffness versus load-cycles curve was inspected. Immediately following the rest period, a strong spike in pseudostiffness was observed.

www.EngineeringEBooksPdf.com

The strong pseudostiffness recovery diminished rapidly over the next few loading cycles. The cumulative, residual effect of pseudostiffness recovery, however, added significantly to the life of the test specimen over the time duration of the experiment. This residual recovery, "healing," was stronger if rest periods were applied before significant damage occurred, that is, early in the experiment. A final outcome was that the binder that exhibited the most significant healing in the Kim et al. (1990) study was consistent with the predictions from the Prapnnachari (1992) study with respect to binder characteristics.

The effect of healing during rest periods is also evident in the permanent deformation characteristics of asphalt mixtures. For example, Bhairampally et al. (2000) demonstrated that the inclusion of rest periods among compressive load cycles extended the time to tertiary damage, and that this extension depended on the type of asphalt binder. Their work concluded that the transition from the secondary phase to the tertiary phase of dynamic compressive creep was related to development and growth of microcracks. Further work by Song et al. (2005) showed this to be true using computer-assisted tomography. Bhairampally et al. (2000) demonstrated that the addition of a filler (in this case, hydrated lime) resulted in reduced rates of damage in the compressive mode of loading because of crack pinning (a damage-control mechanism), and accentuated the effect of healing of microcracks in the mastic. This is in keeping with previous research that demonstrates healing to be more beneficial at lower damage levels.

Little et al. (1987) demonstrated that rest periods (of 24-h duration) applied in traditional flexural beam-bending experiments increased the fatigue life by more than 100%, depending on the type of binder used.

7.2.2 Field studies

Some of the most convincing field data regarding healing were reported by Williams et al. (1998). They selected four pavement sections at the Turner Fairbanks accelerated load facility (ALF), considering a full factorial of two thicknesses: two asphalt layer types over a homogeneous subgrade. Surface wave measurements were made to assess pavement stiffnesses before, immediately after, and 24 h after loading passes. Regardless of the pavement type, the trend was that more healing (recovery of stiffness) was recorded closer to the centerline, suggesting that more fatigue damage results in a greater potential for and a greater amount of microdamage healing. Williams et al. (1998) reported other convincing support for healing using surface wave analysis of pavements at Mn/ROAD pavement sections and on US Highway 70 in North Carolina using designed experiments.

Nishizawa et al. (1997), using four thick asphalt pavements, demonstrated that fatigue cracking did not occur because healing effects at the low-strain and low-damage levels compensated for (offset) crack growth.

The literature holds other very important contributions on the subject of healing during the fatigue damage process in asphalt pavements. This chapter does not attempt to provide an exhaustive review of the literature on this subject, but rather cites work related to the concepts developed in Sections 7.3 through 7.6. For an excellent and

www.EngineeringEBooksPdf.com

thorough review of the literature, the reader is referred to the work of Qiu (2011). His PhD dissertation provides perhaps the most exhaustive and thorough review of the pertinent literature on this subject.

7.3 Hypothesized mechanism(s) of healing in asphalt materials

This section presents a hypothesized mechanism of healing at a micrometer length scale. The proposed mechanism is supported by mechanics-based and/or phenomenological models that can be used to mathematically represent the different processes associated with the mechanism. The second half of this section presents results from experimental and computational models that support the hypothesized mechanism.

7.3.1 Healing: reversal of the fracture process

Healing is generally regarded as the reversal of microdamage within the material that occurs when the external loads that cause microdamage are removed or significantly reduced. It is therefore natural that for any hypothesis to explain the healing process, it must start from an understanding of the processes that cause microdamage.

Depending on the length scale of interest, different mechanisms can be used to explain the evolution of microdamage within the material. This is particularly true for materials such as asphalt binders that are complex composites of different organic molecules. At a molecular or slightly higher length scale, microdamage can be regarded as softening of the material due to the action of external loads. Such softening is driven by the rearrangement of different molecular species or components within the material (Schmets et al., 2009; Jahangir et al., 2015). This mechanism and concomitant softening of the material can also be used to explain what is commonly referred to as the thixotropic effect. One school of thought is that the thixotropic effect must be accounted for separately from damage evolution (Shan et al., 2010). On the other hand, such molecular reorganization and softening can be regarded as a precursor to the more commonly recognized form of microdamage due to microcracks or nanocracks at a slightly larger length scale. In summary, microdamage can be regarded as a process that (1) initiates in the form of molecular reorganization, resulting in a loss of stiffness and (2) is followed by formation and growth of microcracks, and also results in a loss of stiffness.

The view of microdamage as a two-step process can be used to hypothesize a mechanism of self-healing in an asphalt binder as a two-step process starting backward from a load-induced microcrack. More specifically, from this viewpoint, healing would entail reversal of crack openings (referred to as crack closing or *crack wetting*), followed by strength gain across the wetted interface (referred to as *intrinsic healing*). From an engineering and material characterization point of view, one is ultimately interested in the magnitude of healing (or damage reversal) as a function of time. This magnitude, $H(t)$, can then be mathematically modeled based on the *rate of crack*

www.EngineeringEBooksPdf.com

wetting, $W(t)$, and rate of intrinsic healing $I_h(t)$. Wool and O'Connor (1981) indicated that because both wetting and intrinsic healing are simultaneous and time-dependent processes, the overall healing process can be modeled using a convolution integral:

$$H(t) = \int_{\tau=-\infty}^{\tau=t} I_h(t-\tau)\frac{\partial W(\tau)}{\partial \tau}\mathrm{d}\tau \tag{7.1}$$

where t is time and τ is a dummy variable.

The lower limit of negative infinity in Equation (7.1) has special significance: it is used to describe healing even when there is microdamage at the crack tip that has not yet advanced to the crack opening stage. This is achieved by considering that the crack is closed and partially healed at $t = 0$. The process of modeling and ultimately measuring factors that dictate self-healing can now be reduced to two issues: (i) understanding the mechanism of wetting and developing an appropriate mathematical model for the same and (ii) understanding the intrinsic healing process and developing an appropriate mathematical model for the same.

7.3.1.1 Crack wetting

Crack wetting can be explained and modeled as a function of fundamental material properties by investigating this problem from a contact mechanics perspective. The rate of autonomous crack wetting in the absence of external forces, as is the case with the self-healing process, can be described by considering the intermolecular surface forces just beyond the point of contact of the two surfaces, as well as the shape change due to these forces. Maugis and Barquins (1983) and Muller et al. (1979) developed such models; the former assumed constant intermolecular surface forces within the cohesive zone beyond the crack tip that dropped to zero beyond this zone (referred to as the Dugdale model), and the latter assumed a more realistic Lennard-Jones type potential to describe the interfacial surface forces beyond the crack tip. Subsequently, Schapery (1989) demonstrated that *although the surface energy may be small, over a long period of time it can produce considerable deformation and contact area growth*. Schapery used the modified correspondence principles to apply elastic solutions to viscoelastic materials and describe the rate of autonomous crack wetting, $\dot{a}$, as a function of fundamental material properties (the exact mathematical form is not required to make the point):

$$\dot{a} = fn(\beta, \sigma_b, \gamma, D_0, D_1, m) \tag{7.2}$$

In this model, the terms D_0, D_1, and m are parameters of the creep compliance function that follow the power law (i.e., $D(t) = D_0 + D_1 t^m$) and can be easily measured for the material of interest; β is the length of the cohesive zone or length over which the intermolecular surface forces are effective; σ_b is the Dugdale stress, or in this case a constant bonding stress, that is assumed to act over the healing process zone and drops to zero beyond this zone; and γ is the surface free energy. The length of the cohesive or healing process zone β is a function of the crack-tip geometry and bonding stress.

www.EngineeringEBooksPdf.com

Schapery (1989) expressed β as a function of σ_b and the time-dependent stress intensity factor K_1, for a sharp crack tip. Hui et al. (2001) expressed β as a function of σ_b for the geometry of two spheres in contact.

7.3.1.2 Intrinsic healing

The second issue is to understand the relationship between the intrinsic healing function and fundamental material properties. The intrinsic healing function is a dimensionless quantity that represents the rate at which a wetted crack interface gains strength or stiffness relative to the undamaged strength or stiffness of the material. The most general form for the intrinsic healing function $I_h(t)$ represents the cumulative effect of (i) instantaneous strength gain due to interfacial adhesion (or, more appropriately, cohesion) at the crack interface due to its surface free energy γ and (ii) time-dependent strength gain due to restructuring of molecules across the interface to achieve a configuration and strength similar to that of the undamaged material. Explicit modeling of molecular restructuring requires that the self-diffusivities of the different molecules and detailed molecular structures be known well in advance. Preliminary work in this direction is presented in Section 7.3.3. Additional work related to the development of such explicit models is underway by other researchers, Zhang and Greenfield (2007). In the absence of an explicit model, a phenomenological model can also be used to represent the intrinsic healing function. For example, Bommavaram et al. (2009) used the Avrami form to express the intrinsic healing function:

$$I_h(t) = I_0 + (1 - I_0)\left(1 - e^{-qt^r}\right) \tag{7.3}$$

In Equation (7.3), I_0 is related to the surface free energy γ, q is a temperature-dependent material constant, and r is a material constant. Bommavaram et al. (2009) were able to determine these parameters using experiments that involved complete instantaneous wetting of two artificially created crack surfaces. These experiments are discussed in Section 7.4 of this chapter.

In summary, the rate of crack wetting is dictated by material properties such as the creep compliance of the material, surface free energy of the binder, and geometric features of the microcrack. Also, the rate of intrinsic healing is dictated by the rate at which molecular restructuring occurs across a wetted crack interface. This is in turn dictated by the self-diffusivity and mobility of the molecules. Figure 7.1 illustrates this

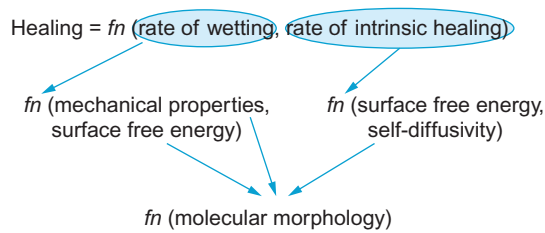


Figure 7.1 Interrelationship between material properties and the healing model.

www.EngineeringEBooksPdf.com

summary. Section 7.3.3 provides evidence for the relationship among molecular morphology, self-diffusivity, and rate of healing, in support of the hypothesized healing mechanism. In addition, Section 7.4 of this chapter provides evidence for the relationship between surface free energy and self-healing of asphalt binders.

7.3.2 Influence of molecular morphology: experimental evidence

Based on the mechanism of healing described in the preceding section, one might expect that asphalt binders containing more molecules with longer chains and fewer branches would have greater mobility and facilitate faster restructuring compared to asphalt binders containing fewer molecules with longer chains and greater branching. This is also based on the reptation model proposed by de Gennes (1971), which indicated that molecular mobility is important in facilitating molecular movement across crack interfaces and strength gain to promote healing. Kim et al. (1990) devised and reported the results from an experiment that evaluated this aspect of the healing hypothesis. They selected three asphalt binders with different chemical composition and measured their healing characteristics.

Kim et al. (1990) fabricated identical asphalt-mixture beam specimens using the three different asphalt binders. They then used a notched-beam fatigue test with intermediate rest periods to measure the healing characteristics of the different asphalt mixtures. They quantified healing in terms of an index based on the relative increase in the dissipated pseudostrain energy immediately after the rest period relative to the dissipated pseudostrain energy just before the rest period.

They proposed the use of two parameters to serve as approximate indicators of molecular mobility (or chain length and branching) related to self-healing: the methylene-to-methyl-hydrocarbon (MMHC) ratio and the methylene-to-methyl-group (CH_2/CH_3) ratio. The MMHC ratio identifies the amount of branching in chains, and the CH_2/CH_3 ratio is indicative of the length of chains. These parameters can be estimated using FTIR spectra. Kim et al. (1990) demonstrated a good correlation between these parameters and the healing index for the selected asphalt binders. Figure 7.2 illustrates a summary of the results reported by Kim et al. (1990). These results demonstrate that the mobility of asphalt molecules is correlated to the rate of self-healing, which is consistent with the hypothesized healing mechanism described in the previous subsection.

7.3.3 Influence of molecular morphology: evidence based on computational modeling

Bhasin et al. (2011) conducted molecular simulations for model asphalt binders created using an ensemble of three different types of molecules, each representing a constituent species (asphaltene, napthene aromatic, and saturates), following the previous work of Zhang and Greenfield (2007). Bhasin et al. (2011) created different asphalt binders by varying the relative proportions of saturates, napthene aromatics, and asphaltenes, as well as by varying the chain length of the molecule used to represent

www.EngineeringEBooksPdf.com

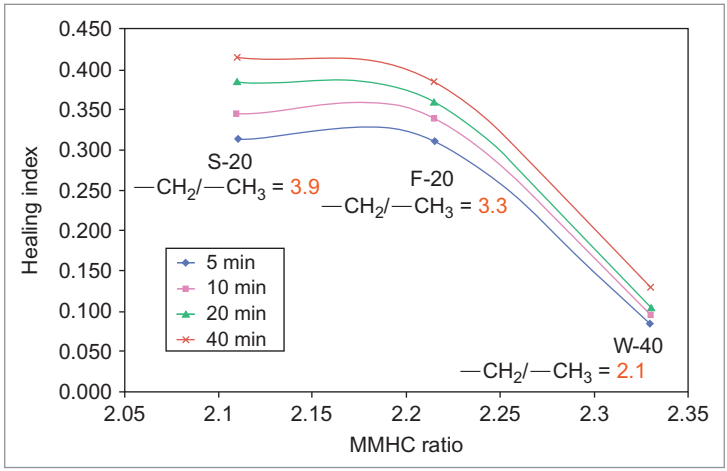


Figure 7.2 Relationship between healing and molecular characteristics of asphalt binders. Adapted from Kim et al. (1990).

the saturates. Structures for the asphaltene and naphthene aromatic molecules were represented using model compounds; these structures were not varied. Table 7.1 presents the composition of the four different binders. The different binders were created to obtain different chain lengths and branching (CH_2/CH_3 and MMHC ratios), and consequently, different self-diffusivity of molecules.

Bhasin et al. (2011) used a commercial software, Materials Studio® by Accelrys Inc., to conduct a molecular dynamics simulation of molecular movement across a simulated crack interface. Figure 7.3 illustrates the layered structure that was used to determine diffusivity by simulating dynamics at 298°K for 50 ps, and the same structure after being subjected to dynamics simulation for 100 ps at 873°K.

Similar to Kim et al. (1990), Bhasin et al. then tried to determine the relationship between molecular length and branching to the self-diffusivity. Because the exact molecular structures were known for the molecular dynamics simulations, the CH_2/CH_3 and MMHC parameters could be directly computed by counting the number

Table 7.1 Composition of asphalt binders used in molecular dynamic simulations

Number	Saturates chain length	Approximate proportions of asphaltene, napthene, and saturates
1	*n*-C23	20–40–40
2		20–20–60
3	*n*-C33	20–40–40
4		20–20–60

www.EngineeringEBooksPdf.com

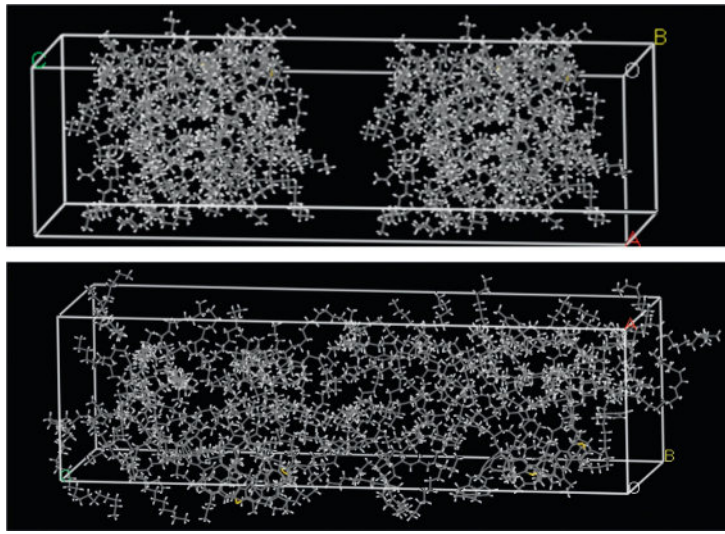


Figure 7.3 Layered structure with an artificial crack interface used for molecular simulations (top) and after being subjected to accelerated healing at elevated temperatures (bottom).

of methylene and methyl groups. Figure 7.4 illustrates that there is a good correlation between chain length and branching of molecules to the self-diffusivity of molecules at the crack interface, and consequently on the healing properties of the binder. The findings based on molecular simulations were consistent with the findings reported by Kim et al. (1990) based on experimental evidence; that is, binders with a molecular composition that result in greater overall mobility tend to heal faster. This, of course, is an extreme simplification of molecular mobility. However, it provides instructive insight into the hypothesis that indeed molecular morphology impacts molecular mobility, and hence impacts healing.

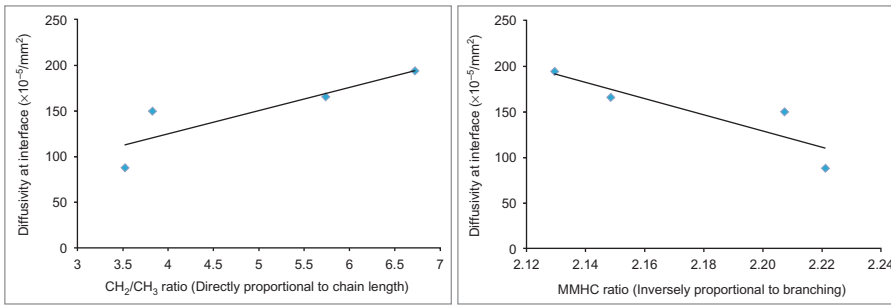


Figure 7.4 Relationship between diffusivity of binder molecules to chain length (left) and branching (right).

www.EngineeringEBooksPdf.com

7.4 Healing in asphalt binders

As discussed in Section 7.3, healing in asphalt binders can be regarded as a two-step process that occurs concurrently in time: (1) wetting of the cracked interface, where the rate of wetting is governed by the surface free energy of the binder, creep compliance of the binder, and geometry of the microcrack and (2) intrinsic healing composed of instantaneous and time-dependent strength gain across the cracked interface. The instantaneous strength gain is hypothesized to be related to the surface free energy of the binder, while the rate-dependent strength gain is related to the mobility of asphalt binder molecules, dictated by their size and self-diffusivity. This section addresses one way of measuring intrinsic healing of different asphalt binders, as well as experimental evidence that supports the hypothesis that the instantaneous component of intrinsic healing is correlated to the surface free energy of asphalt binders.

7.4.1 Measuring intrinsic healing in asphalt binders

Bommavaram et al. (2009) developed a method to measure the intrinsic healing of asphalt binders using the DSR. The test method was subsequently refined by Bhasin et al. (2011) and also used by Qiu (2011) to evaluate healing characteristics of different binders. In fact, Bahia and coworkers (Rad et al., 2014) have recently adapted the same procedure to quantitatively estimate the interdiffusion between virgin binders and aged binders from recycled asphalt pavement as a function of time and temperature. The test method is briefly described here, although the details can be found in the literature (Bhasin et al., 2011; Bommavaram et al., 2009). Readers are encouraged to review the detailed procedure available in the literature to avoid measuring artifacts. Before briefly describing this test method and typical results, it is important to comment on the significance of measuring the intrinsic healing of asphalt binders. Recall that overall healing in an asphalt composite is a function of the extent of damage preceding the rest period (length and geometry of the crack tip and fracture process zone) as well as the inherent properties of the binder. However, the intrinsic healing component is exclusively dependent on the material properties of the binder.

Therefore, for researchers and engineers interested in comparing the healing characteristics among binders (or influence of chemical additives on healing characteristics), it is more beneficial and meaningful to measure the intrinsic healing characteristics of the binder.

In order to measure the intrinsic healing rate of asphalt binders, the parallel plate geometry is used with the DSR (25–40-mm diameter). A 3.5-mm thick bitumen specimen is then affixed onto each one of the two end plates of the DSR. The surfaces of the two specimens are then brought into contact with each other, and the DSR is programmed to adjust and maintain a small compressive normal force. The DSR is then programmed to measure and record the dynamic shear modulus (G^*) at different points in time (typically every 2–5 min) over a period of 1 h. The measurements are made by applying a limited number of load cycles with very small strain amplitudes in order to minimize disturbance to the interface. The same procedure—control

www.EngineeringEBooksPdf.com

test—is then repeated using a single specimen with twice the thickness (the identical size of the composite, two-piece sample). The change in the shear modulus of the two-piece specimen is then normalized with respect to the single specimen to obtain a dimensionless ratio that is representative of the percentage of healing (Figure 7.5).

It is important to emphasize the relevance of the above test protocol to the healing framework described in the previous section. Healing between two bitumen surfaces in contact with each other is modeled by the convolution of wetting and intrinsic healing or strength gain over time (Equation 7.4). The objective of this test method is to obtain the healing function described in Equation (7.5). By bringing the two bitumen surfaces in intimate contact with each other within a short duration of time, the condition of instantaneous wetting is achieved. In this case, the wetting distribution function reduces to a dirac delta function:

$$\frac{\mathrm{d}\phi(\tau)}{\mathrm{d}\tau} = \delta(\tau) \tag{7.4}$$

As a result, the healing function reduces to the following form:

$$H(t) = I_{\mathrm{h}}(t) \tag{7.5}$$

In other words, the macroscopic healing function measured over time can be used to obtain the healing function $R_{\mathrm{h}}(t)$. The procedure assumes that randomization of molecules across the wetted interface during the first few seconds of the test is minimal and is accommodated in the instantaneous healing parameter of the healing function.

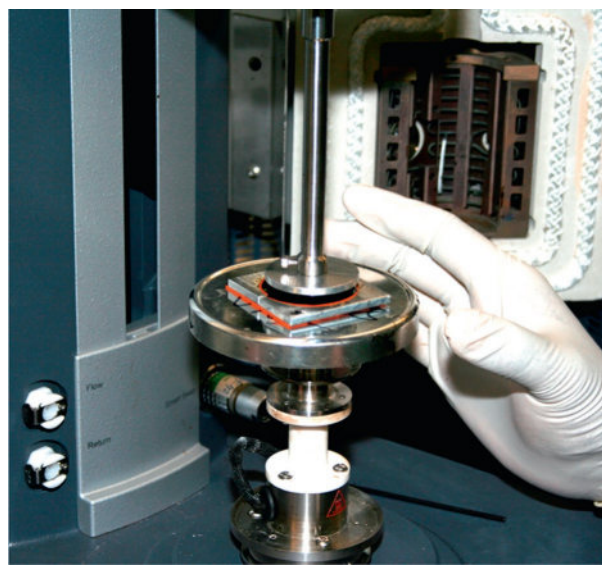


Figure 7.5 Photograph of a typical setup used to measure intrinsic healing of asphalt binders.

www.EngineeringEBooksPdf.com

This assumption may not be valid if the test is conducted at elevated temperatures that entail significant randomization across the interface within short time periods. Also, note that the bitumen specimens are prepared by pouring liquid binder and gradually allowing it to cool at room temperature. This process ensures that the surfaces of the bitumen that come into contact with each other are smooth and free from any irregularities, to facilitate immediate wetting. A trimming process was also added to obtain a smooth, flat surface (Bhasin et al., 2011).

As discussed previously, a modified form of the Avrami equation was used to model the intrinsic healing behavior of an asphalt binder. Equation (7.3) represents the sum effect of (a) instantaneous strength gain due to interfacial cohesion at the crack interface, represented by the parameter I_0 and (b) time-dependent strength gain due to rearrangement and randomization of molecules across the crack interface, represented by $(1-I_0)\left(1-e^{-qt^r}\right)$. The parameter q is a temperature-dependent material constant. The parameter r is a material constant that is used to represent the nature of internal transformation in metals or polymers. Traditionally, this parameter has been assigned an integer value between 1 and 4 for metals, whereas in the case of polymers, the value of r can be a noninteger depending on the types of changes that may occur within the internal structure of the polymer. Based on this rationale, Bommavaram et al. (2009) treated the parameter q as a temperature-dependent material constant, and the parameter r as a material constant. Figure 7.6 illustrates typical results for the intrinsic healing characteristics of three different unaged asphalt binders measured at the same temperature (25 °C). Figure 7.7 illustrates typical intrinsic healing characteristics of another asphalt binder at different temperatures. In summary, it was demonstrated that it is possible to get an approximate measurement for the intrinsic healing characteristics of different asphalt binders, and also that the rate of intrinsic healing increased with an increase in temperature and decreased with aging. These findings are consistent with the previously discussed healing hypothesis, because

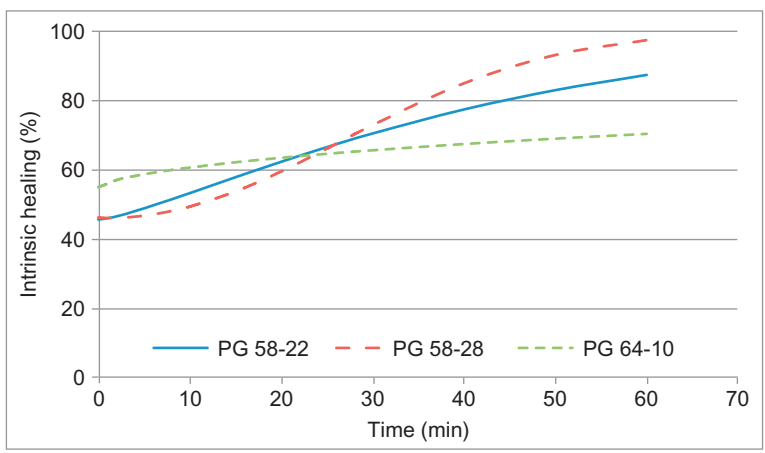


Figure 7.6 Typical results showing the differences in intrinsic healing of different asphalt binders.

www.EngineeringEBooksPdf.com

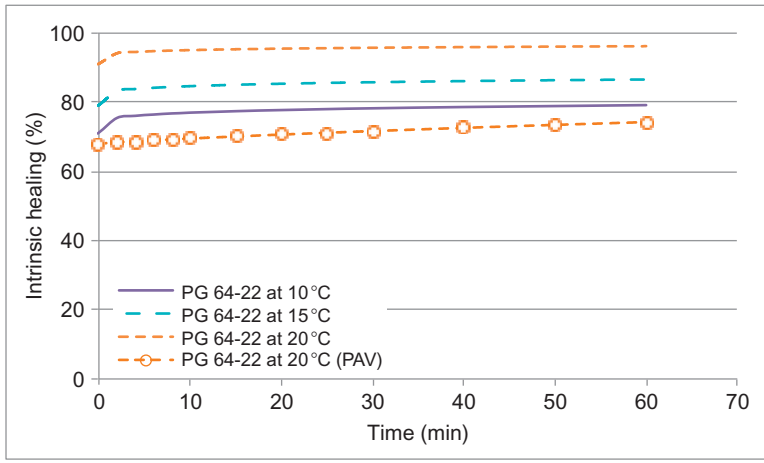


Figure 7.7 Typical results showing the differences in intrinsic healing of an asphalt binder at different temperatures and also due to aging (all binders were RTFO-aged except the one marked PAV).

higher temperature increases molecular mobility, and aging results in more polar molecules that agglomerate to form larger associated entities with lower mobility.

7.4.2 Role of surface free energy in instantaneous intrinsic healing of asphalt binders

As discussed previously, the parameter I_0 reflects the effect of instantaneous healing that is due to the interfacial cohesion between the crack surfaces. In an effort to partially validate this part of the healing hypothesis, as well as the use of the DSR to measure the intrinsic healing of asphalt binders as described in the previous subsection, Bhasin et al. (2008) compared the values of I_0 measured using the DSR-based test method to the work of cohesion W_C for asphalt binders selected from the Strategic Highway Research Program (SHRP) Materials Reference Library, denoted by abbreviations AAD, AAM, and ABD (Jones, 1993). The work of cohesion was calculated based on the surface tension of the asphalt binders, measured using the Wilhelmy plate method. Figure 7.8 compares the values of I_0 to the value of the work of cohesion for three different asphalt binders. As expected, the rank order of the parameter I_0 for the three asphalt binders follows the same order as the work of cohesion or surface free energy determined using the Wilhelmy plate method. Although the data are limited, they support the consistency of the analytical framework and test methods used to obtain the material properties related to healing.

Another approach to partially evaluate the validity of the proposed healing mechanism and the DSR-based test method was to compare the intrinsic healing characteristics of the binders measured using the DSR-based test method to the overall healing

www.EngineeringEBooksPdf.com

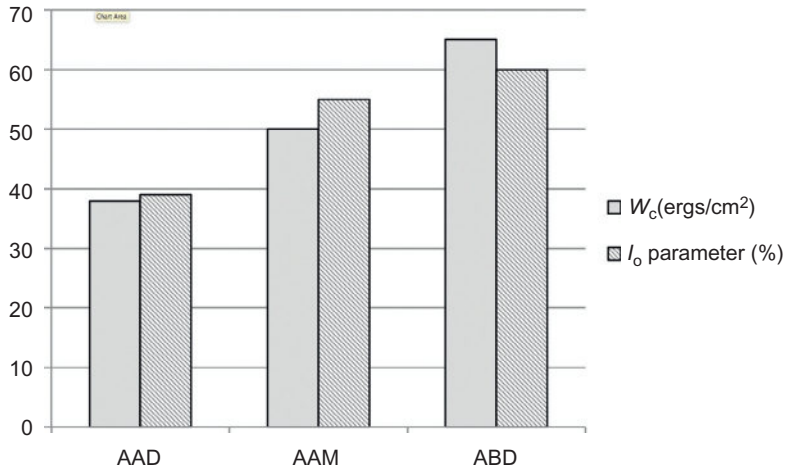


Figure 7.8 Typical results showing that the rank order of work of cohesion is similar to the rank order of the instantaneous intrinsic healing parameter using the DSR test.

of composites produced using these binders. To this end, Little et al. (2001) conducted fatigue tests with and without rest periods on cylindrical test specimens of fine aggregate matrix (FAM). The test specimens were approximately 50 mm tall and 12.5 mm in diameter and comprised asphalt binders mixed with fine aggregates (material smaller than 1.18 mm in nominal diameter). The fatigue test was conducted by fixing one end of the FAM specimen and applying a torsional shear at the other end. A strain amplitude of 0.2% was applied using a sinusoidal wave form at 10 Hz until specimen failure occurred. The stress response, along with shear modulus and phase angle, was continuously recorded throughout the test. The fatigue life of the FAM specimen was quantified using the number of load cycles to failure as well as a crack index parameter derived using a fracture mechanics-based approach and the concept of dissipated pseudostrain energy.

In order to quantify healing for different materials, nine rest periods of 4 min each during the cyclic test were introduced. The rest periods were introduced after cycles that correspond to 2.5%, 5%, 10%, 15%, 20%, 25%, 30%, 40%, and 50% of the fatigue life value for that particular material, measured without any rest period. When rest periods were applied, the crack index parameter was computed using the dissipated pseudostrain energy, measured immediately after the rest period. By comparing this parameter from the test with rest periods to the corresponding value of the parameter from tests without any rest period, it was possible to quantify the influence of healing. A relative decrease in this parameter, which would be associated with positive healing, was then used to quantify the healing potential for each material. Further details of this methodology and typical results due to incorporation of rest periods can be found in Little et al. (2006).

As discussed, both wetting and intrinsic healing functions are required to accurately predict the magnitude of healing in the asphalt materials. While research on

www.EngineeringEBooksPdf.com

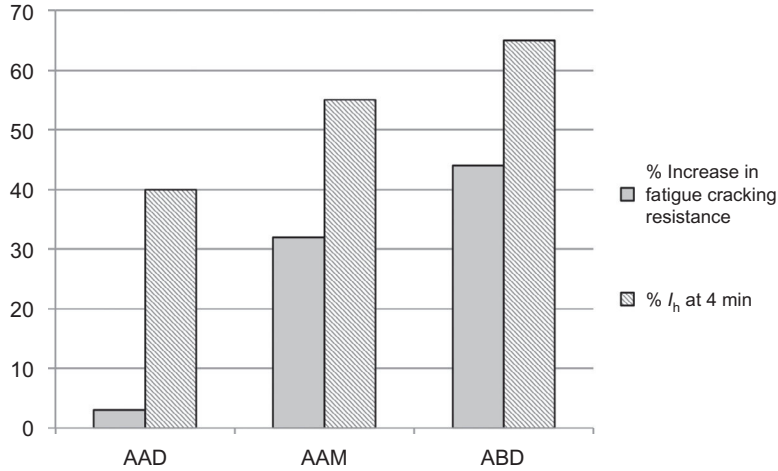


Figure 7.9 Comparison of the intrinsic healing measured using the DSR-based test method to the healing measured for asphalt composites (FAM).

the measurement of parameters related to wetting is ongoing, the intrinsic healing characteristics of the different binders used to produce the FAM specimens can be obtained using the DSR-based test method. Notwithstanding limitations of the approach due to the lack of knowledge of certain wetting parameters (e.g., bonding stress and length of healing process zone), Little et al. (2006) compared the percentage of intrinsic healing at 4 min for each binder to the healing measured using the FAM composites. Figure 7.9 illustrates one set of results from such a comparison. Little et al. (2006) reported that, in general, the rank order of the mixes in terms of the effect of healing on fatigue cracking life was similar to the order based on or predicted by the intrinsic healing function. However, they also commented that parameters that affect the healing function should be considered and used with the general convolution form to get a better prediction of overall healing based on material properties and level of damage.

In summary, the rate of crack wetting is dictated by crack size, crack geometry, asphalt binder properties, and viscoelastic properties of the composite. On the other hand, the rate of strength gain or intrinsic healing is dictated solely by the properties of the asphalt binder. This mechanism can be modeled using a phenomenological model, and the parameters for such a model can be obtained using the DSR-based test method. This test method can also be used to evaluate the intrinsic healing properties of asphalt binders at different temperatures and aging conditions. The advantage of this approach is that it allows one to compare the intrinsic healing properties of different asphalt binders under well-controlled laboratory conditions, without bringing into context the rate of wetting. The former (intrinsic healing) is dictated by the properties of the binder, whereas the latter (wetting) is influenced by both the rheology of the binder and the properties of the mixture (geometry of the binder in the vicinity of the crack) and damage history.

www.EngineeringEBooksPdf.com

7.5 Measuring healing in asphalt mixtures

Section 7.3 of this chapter reviews the micromechanical framework used to characterize healing in asphalt binders. This framework may be considered analogous to fracture mechanics, wherein the interest is primarily on modeling and understanding the relationship between material properties and the growth or healing of a single microcrack. The focus of this section is to present a framework for quantifying the healing in asphalt composites that is analogous to a continuum damage approach. In other words, characterization of growth and self-healing of individual cracks is not the focus; rather, the effect of multiple microcracks' growing and self-healing is averaged over a representative volume.

Section 7.2 of this chapter referenced the findings from several different studies conducted to evaluate the healing characteristics of asphalt composites. In most cases, the approach used in these studies was to quantify healing based on the change in stiffness or a related parameter as a function of one or more rest periods introduced during a fatigue test. Examples of parameters used are the relative increase in complex modulus, relative change in dissipated energy, and relative increase in the number of load cycles to failure. This approach is extremely useful and provides a direct method to compare the relative ability of different asphalt mixes to heal. However, a limitation of this approach is that in most cases, the healing characteristics are defined by the specific test configuration (e.g., duration of the rest period, mode of loading, loading frequency or amplitude). This is analogous to the limitation encountered when fatigue cracking is characterized in terms of the number of cycles to failure or a similar parameter. One approach to overcome this limitation is to use the work potential or viscoelastic continuum damage (VECD) theory.

7.5.1 Continuum approach to quantify healing

Several factors must be considered in developing a continuum-based model to quantify the healing characteristics of an asphalt composite. Specifically, a continuum model and concomitant test method for healing must be capable of obtaining healing characteristics that are:

1. Independent of the testing conditions that are used to induce damage prior to the rest period associated with healing (e.g., stress- or strain-controlled mode of loading, amplitude of loading, frequency of loading).
2. Sensitive to the duration of the rest period during which healing occurs.
3. Sensitive to the level of damage that precedes the rest period.

One approach to accomplish the first requirement is to use work potential theory as a starting point for quantifying the damage evolution in the asphalt composite. Work potential theory, developed by Schapery, is a continuum damage theory that describes the mechanical behavior of an elastic material that experiences incremental damage, using a damage evolution law derived from the principles of thermodynamics. In summary, the theory is based on the consideration that any mechanical, chemical, or thermodynamic process that changes the material state from one state (characterized by the state variable S, stress, and strain) to another requires the same amount of strain energy,

www.EngineeringEBooksPdf.com

irrespective of the path. Work potential theory or elastic continuum damage theory can be extended to describe damage evolution (as in the case of crack nucleation and growth) in viscoelastic materials by using the correspondence principles and a damage evolution law. In fact, Kim and coworkers provide significant evidence demonstrating that this approach can be used to characterize fatigue damage in an asphalt concrete mixture, independent of the specific mode of loading or test conditions, and can potentially be extended to characterize the effect of healing. This approach, referred to as the VECD model, is briefly described in the paragraphs below.

The VECD theory relates the reduction in pseudostiffness C of a specimen subject to external (cyclic or continuous) loads to an internal state variable, S,which represents the state of damage within the specimen. Kim and coworkers (Daniel and Kim, 2002; Kim et al., 1998; Park et al., 1996; Underwood et al., 2010) demonstrated that this damage evolution relationship is unique for a given asphalt mixture and is also independent of the testing conditions (e.g., mode of loading, frequency, amplitude). In other words, the $C-S$ relationship is a true material property that is independent of the testing conditions. In order to obtain this relationship, cyclic or monotonic loading is applied to the test specimens using two or more different loading conditions. One of the three modified correspondence principles is used to transform the time-dependent stress–strain data into a pseudodomain that corresponds to a hypothetical elastic material; based on the theoretical foundation and past results, correspondence principle II (CP-II) is typically found to be more appropriate. The transformations are obtained as

$$\sigma^R = \sigma(t) \tag{7.6}$$

$$\epsilon^R = \frac{1}{E_R}\int_0^t E(t-\tau)\frac{\partial \epsilon(\tau)}{\partial \tau}\mathrm{d}\tau \tag{7.7}$$

In Equations (7.6) and (7.7), $\sigma(t)$ and $\epsilon(t)$ are the time-dependent stress and strain history associated with the viscoelastic material, and the superscript R denotes the transformed stress in the pseudoelastic domain. The term E_R is the reference elastic modulus or the modulus for the pseudoelastic domain (typically taken as unity), and $E(t)$ is the linear viscoelastic relaxation modulus of the material. The pseudostiffness, C, is defined as the slope of ϵ^R versus σ^R. Based on the pseudostress–pseudostrain behavior of asphalt concrete subjected to simple uniaxial cyclic fatigue tests, the constitutive model proposed by Lee and Kim is

$$\sigma^R = C(S)\epsilon^R I \tag{7.8}$$

The strain energy potential is given as

$$W^R = \frac{1}{2} I C(S)\left(\epsilon^R\right)^2 \tag{7.9}$$

In Equation (7.8), the function $C(S)$ is the characteristic damage evolution function for the material and represents the change in pseudostiffness of the material due to damage evolution. The parameter I represents the initial pseudostiffness, introduced to reduce

www.EngineeringEBooksPdf.com

specimen-to-specimen variability. Similar to the Paris law, Schapery proposed that the damage evolution in a viscoelastic material follows a power-law form given as

$$\frac{\partial S}{\partial t} = \left(-\frac{\partial W^R}{\partial S}\right)^{\alpha} \tag{7.10}$$

The following discrete form of this law was developed and demonstrated to be true over several research studies conducted by Kim and coworkers as well as other researchers (Daniel and Kim, 2002; Lee and Kim, 1998; Park et al., 1996; Underwood et al., 2010):

$$S^R \cong \sum_{i=1}^{n} \left(0.5\left(\epsilon_i^R\right)^2 (C_{i-1} - C_i)\right)^{\frac{\alpha}{1+\alpha}} (t_i - t_{i-1})^{\frac{1}{1+\alpha}} \tag{7.11}$$

In Equations (7.10) and (7.11), the term α is related to the material creep and is suggested to take the form of $(1 + 1/m)$ or $1/m$ depending on the type of fracture, where m is the exponent of linear viscoelastic creep compliance. Recent studies (Karki et al., 2015; Palvadi et al., 2012a,b) have also demonstrated that the above approach can be used to obtain the $C(S)$ relationship for other asphalt composites such as FAM comprising aggregates finer than 1.2 mm and asphalt binder. Figure 7.10 illustrates some of the results obtained from these studies.

In the aforementioned studies, researchers used the VECD approach in reverse to characterize healing in asphalt composites in a manner that addressed the second and third requirements listed earlier (sensitive to duration of the rest period and extent of

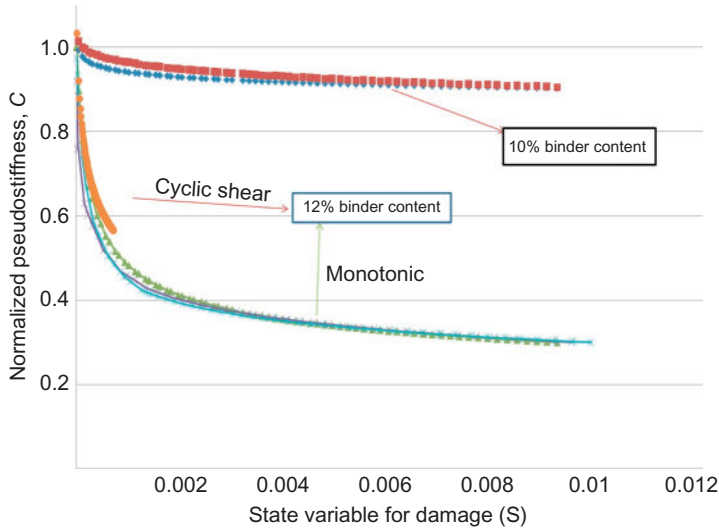


Figure 7.10 Results from cyclic fatigue tests showing a unique $C(S)$ function for each of the two different FAM specimens tested using different loading conditions.

www.EngineeringEBooksPdf.com

damage preceding the rest period). The rationale for using the VECD approach was that the healing characteristics so obtained would be independent of the testing and loading conditions used to induce damage to the material. They start by defining healing as the relative percentage reduction in the damage parameter S and mathematically given as

$$\%\text{Healing}\,(C,t)\overset{\text{def}}{=}\frac{\left[S_f(C,t)-S_i(C)\right]}{S_i(C)}100 \tag{7.12}$$

In Equation (7.12), C represents the pseudostiffness immediately before a rest period is introduced, t denotes the duration of the rest period, and $S_i(C)$ and $S_f(C,t)$ correspond to the internal state variables representing the state of damage before and after the introduction of a rest period, respectively. Note that the state of damage after the rest period is a function of the pseudostiffness of the material C that existed immediately before the introduction of the rest period as well as the duration of the rest period t. The value of $S_i(C)$ can easily be calculated as discussed above, using Equation (7.11). On the other hand, $S_f(C,t)$ is the result of a thermochemical healing process and cannot be calculated directly, because it requires an evolution law that relates S_f to the unknown chemical and thermodynamic forces that drive healing.

An apparently straightforward way to obtain the value of $S_f(C,t)$ is to measure the pseudostiffness of C immediately after the rest period of duration t, and to use this with the $C(S)$ function to determine $S_f(C,t)$. However, experimental results show that the damage evolution in a partially healed specimen immediately following the rest period occurs at a much faster rate compared to the damage evolution rate in the specimen at a similar level of pseudostiffness. This idea is illustrated in Figure 7.11. Consider a specimen that responds to a cyclic fatigue test following the curve C^1 in Figure 7.11. Now consider another test that is conducted using a similar test specimen, but with a rest period introduced at a time when the pseudostiffness of the material reaches a value of C_i. When the loading is resumed, the pseudostiffness of the material recorded would be C_f. However, the material would accumulate damage at a much faster rate (shown by curve C^2) compared to the rate of damage at a similar level of pseudostiffness for the original material (shown by curve C^1). This suggests that although the healing that took place during the rest period resulted in an increase in the *stiffness* of the material, it did not result in a corresponding increase in the *strength* of the material or corresponding reduction in the extent of damage in the material. Similar differences in the damage evolution characteristics of the asphalt mixes immediately after the rest period have been reported in other studies (Lee and Kim, 1998; Little et al., 2001). It is speculated that upon allowing a damaged material to heal, weak bonds are formed across the cracked interface and strength across these interfaces increases with time. The interfaces that only gain partial strength are weaker than the originally intact material and are easier to break, and thus contribute to a faster rate of damage evolution compared to the intact specimen when loads are again applied following rest periods. In conclusion, the stiffness immediately following the rest period is not a good representation of the level of damage reversal in the matrix, and therefore is not recommended as a basis to estimate $S_f(C,t)$, as it would result in an overprediction of healing.

www.EngineeringEBooksPdf.com

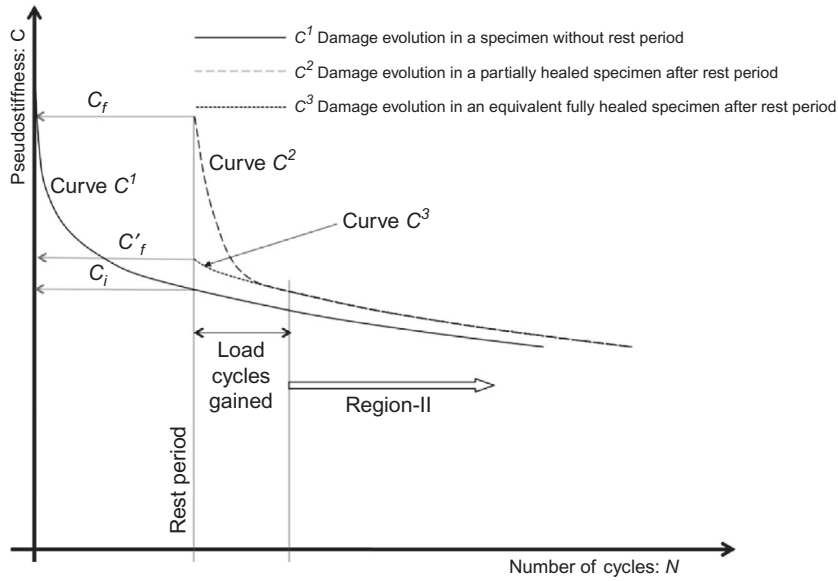


Figure 7.11 Actual and modified C versus N curve represented by curves 2 and 3.

In order to avoid overestimating healing, Palvadi et al. (2012a) and Karki et al. (2015) hypothesized that $S_f(C,t)$ could be back-calculated from data resulting from the application of additional load cycles to a test specimen immediately after the rest period. Using the example of Figure 7.11 once again, this can be explained as follows. The damage evolution curve following the rest period, C^2, eventually takes the same form of the original damage evolution curve C^1. Experimental evidence suggests that, depending on the extent of partial healing, the two curves C^1 and C^2 take the same form (shape) *no later* than the number of cycles at which the pseudostiffness falls below the level before which the rest period was introduced. In other words, the two curves C^1 and C^2 have the same form as before the pseudostiffness dropped below C_i, that is, the value at which the rest period was introduced. Therefore, it is possible to back-extrapolate the curve C^2 (following the same functional form as C^1) and determine the reduced pseudostiffness $C_f^{'}$ immediately following the rest period. This back-extrapolated portion of the curve is shown as C^3 in Figure 7.11. The reduced pseudostiffness can be regarded as the equivalent pseudostiffness of the material with the corresponding extent of reversed damage. The reduced pseudostiffness is also used with the $C(S)$ curve to determine $S_f(C,t)$, and used with Equation (7.12) to compute percentage healing. Readers are encouraged to review the two aforementioned paragraphs and Figure 7.11 carefully to grasp the underlying concept, and also to review the cited literature for more details.

Palvadi et al. (2012a) and Karki et al. (2015) used the aforementioned approach to determine the healing characteristics of FAM specimens fabricated using different types of asphalt binders and aggregates. Palvadi et al. (2012a) applied different

www.EngineeringEBooksPdf.com

durations of rest period at the same level of damage (or pseudostiffness) to determine the influence of the duration of rest period on the healing characteristics. They repeated the test using different specimens of the same material, but varying the level of damage immediately preceding the rest period. Based on these tests, they were able to determine the healing characteristics of the composite as a function of the duration of the rest period, as well as the level of damage immediately preceding the rest period. Karki et al. (2015) used a similar approach, but were able to combine different durations of rest periods at different levels of damage using the same test specimen. By using an algorithm of shifting, they were able to reproduce the base line $C(S)$ curve for the material when there is no rest period, as well as the healing characteristics of the material as a function of the duration of the rest period and level of damage preceding the rest period. Figure 7.12 illustrates a schematic of the protocol that was used to conduct these tests. Figure 7.13 provides validation for the above methodology.

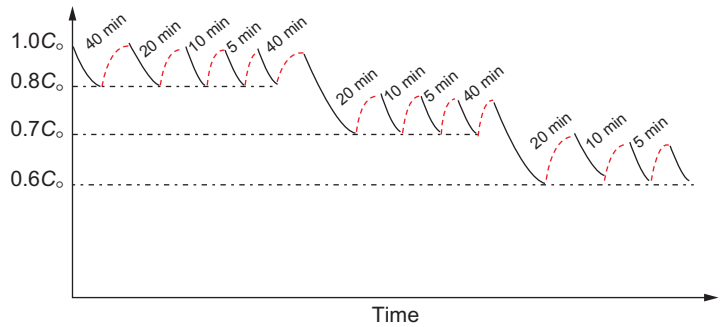


Figure 7.12 Test protocol used to characterize healing as a function of pseudostiffness.

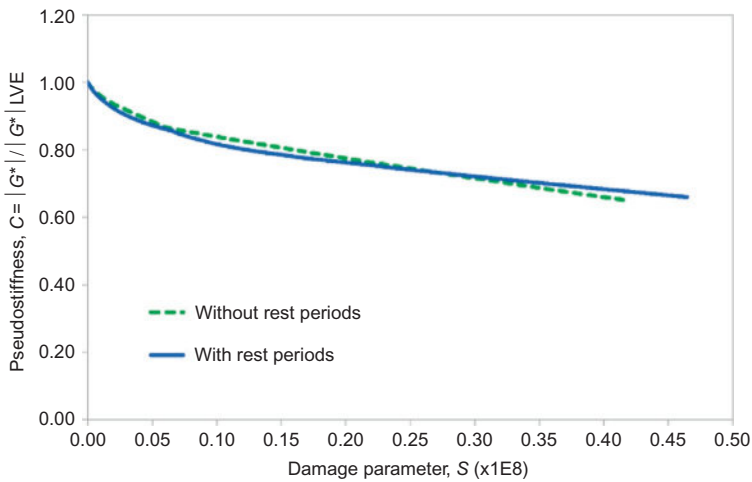


Figure 7.13 Typical results that show the $\boldsymbol{C(S)}$ for a FAM specimen obtained with intermediate rest periods and without any rest periods.

www.EngineeringEBooksPdf.com

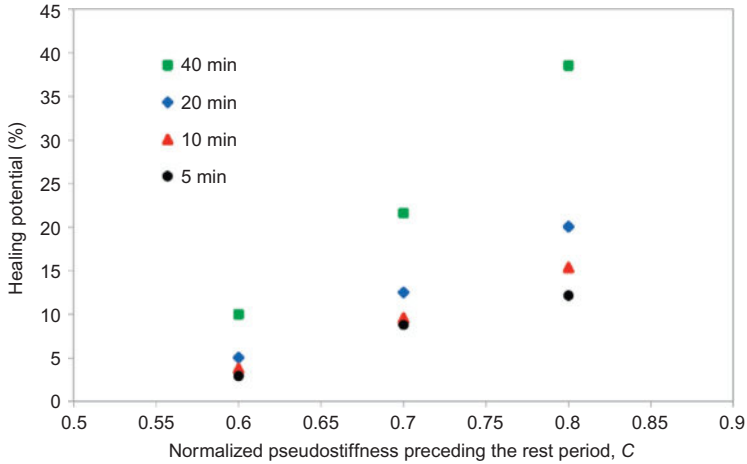


Figure 7.14 Typical results that show the healing characteristics of the binder as a function of the duration of the rest period as well as the level of damage immediately preceding the rest period.

The $C(S)$ curves shown in Figure 7.13 are the same for a given material, irrespective of the fact that some of these curves were obtained with intermediate rest periods and the shifting scheme developed by Karki et al. (2015). In fact, the curves were also the same irrespective of the amplitude of cyclic loading used to induce damage. Finally, Figure 7.14 illustrates the percentage healing for a typical material as a function of both the duration of the rest period and the damage immediately preceding the rest period. As expected, for any given level of damage, longer durations of rest periods resulted in greater percentage healing. Also, higher percentages of healing were achieved when the rest periods were introduced at a lower level of damage. This is expected because larger cracks associated with greater level of damage are unlikely to heal as effectively as smaller cracks.

7.6 Microdamage healing: impact of rest period and thermodynamic considerations

7.6.1 Microdamage healing in the absence of a rest period

It is commonly believed that microdamage healing of asphalt binder and asphalt concrete occurs only during the rest period between the loading cycles at intermediate and high temperatures. While this could be true for elastic media with healing potential, the existence of a rest period between the loading cycles is not the only condition under which microdamage healing occurs in time-dependent materials (e.g., viscoelastic materials) with healing potential, such as asphalt concrete and asphalt binder.

www.EngineeringEBooksPdf.com

Residual (internal) compressive stresses can also aid in the microdamage healing of asphalt concrete. These residual compressive stresses occur even during a cyclic displacement-controlled (CDC) test in tension, where there is no rest period between the loading cycles.

The healing mechanism during the CDC test is illustrated with the aid of Figure 7.15, which shows part of strain and stress responses during the CDC test in tension conducted at 19 °C. In the CDC test, the stress remains tensile during a large portion of the loading history. During the unloading (i.e., when the strain rate is negative), however, compressive stresses are induced in the specimen. These compressive stresses cause the microcrack free surfaces to wet (i.e., get close to each other) and undergo healing and crack closure. This effect can be explained based on the fading memory of viscoelastic

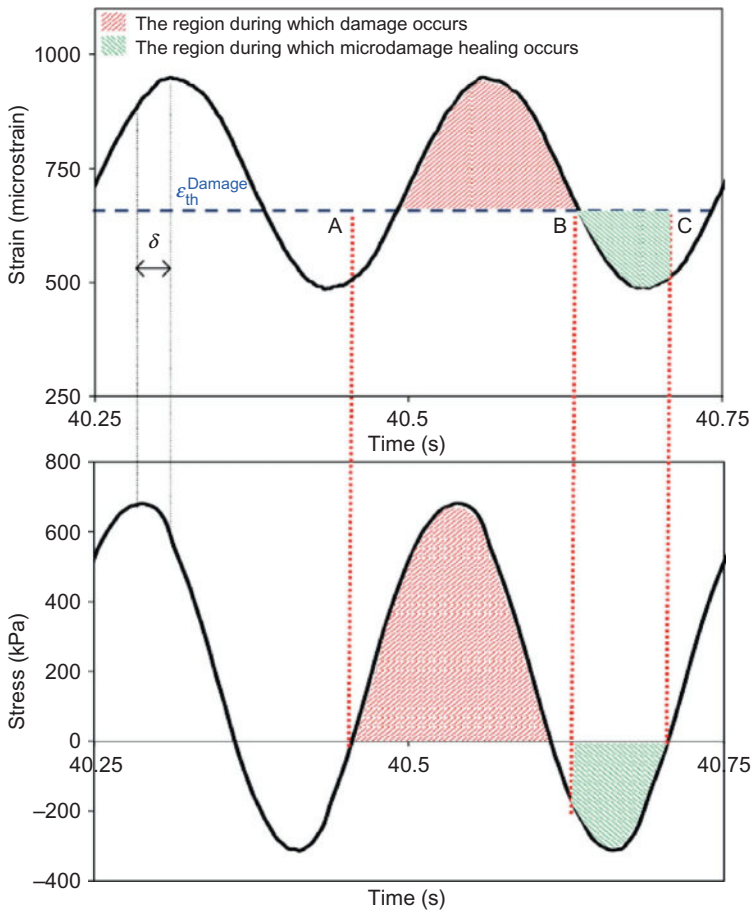


Figure 7.15 Schematic representation of the strain and stress responses for a tensile CDC test and the stages during which microdamage nucleation/growth and microdamage closure/healing occur, with δ being the lag between stress and strain responses.

www.EngineeringEBooksPdf.com

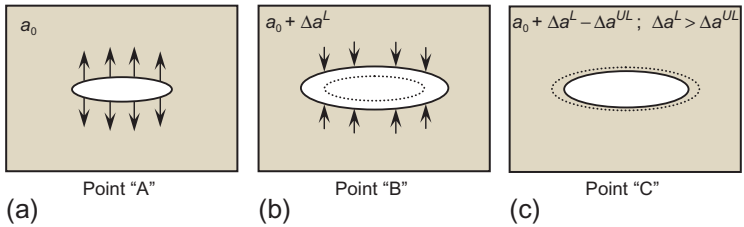


Figure 7.16 (a–c) Schematic representation of the crack growth and crack closure/healing during one cycle of a tensile CDC test.

materials and the lag between stress and strain responses, which is signified by the term δ, as shown in Figure 7.15. As explained by Coleman (1964), fading memory is referred to the assertion that the deformations experienced in the distant past should have less effect on the present values of the stress than deformations that occurred in the recent past (e.g., Coleman and Noll, 1961; Coleman, 1964).

In order to illustrate the effect of the fading memory, assume that a viscoelastic medium contains a single microcrack of length a_0 at point "A," Figure 7.16, and the damage growth occurs when the tensile strain exceeds a threshold value (i.e., $\varepsilon_{th}^{Damage}$). Moving from point "A" to point "B" in Figure 7.15, the strain remains larger than $\varepsilon_{th}^{Damage}$ and the induced stresses in the viscoelastic medium are also tensile. Therefore, the microcrack length increases by Δa^L, such that the crack length at point "B" reaches $a_0 + \Delta a^L$, Figure 7.16. However, fading memory causes the stresses induced in the material to relax and fade away with time.

The increase in the strain level during the preceding loading stage has less effect on the stress level than the decrease in the strain level during the current unloading stage. Obviously, the negative increment in the stress due to the decrease in the strain level during the unloading stage is more than the positive increment in the stress due to the increase in the strain level during the preceding loading stage. Therefore, the viscoelastic medium feels compressive stresses at some point during the unloading stage, although the total strain is still tensile. Therefore, the crack length decreases when moving from point "B" to point "C" by the increment of Δa^{UL}. The induced stresses are compressive during a small portion of the loading and deformation history for the tensile CDC test, such that Δa^L is always greater than Δa^{UL} (i.e., $\Delta a^L > \Delta a^{UL}$). Therefore, microcracks still propagate and increase in length when moving from point "A" to point "C." However, accurate estimation of the damage density requires the incorporation of both Δa^L and Δa^{UL} components.

The schematic analysis shown in Figures 7.15 and 7.16 illustrates microdamage healing of the asphalt concrete materials and that, in fact, microdamage healing can occur even during the cyclic tensile loading scenarios. This phenomenon makes it vital to incorporate the microdamage healing effect in order to accurately predict fatigue damage of asphalt concrete materials. This observation can also help explain the impact of healing at low levels of damage (low strain amplitude), such as those designed for perpetual pavements.

www.EngineeringEBooksPdf.com

7.6.2 Thermodynamics of damage and microdamage healing processes

One of the most important issues associated with damage and microdamage processes is how energy is stored and dissipated as the material experiences damage and microdamage healing. This issue is usually studied in the context of thermodynamics of irreversible phenomena through introducing internal state variables representing damage and microdamage healing processes. However, in most studies on thermodynamics of self-healing materials, the microdamage healing process is treated similar to the damage process (e.g., Miao et al., 1995; Voyiadjis et al., 2011; Pauli, 2014). From these studies, it can be implied that both damage and microdamage healing are dissipative by nature, such that one can derive expressions for storage and dissipative energies during the microdamage healing process similar to the way that storage and dissipative energies during the damage process are derived. However, one must note that damage and microdamage healing have different mechanisms and should be treated differently. In fact, for ideal self-healing materials, the net dissipated energy during a controlled cycle of damage and complete healing could be zero. In this section, a general thermodynamic framework of damage and microdamage healing is presented, with a specific focus on the mechanism under which damage and microdamage healing processes store and dissipate energy. The framework presented herein should be slightly modified to be applicable to self-healing materials with chemical reactivity, such as the hydration reactions or pozzolanic reactions during the curing of Portland cement.

The framework presented herein is based on the definition of internal and external expenditures of power defined following the framework of Gurtin (2003), but with the consideration of damage and microdamage healing. Experimental observations show that materials with healing potential undergo healing processes under specific conditions, such as during the rest period and under hydrostatic pressure. During the rest period, in particular, external loading is removed, and therefore, the external power might be considered to become zero. However, the microdamage healing process partially continues by consuming some of the energy stored inside the body. Further healing occurs once external energy in the form of heat is supplied to the body. This heat speeds up the healing process, and in some cases is essential for the complete healing process. In these cases, temperature change and evolution are extremely important and cannot be ignored (e.g., Cardona et al., 1999). This can be verified by studying the effect of temperature on the healing process (e.g., Reinhardt and Jooss, 2003; Kessler, 2007; Little and Bhasin, 2007). One may start with the principle of virtual power, which states that the external expenditure of the power P_{ext} due to a virtual motion should be balanced by the internal expenditure of the power P_{int} associated with the same virtual motion (i.e., $P_{\text{int}} = P_{\text{ext}}$). Degrees of freedom of the body are considered to be the displacement vector u, the elastic strain tensor $\boldsymbol{\varepsilon}^e$, the damage density ϕ, the healing variable h, and temperature T, such that the generalized virtual motions are the set consisting of $\left\{\dot{u}, \dot{\varepsilon}^e, \dot{\phi}, \dot{h}, \dot{T}, \nabla\dot{T}\right\}$. It is assumed that these virtual motions are, momentarily, independent. The dependency among these virtual motions will be established later. It should be noted that the rate of temperature $\dot{T}$ change and

www.EngineeringEBooksPdf.com

its gradient $\nabla\dot{T}$ have been added to the usual velocity variables to ensure the generality of the thermodynamic framework and in consideration of the endothermic nature of the healing process. Obviously, conventional energy flux should also be modified according to Maugin and Muschik (1994). The internal and external expenditures of power can be written as

$$P_{\text{int}} = \int_V \left(\overline{\sigma} : \dot{\varepsilon}^e + Y\dot{\phi} - H\dot{h} + \xi\dot{T} + \gamma.\nabla\dot{T}\right) \mathrm{d}V;$$

$$P_{\text{ext}} = \int_V b_i \dot{u}_i \mathrm{d}V + \int_S t_i \dot{u}_i \mathrm{d}S - \int_V \rho \ddot{u}_i \dot{u}_i \mathrm{d}V + \int_S \chi\dot{T}\mathrm{d}S \tag{7.13}$$

The Cauchy stress tensor $\boldsymbol{\sigma}$, the damage force Y, and the healing force H are the generalized thermodynamic forces that conjugate to the elastic strain tensor, damage density, and healing variable, respectively. Two additional generalized thermodynamic forces, ξ and $\boldsymbol{\gamma}$ conjugated to temperature and its gradient, respectively, are defined similar to Cardona et al. (1999). Equation (7.13) shows that the damage process increases the internal expenditure of power, whereas the microdamage healing process decreases the internal expenditure of power. This microdamage healing process can therefore be considered as the inverse of the damage process. On the other hand, the macroscopic body force b, the macroscopic surface traction t, the inertial forces, and the generalized temperature traction χ conjugated to $\dot{T}$ contribute to the external expenditure of power. Applying the principle of virtual power implies

$$\overline{\sigma}_{ij,j} + b_i = \rho\ddot{u}_i, \quad \text{in} \quad V; \quad t_i = \sigma_{ij} n_j, \quad \text{on}\, S \tag{7.14}$$

$$\chi = \gamma_i n_i; \quad \text{on}\, S \tag{7.15}$$

$$Y = 0; \quad \text{in}\, V \tag{7.16}$$

$$-H\dot{h} + \left(\xi - \gamma_{i,i}\right)\dot{T} = 0; \quad \text{in}\, V \tag{7.17}$$

where n denotes the outward unit normal on the boundary S. Equations $(7.14)_1$ and $(7.14)_2$ represent the local static/dynamic macroforce balance and the boundary traction as the density of the surface forces, respectively. Equation (7.15) defines the boundary traction for the thermodynamic forces conjugate to $\dot{T}$. Equation (7.16) defines the damage microforce balance (Fremond and Nedjar, 1996) that will be used to derive the dynamic viscodamage nucleation and growth conditions (Abu Al-Rub and Darabi, 2012; Darabi et al., 2012a). The virtual motion fields have not been removed in Equation (7.17). This new and nonclassic equation will be referred to as the *microdamage-healing microforce balance*, which will be used to derive microdamage healing condition and evolution functions. Equation (7.17) reduces to the following equation when the gradient of the rate of temperature is neglected (i.e., $\nabla\dot{T} \cong 0$):

$$-H\dot{h} + \xi\dot{T} = 0 \tag{7.18}$$

www.EngineeringEBooksPdf.com

Equation (7.18) clearly shows the dependency of the healing process on the rate of temperature change. Roughly speaking, Equation (7.18) states that additional power provided as external heat is required for the healing process to occur. This is in agreement with the endothermic nature of the healing process. This equation can be explained even for the isothermal conditions for which the body V is in contact with a reservoir maintaining a constant temperature. In this case, the healing process is accompanied by the absorption of the heat from its surrounding area. This process causes temperature drop within the area in which healing occurs. The reservoir will then compensate for this temperature drop by supplying the heat to the body V, guaranteeing the isothermal condition. However, the timescale for achieving the isothermal condition is of the order of the timescale required for the healing phenomenon, which makes it impossible, for practical purposes, to ignore this transient region during the healing process. Therefore, the rate of the heat supply is directly correlated to the rate of the healing process. At the first approximation, one can assume a linear relationship between the rate of the temperature change and the healing rate (i.e., $\xi\dot{T} = K\dot{h}$), such that the microdamage-healing microforce balance will be simplified to the following form in the absence of the temperature gradient:

$$H - K = 0 \tag{7.19}$$

It is assumed that, for the isothermal conditions, the Helmholtz free energy ψ depends on the elastic strain tensor $\boldsymbol{\varepsilon}^e$, the damage density ϕ, and the healing variable h, such that

$$\psi = \psi(\varepsilon^e, \phi, h) \tag{7.20}$$

By combining the first and the second laws of thermodynamics (i.e., balance of energy and entropy imbalance, respectively), and conservation of mass, and taking the time derivative of the resulted Clausius–Duhem inequality for the isothermal conditions, $\int_v \rho\dot{\Psi}\mathrm{d}V \le P_{\mathrm{int}}$, (c.f., Lemaître and Chaboche, 1990), the following expressions can be derived:

$$\overline{\sigma} = \rho\frac{\partial \Psi}{\partial \varepsilon^e};\ \ \Pi = \left(Y - \rho\frac{\partial \Psi}{\partial \phi}\right)\dot{\phi} - \left(H + \rho\frac{\partial \Psi}{\partial h}\right)\dot{h} + K\dot{h} \ge 0 \tag{7.21}$$

where Π is the rate of the energy dissipation. Equation (7.21) expresses the dissipated energy during damage and microdamage processes. The rate of the energy dissipation during the damage process Π^{vd} and during the microdamage healing process Π^h can be expressed as follows:

$$\Pi^{vd} = \left(Y - \rho\frac{\partial \Psi}{\partial \phi}\right)\dot{\phi};\ \ \Pi^h = -\left(H + \rho\frac{\partial \Psi}{\partial h}\right)\dot{h} + K\dot{h} \tag{7.22}$$

such that the total rate of energy dissipation is $\Pi = \Pi^{vd} + \Pi^h \ge 0$.

www.EngineeringEBooksPdf.com

At a specific location within the material at a specific time t, the material can either undergo the damage process or undergo the microdamage healing process. Therefore, the rate of the microdamage healing variable is zero during the damage process and vice versa, such that $\Pi = \Pi^{vd} \geq 0$ during the damage process and $\Pi = \Pi^{h} \geq 0$ during the healing process.

A close look at Equation $(7.22)_2$ shows that part of the required internal power for the microdamage healing process is provided by the stored energy due to the microdamage healing processes. In other words, the microdamage healing process causes the stored energy to decrease. This released energy (provided by the decrease in the stored energy) is derived from the surface free energy on the faces of the cracks that participate in the healing process as well as from, in certain systems, the increase in configurational entropy. For example, in a bitumen system, the introduction of a crack face probably establishes a preferred orientation of aliphatic, polynuclear aromatic, and naphtenic aromatics. During the healing process, a reorganization of these phase or components across the crack interface contributes to some degree to the reestablishment of strength (healing), resulting in an increase in configurational entropy and a decrease in free energy. In fact, Bhasin et al. (2011) established, using molecular dynamics, that the composition of the bitumen affects the rate or reorganization across an interface. This released energy is spent for the partial microdamage healing process. The extra required energy for the microdamage healing process (i.e., shown by $K\dot{h}$) comes from the external heat energy (i.e., $\xi\dot{T} = K\dot{h}$). For the hypothetical completely self-healing materials, this extra energy is not required (i.e., $K = 0$), such that the microdamage healing process does not dissipate energy and can be considered as a reversible process. However, this condition does not occur in reality.

Equation $(7.21)_2$ contains terms that are only a function of the Helmholtz free energy, which can be defined as energetic thermodynamic conjugate forces. One can define those as the energetic terms as follows:

$$\Pi = (Y - Y^{\text{ene}})\dot{\phi} - (H - H^{\text{ene}})\dot{h} + K\dot{h} \geq 0; \quad Y^{\text{ene}} \equiv \rho\frac{\partial \Psi}{\partial \phi} \quad \text{and} \quad H^{\text{ene}} \equiv -\rho\frac{\partial \Psi}{\partial h} \tag{7.23}$$

where Y^{ene} and H^{ene} are energetic components of the thermodynamic forces conjugated to ϕ and h, respectively. Equation (7.23) shows that the rate of the energy dissipation resulting from the damage process is positive only if the thermodynamic force conjugated to the damage variable has both energetic and dissipative components, such that the rate of the energy dissipation during damage and microdamage healing can be written as

$$\begin{aligned} &\Pi = \Pi^{h} = \left(-H^{\text{dis}} + K\right)\dot{h} \geq 0; \quad \dot{\phi} = 0 \,(\text{during the microdamage healing process}) \\ &\Pi = \Pi^{vd} = Y^{\text{dis}}\dot{\phi} \geq 0; \quad \dot{h} = 0 \,(\text{during the damage process}) \end{aligned} \tag{7.24}$$

where $Y^{\text{dis}} = Y - Y^{\text{ene}}$ and $H^{\text{dis}} = H - H^{\text{ene}}$ are dissipative components of the damage- and microdamage-healing conjugate forces, respectively.

www.EngineeringEBooksPdf.com

The thermodynamic framework described herein shows that both damage- and microdamage-healing thermodynamic forces should have energetic and dissipative components. This is in line with the pioneering work of Ziegler (1977), which states that the proper estimation of the stored energy and energy dissipation requires the thermodynamic conjugate forces to have both energetic and dissipative components. The energetic and dissipative terms mean that the thermodynamic conjugate forces are derived from the Helmholtz free energy and the rate of the energy dissipation, respectively. Obviously, in order to formulate constitutive relationships for the energetic and dissipative conjugate forces, one needs to know how the material stores energy (which helps in assuming a mathematical form for the Helmholtz free energy) and how the material dissipates energy (which helps in assuming mathematical forms for the rate of the energy dissipation).

The dissipative components of the thermodynamic conjugate forces can be identified using the maximum rate of energy dissipation principle and utilizing the mathematics of multiple variables, such that

$$Y^{\text{dis}} = \lambda^{vd}\frac{\partial \Pi}{\partial \dot{\phi}}; \quad \lambda^{vd} = \Pi \Big/ \left(\frac{\partial \Pi}{\partial \dot{\phi}}\dot{\phi}\right) \tag{7.25}$$

$$H^{\text{dis}} - K = -\lambda^{h}\frac{\partial \Pi}{\partial \dot{h}}; \quad \lambda^{h} = \Pi \Big/ \left(\frac{\partial \Pi}{\partial \dot{h}}\dot{h}\right) \tag{7.26}$$

where λ^{vd} and λ^{h} are viscodamage- and microdamage-healing Lagrange multipliers, respectively.

This concludes the general thermodynamic framework for derivation of damage- and microdamage-healing constitutive relationships with specific focus on accurate estimation of stored and dissipated energies. The specific form of the constitutive relationship can be derived by assuming proper mathematical forms, depending on the material type, for the Helmholtz free energy and the rate of the energy dissipation function.

7.6.3 Incorporation of microdamage healing in constitutive relationships

This section briefly presents the constitutive relationships that were developed by the authors and their collaborators and that were implemented in a finite element (FE) package referred to as PANDA, an acronym for Pavement Analysis using Nonlinear Damage Approach, in order to illustrate the significance of including microdamage healing effects to accurately predict the response of asphalt concrete. Readers are referred to the related publications on PANDA for more details (Huang, 2008; Abu Al-Rub et al., 2010; Darabi et al., 2011, 2012a,b,c, 2013; Abu Al-Rub and Darabi, 2012; Rahmani et al., 2013; Shakiba et al., 2013).

The continuum damage-healing mechanics framework (Darabi et al., 2012a), which is an extension of continuum damage mechanics (CDM) (Kachanov, 1958)

www.EngineeringEBooksPdf.com

theories for materials with healing potential, was used to couple damage and healing with other mechanisms occurring in asphalt concrete. This framework presents the stress tensor in the healing space and relates it to the nominal stress tensor as a function of damage and healing variables, such that

$$\overline{\sigma}_{ij} = \frac{\sigma_{ij}}{1-\phi_{\text{eff}}}; \quad \phi_{\text{eff}} = \phi(1-h) \tag{7.27}$$

where the superscript "−" designates the healing space, ϕ is the damage density, and h is the microdamage healing variable. This framework facilitates the coupling of damage and healing with the time-dependent viscoelastic (i.e., recoverable part of deformation) and viscoplastic (i.e., irrecoverable part of deformation) response of asphalt concrete. Schapery's (1969) nonlinear viscoelastic constitutive relationship is implemented in PANDA to describe the nonlinear viscoelastic response of asphalt concrete, such that

$$\varepsilon_{ij}^{\text{nve},t} = g_0\left(\overline{\sigma}_{ij}^t, T^t\right) D_0 \overline{\sigma}_{ij}^t + g_1\left(\overline{\sigma}_{ij}^t, T^t\right) \int_0^t \Delta D(\psi^t - \psi^\tau) \frac{\mathrm{d}\left(g_2\left(\overline{\sigma}_{ij}^t, T^\tau\right)\overline{\sigma}_{ij}^t\right)}{\mathrm{d}\tau} \mathrm{d}\tau \tag{7.28}$$

where D_0 is the instantaneous compliance; ΔD is the transient compliance; g_0, g_1, and g_2 are nonlinear parameters; and the term ψ^t is the reduced time in which the temperature effect is incorporated.

PANDA uses the Perzyna-type hardening viscoplastic constitutive relationship as outlined in Masad et al. (2005), Tashman et al. (2005), and Huang et al. (2011), along with the hardening-relaxation viscoplasticity introduced by Darabi et al. (2012c) to describe permanent deformation of asphalt concrete materials. The evolution of the viscoplastic strain $\dot{\varepsilon}_{ij}^{vp}$ using the Perzyna-type constitutive relationship can be written as

$$\dot{\overline{\varepsilon}}_{ij}^{vp} = \Gamma^{vp}(T)\langle\Phi(f)\rangle^N \frac{\partial g}{\partial \overline{\sigma}_{ij}}; \quad f = \overline{\tau}^{vp} - \alpha\overline{I}_1 - \kappa(p) \tag{7.29}$$

where Γ^{vp} is the viscoplastic fluidity parameter such that $1/\Gamma^{vp}$ represents the viscoplasticity relaxation time, N is the viscoplastic rate sensitivity exponent, Φ is the overstress function, f is the yield surface, g is the plastic potential, α is a material parameter related to the material's internal friction, and $\kappa(p)$ is the isotropic hardening function. To address the limitations of the classical hardening viscoplasticity theories and enable PANDA to accurately predict the response of asphalt concrete subjected to cyclic loading, Darabi et al. (2012c) introduced the concept of the hardening-relaxation memory surface and proposed an evolution function for the rate of hardening.

The damage constitutive relationship proposed by Darabi et al. (2013) is implemented in PANDA, such that

www.EngineeringEBooksPdf.com

$$\dot{\phi} = \Gamma^{vd}(T)\left\langle \frac{\overline{Y}}{Y_0} \right\rangle^{q} (\varepsilon_{\text{eff}})^{k} \tag{7.30}$$

where Γ^{vd} is the viscodamage fluidity parameter; Y_0 is the reference damage force that can be assumed to be unity; k is a material parameter; and ε_{eff} is the effective total strain, defined as $\varepsilon_{\text{eff}} = \sqrt{\varepsilon_{ij}\varepsilon_{ij}}$. A modified Drucker–Prager function is assumed for the damage force $\overline{Y}$, such that

$$\overline{Y} = \overline{\tau}^{vd} - \alpha \overline{I}_1; \quad \overline{\tau}^{vd} = \frac{\sqrt{3\overline{J}_2}}{2}\left[1 + \frac{1}{d^{vd}} + \left(1 - \frac{1}{d^{vd}}\right)\frac{3\overline{J}_3}{\sqrt{3\overline{J}_2^3}}\right] \tag{7.31}$$

The terms $\overline{I}_1$, $\overline{J}_2$, and $\overline{J}_3$ are stress invariants. The damage evolution function is sensitive to the confinement level, distinguishes the damage evolution in extension and contraction, and is sensitive to the mode of loading.

As mentioned in the previous section, accurate prediction of fatigue damage of asphalt concrete requires the incorporation of both damage and microdamage healing mechanisms. The microdamage-healing constitutive relationship implemented in PANDA is postulated to reflect the fundamental mechanisms occurring during the microdamage healing process, such that (Abu Al-Rub et al., 2010)

$$\dot{h} = \Gamma^{h}(T)(1 - \phi_{\text{eff}})^{b_1}(1 - h)^{b_2} \tag{7.32}$$

where $\dot{h} = \mathrm{d}h/\mathrm{d}t$ is the rate of the healing variable and $\Gamma^{h}(T)$ is the healing fluidity parameter that determines how fast the material heals, which is a function of temperature T. Equation (7.32) shows that at low damage density and at the beginning of the healing process, that is, when $h \approx 0$, the microdamage healing variable has its maximum growth rate, that is, $\dot{h} \approx \Gamma^{h}$. Therefore, Equation (7.32) suggests that the microdamage healing variable initially evolves rapidly with the rate of Γ^{h}, and then the evolution rate decreases as the healing variable increases. The fast initial evolution of the microdamage healing variable resembles the wetting process at the microscale. Abu Al-Rub et al. (2010) showed that the microdamage-healing fluidity parameter Γ^{h} can be related to fundamental properties of material, such as surface energy, viscoelastic properties, and properties of the fracture process zone. As more diffusion occurs between crack faces, the rate of time-dependent healing decreases, but the overall amount of healing increases. This history dependency is represented by the last term in Equation (7.32).

7.6.4 Significance of microdamage healing in the cyclic response of asphalt concrete

This subsection presents examples of results from repeated creep-recovery loading in both tension and compression as well as the CDC loading in tension to demonstrate the necessity of incorporating a viable microdamage-healing constitutive relationship to accurately predict the c response of asphalt concrete under such loading scenarios.

www.EngineeringEBooksPdf.com

7.6.4.1 Significance of microdamage healing during cyclic loading in both tension and compression

The material properties associated with the PANDA model were identified for a specific material by Darabi et al. (2012a). The viscoelastic, viscoplastic, and viscodamage material properties were used to predict independent (i.e., tests that were not used for identification of material properties) repeated creep-recovery tests in both tension and compression. Figure 7.17 shows the experimental results and model predictions for repeated creep-recovery tests in compression and tension with the applied stress of 1500 and 300 kPa, respectively. The loading time and rest period in both tension and compression was 60 and 1500 s, respectively. The test results for long resting times were selected in order to provide enough time during the rest period for the induced microcracks to heal.

As shown in Figure 7.17, the model without the microdamage healing component predicted shorter fatigue life compared to experimental measurements. In other words, the model predicted higher creep strains compared to experimental data. This effect is due to the fact that the damage density in the viscodamage constitutive relationship is irreversible; hence, it does not allow for damage recovery or healing during the rest period. This subsection shows that including the microdamage healing component significantly improves the ability to predict the cyclic creep-recovery response of asphalt concrete. As shown in Figure 7.17a and b, when microdamage healing is not incorporated, the model predicts failure after only six cycles. However, experimental measurements and model predictions that include the aforementioned microdamage-healing evolution function agree well that the material can indeed sustain the load for many more loading cycles.

Another test (refer to Kim et al. (2008) for more information on the experimental study) that was used to demonstrate the effect of microdamage healing is the CDC test in tension (refer to Darabi et al. (2013) for details on data analysis to identify the PANDA material properties). Once PANDA was calibrated, independent CDC tests at different temperatures, displacement levels, and frequencies were used to

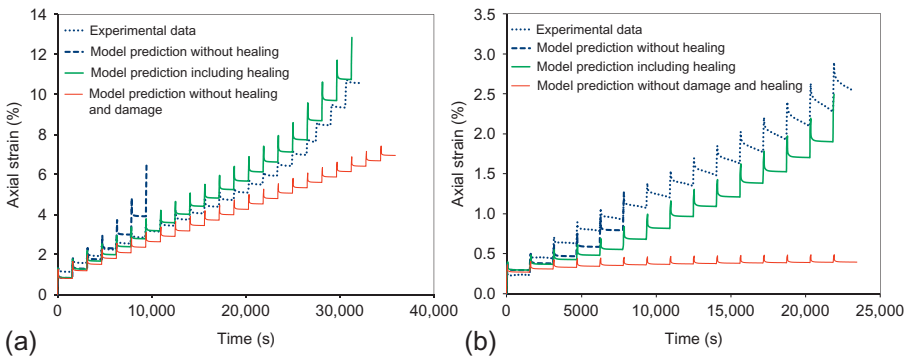


Figure 7.17 Model predictions compared to experimental results of repeated creep-recovery tests at $T = 20$ °C (a) in compression with the applied stress of 1500 kPa, loading time: 60 s, rest period: 1500 s; (b) in tension with the applied stress of 300 kPa, loading time: 60 s, rest period: 1500 s.

www.EngineeringEBooksPdf.com

investigate the significance of microdamage healing during a cyclic test in tension in the absence of the rest period. As emphasized in this chapter, microdamage healing can occur during the CDC test. The displacement input during CDC can be written as

$$\Delta = \frac{\Delta_{\max}}{2}[-1 + \cos(2\pi ft)] \tag{7.33}$$

where f is the frequency. The term $\Delta_{\max}$ is the displacement amplitude applied at the end plates, such that $\Delta_{\max}/\ell$ can be considered as the amplitude of the average strain applied to the specimen, with ℓ being the specimen height. The averaged linear variable differential transformers' (LVDTs') strains should be considered as the input strain for validation and simulation purposes because it measures the strain in the middle of the specimen, where stress and strain can be assumed to be uniformly distributed. Figure 7.18a shows the LVDT strain input for the CDC test at 19 °C when the

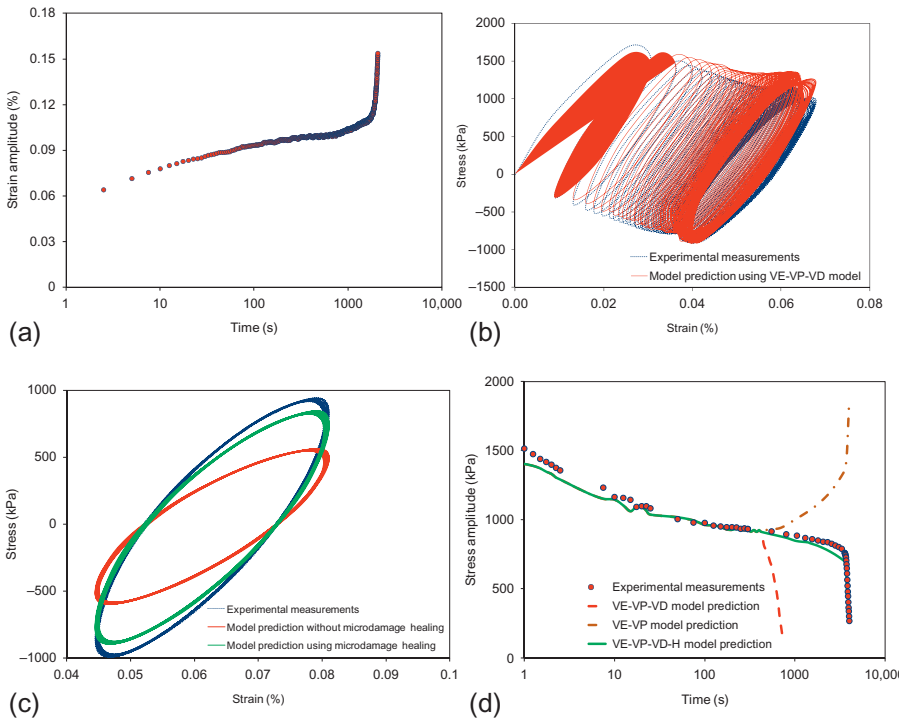


Figure 7.18 Responses during the CDC test at 19 °C when the amplitude of the average strain applied to the specimen is 1200 $\mu\varepsilon$. (a) Average amplitude of the strain measured at LVDTs. (b) Stress–strain response for the experimental measurements as compared to model predictions using the VE–VP–VD model for cycles 1–50. (c) Stress–strain response for the experimental measurements as compared to model predictions for cycles 2200–2250. (d) Measured and predicted stress amplitudes. The microdamage healing model VE–VP–VD–H (where "H" signifies consideration of healing) significantly enhances the prediction of the stress response, stress amplitude, and the dissipated energy.

www.EngineeringEBooksPdf.com

amplitude of the average strain is 1200 $\mu\varepsilon$. Figure 7.18b shows that the viscoelastic–viscoplastic–viscodamage (VE–VP–VD) model predictions are in agreement with the experimental measurements during the initial loading cycles. However, the coupled VE–VP–VD significantly underestimates the stress output as the number of loading cycles increases; see Figure 7.18c.

Model predictions using the viscodamage model predict premature failure for the material, while the experimental measurements show that the material is capable of sustaining loads for much longer time. As discussed before, this discrepancy is related to the inability of the model to account for crack closure and the microdamage healing during the cyclic strain-controlled tests. Figure 7.18c shows that the microdamage healing model significantly enhances the prediction of the stress response as well as the dissipated energy during the intermediate cycles. Figure 7.18d shows that the model without microdamage healing underestimates the stress level and predicts premature failure almost by a factor of four, while the model prediction with the microdamage healing agrees well with experimental measurements.

The results shown in this subsection clearly demonstrate the inevitable need for incorporation of microdamage healing effects in constitutive relationships in order to accurately predict the fatigue damage response of asphalt concrete.

7.7 Future directions

Future directions that can be taken to better understand the process of healing and to better utilize the benefits of healing can be separated into three general categories: (a) fundamental properties and mechanisms that promote and accommodate healing, (b) laboratory measurements of healing properties of mastics and/or mixtures that can be used in constitutive models to evaluate the impact of healing, and (c) investigations of mechanisms at the nano to macro scale that will enhance the healing process *in situ*.

Considerable improvement can be made in understanding and developing a model of the process of healing. It is logical that healing of microcracks is aided by the ability of the binder to flow across crack faces and wet crack surfaces, and models discussed in this chapter support such a mechanism. However, the key surface free energy properties (Lifshitz-van der Waals and Lewis acid/base components) of the binder, which have been shown to be keyed to chromatographic fractions of the asphalt binder (Pauli, 2014), require more reliable methods of measurement, such that the values of these parameters are true material properties and not test dependent. Pauli (2014) states that *healing is speculated to be influenced by variations in flow properties and compatibility amongst asphalts derived from different crude sources*. More work is required to quantify flow activation energies and their relationship to surface free energy. Atomic force microscopy (AFM) has proven valuable in assessing the impact of the microstructure of asphalt and the potential impact of asphalt phases on performance. Allen et al. (2012) demonstrated substantial differences in the compliance properties among at least three microstructural phases of asphalt binders. Jahangir et al. (2015), using finite element modeling and AFM, showed stress concentrations that develop in interstitial regions among phases, and how such regions

www.EngineeringEBooksPdf.com

foster the development of phase separation (load-induced phase separation (LIPS)) in regions of highest compliance that are the beginning of damage and therefore could be where the process of healing begins. An understanding of how these zones can be the locus of damage as well as healing can be enhanced by continued AFM and finite element analyses.

Of course, factors such as oxidative aging and crystallization of oil components of the asphalt binder (including crystallizing paraffin waxes and surface (of crack face) structuring) and thermal stress buildup must impact the healing process. Extending laboratory testing methods, such as those presented in this chapter to accommodate laboratory protocols to mimic the aging and hardening processes and characterize the resulting healing properties, would be a substantial step forward. Alternatively, applying evolution functions such as those developed by Darabi et al. (2012a) and Abu Al-Rub et al. (2013) for aging to adjust healing measurements may be an acceptable solution, but will require extensive validation.

This chapter has illustrated several concepts that are important in order to promote a significant impact of healing in the fatigue damage process. These are that healing is most significant if rest periods occur before significant damage occurs, and that healing is a function of the length of the rest period and the ability of the binder to flow and wet (temperature dependent). Therefore, modifications to asphalt mixtures to promote healing and validation of their efficacy through file monitoring hold promise as a means of extending the life of our asphalt pavement infrastructure.

References

Abu Al-Rub, R.K., Darabi, M.K., 2012. A thermodynamic framework for constitutive modeling of time- and rate-dependent materials, part I: theory. Int. J. Plast. 34, 61–92.

Abu Al-Rub, R.K., Darabi, M.K., Little, D.N., Masad, E.A., 2010. A micro-damage healing model that improves prediction of fatigue life in asphalt mixes. Int. J. Eng. Sci. 48, 966–990.

Abu Al-Rub, R.K., Darabi, M.K., Kim, S.M., Little, D.N., Glover, C.J., 2013. Mechanistic-based constitutive modeling of aging in hot asphalt mixtures and its effect on the cracking potential and fatigue life of asphalt pavements. Constr. Build. Mater. 41, 439–454.

Allen, R., Little, D., Bhasin, A., 2012. Structural characterization of micromechanical properties in asphalt using atomic force microscopy. J. Mater. Civ. Eng. 24 (10), 1317–1327.

Bhairampally, R.K., Lytton, R.L., Little, D.N., 2000. Numerical and graphical method to assess permanent deformation potential for repeated compressive loading of asphalt mixtures. Transport. Res. Rec. 1723, 150–158.

Bhasin, A., Little, D.N., Bommavaram, R., Vasconcelos, K.L., 2008. A framework to quantify the effect of healing in bituminous materials using material properties. Int. J. Road Mater. Pavement Design 9, 219–242.

Bhasin, A., Bommavaram, R., Greenfield, M.L., Little, D.N., 2011. Use of molecular dynamics to investigate self-healing mechanisms in asphalt binders. J. Mater. Civil Eng. 23, 485–492.

Bommavaram, Reddy R., Bhasin, A., Little, D.N., 2009. Determining intrinsic healing properties of asphalt binders: role of dynamic shear rheometer. Transport. Res. Rec. 2126 (1), 47–54.

www.EngineeringEBooksPdf.com

Cardona, J.-M., Forest, S., Sievert, R., 1999. Towards a theory of second grade thermoelasticity. Extracta Math. 14, 127–140.

Carpenter, S.H., Shen, S., 2006. A dissipated energy approach to study HMA healing in fatigue. In: 85th Annual Meeting of the Transportation Research Board, Washington, DC.

Coleman, B.D., 1964. On thermodynamics, strain impulses, and viscoelasticity. Arch. Ration Mech. An. 17, 230–254.

Coleman, B.D., Noll, W., 1961. Foundations of linear viscoelasticity. Rev. Mod. Phys. 33, 239–249.

Daniel, J.S., Kim, Y.R., 2002. Development of a simplified fatigue test and analysis procedure using a viscoelastic, continuum damage model. J. Assoc. Asphalt Paving Technol. 71, 619–650.

Darabi, M.K., Abu Al-Rub, R.K., Masad, E.A., Huang, C.-W., Little, D.N., 2011. A thermo–viscoelastic–viscoplastic–viscodamage constitutive model for asphaltic materials. Int. J. Solids Struct. 48, 191–207.

Darabi, M.K., Abu Al-Rub, R.K., Little, D.N., 2012a. A continuum damage mechanics framework for modeling micro-damage healing. Int. J. Solids Struct. 49, 492–513.

Darabi, M.K., Abu Al-Rub, R.K., Masad, E.A., Little, D.N., 2012b. A thermodynamic framework for constitutive modeling of time- and rate-dependent materials, part II: numerical aspects and application to asphalt concrete. Int. J. Plast. 35, 67–99.

Darabi, M.K., Abu Al Rub, R.K., Masad, E., Huang, C.W., Little, D., 2012c. A modified viscoplastic model to predict the permanent deformation of asphaltic materials under cyclic-compression loading at high temperatures. Int. J. Plast. 35, 100–134.

Darabi, M.K., Abu Al Rub, R.K., Masad, E., Little, D., 2013. Constitutive modeling of fatigue damage response of asphalt concrete materials with consideration of micro-damage healing. Int. J. Solids Struct. 50, 2901–2913.

De Gennes, P.G., 1971. Reptation of a polymer chain in the presence of fixed obstacles. J. Chem. Phys. 55 (2), 572–579.

Fremond, M., Nedjar, B., 1996. Damage, gradient of damage and principle of virtual power. Int. J. Solids Struct. 33, 1083–1103.

Gurtin, M.E., 2003. On a framework for small-deformation viscoplasticity: free energy, microforces, strain gradients. Int. J. Plast. 19, 47–90.

Huang, C.W., 2008. Development and numerical implementation of nonlinear viscoelastic-viscoplastic model for asphalt materials. PhD dissertation, Texas A&M University.

Huang, C.W., Abu Al Rub, R.K., Masad, E.A., Little, D., Airey, G., 2011. Numerical implementation and validation of a nonlinear-viscoelastic and viscoplastic model for asphalt concrete mixes. Int. J. Pavement Eng. 12, 433–447.

Hui, C.Y., Baney, J.M., Lin, Y.Y., 2001. Mechanics of the JKR (Johnson–Kendall–Roberts) adhesion test. In: Mittal, K.L. (Ed.), In: Adhesion Measurement of Films and Coatings, 2, VSP, Boston, pp. 299–328.

Jahangir, R., Little, D., Bhasin, A., 2015. Evolution of asphalt binder microstructure due to tensile loading determined using AFM and image analysis techniques. Int. J. Pavement Eng. 16, 337–349.

Jones, D.R., 1993. SHRP Material Reference library: asphalt cements: a concise data compilication. Report No. SHRP-A-645.

Kachanov, L.M., 1958. On time to rupture in creep conditions (in Russian). Izv. AN SSSR. Otd. Tekh. Nauk 8, 26–31.

Karki, P., Li, R., Bhasin, A., 2015. Quantifying overall damage and healing behavior of asphalt materials using continuum damage approach. Int. J. Pavement Eng. 16 (4), 350–362.

Kessler, M.R., 2007. Self-healing: a new paradigm in materials design. Proc. Instit. Mech. Eng. G J. Aerospace Eng. 221, 479–495.

www.EngineeringEBooksPdf.com

Kim, Y.R., Little, D.N., Benson, F.C., 1990. Chemical and mechanical evaluation of healing mechanisms in asphalt concrete. J. Asphalt Paving Technol. 59, 240–275.

Kim, R.Y., Lee, H.J., Little, D.N., 1998. Fundamental Properties of Asphalts and Modified Asphalts, vol. 4. Texas A&M University, Texas, Final Report.

Kim, Y.R., Guddati, M.N., Underwood, B.S., Yun, T.Y., Subramanian, V., Savadatti, S., Thirunavukkarasu, S., 2008. Development of a multiaxia viscoelastoplastic continuum damage model. Final report, DTFH61-05-RA-00108 Project.

Lee, H.J., Kim, Y.R., 1998. Viscoelastic continuum damage model of asphalt concrete with healing. J. Eng. Mech. 124 (11), 1224–1232.

Lemaître, J., Chaboche, J.-L., 1990. Mechanics of Solid Materials. Cambridge University Press, Cambridge, UK.

Little, D.N., Bhasin, A., 2007. Exploring mechanisms of healing in asphalt mixtures and quantifying its impact. In: van der Zwaag, S. (Ed.), Self healing Materials. Springer, Dordrecht, The Netherlands, pp. 205–218.

Little, D.N., Bhasin, A., Hefer, A., 2006. Final report for NCHRP RRD 316: using surface energy measurements to select materials for asphalt pavement. Transportation Research Board of the National Academies, Washington, DC, p. 196.

Little, D.N., Prapnnachari, S., 1991. Investigation of the microstructural mechanisms of relaxation and fracture healing in asphalt. Annual Report to the Air Force Office of Scientific Research.

Little, D.N., Kim, Y.R., Benson, F.C., 1987. Investigation of the mechanism of healing in asphalt. Report to the National Science Foundation, Texas A&M University, Texas.

Little, D.N., Lytton, R.L., Williams, A.D., Chen, C.W., 2001. Microdamage Healing in Asphalt and Asphalt Concrete, Volume I: Microdamage and Microdamage Healing. Project summary report, DTFH61-92-C-00170, Texas Transportation Institution, College Station, TX, Research Report 7229.

Lytton, R.L., Uzan, J., Fernando, E.G., Roque, R., Hiltunen, D., Stoffels, S.M., 1993. Development and validation of performance prediction models and specifications for asphalt binders and paving mixes. SHRP A-357 Project Report.

Masad, E., Tashman, L., Little, D., Zbib, H., 2005. Viscoplastic modeling of asphalt mixes with the effects of anisotropy, damage and aggregate characteristics. Mech. Mater. 37, 1242–1256.

Maugin, G.A., Muschik, W., 1994. Thermodynamics with internal variables, part I. General concepts. J. Non-Equilib. Thermo. 19, 217–249.

Maugis, D., Barquins, M., 1983. Adhesive contact of sectionally smooth-ended punches on elastic half-spaces: theory and experiment. J. Phys. D. Appl. Phys. 16 (10), 1843–1874.

Miao, S., Wang, M.L., Schreyer, H.L., 1995. Constitutive models for healing of materials with application to compaction of crushed rock-salt. J. Eng. Mech. 121, 1122–1129.

Muller, V.M., Yushchenko, V.S., Derjaguin, B.V., 1979. On the influence of molecular forces on the deformation of an elastic sphere and its sticking to a rigid plate. J. Colloid Interface Sci. 77, 91–99.

Nishizawa, T., Shimeno, S., Sekiguchi, M., 1997. Fatigue analysis of asphalt pavements with thick asphalt mixture layer. In: 8th Inernational Conference on Asphalt Pavements, Seattle, Washington, pp. 969–976.

Palvadi, S., Bhasin, A., Little, D.N., 2012a. Method to quantify healing in asphalt composites by continuum damage theory in fine aggregate asphalt specimen. In: 7th RILEM International Conference on Cracking in Pavements, Delft, The Netherlands, pp. 1115–1123.

Palvadi, S., Bhasin, A., Motamed, A., Little, D.N., 2012b. Quantifying Healing based on viscoelastic continuum damage theory in fine aggregate asphalt specimen. In: 7th RILEM International Conference on Cracking in Pavement, Delft, the Netherlands, pp. 1115–1123.

www.EngineeringEBooksPdf.com

Park, S.W., Kim, R.Y., Schapery, R.A., 1996. A viscoelastic continuum damgae model and its application to uniaxial behavior of asphalt concrete. Mech. Mater. 24 (4), 241–255.
Pauli, A.T., 2014. Chemomechanics of damage accumulation and damage-recovery healing in bituminous materials. Dissertation, Delft University of Technology, The Netherlands.
Petersen, J.C., 1984. Chemical composition of asphalts related to asphalt durability: state of the art. Transportation Research Board No 999. pp. 13–30.
Prapnnachari, S., 1992. Investigation of the microstructural mechanism of relaxation in asphalt. PhD dissertation, Texas A&M University.
Qiu, J., 2011. Self healing of asphalt mixtures towards a better understanding of the phenomenon. PhD dissertation, TU Delft.
Rad, F.Y., Sefidmazgi, N.R., Bahia, H., 2014. Application of diffusion mechanism. Transport. Res. Rec. 2444 (1), 71–77.
Rahmani, E., Darabi, M.K., Abu Al-Rub, R.K., Kassem, E., Masad, E., Little, D., 2013. Effect of confinement pressure on the nonlinear-viscoelastic response of asphalt concrete at high temperatures. Constr. Build. Mater. 47, 779–788.
Reinhardt, H.W., Jooss, M., 2003. Permeability and self-healing of cracked concrete as a function of temperature and crack width. Cem. Concr. Res 33, 981–985.
Schapery, R.A., 1969. Further Development of a Thermodynamic Constitutive Theory: Stress Formulation. Purdue University, Purdue Research Foundation, Lafayette, IN.
Schapery, R.A., 1989. On the mechanics of crack closing and bonding in linear viscoelastic media. Int. J. Fract. 39, 163–189.
Schmets, A.J.M., Kringos, N., Scarpas, A., Duif, C., Schitter, G., Pauli, T., 2009. First-principles investigation of the multiple phases in bituminous materials: the case of asphaltene stacking. Adv. Testing Charact. Bituminous Mater. 1, 143–150.
Shakiba, M., Abu Al Rub, R.K., Darabi, M.K., You, T., Masad, E., Little, D., 2013. A continuum coupled moisture-mechanical damage model for asphalt concrete. Transport. Res. Board 2372, 72–82.
Shan, L., Tan, Y., Underwood, S., Kim, Y., 2010. Application of thixotropy to analyze fatigue and healing characteristics of asphalt binder. Transport. Res. Rec. 2179, 85–92.
Shell Pavement Design Manual, 1978. Shell International Petroleum Company Ltd., London.
Song, I., Little, D.N., Masad, E., Lytton, R., 2005. Comprehensive evaluation of damage in asphalt mastics using x-ray ct, continuum mechanics, and micromechanics. J. Assoc. Asphalt Paving Technol. 74, 885–920.
Tabatabaee, H., Bahia, H., 2014. Establishing use of asphalt binder cracking tests for prevention of pavement cracking. Road Mater. Pavement Design 15, 279–299.
Tashman, L., Masad, E., Little, D., Zbib, H., 2005. A microstructure-based viscoplastic model for asphalt concrete. Int. J. Plast. 21, 1659–1685.
Underwood, B.S., Kim, Y.R., Guddati, M.N., 2010. Improved calculation method of damage parameter in viscoelasic continuum damage model. Int. J. Pavement Eng. 11 (6), 459–476.
Voyiadjis, G.Z., Shojaei, A., Li, G., 2011. A thermodynamic consistent damage and healing model for self healing materials. Int. J. Plast. 27, 1025–1044.
Williams, D., Little, D.N., Lytton, R.L., Kim, Y.R., Kim, Y., 1998. Microdamage healing in asphalt concrete, volume II: laboratory and field testing to assess and evaluate microdamage and microdamage healing. DTFH61-92-C-00170, Research Report 7229.
Wool, R.P., O'Connor, K.M., 1981. A theory of crack healing in polymers. J. Appl. Phys. 52 (10), 5953–5963.
Zhang, L., Greenfield, M.L., 2007. Analyzing properties of model asphalts using molecular simulation. Energy Fuel 21 (3), 1712–1716.
Ziegler, H., 1977. An Introduction to Thermodynamics. North-Holland Pub. Co., Amesterdam.

www.EngineeringEBooksPdf.com

The fatigue cracking of asphalt mixtures in tension and compression

8

R.L. Lytton[1], *Y. Zhang*[2], *X. Luo*[2], *R. Luo*[2]
[1]Texas A&M University, College Station, TX, USA; [2]Texas A&M Transportation Institute, College Station, TX, USA

8.1 Introduction

All properties of an asphalt mixture must be based upon the properties of the mixture in an undamaged state. Subsequent tests of the mixture in different stress or strain states at a level to cause damage can be referred to this undamaged state to assess the degree to which the mixture has been changed. All forms of such change from an original state by such damaging processes as fatigue, plasticity, healing, moisture damage, and aging can only be properly assessed by comparison with an accurately measured undamaged state. The properties addressed in this chapter are engineering properties. In order to be useful to engineers, these properties must be measured with tests that can be conducted quickly, accurately, and repeatably, with consistent results. Moreover, the tests must measure true properties of the mixtures so that they can be put into a catalog of typical properties that can be used by engineers in the design of mixtures, pavements, and specifications for construction quality control and assurance and for the prediction of the future performance of the pavement as it is constructed. This chapter summarizes the results of the testing and analysis methods developed to provide the engineering properties of asphalt mixtures in tension and compression (as expected, they are different) both in the undamaged and the damaged states. Five categories of mixture properties are summarized here:

- Isotropic viscoelastic properties of asphalt mixtures in tension;
- Anisotropic viscoelastic properties of asphalt mixtures in compression;
- Permanent deformation of asphalt mixtures in compression;
- Fatigue, endurance limit, and healing of asphalt mixtures in tension;
- Fracture of asphalt mixtures in compression.

Under each heading, the objective and scope of the developments, the tests, analyses, models, and findings will be summarized. Under each topic, the reader will be directed to the published works in which the details of each development can be found.

Advances in Asphalt Materials. http://dx.doi.org/10.1016/B978-0-08-100269-8.00008-8
© 2015 Elsevier Ltd. All rights reserved.

www.EngineeringEBooksPdf.com

8.2 Isotropic viscoelastic properties of asphalt mixtures in tension

The first test protocol to determine undamaged tensile properties of an asphalt mixture was to determine the master curves of the complex modulus and phase angle of an asphalt mixture. Figures 8.1 and 8.2 present the constructed master curves of the magnitude and phase angle of the undamaged tensile complex modulus, respectively, at the reference temperature of 20 °C.

The test protocol applied a uniaxial monotonically increasing tensile stress to the test specimen. The relationship between the relaxation modulus and the complex modulus was used to determine the complex modulus as a complex function of frequency. The test and data analysis protocol were performed on the same specimen at three temperatures, so master curves of the magnitude and phase angle of the complex modulus were constructed

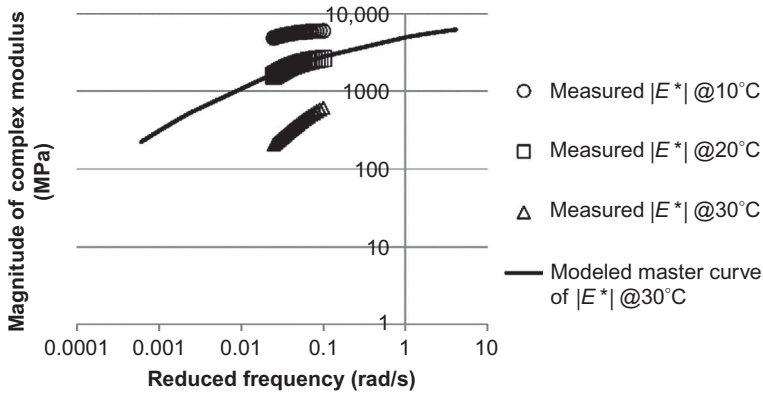


Figure 8.1 Master curve of magnitude of tensile complex modulus at 20 °C.

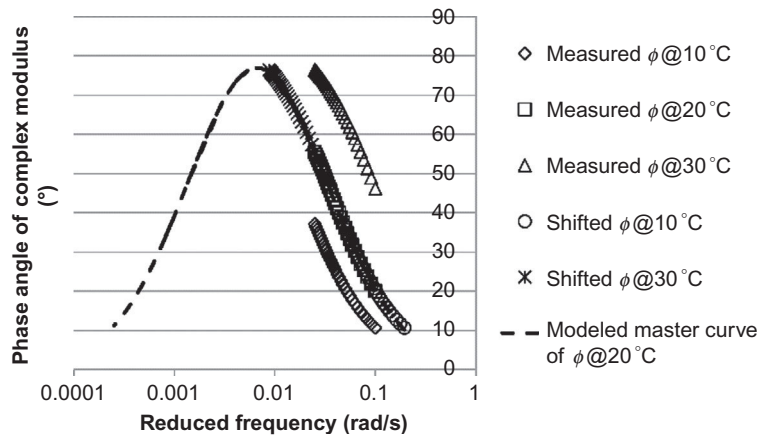


Figure 8.2 Master curve of phase angle of tensile complex modulus at 20 °C.

www.EngineeringEBooksPdf.com

using the time–temperature superposition principle. The master curves of the magnitude and phase angle of the complex modulus were fitted with mathematical functions that were reported in the literature and were modified to be more comprehensive. As seen in Figure 8.2, the maximum phase angle in tension rises to nearly 80°, which is considerably greater than the maximum phase angle in compression. The test protocol requires only 10 min to complete at each temperature.

A second test protocol was to determine the tensile properties of an asphalt mixture that are undamaged under repeated loading. These are the properties that provide the baseline from which to determine the amount of damage that is done by repeated loading. The test is a controlled-strain repeated direct tension (RDT) test and it is useful both for characterizing the viscoelastic properties of undamaged asphalt mixtures and, under damaging strain levels, assessing fatigue cracking accompanied by plastic deformation. The strain curve in a loading cycle of the controlled-strain RDT test is a standard Haversine wave with only a tensile portion, whereas the stress curve has a tensile portion and a compressive portion (quasicompression) because of the viscoelastoplastic nature of the asphalt mixture. Usually, the material properties in the tensile stress portion (the tensile properties) are used, while those in the compressive stress portion (the quasicompressive properties) are neglected. This leads to nonnegligible errors in estimating the dissipated strain energy (DSE) and characterizing the damage (such as cracking and permanent deformation) generated in the material. The objective of this test protocol is to obtain complete material properties and accurate amounts of dissipation and storage of energy of this test method as the foundation of damage characterization. This protocol provides methods to simulate the stress and strain for the tensile and compressive stress portions separately so as to determine the tensile and quasicompressive properties, respectively. The difference between the tensile and quasicompressive properties is investigated using statistical analysis. It is found that the tensile properties of an asphalt mixture are different from the quasicompressive properties, due to the crack opening and closure within each loading cycle. The DSE calculated using both the tensile and quasicompressive properties is larger compared to the traditional method using only the tensile properties, indicating an underestimation of the damage by the traditional method. In addition, the recoverable strain energy (RSE) is investigated to examine the ability of an asphalt mixture to store and recover energy. A new perspective in terms of the integration method is provided to determine the actual amount of the RSE in a loading cycle.

The results of these tests conducted at a damaging level are discussed in a subsequent section on the fatigue, endurance limit, and healing of asphalt mixtures.

Details of the measurements that were made with both test protocols, the analysis of the test data, and the resulting undamaged viscoelastic properties of a variety of asphalt mixtures with different binders, air voids, and aging can be found in Luo and Lytton (2010), Luo et al. (2013d), and Luo (2012).

8.3 Anisotropic viscoelastic properties of asphalt mixtures in compression

An asphalt mixture in compression behaves distinctly differently from the same mixture in tension for several reasons. Because of the orientation of the aggregates in the mixture after compaction, with the long axis tending to lie flat, the undamaged

www.EngineeringEBooksPdf.com

properties of the mixture in compression are anisotropic. The mixture responds viscoelastically to imposed stresses and strains. When it is damaged by high levels of stress or strain, it undergoes both plastic deformation and anisotropic cracking. As with the tensile properties, it is necessary to measure the undamaged properties so as to determine the amount of damage that is done by subsequently applied higher levels of stress or strain. What has been developed is a very rapid, inexpensive, and simple method, which is also an accurate method for measuring the undamaged properties. The details of the measurements and the analysis of the test data that are produced are found in Zhang (2012) and Zhang et al. (2011, 2012a).

The first part of the testing procedure is to use what has been termed the "hot dog" test because it uses an actual hot dog cooker rotator to rotate a cylindrical asphalt sample under a digital scanner, which records the outline of each aggregate on the circumference of the cylindrical asphalt sample. This apparatus is illustrated in Figure 8.3. Analysis of the exposed area, shape, and inclination of each aggregate in the lateral scan produces a single number, which is a measure of the degree of anisotropy. The measure is called the modified "vector magnitude" and ranges from 0 for purely isotropic to 1.0 for purely anisotropic aggregate orientation. Most asphalt mixtures fall between 0.2 and 0.5. This test requires approximately 3 min to complete. Careful measurements of the modulus ratio between the stiffer axial modulus and the less stiff radial modulus were correlated with this modified "vector magnitude," with the result shown in Figure 8.4. The details of this test and the relationship of the modified "vector magnitude" to the modulus ratio are found in Zhang et al. (2011).

The second part of the testing procedure is to use a set of three test configurations: a uniaxial creep test in compression, a uniaxial creep test in tension, and a diametrically loaded indirect tension creep test. The sample is never subjected to a damaging level of strain in any of the three test configurations. The tests are conducted as creep tests and the data are analyzed as with the undamaged tensile properties, using the Laplace transform and the elastic–viscoelastic correspondence principle. The tests are run at three temperatures, and the test results are analyzed together to produce the master curves of



Figure 8.3 Digital lateral scanner (i.e., hot-dog tester) of an asphalt mixture sample.

www.EngineeringEBooksPdf.com

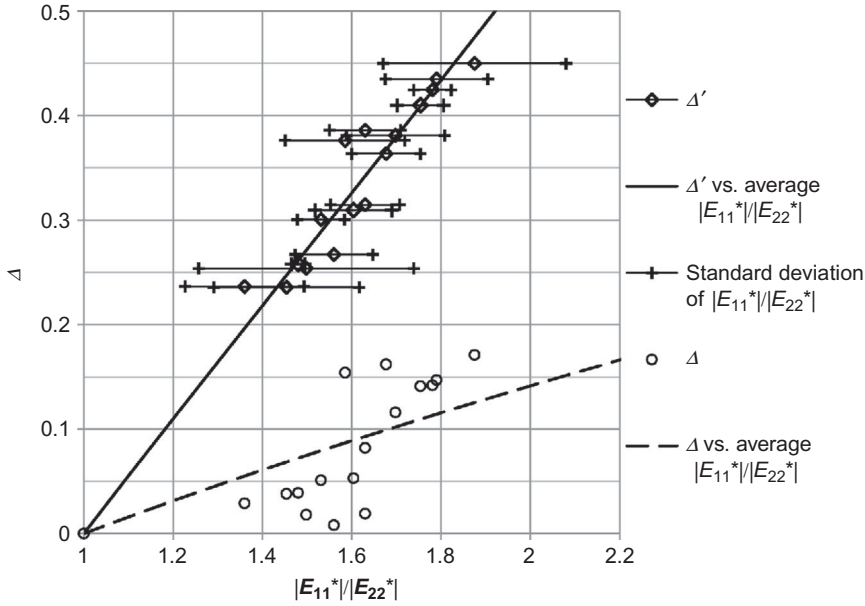


Figure 8.4 Relationship between vector magnitude and anisotropic modulus ratio (modified vector magnitude Δ' considers orientation, shape, and size of both coarse and fine aggregates, thus it shows a better relationship with the anisotropic modulus ratio compared to the vector magnitude that only considers the aggregate orientation).

the axial and radial compressive complex moduli and their complex Poisson's ratios and the axial tensile complex modulus. All of the complex moduli and complex Poisson's ratios are viscoelastic, and each has a magnitude and phase angle. Examples of the master curves of the complex modulus magnitudes and phase angles determined by this protocol are shown in Figures 8.5 and 8.6, respectively. As illustrated in the figures, the magnitude of the radial compression modulus is always smaller than that of the axial compressive modulus. The magnitude of the tensile modulus is closer to that of the radial modulus at the lower frequencies of loading and is closer to the axial modulus with the higher loading frequencies. Consistent with anisotropic elastic theory, the magnitudes of the Poisson's ratios exceeded 0.5 in the lower loading frequencies. The maximum modulus phase angle in compression was around 40°, and the maximum phase angle in tension was around 80°. The compression result is in agreement with published results for compressive tests, and the tensile results are in agreement with the results of the tensile tests noted above. New models (i.e., the β-model) of the phase angles of the complex moduli and Poisson's ratios as they vary with frequency were developed to match the measured data. The details of the test configurations and the master curves of the complex modulus magnitudes and phase angles are found in Zhang et al. (2012a).

www.EngineeringEBooksPdf.com

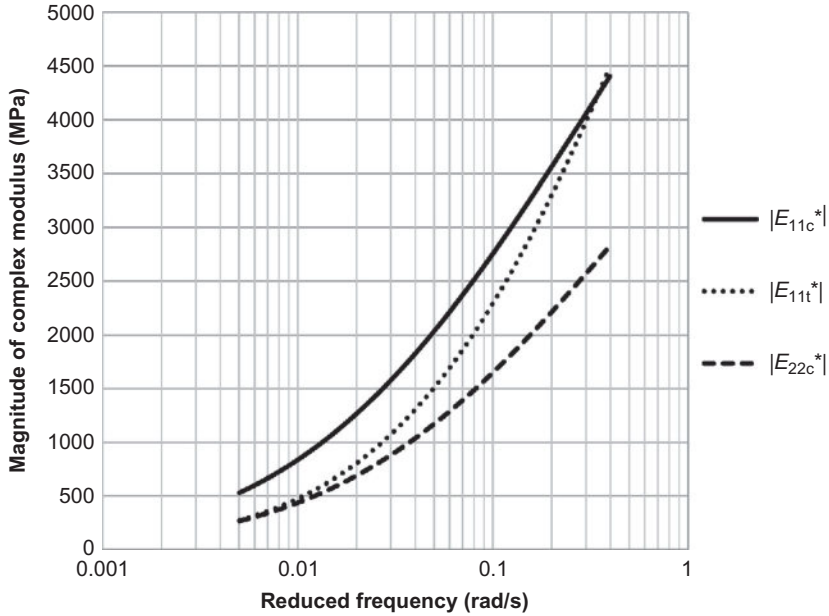


Figure 8.5 Master curves of the magnitude of complex moduli for asphalt mixtures at 20 °C (E_{11c}* is the axial compressive modulus; E_{11t}* is axial tensile modulus; E_{22c}* is the radial compressive modulus; one can find that $|E_{11c}^*| \neq |E_{11t}^*|$ and $|E_{11c}^*| > |E_{22c}^*|$).

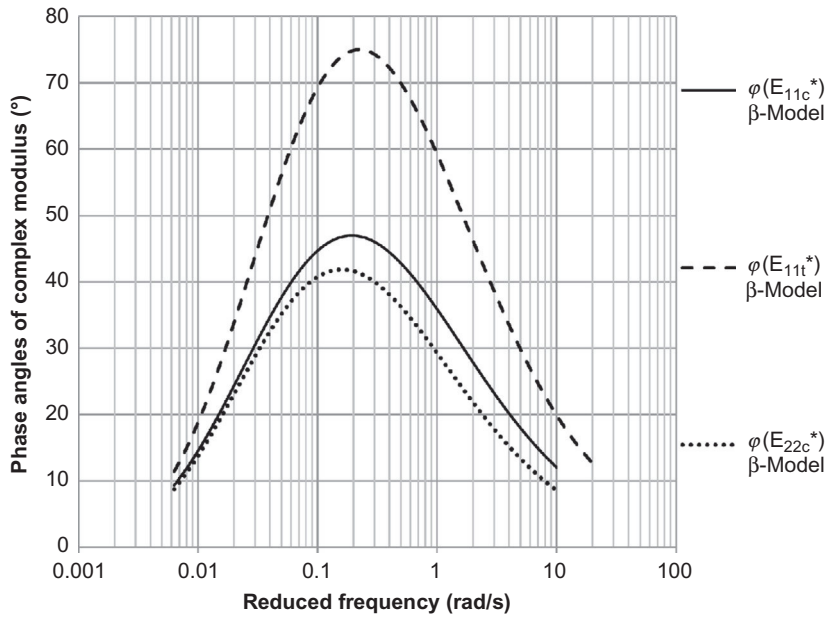


Figure 8.6 Master curves of the phase angle of complex moduli asphalt mixtures at 20 °C (E_{11c}* is the axial compressive modulus; E_{11t}* is axial tensile modulus; E_{22c}* is the radial compressive modulus).

www.EngineeringEBooksPdf.com

8.4 Permanent deformation of asphalt mixtures in compression

Extensive studies indicate that one of the main resources for rutting is the permanent deformation developed in the asphalt mixture layers, which is primarily attributed to the irrecoverable shear deformation under heavy truck loads and a high environmental temperature. To accurately model and predict the permanent deformation occurring in the asphalt mixture layers, a variety of mechanistic models based on viscoplasticity theories have been proposed and widely employed as constitutive relations in the continuum mechanistic modeling. The continuum mechanistic models for asphalt mixtures have an advantage in their computational simplicity; that is, the material responses such as permanent deformation can be easily predicted once the model parameters are provided. However, some problems exist in those models that impede their wide application. Several significant problems of the existing viscoplastic models for asphalt mixtures are presented in the following.

First, the inherent anisotropy of asphalt mixtures has not been well addressed in the constitutive modeling. Asphalt mixture is an inherently anisotropic viscoelastic material, according to published discussions, which indicated that without consideration of inherent anisotropy caused by the preferentially oriented granular particles (e.g., soils, sands, and aggregates) in the constitutive formulation, some important material properties such as noncoaxial and dilatant behaviors would not be accounted for properly.

Second, in addition to considering the inherent anisotropy, the stress-induced anisotropy should also be taken into account in the constitutive models of the asphalt mixture. In fact, the anisotropic cracks that form due to the damaging levels of stress are the cause of the stress-induced anisotropy. These cracks dominate the evolution of the permanent deformation when the material has reached the peak of the stress–strain curves, as well as in high stress levels and long loading periods. For instance, the anisotropic viscofracture controls the properties of the asphalt mixture in the softening stage after the peak stress in a strength test, and in the tertiary flow stage in a repeated destructive stress test.

Third, a nonassociated viscoplastic flow rule must be used in the viscoplastic model of the asphalt mixture. The nonassociated flow rule indicates that the direction of the incremental viscoplastic strain is not parallel to the direction of the incremental stress. Many studies have indicated that the viscoplastic deformation of asphalt mixtures and granular materials in general is nonassociated, and an associated flow rule (directions are the same for incremental strain and stress) overestimates the dilation of the asphalt mixture. Thus, it is very important to accurately determine the viscoplastic potential that has a different inclination and orientation than the viscoplastic yield surface because of the nonassociated flow rule.

Fourth, a comprehensive viscoplastic yield surface must be proposed to provide a yield function for an asphalt mixture that satisfies both mechanical and mathematical requirements. The mechanistic requirements for the yield surface must include:

www.EngineeringEBooksPdf.com

(1) The differences between compression, tension, and extension;
(2) Material cohesion and internal friction;
(3) Dilation and strain hardening mechanism;
(4) The temperature and strain rate dependence.

The mathematical requirements for the yield surface include:

(1) A smooth yield function;
(2) A convex yield function.

The shortcomings of the existing yield surface models for asphalt mixtures are presented in detail in Zhang (2012) and Zhang et al. (2013a). Zhang (2012) also proposes a comprehensive viscoplastic yield surface that satisfies all of the requirements, and presents the data that proves it.

In order to develop a model that fulfills all of the mechanical and mathematical requirements, a modified effective stress method was adopted to integrate both the inherent anisotropy and the stress-induced anisotropy in the viscoplastic constitutive model. Next, an extended Perzyna-type viscoplastic constitutive model was developed to incorporate the comprehensive yield surface described above. Laboratory experiments were used to determine the model parameters for a variety of asphalt binders, air voids, and levels of aging of the mixtures tested. The tests proved to be simple to use as well as rapid, accurate, and repeatable. The results of analyzing the test data showed that the model properties that can be determined with this approach overcome the shortcomings of the existing models.

More specifically, the model that was developed and validated is a generalized Drucker–Prager (GD–P) viscoplastic yield surface model for asphalt mixtures, in which a smooth and convex octahedral yield surface function was developed to characterize the full range of the internal friction angles from 0° to 90°. By way of contrast, the widely used extended Drucker–Prager (ED–P) yield function was demonstrated to be applicable only for a material that has an internal friction angle less than 22°, due to the convexity criterion of the yield surface. All of the asphalt mixtures tested had friction angles greater than 30°. The GD–P model was formulated based on fabric tensor modified stresses to consider the inherent anisotropy of asphalt mixtures that is due to inclined aggregates. Lab tests proved that permanent deformation using existing models will be underestimated without considering material anisotropy and convexity of yield surface. Permanent deformation is used to predict the rut depth, and this is largely related to wet weather accident rates. Consequently, an underprediction of the amount of permanent deformation is on the unsafe side.

Because of the approach taken with the material testing, it was possible to make the measurements and analyze the results to produce material properties in a very short time. Table 8.1 shows the time required for each of the tests that will completely characterize the properties of an asphalt mixture in compression. It must be emphasized that despite the comprehensive nature of the material properties that can be generated by these simple tests, they can all be conducted in the span of 1 day.

The total strains that are generated in the destructive repeated compressive load test are the simultaneous accumulation of five different types of strain: elastic, plastic,

www.EngineeringEBooksPdf.com

Table 8.1 Testing methods and outcomes for compressive viscoplastic permanent deformation and viscofracture fatigue characterization and required testing time

Material properties	Test methods	Time required for testing	Test outcomes
Anisotropy	Lateral surface scanning "hot dog" test	<5 min	Vector magnitude
Viscoelasticity	Compressive/tensile creep test	<5 min	Anisotropic
	Indirect tensile creep test	<5 min	Creep compliance, relaxation modulus, complex modulus, complex Poisson's ratio
	Nondestructive repeated compressive load test	~20 min	
Viscoplasticity and viscofracture	Uniaxial/triaxial compressive strength tests	<10 min	Yield strength Strain hardening Temperature and rate factors
	Destructive repeated compressive load test	~2 h	Damage density Paris' law parameters

viscoelastic, viscoplastic, and viscofracture. Making maximum use of the concept of pseudostrain and defining the reference modulus as the Young's modulus of the material, this approach has developed a unique and very useful method of separating the strains from one another at all times during the testing process. Separating the strains has the formal name of "strain decomposition." A detailed description of the process of strain decomposition, the reasoning behind it, and some data illustrative of it are shown in Zhang et al. (2012b, 2013b, 2014). Figure 8.7 illustrates the typical results of the axial strain decomposition.

The strain superscripts T, ve, vp, and vf indicate the total, viscoelastic, viscoplastic, and viscofracture strains, respectively. It is noted that the elastic and plastic strains were combined into viscoelastic and viscoplastic strains, respectively. Because of the anisotropic nature of an asphalt mixture in compression, a similar strain decomposition process must be done in the radial direction in a cylindrical test specimen as well. There are three phases in the destructive compression testing of an asphalt mixture. Phase I is when the strain is rapidly increasing at the beginning of the test;

www.EngineeringEBooksPdf.com

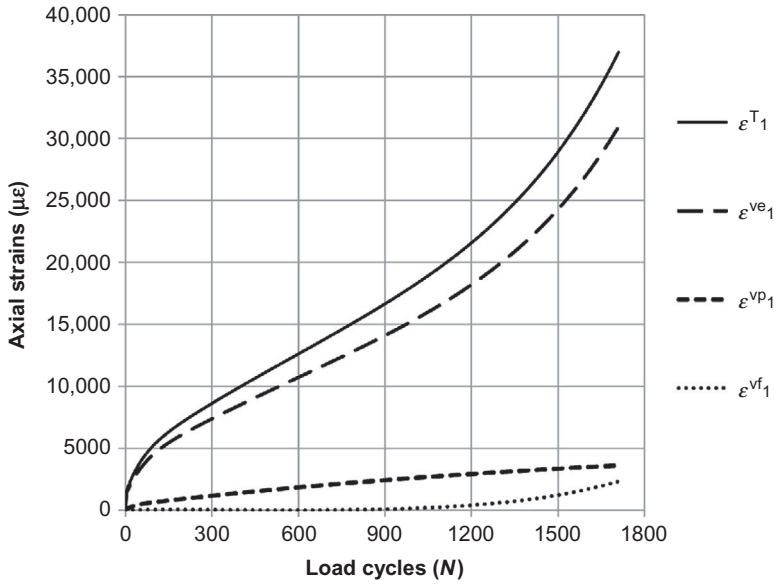


Figure 8.7 Axial strain decomposition for an asphalt mixture. (Strain decomposition was performed by using pseudostrain concept. The viscoplastic strain and the viscofracture strain were employed to characterize permanent deformation and compressive cracking, respectively.)

Phase II is when the strain is increasing at a steady rate; and Phase III begins at the so-called flow point where the viscofracture strain begins to grow. The "flow point" in Figure 8.7 is at around 1000 load repetitions. Figure 8.7 also illustrates another important point: most of the total strain is made up of the viscoelastic strain.

The use of the pseudostrain concept also permitted a simple determination of the cohesive shear strength, C; the internal friction angle, φ; and the two yield function parameters, α and κ_0, based on the straight-line portion of the stress versus pseudostrain graph, as illustrated in Figure 8.8. Beyond the initial yield point, the strain-hardening function (from the initial yield point to the ultimate yield strength) and the strain softening function (beyond the ultimate yield strength point) parameters can be found. "Strain softening" is explained entirely by the viscofracture that occurs beyond the ultimate yield strength. The ultimate yield strength occurs at the "flow point." All of these relations become very clear when the stress is plotted versus the pseudostrain. The slope of the initial portion of the stress–pseudostrain curve is the Young's modulus.

The clarity provided by the pseudostrain concept carries over into the formulation of the yield function, a detailed description of which is provided in Zhang (2012). Figure 8.9 shows the trace of the yield function on the octahedral plane for the entire

www.EngineeringEBooksPdf.com

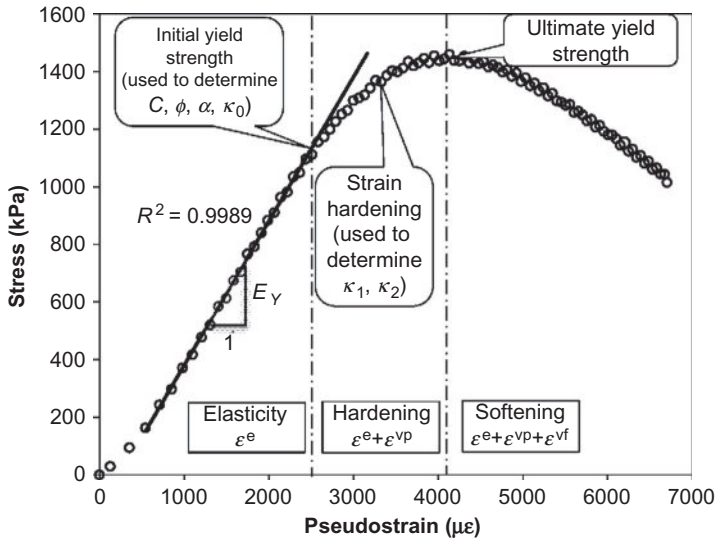


Figure 8.8 Stress versus pseudostrain in a uniaxial compressive strength test of an asphalt mixture (showing the use of strain decomposition in the determinations of yield strength and strain hardening during viscoplastic deformation).

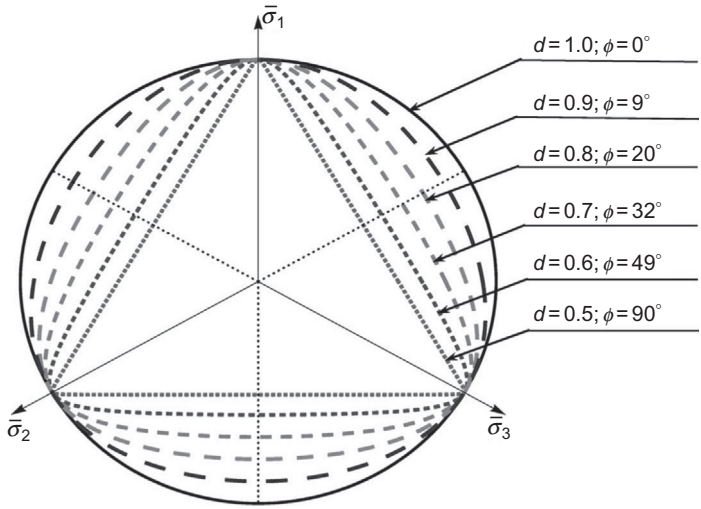


Figure 8.9 Generalized Drucker–Prager yield surfaces on the octahedral plane (showing convex yield surfaces over the full range of internal friction angles from 0° to 90°).

www.EngineeringEBooksPdf.com

range of internal friction angles, from 0° to 90°, that can be represented by the new GD–P yield function. The factor "*d*" shown in the figure is the ratio of the yield stress in extension to the yield stress in compression. The 0° yield function is for a purely cohesive material, and the GD–P model is reduced to a Drucker–Prager model.

The detailed data that are presented in Figure 8.10 are an illustration of the superiority of this new formulation of the GD–P yield function over the ED–P yield function. As noted above, the new GD–P is capable of retaining a convex yield surface for all possible values of the friction angle. In contrast, the ED–P yield function becomes concave at and above friction angles of 22°, thus violating one of the mathematical requirements of a valid yield function. The dotted line in the figure is the widely used ED–P yield function, and is plotted using the measured friction angles of this asphalt mixture of 46° with a 4% air void content. The ED–P yield function is clearly concave and predicts a yield stress that is larger than the measured values of the yield stress. This is what leads to an underestimate of the amount of permanent deformation and thus rutting by the ED–P yield function. In contrast, the solid line is the yield function from the new GD–P yield function, which is not only convex but also correctly predicts the values of the yield stress. This will lead to larger and more realistic predictions of permanent deformation and rutting. Because this prediction is directly related to wet weather accident rates, the use of the more accurate method is desirable.

The model of permanent deformation in compression that has been developed satisfies all of the mechanical and mathematical requirements that were listed at the

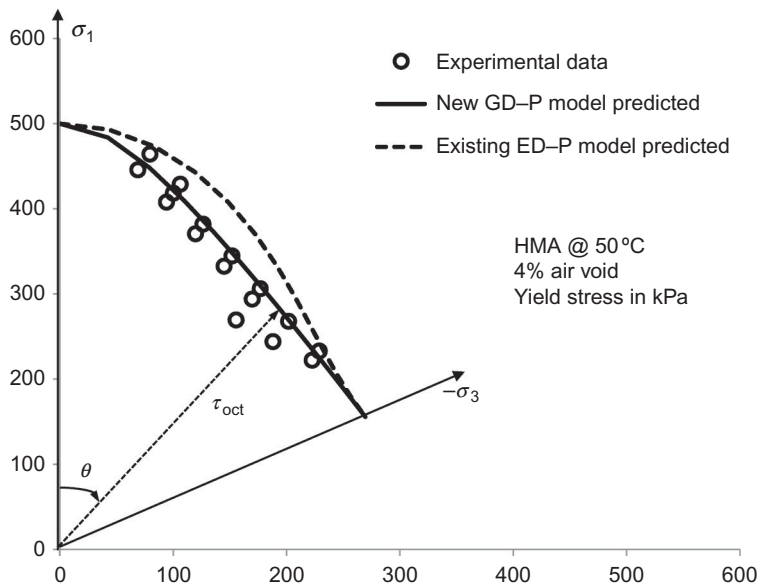


Figure 8.10 Comparisons of yield octahedral shear stresses between experimental data and the predictions from the proposed generalized Drucker–Prager (GD–P) model and the existing extended Drucker–Prager (ED–P) model for asphalt mixtures with 4% air void content.

www.EngineeringEBooksPdf.com

beginning of this section on permanent deformation. In the process, a new and very simple method has been developed to determine the anisotropic characteristics of asphalt mixtures: a strain decomposition method has been formulated and used showing the simplicity and accuracy that can be achieved by making maximum use of the pseudostrain concept, and a new GD–P yield function and its corresponding nonassociated plastic potential function have been proposed and proven by actual measurement to overcome the shortcomings of the widely used ED–P yield function. Perhaps most significant of all, from a practical point of view, is the short time required to complete all of the testing that is needed to generate all of these material properties, as spelled out in Table 8.1. Everything can be completed in 1 day!

8.5 Fatigue, endurance limit, and healing of asphalt mixtures

Fatigue in asphalt mixtures occurs because of the growth of cracks in the mixture. The cracks begin as air voids that have been compressed during the compaction process, and as microcompositional flaws in the binder, which are commonly known as "bee" structures. It is from these damaged nuclei that the cracks will begin to grow. Crack growth can occur as both adhesive and cohesive fractures within the same mixture. Adhesive fracture occurs in the thin films of binder that coat the aggregates in a mixture. In adhesive fracture, cracks grow along the interface between the aggregate and the binder. Cohesive fracture occurs entirely within the binder in the thicker films. Moisture damage to an asphalt mixture is principally an adhesive crack at the interface on which moisture has intruded and has debonded the asphalt from the aggregate surface.

8.5.1 Energy-based mechanistic approach

The method used to predict the fatigue of asphalt mixtures summarized here is called the energy-based mechanistic (EBM) approach, and it is explained in more detail in Luo et al. (2013a,b,c, 2014). It is a purely mechanical approach based on a continuum concept called distributed continuum fracture (DCF), and simple mechanical principles (force equilibrium and energy balance). The DCF is developed especially to model the evolution of a multitude of randomly distributed air void or crack systems in asphalt mixtures. It is impracticable and unnecessary to simulate chaotic air void or crack systems by their exact structures and compositions. Instead, the DCF is built making use of some concepts of the continuum damage mechanics (CDM) to maintain the advantages of simplicity and effectiveness. It further introduces a direct description of damage evolution in terms of evolving cracks for greater accuracy and efficiency in damage characterization. Two characteristic variables are adopted in the DCF: (1) one characteristic variable is to measure the size of air voids or cracks, called average air void size or average crack size, which is defined based on an equal energy consumption principle and (2) the other characteristic variable is to represent the actual mechanical responses of the intact material due to damage, called true stress for cracking and true internal stress for healing.

www.EngineeringEBooksPdf.com

In the EBM approach, the undamaged properties of a mixture remain unchanged as the cracks grow. What does change as the damage increases are the "apparent properties," which are derived directly from the measurements that are made on the sample that is being loaded repeatedly. The relations between the "apparent properties" and the undamaged properties are formulated as balance equations in which the apparent forces and energies are equated to the "true" forces and energies. Using these balance equations and the undamaged properties of the mixture, it is possible to determine the true stress in the material, which changes as the damage increases. As an illustration of this approach, the relationship between apparent and true stress is given below

Force balance between apparent configuration and true configuration

$$P = \sigma^{A} A = \sigma^{T}(A - S), \tag{8.1}$$

where σ^{A} is the apparent stress, σ^{T} is the "true" stress, A is the full cross-sectional area, and S is the cross-sectional area that is lost due to the presence of cracks or voids.

The apparent stress is calculated from the total load divided by the total cross-sectional area, whereas the true stress is the total load divided by the total area minus the "lost area" due to the cracks or air voids in the cross section. The true stress is a continuum stress, that is, it is a mean stress averaged over the cross section of a representative volume element. This true stress is only slightly larger than the apparent stress, because the ratio of the cracked area to the total cross-sectional area rarely exceeds 25% when the material is considered to have failed in a beam fatigue test. The ratio of the lost area to the total cross-sectional area is called the "damage density."

The same reasoning is used with the energy balance equations: the apparent energy as measured is equated with the true energy, which is calculated using the undamaged properties of the intact cross section. There are several energy balance equations that are used in characterizing the fatigue properties of an asphalt mixture: DSE balance, RSE balance, dissipated pseudostrain energy (DPSE) balance, and recoverable pseudostrain energy (RPSE) balance. Details of these energy balance equations can be found in Luo et al. (2013a,b, 2014). Using all of the force and energy balance equations together gives a sufficient number of equations to successfully determine the true stress and damage density as well as the number and mean radius of the cracks that make up the damage density with each load repetition.

In order for all of these to be calculated with each load repetition, it is absolutely necessary to adhere to a consistent and rigorous use of the pseudostrain concept. The essential aspect in determining the pseudostrain is to identify the reference state, in which the material properties (such as modulus and phase angle) are used to calculate the pseudostrain. The reference state is illustrated in Figure 8.11 with the aid of a typical stress–strain curve under tension. As the strain level increases, the material passes through the linear viscoelastic phase, and then the nonlinear viscoelastic phase, and

www.EngineeringEBooksPdf.com

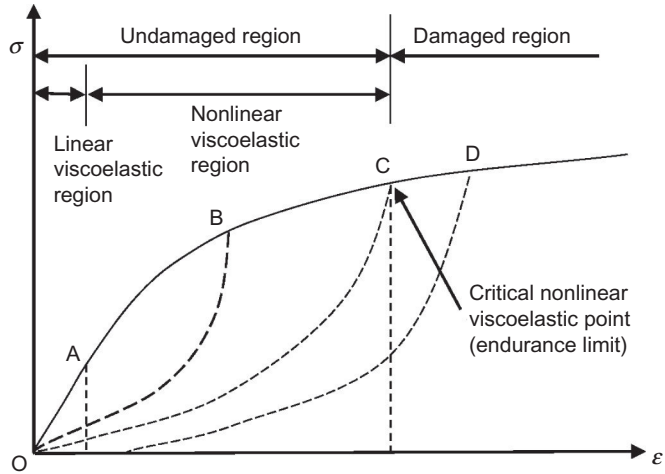


Figure 8.11 Typical stress–strain curve of an asphalt mixture in tension.

then the damaged phase. The threshold between the nonlinear viscoelastic phase and the damaged phase is the critical nonlinear viscoelastic point, or endurance limit for fatigue. The difference between the linear and nonlinear phases is that in the linear phase, all energy that is put into the mixture is recovered, whereas in the nonlinear phase, there is a loss or dissipation of energy. Beyond the endurance limit, the material properties of the mixture begin to change: the apparent modulus decreases and the apparent phase angle increases. If the state of the stress and strain in the mixture is exactly at the endurance limit, cracks are not growing, but energy is being dissipated and most of the energy is recovered. It is the pseudostrain energy balance at the endurance limit that allows the bond energy to be measured directly.

8.5.2 Characterization of fatigue damage

The traditional two phases of crack growth (i.e., crack initiation and crack propagation) are actually parts of a single process that has three recognizable phases: formative, coalescent, and unitary. All three phases are governed by the same crack growth rule: a modified form of Paris' law. The three phases are illustrated in Figure 8.12. The "formative" phase starts with the air voids as the initial flaws from which the cracks begin to grow. As the damage density and true stress increase, the larger "bee" structures are fractured and join the air voids as locations from which these cracks can grow. The formative phase ends when the larger cracks begin to merge with the smaller ones and reduce the total number of cracks.

In the "coalescent" phase, the larger cracks continue to incorporate the smaller cracks and reduce the total number of cracks that are growing. Finally, when the number of cracks has coalesced into a single crack, the crack growth enters the "unitary" phase. All three phases are governed by a modified form of Paris' law, which is (Luo et al., 2013c):

www.EngineeringEBooksPdf.com

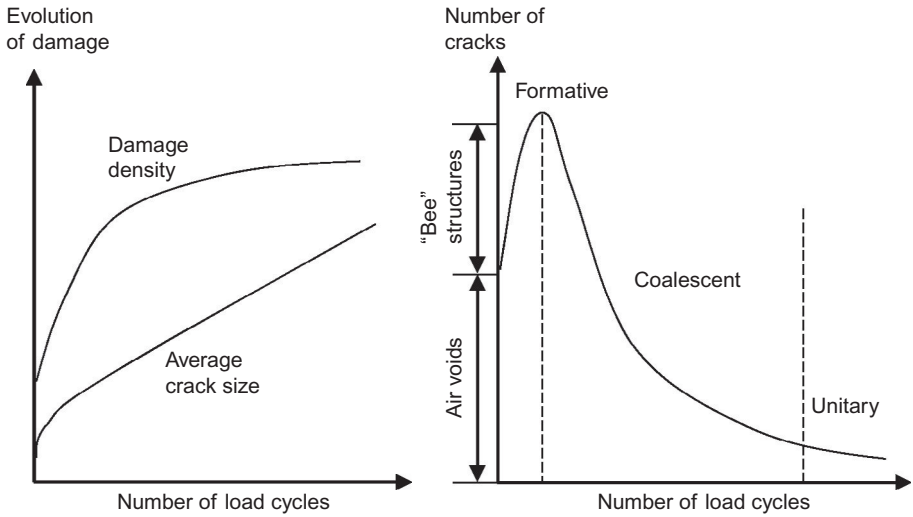


Figure 8.12 Three phases of crack growth.

Pseudo *J*-integral Paris' law in terms of damage density

$$\frac{d\phi}{dN} = A'(\Delta J_R)^{n'}, \tag{8.2}$$

where ϕ is the damage density, N is the number of load cycles, $\triangle J_R$ is the pseudo J-integral, and A' and n' are the modified Paris' law parameters. In the first two phases of crack growth, formative and coalescent, the damage density is given by

Definition of damage density

$$\phi = \frac{m\pi\bar{c}^2}{A}, \tag{8.3}$$

where m is the number of cracks and $\bar{c}$ is the mean crack radius. As with the true stress, the number of cracks and the mean crack radius are both continuum properties because they are averages within a representative volume element. When the crack is in the unitary phase of crack growth, the damage density is defined as

www.EngineeringEBooksPdf.com

Damage density in the unitary phase of crack growth

$$\phi = \frac{\pi \bar{c}^2}{A}, \tag{8.4}$$

where $\bar{c}$ is the current radius of the crack. All three phases are predicted with the same modified Paris' law parameters, A' and n'. Thus, by using the damage density as the focus of the modified Paris' law, there is no need to partition the crack growth into two distinct phases, initiation and propagation, each of which requires its own set of fracture properties.

Fatigue cracks grow under tensile, shear, and compressive stresses. Thermal and shrinkage stresses are tensile; traffic imposes all three types of stresses. Paris' law parameters have been developed for both tension and compression repeated loadings. The innovative testing and data analysis protocols that were developed and are reported here are capable of completely characterizing an asphalt mixture in 1 day, including the full master curves of the complex moduli and Poisson's ratios and the fatigue and healing properties in both tension and compression.

Fatigue cracking and permanent deformation develop simultaneously in asphalt mixtures under repeated destructive loading, regardless of temperature. Because these two distinctly different damage mechanisms always occur together, it is not possible to obtain pure cracking damage or pure permanent deformation damage in any asphalt mixture by varying the temperature or loading level. The EBM approach proposed here is able to separate fatigue cracking from permanent deformation in terms of energy consumption (Luo et al., 2013a). Specifically, the DPSE expended on cracking is separated from that expended on permanent deformation. Examples of this showing the relative amounts of DPSE that are available to cause fracture and permanent deformation separately are shown in Luo et al. (2014).

Controlled-strain RDT tests (Luo et al., 2013d) are performed on asphalt mixture specimens to determine their nondestructive properties, critical nonlinear viscoelastic properties, and destructive properties. The RDT test is a constant strain test that is made at several different strain levels: undamaged and damaged. The tests that are made in the undamaged strain levels provide the benchmark undamaged properties of the mixture (i.e., critical nonlinear viscoelastic point). The tests that are made in the damaged strain levels determine the amount of damage, that is, the departure from the undamaged condition that has been done with repeated loads. The total DPSE, which is the amount of energy dissipated for the fatigue damage, including both fatigue cracking and permanent deformation, is calculated based on the critical nonlinear viscoelastic properties in order to separate both linear and nonlinear viscoelastic effects from the strain energy that is available to cause damage.

Figure 8.13 illustrates typical results of the contrast between apparent and true stress and the characteristic damage densities measured in the RDT tests for two asphalt mixtures, one with an initial air void content of 4% (Type 1) and the other

www.EngineeringEBooksPdf.com

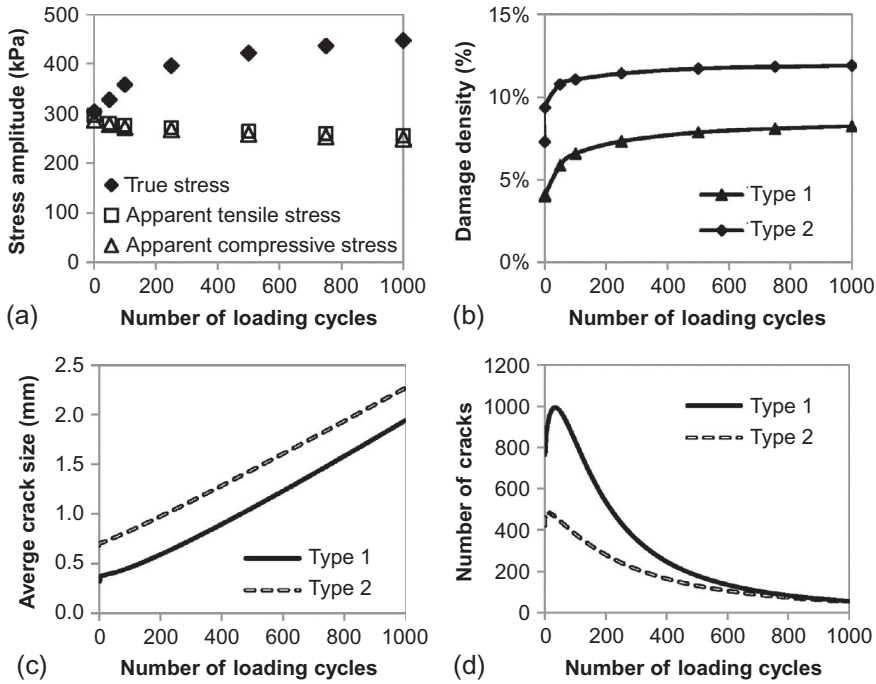


Figure 8.13 Primary results of fatigue characterization of asphalt mixtures. (a) True and apparent stresses; (b) evolution of damage density; (c) evolution of average crack size; and (d) evolution of number of cracks.

having an initial air void content of 7% (Type 2). There is a tensile portion and a compressive portion within each cycle of the RDT test, and the apparent stresses in each portion are shown in Figure 8.13a. Both apparent stresses appear to decrease with increasing loading cycles. However, taking into account the growth of the cross-sectional area of cracks under repeated destructive loading, the true stress actually increases.

Figure 8.13b shows the increase of damage density in both mixtures with increasing numbers of destructive loading cycles. The average crack size with increasing loading cycles is shown in Figure 8.13c, and the number of such cracks is shown in Figure 8.13d. All of these are calculated directly from the data that are measured with each loading cycle while using the true stress and energy balance concepts described above.

By applying the modified Paris' law to the data of damage density versus number of load cycles such as in Figure 8.13b, the modified Paris' law coefficient, A', and its exponent, n', can be determined. There is a unique linear relationship between the log A' and n', as shown in Figure 8.14. All of this is explained and illustrated in detail in Luo et al. (2013c). In that reference, the influence of different binders, air voids, and aging on the fracture of asphalt mixtures is demonstrated and explained. In addition, the measured material properties that govern the rate of crack growth are tabulated.

www.EngineeringEBooksPdf.com

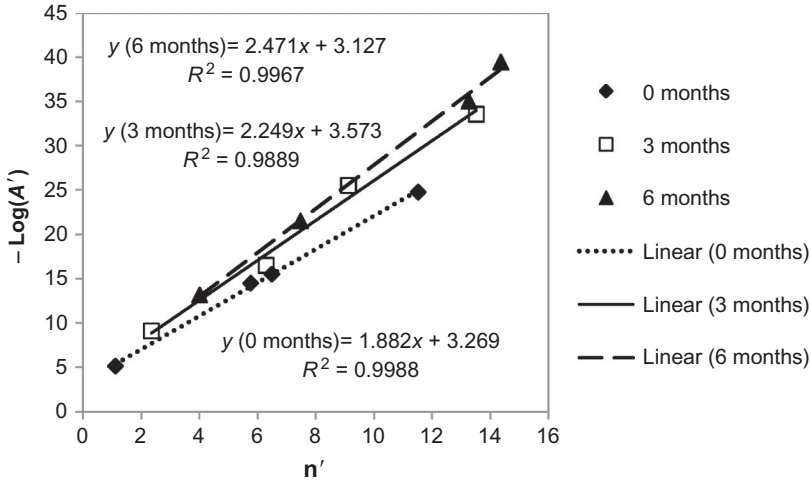


Figure 8.14 Relationship between modified Paris' law A' and n' for unaged and aged mixtures in tension.

8.5.3 Characterization of healing and recovery

Healing occurs when the load is removed and the material is allowed to rest. Therefore, healing usually accompanies the recovery of a material. Recovery of a material refers to a process in which the deformed material reduces its stored energy and restores its deformation after the load is removed. In all previous fatigue studies, major attention has been paid to the loading phase of a material, while much less attention has been paid to the unloading phase, or the recovery phase. Even though there is some literature addressing this issue, the testing and analysis methods are empirical or phenomenological, which emphasize correlation and not causation. This shortcoming is overcome using the internal stress.

The internal stress is the key to deriving the true mechanical properties in the recovery phase because it is the principal driving force for the recovery. A creep and step-loading recovery (CSR) test is developed in Luo et al. (2013e) to directly measure the internal stress during the recovery of an asphalt mixture specimen. The internal stress measured by the CSR test is used to define a new type of material property: the recovery modulus, which is an indicator of the material's capability to recover. The characteristics of the recovery modulus are presented in Luo (2012) in terms of different loading levels, mixture compositions, temperatures, and aging periods, respectively.

From a mechanical point of view, two driving forces promote healing of asphalt mixtures: internal stresses that push the crack closed, and the attraction of the two crack faces for one another. The stronger of these two are the internal stresses. With the measurement of the internal stresses, the EBM approach developed to characterize fatigue damage and model crack growth is applicable to model healing as well. The DCF is still used to model a multitude of randomly distributed air void or crack systems in asphalt mixtures. The two basic mechanical principles (force equilibrium and energy balance) are used to connect

www.EngineeringEBooksPdf.com

the true responses of the intact material to the apparent measurements on the bulk specimen, which consists of the intact material and distributed air voids or cracks. Due to the presence of healing in asphalt mixtures, the measured stress and strain of the bulk specimen are different from the true stress and strain of the intact material. The stress, strain, and energy of the bulk specimen are defined as "apparent stress," "apparent strain," and "apparent energy," respectively, which are measured from the test data. In contrast, the stress, strain, and energy of the intact material are defined as "true stress," "true strain," and "true energy," respectively. The apparent energy and true energy obey the energy balance equations, including the DSE balance equation, RSE balance equation, DPSE balance equation, and RPSE balance equation. Details of the formulations and how to use these equations to model healing in presented in Luo (2012).

Figure 8.15a illustrates typical results of the contrast between apparent and true stresses in a CSR test. The true creep stress and true internal stress are larger than their apparent counterparts. Figure 8.15b shows the change of the damage density of two different asphalt mixtures during the creep phase and the recovery phase. Using the energy balance equations in the EBM approach, the reduction of the damage density is quantified during the recovery phase and the healing curve is generated based on the percent reduction of the damage density. The healing curve is defined as the normalized extent of healing versus the rest time. The normalized extent of healing is defined in the following way:

Definition of healing in terms of damage density

$$h = \frac{\phi_{fc} - \phi_i}{\phi_{fc} - \phi_0}, \quad h \in [0, 100\%], \tag{8.5}$$

where h is the normalized extent of healing; ϕ_{fc} is the initial damage density before healing starts or, equivalently, the final damage density at the end of the creep phase; ϕ_i is the damage density at any data point i during the recovery phase; and ϕ_0 is the initial damage density, which equals the air void content. Figure 8.15c and d presents some examples of the healing curves, which illustrate the principal characteristics of the healing process.

Figure 8.15c and d shows that healing is slower in an aged mixture and in a mixture with higher air void content. Not shown in the figure is the observed fact that the mixtures heal faster at high temperatures. Initial and final healing rates depend upon the relative magnitudes of the nonpolar and polar bond energies of the asphalt mixture. The initial rate depends inversely upon the nonpolar bond energy, and the final rate depends directly upon the polar component of the bond energy. There are wide ranges of the amount of healing between mixtures. Because healing is the antifracture, it is a major component of the well-known shift factor from laboratory fatigue to observed field fatigue lives. As shown in Figure 8.15, the longer the rest period between traffic load applications, the more healing can occur and the longer the field fatigue life of the pavement. Figure 8.15 also shows that a substantial amount of healing can occur in a matter of a few minutes.

Perhaps the most significant practical feature of applying these tests for fracture, healing, and the endurance limit are that, as with the compressive testing, the entire characterization

www.EngineeringEBooksPdf.com

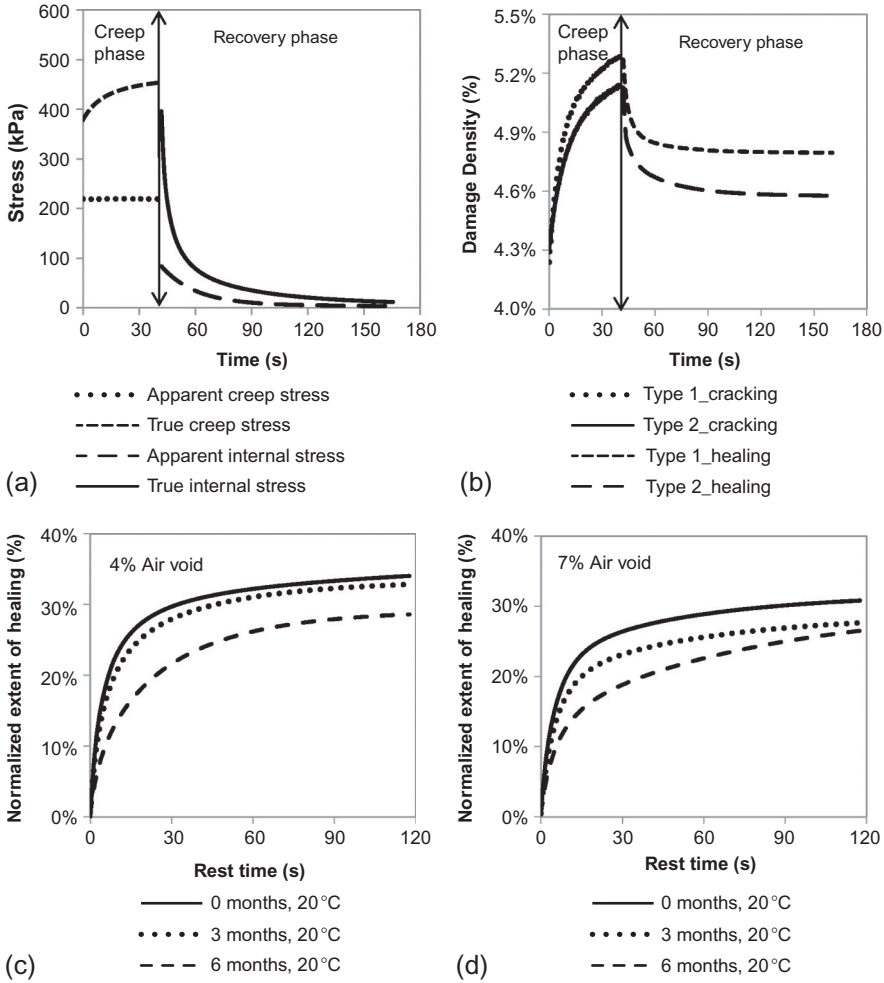


Figure 8.15 Primary results of healing characterization of asphalt mixtures. (a) Apparent and true stresses; (b) evolution of damage density; (c) healing curves of 4% asphalt mixtures; and (d) healing curves of 7% asphalt mixtures.

can be completed in 1 day. The testing times are very short, as seen in Table 8.2, requiring only a matter of minutes for each test. The greatest amount of time that is required in the whole process is the 2 h required to change the temperature of the sample.

8.6 Fracture of asphalt mixtures in compression

When a paving asphalt mixture is subjected to a destructive compressive load, it experiences a sequence of three deformation stages: primary stage, secondary stage, and tertiary stage. During the primary and secondary stages, permanent deformation

www.EngineeringEBooksPdf.com

Table 8.2 Testing methods and outcomes for fatigue and healing characterization

	Test methods	Testing procedure	Testing time	Test outcomes
Fatigue	Controlled-strain repeated direct tension (RDT) test	Three to four nondestructive tests at different loading levels	3–4 min for each loading level	Apparent and true complex modulus Endurance limit Mixture bond energy
		One destructive test	16 min	Damage density, average crack size, and number of cracks Modified Paris' law parameters Ratio of cracking to permanent deformation
Healing	Creep and step-loading recovery (CSR) test	One nondestructive test	3–4 min	Apparent and true creep compliance Recovery modulus
		One destructive test	3–4 min	Damage density and average crack size Healing curve and healing rates

(rutting) accumulates based on a strain (or work) hardening mechanism. The work done by the repeated load accumulates energy in the asphalt mixture, which yields a stiffer material. The asphalt mixture reaches a point at which it is so stiff that the microcracks and voids start to grow and propagate to macrocracks in the tertiary stage. This point is actually the initiation of the tertiary stage, and is defined as the flow number in the repeated load test or the flow time in the static creep test. The increase of the crack size leads to the loss of the area of the intact material, which is the major reason for the degradation of the modulus. The cracks that appear in the tertiary stage in turn accelerate the development of permanent deformation and eventually reduce the service life of pavements. In order to accurately predict the field performance of asphalt pavements, there is a need to perform the fundamentally mechanistic modeling and laboratory evaluation of the fracture that occurs in the tertiary stage of asphalt mixtures. This has been done and is reported in Zhang et al. (2013b, 2014).

The characteristics of fracture in tension and compression are distinctly different for several reasons. The microstructure of asphalt mixtures in compression is

www.EngineeringEBooksPdf.com

anisotropic, which leads to different values of the Paris' law parameters in the directions normal and parallel to the direction of compaction. The degree of the anisotropy is determined by the size, shape, and orientation of the aggregate particles in the mixture. The percentage of air voids is critical in the compressive fracture of asphalt mixtures. The low air void percentages such as those that develop in the wheel paths tend to experience brittle-type fractures, which are principally vertical cracks. The higher percentages of air voids experience ductile fractures, with the cracks forming along nearly horizontal planes.

One of the interesting observations in the repeated loading compression testing is that the flow number can be determined as the number of loading cycles at which the apparent phase angle begins to grow. The data show conclusively that this flow point is precisely the point at which the compressive cracks begin to grow and the visco-fracture strains start to accumulate.

An asphalt mixture has a different cracking mode in compression than that in tension. It is well known that the cracks grow in the direction that is perpendicular to the direction of stress in tension. To demonstrate the cracking mode of the asphalt mixture in compression, some of the asphalt mixture specimens were painted on the lateral surface by white plaster before the tests. Figure 8.16 shows the asphalt mixture specimen after the destructive test. It can be seen from the figure that some of the cracks are illustrated as splitting cracking, growing along the vertical direction that is the same direction as the stresses, while some of the cracks are shown as diagonal cracks, propagating in the diagonal directions.

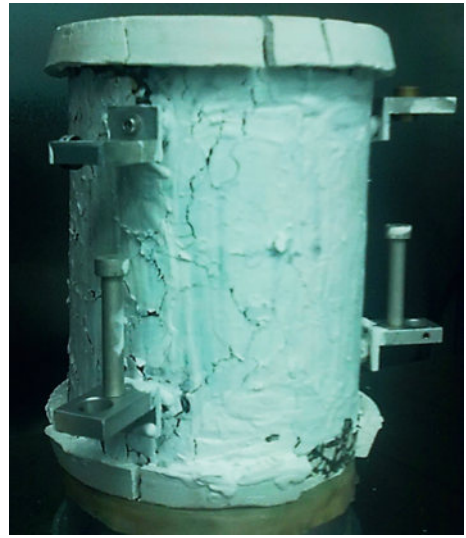


Figure 8.16 An asphalt mixture specimen painted by white plaster on surfaces after destructive test (showing that the cracks under compressive load tend to grow along the direction of the external load).

www.EngineeringEBooksPdf.com

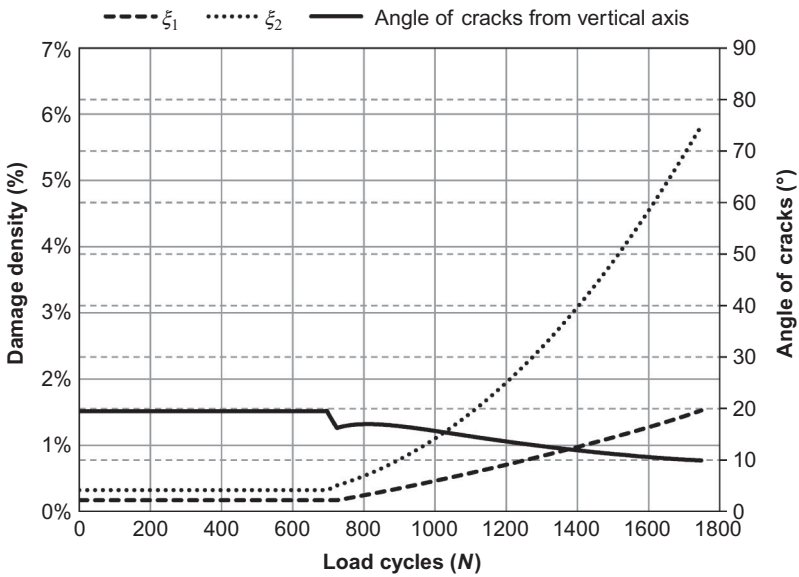


Figure 8.17 Damage densities and angle of cracks for an asphalt mixture with 4% air voids (showing brittle fracture with splitting cracks for relatively stiff asphalt mixtures).

Figure 8.17 shows the axial and radial damage densities for an asphalt mixture with a 4% air void content, and Figure 8.18 shows the axial and radial damage densities for an asphalt mixture with a 7% air void content. The symbols ξ_1 and ξ_2 in both Figures 8.17 and 8.18 are the axial and radial damage densities, respectively. All of these measures of cracking in both samples, including the axial and radial damage density and the orientation of the cracks relative to the vertical axis, are calculated from the measured data. It can be concluded that the asphalt mixture with 4% air void content has a higher radial damage density and a lower axial damage density, while the asphalt mixture with 7% air void content has a lower radial damage density and a higher axial damage density. The same conclusion is found for all of the tested asphalt mixtures that vary with two binders (Valero, NuStar), two air void contents (4%, 7%), and three aging periods (0-, 3-, and 6-month 60 °C aged).

In fact, the asphalt mixture with the 4% air void content is stiffer than the asphalt mixture with the 7% air void content and has more axial cracks during fracture, which is called brittle fracture, and has a splitting cracking mode. The axial cracks have a larger projection area on the circumferential surface, which yields a higher radial damage density. In contrast, the asphalt mixture with the 7% air void content is relatively soft and tends to have a ductile fracture, and has a diagonal cracking mode. The cracks grow along the diagonal plane that is the plane of the maximum shear stress, which yields a larger projection area on the horizontal cross section and eventually causes a higher axial damage density. The low air void content of the mixture in Figure 8.17 is typical of the condition that develops in the wheel path after the passage of multiple tire loads. The anisotropic nature of the mixture combined with the low air void

www.EngineeringEBooksPdf.com

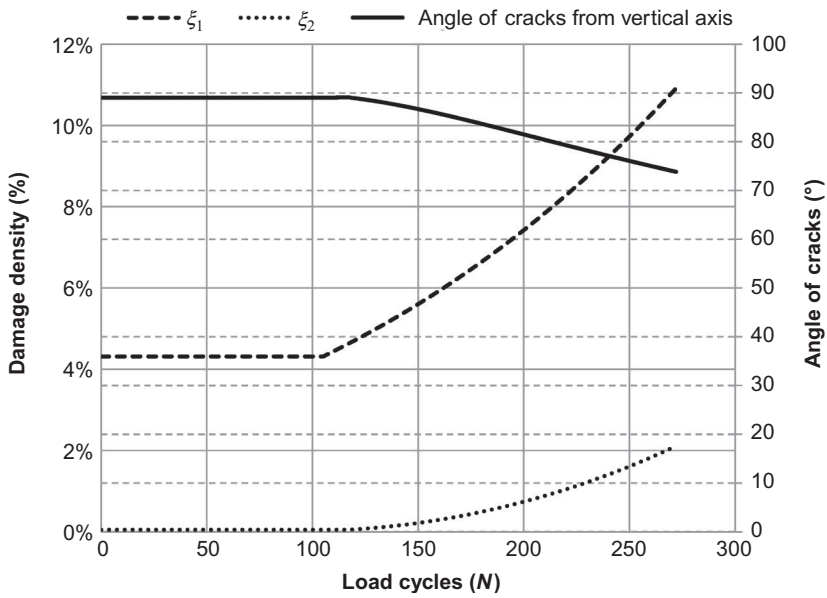


Figure 8.18 Damage densities and angle of cracks for an asphalt mixture with 7% air voids (showing ductile fracture with diagonal cracks for relatively soft asphalt mixtures).

content induces a vertical crack in the wheel path. This is probably the origin of alligator cracking and top-down cracking, which at its beginning is a low severity level longitudinal crack in the wheel path.

The nature of these compressive cracks is anisotropic, with a different amount of vertical and horizontal cracking depending on whether the mixture is behaving as a brittle or a ductile material. Knowing the damage density in both the vertical and the horizontal directions, the directional modified Paris' law parameters can be determined exactly as with the tensile fatigue parameters. Figure 8.19 shows the graph of both sets of axial and radial fracture parameters for a wide variety of mixtures, binders, air void levels, and laboratory aging. The subscript 1 denotes the axial parameters, and the subscript 2 indicates the radial parameters.

Once the material constants (A_i and n_i) are determined, the evolution of the directional damage densities due to a variety of apparent traffic stress histories can be predicted. The objectives of this are to provide a mechanistic characterization method for the damage modeling of the asphalt mixtures in the tertiary stage, and to provide a method to determine the anisotropic damage densities, whether in a laboratory sample or in an asphalt pavement. Based on the mechanistic analysis and the laboratory testing on the fracture properties of asphalt mixtures in compression, the following findings can be achieved:

(1) The asphalt mixture does fracture in the tertiary stage under a destructive compressive load. The deformation caused by the formation and propagation of the cracks are viscofracture strains, which are determined by the strain decomposition of the total measured axial strain.

www.EngineeringEBooksPdf.com

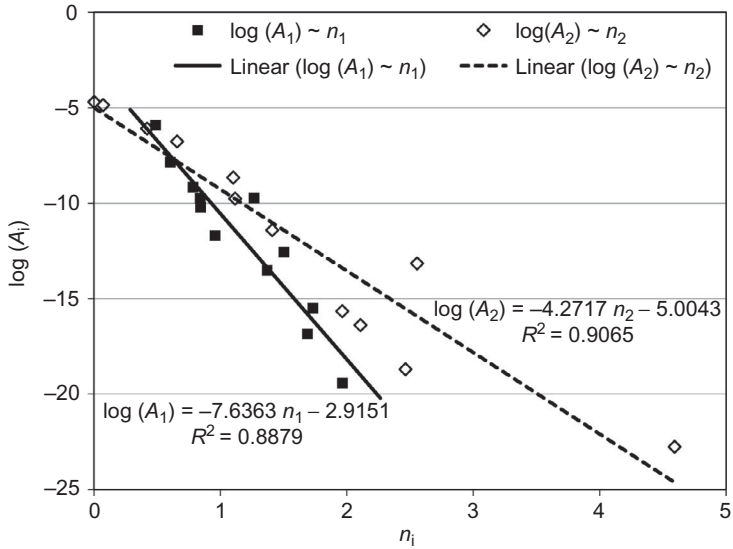


Figure 8.19 Relationships between coefficients of the modified Paris' law for asphalt mixtures in compression (A_1 and n_1 are coefficients of modified Paris' law for axial damage density, and A_2 and n_2 are coefficients of modified Paris' law for radial damage density).

The axial and radial viscofracture strains are employed to determine the axial and radial damage densities, based on CDM and geometric analysis of the cracks.

(2) The asphalt mixture with 4% air void content has more axial cracks during viscofracture, which is a brittle fracture, and has a splitting cracking mode. The axial cracks have a larger projection area on the circumferential surface, which yields a higher radial damage density. In contrast, the asphalt mixture with 7% air void content is relatively soft and tends to have a ductile fracture and a diagonal cracking mode. The cracks grow along a diagonal plane that is the plane of the maximum shear stress, which yields a larger projection area on the horizontal plane and eventually causes a higher axial damage density.

(3) The viscofracture properties of an asphalt mixture in compression are characterized by the anisotropic damage densities and true stress. Both damage densities and true stress increase with load cycles, which indicates that the extra plastic strain observed in the tertiary stage is produced by an increase of true stress. Consequently, the permanent deformation is accelerated by the occurrence of cracks in the tertiary stage.

(4) Anisotropic Paris' laws in terms of damage densities are employed to accurately characterize the evolution of the viscofracture of the asphalt mixtures in compression. The material constants in Paris' law are temperature independent and can be employed to predict the fracture properties of the asphalt mixtures in compression.

8.7 Summary and conclusions

Several important developments are summarized in this chapter. This includes new, rapid, and accurate methods to determine the undamaged properties of asphalt mixtures

www.EngineeringEBooksPdf.com

in both tension and compression. With these measurements, it is observed that the properties are distinctly different: in tension, the asphalt mixture is practically isotropic, whereas in compression, the mixture is anisotropic with a modulus ratio that ranges between 1.2 and 2.0. All of the moduli are viscoelastic and vary with frequency, but the tensile modulus varies between the horizontal modulus at the low frequencies and the vertical modulus at the high frequencies. The modulus phase angles peak at around 40° for compressive moduli and at around 80° for tensile moduli. All of the Poisson's ratios are also viscoelastic, having both a magnitude and phase angle. The compressive Poisson's ratios, being anisotropic, have values that are greater than 0.5 at the lower frequencies. This is a result that is expected from anisotropic elastic theory.

Tensile fracture depends principally upon the undamaged tensile properties of the mixture and on the adhesive and cohesive bond energies that are derived from the surface energies of the binder and aggregates in the mixture. There is a uniquely linear relationship between the Paris' law exponent, n, and the log of the coefficient, A. Between applications of the tensile stress, residual compressive stresses form in the mixture, close the cracks, and promote healing. A novel test method is described in the tensile fatigue section of this chapter, which is capable of measuring these residual stresses, requiring only a few minutes to complete the test sequence. Healing rates increase with higher temperatures and decrease with aging, moisture, and increasing air voids. The healing rates and the level of healing that can be achieved can be predicted reliably using original undamaged properties, which include the tensile compliance and surface energies.

One of the interesting findings of the tension fatigue testing is that there is a strain level above which cracks begin to grow and below which cracks will not grow. This strain level can be found easily and experimentally in a matter of minutes. This strain level varies slightly with the air voids, aging, and different binders, and is identified and tabulated as the endurance limit for fatigue. Another interesting capability that this approach provides is the ability to separate the amount of DPSE that goes into cracking from that which is available for plastic deformation. This ability to show how much of the dissipated energy that a given material channels into each of the two major kinds of structural distress in asphalt pavements may prove decisive in the selection of materials for pavement construction.

Permanent deformation of asphalt mixtures in compression can be characterized with new, rapid, and accurate methods that are similar in concept to those that were developed for the undamaged properties. The need for accuracy required several new developments, which treated the asphalt mixtures as anisotropic and were able to separate with each load cycle several types of strain that occur simultaneously, including elastic, plastic, viscoelastic, viscoplastic, and viscofracture strains. The strain decomposition method that was developed is demonstrated in this chapter and explained in the references. In addition, because of the high levels of internal friction angle that are characteristic of asphalt mixtures, it was necessary to formulate a new plasticity yield criterion, which has been termed the GD–P yield function. With this formulation, it is possible to determine the temperature and strain rate dependence of the strain hardening property of an asphalt mixture, which occurs after the material has yielded. The testing for all of this can be accomplished in a single day. And the properties that are measured can be tabulated and cataloged.

www.EngineeringEBooksPdf.com

The ability to separate the viscoplastic strain from the viscofracture strain that occurs in the tertiary stage of compression testing made it possible to determine the material properties that govern the growth of cracks in an anisotropic mixture. It was found that the mixture can behave as a brittle or a ductile mix, depending on the level of air void content of the mixture. The anisotropic fracture of a mixture in compression with low air voids, such as those that occur in a wheel path after the passage of much traffic, will act in a brittle way and generate a vertical crack in the wheel path. This is commonly defined as the low severity level of alligator cracking. The vertical and horizontal fracture properties are actual properties of the asphalt mixture and are independent of temperature. They, too, can be tabulated and cataloged.

This chapter summarizes many developments, discoveries, new capabilities, and surprises. Consistent with the principles of mechanics, the governing principles of DCF and plasticity have been developed and applied to tensile fracture and healing and anisotropic compressive plasticity and fracture of asphalt mixtures of different compositions, stress levels, and exposure histories. All of these properties have important implications for how these mixtures perform in actual service. The testing protocols and data reduction analyses that have emerged are simple, accurate, repeatable, and quick. All of the undamaged and damaged properties of an asphalt mixture can be determined by testing that is completed in 1 day. Both the tests and the data reduction and analyses require standard testing equipment and readily available computer hardware and software.

The properties that are produced by these tests and analyses are actual properties of these materials. They can be cataloged and used as a basis for comparison and selection of the best binder–aggregate combination and composition to use for a given pavement project. The archived properties can also be used in design studies to select the best pavement structure and asphalt–aggregate combinations for an extended service life. These are the concepts, results, and products that provide the engineering properties of asphalt mixtures that will make it possible to design mixes and pavement structures and provide performance-based specifications.

8.8 Future trends

Space limitations have made it necessary to leave out several recent advances of the ideas and principles that have been presented in this chapter. First, the genuine material properties of asphalt mixtures determined in this chapter are very valuable in the development of specifications, as they can be cataloged and, once measured, need not be measured again except to verify that they have not changed. Second, the mechanical principles developed in this chapter can be employed to predict the future performance of the asphalt mixtures when they are placed in service under traffic and weather. Accurate predictions of the expected values and variances of the future development of fatigue in these asphalt mixtures will make possible and practical performance-based specifications, warranties, and increasing use of the design-build-operate-maintain contracts of roadway networks. Accurate predictions will

www.EngineeringEBooksPdf.com

provide realistic estimates of reliability and risk and make possible financing arrangements that cannot be undertaken with present prediction methods. It will also make possible optimal management of roadway networks to make better use of the available funding for transportation. Third, applying the test results and mechanical models shown in this chapter to computer prediction methods will make it possible to make realistic evaluations of a mixture's future fatigue and healing behavior and its resistance to such material hazards as aging and moisture damage. It will be possible to make adjustments to the mixture design before proposing a job mix formula, and to identify the quality control/assurance testing that needs to be done in construction to achieve the desired levels of reliability. Fourth, the use of the mechanical principles summarized in this chapter and the resulting simplicity in testing and analysis will be applied in the determination of how the properties of these mixtures and their components will change with exposure in service. Using these same testing and analysis principles, it will be possible to measure the rheological and aging activation energies of mixtures rather than of the binders, as is done at present. Further, it will be possible to determine how these properties will be altered with additives and modifiers, and how they will deteriorate with exposure to moisture and solar radiation. Future developments will be viscoelastic crack growth criteria for mixtures in tension and compression, which are similar to the Griffith crack growth criterion that was developed in the 1920s for elastic materials. This will make it possible to determine the needed properties of the components of the mixtures, such as the binder, at the time of construction, in order to provide a reliable expected service life.

In sum, mechanical principles, rapid and accurate characterization of mixture properties, and accurate computer predictions of the expected values and variances of fatigue service lives are the future trends that can be expected of the subjects that are summarized in this chapter.

References

Luo, X., 2012. Characterization of fatigue cracking and healing of asphalt mixtures. Ph.D. Dissertation, Texas A&M University, College Station, TX.

Luo, R., Lytton, R.L., 2010. Characterization of the tensile viscoelastic properties of an undamaged asphalt mixture. J. Transp. Eng. ASCE 136 (3), 173–180.

Luo, X., Luo, R., Lytton, R.L., 2013a. Characterization of fatigue damage in asphalt mixtures using pseudo strain energy. J. Mater. Civ. Eng. ASCE 25 (2), 208–218.

Luo, X., Luo, R., Lytton, R.L., 2013b. Energy-based mechanistic approach to characterize crack growth of asphalt mixtures. J. Mater. Civ. Eng. ASCE 25 (9), 1198–1208.

Luo, X., Luo, R., Lytton, R.L., 2013c. A modified Paris' law to predict entire crack growth in asphalt mixtures. Transp. Res. Rec. 2373, 54–62.

Luo, X., Luo, R., Lytton, R.L., 2013d. Characterization of asphalt mixtures using controlled-strain repeated direct tension test. J. Mater. Civ. Eng. ASCE 25 (2), 194–207.

Luo, X., Luo, R., Lytton, R.L., 2013e. Characterization of recovery properties of asphalt mixtures. Constr. Build. Mater. 48, 610–621.

Luo, X., Luo, R., Lytton, R.L., 2014. Energy-based mechanistic approach for damage characterization of pre-flawed visco-elasto-plastic materials. Mech. Mater. 70, 18–32.

www.EngineeringEBooksPdf.com

Zhang, Y., 2012. Anisotropic characterization of asphalt mixtures in compression. Ph.D. Dissertation, Texas A&M University, College Station, TX.

Zhang, Y., Luo, R., Lytton, R.L., 2011. Microstructure-based inherent anisotropy of asphalt mixtures. J. Mater. Civ. Eng. 23 (10), 1473–1482.

Zhang, Y., Luo, R., Lytton, R.L., 2012a. Anisotropic viscoelastic properties of undamaged asphalt mixtures. J. Transp. Eng. ASCE 138 (1), 75–89.

Zhang, Y., Luo, R., Lytton, R.L., 2012b. Characterizing permanent deformation and fracture of asphalt mixtures by using compressive dynamic modulus tests. J. Mater. Civ. Eng. 24 (7), 898–906.

Zhang, Y., Luo, R., Lytton, R.L., 2013a. Characterization of viscoplastic yielding of asphalt concrete. Constr. Build. Mater. 47, 671–679.

Zhang, Y., Luo, R., Lytton, R.L., 2013b. Mechanistic modeling of fracture in asphalt mixtures under compressive loading. J. Mater. Civ. Eng. 25 (9), 1189–1197.

Zhang, Y., Luo, R., Lytton, R.L., 2014. Anisotropic characterization of crack growth in the tertiary flow of asphalt mixtures in compression. J. Eng. Mech. ASCE 140 (6), in press.

www.EngineeringEBooksPdf.com

Multiscale modeling approach for asphalt concrete and its implications on oxidative aging

9

B.S. Underwood
Arizona State University, Tempe, AZ, USA

9.1 Introduction

Aging, specifically oxidation of the asphalt cement, has long been recognized as a major distress facilitator in asphalt concrete and, by extension, asphalt pavements. This process causes the material to stiffen and embrittle, and may lead to a higher potential for cracking. Despite its importance, there are many aspects of this phenomenon that are not completely understood after substantial study. Evaluations of oxidation tend to focus on either asphalt cement binder or asphalt concrete, with asphalt cement-based studies being more prevalent. The earliest work focused on understanding the physical and mechanical implications of oxidation (Hubbard and Reeve, 1913; Thurston and Knowles, 1936; Van Oort, 1956; Corbett and Merz, 1975), while later and more recent studies have focused on the chemical-related impacts (Wright, 1965; Lee and Huang, 1973; Jemison et al., 1992; Lunsford, 1994; Liu et al., 1996; Petersen and Harnsberger, 1998; Glover et al., 2008; Prapaitrakul, 2009; Huang and Grimes, 2010).

One of the most important documents on asphalt oxidation was produced by Petersen (2009), who summarized more than half a century's worth of experience and knowledge on the subject. This document follows many of the important developments in the field and begins by explaining oxidation in terms of the coarsely defined molecular components familiar to civil engineers, the saturate–aromatic–resin–asphaltene (SARA) fractions. This coarse understanding is expanded upon by introducing the idea of asphalt functional groups and explaining oxidation using more fundamental nomenclature. Support for the key concepts is provided in the form of experimental studies that explain the types of products that result from oxidation and how these affect the asphalt binder functional groups. Many of these key findings with respect to the molecular-level changes upon oxidation are discussed in Section 9.3. The document also reports on the correlation between asphalt binder chemistry, the changes that occur upon aging and how experimental techniques can monitor these changes, and the associated impacts on mechanical properties. Petersen does not propose any specific model for relating chemical and mechanical properties, but does demonstrate considerable correlation between the two. Of particular note is the observation from laboratory aging studies that oxidation products form first at a fast but decreasing rate, and then afterward form at a constant rate. The binder

Advances in Asphalt Materials. http://dx.doi.org/10.1016/B978-0-08-100269-8.00009-X
© 2015 Elsevier Ltd. All rights reserved.

www.EngineeringEBooksPdf.com

viscosity, measured at 60 °C, is also shown to follow the same trend; however, the precise relationship between oxidation product formation and viscosity change is found to vary by asphalt.

Although Petersen does not introduce a mathematical model in his work, others have taken on this problem, as summarized in Table 9.1. Glover and his colleagues (Jemison et al., 1992; Lunsford, 1994; Liu et al., 1996; Glover et al., 2008; Han, 2011) have focused primarily on modeling the chemical products formed via oxidation and use a dual-rate approach. In this technique, the oxidation process is divided into two regions: fast-rate reaction region and constant-rate reaction region. In the first one, oxidation products form quickly but at a declining rate, whereas in region two the products form at a constant rate. This constant-rate region is modeled using an

Table 9.1 Summary of oxidative aging models for asphalt cement

Model	Primary equations	Comment
Glover model	$\ln\eta(t) = \ln\eta_0 + \Delta\left(\ln\ \eta_j\right) + r_\eta \times t$ $r_\eta = \frac{\mathrm{d}\ \ln\eta}{\mathrm{d}t} = \mathrm{HS} \times \frac{\mathrm{dCA}}{\mathrm{d}t}$ $\frac{\mathrm{dCA}}{\mathrm{d}t} = \mathrm{AP}^\alpha \mathrm{e}^{-E/\mathrm{RT}}$	• Models the rate of oxidation product formation (CA) and uses empirical relationships between these products and mechanical properties
Farrar model	$\frac{1}{G_\mathrm{c}^*(t)} = \frac{1}{G_{\mathrm{c}0}^*} + kt$ $k = \mathrm{AP}^\alpha \mathrm{e}^{-E/\mathrm{RT}}$	• Models the rate of change in crossover modulus using a second-order aging kinetics relationship
Global aging system model	$\log\ \log\eta(t) = \frac{\log\ \log\eta_0 + \mathrm{A}t}{1 + Bt}$ $A, B = f(T, \mathrm{Maat}, \eta_0)$	• Empirical correlation between in-service time and binder viscosity at multiple temperatures
Aging shift factor model	$\lvert G^*\rvert(t) = \frac{G_\mathrm{g}^*}{\left[1 + \left(f_\mathrm{c}/f_\mathrm{ra}\right)^d\right]^{m_\mathrm{e}/d}}$ $f_\mathrm{ra} = f \times a_T \times a_A$	• Phenomenological relationship between changes in linear viscoelastic properties of asphalt binder as a function of loading time/rate/frequency, temperature, and oxidation time
Terms	η = viscosity t = time T = temperature P = pressure η_0 = initial viscosity η_j = rapid growth viscosity CA = carbonyl area (measure of oxidation product formation) HS = hardening susceptibility (empirical factor) r_η = viscosity growth rate in constant growth region	A, E, α = calibration coefficients $G_\mathrm{c}^*(t)$ = crossover modulus as a function of time $G_{\mathrm{c}0}^*$ = initial crossover modulus G_g^* = viscosity growth rate in constant growth region f_c, m_e, d = calibration coefficients a_T = temperature-related shift factor a_A = aging-time-related shift factor

www.EngineeringEBooksPdf.com

Arrhenius expression considering temperature and pressure. Correlations between oxidation product and binder viscosity at 60 °C are used to link chemical and rheological changes. Farrar (2013) suggests that the fast-rate oxidation kinetics may not be practically significant for in-service pavements by using a constant rate model (e.g., a second-order kinetics model) to demonstrate good predictive agreement between the crossover modulus and oxidation time for both short- and long-term aging periods. As in the constant-rate portion of Glover's model, this rate is described using an Arrhenius-type function. This approach has received less attention than the dual-rate method, probably due to the fact that oxidation products in asphalt cement are known to form quickly at first before settling into a more or less constant rate of accumulation. However, the results reported by Farrar could be explained by noting that the relationship between oxidation product and rheological changes may not be linear. Other than the obvious simplification that a single-rate model affords, the direct prediction of a rheological property may also be advantageous.

Other researchers have focused on the mechanical impacts of oxidation alone and attempted to characterize the changes in material properties without direct consideration of the chemical processes. The most well known of these is the global aging system (GAS) model (Mirza and Witczak, 1995), which is based on the large-scale regression of viscosity from at least 47 in-service projects (2308 individual measurements). The model does capture major trends with respect to time (increases in oxidation-related viscosity) and depth in the pavement (decreases in oxidation-related viscosity with depth). Some have questioned its overall validity though, because it has only limited characterization with respect to air void content effects and modified asphalt cements. In addition, it relies solely on the mean annual air temperature as the climate-related input, which does not explicitly consider confounding factors such as sunlight, cloud cover, convective flow, and so on.

Another approach to characterizing the impact of oxidation on mechanical properties is to utilize phenomenological shifting methods. These approaches strive to create aging master curves akin to what is done in a thermorheologically simple analysis of temperature and time effects. Studies conducted by Strategic Highway Research Program (SHRP) researchers suggested that the oxidation impact is too complex to be accurately handled by such methods (Anderson et al., 1994). Nevertheless, various researchers (Shalaby, 2002; Huang and Zeng, 2007; Banerjee et al., 2012) have applied these techniques as a means to characterize the aging impacts. Heretofore, such works have not supplied a theoretical basis for the shifting approach, such as the free-volume concepts used to support time–temperature superposition (Ferry, 1980).

The complexity of the problem increases in the case of asphalt concrete due to the fact that (1) the aging kinetics are highly binder specific and dependent upon temperature; (2) physicochemical interactions may be significant; (3) thermal exposure during the mixing and placement operations can be highly variable and in some cases not very well controlled; and (4) void content can vary. Coincidently, there has been substantially less research to understand and model the aging phenomenon of asphalt mixtures (Bell, 1989; Bell and Sosnovske, 1994; Bell et al., 1994; Anderson et al., 1994; Brown and Scholz, 2000; Airey, 2003; Houston et al., 2005). Despite a lack

www.EngineeringEBooksPdf.com

of attention, evaluation of aging in asphalt concrete is important because the aging of asphalt concrete has direct implications on the performance of the majority of pavements worldwide. Coincident with this importance, the complexity of the relationship between the asphalt binder and asphalt mixture properties makes it impossible to judge the impact of certain conditions on asphalt mixture behavior by simply measuring the properties of the binder.

9.2 A multiscale perspective of asphalt concrete behavior

Along with other mechanisms, oxidative aging is generally interpreted in the framework of a two-scale system: asphalt binder and asphalt concrete. The two materials in this paradigm exist in a related, but separate context and rely on single-step correlations. A multiscale perspective postulates that single-step relationships have limited utility because of the existence of multiple mechanisms that manifest at different length scales. Thus, linking mechanical behaviors of asphalt binder and asphalt mixture in a single step requires the smearing of multiple physical phenomena. Such an approach would then limit the potential to develop meaningful insight into cause-and-effect relationships and to consequently formulate strategies to better design the materials. The scalewise dependencies that exist in asphaltic composites are summarized in Figure 9.1.

At the smallest scale, asphalt cement can be viewed as a composite of hydrocarbons and other elements in multiple complex structures. In this domain, the material is best understood with respect to the chemical properties of the constituent elements, molecular species, and functional groups that compose the bulk asphalt binder. At the next

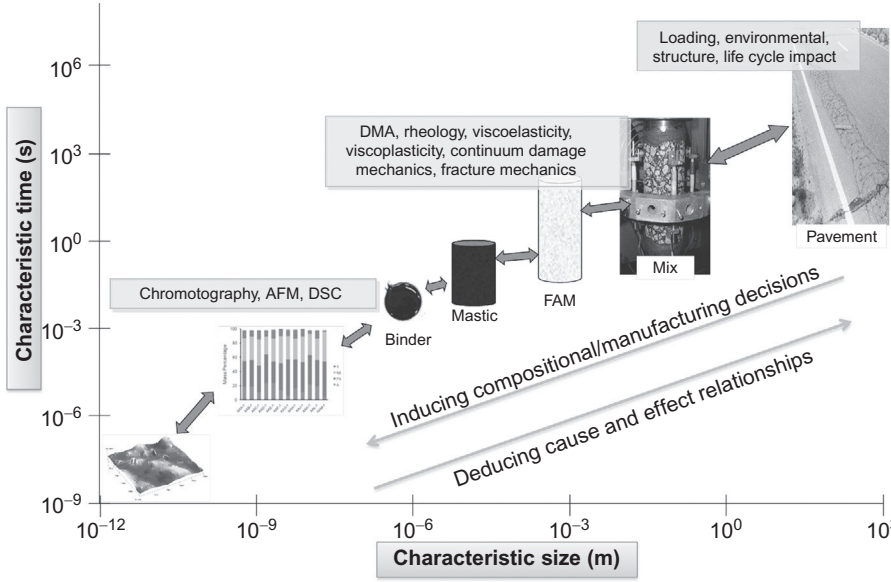


Figure 9.1 Scale dependencies involved in a multiscale interpretation of asphalt concrete.

www.EngineeringEBooksPdf.com

largest scale, asphalt binder is viewed as a dark brown to black semisolid cementitious material with viscous to viscoelastoplastic mechanical properties. Here, behaviors are interpreted primarily in a rheological context either as part of a specification process or as a means to understand the impacts of binder compositional factors on mechanical properties.

The next scale of practical interest is asphalt concrete, which consists of the asphalt binder, graded aggregates from up to 37.5 mm to sizes less than 75 μm, and air in the form of void spaces between the coated aggregates. Although this is the next largest size of practical engineering significance, understanding the mechanical relationship between it and the asphalt binder can be facilitated by further dividing the composition of asphalt concrete into two scales: asphalt mastic and asphalt fine aggregate matrix (FAM). Asphalt mastic is the material consisting of mineral filler (particles smaller than 75 μm) and the asphalt binder. The importance of this scale in establishing the link between asphalt binder and asphalt concrete is the magnification of physicochemical interactions that occur at the interface of the asphalt and aggregate. This scale magnifies the influences of this phenomenon because of the relatively large specific surface of the filler particles. Asphalt FAM consists of the asphalt mastic and the fine aggregate particles, and thus it is synonymous with the mortar phase of portland cement concrete. Like the mortar, FAM forms the material that exists between the coarsest aggregate particles in the mixture. It is the FAM phase that deforms under high-temperature loading and that shows visible cracking under repeated loading at intermediate temperatures. Because mastic is a part of this scale, the physicochemical influences are inherently occurring, but particle contact interactions are the more dominant mechanism.

One goal for multiscale evaluations is to understand physical and chemical mechanisms that occur in a material by carrying out targeted experiments at scales where those mechanisms are most dominant. A second and perhaps more meaningful outcome from these evaluations is the integration of the individual mechanisms into a comprehensive analytical or computational formulation. Such a model can then be used to deduce the cause-and-effect relationships and/or to engineer the composition and internal structure of asphalt concrete to improve the properties and performance.

With respect to oxidative aging, this process has progressed in two separate directions starting at the asphalt binder. To the left (e.g., toward smaller scales), there is impetus to understand the linkages between rheological properties and molecular composition. The goal of moving in this direction is to identify the key molecular components and allow the engineering of asphalt binder to be more resilient to oxidative impacts. To the right (e.g., toward larger scales), the primary motivation is to develop an understanding of the relationship between asphalt rheology, the physicochemical interactions, particle contacts and the role that these play in affecting the properties of the asphalt concrete, and ultimately the performance of asphalt pavements. Performance includes resistance to distresses (fatigue cracking, thermal cracking, rutting, etc.), which involves understanding the behaviors as they relate to viscoelastoplasticity and damage as well as perhaps healing, thixotropy, heat generation, and others. The goal in this document is less ambitious. Here, the behaviors with respect to only linear viscoelasticity (LVE) are explored. For approximating this relationship and understanding the impact of oxidation of the asphalt cement on the asphalt mixture modulus, models

www.EngineeringEBooksPdf.com

are available today that, while not perfect, do provide an approximate and rational link between the scales (Kim et al., 2009). Aging effects may have a more significant influence beyond the LVE conditions, and generalizing observations made on the LVE properties to failure regions is ill advised. However, without a proper understanding of the relationship in the LVE conditions, it is likely that one will not be able to describe the relationships under fatigue or permanent deformation.

9.3 Oxidation at the molecular level

The chemical nature of oxidation in asphalt has been explained and summarized extensively in the literature (Petersen et al., 1994; Petersen and Harnsberger, 1998; Lesueur, 2009; Petersen, 2009), and is thus only briefly mentioned here for completeness. Interested readers will find substantially more detail in the cited references. Understanding the chemical oxidation process in asphalt first requires an understanding of the physical and chemical composition of asphalt at the molecular scale. Asphalt is composed of primarily hydrogen and carbon, which exist in both aliphatic and aromatic forms. Along with the hydrocarbons, other elements such as oxygen and nitrogen, and metals like vanadium can also exist in the form of heteroatoms. Composition is commonly expressed not in terms of specific molecular species, but rather in broad classifications of functional classes and/or as molecular types as determined by solubility. The SARA fractions are distinguished from one another based on their solubility, which broadly correlates with molecular weight and polarity. Different methods do exist for extracting these fractions, and the methods yield different results, so that one must carefully consider the method of evaluation and hence the physical significance of the outcomes. Despite the limits with respect to rigorous physical and chemical correlations, the SARA fraction framework provides a convenient method to view asphalt structure and to interpret the impacts of oxidation.

The oxidation reaction in asphalt can be tracked by measuring the change in certain functional groups in the asphalt cement. Of particular interest are the ketones, anhydrides, and carboxylic acids (e.g., double-bonded oxygen structures or carbonyls), as well as the sulfoxides. Each of these functionalities forms at different rates, with sulfoxides generally forming first and with a rate that slows considerably after a short period, while carbonyls form slowly at first but with a relatively stable rate over time (given constant temperature/pressure conditions) (Petersen et al., 1994). Under nonsteady-state conditions, the rates of oxidation are dependent upon the rate of diffusion and the availability of oxygen to the system. The study of chemical oxidation kinetics has matured to the point where, after some laboratory calibration, it is possible to predict the amount of oxidation product formed during in-service conditions. However, predicting the amount of carbonyls, sulfoxides, or the combined carbonyl-sulfoxide content is not sufficient for predicting the mechanical impacts of oxidation. Such is the case because the exact sensitivity of asphalt rheology to asphaltenes and oxidation products is dependent upon the physical nature of the oxidized products as well as the chemical nature of the lighter molecular weight compounds and their solvent power (Petersen et al., 1994). While it is understood that these factors strongly

www.EngineeringEBooksPdf.com

impact the link between chemical and rheological properties, a complete description of the mechanisms does not yet exist. This statement applies to the traditional rheological measurement in asphalt (viscosity), the more fundamental dynamic shear modulus ($|G^*|$), and more recent high-strain-level measures such as nonrecoverable creep compliance (J_{nr}). Thus, studies that predict oxidation product formation must currently rely on empirical correlations, which themselves are dependent on the breadth of experimental data gathered. Thus, the modeling of fundamental oxidation kinetics has some limitations with respect to predicting the evolution of mechanical properties with time. This is not to say that the fundamental chemical-based evaluation is not important or useful, only that it has limitations, which motivate many to investigate oxidation from a more rheological perspective.

9.4 Effects of oxidation on asphalt materials

9.4.1 Rheology of asphalt cement

It is well known that asphalt binder becomes stiffer as oxidative aging occurs (Hubbard and Reeve, 1913; Petersen et al., 1994). Historically, this effect is quantified with aging indices defined as shown in Equation (9.1).

$$\mathrm{AR} = \frac{A_{age}}{A_{ref}} \tag{9.1}$$

where A_{ref} is the binder property, viscosity or $|G^*|$, at some reference condition; and A_{age} is the same binder property determined after a different level of oxidative aging either in the lab or in service. The advantage of AR is its simplicity and that it works well to quickly show the aging sensitivity of a given material. Its disadvantage is that when defined at a single temperature, it does not provide a full picture of the effects of oxidative aging over the range of conditions that would be experienced under service (Petersen et al., 1994). To demonstrate some of these complications, ARs will be calculated based on both viscosity and $|G^*|$, using the basic form in Equation (9.1), but at various temperatures and frequencies of loading.

A database of 20 different asphalt binders has been compiled to assess the aging effects on viscosity and $|G^*|$; see Table 9.2. As seen in this table, the available binder conditions included original (unaged); rolling thin-film oven (RTFO) aged; pressure aging vessel (PAV) aged at the standard temperature; PAV aged at 110 °C (PAV110); and recovered from an asphalt mixture (REC). At each aging level available for a given binder, viscosity was measured via traditional methods: a gravity-based cross-arm tube viscometer (135 °C), a vacuum-assisted U-tube viscometer (60 °C), a penetrometer (25–5 °C), and a ring-and-ball viscometer. In addition, for each binder, the $|G^*|$ has been measured using a parallel plate rheometer at the combination of temperatures between 5 and 80 °C and frequencies between 100 and 0.1 rad/s. Some of the asphalt binders have beam stiffness measured with the bending beam rheometer (BBR) for temperatures between approximately −30 and −10 °C and for times between 8 and 240 s. Because the binder RTFO is meant to represent

www.EngineeringEBooksPdf.com

Table 9.2 Binder database used for aging study

Project	Binder name	Aging conditions					BBR data available
		Original	RTFO	PAV	PAV110	REC	
ALF	AC 5	✓	✓	✓		✓	✓
	AC 10	✓	✓	✓		✓	✓
	AC 20	✓	✓	✓		✓	✓
	Novophalt	✓	✓	✓		✓	✓
	Styrelf	✓	✓	✓		✓	✓
MnRoad	AC 20	✓	✓	✓		✓	✓
	Pen 120/150	✓	✓	✓		✓	✓
Westrack	Westrack	✓	✓	✓			
Arizona DOT	Para. PG 58-22	✓	✓	✓	✓		
	Para. PG 64-16	✓	✓	✓	✓		
	Nav. PG 70-10	✓	✓	✓	✓		
	Nav. PG 76-16	✓	✓	✓	✓		
	Chev. PG 64-22	✓	✓	✓	✓		
	Chev. PG 76-16	✓	✓	✓	✓		
Witczak	Citgo PG 64-22	✓	✓	✓		✓	
Maryland port authority	Citgo PG 70-22	✓	✓	✓			
	TLA	✓	✓	✓			
	Stylink	✓	✓	✓			
	Novophalt	✓	✓	✓			
	PMB	✓	✓	✓			

the materials after placement, it serves as the datum for comparison between and among materials (e.g., A_{ref}).

9.4.1.1 Viscosity

Viscosity values are determined for all of the asphalt binders in the database using the A and VTS function, Equation (9.2). It is assumed, based on the work of others (Mirza and Witczak, 1995), that a maximum viscosity of 2.7×10^{12} cP exists for all materials.

$$\log(\log(\eta)) = A + \text{VTS}\ \log(T_R) \tag{9.2}$$

where η is the viscosity in cP, A is the intercept of the temperature susceptibility relationship, VTS is the slope of the temperature susceptibility relationship, and T_R is the temperature in Rankine.

The results of viscosity-based aging analysis are shown in Table 9.3 for 5 and 54 °C. Although only 5 and 54 °C are shown, it is noted that the AR values have also been

www.EngineeringEBooksPdf.com

Table 9.3 Viscosity-based aging ratios for study binders at selected temperatures

Binder		Temperature (°C)											
		5						54					
		Experimental				GAS model months		Experimental				GAS model months	
		Original	PAV	PAV110	REC	12	120	Original	PAV	PAV110	REC	12	120
ALF	AC 5	0.21	7.08	–	0.91	58.13	58.13	0.44	3.70	–	1.12	2.01	4.56
	AC 10	0.06	3.22	–	0.69	15.73	15.73	0.19	2.30	–	0.89	1.81	3.60
	AC 20	0.22	9.37	–	2.07	17.59	17.59	0.39	4.52	–	1.72	1.79	3.53
	Novophalt	0.36	4.32	–	4.69	40.87	40.87	0.41	3.72	–	0.76	1.47	2.27
	Styrelf	0.49	2.17	–	1.05	14.61	14.61	0.49	5.39	–	1.66	1.32	1.81
MnRoad	AC 20	0.20	11.47	–	4.66	20.09	20.09	0.39	4.70	–	2.82	1.85	3.77
	Pen 120/150	0.20	12.17	–	9.21	76.57	76.57	0.40	4.38	–	4.08	2.10	5.01
Westrack	Westrack	0.22	2.29	–	–	12.13	12.13	0.42	1.63	–	–	1.84	3.72
Arizona DOT	Para. PG 58-22	0.24	8.30	27.05	–	72.96	72.96	0.41	3.45	8.88	–	2.08	4.89
	Para. PG 64-16	0.38	2.90	2.90	–	2.90	2.90	0.44	3.00	7.06	–	1.74	3.30
	Nav. PG 70-10	0.28	1.00	1.00	–	1.00	1.00	0.59	4.99	6.06	–	1.58	2.67
	Nav. PG 76-16	0.25	2.76	3.90	–	16.29	16.29	0.40	2.02	1.86	–	1.24	1.57
	Chev. PG 64-22	1.14	13.78	19.43	–	25.10	25.10	0.51	3.20	5.40	–	1.85	3.77
	Chev. PG 76-16	0.56	2.55	2.55	–	2.55	2.55	0.58	4.49	8.14	–	1.47	2.29
Witczak	Citgo PG 64-22	0.22	7.64	–	1.31	16.86	16.86	0.43	3.30	–	1.29	1.85	3.79
Maryland Port Authority	Citgo PG 70-22	0.32	7.64	–	–	7.70	7.70	0.47	3.40	–	–	1.67	3.00
	TLA	0.17	1.68	–	–	107.38	107.38	0.34	3.50	–	–	1.80	3.58
	Stylink	0.37	4.39	–	–	6.05	6.05	0.44	3.80	–	–	1.31	1.79
	Novophalt	0.26	1.12	–	–	1.68	1.68	0.31	1.71	–	–	1.38	1.97
	PMB	0.23	1.83	–	–	1.12	1.12	0.17	1.46	–	–	1.05	1.11

Note: Dashes indicate that the A and VTS coefficients were not available for the particular aging condition.

www.EngineeringEBooksPdf.com

computed for −10, 20, and 40 °C, which in total represent the typical range of in-service conditions (ARA, 2004). Only the 5 and 54 °C data are discussed in detail, because the other temperatures generally represent a continuum of responses between those observed at these two temperatures. The AR can be strongly dependent on temperature (see, for example, the MnRoad binders at the PAV aging condition), and can also depend on the specific binder and aging condition examined. No clear correlation exists for predicting how the AR will manifest itself for the PAV condition, given the behavior of the original binder. In some cases, asphalt binders that show significant effect from the RTFO aging show little effect from the PAV aging (see the Maryland PMB). In other cases, such as the MnRoad Pen 120/150 asphalt binder, significant original-to-RTFO aging is observed, and a large RTFO-to-PAV change is also observed. Based on the preceding discussion regarding the chemical interactions at play in the asphalt cement and the associated literature on temperature-dependent oxidation kinetics, these differences are not overly surprising. Note that the Nav. PG 70-10 asphalt shows an AR of 1 at 5 °C due to the assumption that the maximum viscosity of the asphalt binder is 2.7×10^{12} cP. At −10 °C, the Nav. PG 70–10, and many of the other binders, show an AR of 1.

The GAS model has been applied to examine the effects of long-term field exposure on the aging ratio under in-service conditions. This method was chosen in lieu of more advanced and emerging methods because it is based on a large database of in-service materials, and because it adequately captures the basic trend of viscosity change with age. The predicted relationship between the original and RTFO-aged asphalt binder, η_{Original} and η_{RTFO}, respectively, is given by Equation (9.3) if it is assumed that the given asphalts have a standard aging susceptibility. Verification of this assumption for the asphalt binders in this study is shown in Figure 9.2, which demonstrates that the study materials are consistent with those used to develop the

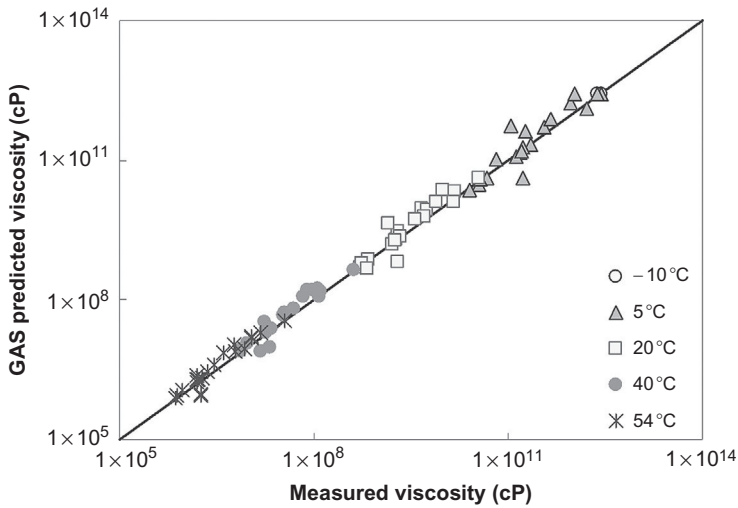


Figure 9.2 Verification of GAS model for original-to-RTFO aging prediction.

www.EngineeringEBooksPdf.com

GAS model. Thus, this model can be used reliably with the study materials to simulating in-service aging.

The second important component of the GAS model is the equation for relating RTFO viscosity to the long-term aged viscosity, η_{aged}, Equation (9.4). Note that the GAS model assumes the RTFO asphalt binder is equivalent to the asphalt binder as it exists immediately after mix and laydown operations (Mirza and Witczak, 1995).

$$\log(\log(\eta_{RTFO})) = 0.054405 + 0.972035\ \log\left(\log\left(\eta_{Original}\right)\right) \tag{9.3}$$

$$\log\left(\log\left(\eta_{aged}\right)\right) = \frac{\log(\log(\eta_{RTFO})) + At}{1 + Bt} \tag{9.4}$$

In Equation (9.4), $A = -0.004166 + 10^{F}(1.41213 + \log(\text{Maat})) + D(\log(\log(\eta_{RTFO})))$, $B = 0.197725 + 0.068384\left(\log\left(10^{F}\right)\right)$, $D = -14.5521 + 10.47662(\log(T_R)) - 1.88161\left(\log(T_R)^2\right)$, $F = 274.4946 - 193.831(\log(T_R)) + 33.9366\left(\log(T_R)^2\right)$, Maat is the mean annual air temperature (assumed equal to 50 °F), and t is the time in months.

The predicted effect of the long-term aging is shown in Table 9.3 for periods of 12 and 120 months. While these predictions capture some overall trends, considering that PAV aging was established to simulate the effect of field exposure for 10–15 years, the magnitudes of these predicted ratios are quite different from experimental values. Experimental ratios do not exceed 13.78 at the temperature of 5 °C, whereas the modeled viscosity ratio may be as large as 100. At 54 °C, the correlation is more reasonable. Furthermore, for heavily modified asphalt binders such as the Maryland Stylink, Novophalt, and PMB asphalt binders, the GAS model actually predicts an AR less than 1 (e.g., softening with aging) at some intermediate temperatures such as 40 °C. This is a mathematical anomaly of the GAS model and could be related to the fact that the model was not calibrated at these temperatures or with these materials. Similar extrapolation issues are also believed to be the cause of the high AR at 5 °C. The fact that the predicted AR values at 5 °C do not change between 12 and 120 months is due to the assumption that the maximum viscosity of asphalt binder is 2.7×10^{12} cP.

9.4.1.2 Linear viscoelastic properties

The development and implementation of the Superpave binder specification has caused $|G^*|$ to replace viscosity as the primary asphalt binder property in much of the United States. The AR calculated from $|G^*|$, unlike that calculated from viscosity, is a function of both frequency and temperature. Because the low end of the temperature range of interest (−10 °C) cannot be accurately measured using the dynamic shear rheometer (DSR), an analytical technique, presented elsewhere, that combines the results from the BBR and DSR tests is utilized (Underwood et al., 2010). The reference (RTFO) and aged asphalt $|G^*|$ are plotted relative to one another in Figure 9.3. Points above the line of equality represent cases where the aged asphalt modulus is greater than the reference, and points below the line represent cases where the aged

www.EngineeringEBooksPdf.com

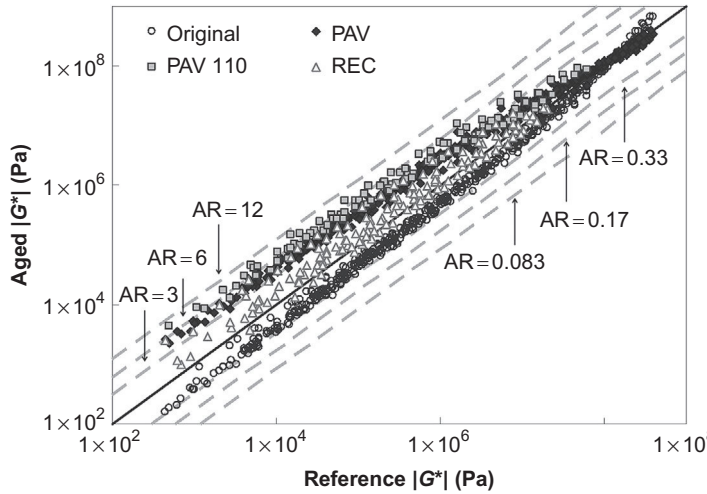


Figure 9.3 Effect of aging on asphalt binder $|G^*|$.

modulus is less than the reference case. The convenience of graphing the data in this way is that different ARs will plot as straight lines offset from the line of equality by an amount directly proportional to the AR. These lines are shown at certain specific AR values to provide a visual guide to the amount of stiffening occurring due to oxidation. Note that asphalt binders with BBR data available are plotted for −10, 5, 20, 40, and 54 °C, whereas the other asphalt binders are shown for only 20, 40, and 54 °C. The recovered asphalt binder samples do not have BBR data, and thus their results are plotted at only 20, 40, and 54 °C.

To properly interpret Figure 9.3, it must be recognized that $|G^*|$ decreases as the temperature increases or the frequency decreases, and therefore the $|G^*|$-based ratios suggest a larger rheological effect from aging at higher temperatures and/or slower frequencies. A comparison of the $|G^*|$ and viscosity-based aging ratios at some selected temperatures is shown in Figure 9.4. For the $|G^*|$-based quantity, the value is computed by averaging the results at frequencies between 1 and 100 rad/s for a given temperature. In this figure, the average AR, both $|G^*|$ and viscosity-based, for all study materials is plotted. Error bars are shown to represent the 75th and 25th percentiles. The reason for compiling all of the data into this single figure is to demonstrate that certain broad patterns exist.

The agreement between the $|G^*|$ and viscosity-based ratios is mostly favorable for the case of the original and recovered asphalt, but not for the PAV and PAV110 conditions. In these latter two aging conditions, the viscosity AR may be as large as 10–18, but the $|G^*|$ ratio never exceeds 7. This difference may be attributed to the fact that some of the viscosity measurements used to generate the A and VTS relationships are nonfundamental quantities. At high temperatures, when kinematic or rotational viscosities are measured, the material is mostly Newtonian and a viscosity measurement is a fundamentally meaningful quantity. However, at lower temperatures, where penetration is measured, the material is shear-rate dependent, and thus viscosity is an

www.EngineeringEBooksPdf.com

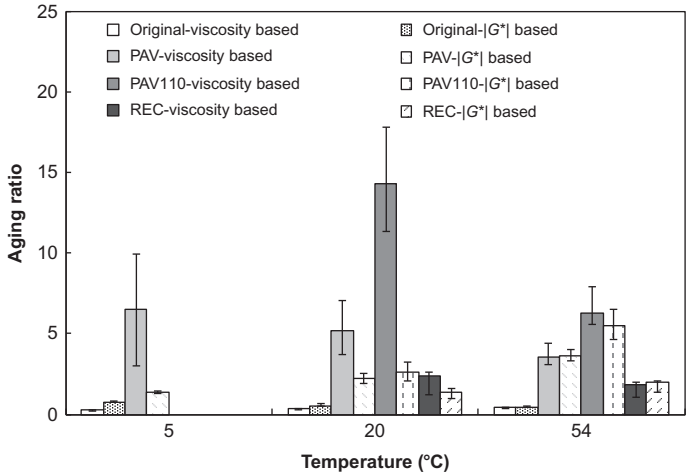


Figure 9.4 Comparison of viscosity-based and $|G^*|$-based aging ratios at selected temperatures.

engineering quantity rather than a fundamental one. It is hypothesized that these shear-rate effects will become more significant as the material stiffness increases, and thus the true effects of oxidative aging are overemphasized for these conditions. Examining only the data at 54 °C, where non-Newtonian effects are reduced (although not eliminated), the agreement between the $|G^*|$ and viscosity-based quantities improves. This is an important observation because many historical studies rely on viscosity values at 60 °C as the primary rheological indicator for oxidation (Petersen, 2009; Lunsford 1994; Glover et al., 2008).

9.4.2 *Viscoelasticity of asphalt concrete*

Oxidation in asphalt concrete is predominantly studied with techniques that first subject compacted asphalt concrete samples to a moderately high temperature (85 °C) for 2–5 days prior to performing mechanical tests (Bell, 1989; Brown and Scholz, 2000; Roque et al., 2010). This standard long-term oxidative aging (LTOA) procedure affects the LVE properties of asphalt concrete. Some specific changes include an increase in modulus at the high and intermediate temperatures, but, similar to the asphalt binder, the modulus at low temperatures does not change much. Based on this general pattern, it is also found that the time dependence of the material changes. Interestingly though, the *t*–*T* (time–temperature) shift factor is not strongly affected by oxidation, except at higher temperatures. The frequency at which the maximum phase angle occurs is delayed to a slower frequency with aging. This change causes the elasticity to be greater at intermediate temperatures, but less at high temperatures. Observing all of these effects, it is generally found that the overall impact of aging is most noticeable in the intermediate temperature range, followed by the high temperatures, and finally the low temperatures.

Some of these behaviors parallel those observed in asphalt binder (observations 1 and 2 above), while others (observations 3 and 4) do not. Such findings reinforce the

www.EngineeringEBooksPdf.com

complicated mechanics that dictate how asphalt binder influences the behaviors of asphalt mixtures. These mechanics have not yet been fully described with analytical or computational methods. Nevertheless, existing simplified tools can capture some of these fundamental differences and provide insight into the impacts of oxidation on asphalt concrete behaviors.

To demonstrate the effectiveness of oxidation on asphalt mixture behavior, a database consisting of dynamic modulus, $|E^*|$, and phase angle, ϕ, measurements from 30 mixtures aged at different laboratory and in-service levels has been compiled; see Table 9.4. The data are available for the unaged, short-term oven aged (STOA), LTOA, plant mixed, and field-aged conditions. In the unaged condition, the asphalt binder is heated to the appropriate mixing temperature and then combined with the aggregate. The mixture is then cooled to compaction temperature, whereupon it is compacted to the appropriate air void level for testing. In this case, the term unaged is somewhat misleading because oxidation could occur during the mixing and compaction process, but the naming is set based on convention. For STOA cases, the mixture was placed into a 135 °C oven for 4 h, then heated to the appropriate compaction temperature, and compacted. The same process was also followed for LTOA; however, after the sample was fabricated, it was subjected to 8 days of conditioning at 85 °C. For mixture evaluations, the STOA served as the reference case.

The impact of laboratory and in-service aging of asphalt concrete mixtures is summarized for the study materials in Figure 9.5. This figure conveys the same type of oxidative aging effect information shown for the asphalt binder in Figure 9.3. In Figure 9.5, the reference modulus is plotted on the x-axis and the moduli at different aging levels (noted in the legend) are plotted on the y-axis. For convenience, lines at aging ratios of 2, 1.5, 0.67, and 0.5 are also shown. First, the field sections are found to show substantial variability, which is attributed to three primary factors: (1) the specimen-to-specimen variability was higher than usual for these materials; (2) the field sections were exposed to aging for only a very short period of time—less than 5 years; and (3) the well-known, but hard to quantify effects of lab-to-field compaction differences are present. Comparisons of the different laboratory-aged materials show that the unaged samples are almost consistently softer and the LTOA-aged samples are almost consistently stiffer than the reference. Cases that do not follow this trend are likely the result of experimental variability because the differences are small. Some mixtures also show a trend toward a reduced aging effect at the extremely low modulus values.

9.5 Linking asphalt binder and asphalt mixture oxidation impacts

Comparing Figures 9.3 and 9.5, it is seen that the mixture-aging ratios are smaller in magnitude than those found for the asphalt binder. This effect can be clearly observed by noticing the spread of data relative to the reference AR lines. This effect could be related to the mismatch in aging conditions between binder and mixture because *unaged* asphalt mixture may not necessarily be the same as original binder, STOA may not

www.EngineeringEBooksPdf.com

Table 9.4 Mixture database used for aging study

Project	Mixture name	Aging conditions					Testing temperatures (°C)	
		Unaged	STOA	Plant Mix	LTOA	Field	Max	Min
NCHRP 9-36	Airblown	✓	✓				4	40
	AAC-1	✓	✓					
	AAF-1	✓	✓					
	AAM-1	✓	✓					
	ABL-1	✓	✓					
	ABM-2	✓	✓					
	Citgoflex	✓	✓					
	Elvaloy	✓	✓					
	ALF PG 64	✓	✓					
	Novophalt	✓	✓					
	EVA	✓	✓					
ALF	ALF AC5		✓			✓	−10	54
	ALF AC5-Base		✓			✓		
	ALF AC10		✓			✓		
	ALF AC20		✓			✓		
	ALF AC20-Base		✓			✓		
	ALF Novophalt		✓			✓		
	ALF Styrelf		✓			✓		
NCSU	AL		✓		✓		−10	54
	A		✓		✓			
AAT	Citgo		✓		✓		4	40
WRI Kansas	Coastal Eldorado			✓	✓		4	40
	Koch Muskogee			✓	✓			
	Royal Trading			✓	✓			
	Sinclair Tulsa			✓	✓			
WRI Nevada	Crown Nevada			✓	✓		4	40
	Crown Canada			✓	✓			
	Sinclair, Wyoming			✓	✓			
	Crown Venezuela			✓	✓			

www.EngineeringEBooksPdf.com

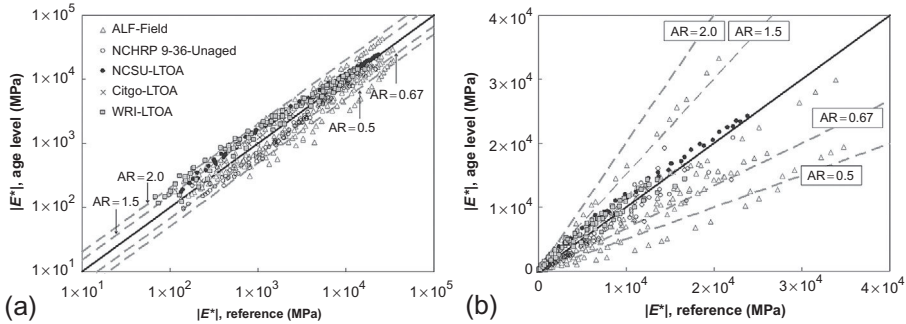


Figure 9.5 Effect of aging on measured $|E^*|$ in (a) logarithmic space and (b) arithmetic space.

equate to RTFO, and LTOA may not equate to PAV. However, numerous research studies have concluded and engineering practice suggests an approximate and *on the average* agreement in material states at these aging conditions (Von Quintus et al., 1991; Bell et al., 1994; Houston et al., 2005). As noted in the introduction, the exact aging time correspondence is dependent upon many confounding factors, but in taking the general guidelines as truth or near truth, it can be concluded that oxidative aging has a less noticeable effect on the mixture modulus than it does on the binder modulus.

The fact that asphalt mixture modulus is less sensitive to oxidation than the asphalt binder can be understood with the aid of a highly simplified physical analog, shown in Figure 9.6. Such a construct is much too simplistic to accurately represent the asphalt mixture, but it does provide a simple analog to broadly explain why differences in sensitivity may exist. If a unit force is applied to this model and if the area of each

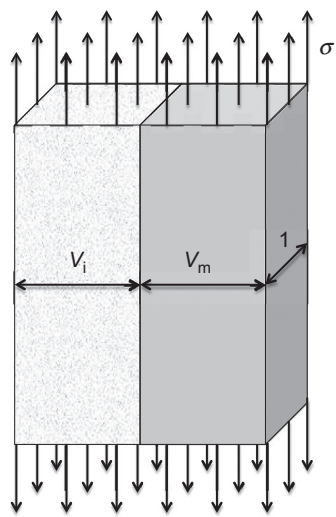


Figure 9.6 Simplified mechanical analog for conceptualizing differences in mixture and binder sensitivity to oxidation.

www.EngineeringEBooksPdf.com

element is set to be proportional to the volume content of the matrix (asphalt binder) and inclusion (aggregate) phases, V_m and V_i, respectively, then the composite modulus, E_c, of the system is given by Equation (9.5).

$$E_c = V_m E_m + V_i E_i \tag{9.5}$$

Now consider two cases wherein the matrix phase has different values: for case one let the matrix modulus, E_m, equal a nondimensional value of 10, and for case two let $E_m = 100$. For both, let the modulus of the inclusion, E_i, equal 1000. If the volume of each phase is taken to be representative of what is typically observed in asphalt concrete ($V_m = 11\%$ and $V_i = 89\%$), then $E_c = 891$ for case one and it equals 901 for case two. Thus, in this scenario, a matrix ratio of 10 results in a composite modulus ratio of 1.01. Obviously, this is a highly idealized scenario using a model that is too simplistic to fully represent asphalt concrete, but it does show that a change in the modulus of the asphalt binder does not translate to equivalent changes in the modulus of the asphalt mixture. In reality, the relationship between the mechanical properties of an asphalt mixture and its asphalt binder is highly complex and dependent upon many diverse physical and physicochemical factors, such as aggregate gradation, void content, thermal history, aggregate surface chemistry and its interaction with the asphalt cement, and so on.

While it is true that as of this writing, a wholly accurate and fully mechanistic model to link known properties of asphalt binder and aggregates to those of the resulting asphalt concrete does not exist, some existing empirical to semiempirical methods do exist for this purpose, and they have been applied to assess their ability to match the quantitative observations in the preceding sections of this paper. In total, four different analytical methods are used: (1) the original Witczak model, (2) the modified Witczak model, (3) the Hirsch model, and (4) the North Carolina State University artificial neural network (NCSU ANN) model. A brief description of these models is given here, but significant literature on each model has been reviewed and presented elsewhere (Kim et al., 2009). The two Witczak models are empirically based regression formulas developed from large databases of modulus measured on widely varying asphalt concrete mixtures. In the original version, viscosity is used as the primary asphalt binder property, while the modified version utilizes the $|G^*|$ and phase angle. Both models use aggregate gradation parameters as well as the volumetric properties of the mixture. The Hirsch model contains a micromechanically motivated function, which includes some empirically calibrated adjustment factors. The NCSU ANN model is based on an artificial neural network approach, with the network trained using a large database of moduli from various asphalt concrete mixtures. Both the Hirsch model and the NCSU ANN model utilize binder $|G^*|$ and mixture volumetric parameters as the input parameters.

The measured original, RTFO, PAV, PAV110, and REC asphalt binder properties are used as input in these models to predict the effect of aging on mixture modulus. Plots similar to that shown in Figure 9.5(a) are created to qualitatively and quantitatively examine the given model's ability to match the trends observed in mixture testing. These plots are shown in Figure 9.7 for each of the models. In Figure 9.7(c), shaded areas are shown to represent conditions where the Hirsch model has not been fully calibrated (Kim et al., 2009). These extrapolation areas are included because users would likely

www.EngineeringEBooksPdf.com

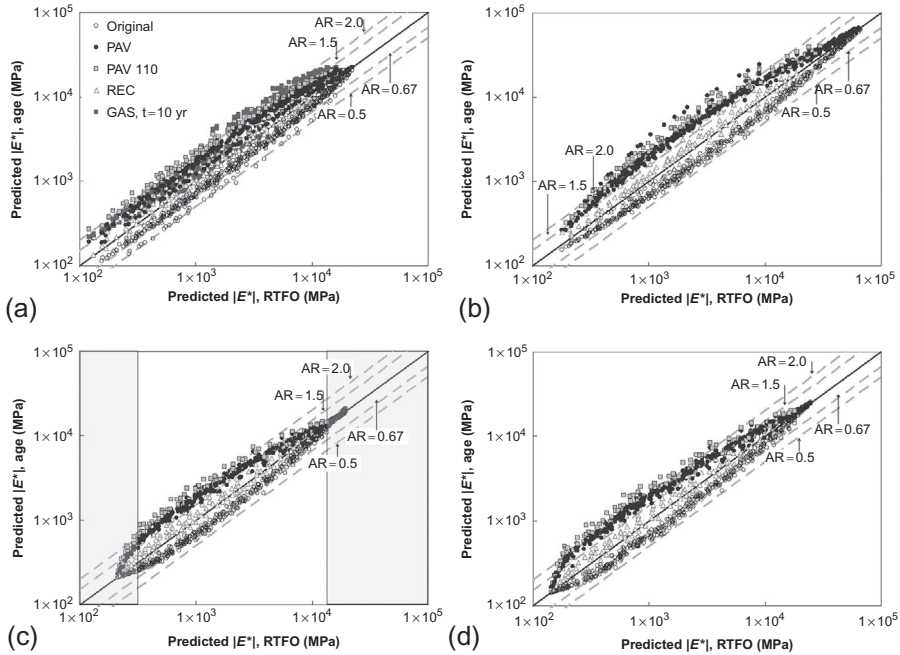


Figure 9.7 Predicted aging susceptibility with existing $|E^*|$ prediction models: (a) original Witczak model, (b) modified Witczak model, (c) Hirsch model, and (d) NCSU ANN model.

apply the model irrespective of extrapolative errors. Long-term aged mixture moduli are predicted using only the original Witczak model because it is the only model that utilizes viscosity (the output from the GAS model) as an input variable.

Comparisons between Figures 9.5(a) and 9.7(a)–(d) show that each predictive model generally matches the magnitude of the aging effect observed in the experiments (observe that the different AR lines are shown for the same level of aging). In addition, all models except the original Witczak predict that aging is most significant at intermediate conditions and becomes less significant at the extremes. This behavior gives a characteristic elliptical shape to the plots in Figure 9.7(b)–(d), but is most pronounced for the Hirsch and NCSU ANN models. Both of these models utilize only the $|G^*|$ and mixture volumetrics as input parameters, but have no parameters to account for aggregate gradation. The original Witczak model suggests that the effect of aging increases as the material softens, but it does not show the characteristic elliptical shape; instead, this model predicts that the influence of aging is very similar at the intermediate and low modulus conditions (e.g., a parabolic shape). The characteristic shape from Figure 9.5(a) varied from slightly elliptical (NCSU-LTOA and Citgo-LTOA series) to parabolic (WRI-LTOA and NCHRP 9-36). These qualitative observations suggest that the original and modified Witczak models are better suited for assessing the impact of asphalt binder aging on the mixture modulus, but that all of the existing models do an adequate job. The better match from the two Witczak models may be

www.EngineeringEBooksPdf.com

related to the fact that they include parameters to directly account for the aggregate gradation, which may indirectly capture some of the influence of aggregate surface characteristics on the aging phenomenon.

Even though the individual models produce different AR values, the predictions in Figure 9.7 show that each captures the fact that a given amount of stiffening in the asphalt binder does not directly translate to an equivalent amount of stiffening in the asphalt mixture. Recall that the influence of aging on the asphalt binder alone was shown in Table 9.3 and Figure 9.3 to regularly result in AR greater than 12 and less than 0.2. The maximum AR value observed from the mixture data shown in Figure 9.5 or predicted from Figure 9.7 is 3.25, while the minimum predicted value (e.g., for the unaged cases) is 0.43. These observations are independent of the exact agreement between mixture and binder aging conditions, and reflect a larger difference in behavior of the two materials. The data and analysis in this and the preceding section shows that the relationship between asphalt binder and mixture stiffness is not a simple one, and as such, a major change in the properties of the asphalt binder does not necessarily translate to a major change in the mixture modulus.

9.6 Sequential multiscale approach for identifying oxidation impacts

As the previous sections demonstrate, the topic of asphalt concrete oxidation contains aspects that are relevant at different length scales. At the smallest scale commonly considered, oxidation is understood with respect to changes in molecular functionalities, while at the next largest scale it is understood with respect to the impacts on asphalt cement rheology. Although a complete description of the mechanisms that relate molecular functionalities and asphalt rheology does not currently exist, a general understanding has evolved, and broadly defined correlations have been developed to aid engineers and scientists in bridging the scale gap. Han (2011) evaluated the oxidation of different asphalts and found a strong relationship between the diffusivity and the low-shear rate limiting viscosity, η_0^*.

$$\frac{D_{O_2}}{T} = 5.21 \times 10^{-12} \left(\eta_0^*\right)^{-0.55} \tag{9.6}$$

This correlation can be further related to the molecular structure of the asphalt by considering asphaltenes to be impermeable to oxygen, and then using a differential micromechanical model based on a generalization of Einstein's suspension model (Mooney, 1951). The significance of Equation (9.6) is that the diffusivity of oxygen in asphalt decreases as the viscosity increases, and that this increase can be attributed to the correlation between viscosity and asphaltene content.

Increases in diffusivity do not necessarily mean an increase in oxidation product, because the rate of carbonyl formation can vary from binder to binder (Liu et al., 1996). Likewise, the formation of carbonyl is not a singular indicator for the impact of oxidation on the physical properties of the asphalt. Complicating these issues even

www.EngineeringEBooksPdf.com

further is the fact that within an asphalt concrete mixture, asphalt binder is intimately bound to filler aggregates; for example, asphalt cement exists in the form of a mastic in the concrete mixture (Delaporte et al., 2007; Underwood and Kim, 2013). As discussed previously, the filler particles can provide both a physical and physicochemical reinforcement effect within the mastic. The importance of this scale from a multiple-scale assembly viewpoint is that these physicochemical influences are magnified so a more direct characterization of the behaviors can be developed. Han evaluated the diffusivity of such mastics and found an overall decrease in diffusion when compared to the asphalt binder alone. This behavior was theorized to be the consequence of the physical interactions and increased diffusion path that result from the addition of mineral filler. Existing models to describe multicomponent systems (Maxwell, Rayleigh, and nonspherical complex models) predicted the change in diffusivity within statistical reason, but on average tended to underestimate the change in diffusion at higher particle concentrations.

During the SHRP, researchers evaluated the oxidation of asphalt mastics using standard laboratory aging procedures (Anderson et al., 1994). A small experimental plan was carried out involving mastics created from five aggregate sources and two asphalt cement binders. Each of the mastics and the binders alone were conditioned in a PAV for 6 days at 60 °C. The SHRP researchers clearly observed an aggregate-dependent interaction in the oxidation, but concluded that the asphalt source effects were greater than the aggregate effects. The SHRP study findings are shown in terms of the aging ratio (oxidized to unoxidized mastic viscosity) in Figure 9.8. Because the goal of this project was to develop performance-based tools for asphalt binder, additional experiments and analysis were not completed to a substantial amount to warrant additional publications. However, as shown in Figure 9.8, the observed trends were inconsistent, and some aggregates resulted in an increase in the aging ratio, while others actually showed a decrease relative to what was observed in the aging of the

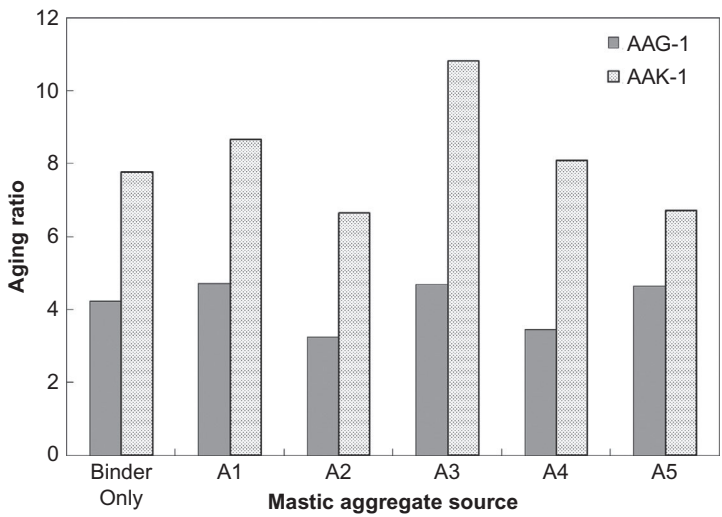


Figure 9.8 Comparison of asphalt binder and asphalt mastic aging ratios from the SHRP study.

www.EngineeringEBooksPdf.com

asphalt binder alone. It is known that there are multiple competing mechanisms that may be responsible for such behaviors. First, for the same volume or mass, the asphalt mastics contains less asphalt binder than an equivalently aged pure binder condition; thus, there exists a greater potential for oxidation. This tendency would be somewhat tempered by the decreased diffusivity of oxygen through asphalt mastics and/or increased film thickness (depending on the oxidation protocol followed), as demonstrated by Han (2011). In addition, it is known from the simplistic micromechanical analysis in Section 9.5 that the mechanical properties of asphalt mastic do not change by an amount equivalently sensitive to changes in asphalt binder. Such a tendency has been confirmed by blending aggregate filler with asphalt that has been aged *a priori*. For this particular experiment, the asphalt binder was aged in a PAV oven at 110 °C for 20 h. The comparisons between aging ratios (based on $|G^*|$ at 60 °C) for the asphalt binder and asphalt mastic are shown as the Case 1 series in Figure 9.9. This figure also shows results for a similar asphalt binder that was blended and aged as a mastic, like in the SHRP project, labeled as Case 2 in the figure. As seen in this figure, the preblended case demonstrates greater aging than the asphalt binder, whereas the SHRP-like aging scenario (e.g., aged mastic) shows less. This finding essentially indicates that the impacts of mineral filler on oxidation should be more carefully considered than has been previously done. Each of the competing behaviors would of course be affected by the peculiar nature of the aggregate filler, along with its interaction with the asphalt binder. While this interaction may not be critically important for distinguishing between asphalt binders, it could be quite important for modeling and investigations that attempt to better engineer asphalt concrete mixtures.

Recently, two separate studies have identified the potential for a nonhomogenous distribution of asphalt binder molecular fractions within the asphalt mastic (Tan and Guo, 2014; Underwood and Kim, 2014). This theory, originally posited by Tunnicliff (1962, 1967) to explain experimental data gathered on mastics, has received support

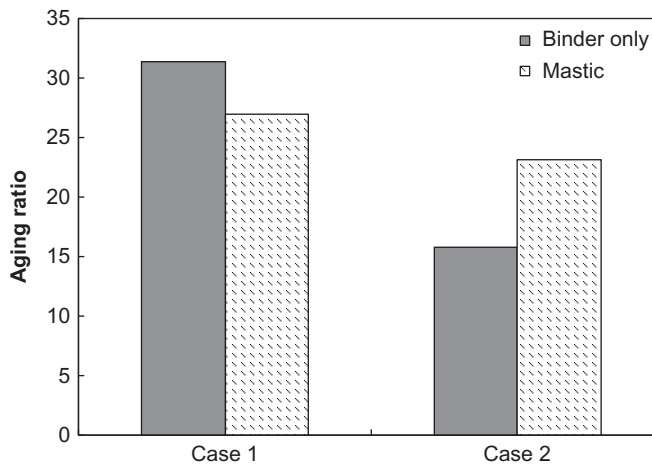


Figure 9.9 Comparison of asphalt binder and asphalt mastic aging ratios for filler blended with aged asphalt and aged mastic from similar material sources aged in the PAV at 110 °C.

www.EngineeringEBooksPdf.com

from different studies carried out over the years (Anderson and Goetz, 1973; Craus et al., 1978; Petersen et al., 1987; Anderson et al., 1992; Kim, 2003). The more recent evaluations have examined the phenomenon from a thermal and rheological perspective, using, in essence, the physical model depicted in Figure 9.10. Comparisons between the traditional two-phase interpretations and the one resulting from the multiphase asphalt framework are shown in Figure 9.11. This figure demonstrates that a multiphase interpretation, when coupled with an appropriate micromechanical formulation, can better explain the time- and temperature-related stiffening, both qualitatively and quantitatively, than models relying on the two-phase interpretation (Underwood and Kim, 2014).

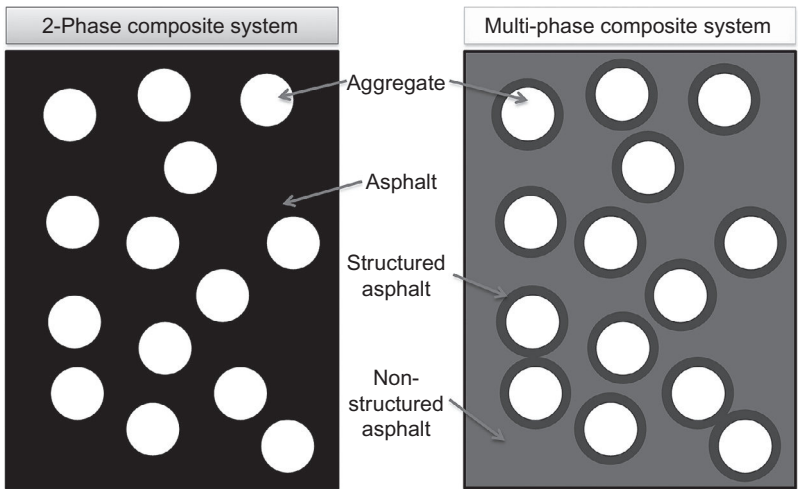


Figure 9.10 Schematic representation of multiphase asphalt structure.

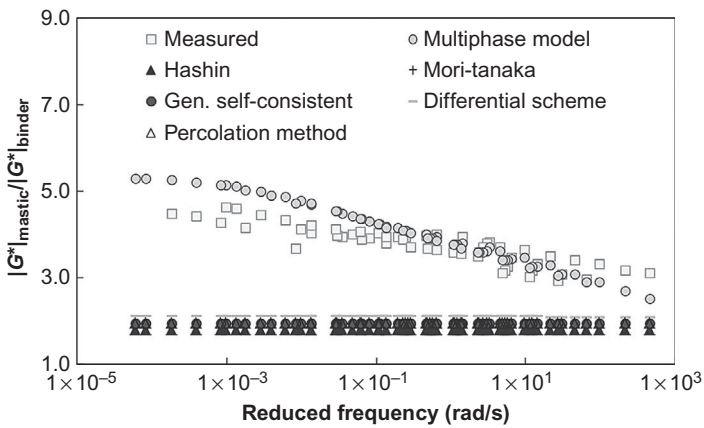


Figure 9.11 Comparison of predicted modulus for a typical asphalt mastic using two-phase and multiphase micromechanical models.

www.EngineeringEBooksPdf.com

The interface layer of asphalt is theorized to have a higher modulus (increased viscosity) due to the preferential adsorption of asphaltenes or other highly polar compounds. Coupling this theory with the correlation shown in Equation (9.6) suggests that the physicochemical interactions would add an additional hindrance to the oxidation pathway. More interestingly though, it suggests that there would exist a preferential oxidation path thorough the asphalt cement such that the process would occur first in the material that is located further from the aggregate particles. This spatially heterogeneous oxidation profile could have important implications in the origination of damage and cracking. Thus, the exact way that the molecular functionalities distribute within the mastic can be an important characteristic for determining both how the asphalt oxidizes within the asphalt concrete and also how this chemical oxidation affects the mechanical properties of the asphalt concrete.

The mastic-related influences are not the only factors affecting the modulus of asphalt concrete. To completely understand the impact of asphalt binder changes on asphalt mixture behaviors, one should also consider what occurs when aggregates are of sufficient volume fraction that they interact together through contact. The intermediate scale that captures a major portion of this interaction is the FAM scale. Understanding the scalewise relationships between it and the asphalt mastic below and the asphalt concrete above can provide the additional information needed to examine oxidative aging impacts in a way that is more complete than is possible with the previously described empirical models. Between asphalt mastic and asphalt FAM, substantial internal structure is developed as the aggregate volume has increased from approximately 20–30% in the mastic to approximately 70–90% in the case of FAM. This phenomenon has been found to evolve along a continuum of structure, which is tracked by a structuralization index (SI) that is related to the volume concentration of aggregate particles, and their characteristic packing behaviors (e.g., gradation, surface texture, and shape). These characteristics evolve in a material-specific manner as a function of the length scale. It has been found that this relationship between the mastic modulus and the structuralized material's properties can be expressed according to Equation (9.7) (Underwood and Kim, 2012):

$$\log\left(|G^*|_{\text{FAM}}\right) = \alpha(\text{SI}) + \frac{\beta}{1 + e^{\chi + \delta(\text{SI})\log\left(|G^*|_{\text{mastic}}\right)}} \tag{9.7}$$

It is found that the functions α and δ are approximately constant for the highly structured FAM scale. Then, differentiating Equation (9.7) with respect to the logarithm of $|G^*|_{\text{mastic}}$, Equation (9.8), it is found that the rate of change in FAM modulus is less than that of the mastic; see Figure 9.12.

$$\frac{d\log\left(|G^*|_{\text{FAM}}\right)}{d\log\left(|G^*|_{\text{mastic}}\right)} = \frac{-\beta\delta\left(e^{\chi + \delta\log\left(|G^*|_{\text{mastic}}\right)}\right)}{\left(1 + e^{\chi + \delta\log\left(|G^*|_{\text{mastic}}\right)}\right)} \tag{9.8}$$

Asphalt mixture is also a highly structured composite, and therefore from Section 9.5 it can be inferred that the mechanical properties of FAM will be less sensitive to

www.EngineeringEBooksPdf.com

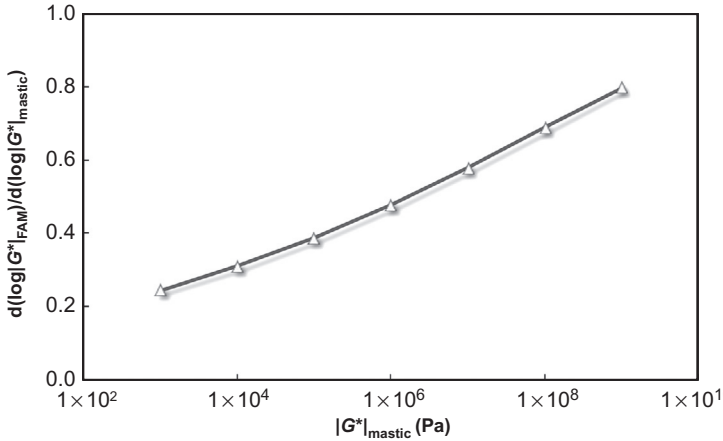


Figure 9.12 Effect of changes in the mastic modulus on the modulus of FAM.

oxidation than asphalt binder. However, by following the multiple-scale linkage approach, it is possible to understand that these differences can be related back to the particle contact mechanism and likely not the particle surface interactions that are dominant at the mastic scale.

FAM can also be linked to the asphalt mixture scale by using relatively well-known micromechanical models. Such models are found to be too simplistic to cover the whole range of scales required to bridge the gap between asphalt binder and mixture. However, because the modulus gradient between FAM and aggregates is not as large as that between asphalt binder and aggregate, the method is found to have sufficient utility for this purpose. Here, the generalized self-consistent method derived by Christensen and Lo (1979) is adopted. This method begins with assumptions of spherical particle shapes, isotropic elasticity, and strain–energy equivalence between the microstructure and an equivalent medium. The model itself reduces to the solution of a quadratic function, Equation (9.9), which relates the mixture modulus, $|G^*|_M$, to the FAM modulus, $|G^*|_F$.

$$A\left(\frac{|G^*|_M}{|G^*|_F}\right)^2 + B\left(\frac{|G^*|_M}{|G^*|_F}\right) + C = 0 \tag{9.9}$$

The expressions for A, B, and C are given in Equation (9.10), and found to be functions of the shear modulus and Poisson's ratio of the aggregate, G_P and v_P, the dynamic shear modulus and Poisson's ratio of the FAM, $|G^*|_F$ and $|v^*|_F$, and the volumetric particle concentration, C_v.

The predictability of Equation (9.9) is demonstrated in Figure 9.13. The scalewise implications of this prediction match are that stiffening of the asphalt FAM will lead to stiffening of the asphalt mixture. However, an incremental increase in modulus of the FAM will not result in an equivalent increment of stiffening in the asphalt mixture. The fact that the volumetric concentration alone can predict the observed stiffening suggests that on average, other coarse aggregate shape descriptors (shape, texture,

www.EngineeringEBooksPdf.com

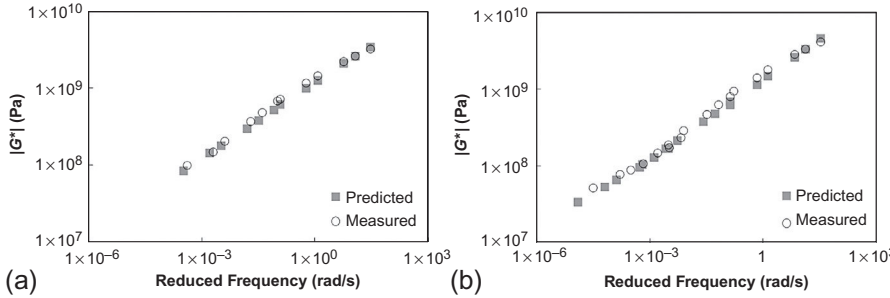


Figure 9.13 (a, b) Predictability of asphalt mixture modulus using a generalized self-consistent model for two different asphalt concrete mixtures.

etc.) are not important factors in the modulus at the mixture scale, which may be one reason why the Hirsch and NCSU ANN models were able to empirically capture the appropriate aging-related mixture stiffening. It is likely that these other characteristics may hold increased importance as one applies higher strain levels that exceed the linear viscoelastic limits of the material.

$$
\begin{aligned}
A &= 8\left(\frac{G_{\mathrm{P}}}{|G^*|_{\mathrm{F}}}-1\right)\left(4-5|v^*|_{\mathrm{F}}\right)\kappa_1 C_{\mathrm{v}}^{10/3}-2\left[63\left(\frac{G_{\mathrm{P}}}{|G^*|_{\mathrm{F}}}-1\right)\kappa_2+2\kappa_1\kappa_3\right]C_{\mathrm{v}}^{7/3}\\
&\quad+252\left(\frac{G_P}{|G^*|_{\mathrm{F}}}-1\right)\kappa_2 C_{\mathrm{v}}^{5/3}-50\left(\frac{G_P}{|G^*|_{\mathrm{F}}}-1\right)\left(7-12|v^*|_{\mathrm{F}}+8|v^*|_{\mathrm{F}}^2\right)\kappa_2 C_{\mathrm{v}}+4\left(7-|v^*|_{\mathrm{F}}\right)\kappa_2\kappa_3\\
B &= -4\left(\frac{G_{\mathrm{P}}}{|G^*|_{\mathrm{F}}}-1\right)\left(1-5|v^*|_{\mathrm{F}}\right)\kappa_1 C_{\mathrm{v}}^{10/3}+4\left[63\left(\frac{G_{\mathrm{P}}}{|G^*|_{\mathrm{F}}}-1\right)\kappa_2+2\kappa_1\kappa_3\right]C_{\mathrm{v}}^{7/3}\\
&\quad+504\left(\frac{G_{\mathrm{P}}}{|G^*|_{\mathrm{F}}}-1\right)\kappa_2 C_{\mathrm{v}}^{5/3}+150\left(\frac{G_{\mathrm{P}}}{|G^*|_{\mathrm{F}}}-1\right)\left(3-|v^*|_{\mathrm{F}}|v^*|_{\mathrm{F}}\right)\kappa_2 C_{\mathrm{v}}+3\left(15|v^*|_{\mathrm{F}}-7\right)\kappa_2\kappa_3\\
C &= 4\left(\frac{G_{\mathrm{P}}}{|G^*|_{\mathrm{F}}}-1\right)\left(5|v^*|_{\mathrm{F}}-7\right)\kappa_1 C_{\mathrm{v}}^{10/3}-2\left[63\left(\frac{G_P}{|G^*|_{\mathrm{F}}}-1\right)\kappa_2+2\kappa_1\kappa_3\right]C_{\mathrm{v}}^{7/3}\\
&\quad+252\left(\frac{G_P}{|G^*|_{\mathrm{F}}}-1\right)\kappa_2 C_{\mathrm{v}}^{5/3}+25\left(\frac{G_{\mathrm{P}}}{|G^*|_{\mathrm{F}}}-1\right)\left(|v^*|_{\mathrm{F}}^2-7|v^*|_{\mathrm{F}}\right)\kappa_2 C_{\mathrm{v}}-\left(7+15|v^*|_{\mathrm{F}}\right)\kappa_2\kappa_3\\
\kappa_1 &= \left(\frac{G_{\mathrm{P}}}{|G^*|_{\mathrm{F}}}-1\right)\left(49-50v_{\mathrm{P}}|v^*|_{\mathrm{F}}\right)+35\left(\frac{G_{\mathrm{P}}}{|G^*|_{\mathrm{F}}}-1\right)\left(v_{\mathrm{P}}-2|v^*|_{\mathrm{F}}\right)+35\left(2v_{\mathrm{P}}-|v^*|_{\mathrm{F}}\right)\\
\kappa_2 &= 5v_{\mathrm{P}}\left(\frac{G_{\mathrm{P}}}{|G^*|_{\mathrm{F}}}-1\right)+7\left(\frac{G_{\mathrm{P}}}{|G^*|_{\mathrm{F}}}+4\right),\ \kappa_3=\left(\frac{G_{\mathrm{P}}}{|G^*|_{\mathrm{F}}}\right)\left(8-10|v^*|_{\mathrm{F}}\right)+\left(7-5|v^*|_{\mathrm{F}}\right)
\end{aligned}
\tag{9.10}
$$

9.7 Summary

The influence of oxidative aging on the viscosity and modulus of asphalt binder and on the modulus of asphalt mixtures has been studied. It was found that very little experimental data have been gathered on the influence of oxidative aging in asphalt

www.EngineeringEBooksPdf.com

mixtures. Surprisingly, no studies were found wherein researchers attempted to study the effects of aging in asphalt binder and asphalt mixture at a consistent aging level and over the entire range of in-service conditions. Because data for direct comparison are not available, an indirect method was adopted wherein materials with vastly different properties were examined at many different aging levels. Using qualitative and quantitative methods, it was shown that oxidative aging may influence the viscosity and linear viscoelastic modulus of asphalt binder by a factor of 10 or more. However, it was also observed that this influence does not directly translate to increases in the modulus of asphalt concrete mixtures. Such a direct translation does not occur due to the complex interactions that can occur within an asphalt concrete mixture, including the mitigating effects of aggregate particles and the fact that asphalt binder typically represents only about 10–15% of the total volume of an asphalt concrete mixture. A rational method that utilizes existing analytical models was shown to predict the influence of asphalt binder aging on mixture modulus with a reasonable degree of accuracy. With this method, engineers can better assess the influence of asphalt binder aging on the modulus of asphalt concrete mixtures.

9.8 Future trends

The fundamental study of asphalt concrete aging has, for the most part, focused on the relevant chemical processes occurring in the asphalt cement. Such an approach is intuitive because it is understood that within the asphalt concrete, it is the asphalt cement that responds to oxidation. However, this approach is fundamentally limited in terms of its applicability to practice, as it does not directly address the impacts of these changes on asphalt mixture nor provide insights that allow engineers to better design materials. New research and evolving paradigms for the structure and modeling of asphalt concrete are providing a new vision for how the oxidation of asphalt cement impacts the properties of asphalt concrete and, by extension, the performance of pavements. Future trends with respect to aging parallel larger trends in the asphalt concrete community that are striving to understand cause-and-effect relationships within the asphalt concrete structure. By better understanding the mechanisms that link different scales, it may be possible to adequately control the mixture variables to mitigate issues that may exist with the available source materials (e.g., not using a material highly sensitive to oxidation in an asphalt concrete that itself is highly sensitive to changes in asphalt binder properties).

While a complete understanding of the asphalt oxidation kinetics does not yet exist, the essential fundamental elements of the process have matured to a point where researchers have the capability to predict the oxidation process at a chemical level. To utilize this understanding, the linkages between chemical/molecular properties and asphalt rheology must be more fundamentally established. Future research will focus on developing these linkages in a less empirical and more rigorously accurate way. For example, many existing relationships are based on a single rheological measure, viscosity at 60 °C, and as it has been seen in this chapter, the actual rheological

www.EngineeringEBooksPdf.com

changes are much more complicated and vary by temperature and frequency of loading. Moving forward, research will continue to emerge on the upscaling of asphalt binder to asphalt mixture characteristics. Although the empirical and semiempirical methods discussed in this chapter show a capability to capture some of the first-order stiffening effects, there still remains considerable scatter. In addition, due to the nature of oxidation to embrittle the asphalt cement, these existing relationships must be expanded upon to relate properties beyond LVE in order to provide meaningful insight into the oxidation phenomena in mixtures. The multiscale paradigm for studying asphalt concrete behavior thus has many potential applications, and can serve as a framework to develop more fundamental-based cause-and-effect relationships that can lead to better engineering of asphalt concrete materials.

9.9 Sources of further information

Oxidation has been and continues to be a relevant issue in the asphalt concrete and asphalt pavement field. Interested readers will find the reports from the SHRP a valuable resource in understanding the phenomenon from a fundamental chemical perspective. A good overall summary of the asphalt binder oxidation studies conducted in the years leading to the SHRP and during the SHRP itself is given by Petersen (2009). Readers may also find the studies of Dr. Charles Glover and his associates (Jemison et al., 1992; Lunsford, 1994; Liu et al., 1996; Glover et al., 2008; Han, 2011) very useful as well. These researchers are integrating the essential framework of chemical oxidation with thermal history profiles for in-service pavements to predict the amount of oxidation product formed during the life of a pavement, and also to link this, in an approximate way, to the asphalt binder rheology.

Practical guidance on laboratory aging protocols exists in the reports of completed and ongoing research projects funded by the National Cooperative Highway Research Program. NCHRP 9-23 (Houston et al., 2005) led to refinement of the laboratory aging procedure for simulating long-term oxidation of the asphalt cement; NCHRP 9-52 (to be completed in November 2014) will establish updated protocols for short-term laboratory aging of asphalt concrete mixture; and NCHRP 9-54 will develop long-term laboratory aging protocols for asphalt concrete mixtures. Although these projects have very applied outcomes, the issues addressed, methods developed, and overall findings can be related to many of the essential concepts discussed throughout this chapter.

References

Airey, G.D., 2003. State of the art report on ageing test methods for bituminous pavement materials. Int. J. Pavement Eng. 4, 165–176. http://dx.doi.org/10.1080/1029843042000198568.

Anderson, D.A., Goetz, W.H., 1973. Mechanical behavior and reinforcement of mineral filler-asphalt mixtures: Technical paper, Publication FHWA/IN/JHRP-73/05. Joint Highway Research Project, Indiana Department of Transportation and Purdue University, West Lafayette, Indiana, http://dx.doi.org/10.5703/1288284313845.

www.EngineeringEBooksPdf.com

Anderson, D.A., Bahia, H.U., Dongre, R., 1992. Rheological properties of mineral filler-asphalt mastics and its importance to pavement performance. In: Meininger, R. (Ed.), Effects of Aggregates and Mineral Fillers on Asphalt Mixture Performance: ASTM STP 1147. ASTM, Philadelphia, pp. 131–153.

Anderson, D.A., Christensen, D.W., Bahia, H.U., Dongre, R., Sharma, M.G., Antle, C.F., Button, J., 1994. Binder characterization and evaluation volume 3: physical characterization, SHRP A-369. Strategic Highway Research Program, Washington, DC.

ARA Inc., 2004. Guide for Mechanistic-Empirical Design of New and Rehabilitated Pavement Structures. National Cooperative Highway Research Program, Washington, DC.

Banerjee, A., Smit, A.F., Prozzi, J.A., 2012. The effect of long-term aging on the rheology of warm mix asphalt binders. Fuel 97, 603–611. http://dx.doi.org/10.1016/j.fuel.2012.01.072.

Bell, C.A., 1989. Aging of asphalt aggregate systems, SHRP-A-305. Strategic Highway Research Program, Washington, DC.

Bell, C.A., Sosnovske, D., 1994. Aging: binder validation, *SHRP-A-384*. Strategic Highway Research Program, Washington, DC.

Bell, C.A., Fellin, M.J., Wieder, A., 1994. Field validation of laboratory aging procedures for asphalt aggregate mixtures. J. Assoc. Asphalt Paving Technol. 63, 45–80.

Brown, S.F., Scholz, T.V., 2000. Development of laboratory protocols for the ageing of asphalt mixtures. In: 2nd Eurasphalt and Eurobitume Congress, Barcelona, Spain.

Christensen, R.M., Lo, K.H., 1979. Solutions for effective shear properties in three phase sphere and cylinders models. J. Mech. Phys. Solids 27, 315–329. http://dx.doi.org/10.1016/0022-5096(79)90032-2.

Corbett, L.W., Merz, R.E., 1975. Asphalt binder hardening in the michigan test road after 18 years of service. Transp. Res. Rec. 544, 27–34.

Craus, J., Ishai, I., Sides, A., 1978. Some physico-chemical aspects of the effect and the role of the filler in bituminous paving mixtures. J. Assoc. Asphalt Paving Technol. 47, 558–588.

Delaporte, B., Di Benedetto, H., Chaverot, P., Gauthier, G., 2007. Linear viscoelastic properties of bituminous materials: from binders to mastics. J. Assoc. Asphalt Paving Technol. 76, 455–494.

Farrar, M.J., 2013. Discussion AIP Gc* kinetics, White paper for NCHRP 9-54, National Cooperative Highway Research Program, Washington, DC.

Ferry, J.D., 1980. Viscoelastic Properties of Polymers. John Wiley and Sons, Inc., New York.

Glover, C.J., Martin, A.E., Chowdhury, A., Han, R., Prapaitrakul, N., Jin, X., Lawrence, J., 2008. Evaluation of binder aging and its influence in aging of hot mix asphalt concrete: literature review and experimental design, Report 0-6009-1. Texas Transportation Institute, College Station, Texas.

Han, R., 2011. Improvement to a transport model of asphalt binder oxidation in pavements: pavement temperature modeling, oxygen diffusivity in asphalt binders and mastics, and pavement air void characterization. Ph.D. Dissertation, Texas A&M University, College Station, TX.

Houston, W.N., Mirza, M.W., Zapata, C.E., Raghavendra, S., 2005. Environmental effects in pavement mix and structural design systems, NCHRP Web-Only Document 113. National Cooperative Highway Research Program, Washington, DC.

Huang, S.C., Grimes, W., 2010. Influence of aging temperature on rheological and chemical properties of asphalt binders. Transp. Res. Rec. 2179, 39–48. http://dx.doi.org/10.3141/2179-05.

Huang, S.C., Zeng, M., 2007. Characterization of aging effect on rheological properties of asphalt-filler systems. Int. J. Pavement Eng. 8, 213–223. http://dx.doi.org/10.1080/10298430601135477.

www.EngineeringEBooksPdf.com

Hubbard, P., Reeve, C.S., 1913. The effect of exposure on bitumens. J. Ind. Eng. Chem. 5, 15–18. http://dx.doi.org/10.1021/ie50049a009.

Jemison, H.B., Burr, B.L., Davison, R.R., Bullin, J.A., Glover, C.J., 1992. Application and use of the ATR, FT-IR method to asphalt aging studies. Pet. Sci. Technol. 10, 795–808. http://dx.doi.org/10.1080/08843759208916021.

Kim, Y.R., 2003. Mechanistic fatigue characterization and damage modeling of asphalt mixtures. Ph.D. Dissertation, Texas A&M University, College Station, TX.

Kim, Y.R., Underwood, B.S., Sakhaei Far, M., Jackson, N., Puccinelli, J., 2009. LTPP computed parameter: dynamic modulus, Final Report for Project: DTFH61-02-D-00139. Federal Highway Administration. Washington, DC.

Lee, D.Y., Huang, R.J., 1973. Weathering of asphalts as characterized by infrared multiple internal reflection spectra. Appl. Spectrosc. 27, 419–490.

Lesueur, D., 2009. The colloidal structure of bitumen: consequences on the rheology and on the mechanisms of bitumen modification. Adv. Colloid Interface Sci. 145, 42–82. http://dx.doi.org/10.1016/j.cis.2008.08.011.

Liu, M., Lunsford, K.M., Davison, R.R., Glover, C.J., Bullin, J.A., 1996. The kinetics of carbonyl formation in asphalt. AIChE J. 42, 1069–1076. http://dx.doi.org/10.1002/aic.690420417.

Lunsford, K.M., 1994. The effect of temperature and pressure on laboratory oxidized asphalt films with comparison to field aging. Ph.D. Dissertation, Texas A&M University, College Station, Texas.

Mirza, M.W., Witczak, M.W., 1995. Development of global aging system for short and long term aging of asphalt cements. J. Assoc. Asphalt Paving Technol. 64, 393–430.

Mooney, M., 1951. The viscosity of a concentrated suspension of spherical particles. J. Colloid Sci. 6, 162–170. http://dx.doi.org/10.1016/0095-8522(51)90036-0.

Petersen, J.C., 2009. A review of the fundamentals of asphalt oxidation: chemical, physicochemical, physical property, and durability relationships, Trans Res Circular, E-C140, Transportation Research Board, Washington, DC.

Petersen, J.C., Harnsberger, P.M., 1998. Asphalt aging: dual oxidation mechanism and its interrelationships with asphalt composition and oxidative age hardening. Transp. Res. Rec. 1638, 47–55. http://dx.doi.org/10.3141/1638-06.

Petersen, J.C., Plancher, H., Harnsberger, P.M., 1987. Lime treatment of asphalt to reduce age hardening and improve flow properties. J Assoc. Asphalt Paving Technol. 56, 632–653.

Petersen, J.C., Robertson, R.E., Branthaver, J.F., Harnsberger, P.M., Duvall, J.J., Kim, S.S., Anderson, D.A., Christensen, D.W., Bahia, H.U., 1994. Binder characterization and evaluation volume 1, SHRP-A-367. Strategic Highway Research Program, Washington, DC.

Prapaitrakul, N., 2009. Toward an improved model of asphalt binder oxidation in pavements. Ph.D. Dissertation, Texas A&M University, College Station, TX.

Roque, R., Zou, J., Kim, Y.R., Baek, C., Thirunavukkarasu, S., Underwood, B.S., Guddati, M. N., 2010. Top-down cracking of hot mix asphalt layers: models for initiation and propagation, NCHRP Report 667. National Cooperative Highway Research Program, Washington, DC.

Shalaby, A., 2002. Modelling short-term aging of asphalt binders using the rolling thin film oven test. Can. J. Civ. Eng. 29, 135–144. http://dx.doi.org/10.1139/l01-086.

Tan, Y., Guo, M., 2014. Interfacial thickness and interaction between asphalt and mineral fillers. Mater. Struct. 47, 605–614. http://dx.doi.org/10.1617/s11527-013-0083-8.

Thurston, R.R., Knowles, E.C., 1936. Oxygen absorption tests on asphalt constituents. J. Ind. Eng. Chem. 28, 88–91. http://dx.doi.org/10.1021/ie50313a023.

www.EngineeringEBooksPdf.com

Tunnicliff, D.G., 1962. A review of mineral filler. J. Assoc. Asphalt Paving Technol. 31, 118–150.

Tunnicliff, D.G., 1967. Binding effects of mineral filler. J. Assoc. Asphalt Paving Technol. 36, 114–156.

Underwood, B.S., Kim, Y.R., 2012. Microstructural association model for upscaling prediction of asphalt concrete dynamic modulus. J. Mater. Civ. Eng. 25, 1153–1161. http://dx.doi.org/10.1061/(ASCE)MT.1943-5533.0000657.

Underwood, B.S., Kim, Y.R., 2013. Microstructural investigation of asphalt concrete for performing multiscale experimental studies. Int. J. Pavement Eng. 14, 498–516. http://dx.doi.org/10.1080/10298436.2012.746689.

Underwood, B.S., Kim, Y.R., 2014. A four phase micro-mechanical model for asphalt mastic modulus. Mech. Mater. 75, 13–33. http://dx.doi.org/10.1016/j.mechmat.2014.04.001.

Underwood, B.S., Sakhaei Far, M.S., Kim, Y.R., 2010. Using limited purchase specification tests to perform full linear viscoelastic characterization of asphalt binder. J. Test. Eval. 38, 558–567. http://dx.doi.org/10.1520/JTE102591.

Van Oort, W.P., 1956. Durability of asphalt—it's aging in the dark. J. Ind. Eng. Chem. 48, 1196–1201. http://dx.doi.org/10.1021/ie50559a033.

Von Quintus, H.L, Scherocman, J.A., Hughes, C.S., Kennedy, T.W., 1991. Asphalt-aggregate mixture analysis system, NCHRP Report 338. National Cooperative Highway Research Program, Washington, DC.

Wright, J.R., 1965. Weathering: theoretical and practical aspects of asphalt durability. In: Hoiberg, A.J. (Ed.), In: Bituminous Materials: Asphalts, Tars and Pitches, vol. 2. Interscience Publishers, New York (Chapter 8).

www.EngineeringEBooksPdf.com

Moisture damage in asphaltic mixtures

10

A. Varveri[1], J. Zhu[2], N. Kringos[2]
[1]Delft University of Technology, Delft, The Netherlands; [2]KTH Royal Institute of Technology, Stockholm, Sweden

10.1 Introduction

The development of sustainable road infrastructure requires, among other things, the construction of asphalt pavements with enhanced durability characteristics. From the moment of construction and continuing during their service life, asphalt pavements are continuously exposed to a combination of traffic loading and environmental influences. Environmental conditions such as fluctuating temperature, humidity, precipitation, oxygen, freeze-thaw cycles, and ultraviolet (UV) radiation influence the material properties constantly. To counteract these influences, an increase in the operational and maintenance costs is needed in order to fulfill the desired service life of the pavement system. Global warming and climate change events such as temperature extremes, high mean precipitation, and rainfall intensity may further increase the probability and rate of pavement deterioration. There is thus a strong need to obtain an improved understanding of the influence of environmental factors on the long-term performance of asphalt pavements. Of all the potential damages, moisture damage has been identified as a major contributor to premature failure of asphalt pavements and can result in various distresses such as stripping, raveling, rutting, and cracking. Figure 10.1 illustrates the effect that water can have on pavement-wearing courses.

An improved understanding of moisture-induced damage phenomena in asphalt pavements can have a significant impact on road maintenance expenditure, particularly in countries that suffer from large amounts of rainfall. Even though the mechanisms related to moisture damage were identified in the early 1970s, they are today still not understood to the extent that we have been able to mitigate the problem. Current moisture-damage sustainability evaluation methods for asphalt mixtures are still primarily based on the empirical test methods, and the pavement engineer today does not have many new tools to assist him or her in preventing moisture damage at large or to make accurate moisture damage predictions. In the recent past, however, focused computational methods were developed to characterize and predict the moisture sensitivity of asphalt mixtures, based on the fundamental and theoretical mechanisms. From a practical point of view, some additives (e.g., hydrated lime and amines) have been used in asphalt pavements to minimize moisture-damage-related distresses. But more new and efficient additives and field techniques are still required.

Advances in Asphalt Materials. http://dx.doi.org/10.1016/B978-0-08-100269-8.00010-6
© 2015 Elsevier Ltd. All rights reserved.

www.EngineeringEBooksPdf.com



Figure 10.1 Deteriorated pavements due to water-induced damage. (a) Raveling caused by segregation. (b and c) pothole formation.
Reprinted from Pavement Interactive (http://www.pavementinteractive.org/).

This chapter focuses on moisture damage in asphalt mixtures (hot mix asphalt mixtures, unless otherwise specified), aiming to give a comprehensive overview of the mechanisms, modeling, characterization, and prevention of moisture damage. The potential trends of research on moisture damage in asphalt mixtures in the future are discussed. Though we have tried to be comprehensive in our references, our main aim was to categorize the current developments and possibilities to further stimulate research and transfer to practice. Furthermore, we would like to note the importance of frost heave and freeze-thaw damage as a part of the family of moisture-induced damage mechanisms, which we have not included explicitly in this chapter, as there already exist comprehensive books on these subjects.

10.2 Moisture[1] damage in asphalt mixtures

Moisture damage is a rather complicated mode of distress in asphalt pavements, due to the combination of physical, chemical, thermodynamic, and mechanical processes (Caro et al., 2008a; Kringos et al., 2008a) that occur during the interaction of water with the asphalt constituents. A great number of factors, such as the physicochemical properties of bitumen and aggregates and their interaction, the mixture characteristics (percentage, size, and interconnectivity of air voids and hence permeability), type of traffic loading, and quality control during construction, can influence the susceptibility of a mixture to moisture damage. The variability of the abovementioned factors introduces a higher level of complexity to the problem and causes additional difficulties in predicting and preventing moisture-induced damage in asphalt pavements. What further complicates the "clear" identification of moisture damage is that it is

[1] The terms *moisture* and *water* are used interchangeably throughout this chapter. However, *water* refers to the liquid state of water, while *moisture* to the vapor state; when necessary, a clear distinction between them is made.

www.EngineeringEBooksPdf.com

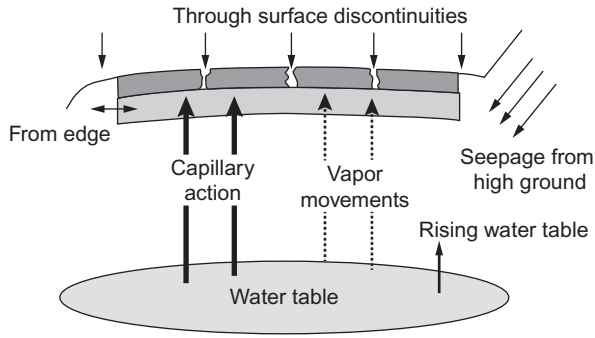


Figure 10.2 Sources of moisture in pavement structures.
After Christopher et al. (2006).

highly coupled to "other" damage mechanisms, and moisture can induce the start of new or the aggravation of existing damage mechanisms. To thus clearly define the resulting visible damage as "moisture damage" becomes challenging, and it becomes important to explain the mechanisms themselves.

As illustrated in Figure 10.2, water can accumulate in asphalt pavements due to a number of reasons (Kandhal, 1992). The most common source is atmospheric precipitation, which supplies water in the form of rainfall, hail, mist, or dew. Water enters the body of the pavement through its surface discontinuities. Specifically, the air voids and cracks in the surface of a pavement, the shoulder edges, and the joints formed between adjacent asphalt mats during construction provide easy access paths for surface water. Alternatively, water can enter into pavement structures due to capillary action, water vapor movement, or upward flow from a high groundwater table or an artesian aquifer. In the case of open-graded pavements (also named drainage asphalt or silent asphalt), the top mixtures are designed to have high levels of interconnected air voids to enable the fast drainage of the surface water. In this section, the mechanisms related to moisture-induced damage and the theories describing the cohesion of asphalt binder and its interactions with mineral aggregates under the influence of moisture are discussed.

10.2.1 Mechanisms associated to moisture damage

Moisture damage in asphalt pavement is most visible through the loss of aggregates (named stripping or raveling) and the appearance of potholes on its surface. Though the failure of adhesion between different pavement layers (partly) due to moisture infiltration can be the cause of the latter damage, potholes can also be caused by a similar mechanism as raveling—namely, the loss of the bond between the mineral aggregate and the asphalt binder (i.e., bitumen plus mineral filler) and/or the loss of strength and stiffness of the mastic itself (Kiggundu and Roberts, 1988). These are often referred to as adhesive and cohesive failure modes, respectively. In the literature, five mechanisms are proposed in an attempt to explain moisture damage: detachment, displacement, spontaneous emulsification, pore pressure development, and hydraulic scouring. Depending on the traffic loading and environmental

www.EngineeringEBooksPdf.com

conditions, the binder and aggregate characteristics, and mixture type, one damage mechanism or a combination thereof can lead to adhesive or cohesive failure.

Majidzadeh and Brovold (1968) define detachment as the separation of the bituminous film of the aggregate surface due to the presence of water, assuming a continuous film without the presence of cracks. In this case, the existence of moisture in the interface can be only attributed to the molecular process of diffusion (Cheng et al., 2003). According to Kringos et al. (2008a), when a bituminous film is exposed to a moist environment, moisture gradually starts infiltrating through the film toward the adhesive interface zone. Depending on the moisture diffusion characteristics and on the thickness of the bituminous film, the amount of moisture in the interface varies with time. Once moisture reaches the interface, it will progressively cause stripping of the asphalt binder from the aggregate. Figure 10.3 shows a schematic of the diffusion process.

An additional mechanism that also results in separation of the binder film from the aggregate is displacement (Tarrer and Wagh, 1991). In this case, stripping of the binder from the aggregate surface involves a disruption in the bituminous film. Two possible explanations are given for the detachment and displacement mechanisms, based either on thermodynamic or chemical considerations. These theories are discussed in detail later in this chapter (see Section 10.2.2).

Stuart (1990) and Labib (1992) refer to spontaneous emulsification as an additional moisture-induced damage mechanism. Generally, spontaneous emulsification occurs when two immiscible liquids emulsify without the aid of any external thermal or mechanical energy source (López-Montilla et al., 2002). Depending on the nature of the liquids involved, it may take from a few minutes to several days for the process to complete. Davies and Rideal (1963) discussed three mechanisms by which spontaneous emulsification can be produced: interfacial turbulence, negative interfacial tension, and "diffusion and stranding." According to the diffusion theory, during the diffusion process, regions of local supersaturation are produced, and emulsion droplets are formed due to phase transformation at those regions. For asphalt mixtures, it has been observed that long conditioning periods can cause emulsification at the surfaces of the samples, which are in direct contact with water. In this case, water diffuses into the asphalt specimen, weakens the binder, and forms water-bitumen emulsions for asphalt binders that are unstable in water.

Hydraulic scouring is reported as an additional water damage mechanism. The action of a vehicle tire over a saturated pavement can cause abrasion of the asphalt binder from

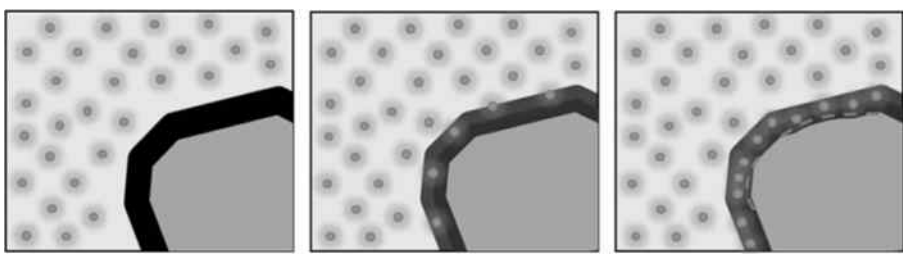


Figure 10.3 Damage of the asphalt binder and the binder–aggregate interface due to moisture diffusion.
After Varveri et al. (2014).

www.EngineeringEBooksPdf.com

the aggregates, resulting in fine aggregates to become loose and ultimately dislodge from the pavement. This mechanical scraping can be aggravated by the presence of abrasives, such as dust, on the surface of the pavement (Asphalt Institute, 1987).

Unlike hydraulic scouring, which is a phenomenon that occurs at the pavement surface, the repeated action of traffic loading over a saturated pavement can result in excessive pressure buildup in the macropores or internal erosion of the binder due to the presence of water flow, depending on the drainage conditions. The latter process is also mentioned as desorption and modeled via an advective transport model (Kringos et al., 2008a). Generally, it is assumed that the permeability of a pavement is proportional to its air void content. Choubane et al. (1997), Cooley et al. (2001), and Chen et al. (2004) performed falling-head permeability tests on dense- and open-graded asphalt mixtures. In every case, an exponential relationship was found to exist between permeability and air-void content, as shown in Figures 10.4–10.6.

In reality, permeability is affected also by other factors, such as aggregate gradation and shape, lift thickness, density homogeneity, and compaction method (Mallick et al., 2003; Caro et al., 2008a). However, it has been shown that the air void content has a strong effect on permeability, and therefore on the susceptibility of asphalt mixtures against water damage. Additionally, the design of a mixture and consequently its permeability characteristics dictate the occurrence of either pressure development or binder erosion. In the undrained case, at which water is entrapped in the air-void network of the pavement, water will dilate and contract due to the incompressibility of the liquid under the effect of dynamic traffic loading and will encourage high pressure in the saturated pores, which may cause additional stresses in the material. The process of the pore pressure buildup will ultimately lead to the cracking of the binder film or the growth of the microcracks in the asphalt mixture, thus facilitating the ingression of water to the interface of the asphalt binder with the aggregate, as shown in Figure 10.7. In the literature, this phenomenon is referred to as pumping action (Taylor and Khosla, 1983; Kiggundu and Roberts, 1988; Kandhal, 1992).

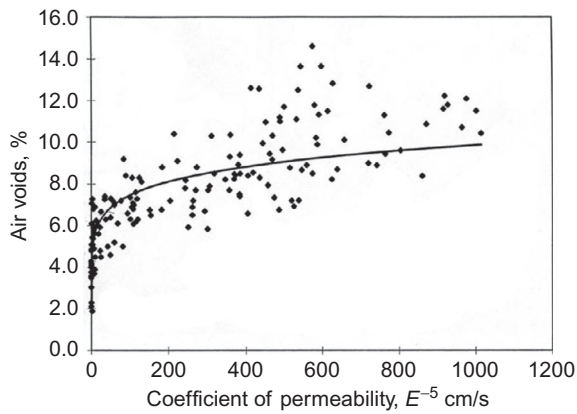


Figure 10.4 Relationship between air voids (%) and permeability (cm/s) for coarse-graded Superpave mixes.
After Choubane et al. (1997).

www.EngineeringEBooksPdf.com

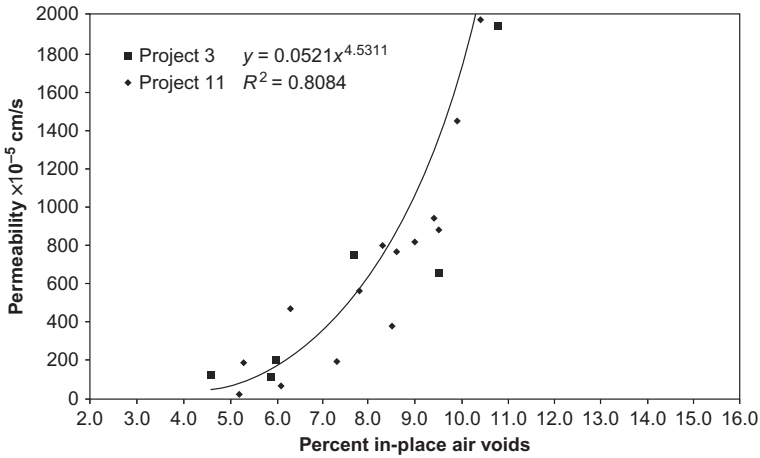


Figure 10.5 Relationship between permeability (cm/s) and in-place air voids (%) for 19.0 mm nominal maximum aggregate size (NMAS) mixes.
After Cooley et al. (2001).

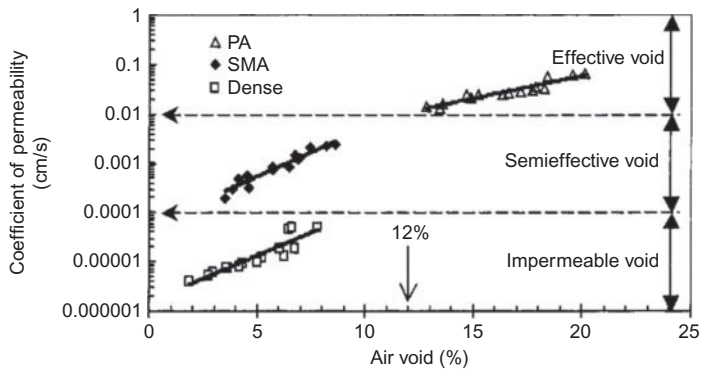


Figure 10.6 Relationship between permeability (cm/s) and air void content (%) for porous, stone mastic, and dense asphalt mixtures. Three types of voids (effective, semieffective, and impermeable) are identified.
After Chen et al. (2004).

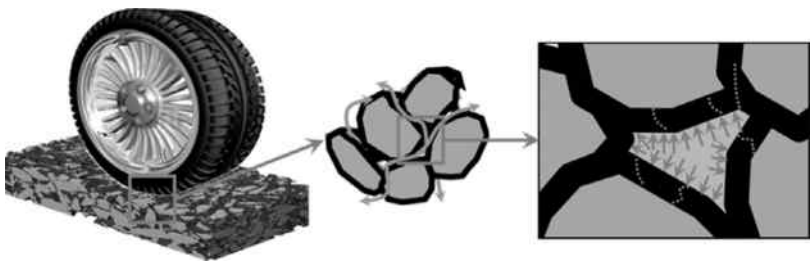


Figure 10.7 Cracking of the asphalt binder due to pumping action.
After Varveri et al. (2014).

www.EngineeringEBooksPdf.com

On the other hand, high permeable pavements have a high percentage of air voids that are interconnected and allow water to flow through the pore network. The design of pavements with high permeability ensures the reduction of surface runoff and improves driving safety. However, the action of fast water flow through the interconnected pores may create an erosion effect due to the high water pressure gradients against the binder film (Kringos et al., 2008a).

Though pumping action could often be related to mixtures with nonconnected air voids, one can also consider that open-graded mixtures that originally start with good connected air voids will eventually clog with dirt from the pavement surface, thus increasing the risk of trapped water. Open-graded mixtures can therefore first be exposed to a dominant erosion issue, followed by a pumping action challenge over time, when some of the permeability reduces. But it could be hypothesized that erosion of mastic is also a function of the age of the mastic film, depending on the start properties and the moisture diffusion propensity.

10.2.2 Adhesion and cohesion failure theories

In the previous section, the basic water damage mechanisms in asphalt mixtures were discussed in relation to their mode of infiltration. In general, moisture damage reveals itself through two modes of failure: adhesion and cohesion. Adhesion is defined as the attraction process between unlike molecules that are brought into contact in such a way that the adhesive binds to the applied surface or substrate. In contrast, cohesion is the attraction between similar molecules, mainly as the result of chemical bonds that are formed between the individual components of the substance. Thus, in bituminous mixtures, cohesion may be defined as the internal strength of the asphalt binder due to various interactions that keep the mass together, whereas adhesion is the bonding of the mineral aggregate with the asphalt binder due to various interactions at the aggregate–binder interface. The adhesion and cohesion failure modes are shown schematically in Figure 10.8. Considering that the load-carrying capacity of the mixture comes from the aggregate skeleton, and the ability of the mixture to dampen the traffic loads (thus making asphalt very comfortable to drive over) comes from the mastic matrix, the adhesive and cohesive bonds are equally important and should be maintained at a high quality for as long as possible.

In the following section, adhesion and cohesion theories are briefly discussed. According to Terrel and Shute (1989), four main theories exist to fundamentally describe adhesive bonding between aggregates and asphalt binders: chemical bonding, molecular orientation, thermodynamic theory, and mechanical theory. Also, the weak boundary layer theory (Bikerman, 1967) is used to describe poor adhesion in aggregate–bitumen systems.

The thermodynamic theory suggests that adhesion occurs due to the molecular contact between adhesive and substrate and the interfacial forces that develop between them. The degree of contact between the two materials is governed by their wetting characteristics, which in turn depend on the relative surface energies of the adhesive and substrate materials. A high degree of wetting is essential for attaining good adhesive bonding. The work of adhesion, under ideal circumstances, is the reversible

www.EngineeringEBooksPdf.com

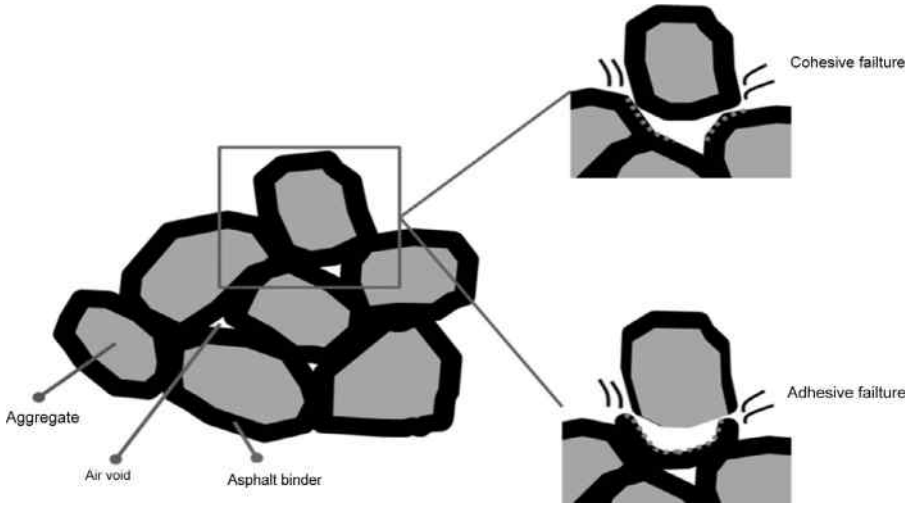


Figure 10.8 Adhesive and cohesive failures due to water damage.
After Varveri (2015).

thermodynamic work that is needed to separate two materials from each other. Physically, it shows the level of attraction between two materials: the higher the work of adhesion between the materials, the more thermodynamically stable the bond between them. Equation (10.1) shows the work of adhesion W for a solid–liquid combination. This relation was proposed by Dupré (1869):

$$W = \gamma_s + \gamma_l - \gamma_{sl} \tag{10.1}$$

where γ_s and γ_l are the surface energy of the solid and liquid phases, respectively, and γ_{sl} is the interfacial surface tension. A relative measure of surface energy is contact angle θ, which is the angle between the tangent to the solid–liquid interface and the tangent to the liquid–air interface, as shown schematically in Figure 10.9. In principle, the smaller the contact angle, the lower the surface tension of the liquid and the greater the degree of wetting allowed. Contact angles greater than 0° but less than 90° (i.e., $0° < \theta < 90°$) relate to high wettability, whereas values that exceed 90° relate to low wettability, a process sometimes referred to as dewetting. In the second case, droplets of liquid will form on the substrate surface (da Silva et al., 2011).

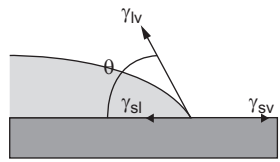


Figure 10.9 Equilibrium contact angle on an ideal surface.
After Bonn et al. (2009).

www.EngineeringEBooksPdf.com

There are different techniques for measuring the contact angles required for the calculation of the surface energy of materials. Bagampadde et al. (2004) provide a summary of the methods used to determine surface and interfacial tension; see Table 10.1. The applicability of the techniques depends highly on the physical state of the material (i.e., liquid or solid) as well as on the temperature at which the surface energy needs to be determined; consequently, every single technique has its own limitations (van Lent, 2013).

Earlier, a surface energy approach for the determination of the thermodynamic properties of various bitumen and aggregate types was developed (Cheng et al., 2002; Little and Jones, 2003; Lytton et al., 2005; Masad et al., 2006; Bhasin and Little, 2007). Based on this methodology, the nonpolar (Liftshitz–van der Waals) and the polar (acid–base) components of surface energy were determined and associated to fracture and healing processes in bituminous mixtures. Cheng et al. (2002) stated that water increases the polar component and reduces the total fracture bond

Table 10.1 Various methods for the determination of surface and interfacial tensions

Method	θ	Static values	Dynamic values	Surface tension	Interfacial tension	High T, p capability
Jaeger bubble pressure	×	√	×	√	×	√
Capillary rise	×	√	≈	√	×	×
Wilhelmy plate apparatus	√	√	≈	√	√	×
DuNouy ring tensiometer	×	√	×	√	√	×
Drop weight	×	√	×	√	√	√
Drop volume	×	√	×	√	√	√
Pendant drop	×	√	√	√	√	√
Free hanging thread	×	√	×	√	×	×
Sessile drop	√	√	√	√	√	√
Oscillating jet	×	√	√	√	×	×
Spinning drop	×	√	≈	√	√	×
Max. bubble pressure	×	√	√	√	√	√
Captive drop	×	√	≈	√	×	×
Surface laser light scattering	×	√	√	√	≈	√
Tilting plate	√	√	≈	√	√	×

× shows lack of capability of the technique to determine the respective property.
√ refers to capability of the technique to determine the respective property.
≈ means that the technique gives approximate value of the respective property.
T = temperature and p = pressure.
Source: Bagampadde et al. (2004).

www.EngineeringEBooksPdf.com

energy; consequently, it is beneficial to have a greater polar acid–base component and a lower nonpolar component.

Lytton et al. (2005) performed surface energy measurements utilizing the Universal Sorption Device (USD) and the Wilhelmy plate (WP) tests. The surface energies of various bitumen and aggregate types were determined, and the adhesive bond energy of the bitumen–aggregate interface was calculated under dry and wet conditions. The work of adhesion was found to be negative in the presence of water for the majority of bitumen–aggregate systems, as shown in Table 10.2. The results indicate that water damage is a thermodynamically favorable phenomenon; thus, the asphalt–aggregate bond stability is compromised in the presence of water.

Later, Kringos et al. (2008c) determined the work of adhesion as well as the mechanical strength of the bond for six different combinations of aggregates and unmodified as well as modified asphalt binders. The results of both approaches were used as a screening tool, by which a selection of the optimum combinations of asphalt binders and aggregates was performed. A comparison between the rankings resulted

Table 10.2 Work of adhesion at the asphalt–aggregate interface in dry and wet conditions

Mixture ID	Aggregate type	Adhesive wet (erg/cm^2)			Adhesive wet (erg/cm^2)		
		ΔG^a Dry	ΔG^{LW} Dry	ΔG^{AB} Dry	ΔG^a Wet	ΔG^{LW} Wet	ΔG^{AB} Wet
1	Granite	140.61	57.10	83.51	−193.99	−4.91	−189.08
2	Granite	104.72	72.97	31.75	−228.93	−1.09	−230.02
3	Quartzite	114.0	54.38	59.62	−139.43	−7.42	−132.01
4	Light sandstone	91.57	55.09	36.48	−61.99	−7.66	−54.34
4	Dark sandstone	103.38	55.75	47.63	−95.25	−7.88	−87.36
5	Gravel	93.36	53.77	39.59	−75.20	−7.21	−68.0
5	TXI limestone	118.87	53.95	64.92	−151.14	−7.27	−143.87
6	Light sandstone	99.61	74.51	25.10	−53.49	−0.29	−53.78
6	Dark sandstone	107.31	75.40	31.90	−90.86	−0.30	−91.16
7	Limestone	87.49	83.42	4.07	−115.58	−4.76	−120.34
7	Gravel	94.56	87.26	7.29	−160.22	−5.33	−165.55
8	Limestone	81.27	66.0	15.27	−119.82	−1.98	−117.84
8	Gravel	90.92	69.04	21.89	−161.87	−2.22	−159.65

Notes: ΔG^a denotes the Gibbs free energy of adhesion; ΔG^{LW} and ΔG^{AB} denote the Lifshitz–van der Waals and the acid–base components, respectively. ΔG^a results from the addition of the individual components.
Source: Lytton et al. (2005).

www.EngineeringEBooksPdf.com

from the work of adhesion, as calculated from the thermodynamic theory, and the measured bond energy from the direct tension tests was made. From this research, it was argued that though the thermodynamic properties could not be used to directly quantify the engineering strength, they were capable of identifying the best and the worst combinations, and they found moisture-resistance performance ranking similar for both approaches. Only the binder–aggregate combination that included highly modified mastic gave a considerable difference in the ranking between the two approaches; in this case, the measured bond strength showed a better ranking than the surface energy approach. From this, it was hypothesized that polymers create a different type of bonding with the stones, which cannot be mainly described by surface energy forces.

It could be commented here that all the standard surface free energy (SFE) models are simplifications based on one or two assumed dominating types of interaction. However, to get the true interaction, all electromagnetic interaction (static and dynamic) between the molecules at all frequencies should be integrated. The acid–base model assumes that electrostatic forces are dominating, that is, that permanent charge separations (permanent dipoles to ions) are the main contributors to the interaction. Where this is not the case (e.g., most commodity polymers), models that divide the interaction into a dispersive and a polar parts make a better fit. Bitumen is by and large a nonpolar material, and therefore, this second type of model can be found to apply best. The Strategic Highway Research Program (SHRP) experimentally concluded that about two-thirds of the adsorption energy of bitumen on aggregates was dispersive in nature, and one-third was polar. Based on these observations, one should be careful in applying the acid–base theory from adhesive technology directly to bitumen, as modern adhesives are based on the very polar polymers.

Until now, most research studies have determined the contact angles and surface tension for various bitumen–aggregate combinations macroscopically, considering bitumen as a continuous material. In a recent study, Fischer et al. (2012) investigated the interaction of the individual components of bitumen microstructure with the interface of solid particles using atomic force microscopy (AFM). For the measurements, pen grade 70–100 bitumen and four flat mineral surfaces (i.e., mica, limestone, marble, and quartz glass) representing different asphalt filler materials were used. Two different microstructural phases of bitumen, sometimes referred to as the catana phase/peri phase and the perpetua phase, were considered. The different constituents of the phases within bitumen were expected to interact differently with the solid aggregate surfaces, according to their chemical nature. The results showed that all measured contact angles were low (from 4° to 14°), showing a good wetting of the mineral surfaces by bitumen.

For all cases, the contact angles determined for the catana phase/peri phase were found to be smaller than the contact angles determined for the perpetua phase, indicating that the peri phase/catana phase, compared to the perpetua phase, has a greater affinity for the substrate (Figure 10.10). Also, it was observed that there was no difference in the wetting abilities of bitumen onto dry mineral surfaces with different surface chemistry; possibly, more important for the adhesion strength between mineral surfaces and bitumen is the surface texture of the mineral. Khan et al. (2014) further investigated pure minerals using the sessile drop method. From this work, utilizing Fowke's additive

www.EngineeringEBooksPdf.com

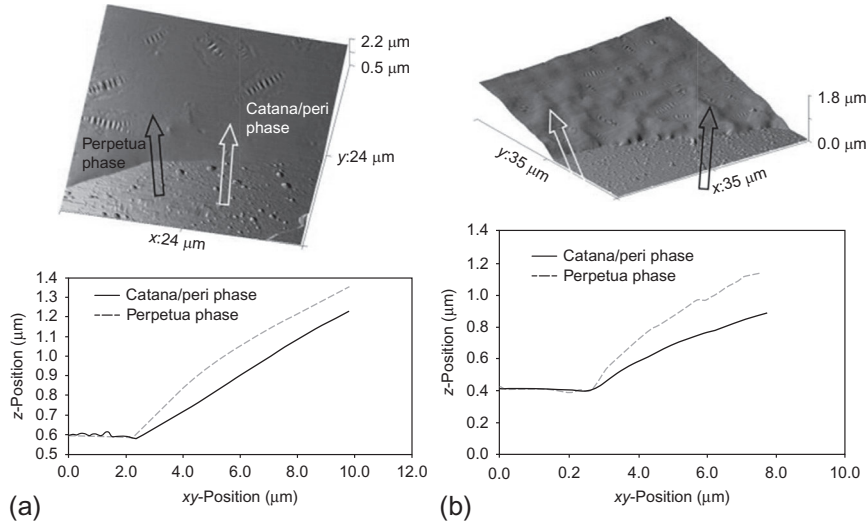


Figure 10.10 Three-dimensional plot of the topology of the contact area between bitumen and (a) a calcite and (b) a mica surface, as measured by AFM in tapping mode. Also, the surface profile for the wetting areas of the two different phases is plotted.
After Fischer et al. (2012).

nature of the forces, bitumen and water were found to roughly equally strongly be adsorbed to plagioclase and calcite, whereas water was found to displace bitumen from quartz, gypsum, potassium feldspar, and mica surfaces.

According to the molecular orientation theory, the molecules in asphalt binder orient themselves in the direction of polarization of the aggregate ions in order to minimize the repulsion energy developed between them (Hicks, 1991). The various functional groups of bitumen migrate toward the aggregate surface, resulting from the electric field caused by the dipole charges of the functional groups on the aggregate surface. The bitumen functional groups align in accordance with the electrical field around the aggregate (van Lent, 2013). Because of the high polarity of water molecules, the surface of the aggregate tends to prefer water against bitumen, thus causing a debonding in the aggregate–binder interface.

The chemical-bonding theory suggests that adhesion depends on the pH and the chemical reactions between the functional groups of both the aggregate and the asphalt binder. Some believe that these bonds produce new compounds upon formation (Kiggundu and Roberts, 1988). Tarrer and Wagh (1991) state that changes in the pH of the microscopic water accumulations at the mineral aggregate surface can alter the type of polar groups adsorbed, thus leading to the buildup of negatively charged electrical double layers on the aggregate and asphalt interface. Consequently, the drive to reach equilibrium attracts more water and leads to physical separation of the asphalt from the aggregate.

An additional theory that is used to describe adhesive failure in the aggregate–binder interface is the weak boundary layer theory. According to this theory, adhesive

www.EngineeringEBooksPdf.com

failures may occur due to the presence of an interface region of low cohesive strength (Packham, 1992). Examples of weak boundary layers in asphalt mixtures involve surfaces of aggregates containing much dust or other dissolvable compounds in specific environments. Labib (1992) states that the weak boundary layer that is responsible for failure may be intrinsic to the aggregate; alternatively, the outer layers of the aggregate may become weak due to the formation of complexes between the aggregate surface and the binder's surface groups.

The mechanical theory describes adhesion as the mechanical interlocking of asphalt binder to the aggregate surface. Hot bitumen flows and penetrates the microcavities, pores, and other irregularities on the aggregate. When the binder hardens, both substrates are held together mechanically, similar to a turned key in a lock that cannot be pulled out easily. It is generally accepted that aggregates with porous, slightly rough surfaces enhance the mechanical interlocking effect and promote a better adhesive bond (Hefer and Little, 2005). One way that roughness benefits adhesion is by increasing the contact surface between the aggregate and the binder. Considering that interfacial interaction is important for adhesion, an increase in the surface area, possibly by a very high factor, raises the surface energy when expressed per unit of nominal area (Packham, 2003). However, because the roughness of the aggregate affects its wettability characteristics, aggregates with increased surface texture may result in incomplete wetting by the bitumen (Hefer and Little, 2005).

In contrast to the aforementioned theories that describe adhesive failure between asphalt binder and aggregates, cohesion failure refers to failure within the asphalt binder itself due to the interaction with water or moisture. Cohesion is defined as the internal strength of the binder due to the intermolecular forces between similar molecules and is influenced by the binder's rheological properties. Moisture enters into the binder film through diffusion and, due to physicochemical interactions, softens the binder, and therefore, reduces its cohesive strength and stiffness (Hicks, 1991). Cohesive failure can occur due to spontaneous emulsification and expansion of the void system due to saturation (Stuart, 1990). Additionally, the weakening of the binder due to moisture alters its desorption characteristics and can actually assist the erosion effect due to fast water flow, sometimes referred to as dispersion of the binder (Kringos et al., 2008a).

Das et al. (2014) performed extensive aging studies of bitumen samples in which oxygen and ultraviolet (UV) aging were considered. They formulated a hypothesis that when bitumen is exposed to air or sunlight, the combination of oxidation and UV radiation may create a thin film of less soluble (in *n*-alkane medium) hydrocarbon molecules upon the exposed surface. Because these aging products are mainly polar compounds, they posed that the thin film might be soluble in water. To validate their hypothesis, they performed aging experiments, where bitumen samples were exposed to air and UV conditioning for 30 days, after which they were carefully washed with distilled water. Before and after the conditioning and washing, the samples were investigated under the AFM. From this, the authors concluded that UV aging can indeed create a water-soluble film. These findings mean that the mastic films would get thinner and thinner over time (on the top of the pavement), making moisture infiltration a larger problem. This, combined with an increasing brittleness of the asphaltic

www.EngineeringEBooksPdf.com

mix given the thinner films that get more susceptible to aging, could have severe consequences of fast and unexpected deterioration of the overall structure. From this work, it can be concluded that more studies are needed in which the interplay between asphalt material aging and moisture-induced damage is investigated.

10.3 Constitutive modeling of moisture damage

Constitutive modeling is an important way to help understand the possible fundamental processes that govern moisture damage and to identify the key factors that control these processes in asphalt mixtures. With the advent of today's computer power, computation times and space issues have largely been reduced. An effective model can be used to estimate in-time performance of asphalt pavements under specific environmental conditions and traffic loading. This means that, relatively fast and at low cost, a great variety of parameters can be investigated before the structure is actually built. This allows for new material and new designs to be investigated, and the risks involved with these to be minimized. Validation of such models must, of course, be rigidly applied for great confidence in the outcomes of such models.

In this following section, the constitutive models specifically developed to simulate moisture damage phenomena in asphalt mixtures are discussed, as they take into account the previously described mechanisms.

10.3.1 Modeling of water flow and pumping action in asphalt mixtures

In the previous sections, it was stated that the introduction of moisture in the pavement can assemble a water flow pattern inside the asphalt mixtures (especially in the case of open-graded mixtures). Numerical modeling of flow fields can thus help one to understand the nature of moisture flow and its relationship with the structure and permeability of the mixtures. The possible flow velocity and pressure ranges can then become important parameters for understanding the flow patterns, and assist further simulations of moisture damage at the microstructural level.

Researchers (Kutay et al., 2007a,b; Masad et al., 2007) have developed three-dimensional (3D) numerical models to simulate moisture flow into asphalt mixtures, using incompressible fluid flow models. The results showed that most asphalt mixtures have anisotropic and heterogeneous internal pore structures; subsequently, the horizontal permeability of asphalt mixtures could be several times higher than the vertical permeability, as shown in Figure 10.11. Until that time, only vertical permeability of asphalt mixtures was characterized, and realizing the possible dominance of the horizontal water movement was an important improvement in the understanding of water infiltration into asphalt pavements.

However, the aforementioned models did not consider the effects of traffic loading. As discussed in the previous sections, moving wheel pressure can create fast water flow fields in asphalt mixtures by pumping action. Kettil et al. (2005) implemented

www.EngineeringEBooksPdf.com

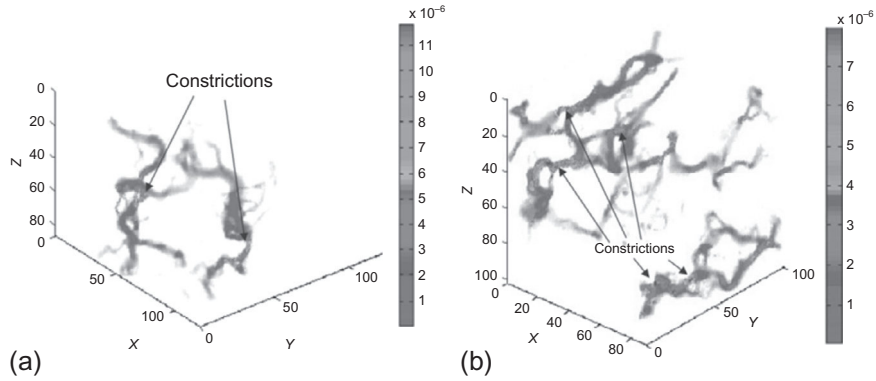


Figure 10.11 Velocity distribution in pore structure of an SMA specimen after steady-state flow is achieved in (a) *z*-direction and (b) *y*-direction; bar represents magnitude of velocity in mm/s. After Kutay et al. (2007a).

a porous media formulation using the finite element method (FEM) to simulate water flow induced by the moving wheel on a saturated asphalt pavement. For the simulations, a two-dimensional (2D) mesh of a three-layer pavement system was employed. For the top layer, two variants of asphalt mixtures were used, which differed in terms of their stiffness, porosity, and permeability: a "hard" mixture with low porosity, high stiffness, and low permeability and a "soft" mixture with high porosity, low stiffness, and high permeability.

From the simulation results, it was found that high water pressures, up to 2 MPa, were developed for the "hard" mixture, while the relative water velocity was low. The phenomenon of pumping action was observed for the "hard" asphalt; specifically, the water was squeezed out from the asphalt mixture under loading and sucked back, when the load was removed. In contrast, for the "soft" asphalt, water pressure was found to be low, and the relative water velocity was higher than for the "hard" asphalt. In this case, water flow was directed upward in front of the wheel loading and downward behind the wheel loading. Figure 10.12 illustrates the displacement, water velocity, and pressure across and along the traffic direction for both mixtures.

Based on the moisture damage mechanisms discussed previously, two different phenomena can be observed. For high permeable pavements such as the "soft" mixture case, the effect of traffic results in the development of fast water flows that can result in binder erosion. On the other hand, for pavements with low permeability, as is the case for "hard" asphalt, water cannot flow through the pavement; as a result, high pressures are developed in the saturated pores of the structure.

Kringos (2007) simulated the generation of water pressure in the macropores of asphalt mixtures under traffic loading using a micromechanical mesh of two aggregates coated with a binder film and a saturated pore between them. It was found that under the imposed loading cycles, water pressure reached a local maximum value of 0.20 MPa, as shown in Figure 10.13. The extra stresses developed within the material were found to possibly cause further mechanical damage.

www.EngineeringEBooksPdf.com

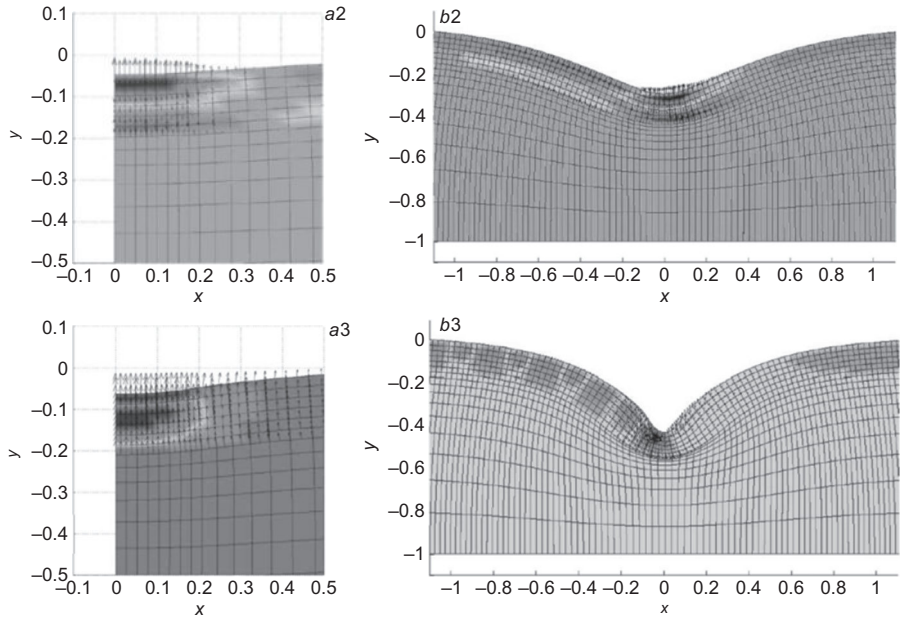


Figure 10.12 Two-dimensional finite element models of saturated asphalt pavement. Displacement (deformed mesh), water velocity (arrows), and pressure (color) plots for "hard" asphalt (a2) and "soft" asphalt (a3) across the traffic direction and "hard" asphalt (b2) and "soft" asphalt (b3) along the traffic direction.
After Kettil et al. (2005).

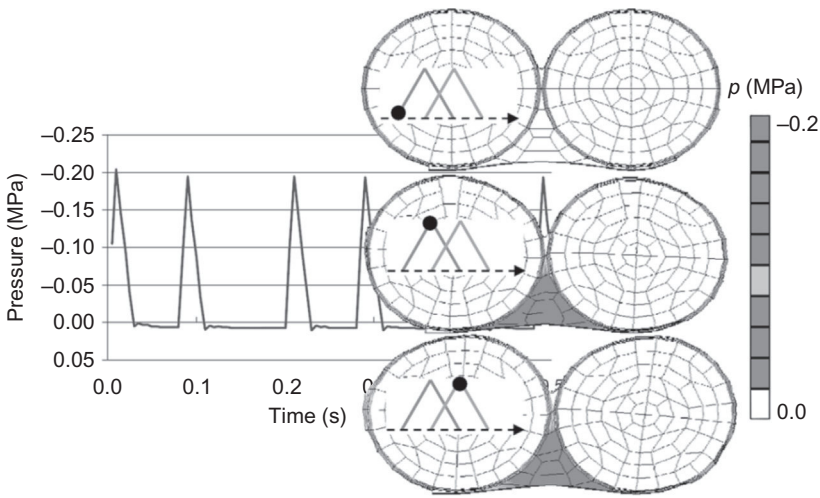


Figure 10.13 Water pressure developed in the macropore.
After Kringos (2007).

www.EngineeringEBooksPdf.com

Considering that asphalt mixtures are exposed to water flows, Kringos (2007) modeled the desorbed mastic particles that were eroded and being transported via the water out of the mixture; therefore, they no longer contribute to the physical or mechanical characteristics of the asphalt mixture. The loss of mastic concentration is a function of the desorption coefficient K_d and was expressed by the normalized density of the mastic

$$\hat{\rho} = \frac{\rho(x,t)}{\rho_o}, \tag{10.2}$$

where ρ_o is the undamaged mastic density. This means that for $\hat{\rho} = 1.0$, no mastic has been lost, and in the extreme case of $\hat{\rho} = 0.0$, all mastic is lost. The relationship between the actual weakening of the material as a function of mastic density does not have to be linear. The damage in the mastic film, due to loss of mass, is therefore expressed as

$$d_{\hat{\rho}} = 1 - \hat{\rho}^{\alpha_{\hat{\rho}}}, \tag{10.3}$$

where $\alpha_{\hat{\rho}}$ is the moisture susceptibility parameter of asphalt mastic in the presence of water pressure gradients. Based on this formulation, the loss of asphalt mastic was simulated, as illustrated in Figure 10.14, under the defined loading cycles.

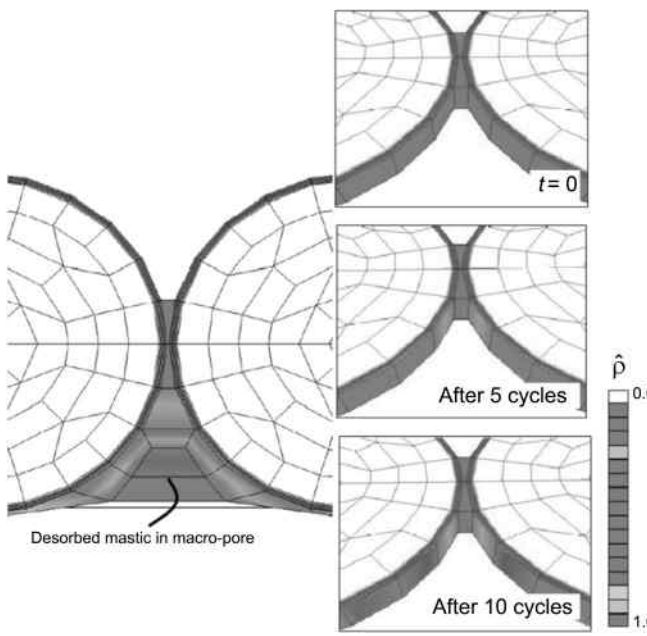


Figure 10.14 Loss of asphalt mastic after 10 loading cycles.
After Kringos (2007).

www.EngineeringEBooksPdf.com

10.3.2 Micromechanical modeling of combined physical–mechanical moisture-induced damage

Moisture-induced damage in asphalt pavements results from a combination of different deterioration processes, which can be divided into physical and mechanical, as shown in Figure 10.15. However, as discussed earlier, it is the synergistic effects of concurrently or successively acting environmental and mechanical loads that eventually result in stripping of aggregates from the pavements' surface, or in more severe damage forms such as raveling.

As soon as moisture is introduced into the structure of asphalt mixtures in the form of liquid or vapor water, the infiltration of moisture into the materials becomes a critical process that needs to be understood. For dry aggregates well coated with a continuous mastic film without any cracks, moisture can only reach the binder–aggregate interface by moving through the binder film (Cheng et al., 2003). This is of course assuming that water was not already present in the system upon construction. The movement of moisture through the binder can be hypothesized to be a process that occurs at the molecular level and can be approached following Fick's second law of diffusion (Fick, 1855):

$$\frac{\partial C}{\partial t} = \underset{\approx}{D}\nabla^2 C \tag{10.4}$$

where C is the current concentration in the material. The diffusivity of the material is determined by the diffusion tensor $\underset{\approx}{D}$, which is expressed as

$$\underset{\approx}{D} = \sum_{i,j} D_{ij}\underline{e}_i \otimes \underline{e}_j = \alpha_m \tau \delta_{ij} \tag{10.5}$$

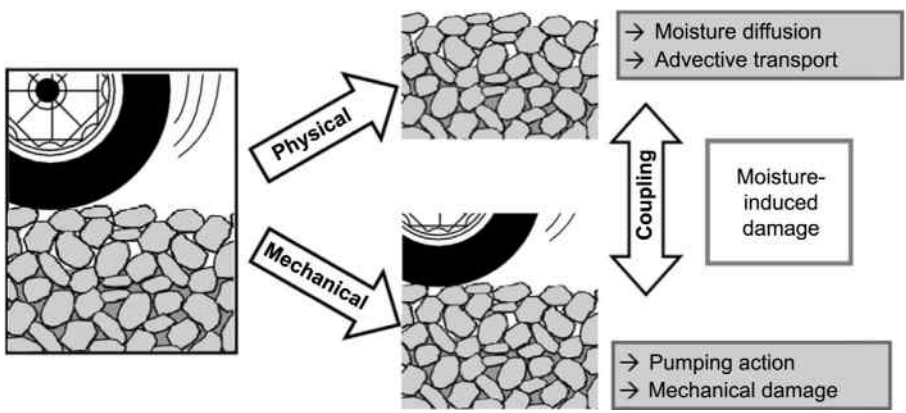


Figure 10.15 Approach toward combined physical–mechanical moisture-induced damage (Kringos, 2007).

www.EngineeringEBooksPdf.com

where α_m is the molecular diffusion coefficient, τ is the tortuosity of the material, and δ_{ij} is the Kronecker delta. As moisture accumulates in the binder, its properties change, thus causing a decrease in cohesive strength and consequently an overall reduction in stiffness and strength of the asphalt pavement. Consequently, under the application of mechanical loading, the degradation of the pavement due to moisture is revealed.

Over the years, constitutive models have been developed to simulate the response of the bituminous materials under the combined effect of long-term moisture diffusion and mechanical loading. Although different geometries, material properties, and constitutive models were used in these studies, all studies focused on the principle of coupling the physical and mechanical processes into a single moisture-induced damage model for asphalt mixtures.

Kringos (2007) developed a computational tool, named RoAM (raveling of asphalt mixes), which was coupled with the finite element system CAPA-3D, to model the combined physical–mechanical moisture damage in asphalt mixtures. An elasto viscoplastic model was adjusted to incorporate the degradation effects of moisture, and the resulting damage was expressed in the form of equivalent plastic deformation parameter ξ. Moisture diffusion through asphalt mastics can cause both adhesive and cohesive failures; therefore, moisture damage functions were expressed, for all components of asphalt mixtures (i.e., asphalt mastics, aggregates, and mastic–aggregate interfaces), as

$$d_\theta = f(\theta) \tag{10.6}$$

where θ is the moisture content, defined as the ratio of moisture concentration with respect to the maximum moisture concentration that the material can absorb. Expressions for the moisture damage functions were determined for both adhesive and cohesive failures. Copeland et al. (2006, 2007) and Kringos et al. (2008b,c) studied the relationship between moisture content and damage at the mastic–aggregate interface. Based on these studies, it was postulated that the development of moisture damage at the interface increases as a function of moisture concentration and can be defined as

$$d_\theta^{\text{if}} = 1 - e^{-\alpha_\theta^{\text{if}}\sqrt{\theta}} \tag{10.7}$$

where $\alpha_\theta^{\text{if}}$ is the moisture susceptibility parameter of mastic–aggregate interfaces. The susceptibility parameter for the particular mastic–aggregate combinations tested was found to be $\alpha_\theta^{\text{if}} = 3.76$. For simplicity and due to the lack of experimental evidence, the evolution of damage for asphalt mastics due to the presence of moisture was at that time defined as

$$d_\theta^{\text{mst}} = 1 - e^{-\alpha_\theta^{\text{mst}}\sqrt{\theta}} \tag{10.8}$$

Based on the above, moisture diffusion and the resulting damage were simulated using a 2D finite element mesh consisting of two stones, which was coated with a mastic film. The aggregate–mastic interface was also modeled to simulate the response of the adhesive bond. Figure 10.16 illustrates the infiltration of moisture into the asphalt mastic and toward the mastic–aggregate interface, as modeled by Kringos (2007).

www.EngineeringEBooksPdf.com

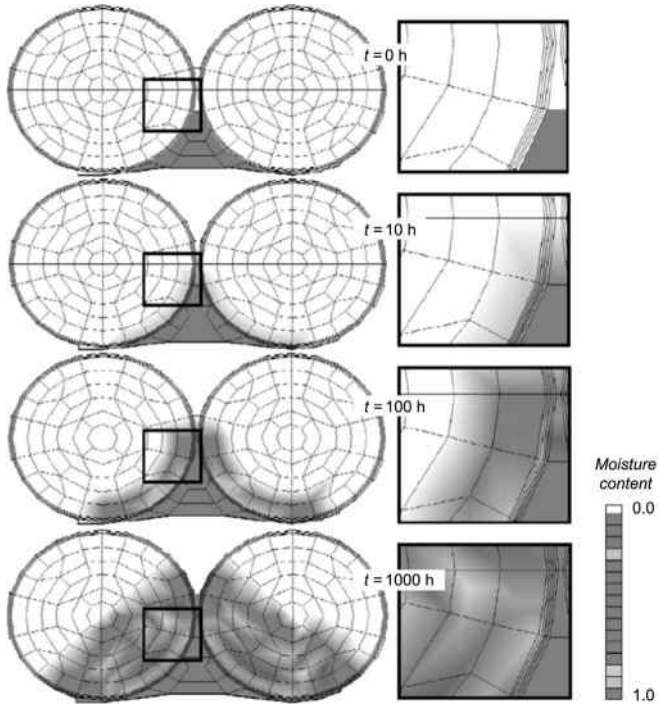


Figure 10.16 Moisture diffusion simulation with $D_{agg} = 0.01$ mm^2/h and $D_{mst} = 0.015$ mm^2/h. After Kringos (2007).

In the simulations, moisture damage development within the aggregates was disregarded; consequently, damage due to moisture diffusion was described by determining the moisture diffusion coefficients of asphalt mastics D_{mst} and the moisture susceptibility parameters α_θ^{mst} and α_θ^{if}. As shown in the previous section, Kringos (2007) considered also the effect of pumping action and binder erosion.

Caro et al. (2009) coupled the effects of moisture diffusion and mechanical loading to quantify the level of damage within asphalt mixtures. Similarly, based on Fick's laws of diffusion, Caro et al. (2009) computed the moisture concentration profiles in a finite element mesh, composed of two real-shaped coarse aggregates embedded in continuous mastics, as shown in Figure 10.17. The results indicated that the diffusivity characteristics of the asphalt matrix and aggregates, as well as the bond strength of the aggregate–matrix interface, have great influence on the moisture susceptibility of the mixtures.

The adhesive failures at the mastic–aggregate interfaces and the cohesive failure of the mastic were simulated using the cohesive zone-modeling technique. Damage was evaluated based on the location and time for crack initiation and propagation at the mastic-aggregate interfaces and on the level of strains and stresses within the bulk of asphalt mastics. Figure 10.18 illustrates the responses of two types of mastics

www.EngineeringEBooksPdf.com

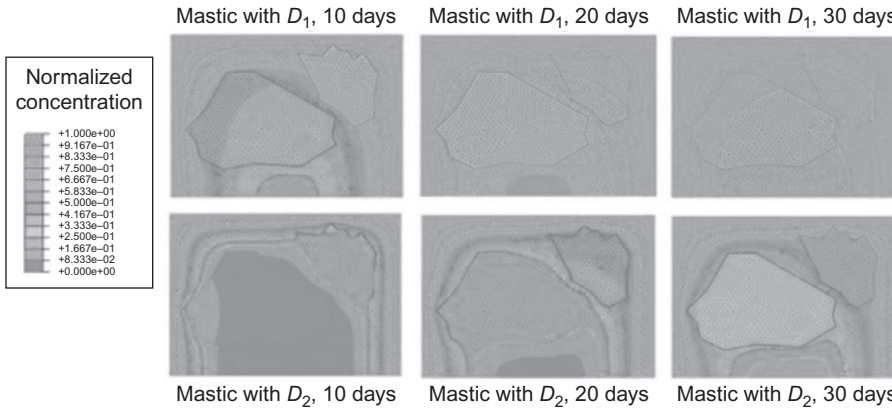


Figure 10.17 Normalized moisture concentration profiles for two mastics with different diffusivity characteristics.
After Caro et al. (2009).

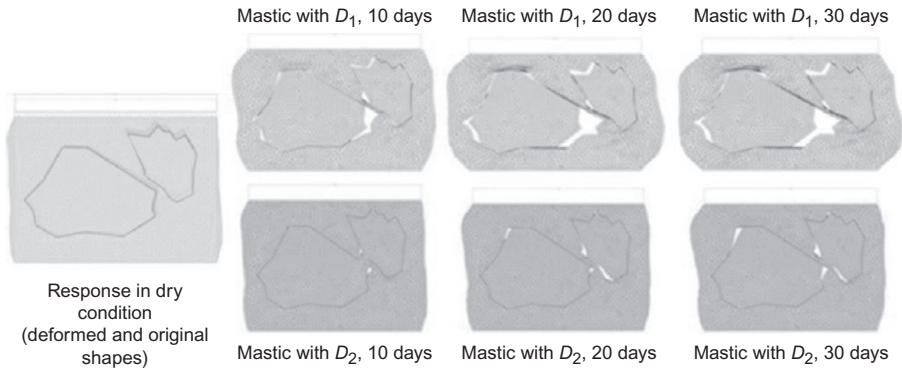


Figure 10.18 Response of the aggregate–mastic system after application of the mechanical loading of 0.2 N/s for a total time of 30 s for specimens subjected to different moisture-conditioning periods.
After Caro et al. (2009).

after mechanical loading for the dry case and for the moisture-conditioned cases. In this model, the mechanisms of advective transport and pumping action were not considered.

Graham (2009) modified the nonlinear viscoelastic–viscoplastic model developed by Huang (2008) to couple the effects of moisture and mechanical loading on asphalt mixtures. In this study, the moisture history was taken into consideration by introducing the moisture content as a function of time. However, Mehrara and Khodaii (2013) stated that moisture-induced damage in asphalt mixtures may be partly healed during the absence of moisture and suggested that a parameter related to the healing of the material needs to be included.

www.EngineeringEBooksPdf.com

Finally, Varveri et al. (2015) developed a viscoelastic damage model that introduces material damage as an internal state variable, which represents the irreversible physical processes within the microstructure of the material. In this implementation, damage was assumed to be a combination of moisture-induced damage and damage due to mechanical loading. The evolution law for the mechanical damage was considered to be a function of the total dissipated viscous work W in the viscoelastic component and was described as

$$d_m = 1 - e^{-k \cdot W^r} \tag{10.9}$$

where k and r are damage-related parameters. Similar to the previous work, moisture damage in the binder was defined as a function of moisture content at various times and was described as

$$d_\theta = 1 - e^{-a\sqrt{\theta}} \tag{10.10}$$

According to Varveri et al. (2015), the response of asphalt mixtures is governed by the contribution and the interaction of the various constituents as well as by their geometrical characteristics. Specifically in the case of moisture diffusion, where air voids facilitate the ingress of moisture to the mastic and eventually to the aggregate–mastic interface, the inclusion of the air-void phase in the numerical simulations of moisture damage is critical. For that reason, in this study, three-dimensional (3D) micromechanical finite element meshes produced from X-ray computed tomography (CT) scans were employed. Two different types of mixtures, a gap-graded (stone mastic asphalt (SMA)) and open-graded (porous asphalt (PA)) mixtures, were scanned using X-ray computed tomography, and their internal morphology was reconstructed by means of advanced imaging techniques. From statistical analysis performed in both meshes, the percentage of air voids was 4.4% and 23.7% for the SMA and the PA mixture, respectively. In addition, it was found that pore connectivity reached almost 90% for the PA mixture, while for the dense mixture only 10% of the pores were interconnected.

The analysis was performed in a staggered scheme: first, moisture diffusion simulations were performed to determine the moisture concentration profiles of both mixtures, and then the mechanical load was applied. The normalized moisture concentration profiles, along the diameter of the PA and the SMA specimens at different time intervals, are shown in Figures 10.19 and 10.20, respectively. For the presentation of the results, a number of nodes were selected as output locations for the moisture concentration values. All the selected nodes are lying on the diameter of the specimens and are located 1 mm above the bottom surface of the samples. The results demonstrated the effect of air-void content and connectivity on the amount of moisture that is present in an asphalt specimen at any given time. After 5 days of diffusion, and for the same diffusivity properties, it was shown that the porous mixture had greater values of moisture concentration compared to the dense mixture, because of its higher total air-void content and the greater diffusion rates associated with the air-void phase.

After each moisture-conditioning phase, the micromechanical finite element (FE) meshes, with material characteristics updated for moisture damage, were subjected to

www.EngineeringEBooksPdf.com

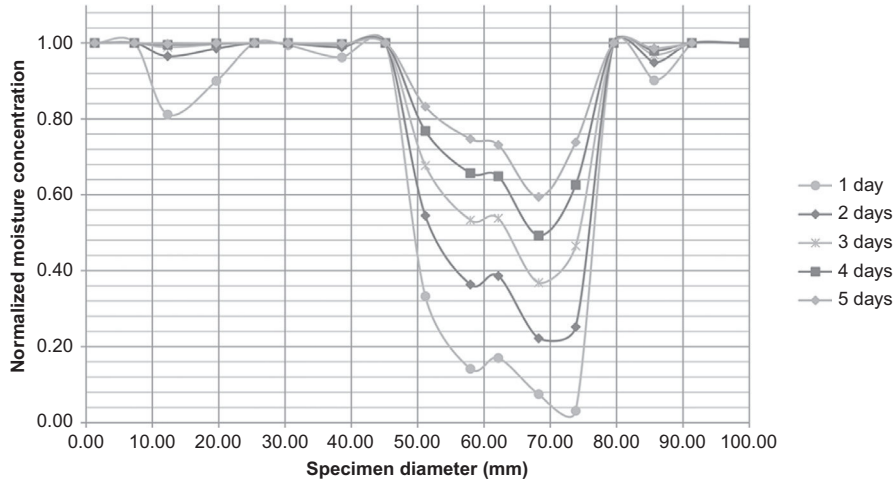


Figure 10.19 Moisture concentration profile within the PA specimen at different time intervals. After Varveri et al. (2015).

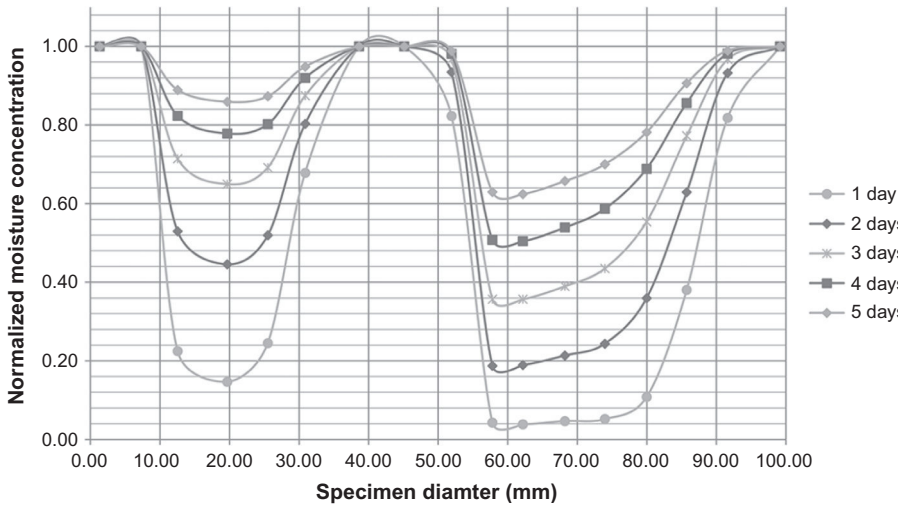


Figure 10.20 Moisture concentration profile within the SMA specimen at different time intervals. After Varveri et al. (2015).

mechanical loading. Loading was applied diametrically across the circular cross section of the cylindrical specimen, replicating the loading conditions during an indirect tensile test. The damage distribution for both mixtures after specified periods of moisture conditioning is shown in Figures 10.21 and 10.22.

The results demonstrated the strong relationship between the amount of moisture in the binder and the overall level of damage development in the asphalt mixtures.

www.EngineeringEBooksPdf.com

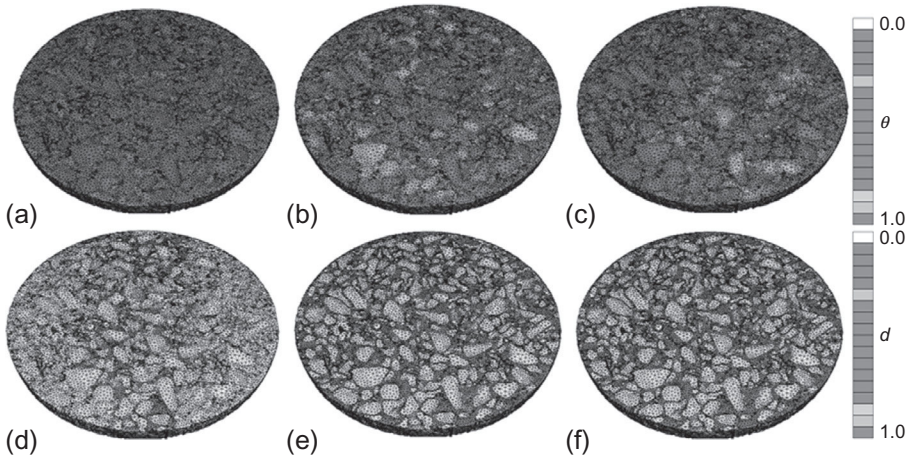


Figure 10.21 Moisture concentration and damage distribution in the porous mixture after 0 h (a and d), 48 h (b and e), and 120 (c and f) h of moisture diffusion.
After Varveri et al. (2015).

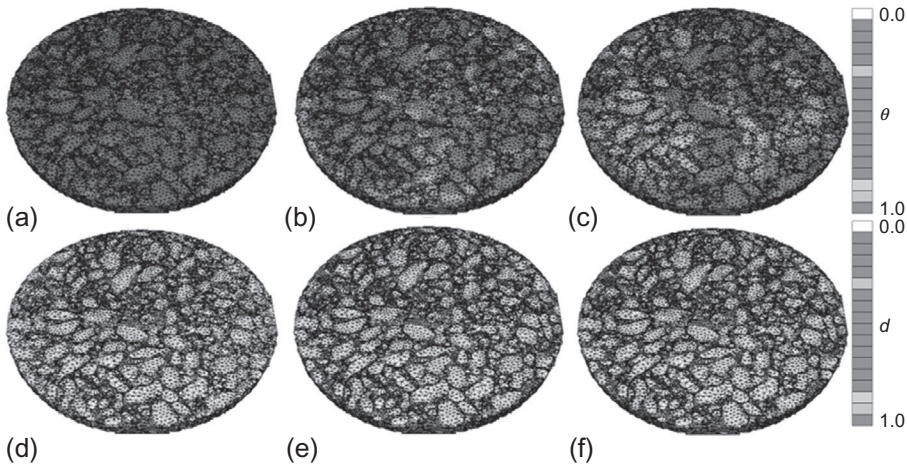


Figure 10.22 Moisture concentration and damage distribution in the dense mixture after 0 h (a and d), 48 h (b and e), and 120 h (c and f) of moisture diffusion.
After Varveri et al. (2015).

Damage was found to be higher on those areas in the specimen that had their mechanical properties already degraded by moisture. Also, by varying the properties of the binder, it was indicated that the choice of mixture components less susceptible to moisture damage is of paramount importance. For the porous mixture, the use of a less moisture-sensitive binder resulted in lower reduction in strength, from 43% to 18.5%, compared to the dry case.

www.EngineeringEBooksPdf.com

The aforementioned micromechanical models can assist researchers in drawing insights toward the interactions of the various mixture constituents and the influence of certain mixture variables on mixture properties, and subsequently their effect on overall mixture performance. As stated earlier, moisture damage is a rather complex pavement distress. Each mixture constituent has its particular physical properties that control the long- and short-term moisture-induced damage mechanisms; consequently, the rate of moisture ingress into the mixture is influenced, thus affecting the rate of degradation. Varveri et al. (2015) demonstrated the effect of using binders with high resistivity against moisture in the preparation of porous asphalt mixtures and quantified the benefits that would arise due to this choice. Similarly, the mechanical properties of mixture constituents can alter the response of asphalt mixtures. Given the fact that asphalt is a composite material, one can understand the implications that arise due to mix design. For example, the performance of an asphalt binder (i.e., bitumen plus filler) with high filler content against moisture damage will be different compared to that of a binder prepared with the same bitumen but lower filler content. In terms of moisture damage physical processes, high filler concentration is associated with high rates of diffusion in the binder (considering that bitumen has a lower diffusion coefficient than the filler). On the other hand, a filler-rich binder will have a higher stiffness compared to a binder with low concentration of filler particles. All these variations play an important role in estimating the susceptibility characteristics of asphalt mixtures. Micromechanical modeling can be used to perform sensitivity analyses aiming to develop new mixture designs with enhanced characteristics against moisture damage, thus reducing the risk of failure.

Moreover, mixture susceptibility to moisture damage is affected by the geometrical and morphological characteristics of the material microstructure. The use of micromechanical models, in contrast to macromechanical models, enables the investigation of different mixtures types, such as gap- and open-graded mixtures. Imaging techniques are used to capture the particularities of the internal structure, and a better understanding of characteristics such as air-void connectivity, structure of the aggregate skeleton, and binder film thickness can be attained.

It is expected that successfully developed micromechanical FE models constitute a tool for the design of mixtures with optimized moisture susceptibility properties, and allow the addition of new materials in mix design to be investigated. These models can be used as computational platforms where simulations of laboratory tests can be performed that will provide useful insights and practical recommendations to the pavement community.

10.4 Experimental characterization and mixture design of asphalt mixtures for moisture damage

10.4.1 Test methods to characterize moisture damage

Moisture susceptibility of asphalt mixtures can largely vary, depending on the material component parameters, their interaction, their mix design, and their in-time degradation. One can, for example, think of a mixture that has very low aggregate–stone

www.EngineeringEBooksPdf.com

bond strength, yet due to its design moisture may take such a long time to penetrate at the interfaces that it may not be the most feared damage mechanism. Similarly, mixtures that have very high moisture permeability but a very slow mechanical degradation when exposed to moisture may not be moisture sensitive. Therefore, it is crucial to determine the degree-of-function loss for a given asphalt mixture and its individual components under a relevant time frame. In terms of specifications and standards, threshold values are usually expected to distinguish between materials that are susceptible, or not, to moisture damage. The complexity of moisture-induced damage phenomena makes it difficult to find a unique way to comprehensively evaluate and estimate the future performance of the materials (Solaimanian et al., 2003). However, many test methods have been developed to characterize the moisture susceptibility of asphalt mixtures (Airey and Choi, 2002). In a review paper, Caro et al. (2008b) classified the developed test methods into three categories based on their generic nature: subjective qualification, quantification by a performance index, and tests that use the ratio of a single or multiple performance parameters to assess moisture damage (moisture damage ratio (MDR)). The various classifications are shown in Tables 10.3–10.6.

Of all the test methods, the modified Lottman test is the most popular for characterizing moisture susceptibility of asphalt mixtures. The test resulted from the

Table 10.3 Subjective qualification tests

Test	Reference	Assessment of damage
Rolling bottle method	CEN prEN 12697-11	Visual estimation of the amount of binder retained in the mixture
Ancona stripping test	Bocci and Colagrande (1993)	Visual estimation of the total percentage of material stripped (Airey and Choi, 2002)
Boiling water test	American Society for Testing and Materials, ASTM D 3625	Visual estimation of the amount of binder loss. Retained coating between 85% and 90% is considered acceptable
Film stripping	California test 302-1999'	Visual estimation of the total percentage of material stripped
Static immersion test	American Association of State Highway and Transportation Officials, AASHTO T182 ASTM D 1664	Visual estimation of the total area of the coated aggregate as above or below 95% (discontinued by ASTM)
Ultrasonic method	Vuorinen and Valtonen (1999)	Visual estimation of material stripped. It can also include the assessment of the weight of material released from the aggregate
Chemical immersion test	Kennedy et al. (1983)	Concentration of sodium carbonate required to produce stripping (identified visually). This value is considered a measure of adhesiveness

Source: Caro et al. (2008b).

www.EngineeringEBooksPdf.com

Table 10.4 Tests of quantification by a performance index

Test	Reference	Performance index (damage parameter)
First proposal of ultrasonic method	Vuorinen and Valtonen (1999)	Loss of weight of a polished stone test specimen of 2 cm × 8 cm coated with 2 g of asphalt binder after the application of ultrasound under water (Airey and Choi, 2002)
Ultrasonic-accelerated moisture-conditioning procedure (UAMC)	McCann and Sebaaly (2001)	Percentage loss in weight of original sample after subjecting it to an ultrasonic bath. The lost material corresponds to small particles of aggregate that are dislodged from larger aggregates when ultrasonic energy is applied
	McCann et al. (2005)	Recently, the authors proposed the use of the rate at which the small particles are released as the asphalt recedes along the surface of the aggregate as a *performance index* that characterizes damage
Net adsorption test (NAT)	SHRP Designation-001 Curtis et al. (1993)	Net adsorption is defined as the amount of asphalt binder that remains on the aggregate after aqueous desorption. The value is measured based on the amount of binder that is adsorbed onto the aggregate surface from a toluene solution and the amount of binder that is desorbed (i.e., removed) by the addition of water to the mixture (Airey and Choi, 2002)
Modified net adsorption test	Walsh et al. (1996)	Same principle as NAT but with modifications in the preparation of the aggregates (Airey and Choi, 2002)
Pneumatic pull-off	Youtcheff and Aurilio (1997)	Adhesive bond of asphalt binders based on the burst pressure required to debond the binder from a stone as a function of time while exposed to water (tensile and bonding strength in different moisture conditions) (Solaimanian et al., 2003)
Texas freeze-thaw pedestal method	Kennedy and Anagnos (1984)	Thermal cycles required for causing crack initiation in an asphalt mixture
Boiling water stripping test	Belgium Road Research Center (BRRC) Procedure ME 65-91	Stripping rate calculated from a calibration curve of acid consumption against percentage of uncoated material. The curve is obtained from mixtures with coated and uncoated aggregates in different ratios that are subjected to chemical attacks

Continued

www.EngineeringEBooksPdf.com

Table 10.4 Continued

Test	Reference	Performance index (damage parameter)
Hamburg wheel-tracking test	Texas Department of Transportation TxDOT standard Tex-242-F, 2004	The test uses wheel tracking to simulate traffic conditions on compacted specimens that are immersed in water. Stripping is identified with the presence of a sudden inflection point in the plastic deformation during the application of cyclic load
Moisture vapor susceptibility (MVS)	California test 307, 1999	Stabilometer value at which the effect of moisture on mixtures is imminent. The stabilometer value is calculated following the test C 366
Methylene blue test	Ohio Department of Transportation (supplement 1052)	The test identifies the concentration of plastic fines (including clay and organic material) in the mix that can promote emulsification of asphalt in the presence of water (Kandhal et al., 1998)

Source: Caro et al. (2008b).

Table 10.5 Tests that use a single-parameter performance function in MDR evaluation

Test/work	Standards/ references	Material property used in the single-index performance function for MDR	Comments
Lottman	NCHRP 246, Lottman (1982)	Indirect tensile strength and stiffness	
Modified Lottman	AASHTO T283	Indirect tensile strength and stiffness	Commonly known as tensile strength ratio (TSR)
Tunnicliff and Root procedure	ASTM D 4867	Indirect tensile strength	Commonly known as tensile strength ratio (TSR)
Duriez test	NFP 98-251-1	Unconfined compression strength and Marshall stability	
Marshall stability test	AASHTO T245	Marshall stability	
Immersion compression test	AASHTO T165, ASTM D 1075	Compressive strength (wet over dry values)	The MDR in this case is referred to as the index of retained strength (IRS)

www.EngineeringEBooksPdf.com

Table 10.5 Continued

Test/work	Standards/ references	Material property used in the single-index performance function for MDR	Comments
Bitutest protocol	Scholz (1995)	Indirect stiffness modulus using the Nottingham asphalt tester	
Environmental conditioning system (ECS) with dynamic modulus	Al-Swalimi and Terrel (1992); NCHRP 9-19, 9-29, and 1-37	Dynamic modulus using ECS (Solaimanian et al., 2003, 2006)	
ECS with flow number		Flow number using ECS (Solaimanian et al., 2003, 2006)	
ECS with flow time		Flow time using ECS (Solaimanian et al., 2003, 2006)	
Flexural fatigue beam test with moisture conditioning	Shatnawi et al. (1995)	Fatigue life following AASHTO TP-8	
Disk-shape compact tension (DCT) fracture test	Apeagyei et al. (2006)	Fracture energy (G_f), Fracture strength (S_f)	
Dynamic mechanical analysis (DMA) of fine aggregate mixtures (FAM)[a] for analyzing moisture damage of mixtures	Song et al. (2005) and Masad et al. (2006a)	Fatigue life, N_f (number of cycles to failure under strain-controlled conditions)	Conducted on FAM using torsion strain-controlled conditions. There is no threshold value that separates good and poor performance of mixtures
		Reduction in the dynamic modulus at fatigue life (G^*/G')	Small values are desirable
Static creep test	Abo-Qudais and Al-Shweily (2007)	Accumulated microstrain	Comparison of accumulated microstrain after 60 min of loading
Pull-off test	Copeland et al. (2007)	Tensile strength of the binder–rock interface	

Continued

www.EngineeringEBooksPdf.com

Table 10.5 Continued

Test/work	Standards/ references	Material property used in the single-index performance function for MDR	Comments
Saturation aging tensile stiffness (SATS)	Collop et al. (2004) and Airey et al. (2007)	Tensile stiffness modulus	Calculated at 20 °C using the Nottingham Asphalt Tester (NAT)
Surface energy measurements (Wilhelmy plate and Universal Sorption Device)	Bhasin et al. (2006a,b, 2007), Masad et al. (2006a), and Little and Bhasin (2007)	Adhesive bond between aggregates and asphalt binders (ΔG_{AS}) and the potential of water to debond the asphalt (ΔG_{WAS})	

[a]FAM represent the fine matrix of asphalt mixture. They are composed by asphalt binder and the fine portion of the aggregates (passing the sieve 1.18 mm).
Source: Caro et al. (2008b).

combination of the Lottman and Tunnicliff and Root tests. Other variants of the modified Lottman test method are being used all over the world. The test involves the comparison of a dry control set of samples with samples subjected to vacuum saturation and freeze-thaw conditioning. The damage due to moisture is evaluated on the basis of the indirect tensile strength test. The percentage loss of tensile strength of the mixture, widely known as tensile strength ratio (TSR), is used to evaluate the moisture sensitivity of the mixtures. The tensile strength ratio is expressed as

$$\mathrm{TSR}(\%) = \frac{S_2}{S_1} \times 100 \tag{10.11}$$

where S_1 and S_2 are the average tensile strengths of the control and the conditioned set of samples, respectively. The minimum TSR values, which are required to determine if a mixture is moisture susceptible, are typically between 0.70 and 0.90.

However, despite the test's popularity, modified Lottman test results are known to be rather variable, not necessarily accurately describing moisture susceptibility. Several drawbacks have been reported about the test: poor correlation with field performance, high dependency on sample geometry, mechanical loading application that is not representative of the actual conditions, and ineffective and long moisture-conditioning protocols. Kringos et al. (2009) and Azari (2010) analyzed the moisture infiltration process and the structural nature of the modified Lottman test. It was concluded that the microcracks induced by the vacuum suction procedure may increase the variability of the test. Also, the conditioning protocol of the test fails to capture the time frame over which moisture infiltration occurs and disregards the short-term moisture processes related to pumping action. This could thus lead to erroneous conclusions regarding moisture susceptibility of the mixtures, leading to moisture damage sensitive pavements when applying these mixtures.

www.EngineeringEBooksPdf.com

Table 10.6 Examples of quantification using multiple parameter MDR

References	MDR	Function for MDR	Tests required	Indices for the performance function
Birgisson et al. (2003)	MDR_2	N_f number of cycles for the crack to grow 1-in. long under cyclic loading in Superpave indirect tensile (IDT) test	Tensile strength, resilient modulus, and creep compliance tests	Creep strain energy per cycle, creep strain energy limit (to produce failure), creep properties, and tensile strength
Birgisson et al. (2004)	MDR_3	ER	Strength tests, resilient modulus, and creep compliance tests (Superpave IDT)	Tensile strength, resilient modulus, fracture energy limit to failure, dissipated creep strain energy (DCSE) limit, and creep properties
Song et al. (2005)	MDR_4	Ratio between the apparent and the initial shear modulus	Shear oscillation test in DMA	Viscoelastic properties, change in pseudostiffness, and reference shear strain at each cycle
Zollinger (2005), Masad et al. (2006a), and Caro et al. (2008)	MDR_5 and MDR_6	Crack growth index	Shear oscillation and relaxation modulus in DMA; USD and WP on aggregates and binders, respectively	Viscoelastic properties (m and E_1), reference modulus, change of pseudostrain energy with respect to load cycles, and adhesive bond energy (from the surface energy of aggregates and binders)
Arambula et al. (2007a,b)	MDR_5	Crack growth model, but including the material tensile strength	Relaxation modulus, tensile strength, repeated uniaxial tensile in mixtures; USD and WP on aggregates and binder, respectively	Viscoelastic properties (m and E_1), reference modulus, change of pseudostrain energy with respect to load cycles, and adhesive bond energy at the aggregate–binder interface, tensile strength

Source: Caro et al. (2008b).

www.EngineeringEBooksPdf.com

An attempt to evaluate the relationship between the performance of asphalt pavements (as given by the pavement distress index (PDI)) in the field and the TSR values measured in the laboratory was made by Kanitpong and Bahia (2008). The analysis indicated that there was no relationship between the PDIs and the TSR values for the total of 21 pavement sections under study. In addition, the TSR values could not correlate to common distresses such as rutting and raveling, which are associated to moisture damage. It was also reported that the TSR data could only show the effect of antistripping additives, but again, they did not correlate to performance.

The relationship between permeability and tensile strength ratio was investigated by Birgisson et al. (2005). Permeability was found not to correlate well with the TSR values; this mismatch was attributed to the high variability of the indirect tensile test and to the microstructural characteristics of the mixtures. Differences were also observed during the saturation procedure of fine- and coarse-graded mixtures. The requirement of a minimum level of saturation could not be achieved with the same number of vacuum cycles for all mixtures. The researchers suggested that the mixture should be subjected to a single vacuum saturation cycle and find its own level of saturation that reflects better its physical sensitivity to moisture.

Overall, the test methods currently used to characterize a mixture in terms of its sensitivity to moisture damage show poor repeatability and do not correlate well with field observations. The development of a new test that simulates the relevant load levels in the field and takes into account the various moisture failure mechanisms in a relevant time frame is therefore necessary. Such a test could possibly provide the asphalt community with results that can be used in performance prediction.

10.4.2 Parameter determination for modeling of moisture damage

The standard mechanical asphalt tests today cannot provide the parameters necessary for modeling moisture damage. Parameter determination for physicochemical models involves the use of special tests that allow the measurement of more fundamental material properties. The parameters required for modeling moisture-related processes mainly include the measurement of moisture diffusion coefficients of mixture components (aggregates and asphalt binders), as well as the desorption characteristics of asphalt binders. Table 10.7 summarizes previous studies that were carried out for the determination of the moisture diffusion coefficients of asphalt binders.

Among these studies, various methods were employed: monitoring the change of total suction in specimens with time (Kassem et al., 2006), measuring the weight increase of specimens after submerged under water (Vasconcelos et al., 2011), and using gravimetric methods (Kringos et al., 2008b; Arambula et al., 2010; Apeagyei et al., 2013). It is observed that there are differences in the measured values among the various studies, which could be due to the differences in experimental setup and testing conditions (Apeagyei et al., 2013), differences in the binder mixture, and slightly different definitions of moisture diffusion and infiltration. Figures 10.23 and 10.24 illustrate the experimental setups used by Kassem et al. (2006) and Arambula et al. (2010), respectively.

www.EngineeringEBooksPdf.com

Table 10.7 Reported asphalt mastic diffusion coefficients

Reference	Blend proportions (by weight)	$D \times 10^{-12}$ (m^2/s)	Specimen characteristics and experimental conditions
Kassem et al. (2006)	Aggregate: 52.4%, sandstone: 35.0%, igneous screening: 4.6%, hydrated lime asphalt: 8.0%, PG 76-22	10.26	Cylindrical specimens, 50 mm in diameter and 50 mm in height, sitting in a shallow water bath at 25 °C, while measuring the change in the logarithm of total suction using a psychrometer embedded in the middle specimen and placed 5 mm above the bottom end of the specimen. Aggregate size passing sieve number 16 (1.18 mm). Air voids not specified
	Aggregate: 66.2%, natural sand: 25.8%, limestone sand asphalt: 8.0% (PG 64-22 and PG 64-28)	9.72 and 24.30	
Kringos et al. (2008c)	Aggregate: 50.0%, crushed sand: 25%, lime asphalt: 25%, binder (Pen 70/100, Cariphalt XS, Sealoflex)	0.13–3.08	Gravimetric sorption method applied to 30×30 and 1 mm thick specimens placed inside an 85% relative humidity chamber at 25 °C. Aggregate size (top size 1.18 mm). Air voids not specified
Arambula et al. (2010)	Aggregate: 47.3%, diabase: 42.5%, sand: 1.7%, dust asphalt: 8.5%, PG 70-22	25.444	Gravimetric method (ASTM E96 (ASTM, 2005)), wet cup/dry cup method applied to cylindrical ensembles containing 70 mm diameter and 4–5-mm thick specimens, where three ensembles were placed in a chamber with 15% relative humidity at 35 °C. Aggregate size passing sieve number 4 (4.75 mm). Air voids between 11% and 13%. Used Fick's first law to estimate D
Vasconcelos et al. (2011)	Aggregate: N/A, asphalt: 8.9% (PG 85-*XX*, *XX* = 10, 22, 28)	0.78–2.23	23.9 °C temperature conditioning by submerging in water for 21 months and measuring saturated surface dry (SSD) with time using a sensitive mass balance. Aggregate size passing 1.18-mm sieve. Air voids between 7% and 11%. Specimen size 12-mm diameter by 50-mm thick
	Aggregate: N/A, asphalt: 8.9% (PG 85-*XX*, *XX* = 10, 22, 28)	2.21–4.90	37.8 °C temperature conditioning by submerging in water for 14 months and measuring SSD with time using a sensitive mass balance. Aggregate size passing 1.18-mm sieve. Air voids between 7% and 11%. Specimen size 12-mm diameter by 50-mm thick

N/A = data not available.
Source: Apeagyei et al. (2013).

www.EngineeringEBooksPdf.com

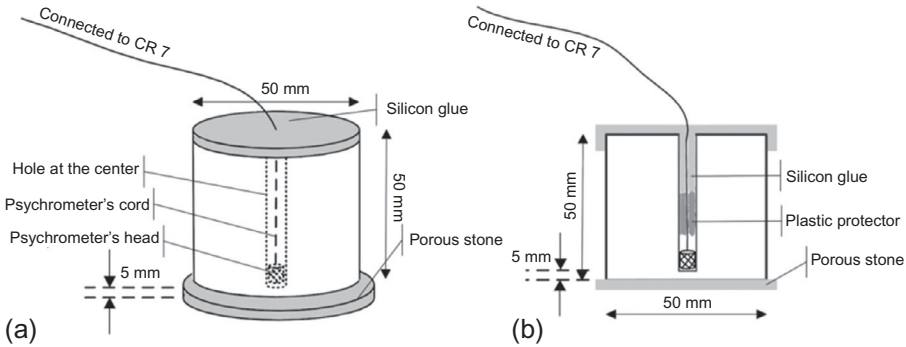


Figure 10.23 Experimental setup used by Kassem et al. (2006): (a) schematic view and (b) cross section.

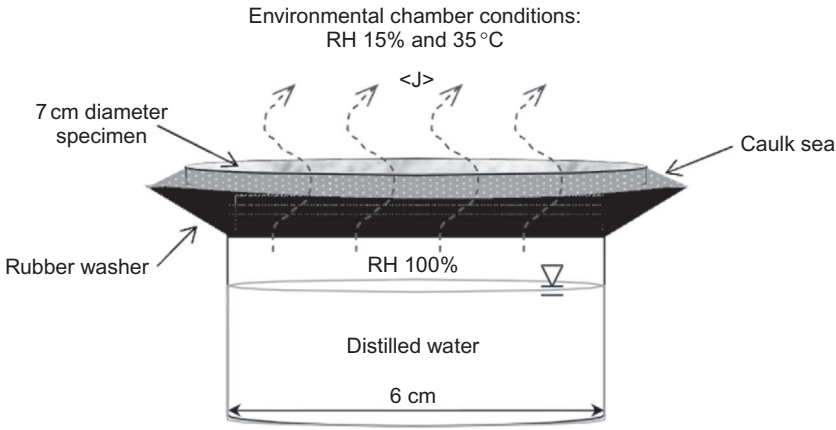


Figure 10.24 Experimental setup used by Arambula et al. (2010): the curved arrows represent the molar flux from inside the container with saturated water vapor pressure to the environmental chamber.

In contrast to diffusion coefficients, there are no data available for the desorption coefficients of asphalt binders. Nevertheless, Kringos et al. (2008b) mentioned a rather simple test, equivalent to the hollow cylinder test with fluid flow used frequently in soil-engineering laboratories (Papamichos, 2010). In the test, a controlled water pressure field is applied on a simplified binder core. The velocity of the flow should simulate the representative water flow in the pavement due to pumping action. The loss of binder mass is recorded at different time intervals. From the test, the binder desorption due to water flow might be measured and desorption curves may well be developed. Additionally, one could further explore the use of the Hamburg test (Izzo and Tahmoressi, 2007) and further analyze, for example, the residue in the water coming from the test. Though this test could be considered a very harsh test that includes

www.EngineeringEBooksPdf.com

several damage mechanisms at the same time (thus making it hard to filter out specific material parameters), it may be one of the most relevant tests used in practice today.

10.4.3 Guidelines for mix design of moisture-resistant asphalt mixtures

Apart from a well-designed pavement drainage system, a key parameter in preventing moisture damage of asphalt mixtures is the careful design of the mixtures in terms of binder content and aggregate gradation. The selection of asphalt mixture type (i.e., dense-, gap-, or open-graded) should be performed properly, according to the climate and traffic conditions of the particular area. It is generally believed that dense- and open-graded mixtures may be more sensitive to stripping problems than gap-graded mixtures; however, this does not imply that these mixtures cannot be effectively used without exhibiting moisture damage (D'Angelo and Anderson, 2003). As discussed in the previous sections, moisture damage has a very close relation to permeability, air void percentage, and aggregate structure. Therefore, it is critical to apply the appropriate compaction effort so that the mixtures are properly densified under traffic and ultimately achieve the desired air voids. Poor compaction in asphalt pavements results in high air-void content, which might cause moisture damage problems.

Furthermore, focus should be placed on selecting the individual mixture components. A selection of aggregates, asphalt binders, mineral fillers, and additives, as well as aggregate–binder combinations with improved characteristics against moisture damage, should be made. Especially for porous mixtures, which are significantly affected by moisture damage, binders with enhanced properties could be further considered (Varveri et al., 2015). Similarly, the dust content of mineral aggregates should be controlled properly. As discussed in the previous sections, excess dust coating of the aggregates facilitates the creation of weak boundary layers in asphalt mixtures and does not promote good adhesion between the aggregate and the asphalt binder.

Another way to prevent moisture damage is the addition of antistripping agents, which can alter the chemical and physical properties of the mixture components, thus improving their adhesive and cohesive properties. Based on the work of Bagampadde et al. (2004), typical additives for preventing moisture damage of asphalt mixtures are listed in Table 10.8.

In order to evaluate the moisture sensitivity of the designed mixtures, related performance tests should be carried out during mix design.

10.5 Outlook for the future

Though several new tests and computational models have been developed throughout the years that could be successfully applied to simulate moisture-induced damage in materials, not many of them are in fact applied in daily engineering design questions. This could be partly explained by how the current market functions. But the new types of innovative procurement contracts that include design-build and maintain principles could in fact bring a significant change in this. Business as usual, or applying

www.EngineeringEBooksPdf.com

Table 10.8 Additives for preventing moisture damage of asphalt mixtures

Additives		Proposed mechanisms of action
Mineral additives	Hydrated lime	• Reaction between calcium and aggregate silicate and aluminate surfaces forming products that bond strongly with asphalt binders, even in the presence of water • Consolidation of the fine coatings on aggregate surfaces through ion exchange/pozzolanic reactions between calcium- and silica-producing calcium-rich bonding sites for binder acidic polars • Reaction with carboxylic acids and 2-quinolones, so that few of them are available for adsorption • Inhibition of microbial activities
	Cement	• Hydration of cement
Liquid additives	Surfactants (mainly amines)	• Interaction of nitrogen lone electron pair with acid sites on silica surfaces, thereby improving adhesion • Action as Lewis bases that acquire protons from acidic groups in asphalt binders forming products that are attracted by the aggregate surfaces • Action like cationic surfactants by reducing the surface tension of the asphalt binders
	Silane-coupling agents (mainly $(RO)_3SiR_1$)	• Hydrolysis of organofunctional silane yielding silanol, which condenses rapidly to form a siloxane structure with a lipophilic part that remains solubilized in asphalt binders, while the inorganic end reacts with siliceous aggregate surfaces
Others	Sulfur-based additives	• Action as extender for asphalt binders
	Polymeric additives	• Action as modifier for asphalt binders • Pretreatment to aggregates, forming a protective barrier on the aggregate surfaces

Source: Bagampadde et al. (2004).

traditional designs may then in fact mean companies are not competitive in a global market or no longer fulfill new environmental, social, or economic sustainability requirements. This means that proper explanation of new models, the possibly needed new tests, and how to embed these in current state-of-the practice should become part of the effort in the research community. It also means that industry and academia will start having common vocabulary to use and an enhanced understanding of each other's domains, which could all contribute to ensuring an increase of innovation in the field.

In conclusion, we can add the common wisdom, "water gets everywhere." This certainly is the case for pavement. So it is of crucial importance that modern pavement

www.EngineeringEBooksPdf.com

engineers understand the basic mechanisms in which moisture can infiltrate and damage the pavement, both over short- and long-term periods. Micromechanical modeling is of paramount importance in understanding the possible fundamental processes that govern moisture damage and identifying the key factors that control these processes. Such models can serve as a relatively fast and inexpensive way to investigate a great variety of parameters before the structure is actually built. This allows for new material and new mixture designs to be investigated, and the risks involved with these to be minimized. Only this type of understanding can lead to universally applicable knowledge—tools that are not only "practical" but are also effective over the long term and that allow engineers to place moisture damage in the context of other damage mechanisms.

Acknowledgments

The authors would like to express their appreciation to S. Avgerinopoulos for his valuable and constructive suggestions during the writing of this chapter. His willingness to give his time so generously has been very much appreciated.

References

Abo-Qudais, S., Al-Shweily, 2007. Effect of aggregate properties on asphalt mixtures stripping and creep behavior. Constr. Build. Mater. 21, 1886–1898.

Airey, G.D., Choi, Y.K., 2002. State of the art report on moisture sensitivity test methods for bituminous pavement materials. Road Mater. Pavement Des. 3 (4), 355–372.

Airey, G.D., Collop, A.C., Zoorob, S.E., Elliot, R.C., 2007. Moisture damage assessment of asphalt mixtures using the UK SATS test. 86th TRB Annual Meeting Compendium of Papers, Transportation Research Board, Washington, DC.

Al-Swalimi, S., Terrel, R.L., 1992. Water sensitivity of asphalt–aggregate mixtures test development. SHRP-A-403, Strategic Highway Research Program. National Research Council, Washington, DC.

Apeagyei, A.K., Buttlar, W.G., Dempsey, B.J., 2006. Moisture damage evaluation of asphalt mixtures using AASTHO T 283 and DC(T) fracture test. 10th International Conference on Asphalt Pavements (ISAP), 742–753.

Apeagyei, A.K., Grenfell, J.R., Airey, G.D., 2013. Evaluation of moisture sorption and diffusion characteristics of asphalt mastics using manual and automated gravimetric sorption techniques. J. Mater. Civil Eng. 26, 8.

Arambula, E., Caro, S., Masad, E.A., 2010. Experimental measurement and numerical simulation of water vapor diffusion through asphalt pavement materials. J. Mater. Civil Eng. 22 (6), 588–598.

Arambula, E., Masad, E., Epps, A., 2007a. The influence of crack growth distribution on the moisture susceptibility of asphalt mixes. J. Mater. Civil Eng. ASCE 19 (8), 655–664.

Arambula, E., Masad, E., Epps, A., 2007b. Moisture susceptibility of asphalt mixtures with known field performance using dynamic analysis and a crack growth model. Transport. Res. Rec. 2001 (1), 20–28.

Asphalt Institute, 1987. Cause and prevention of stripping in asphalt pavements. Educational Series No. 10 (ES-10), second ed. Asphalt Institute, Maryland, USA.

www.EngineeringEBooksPdf.com

Azari, H., 2010. Precision estimates of AASHTO T283: resistance of compacted hot mix asphalt (HMA) to moisture-induced damage. National Cooperative Highway Research Program. Transportation Research Board of the National Academies.

Bagampadde, U., Isacsson, U., Kiggundu, B.M., 2004. Classical and contemporary aspects of stripping in bituminous mixes. Road Mater. Pavement Des. 5 (1), 7–43.

Bhasin, A., Masad, E., Little, D., Lytton, R., 2006a. Limits on adhesive bond energy for improved resistance of hot mix asphalt to moisture damage. Transport. Res. 1970, 3–13.

Bhasin, A., Chowdhury, A., Button, J., Little, D.N., 2006b. Evaluation of material property tests to predict moisture susceptibility of HMA. 10th International Conference on Asphalt Pavements (ISAP), 701–710.

Bhasin, A., Little, D.N., 2007. Characterization of aggregate surface energy using the universal sorption device. J. Mater. Civil Eng. 19, 634–641.

Bhasin, A., Little, D.N., Vasconcelos, K.L., Masad, E., 2007. Used of surface free energy to identify moisture sensitivity of materials for asphalt mixtures. 86th TRB Annual Meeting Compendium of Papers, Transportation Research Board, Washington, DC.

Bikerman, J.J., 1967. Causes of poor adhesion. J. Ind. Eng. Chem. 59 (9), 40–44.

Birgisson, B., Roque, R., Page, G., 2003. Evaluation of water damage using hot mix asphalt fracture mechanics. J. Assoc. Asphalt Paving Technol. 73, 424–462.

Birgisson, B., Roque, R., Page, G., 2004. The use of a performance based fracture criterion for the evaluation of moisture susceptibility in hot mix asphalt. Transport. Res. Rec. 1891, 51–61.

Birgisson, B., Roque, R., Tia, M., Masad, E.A., 2005. Development and evaluation of test methods to evaluate water damage and effectiveness of antistripping agents. Final report. University of Florida, Gainesville.

Bocci, M., Colagrande, S., 1993. The adhesiveness of modified road bitumen. 5th Eurobitumen Congress, Paper 1.61, Stockholm, Sweden.

Bonn, D., Eggers, J., Indekeu, J., Meunier, J., Rolley, E., 2009. Wetting and spreading. Rev. Mod. Phys. 81 (2), 739–805.

Caro, S., Masad, E., Airey, G., Bhasin, A., Little, D., 2008. Probabilistic analysis of fracture in asphalt mixtures caused by moisture damage. Transport. Res. Rec. 2057, 28–36.

Caro, S., Masad, E., Bhasin, A., Little, D.N., 2008a. Moisture susceptibility of asphalt mixtures, part 1: mechanisms. Int. J. Pavement Eng. 9 (2), 81–98.

Caro, S., Masad, E., Bhasin, A., Little, D.N., 2008b. Moisture susceptibility of asphalt mixtures, part 2: characterisation and modelling. Int. J. Pavement Eng. 9 (2), 99–114.

Caro, S., Masad, E., Bhasin, A., Little, D., 2009. Coupled micromechanical model of moisture-induced damage in asphalt mixtures. J. Mater. Civil Eng. 22 (4), 380–388.

Chen, J.S., Lin, K.Y., Young, S.Y., 2004. Effects of crack width and permeability on moisture-induced damage of pavements. J. Mater. Civil Eng. 16 (3), 276–282.

Cheng, D., Little, D.N., Lytton, R., Holste, J., 2002. Use of surface free energy properties of the asphalt–aggregate system to predict damage potential. J. Assoc. Asphalt Paving Technol. 71, 59–88.

Cheng, D., Little, D.N., Lytton, R.L., Holste, J.C., 2003. Moisture damage evaluation of asphalt mixtures by considering both moisture diffusion and repeated-load conditions. Trans. Res. Rec. J. Trans. Res. Board 1832, 42–49.

Choubane, B., Page, G.C., Musselman, J.A., 1997. Investigation of water permeability of coarse graded Superpave pavements. Research report FL/DOT/SMO/97-416. Florida Department of Transportation.

Christopher, B.R., Schwartz, C., Boudreau, R., 2006. Geotechnical Aspects of Pavements. National Highway Institute, Federal Highway Administration, Washington, DC.

www.EngineeringEBooksPdf.com

Collop, A.C., Choi, Y., Airey, G.D., Elliott, R.C., 2004. Development of the saturation ageing tensile stiffness (SATS) test. ICE J. Transport 157, 163–171.

Cooley Jr., L.A., Brown, E.R., Maghsoodloo, S., 2001. Development of critical field permeability and pavement density values for coarse-graded Superpave pavements. Report 01-03. National Center for Asphalt Technology, Auburn University, Alabama

Copeland, A., Kringos, N., Scarpas, A., Youtcheff, J., 2006. Determination of bond strength as a function of moisture content at the aggregate–mastic interface. In: Proceedings of the 10th Conference of the International Society for Asphalt Pavement (ISAP), pp. 709–718.

Copeland, A., Kringos, N., Youtcheff, J., Scarpas, A., 2007. Measurement of aggregate–mastic bond strength in the presence of moisture: a combined experimental–computational study. In: 86th TRB Annual Meeting Compendium of Papers, No. 07-1829. Transportation Research Board, Washington, DC.

Curtis, C.W., Ensley, K., Epps, J., 1993. Fundamental properties of asphalt–aggregate interactions including adhesion and adsorption, Strategic Highway Research Program Project SHRP-A-341, The National Academies Press, Washington, DC.

D'Angelo, J., Anderson, R.M., 2003. Material production, mix design, and pavement design effects on moisture damage. In: Moisture Sensitivity of Asphalt Pavements: A National Seminar, San Diego, California. National Academies Press, Washington, DC.

da Silva, L.F.M., Öchsner, A., Adams, R.D., 2011. Handbook of Adhesion Technology. Springer, Berlin/Heidelberg.

Das, P.K., Kringos, N., Birgisson, B., 2014. Microscale investigation of thin film surface ageing of bitumen. J. Microsc. 254, 95–107.

Davies, J.T., Rideal, E.K., 1963. Interfacial Phenomena. Academic Press, New York.

Dupré, A., 1869. Theorie Mechanique de la Chaleur. Gauthier-Villars, Paris.

Fick, A., 1855. On liquid diffusion. Philos. Mag. J. Sci. 10 (63), 30–39.

Fischer, H.R., Dillingh, E.C., Hermse, C.G.M., 2012. On the interfacial interaction between bituminous binders and mineral surfaces as present in asphalt mixtures. Appl. Surf. Sci. 265, 495–499.

Graham, M.A., 2009. Viscoelastic–viscoplastic damage model for asphalt concrete. M.Sc. thesis. Texas A&M University, USA.

Hefer, A., Little, D.N., 2005. Adhesion in bitumen–aggregate systems and quantification of the effects of water on the adhesive bond. Report ICAR/505-1. Texas Transportation Institute, Texas A&M University System, College Station, Texas, USA.

Hicks, R.G., 1991. Moisture Damage in Asphalt Concrete, NCHRP Synthesis of Highway Practice 175. TRB, National Research Council, Washington, DC.

Huang, C.W., 2008. Development and numerical implementation of nonlinear viscoelastic–viscoplastic model for asphalt materials. Doctoral dissertation. Texas A&M University, USA.

Izzo, R.P., Tahmoressi, M., 2007. Use of the Hamburg Wheel-Tracking device for evaluating moisture susceptibility of hot-mix asphalt. Transport. Res. Rec. 1681, 76–85.

Kandhal, P.S., 1992. Moisture susceptibility of HMA mixes: identification of problem and recommended solutions. Report 92-01. National Center for Asphalt Technology, Auburn University, Alabama.

Kandhal, P.S., Lynn, C.Y., Parker, F., 1998. Test for plastic fines in aggregates related to stripping in asphalt paving mixtures. J. Assoc. Asphalt Paving Technol. 68, 459.

Kanitpong, K., Bahia, H.U., 2008. Evaluation of HMA moisture damage in Wisconsin as it relates to pavement performance. Int. J. Pavement Eng. 9 (1), 9–17.

Kassem, E., Masad, E., Bulut, R., Lytton, R., 2006. Measurements of moisture suction and diffusion coefficient in hot-mix asphalt and their relationships to moisture damage. Transport. Res. Rec. 1970 (1), 45–54.

www.EngineeringEBooksPdf.com

Kennedy, T.W., Anagnos, J.N., 1984. Modified test procedure for Texas freeze-thaw pedestal test. Center for Transportation Research (CTR), University of Texas at Austin, Austin, Project 3-0-79-253-7.

Kennedy, T.W., Roberts, F., Lee, K., 1983. Evaluation of moisture effects on asphalt concrete mixtures. Transport. Res. Rec. 911, 134–143.

Kettil, P., Engström, G., Wiberg, N.E., 2005. Coupled hydro-mechanical wave propagation in road structures. Comput. Struct. 83 (21), 1719–1729.

Khan, A., Redelius, P., Kringos, N., 2014. Surface energy measurements and wettability investigation of different minerals and bitumen for cold asphalts. Paper-933. ISAP, Raleigh, NC, USA.

Kiggundu, B.M., Roberts, F.L., 1988. Stripping in HMA mixtures: state-of-the-art and critical review of test methods. Report 88-02. National Center for Asphalt Technology, Auburn University, Alabama.

Kringos, N., 2007. Modeling of combined physical–mechanical moisture induced damage in asphaltic mixes. Doctoral dissertation. Delft University of Technology, The Netherlands.

Kringos, N., Scarpas, A., Kasbergen, C., Selvadurai, P., 2008a. Modelling of combined physical mechanical moisture-induced damage in asphaltic mixes, part 1: governing processes and formulations. Int. J. Pavement Eng. 9 (2), 115–118.

Kringos, N., Scarpas, A., Copeland, A., Youtcheff, J., 2008b. Modelling of combined physical–mechanical moisture-induced damage in asphaltic mixes, part 2: moisture susceptibility parameters. Int. J. Pavement Eng. 9 (2), 129–151.

Kringos, N., Scarpas, A., de Bondt, A., 2008c. Determination of moisture susceptibility of mastic–stone bond strength and comparison to thermodynamical properties. J. Assoc. Asphalt Paving Technol. 77, 435–478.

Kringos, N., Azari, H., Scarpas, A., 2009. Identification of parameters related to moisture conditioning that cause variability in modified Lottman test. Transport. Res. Rec. 2127 (1), 1–11.

Kutay, M.E., Aydilek, A.H., Masad, E., 2007a. Estimating directional permeability of hot-mix asphalt by numerical simulation of microscale water flow. Transport. Res. Rec. 2001 (1), 29–36.

Kutay, M.E., Aydilek, A.H., Masad, E., Harman, T., 2007b. Computational and experimental evaluation of hydraulic conductivity anisotropy in hot-mix asphalt. Int. J. Pavement Eng. 8 (1), 29–43.

Labib, M.E., 1992. Asphalt–aggregate interactions and mechanisms for water stripping. Am. Chem. Soc. Div. Fuel Chem. 37, 1472–1481.

Little, D.N., Bhasin, A., 2007. Using surface energy measurements to select materials for asphalt pavements. National Cooperative Highway Research Program (NCHRP) report 09-37, National Academies Press, Washington, DC.

Little, D.N., Jones, D.R., 2003. Chemical and mechanical processes of moisture damage in hot-mix asphalt pavements. In: Proceedings of the Moisture Sensitivity of Asphalt Pavements—A National Seminar, California.

López-Montilla, J.C., Herrera-Morales, P.E., Pandey, S., Shah, D.O., 2002. Spontaneous emulsification: mechanisms, physicochemical aspects, modeling and applications. J. Disper. Sci. Technol. 23 (1–3), 219–268.

Lottman, R.P., 1982. Predicting moisture-induced damage to asphaltic concrete: field evaluation. National Cooperative Highway Research Program 246, National Academies Press, Washington, DC.

Lytton, R.L., Masad, E.A., Zollinger, C., Bulut, R., Little, D.N., 2005. Measurements of surface energy and its relationship to moisture damage. Technical report no. TX-05/0-4524-2. Texas A&M Transportation Institute, College Station, Texas.

www.EngineeringEBooksPdf.com

McCann, M., Anderson-Sprecher, R., Thomas, K.P., Huang, S., 2005. Comparison of moisture damage in hot mix asphalt using ultrasonic accelerated moisture conditioning and tensile strength test results. 84th TRB Annual Meeting Compendium of Papers, Transportation Research Board, Washington, DC.

McCann, M., Sebaaly, A., 2001. Quantitative evaluation of stripping potential in hot mix asphalt using ultrasonic energy for moisture accelerated conditioning. Transport. Res. Rec. 1767, 48–59.

Majidzadeh, K., Brovold, F.N., 1968. Special Report 98: State of the Art: Effect of Water on Bitumen–Aggregate Mixtures. Highway Research Board, National Research Council, National Academy of Sciences and National Academy of Engineering, Washington, DC.

Mallick, R.B., Cooley, Jr., L.A., Teto, M.R., Bradbury, R.L., Peabody, D., 2003. An evaluation of factors affecting permeability of Superpave designed pavements. Report 03-02. National Center for Asphalt Technology, Auburn University, Alabama.

Masad, E., Zollinger, C., Bulut, R., Little, D.N., Lytton, R.L., 2006. Characterization of HMA moisture damage using surface energy and fracture properties. J. Assoc. Asphalt Paving Technol. 75, 713–754.

Masad, E., Al Omari, A., Chen, H.C., 2007. Computations of permeability tensor coefficients and anisotropy of asphalt concrete based on microstructure simulation of fluid flow. Comput. Mater. Sci. 40 (4), 449–459.

Mehrara, A., Khodaii, A., 2013. A review of state of the art on stripping phenomenon in asphalt concrete. Construct. Build. Mater. 38, 423–442.

Packham, D.E., 1992. Handbook of Adhesion. Longman Group, London, UK.

Packham, D.E., 2003. Surface energy, surface topography and adhesion. Int. J. Adhes. Adhes. 23 (6), 437–448.

Papamichos, E., 2010. Erosion and multiphase flow in porous media. Eur. J. Environ. Civil Eng. 14 (8–9), 1129–1154.

Scholz, T.V., 1995. Durability of bituminous paving mixtures. PhD Thesis, University of Nottingham.

Shatnawi, S.R., Nagarajaiah, M., Harvey, J., 1995. Moisture sensitivity evaluation of binder-aggregate mixtures. Transport. Res. Rec. 1492, 71–84.

Solaimanian, M., Fedor, D., Bonaquist, R., Soltani, A., Tandon, V., 2006. Simple performance test for moisture damage prediction in asphalt concrete. J. Assoc. Asphalt Paving Technol. 75, 345–380.

Solaimanian, M., Harvey, J., Tahmoressi, M., Tandon, V., 2003. Test methods to predict moisture sensitivity of hot mix asphalt pavements. In: Moisture Sensitivity of Asphalt Pavements: A National Seminar, San Diego, California. National Academies Press, Washington, DC.

Song, I., Little, D.N., Masad, E., Lytton, R.L., 2005. Comprehensive evaluation of damage in asphalt mastics using X-ray CT, continuum mechanics, and micromechanics. J. Assoc. Asphalt Paving Technol. 74, 885–920.

Stuart, K.D., 1990. Moisture damage in highway mixtures—a state of the art report. FHWA-RA-90-019. Washington, DC.

Tarrer, A.R., Wagh, V., 1991. The effect of the physical and chemical characteristics of the aggregate on bonding. Strategic Highway Research Program. National Research Council, Washington, DC.

Taylor, M.A., Khosla, N.P., 1983. Stripping of asphalt pavements: state-of-the-art. Transport. Res. Rec. 911, 150–158.

Terrel, R.L., Shute, J.W., 1989. Summary report on water sensitivity. SHRP-A/IR-89-003, Strategic Highway Research Program. National Research Council, Washington, DC.

www.EngineeringEBooksPdf.com

van Lent, D.Q., 2013. Interfacial Interactions and Mass Transfer at the Interfacial Region of Bituminous Hydrocarbon Mixtures. Technische Universiteit Delft, The Netherlands.

Varveri, A., 2015. Coupled environmental–mechanical causes of damage in AC mixtures. Doctoral thesis in preparation. Delft University of Technology, The Netherlands.

Varveri, A., Avgerinopoulos, S., Scarpas, A., Collop, A., Erkens, S., 2014. On the combined effect of moisture diffusion and cyclic pore pressure generation in asphalt concrete. In: 93rd TRB Annual Meeting Compendium of Papers, No. 14-1195. Transportation Research Board, Washington, DC.

Varveri, A., Avgerinopoulos, S., Kasbergen, C., Scarpas, A., Collop, A., 2015. The influence of air void content on moisture damage susceptibility of asphalt mixtures: a computational study. Transport. Res. Rec. in press.

Vasconcelos, K.L., Bhasin, A., Little, D.N., Lytton, R.L., 2011. Experimental measurement of water diffusion through fine aggregate mixtures. J. Mater. Civil Eng. 23 (4), 445–452.

Vuorinen, M.J., Valtonen, J.P., 1999. A new ultrasound method for measuring the resistance to stripping. Eurobitume Workshop 99: Performance related properties for bituminous binders, European Bitumen Association, Luxembourg.

Walsh, G., Jamieson, I., Thorton, J., O'Mahony, M., 1996. A modified SHRP net adsorption test. 1st Eurasphalt & Eurobitumen Congress, Strasbourg.

Youtcheff, J., Aurilio, V., 1997. Moisture sensitivity of asphalt binders: evaluation and modeling of the pneumatic adhesion test results. 42nd Annual Conference of the Canadian Technical Asphalt Association, Ottawa, 180–200.

Zollinger, C., 2005. Application of surface energy measurements to evaluate moisture susceptibility of asphalt and aggregates. MSc Thesis, Texas A&M University, College Station, Texas.

www.EngineeringEBooksPdf.com

11 Advances in the development of alternative binders from biomass for the production of biosourced road binders

E. Chailleux[1], M. Audo[1], S. Goyer[2], C. Queffelec[3], O. Marzouk[2]
[1]IFSTTAR, Centre de Nantes, Bouguenais, France; [2]CEREMA, Saint-Brieuc, France;
[3]CEISAM, Université de Nantes, Nantes, France

11.1 Introduction

Most bitumens traditionally used in pavement application come from the petroleum oil refinery process. Only 10% of these oils can be used as materials for roads. Moreover, this natural resource is, of course, finite. Production will begin to decrease within a few years. The question is not "if" but "when" the peak oil will arrive. Meanwhile, supply difficulties have begun to appear (Lavoie, 2011). Refinery strategies are changing, and some chemical compounds, like butadiene or some bitumen grades, could be lacking in the near future. Hence, the questions facing this problem are "Do alternatives to petroleum bitumen exist?" and "What about their performance?"

More and more publications and patents are published on this subject. The present chapter will try to review some of these publications to understand what natural resources are used, which processes are used for the transformation, and what is the durability of the alternative binders already tested at full-scale.

In the first section, alternative binders developed for full replacement are presented. The use of one type of alternative binder made of vegetable oils and wood coproducts, which is the more developed one, is especially described. Then, some input concerning alternative binders developed for partial replacement, followed by vegetable flux and surfactants, is given.

11.2 Alternative binders developed for full replacement

11.2.1 Binder from vegetable oils and wood coproducts

All patents and publications that propose to use vegetable oil and wood coproducts to produce a binder as an alternative to bitumen are based on the same principle: a high molecular weight material, generally from the wood industry (natural resin or chemically modified), is mixed with viscous oil (mineral or vegetable). Some consistency agents like polymers are added to optimize the rheology. The blend is carried out at temperatures

Advances in Asphalt Materials. http://dx.doi.org/10.1016/B978-0-08-100269-8.00011-8
© 2015 Elsevier Ltd. All rights reserved.

www.EngineeringEBooksPdf.com



Figure 11.1 Products used to manufacture a vegetable binder with blending at high temperature.

above the melting point of products. During this manufacturing, there is no chemical reaction. At ambient temperatures, the blend appears to be a suspension of particles (agglomerates of resin molecules) in a viscous matrix (oil). Consistency of this material is the consequence of a physical interaction between both phases (see Figure 11.1).

The first patent using vegetable oil was published in 1991 (Pinomaa, 1991). A tall oil resin, a byproduct from the paper industry, was mixed with vegetable oil and a polymer. Then, some inorganic pigments were added to dye the binder. Surprisingly, this type of binder was first designed to be dyeable and not environmentally friendly. About 10 years later, major contractors and oil companies in France proposed their own vegetable binders, all based on the same concept. Table 11.1 presents different commercial binders and compositions.

Due to the consistency of those vegetable binders, their manufacturing process, similar to the petroleum one, is done at lower temperatures (about 40 °C), which is a real gain of energy. It is worth mentioning that only the binder Vegecol® from Colas can be defined as a 100% vegetable binder, because no petroleum polymer is used in the formulation.

But the major issue of these alternative binders is the price. Indeed, the price of vegetable binders or synthetic binders is higher than that of a petroleum binder, resulting in an asphalt mix that could cost four times more. At present, they are, therefore, less competitive (even though the cost of petroleum bitumen is on the rise) due to the strong increase in mineral oil prices. For those reasons, but also for the high tonnage needed, these binders are right now almost exclusively developed on bicycle paths, on parking lots, and on pedestrian alleyways, where their transparent color enhances the natural color of aggregates.

11.2.1.1 Physical properties of vegetable oil–rosin binders

Consistency

The consistency of this type of binder is created by adjusting the rosin-to-oil ratio and then using a consistency agent, like polymer. In Table 11.2, the consistency of pure bitumen 50–70 is compared with vegetable binders with various percentages of oil and resin. Thus, ring-and-ball temperature, penetrability, and glass transition temperature tests show that binders 1 and 2 have similar characteristics as bitumen 50–70. So in

www.EngineeringEBooksPdf.com

Table 11.1 Composition of some industrial vegetable binders (percentages are given for the total binder weight)

Commercial name	Company	Resin	Oil	Polymer	Additives	Reference
–	–	Tall oil resin, from wood or terebenthine	Mineral vegetable oil, or tall oil 15–20%	PP[a], PE[b], PA[c], SB[d] 2–15%	Inorganic pigments (TiO_2, Cr_2O_3)	Pinomaa (1991)
Vegecol®	Colas	Natural or modified rosins[e] (modification by esterification or maleinization) 40–70%	Linseed, ricin, or wood oil. Nonmodified or from distillation or chemically modified 40–70%	–	Co, Zr, and Mn salt	Colas (2004a)
Biophalt®	Eiffage	Natural or modified rosins, terpenes—(solid or modified) 1–10%	Tall oil pitch	1–20%	Wax 1–40% Fibers—additives 2–10% Flux 2–25% Sicatif Co, Va, Ca, or Mn salt 2–30%	Eiffage (2007)
Floraphalte®	Shell	Rosin ester 20–90%	Colza, palm oil, or tall oil 10–80%	Functionalized EVA[f] by silanes 1–10%	–	Shell (2010)
Séquoia®	Eurovia	Natural or modified rosins, terpenes 40–60%	Polyester carried or by polycondensation of rapeseed, sunflower, soybean, palm oil, or tall oil with polyacids and polyols 40–60%	SB, EVA 5–10%	UV-protecting agent Structuring and reinforcing agents Rheology modifier agent Ti, Zn, or Fe salts	Eurovia (2010)

[a]Polypropylene.
[b]Polyethylene.
[c]Polyamide.
[d]Styrene-butadiene.
[e]Residue from the distillation of turpentine, coming from coniferous trees.
[f]Ethylene-vinyl acetate.

www.EngineeringEBooksPdf.com

Table 11.2 Physical properties of bitumen 50–70 and vegetable binders

Material	Resin/ oil (%)	Glass transition temperature (°C)	Ring-and-ball temperature (°C)	Penetrability
Binder 1 (Vegecol®)	75/25	−3	46.9	58
Binder 2 (Vegecol®)	82/18	−2	47.8	56
Binder 3 (Floraphalte®)	–	–	89	45
Bitumen 50–70	–	6	50.7	52

Source: Trigallez et al. (2009) and Lecomte et al. (2009).

this case, the vegetable binders tested could replace bitumen 50–70. It could be noted that the glass transition of vegetable binders is low in comparison to that of conventional binders. Another example comes from the Shell company: the Floraphalte®, which has penetrability close to 70/100 grade.

Properties related to manufacturing

Ballie et al. (2004) showed that the viscosity values of the plant-based binder developed by Colas are considerably lower than 35/50 bitumen. Consequently, it is possible to manufacture hot mixes at a lower temperature than that of bituminous mixes. The coating temperature can be reduced to 40–50 °C, without any reduction in workability.

Nevertheless, this type of alternative binder is highly susceptible to a polymerization process that leads to a hardening of the material, especially when it is exposed to high temperatures. For this reason, generally a low viscosity or high penetration grade can been used in order to take into account the curing effect during manufacturing. As an example, Floraphalte® binder (Lecomte et al., 2009) keeps good oxidation resistance after Rolling Thin Film Oven Tester (RTFOT) up to 160 °C. From 170 °C, the binder hardens very quickly due to oxidation and the polymerization process.

The evolution of the binder was also studied after the coating phase. Samples of uncompacted mixes were maintained for 4 h in an oven (at 130 or 170 °C). Table 11.3 shows that at 170 °C, properties of the binder change very quickly with time. Indeed, after 4 h, the penetrability decreases dramatically (penetrability after 4 h reaches 9 1/10 mm, namely 10% of its initial penetrability). At 130 °C, the characteristics of the binder are less time dependent; the binder loses only a penetrability grade (Lecomte et al., 2009). The authors concluded that during the storage phase of the binder and asphalt manufacturing, the binder should not be above 160 °C.

Mechanical properties at an early age

The water resistance test on Floraphalte® (EN standard protocol NF 98-251-1) shows high values for compressive strength, with and without immersion (r and R) ($R = 10.5$, $r = 7.7$) (Lecomte et al., 2009). Moreover, the hardening of this binder is observed

www.EngineeringEBooksPdf.com

Table 11.3 Floraphalte®—evolution of penetrability and softening temperature depending on the exposure time in oven

Temperature (°C)	Exposure time (h)	Penetrability (1/10 mm)	Softening temperature (°C)
130	0	88	46.2
	2	52	49.6
	4	43	51.4
170	0	95	45.4
	2	23	53.8
	4	9	58
Initial binder (before mixing)		79	48.2

Source: Lecomte et al. (2009).

during the conditioning phase (with or without immersion). This observation has been also made for the Vegecol® binder (Colas, 2004a). But at a very early age, the compressive strength of water-immersed cores appears to be very low. This study showed that it is necessary to have a curing time to increase compressive strength. All of the coated and compacted specimens were stored up to 60 days before testing at 18 °C and 50% humidity. The compressive strength of samples after storage in air at 18 °C and compressive strength after water immersion both evolve over time. The increase from 4 to 13 MPa in compressive strength seems to slow down after 60 days. The authors suggested a stabilization of this evolution due to the end of the polymerization mechanism. Nevertheless, the ratio between both strengths appears to be stable with time and remains around 0.7.

The hardening of the binder at room temperature has a strong influence on the complex modulus. Stiffness could increase a lot over time in comparison to conventional mixes (see Table 11.4). Pouget and Loup (2013) also showed that the phase angle decreases at the same time (decrease is between 20° and 35°) after 12 months. From a general point of view, it seems necessary to take into account a curing time to reach a certain modulus. The modulus increase does not appear to affect cracking properties. Indeed, for the curing time studied, fatigue performance of Vegecol® appears to be very high (Trigallez et al., 2009) in comparison to conventional mixes with a similar penetrability grade. On the other hand, low temperature tensile properties for both mixes made with Biophalt® are also close to what can be found with conventional binders (Pouget and Loup, 2013).

11.2.1.2 Field experience feedback

Some experimental road work sites have been achieved, especially in France. Currently, not much data are available concerning their long-term behavior, because the first test sections were realized in the 2000s. Nevertheless, initial feedback showed that, in some cases (not yet fully understood), aging issues of the binder occurred. For some vegetable binders, experimental sites showed significant damage after 4–7 years

www.EngineeringEBooksPdf.com

Table 11.4 Evolution of some mechanical properties with time of three mixes made with vegetable binders

	Vegecol® type (Trigallez et al., 2009)	Biophalt® type 1 (Pouget and Loup, 2013)	Biophalt® type 2 (Pouget and Loup, 2013)
$\|E^*\|$ (15 °C, 10 Hz)	1 month: 5100 MPa 9 months: 5600 MPa	0 months: 4300 MPa 6 months: 10,100 MPa 12 months: 12,900 MPa	0 months: 1800 MPa 6 months: 6400 MPa 12 months: 10,700 MPa
Stress at break at −10 °C (in tension)	–	0 months: 5.00 MPa 6 months: 4.00 MPa 12 months: 3.73 MPa	0 months: 2.84 MPa 6 months: 3.78 MPa 12 months: 4.40 MPa
Temperature at break (in Thermal Stress Restrained Specimen Test (TSRST))	–	0 months: −29.5 °C 6 months: −27.9 °C 12 months: −23.6 °C	0 months: −29.0 °C 6 months: −25.4 °C 12 months: −25.7 °C
Fatigue performance (ε_6)	1 month: 129 μstrain 9 months: 161 μstrain		

of service life (large number of transverse and longitudinal cracks, alligator cracking; see Figure 11.2).

Some samples have been cored from cracked areas (after 5 and 7 years of service life). Moduli of the samples were measured using indirect tensile tests (see Figures 11.3 and 11.4). The moduli measured were very high (up to 14,000 MPa), especially for products designed for surface courses. These moduli are similar to those of high modulus asphalt mixes, but the rheological behavior appears to be strongly different. Indeed, the mixes with vegetable binders have an elastic behavior instead of a viscoelastic behavior. They appear to be no longer thermal and time dependent. This means that the ability to relax stress, which is generally observed for usual bituminous materials, is lost at this age. This may explain the fragility observed on experimental sites. It also means that the curing process of this type of vegetable binder, which leads to an increase of the modulus, could lead also to a decrease of the viscous component. The material becomes finally brittle at service temperature.

11.2.2 Binders based on microalgae

Microalgae are one of the most promising alternative biomasses, as they present several advantages compared to other terrestrial plants: high biomass production (Figure 11.5), high growth rate, high photosynthetic yield, high lipid content (until

www.EngineeringEBooksPdf.com



Figure 11.2 Example of cracked pavement made with vegetable binder.

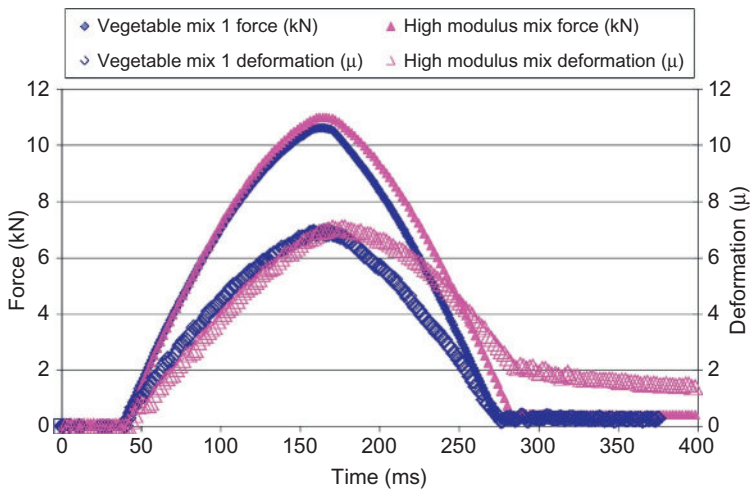


Figure 11.3 Impulse load (124 ms, ~11 kN) and deformation response in indirect tensile test for a mix made with vegetable binder (7 years, cored on site) in comparison with a high modulus asphalt mix.

80 wt.% under stressing conditions and for some particular species), and no competition with human feeding.

In the future, microalgae could be an extraordinary source for feeding, chemicals, or biomedical molecules (Vilchez et al., 1997). But the microalgae industry can be viable only if all fractions of the biomass can be valorized, as for petroleum. This is why it is interesting to explore the possibility of developing an alternative binder based on the microalgae byproducts.

It has been shown (Audo et al., 2012) that the design of microalgae-based road binders should be feasible using extracted lipids. The isolated lipid fraction of

www.EngineeringEBooksPdf.com

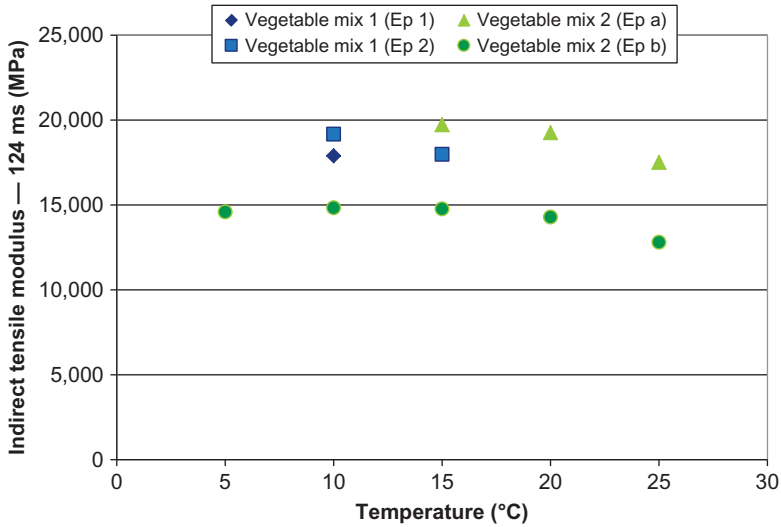


Figure 11.4 Indirect tensile modulus of mixes made with vegetable binder (cored on site several years after construction), according to temperature.

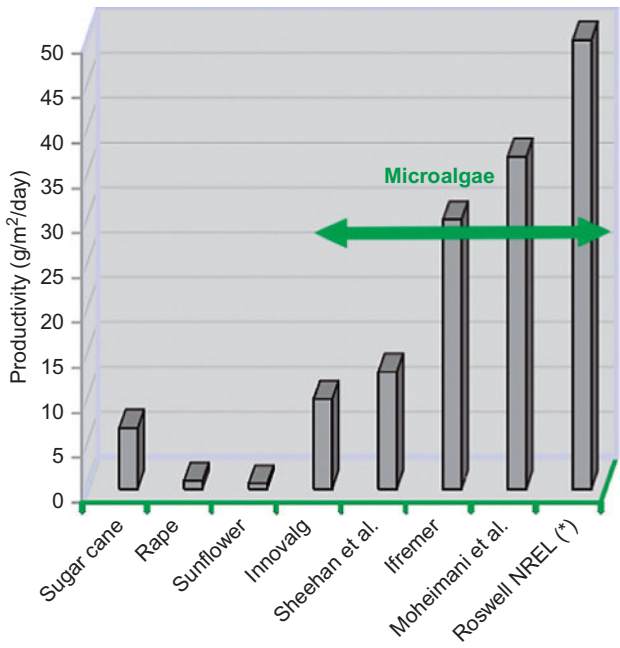


Figure 11.5 Oil productivity of several biomasses.
Adapted with permission from Cadoret and Bernard (2008).

www.EngineeringEBooksPdf.com

Scenedesmus sp. microalgae is made of a fatty acid polymer (algaenans) suspended in a free fatty acid oil (principally palmitic, stearic, oleic, linoleic, and linolenic acids). This lipid fraction appears to be a hot-melted viscoelastic material. The complex modulus norm of microalgae extracts, measured at 1 Hz, is compared to two paving-grade asphalts (Figure 11.6). On the temperature range tested, microalgae lipid extracts show a thermosusceptibility similar to that of asphalt. It seems possible to adjust the rheological properties of the material by tuning the algaenan content. In this way, it might be possible to obtain alternative road binders with the same rheological properties as asphalts.

Hydrothermal liquefaction has also been used to transform microalgae biomass into biobinder (Queffelec et al., 2014). This process allows the transformation of wet biomass, avoiding a drying step, and consequently permits energy saving. Half of the total biomass can be converted by the thermochemical process into an oily hydrophobic phase (Figure 11.7). The rheology of the hydrophobic phase depends on the liquefaction-operating conditions and in some cases can be comparable to conventional bitumen. Even if the concept of producing this type of biobinder has been verified, it has not yet been tested in a full-scale experiment.

Nevertheless, mixes prepared from this hydrophobic phase in the lab show promising behavior. For example, isotherms of the complex modulus at 15 °C of two stone mastic asphalt (SMA) mixes, prepared with conventional bitumen and with the hydrophobic phase from hydrothermal liquefaction (algae binder), are presented in Figure 11.8. In this example, the modulus and the phase angle appear to be in different domains, but describe the same trend in black space. It suggests that the algae binder has a lower penetration grade than the 50/70 used as the bitumen reference. It also means that it would

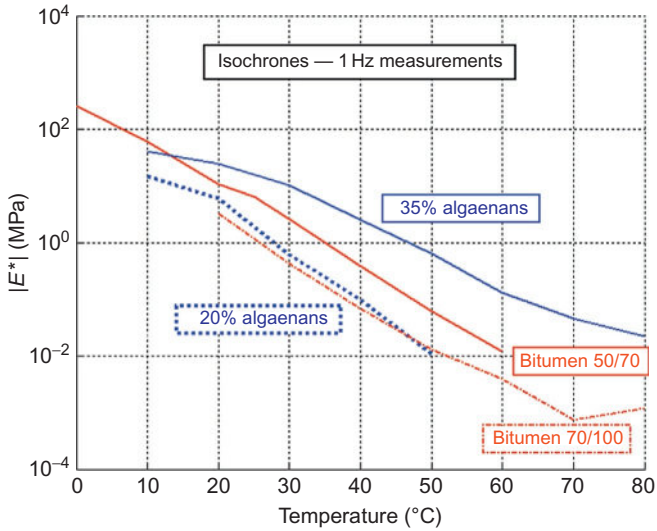


Figure 11.6 Rheological comparison between microalgae extracts and bitumen (Audo et al., 2012).

www.EngineeringEBooksPdf.com



Figure 11.7 Hydrophobic fraction after hydrothermal liquefaction on microalgae.

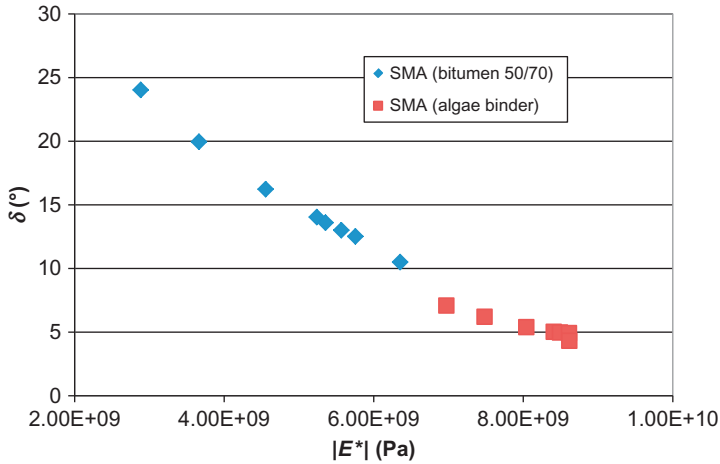


Figure 11.8 Complex modulus at 15 °C, from 1 to 100 Hz, measured on SMA mixes made of a conventional bitumen and an algae binder, plotted in a black diagram.

be possible to adjust the algae binder rheology by modifying the hydrothermal liquefaction parameters in order to obtain the same behavior as that of conventional bitumen. The other important observation concerns the behavior of the SMA mix made of algae binder during aging (Figures 11.9 and 11.10). SMA mixes were exposed to ultraviolet (UV) (60 W/m^2) and air flux at 60 °C during 600 h. The norm of the complex modulus (at 15 °C, 1 Hz) of the algae binder mix appears to be relatively stable in comparison to that of the conventional mix. The relative evolution of the phase angle measured on the algae binder mix is more pronounced than the norm of the complex modulus but remains below the evolution of the conventional mix phase angle. This algae binder, aged with the mineral phase, has an interesting behavior, because the complex modulus appears to

www.EngineeringEBooksPdf.com

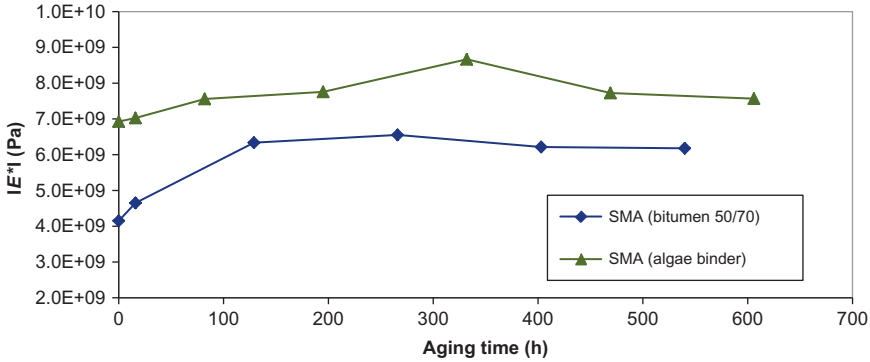


Figure 11.9 Norm of the complex modulus at 15 °C, 1 Hz, measured on SMA mixes made of a conventional bitumen and an algae binder, plotted according to the aging time.

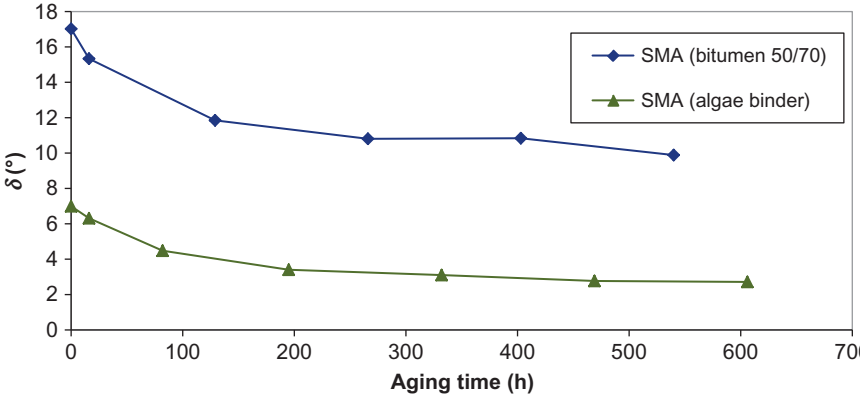


Figure 11.10 Phase angle at 15 °C, 1 Hz, measured on SMA mixes made of a conventional bitumen and an algae binder, plotted according to the aging time.

be stable with time. Of course, the optimization of this alternative material will have to be done. Indeed, it could have a brittle behavior at low temperature, as seen from the phase angle value, which is very low in comparison to the phase angle of the SMA mix made of a conventional 50/70 bitumen.

11.2.3 Binders based on other raw materials

The actual research does not focus exclusively on vegetable oils, and numerous original projects have been recently developed by academic laboratories. In 2008, the University of Picardie patented the development of a binder obtained from protein components and vinegar (or other organic acids from the vegetable world; Université de Picardie Jules Vernes, 2008). Dissolving proteinaceous material in acidic

www.EngineeringEBooksPdf.com

conditions causes a coagulation of the proteins and a loss in functionality (loose primary structure), leading to the formation of a thermosetting rubber mixture. This invention offers a dramatic advantage because it valorizes an abundant and unused resource, which is hemoglobin. Coming from the slaughtering of animals, the amount of hemoglobin recovered is more than 140,000 t in Germany, 100,000 t in Great Britain, and 80,000 t in France. This concept could certainly be transferred to other protein compounds, such as casein.

In 2010, the Polytechnic National Institute of Toulouse patented a road binder made from cellulosic biomass, the most abundant biomass on Earth (INP de Toulouse, 2010). The principle is the following: an esterification between the alcohols on the glucose units of cellulose and fatty acids has been performed, thus leading to a hydrophobic material (originally, cellulose is hydrophilic), which is required for a road binder (Figure 11.11, Table 11.5). The number of alcohol functions substituted (by glucose unit) and the choice of fatty acids enabled modulation of the rheological properties of the final material.

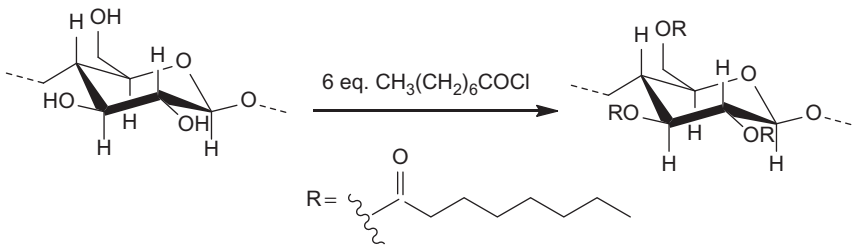


Figure 11.11 Esterification of cellulose by octanoyl chloride, leading to a substitution degree of DS = 3.

11.3 Binder developed for partial replacement

More recently, an American team succeeded in valorizing hog manure by obtaining oil after hydrothermal liquefaction (Fini et al., 2011). This process dovetails perfectly with the American government's environmental policy of tightening its laws about manure from pig farms to avoid overapplication as cheap sources of fertilizer or accidental spills in the environment. The potential of this biooil was studied as an additive for bitumen 50/70, with various concentrations of 2%, 5%, and 10%. The study showed that adding the biooil into the bitumen led to a decrease of the viscosity, which is particularly important as the concentration of biooil increases, resulting in a decrease of the compaction and mixing temperature. Moreover, adhesion properties of the modified bitumen seemed improved in comparison with those of conventional bitumen.

Other thermochemical processes can be applied to biomass, such as pyrolysis (a process where the dried biomass is decomposed in a few seconds without oxygen, within a temperature range of 500–1000 °C, and heating rates of 1000 °C/min), which

www.EngineeringEBooksPdf.com

Table 11.5 Summary of the nonindustrialized alternative binders for road application

Raw material	Technique	Remarks	Reference
Hemoglobin	Chemical denaturation with organic acid	Modification is possible with vegetable oil	de Picardie Jules Verne (2008)
Cellulosic biomass	Esterification by fatty acid chloride	Rheology depends on the fatty acid and the substitution	INP de Toulouse (2010)
Swine manure	Hydrothermal liquefaction	Use as an additive in bitumen	Fini et al. (2011)
Woody biomass	Fast pyrolysis	Modifications are possible by adding polymers or use as additive in bitumen	Williams et al. (2011)

has been applied mostly to woody biomass (Williams et al., 2011). The oil obtained after pyrolysis can be used directly as a binder, it can be modified by a synthetic polymer, or it can be used in a mixture with conventional bitumen (Table 11.5).

11.4 Vegetable fluxes and surfactants

Vegetable resources have mostly been used to produce fluxes, which reduce binder viscosity and improve the workability of mixes. Fluxes usually come from petroleum oil or coal. After laying the mix, volatile components evaporate, leading to an increase of the hardness of the binder. But these vapors are potentially dangerous for workers. Alternative fluxes, developed to circumvent this problem, are mostly composed of fatty acid esters. In 1997, the SAADA company provided Bioflux®, which is composed mainly of fatty acid methyl esters, produced by transesterification of vegetable oils. Metallic salts like cobalt, manganese, and zirconium were added in order to catalyze the polymerization reaction taking place between the ester chains and oxygen (Figure 11.12).

In this case, hardening of the binder is the consequence of a chemical reaction and not an evaporation (SAADA, 1997), which is interesting from an environmental point of view, because there are no emissions of organic volatile compounds. In 2001, Oléoroute (cofunded by Appia, now Eiffage) commercialized a similar product called Oléoflux 18®, produced by the transesterification of sunflower oil.

Some years later, a patent from Colas was published (Colas, 2004b). Partially unsaturated, natural fatty material was used. About 15% of these unsaturations were functionalized with oxygenated functions: ether, epoxy, or anhydride maleic. These chemical groups have the possibility of reacting with some molecules present in the bitumen in order to get the expected rheology.

www.EngineeringEBooksPdf.com

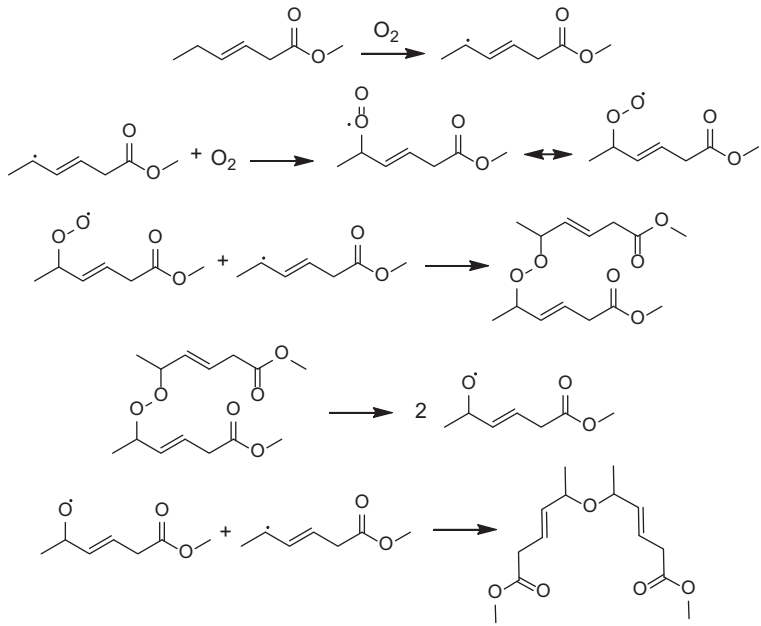


Figure 11.12 Polymerization reaction of methyl hexanoate with oxygen.

Recently, the Valagro company proposed to use fatty acid esters or diesters and polyglycerol as surfactants to produce emulsified bitumen or other hydrocarbon binders (Valagro, 2011).

11.5 General remarks about alternative binder development

Various experiences in the development of alternative binders showed that some properties have to be reinforced. Indeed, in order to have at least the same potential durability as conventional bitumen, efforts must be made to improve these new materials for road application. Generally, the oxygen content inside binder extracted from biomass is high in comparison to that of usual bitumen. This leads to a higher sensitivity to oxidation mechanisms, also favored by the presence of unsaturated chemical links (derived from fatty acids). The consequence for mechanical properties is a loss of viscous properties, with the material finally evolving toward a more brittle state. Further developments need to address this point by working on thermochemical processes that reduce oxygen content, or on special additives able to inhibit oxidation or polymerization mechanisms. Moreover, conventional bitumen came from a distillation process carried out at high temperature (~350 °C) under vacuum. This means that bitumen can be considered a nonvolatile material at manufacturing temperature

www.EngineeringEBooksPdf.com

(∼160 °C) and at service temperature (up to 60 °C). Considering the manufacturing processes used to produce the alternative binders presented in this chapter, the probability of having volatile components is high and could partially explain the instability in time that has been observed. To improve alternative solutions, new materials will have to be developed in order to reduce volatile components by using, for example, a final distillation process. One idea could be also to work on the reduction of manufacturing temperature by using emulsified alternative binders. In that regard, in the future, it will be very important to prove that alternative binders are safe for workers to handle, and safe for the environment. Fume emission measurements will have to be carried out, and the impact on aqueous species will have to be assessed. Finally, it is interesting to imagine that in the next generation, alternative binders might be developed to facilitate recycling, using the existing bitumen mixed with renewable materials.

11.6 Conclusions

Currently, many alternatives to bitumen have been proposed. However, they are not all industrialized yet, because an optimal alternative road binder must satisfy several criteria, which are sometimes difficult to combine:

- Properties similar to petroleum bitumen,
- Viscoelasticity,
- The use of crops that do not compete with human feeding production,
- A production cost competitive with that of petroleum binders.

The most advanced field experiences, mainly in France, show that it is possible to totally replace conventional bitumen with a material made of vegetable oil and a coproduct from the wood industry (especially rosin). Nevertheless, evolution of this type of material with time is not fully understood. In comparison to conventional mixes, mechanical properties of these vegetable mixes, which are initially viscoelastic thermodependent, tend to be purely elastic.

Research should now focus on new production technologies, but also, and above all, on new raw material sources. Indeed, vegetable binders that are actually marketed are based on the edible oil. In the biofuel areas, news and pressure caused by the recent turmoil in the food market have shown the disastrous implications of the use of edible oils. It seems very difficult to reconcile global industrialization with the use of food resources.

Research on new biomasses that do not compete with human feeding production is actually under intense development. Interesting work has been done based on the microalgae, which seems to be a promising biomass source in the future. It offers the most credible alternative to petroleum fuels, and it has been proven that it could also be used to produce a biobinder. Also, very interesting studies in the United States dealing with the hydrothermal liquefaction of swine manure have been published. In the near future, this could be a response to environmental issues of animal husbandry as well as partial bitumen replacement.

www.EngineeringEBooksPdf.com

References

Audo, et al., 2012. Relationship between microalgae lipid extracts composition and rheological properties. In: ISAP.

Ballie, M., Poirier, J.-E., Delcroix, T., 2004. Vers une nouvelle route ? Végécol, une gamme de liants végétaux pour enrobés et revêtements esthétiques. RGRA n°834, December 2004.

Cadoret, J.-P., Bernard, O., 2008. La production de biocarburant lipidique avec des microalgues: promesses et défis. J. Soc. Biol. 202 (3), 201–211.

Colas, 2004a. Liant de nature végétale pour la réalisation de matériaux pour le bâtiment et/ou les travaux publics. EP1466878 (A1).

Colas, 2004b. Obtention de liants routiers à base de bitume et d'une nouvelle gamme de fluxants d'origine naturelle fonctionnalisés. EP1645595 (A1).

Eiffage, 2007. Composition comprenant une fraction organique pour la réalisation d'une couche et/ou d'un revêtement de voie ou de bâtiment. FR2915204 (A1).

Eurovia, 2010. Liant synthétique essentiellement à base de matières issues de ressources renouvelables, en particulier d'origine végétale, et ses applications en technique routière. FR2955586 (A1).

Fini, E.H., Kalberer, E.W., Shahbazi, A., Basti, M., You, Z., Ozer, H., Aurangzeb, Q., 2011. Chemical characterization of bio-binder from swine manure: a sustainable modifier for asphalt binder. J. Mater. Civ. Eng. 23, 1506–1513.

INP de Toulouse, 2010. Coating material for road construction. WO2010/003838 (A1).

Lavoie, C., 2011. Le bitume: approvisionnement, production et marché. http://www.bitumequebec.ca/assets/application/publications/47481a992acb429_file.pdf.

Lecomte, M., Nadjar, H., Poncelet, K., 2009. Développement d'un nouveau liant clair issu de ressources végétales renouvelables pour enrobés colorés. Congrès belge de la Route, Gand (Belgique).

Pinomaa, O., 1991. Dyeable pavement material. US5021476 (A).

Pouget, S., Loup, F., 2013. Thermo-mechanical behavior of mixtures containing biobinders. Road Mater. Pavement Des. 14 (S1), 212–226.

Queffelec, C., Chailleux, E., Audo, M., Paraschiv, M., Legrand, J., Lépine, O., Bujoli, B., 2014. Hydrothermal liquefaction as a route to transform microalgae residues in bio-asphalt. In: ALG'N'CHEM, Poster, Montpellier, March 31–April 3.

SAADA, 1997. Liant bitumineux, composition et utilisation. FR2768150 (A1).

Shell, 2010. Binder composition and asphalt mixture. WO2010128105 (A1).

Trigallez, J., Ballie, M., Delcroix, T., 2009. Liant innovant d'origine végétale pour enrobés routiers et revêtements de voirie. Congrès belge de la Route, Gand (Belgique).

Université de Picardie Jules Vernes, 2008. Procédé de fabrication d'un liant, notamment destiné à l'élaboration et/ou l'enrobage de granulats ou encore entrant dans la composition de matrices pour la fabrication de biocomposites. FR2935375 (A1).

Valagro, 2011. Procédé de préparation d'une composition tensioactive à base de bio-tensioactifs non-ioniques d'origine naturelle. FR2972191 (A1).

Vilchez, C., Garbayo, I., Lobato, M.V., Vega, J.M., 1997. Microalgae-mediated chemicals production and wastes removal. Enzyme Microb. Technol. 20 (8), 562–572.

Williams, C.R., Mohamed Metwally, M.A.R., Brown, R.C., 2011. Bio-oil formulation as an asphalt substitute. WO2011/153152 (A2).

www.EngineeringEBooksPdf.com

Blending of virgin bitumen and RA binder in mixtures with high amounts of RA

12

M. Mohajeri[1,2], *A.A.A. Molenaar*[2], *M.F.C. Van de Ven*[2]
[1]Gebr. Van der Lee contractors, Lelystad, The Netherlands; [2]Delft University of Technology, Delft, The Netherlands

12.1 Introduction

In the Netherlands, hot mix asphalt (HMA) containing high percentages of reclaimed asphalt (RA) are being produced either by a batch plant to which a parallel drum is attached to preheat the RA to approximately 130 °C or by means of a double barrel drum. In the double barrel drum, virgin aggregates (VAs) are preheated in the inner drum and then mixed with moist RA at ambient temperature in an outer drum that is folded around the inner drum. In the outer drum, the virgin fines (filler) and bitumen also are added. Because the mixing temperature is between 160 and 180 °C, the VAs have to be preheated to (very) high temperatures, especially when high RA percentages are used. In the Netherlands, using 50% RA is a common practice for all base, binder, and wearing course mixtures. RA is not allowed in SMA and porous asphalt.

It is not uncommon to preheat the VAs to 320 °C and higher in the double drum mixer to obtain a mixing temperature of 160 °C. Especially when the RA is moist, moisture contents of 5% are not uncommon; even higher preheating temperatures are required.

Also in a batch plant, the VAs are heated to fairly high temperatures even when the RA is preheated in a parallel drum to 130 °C. The VAs should be heated to higher temperatures when larger amounts of RA are used.

It might be very well that the heat transfer between superheated aggregates and binders may locally damage both the RA binder and virgin bitumen (VB). Therefore, it is essential to study the effect of this kind of harsh heat transfer on the binder properties.

The target temperature of the mixture (160–180 °C) is usually achieved by adjusting the preheating temperature of aggregates in both the batch plant and the double drum mixer. However, the first question is whether the superheating of VAs will soften the RA binder enough that RA will coat the VAs before the VB is added. The second question is whether the RA and virgin binder will blend such that a homogeneous binder is obtained.

These two questions initiated the research that is presented in this chapter.

Advances in Asphalt Materials. http://dx.doi.org/10.1016/B978-0-08-100269-8.00012-X
© 2015 Elsevier Ltd. All rights reserved.

www.EngineeringEBooksPdf.com

12.2 Research approach

Being able to answer these questions implies that one is able to determine the amount and characteristics of the binder coating the RA and VAs after mixing. However, the major difficulty in studying the interaction between RA binder and VB is the separation of RA aggregates from VA in the recycled mixture, inasmuch as each aggregate particle is coated with black binder, and the shape of the RA and VA particles is similar.

Because distinction by color differences between aggregates was not applicable, a novel method was devised in this research by using mono-size glass beads (GBs) as artificial aggregates instead of real aggregates. RA could then be separated from VA because of different shapes and sizes. It will be shown that a combination of GB and RA was a good representation of a real mixture.

Three mixture combinations were designed to study the effect of superheating in HMA recycling by replacing real stone aggregates with GBs. They will be explained in detail in one of the next sections.

Also, an aging method is adopted to create artificial RA binder. This method is using the rotating cylinder aging test (RCAT). First, two grades of bitumen were aged using different aging periods. Second, their chemical and physical properties were determined. The properties of the aged binder were compared with those of real RA binder. Then, a decision was made on choosing the aging protocol.

Once artificial RA aggregates are separated from VAs, their binders have to be extracted for further analysis. In the case of real mixtures, a centrifugal extraction method along with a rotary evaporation setup is used to obtain sufficient amount of binder for analysis. However, current extraction and recovery setups are not suitable if small amounts of bitumen have to be recovered. Therefore, the commonly used extraction and recovery method had to be adapted. A simple extraction and recovery method was devised based on solvent extraction and cabinet evaporation. The efficiency of extraction and recovery was also investigated.

Different layers of binders around aggregates were assumed to be present. This assumption was based on results reported by Noureldin and Wood (1989) and Huang et al. (1929), which will be discussed later. Inspired by their work, the effectiveness of separating the bituminous coating of aggregate particles into different layers was examined. If a layered system indeed appears to exist, then it should be determined how mixing of superheated aggregates with cold RA affects the binder properties of the different layers, and if it is affecting the blending efficiency.

The following actions were therefore undertaken:

- An aging protocol was adopted.
- An extraction and recovery method was developed.
- The effectiveness and usefulness of a stage extraction method based on soaking in solvent was evaluated.
- Three types of mixtures were produced.
- Rheological and chemical properties of binders were compared.

www.EngineeringEBooksPdf.com

12.3 Mixtures

In this study, three mixtures were tested; they are briefly described hereafter.

12.3.1 Mixture 1

GBs of 5 mm (GB5) were coated with aged binder to create artificial RA. No filler was used in this mixture because experience has shown that there is always a chance that some filler traces might be present in the recovered binder. Presence of filler would of course have an effect on the outcomes of the test to be performed on the recovered binder. GBs of 8 mm (GB8) were used to represent the VA in this mixture type. First, GB8 was superheated to 300 and 400 °C prior to mixing with GB5. Second, 50% (by mass) of superheated GB8 was mixed within 30 s with 50% (by mass) of precoated GB5. These two temperatures were selected to study the effect of temperature. Mixture 1 is identified in this chapter by "300–" and "400–." The workflow in preparing mixture 1 is illustrated in Figure 12.1.

12.3.2 Mixture 2

Similar combinations of GB sizes, percentage, and temperatures were used once again. The only difference was that 1% VB was also added during mixing. Mixture 2 is identified by "300+" and "400+." The plus sign indicates the addition of VB,

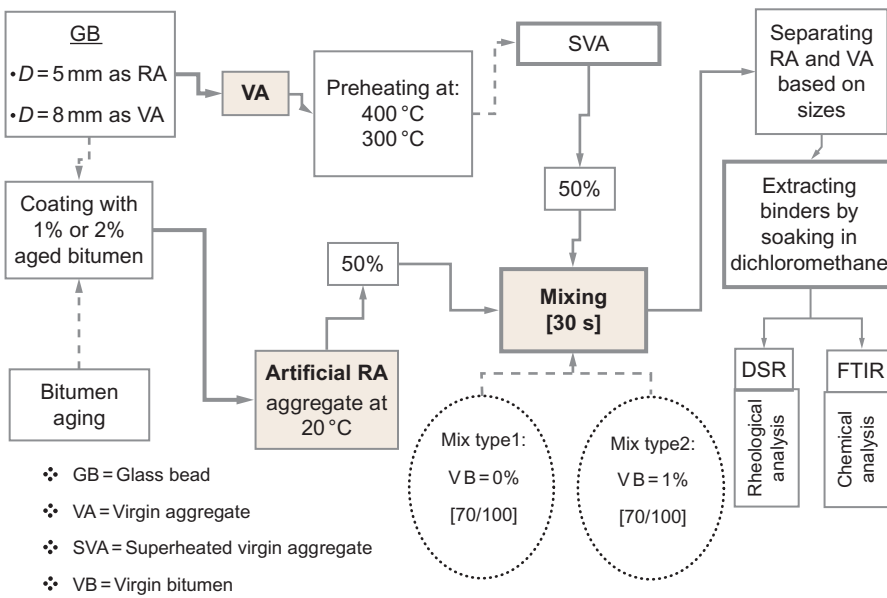


Figure 12.1 Experimental plan for mixtures 1 and 2.

www.EngineeringEBooksPdf.com

while the minus sign used in indicating the two mixture 1 types implicates no addition of bitumen. The workflow of the experiments on mixture 2 is also illustrated in Figure 12.1.

12.3.3 Mixture 3

A real asphalt mixture was produced with 50% real RA. Only VAs were replaced by GBs of different sizes. Filler, sands, and VB were added following the procedure described in the Dutch standard. GB sizes to be used were determined with respect to mixture gradation requirements. GBs were superheated to 515 °C prior to mixing; the real RA contained 4% moisture. The mixing time was set to 30 s. Figure 12.2 shows the workflow for preparing this mixture.

12.4 Materials and processes

As noted, artificial materials (GB and aged bitumen) were used to simulate real aggregates and RA binder. The material properties and preparation procedure will be discussed in this section.

Three preliminary studies were required before conducting the main study on the effect of superheating. As noted earlier, first, the effectiveness and usefulness of stage extraction by soaking bituminous material in a solvent had to be investigated. Second, a convenient binder extraction and recovery method had to be developed. Third, an

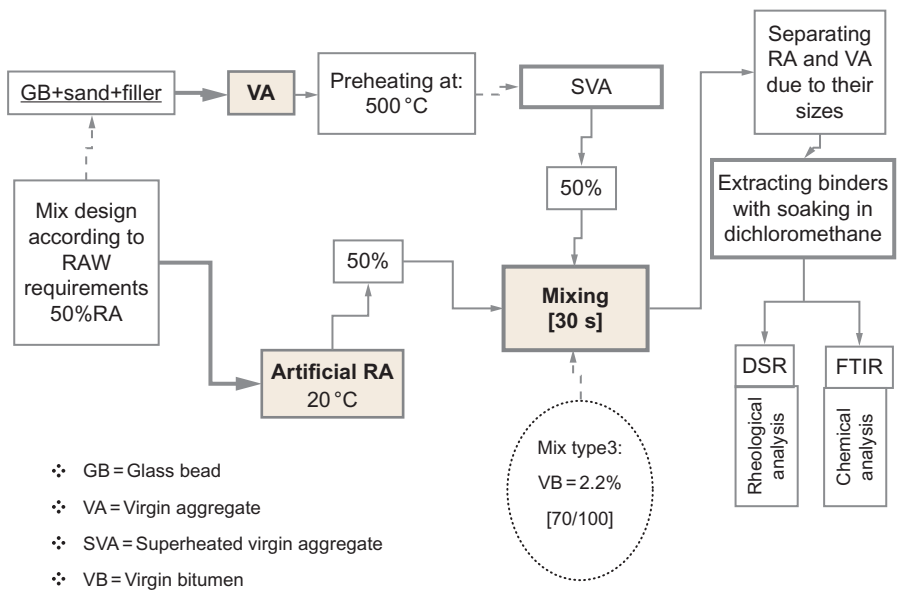


Figure 12.2 Mixing process of mixture 3.

www.EngineeringEBooksPdf.com

appropriate aging protocol had to be established to obtain an artificial aged binder with properties as close as possible to those of a real RA binder.

This section will focus on developing these three processes as well as other material preparation techniques. The mixture designs, mixing process, and sample preparation will be discussed here as well.

12.4.1 Developing an extraction and recovery method

In HMA recycling studies, binder extraction and recovery are essential processes in regaining the binder from RA. The binder is primarily needed for rheological analysis prior to designing a mixture. In addition, the chemical composition of RA binder or any aged binder would be required for studying the effect of aging on the original binder. Extraction was first done by soaking an AC mixture into a solvent, dichloromethane CH_2Cl_2, at ambient temperature to separate aggregate, sand, and filler from the binder. Second, the mineral fraction was separated from the binder solution in a centrifuge. These two steps of extraction are commonly practiced in the Netherlands according to *NEN 3971(1991): Recovery of bitumen from asphalt for qualitative testing purposes*. The bitumen solution is usually brought to a rotary evaporation system to separate the solvent at a rather high temperature according to EN12697-3.

These extraction and recovery setups are not suitable when small amounts of bitumen must be recovered, as is the case in this study. Therefore, another extraction and recovery method had to be developed.

The newly developed method is based on solvent extraction and cabinet evaporation. The efficiency of extraction and recovery was also investigated. The method used here is referred to as the solution spreading extraction method (SSEM):

- First, a small amount of aggregate (about 50 g) is washed manually in dichloromethane by agitating with a spatula for half an hour. One hundred milliliters of solvent is usually sufficient to get the aggregates clean. Because the main goal is to get only sufficient binder for dynamic shear rheometer (DSR) and FTIR tests, it was not really necessary to obtain thoroughly cleaned aggregate particles.
- Second, the filler is separated in a desk centrifuge in the laboratory. The solution is filtered with a microfilter (0.6 μm), and centrifuging is done at 3700 rpm for 30 min.
- Third, the solution is gently taken from the centrifuge container with special care to avoid remixing it with filler sediment.
- The residual solution is spread on a surface of silicon paper with dimension of 25×25 cm^2 to facilitate the evaporation of solvent at ambient temperature in a vacuum cabinet.
- After 24 h, the residual thin film of binder is brought into an oven at 50 °C for 3 h to ensure thorough evaporation of the solvent.

The experiment plan related to this preliminary study is shown in Figure 12.3.

- Two binders were tested: 70/100 VB (A1) (3.66 g) + filler Wigro (4 g) + 100 ml dichloromethane.
- RCAT 163 °C–24 h aged 70/100 bitumen (4.0 g) + filler Wigro (4 g) + 100 ml dichloromethane.

www.EngineeringEBooksPdf.com

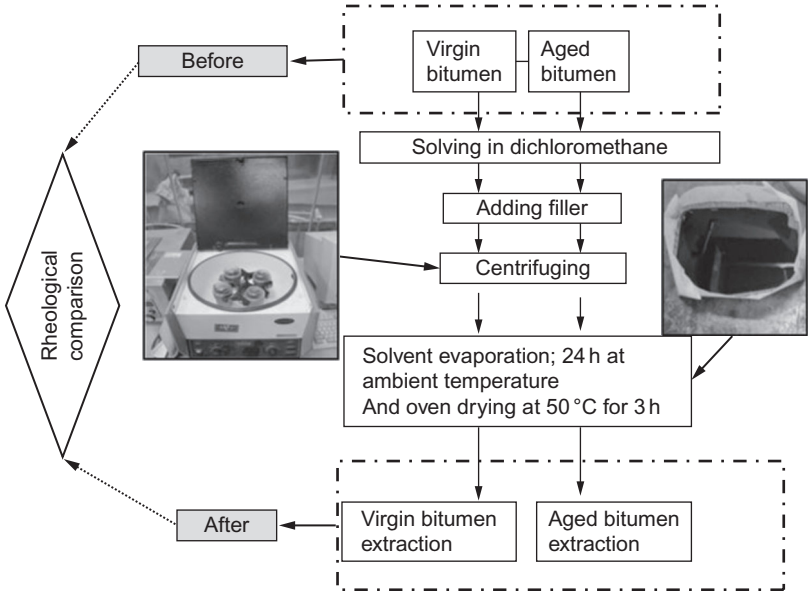


Figure 12.3 Solution spreading extraction method (SSEM).

After binder recovery, they were tested in a DSR to compare the properties of the extracted binder (from SSEM) with the properties of the original bitumen. The DSR was conducted with a parallel plate geometry, using plates with a diameter of 25 mm and a 1-mm thick layer of binder in between.

Master curves for the complex shear modulus G^* were developed, and these are shown in Figure 12.4; G^* values at 20 °C and various frequencies are also shown

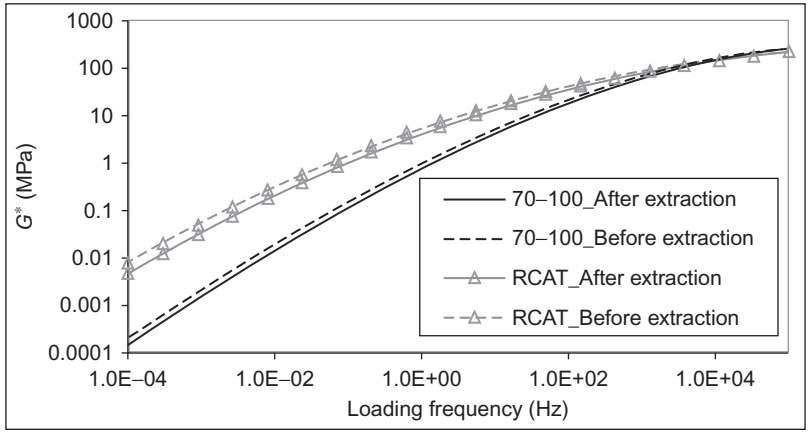


Figure 12.4 Comparison of G^* master curves (at 20 °C) before and after extraction following SSEM.

www.EngineeringEBooksPdf.com

Table 12.1 Decrease in G^* values after extraction following SSEM

Frequency	0.1 Hz	1 Hz	10 Hz	20 Hz	100 Hz
RCAT_Before extraction (GPa)	1.46	5.47	16.52	22.13	40.76
RCAT_After extraction (GPa)	1.10	4.42	14.27	19.46	37.20
Decrease in G^* value	**−25%**	**−19%**	**−14%**	**−12%**	**−9%**
70/100_Before extraction (GPa)	0.15	1.01	5.37	8.43	21.75
70/100_After extraction (GPa)	0.11	0.78	4.33	6.89	18.36
Decrease in G^* value	**−24%**	**−22%**	**−19%**	**−18%**	**−16%**

in Table 12.1. It turns out that the shear modulus of the binder extracted by SSEM is in reasonable agreement with that of the original binder. Nevertheless, the G^* values are slightly lower after SSEM. This reduction might be because small amounts of solvent are still left in the binder. The reduction of 10–20% in G^* values appeared to be valid for both the aged and VB.

12.5 Stage extraction

12.5.1 Background

Stage extraction has been practiced since 1980 by a number of researchers (Noureldin and Wood, 1989; Huang et al., 1929). It is a process of extracting binder from RA particles, layer by layer. It is repeatedly assumed that if an RA aggregate is soaked in a solvent for given periods, the recovered binder corresponding to each soaking time represents a layer of bitumen.

Noureldin and Wood (1989) conducted a test on a recycled mixture by applying a rejuvenator on RA aggregates. They soaked RA aggregates in a solvent and took four binder solutions. After recovery of the binder from each solution, they measured its penetration and viscosity. The penetration test results of the four imaginary layers are shown in Figure 12.5.

They concluded that the outer microlayers around RA aggregates are stiffer than the inside layers because of the exposure to oxidation. They believed that the very inner layer is slightly harder because of the absorption of light fractions by the stone. After treating the RA with a rejuvenating product, the outer layers became significantly softer.

A similar concept was used by Huang et al. (1929) to extract four layers of binder (Figure 12.6). After conducting DSR tests, they claimed that the inner layers are stiffer than the outer layers (Figure 12.7), implying that inner layers are RA binders that are not completely blended with the added VB.

www.EngineeringEBooksPdf.com

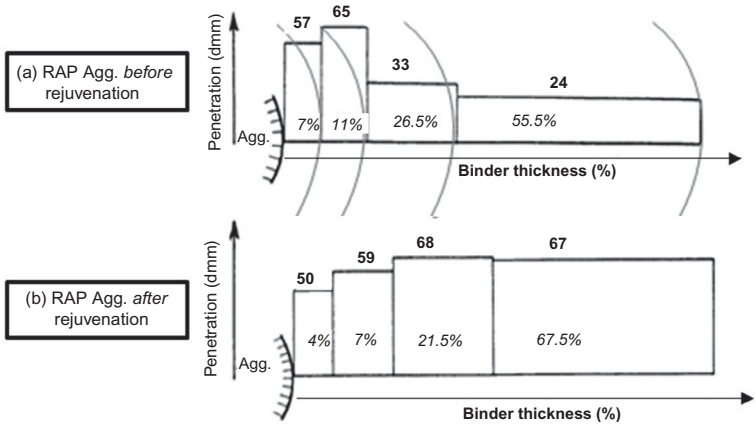


Figure 12.5 Penetration results of imaginary layers on reclaimed asphalt pavement (RAP) and rejuvenated RAP by Noureldin and Wood (1989).

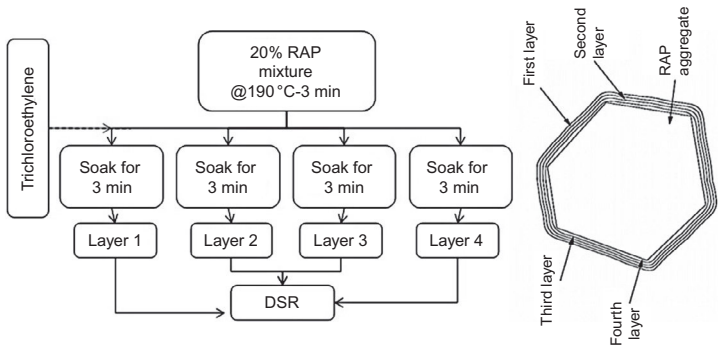


Figure 12.6 Process of stage extraction, according to Huang et al. (1929).

In both studies, only one variable was taken into account: soaking time. Then, it was assumed that the solvent would take an equal amount of binder from every aggregate particle. As will be shown hereafter, this assumption is only true if all the aggregate particles have the same size, whereas the aggregate sizes in the mentioned experiments ranged from 20 to 20,000 μm. It will be shown hereafter that the aggregate sizes have to be taken into account as an extra variable.

A test program was therefore conducted here to examine the appropriateness of the stage extraction method by including aggregate size as an extra variable.

www.EngineeringEBooksPdf.com

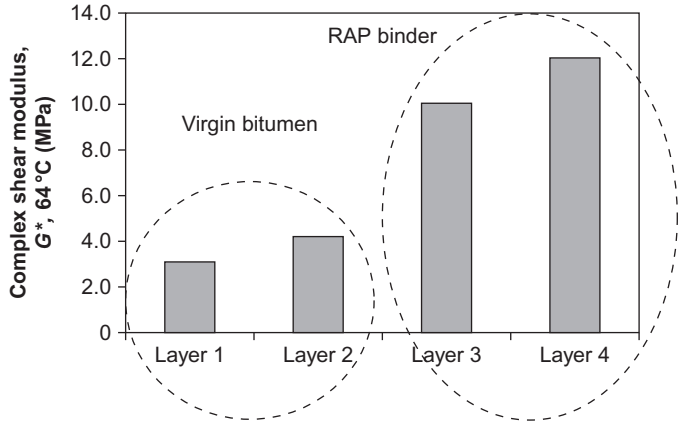


Figure 12.7 G^* values of imaginary layers of bitumen, according to Huang et al. (1929).

12.5.2 Extraction test at two layers

One hundred fifty grams of RA aggregates were screened into three fractions of 0–2, 2–5, and 5–11 mm. Then, each fraction was soaked in 50 ml dichloromethane for 5 min at room temperature (see Figure 12.8). The first binder solution was poured and stored in a separate container. The remaining aggregates were thoroughly washed with another 50 ml dichloromethane until the aggregates became apparently clean. The first and second solutions were centrifuged for 30 min at a speed of 370 rpm to separate the fillers. After filtration, both solutions were recovered following the SSEM.

The recovered binders were tested with the DSR to measure G^* values at different temperatures and frequencies. The results are shown in Figure 12.9.

According to this figure, the effect of the two variables, being the size of the aggregates and the imaginary layers, is considerable. The figure shows that the second extractions are slightly softer than the first ones. However, in the fraction of 2–5 mm, they are almost equal.

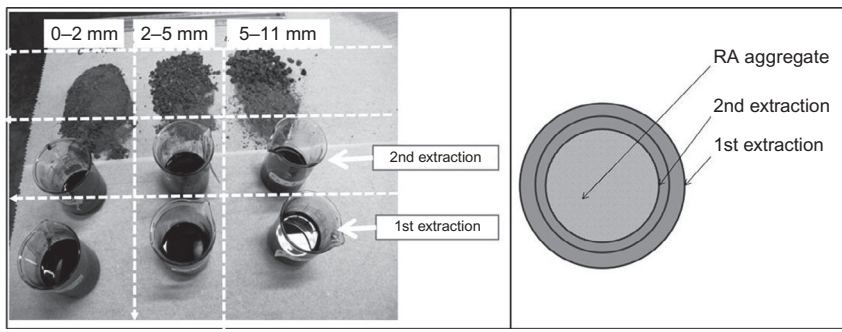
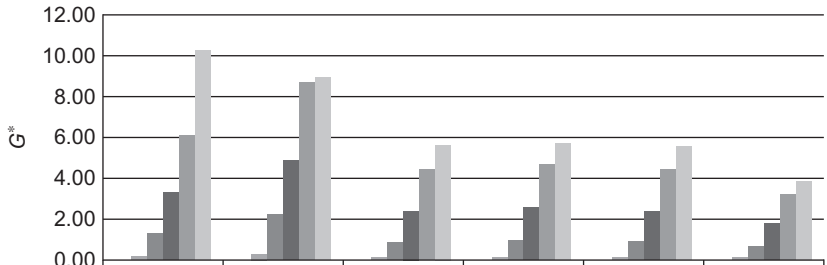


Figure 12.8 Extracting binder at two imaginary layers from different sizes of RA.

www.EngineeringEBooksPdf.com



	0–2 mm first extraction	0–2 mm second extraction	2–5 mm first extraction	2–5 mm second extraction	8–11 mm first extraction	8–11 mm second extraction
0.001 Hz	0.032	0.048	0.017	0.023	0.020	0.016
0.01 Hz	0.218	0.326	0.135	0.166	0.152	0.115
0.1 Hz	1.312	2.225	0.864	0.982	0.904	0.668
1 Hz	3.301	4.886	2.404	2.595	2.430	1.780
4 Hz	6.097	8.714	4.430	4.684	4.446	3.241
10	10.269	8.901	5.650	5.694	5.547	3.818

Figure 12.9 G^* values of imaginary layers around different aggregate sizes at the reference temperature of 25 °C.

Therefore, it could be concluded that aggregate size may influence the properties of their binder films, inasmuch as finer sizes cause more aging of the binder.

There are a number of differences between fine and coarse aggregates that could affect the aging of their film binder:

- The larger surface area of fine aggregates provides more surface for short-term aging (STA).
- The difference in absorption properties of fine and coarse aggregates.

Visual observation during manual washing of the aggregates revealed the fact that not every aggregate size loses its binder at the same time, inasmuch as it took the finer fraction (0–2 mm) almost twice the time as the coarser fractions to get thoroughly cleaned. This is most probably because of the different binder contents of each aggregate size, due to their specific surface (see also Table 12.2). Also, differences in texture and surface polarity between the coarse and fine aggregates might have had an influence.

Table 12.2 Extracted RA binder properties

Property	Unit	
Penetration @ 25 °C (# @15 °C)	0.1 mm	21
Softening point $T_{R\&B}$	°C	59
Penetration index	()	−0.8
Density, 25 °C	kg/m^3	1035

www.EngineeringEBooksPdf.com

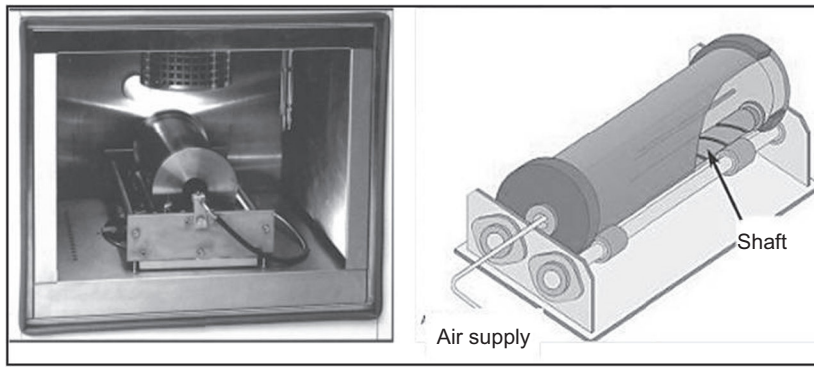


Figure 12.10 Rotating cylinder aging test (RCAT) (den Berg, 2011).

The main conclusion is that a number of factors influence the properties of the binder recovered at different stages (as experienced in previous studies). Although binder properties of extracted binders at different stages were different, the assumption of detecting different binders by stage extraction is debatable, especially when the extraction is performed on a mixture that contains different aggregate sizes.

12.6 Materials

12.6.1 Artificial RA binder

To make artificial RA binder (for GB coating), an STA method and long-term aging (LTA) method had to be adopted. According to the European norm, there are mainly three methods available for accelerated bitumen aging: RTFOT,[1] PAV,[2] and RCAT.[3] A summary of these aging testing methods is made by Hagos (2008).

12.6.1.1 The rotating cylinder aging test

The RCAT accelerated aging method was developed by the Belgian Road Research Center (BRRC) to simulate both STA and LTA of bitumen. This method is suitable to age considerable amounts of bitumen (500 g) to be used in further studies.

The method consists of an oven for temperature control, a steel cylinder, and a rotating system to maintain constant rotation of the horizontally placed cylinder. A stainless steel roller is also freely rotating inside the cylinder to keep the film thickness constant. A constant flow of air or oxygen is blown into the rotating cylinder to accelerate the aging process (see Figure 12.10).

[1] Rolling thin-film oven test.

[2] Pressure aging vessel [EN 14769].

[3] Rotating cylinder aging test [EN 15325].

www.EngineeringEBooksPdf.com

In this study, the available RCAT oven in the laboratory was not equipped with an oxygen supply, and therefore air was used in the process at a flow rate of 4.5 l/h. The STA and LTA were done together, using one temperature (163 °C) for a total duration of 24 h. The development of aging was monitored by taking samples at 0, 4, 8, and 24 h. These samples were used for penetration, $T_{R\&B}$, FTIR, and DSR tests to study the progress of aging during the RCAT test. The results were compared with those obtained on a real RA binder, which was taken as a reference.

Two grades of bitumen were used in this study: Q8 70/100 and Q8 40/60. The test program is shown in Figure 12.11.

A summary of the initially measured properties of the extracted RA binder is listed in Table 12.2.

12.6.1.2 Rheological evaluation of aged binders

As mentioned earlier, penetration and softening-point tests were carried out to determine the change of these rheological parameters as a function of aging time. The results are shown in Figure 12.12.

A DSR (AR2000ex) was used in the research to measure the complex shear modulus (G^*) and the phase angle (δ) between shear stress and shear strain. The machine has a torque capacity of 0.2 Nm and is equipped with an environmental test chamber. G^* and δ values are measured at different temperatures and loading frequencies. The results were used to create master curves of the shear modulus (G^*) and phase angle (δ).

The master curves of the aged binders along with the VB are illustrated in Figures 12.13 and 12.14, respectively. DSR measurement results of a real RA binder are illustrated in both charts to facilitate the comparison of artificial aged binders with

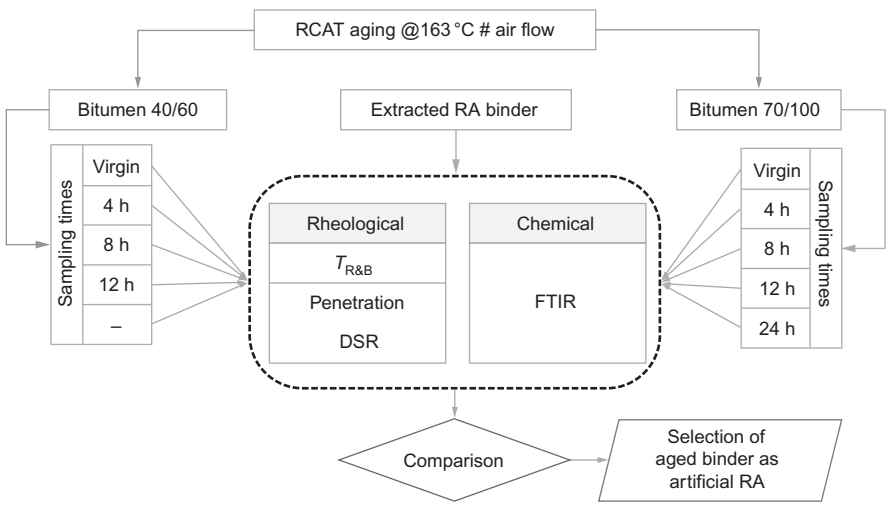


Figure 12.11 Process of selecting an artificial RA binder.

www.EngineeringEBooksPdf.com

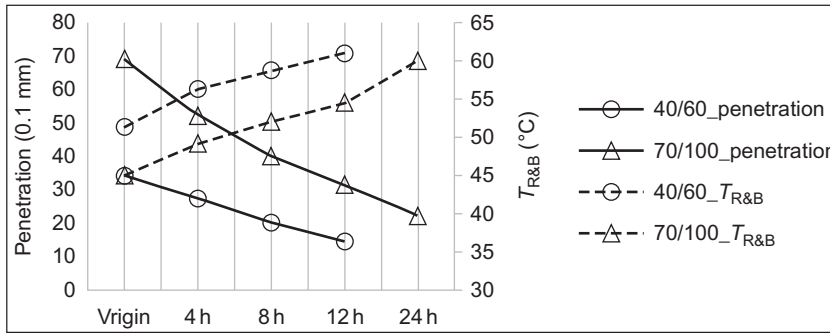


Figure 12.12 Penetration results at 25 °C and softening points ($T_{R\&B}$) of binders aged with RCAT at 163 °C.

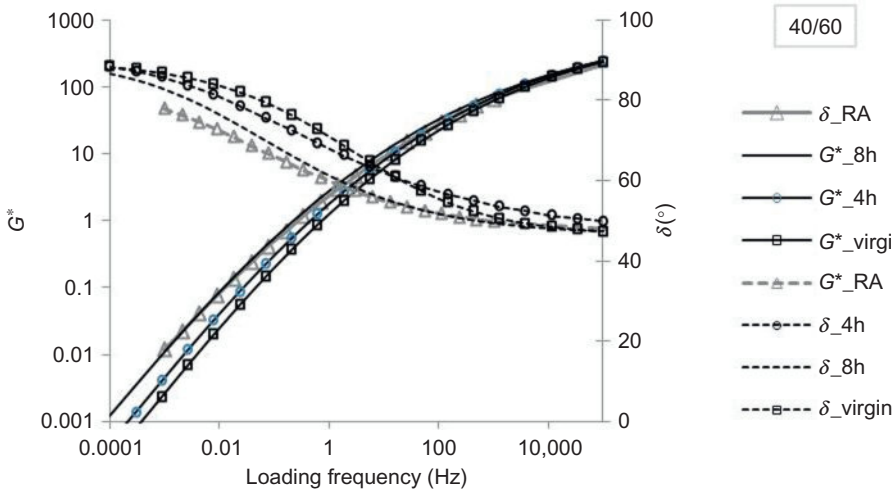


Figure 12.13 DSR master curves at 20 °C on RCAT aging of 70/100 bitumen.

a real RA binder. It turned out that RCAT aging of 70/100 bitumen at 163 °C and 24 h produces a binder that is closest to the real RA binder.

12.6.2 Glass beads

GBs are widely used in industry and research. In industry, they are mainly used for blasting surfaces. In research, they are used in simulating particle flow in industrial processes. They are available in different sizes and even in microscales. Their sizes are very precise.

As mentioned before, the regular size and shape of GBs were the reason for using them in this study. However, the smooth surface of GBs is a critical drawback in comparison with the natural, usually rough, surface of normal aggregates.

www.EngineeringEBooksPdf.com

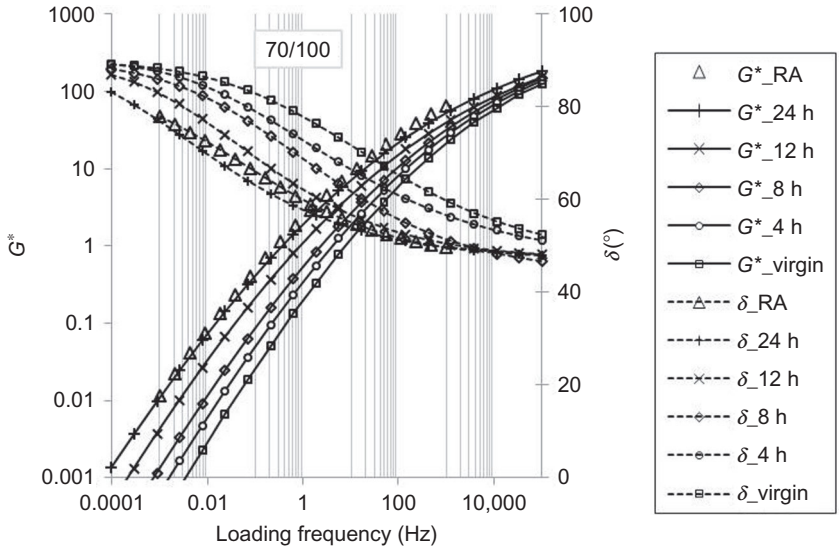


Figure 12.14 DSR master curves at 20 °C on RCAT aging of 40/60 bitumen.

In this research, GBs of different sizes were used to simulate RA and VA. Two available sizes of borosilicate GBs were used in mixtures 1 and 2: 5 and 8 mm. In mixture 3, other sizes (i.e., 13 and 20 mm) were used as well. They are identified as GB5, GB8, GB13, and GB20.

The GBs used in this research contain primarily silica and boron oxide, which makes them more resistant to thermal shocks than any other common glasses. Table 12.3 shows the comparison between the chemical and physical properties of borosilicate GBs and granite stones.

The volumetric properties of GB5 and GB8 are presented in Table 12.4. The volumetric properties are needed to determine the required amount of binder to achieve the intended film thickness. The weight of the particles of each size was calculated by

Table 12.3 Chemical land physical properties of borosilicate and granite stone

	Borosilicate GB		Granite stone	
Chemical composition	**SiO_2** **B_2O_3** **Na_2O**	**81.20%** **12.40%** **2.93%**	**SiO_2** **Al_2O_3** **K_2O**	**72%** **14%** **4%**
Coefficient of thermal expansion	3×10^{-6}/°C at 20 °C		5×10^{-6}/°C at 20 °C	
Thermal conductivity	1.2–1.4 W/(m · K)		1.73–3.98 W/(m · K)	
Melting point	1600 °C		1215–1260 °C	
Density	2.23 kg/m^3		2.70 kg/m^3	

www.EngineeringEBooksPdf.com

Table 12.4 Glass bead properties and bitumen mass required to obtain intended film thickness around the GB particles

Volumetric property of GB	Unit	GB5	GB8
Specific density	kg/mm^3	2.23×10^{-6}	2.23×10^{-6}
Diameter ($2r$)	mm	5	8
Surface area ($4\pi r^2$)	mm^2	78.5	201.1
Volume ($4\pi r^3/3$)	mm^3	65.4	267.9
Mass (kg)	kg	1.46E − 4	5.98E − 4
No. of particles in 1 kg aggregate	1/kg	6855	1674
Total surface area of 1 kg aggregate	mm^2/kg	538,117	336,323
Coating per 1.0 (% m/m) bitumen	μm	18	29

dividing the weight of a number of beads by that number. It turns out that 1% mass ratio of bitumen to GB results in 18 μm coating on 1000 g of 5 mm beads. Therefore, a mass ratio of bitumen to GB of 2% is needed to achieve 36 μm film thicknesses. The 36 μm film thickness was selected because this formed a stable bitumen coating around GBs. This percentage was used later to prepare artificial RA with 5 mm beads and aged bitumen.

12.6.3 Mixtures

As mentioned before, three mixtures had to be prepared in the laboratory with artificial aggregates. The mixing procedure of each mixture type is explained hereafter.

12.6.3.1 Mixture 1

In these mixtures, GB5 had to be covered with 2% (by weight) aged bitumen (RCAT163 °C_70/100@24 h), which was chosen during the preliminary aging tests discussed earlier. Two kilograms of GB5 was premixed with 2% aged binder at 150 °C to prepare the artificial RA. A Hobart pan mixer with a spiral dough hook (see Figure 12.15) was used to coat GB5 with aged binder within 3 min to ensure a homogenous coating. Because pure bitumen was used without any filler, it was important to carefully clean all mixing equipment prior to any mixing.

The precoated GB5 was cooled down with a fan ventilator while it was spread on silicone paper on a table. After cooling using a fan ventilator for 1 h, the mixture was stored for 3 h at room temperature (23 °C) and 24 h in a climate room (15 °C) to make it brittle enough to be broken into single particles by means of slight hammering (Figure 12.16). The separated particles were stored at −5 °C to avoid sticking together again. Then, 500 g of GB8 (as VA) was preheated to 300 °C in an oven for 3 h. After this, the precoated GB5 particles (500 g at 15 °C) were mixed in a pan mixer together with the GB8 particles for 30 s.

www.EngineeringEBooksPdf.com



Figure 12.15 Mixer setups and thermography of a mixture.

Figure 12.16 Hammering the cooled artificial RA to loosen the particles at 15 °C.



The heat exchange between the preheated bold G8 particles and the coated GB5 particles during mixing was measured by means of the infrared thermography method. As can be seen in Figure 12.15, the GB5 particles started to stick to each other as soon as they were added to the mixer, because of their precoating. For this reason, manual agitation lasting 10 s by means of a steel spatula was done before mechanical mixing started; this improved mixing considerably. One similar mixture was prepared in which the GB8 was preheated to 400 °C. After mixing and cooling down, the particles of the mixture were separated by means of slight hammering.

A special sieve was prepared with openings of 6 mm to separate the GB5 particles from GB8. A few small particles still remained on the sieve, and had to be separated manually (see Figure 12.17).

In the next step, the binders covering the GB5 and GB8 particles were recovered using the SSEM extraction and recovery method. Initially, it was intended to extract binders in two stages, as explained in the previous section. However, the GBs lost their binder as soon as they were soaked in the solvent. Two factors caused the quick solving of the binders around the GBs: lack of texture on the GB surface, and the fact that pure bitumen (without filler) was used in the experiment.

www.EngineeringEBooksPdf.com



Figure 12.17 Sieving and separating GB5 from GB8.

Table 12.5 Identification of binders extracted from GB5 and GB8 (mixture 1)

Mixture ID	Explanation
300 – V5	Extracted binder from **GB5**; mixture **1**; preheating temperature at **300 °C**
300 – V8	Extracted binder from **GB8**; mixture **1**; preheating temperature at **300 °C**
400 – V5	Extracted binder from **GB5**; mixture **1**; preheating temperature at **400 °C**
400 – V8	Extracted binder from **GB8**; mixture **1**; preheating temperature at **400 °C**

Consequently, only one stage extraction was applied on GB5 and GB8 for each mixture. The extracted binders are identified with the coding system explained in Table 12.5. These binders were to be used for further analysis.

12.6.3.2 Mixture 2

As mentioned in the experimental design section, mixture 2 was quite similar to mixture 1 in the sense of preheating temperature and mixing. The only two differences compared to mixture 1 were:

- GB5 is precoated with 1% aged bitumen (it was 2% in mixture 1).
- The same weight of superheated GB8 particles (VA) and 1% VB is added during 30 s of mixing time.

Given the fact that both mixture types contain 50% GB5 and 50% GB8, it turns out that the final binder content of all mixtures is 1% by mass.

Other procedures such as preheating, storing, particle separation, and binder extraction and recovery were similar to those used to prepare mixture 1. The identification system for the binders extracted from mixture 2 is shown in Table 12.6.

12.6.3.3 Mixture 3

In this mixture, some fractions of VAs were replaced by different sizes of GBs: GB5, GB8, GB13, and GB20. First, a mixture containing 50% RA was designed. A 70/100 pen bitumen was used as VB to be added during mixing. The target bitumen content of the mixture was set to 4.3% by mass. Given the fact that the RA contained 4.3%

www.EngineeringEBooksPdf.com

Table 12.6 Identification of binders extracted from GB5 and GB8 (mixture 2)

Mixture ID	Explanation
300+V5	Extracted binder from **GB5**; mixture **2**; preheating temperature at **300 °C**
300+V8	Extracted binder from **GB8**; mixture **2**; preheating temperature at **300 °C**
400+V5	Extracted binder from **GB5**; mixture **2**; preheating temperature at **400 °C**
400+V8	Extracted binder from **GB8**; mixture **2**; preheating temperature at **400 °C**

bitumen, half of this amount (2.15% by mass) of VB had to be added. The modifications of aggregate gradation as well as the required GBs are presented in Table 12.7 and Figure 12.18. The other mixing conditions and materials are listed briefly below:

- RA: 50%
- VB: 70/100
- Bitumen content: 4.3% (on 100% of aggregate by mass)
- Mixing time: 30 s
- Preheating temperature of VAs: 515 °C
- RA moisture content: 4%

The final mixture temperature was 170 °C. The mixture was kept in an oven at 170 °C for 30 min before compacting it with a Marshall compaction hammer with 40 blows at each side. Normally, 50 blows are applied on each side, but because the GBs could break during Marshall compaction, the number of blows was reduced to 40. The virgin materials, including the GBs, as well as the final mixture are illustrated in Figure 12.19. The GBs could manually be separated from the loose mixture because

Table 12.7 Gradation adjustments for mixture 3

Size (mm)	RAP	50% RAP (% m/m)	Virgin material (% m/m)	Target	GB sizes intended to replace corresponding virgin aggregates
>C22.4	0	0	**1.2**	1.2	**GB20**
C22.4–C16	6	3	**9.2**	12.2	**GB20**
C16–C11.2	11	5.5	**1.1**	6.6	**GB13**
C11.2–C8	14	7	**13.2**	20.2	**GB8**
C8–C5.6	9.2	4.6	**2.4**	7	**GB5**
C5.6–C2	16.3	8.2	**1.7**	9.8	
River sand (0/2)	35.7	17.9	**19.2**	37	
<0.063	7.8	3.9	**2.1**	6	
Total (%)	100	50	**50**	100	
Bitumen	4.3	2.15	**2.35**	4.5	

www.EngineeringEBooksPdf.com

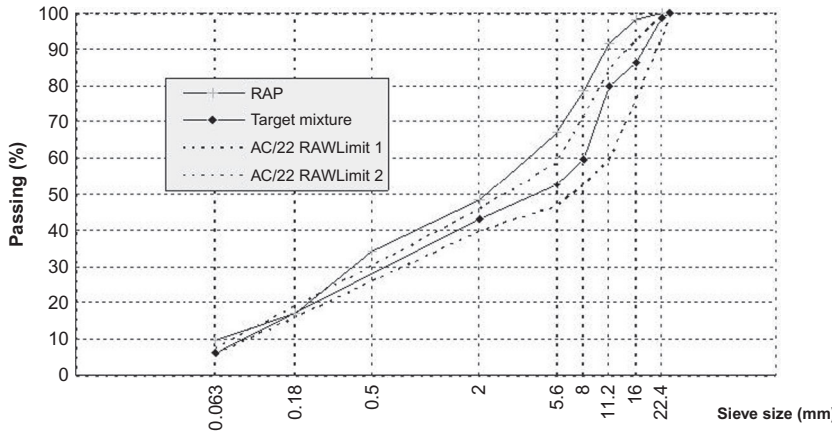


Figure 12.18 Gradation curves of the target mixture, the available RAP, and gradation limitations.

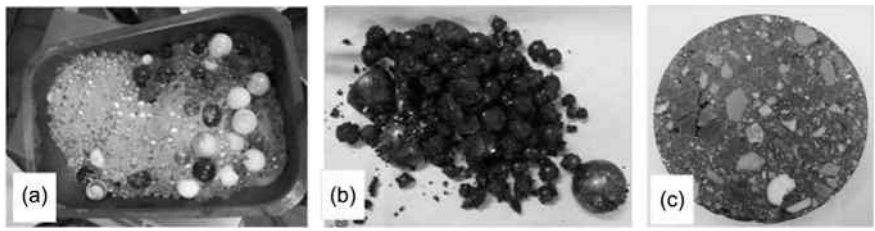


Figure 12.19 Materials and mixing process used in mixture 3. (a) GB, sand, and filler representing virgin aggregates. (b) Loose mixture after mixing with 50% RA. (c) Marshall-compacted specimen.

of their shapes. The binder attached to the GBs and real aggregates were separately extracted and recovered for further analysis. In the remainder of the analysis, the binder extracted from the GBs is called "GB binder." The binder extracted from the mineral aggregates is called "stone binder."

12.7 Results and analysis

The extracted binders were used for rheological and chemical analyses. G^* values were determined at different temperatures and frequencies by means of a DSR, using parallel plates with a diameter of 25 mm to create master curves. The same binders were used for ATR/FTIR analyses, the results of which will be presented for each mixture type. Peak area values in the FTIR spectra were utilized to determine the carbonyl index ($1700\ cm^{-1}$) and sulfoxide index ($1039\ mm^{-1}$) as indicators of chemical changes due to superheating.

www.EngineeringEBooksPdf.com

It has to be noted once again that GB5 stands for GB (5 mm), which was prepared as an artificial aggregate by precoating it with aged binder. Artificial VAs are represented by GB8, which are superheated prior to mixing at temperatures of 300 and 400 °C. In mixture 1, GB5 was coated with 2% aged bitumen. GB5 in mixture 2 was precoated with 1% aged bitumen and 1% VB, which was being added during mixing. Comparison of the binder content on each group of aggregates (GB5 and GB8) will determine the amount of binder transfer from GB5 to GB8.

12.7.1 Mixture 1

Figure 12.20 shows that 0.8% of GB5 binder was transferred to GB8. This implies that 1.2% of the bitumen stayed at the GB5 particles. This can be explained in the following way. Mixture 1 contained, in terms of weight, the same amount of GB8 and GB5 particles. This implies that the total surface area of the GB5 particles was 1.6 times larger than the total surface area of the GB8 particles (see also Table 12.4). The fact that the GB5 particles, with their total surface area being 1.6 times that of the GB8 particles, were carrying 1.5 times more bitumen in total than the GB8 particles implies that per unit of surface area, the GB5 and GB8 particles carried about the same amount of bitumen. This amount was similar at both superheating temperatures. This reveals

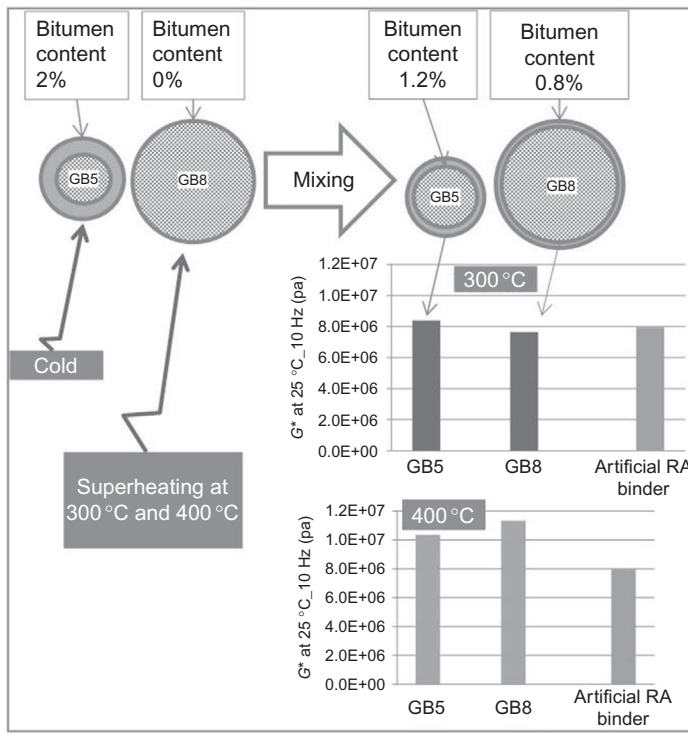


Figure 12.20 *G** results obtained on binders recovered from mixture 1.

www.EngineeringEBooksPdf.com

that cold RA (GB5) could share to a large extent its binder with superheated aggregates at even short periods of mixing (30 s). Comparison between the shear modulus of GB5 and GB8 binders (at 300 °C superheating temperature) shows no severe change or damage of the binder properties. However, superheating at 400 °C has increased the G^* value of the GB5 binder as well as that of the GB8 binder. G^* values of the original aged binder (being RCAT_70/100@24 h) are also shown in the charts as the property of the binder before mixing.

Furthermore, the GB8 binder has become slightly stiffer than that of GB5. Direct exposure of the binder to superheated aggregates (400 °C) accounts for the difference between the binders coating GB5 and GB8.

The FTIR test was conducted on each extracted binder to study the chemical changes, particularly due to oxidation. The FTIR spectra related to mixture 1 are presented in Figure 12.21. The aging indices of CO and SO are determined by calculating peak area values and are given in Table 12.8. A comparison of aging indices between the different groups of extracted binders (from mixture 1) is given in Figure 12.22. As can be seen, the binders of the 400 °C mixtures show more oxidation compared to those of the 300 °C

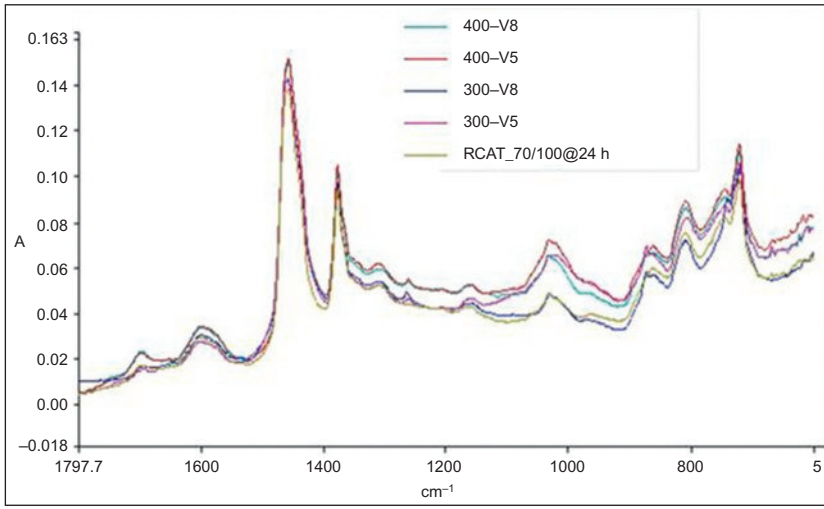


Figure 12.21 FTIR spectra of binder from mixture 1.

Table 12.8 Peak values in the FTIR spectra (mixture 1)

	A1030	A1375	A1460	A1600	A1700	ISO	ICO
300 – V5	0.6407	0.9936	4.8442	0.5447	0.0558	0.110	0.010
300 – V8	0.6786	1.1399	4.6757	0.7474	0.0898	0.117	0.015
400 – V5	0.6266	0.9217	4.2226	0.5139	0.1093	0.122	0.021
400 – V8	0.764	1.1313	4.8113	0.8059	0.107	0.129	0.018

www.EngineeringEBooksPdf.com

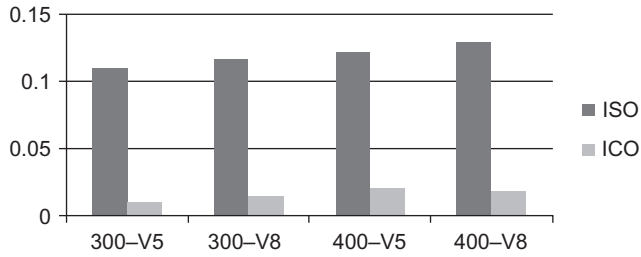


Figure 12.22 Aging indices from mixture 1.

mixtures. It is also evident that the binder coating GB8 has higher aging indices than the binder coating GB5, confirming the effect of direct exposure to superheated aggregates.

12.7.2 Mixture 2

As can be seen from Figure 12.23, the GB8 particles are carrying the same amount of bitumen as the GB5 particles after being mixed with the GB5 particles carrying 1% of bitumen and the 1% added VB. In contrast to what happened to mixture 1, the bitumen

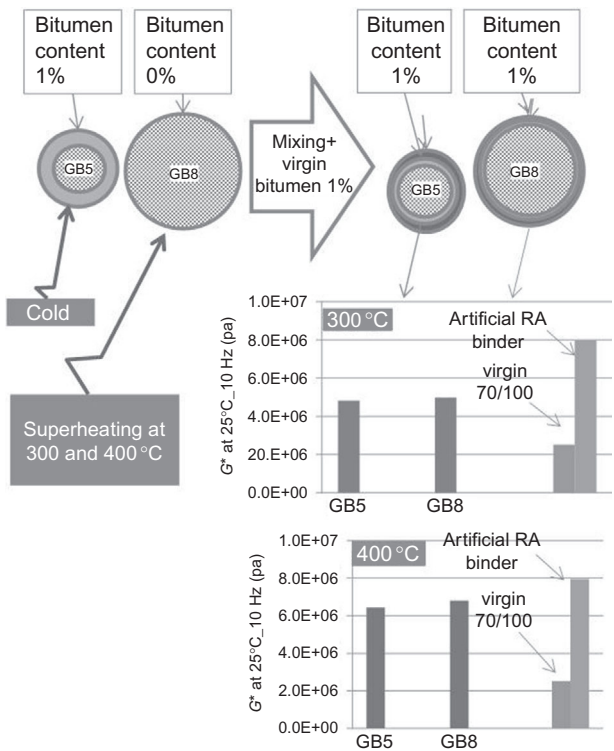


Figure 12.23 G^* values obtained on the binder recovered from the GB5 and GB8 particles in mixture 2.

www.EngineeringEBooksPdf.com

now seems *not* to be divided according to the surface area ratio of GB5 and GB8. It is, however, very difficult to say how much of the artificial aged binder on the GB5 particles was transferred to the GB8 particles. Although the G^* values determined on the bitumen coming from the GB8 particles are slightly higher than those determined on the bitumen coming from the GB5 particles, this does not reveal anything about the composition of the binder coming from the GB5 and GB8 particles. The only conclusion that perhaps can be made is that the superheated GB8 particles had almost the same effect in terms of aging on the bitumen that finally coated both GB sizes.

In Figure 12.23, the shear moduli of the binders extracted from GB5 and GB8 after mixing are compared with those of binders before mixing (VB and artificial aged bitumen). At both preheating temperatures, the G^* values of the GB5 and GB8 binders are between those of the original binders. This shows the effect of blending between the two binders. At 300 °C, the GB8 binder has become slightly stiffer than that of GB5 mixture 1, most probably because of the exposure to superheated particles. The same trend is observed in the other mixture, where the superheating temperature was 400 °C.

Increasing the superheating temperature from 300 to 400 °C caused more aging on both the GB5 and GB8 binders.

The results allow us to check the validity of the log-pen rule, which is normally used to determine the grade of VB to be used in recycling. The rule is

$$A \times \log\left(\text{pen}_{\text{virgin}}\right) + B \log\left(\text{pen}_{\text{RA}}\right) = (A+B)\ \log\left(\text{pen}_{\text{mixture}}\right) \tag{12.1}$$

where A, % of VB; $\text{pen}_{\text{virgin}}$, penetration of the VB added; B, % of bitumen coming from the RA; pen_{RA}, penetration of the bitumen of the RA; $\text{pen}_{\text{mixture}}$, penetration of the bitumen of the recycled mixture; and $A+B$, 100.

It is assumed that this rule is also applicable to determine the G^* of the bitumen of the recycled mixture.

Because $G_{\text{virgin}}^* = 2.47 \times 10^6$ Pa and $G_{\text{aged}}^* = 8 \times 10^6$ Pa, one would expect the G_{mixture}^* to be equal to 4.42×10^6 Pa. The figure shows that in the case of the 300 °C preheated aggregates, the G^* of the bitumen coming from GB5 equals 4.82×10^6 Pa, and is 4.94×10^6 Pa for the bitumen coming from the GB8 particles. In this case, it looks like the $\log(G^*)$ rule seems to be valid. However, it is clear that in the case when the virgin GB8 aggregate was preheated to 400 °C, the $\log(G^*)$ rule is not valid. The G^* of the bitumen coming from both the GB5 and GB8 particles is much higher. Obviously, additional aging due to the superheated aggregates must have occurred in this case.

The effect of adding 1% VB is shown in Figure 12.24, where a comparison is made between mixtures 1 and 2. Figure 12.25 shows the G^* master curves of all extracted binders in one chart. The FTIR spectra for the recovered bitumen from the GB5 and GB8 particles as well as those of the virgin and artificially aged binder are shown in Figure 12.26.

The aging indices ICO and ISO are determined by calculating the peak area values, and the results are shown in Table 12.9. It can be seen that the binders of 400 °C show slightly more oxidation compared to those of the 300 °C mixtures. Because VB is

www.EngineeringEBooksPdf.com

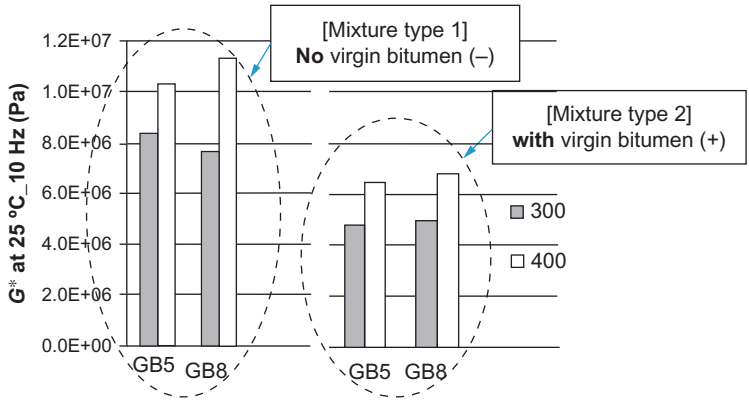


Figure 12.24 Comparison between mixtures 1 and 2.

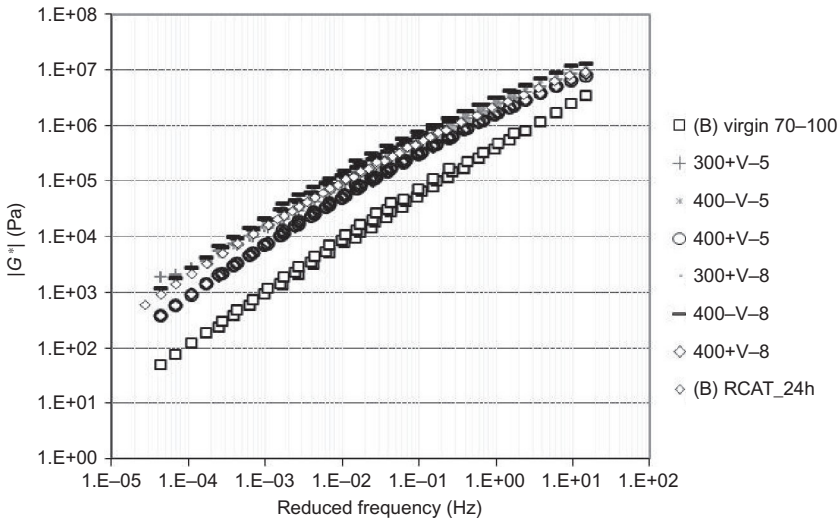


Figure 12.25 *G** values of the binders extracted from mixtures 1 and 2.

added to the mixture, no meaningful relationship could be seen between the aging indices of GB5 and GB8 (Figure 12.27).

12.7.3 Mixture 3

Binder was extracted from the GB and RA aggregates and was then tested in the DSR and FTIR. It has to be reminded that in the further analysis, binders extracted from the GB particles are identified as "GB binder," and the binder extracted from the rest of the aggregates is called "stone binder."

www.EngineeringEBooksPdf.com

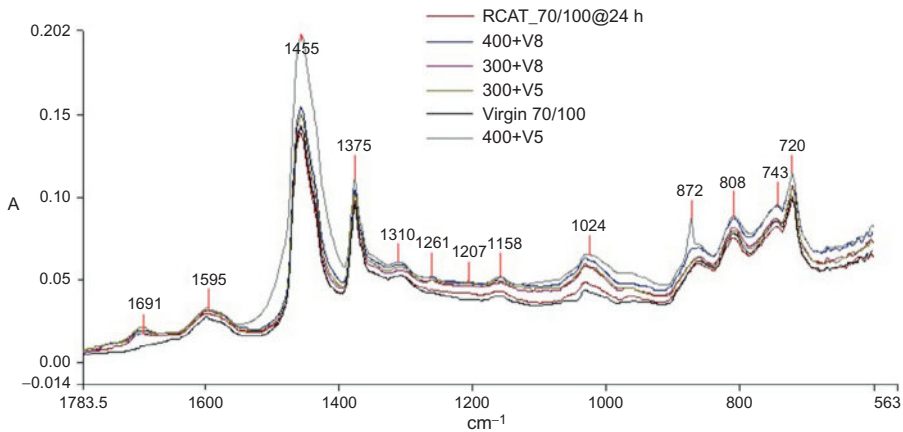


Figure 12.26 FTIR spectra of binders from mixture 2.

Table 12.9 Peak values in the FTIR spectra (mixture 2)

	A1030	A1375	A1460	A1600	A1700	ISO	ICO
300+V5	0.675	1.156	4.871	0.721	0.151	0.112	0.025
300+V8	0.665	0.669	9.626	0.413	0.038	0.065	0.004
400+V5	0.417	0.878	3.594	0.486	0.041	0.093	0.009
400+V8	0.681	1.112	4.876	0.713	0.054	0.114	0.009

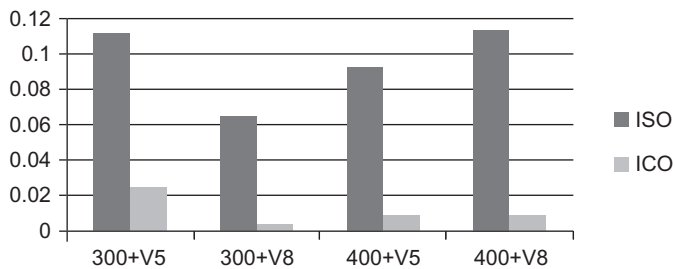


Figure 12.27 Aging indices from mixture 2.

Shear modulus master curves of both binders are shown in Figure 12.28. Master curves of original binders—real RA binder and virgin 70/100 bitumen—are also included to study the effect of superheating and blending after a mixing period of 30 s in a pan mixer. As shown in Figure 12.28, the GB binder is stiffer than the binder extracted from the rest of the mixture (stone binder), implying the effect of direct exposure of the binder to VAs (GB) superheated to 515 °C. The stone binder is

www.EngineeringEBooksPdf.com

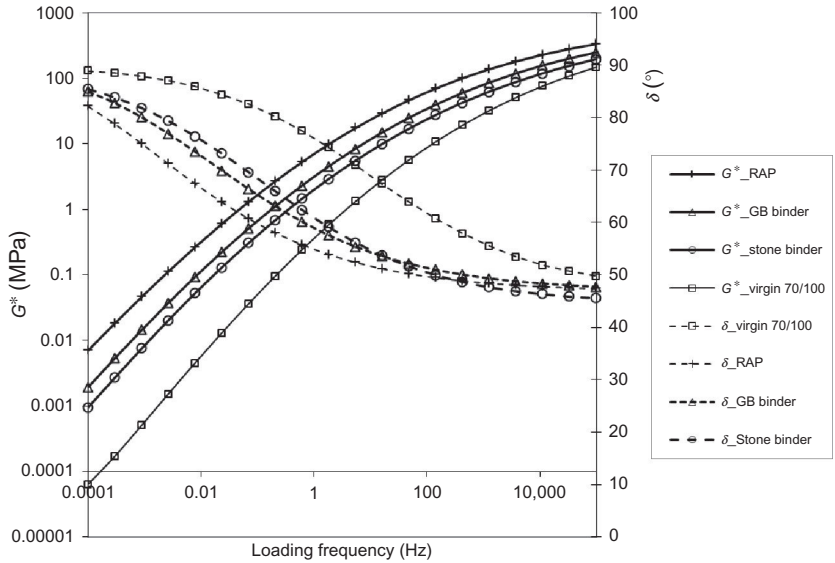


Figure 12.28 *G** master curves of extracted binders in mixture 3.

relatively softer, which implies that it was less affected by the superheated aggregates. The stiffness of the stone binder is between the RA and VB.

Table 12.10 gives more detailed information about the *G** and δ values obtained at various frequencies. Furthermore, penetration values are presented in this table, which

Table 12.10 *G and δ values for the binders recovered from mixture 3 as well as penetration values for these binders calculated from *G** values**

	RAP		GB binder		Stone binder		Virgin 70/100	
***f* (Hz)**	***G**** **(MPa)**	**δ (°)**	***G**** **(MPa)**	**δ (°)**	***G**** **(MPa)**	**δ (°)**	***G**** **(MPa)**	**δ (°)**
0.01	0.323	66.6	0.113	72.7	0.064	75.7	0.006	85.6
0.4	**4.112**	**56.7**	**1.731**	**61.2**	**1.078**	**63.8**	**0.169**	**78.6**
1	7.089	54.9	3.118	58.9	1.979	60.9	0.361	76.1
10	23.578	51.7	11.566	54.3	7.678	54.7	2.033	68.9
20	32.302	51.0	16.372	53.2	11.010	53.3	3.250	66.7
100	61.836	49.7	33.789	51.3	23.418	50.5	8.780	61.7
Predicted penetration	**16**		26		33		**88**	
Log-pen rule based on 50% RAP	**38**							

www.EngineeringEBooksPdf.com

were calculated using the following equation developed by Saal and Labout (see Van den Berg, 2011):

$$\log\left(G^*_{0.4\,\mathrm{Hz};25^\circ\mathrm{C};(\mathrm{MPa})}\right) = 2.923 - 1.9\log\left(\mathrm{pen}_{25^\circ\mathrm{C};(\mathrm{dmm})}\right)$$

Furthermore, Table 12.10 presents the penetration value of the bitumen in mixture 3 as calculated by means of the log-pen rule, which was presented earlier. As one will observe, the penetration of the bitumen recovered from the stone is not too different from the penetration value calculated by means of the log-pen rule. The penetration of the bitumen recovered from the GB particles is, however, much lower than the log-pen rule value. All in all, these results show that full blending of the RA and virgin binder as it is assumed in the log-pen rule certainly did not occur. Furthermore, the table shows that the G^* of the GB binder is approximately 50% of that of the RA binder. The G^* of the stone binder is approximately two-thirds of that of the GB binder.

The FTIR spectra of the binders are illustrated in Figure 12.29. The aging indices of ICO and ISO are determined by calculating the peak area values, and the results are shown in Table 12.11. The indices of the stone, GB, virgin, and RA binders are compared in Figure 12.30. Higher values of ISO and ICO for the GB binder indicate the effect of superheating on directly exposed binder.

12.8 Conclusions

Based on the research results presented here, the following conclusions can be drawn:

1. Extraction of bitumen from asphalt mixtures is a delicate process. Great care should be given to the complete removal of the solvent and the filler.
2. Stage extraction, which is done to determine the presence of a layered bitumen film around aggregate particles, can only be successful if the extraction is done on particles of

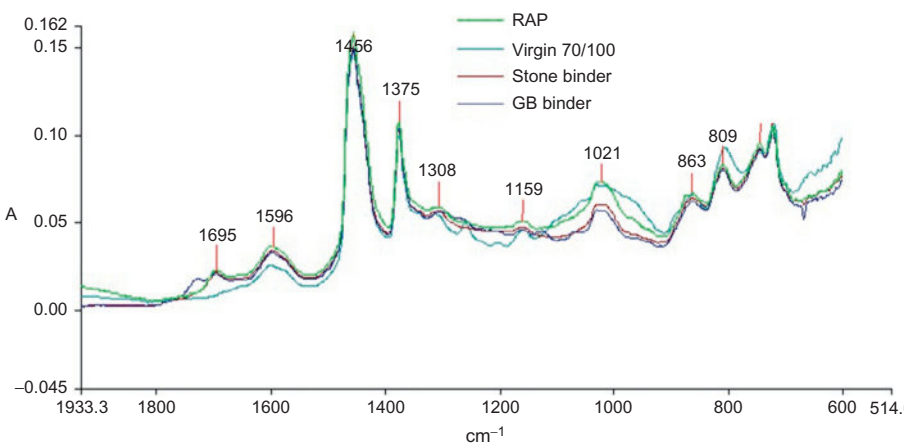


Figure 12.29 FTIR spectra of binder from mixture 3.

www.EngineeringEBooksPdf.com

Table 12.11 Aging indices for mixture 3

	A1030	A1375	A1460	A1600	A1700	ISO	ICO
Stone binder	0.656	1.044	4.191	0.721	0.122	0.125	0.023
GB binder	0.720	1.093	4.020	0.658	0.195	0.141	0.038
Virgin 70/100	0.442	1.064	4.450	0.546	−0.049	0.080	−0.009
RAP	0.817	1.092	4.625	0.796	0.104	0.143	0.018

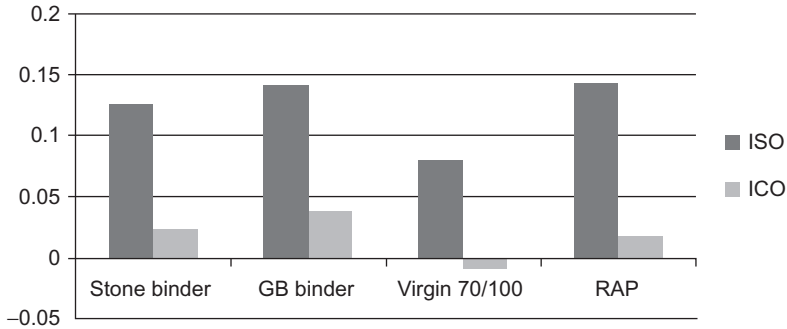


Figure 12.30 Aging indices from mixture 3.

approximately the same size. It has been shown in this research that larger particles will lose their bitumen film easier than will smaller particles. This implies that when stage extraction is done on a mixture consisting of different sized aggregates, one will first recover the bitumen around the coarse aggregates, and in a later stage the bitumen around the finer particles. Such a stage extraction will therefore reveal nothing about the presence of a layered bitumen film around the various particle sizes.

3. G^* measurements on the bitumen recovered by means of stage extraction from different particle sizes showed that the bitumen recovered from the finer particles had a higher G^* than the G^* of the bitumen recovered from the coarser particles.
4. The G^* values obtained on the bitumen recovered from the first extraction (the outer bitumen layer around a particle) were slightly higher than the G^* values obtained on the bitumen from the second extraction (inner layer). The differences were rather small, however, and no clear trend could be discovered.
5. It can be concluded that the RCAT is a useful tool to artificially age VB such that it gets comparable rheological properties as binders that are aged in the field.
6. The GB experiments were very useful for gaining an understanding of the transfer of RA binder from RA aggregates to (super)-heated VAs.
7. The experiments with the asphalt mixture where some of the VAs were replaced by GBs showed that adding virgin binder to the mixture had a significant effect on the G^* of the RA binder coating the RA particles (after separation and recovery).

www.EngineeringEBooksPdf.com

8. Furthermore, it can be concluded that the G^* of the bitumen coating VAs in an RA mixture (in this case, the GBs) is not the same as the G^* of the bitumen coating the RA aggregates.
9. Based on conclusion 7, it is furthermore concluded that full blending of RA and virgin binder does not occur.
10. In line with conclusion 8, experiments furthermore showed that the log-pen rule, which is often used to determine the required penetration of the virgin binder to obtain the desired penetration of the binder of the completed mixture, was not applicable for the investigated mixture. It might, however, still be applicable for mixtures containing lower amounts of RA. Furthermore, it should be noted that the experiments were especially designed to investigate double barrel drum mixing. They therefore allow no conclusions to be made on the applicability of the log-pen rule in the case of preheating the RA material in a different way.

12.9 Future trends

Although much has been learned about blending from the research described in this chapter, it did not solve all the questions and queries. Aspects that certainly need to be investigated are the following:

- The effect of preheating RA on blending should be investigated. Preheating RA in a parallel drum to 130 °C, which is a normal practice in the Netherlands, reduces the need to preheat the VAs to very high temperatures, and because of the smaller temperature difference, a better blending could be obtained.
- Bioproducts like cashew nut oil are currently used to rejuvenate RA binder, and mixtures with 100% RA rejuvenated with such products are already produced. Research on the blending of such products on the RA binder is needed to understand why such products are effective, and when such products will not be effective.
- Because of environmental reasons, warm and half-warm asphalt mixtures with high RA percentages will be used extensively in the near future, and are already used on a large-scale nowadays. Knowledge about blending the RA binder with, for example, foam bitumen is not available at the moment but is essential in order to be able to understand the critical factors determining the quality of such mixtures.
- Blending seems to be an important issue, but questions remain about the effect of imperfect blending on the mechanical characteristics of mixtures with high RA percentages.
- The microstructural mechanisms controlling the blending of old and new bitumen at their mixing interfaces should be studied, because this will allow us at the end to select the right type of virgin binder, given the present RA binder.
- The possibility of studying the binder properties of recycled mixtures without solvent extraction should be studied, because solvent extraction and recovery may alter the properties of original binders.
- Studies on binder characteristics of different fractions of RA would be helpful in understanding the interaction of different sizes of virgin and RA aggregates during mixing at high temperature.
- Numerical modeling of the interaction between old and VB in recycled mixture, with the assumption of different levels of blending (not blended ~ totally blended), would improve the understanding of the importance of blending of bituminous binder.

www.EngineeringEBooksPdf.com

References

Hagos, T., 2008. The effect of aging on binder properties of porous asphalt concrete. PhD dissertation, Delft University of Technology, Delft.

Huang, B., Li, G., Vukosavljedic, D., Shu, X., Egan, B., 1929. Laboratory investigation of mixing hot-mix asphalt with reclaimed asphalt pavement. Transport. Res. Rec. 2005, 37–45.

Noureldin, A.S., Wood, L.E., 1989. Rejuvenator diffusion in binder film for hot-mix recycled asphalt pavement. Transport. Res. Rec. 1115, 51–61.

Van den Berg, W., 2011. The effect of aging on the fatigue and healing properties of bituminous mortars. PhD thesis, Delft University of Technology, Delft.

www.EngineeringEBooksPdf.com

Paving with asphalt emulsions

13

K. Takamura[1], *A. James*[2]
[1]University of California, Davis, CA, USA; [2]Akzo Nobel Surface Chemistry, Chicago, IL, USA

13.1 Introduction

Asphalt emulsions are water-continuous dispersions of fine asphalt droplets, typically 1–10 μm in diameter, manufactured with the aid of a colloid mill. The emulsions may contain between 40% and 80% asphalt by weight. The emulsions have significantly lower viscosity than asphalt itself, and so can be applied at lower temperatures. Consequently, processes using emulsions have lower energy consumption and lower emissions than those using hot asphalt or cutbacks (asphalt solutions in hydrocarbon solvents).

The International Bitumen Emulsion Federation has collected some information on emulsion use in different countries. Approximately 8 million tons of asphalt are used in emulsion form, about 9% of all asphalt usage (Le Bouteiller and Roffe, 2011). The major part is used in spray applications like chip seal, fog seals, and bond coats. The rest is used in asphalt mixtures prepared cold or warm, including in-place techniques. An important application in some countries is microsurfacing, in which a mixture of polymer-modified asphalt emulsion, fine grained aggregate, water, and cement is applied to the surface of an asphalt or cement concrete roadway from a mobile mix-paver to correct deformations, improve skid resistance, and seal the surface.

Conventional asphalt "hot mix" is generally produced at 150 °C or greater at the mixing plant, and subsequently compacted at around 120–140 °C. New technologies, collectively known as warm mix asphalt, allow a reduction in the mixing and compaction temperatures (Capitão et al., 2012; Newcomb, 2007). Asphalt emulsions find use in warm mixes (Crews, 2006) where mix temperatures are reduced to 60–120 °C, and in cold mixes where the materials are generally unheated and mixed at ambient temperatures. The description "half-warm mix" has been used to distinguish warm processes where mixing takes place below 100 °C, avoiding the need to dry the aggregate. Lower mix temperatures mean a reduction in fuel consumption and consequent greenhouse gas emissions, and lower particulate and fume emissions (Newcomb, 2007; Potti et al., 2006). Further environmental benefits accrue if recycled materials are used in the mix, and half-warm mix with emulsion has been used to recycle tar-containing road materials, avoiding hazardous emissions (Dijkink et al., 2000). Characterization of the binder from an emulsion-based warm mix (Davidson et al., 2007; Takamura, 2008) confirms less age hardening of the binder than from hot mix, which should eventually result in less cracking.

A cold mix plant using asphalt emulsion requires less initial capital investment than a conventional hot-mix plant, and is well suited for mobile use. Placing the mix plant

Advances in Asphalt Materials. http://dx.doi.org/10.1016/B978-0-08-100269-8.00013-1
© 2015 Elsevier Ltd. All rights reserved.

www.EngineeringEBooksPdf.com

close to local raw materials and the job site maximizes the environmental benefit. Emulsion mixes are also well adapted for cold in-place stabilization and recycling techniques because the aggregates need not be heated.

For developed countries, the environmental focus has shifted from pollution prevention to sustainable development. The preservation of existing roadways by preventive maintenance is the most financially effective use of available resources (Mamlouk and Zaniewski, 1999; Roberts et al., 1996). Bitumen emulsions are widely used in pavement preservation techniques such as chip seal, fog seal, and microsurfacing, which look to maintain the surface properties of the road while preserving the structural layers beneath. Eco-efficient analysis provides an integrated assessment of the ecological and economic pros and cons of alternative products and processes. Eco-efficiency analysis of preventive maintenance demonstrates that asphalt emulsion-based microsurfacing is more "eco-efficient" than a conventional thin hot-mix overlay. This is because of lower material consumption, less transportation of materials, and lower overall emissions during the life of the treatment (Takamura et al., 2004).

Asphalt emulsions are produced by mixing a water solution of emulsifier, usually a cationic or anionic surfactant, with hot asphalt in a colloid mill. They may contain other ingredients like polymers and solvents, which may be added during or after the emulsion production. Emulsions are graded on their reactivity—how readily they set or break in contact with the aggregates used in road construction and repair—and different reactivities are suitable for different applications. Rapid-setting (RS) grades are the most reactive, slow-setting grades the least, and medium-setting (MS) grades have intermediate reactivity. Asphalt content, solvent content, emulsion viscosity, and storage stability are also often specified, as are the rheological properties of the "residue"—the material remaining after the water has evaporated. The reactivity of the emulsion is determined by its formulation—especially by the concentration and chemical nature of the emulsifier. The actual setting and curing rate in the final application depends on the aggregate chemistry and surface area, temperature, and other environmental conditions. The transformation of the dispersed asphalt phase present in the emulsion to the continuous binder phase in the pavement is a key process in all the applications of asphalt emulsion.

This chapter provides in-depth analysis of emulsion production, emulsion properties, and curing mechanisms through fundamental theories of dispersion stability and rheology, and also discusses emulsion residue characterization, which demonstrates advantages of emulsion-based paving technology.

13.2 Overview of emulsifier chemistry and emulsion recipes

Surfactants are materials that concentrate at surfaces and interfaces. The molecular origins of this surface activity are described in Section 13.3. Surfactants that concentrate at the interface between oil and water are used to stabilize emulsions and are called emulsifiers. Asphalt emulsifiers have separated nonpolar and polar portions in a single

www.EngineeringEBooksPdf.com

molecule. The nonpolar portion is often a single hydrocarbon chain with 12–20 carbon atoms, while the polar portion is a "head group" containing one or more charged centers. Emulsifiers with positively charged head groups produce "cationic" emulsions where the asphalt droplets have positive charge, and emulsifiers with negatively charged head groups produce "anionic" emulsions where the droplets have negative charge. Sometimes nonionic surfactants can be used to produce asphalt emulsion, and emulsion stability in these cases may derive partly from steric effects. The choice and concentration of the emulsifier provide the desired reactivity and performance of the emulsion. Generally, rapid-set emulsion grades use low levels of emulsifier (0.15–0.4% active material basis emulsion), while slow-setting emulsions may use 1.5% or even higher. Expressed on the water portion of the emulsion, the emulsifiers may range in concentration from 0.01 to 0.2 M. Emulsifiers used in RS grades are selected to be sensitive to the small changes in pH and ion concentrations that occur when emulsion is in contact with aggregates. Emulsifiers used in slower setting grades are designed to be less sensitive to these changes, for instance by the inclusion of nonionic or amphoteric surfactant components, or molecules offering some steric stability.

Anionic emulsifiers contain oxygen. For anionic RS and MS asphalt emulsions, the most often used emulsifier chemistries are the sodium or potassium salts of C16–24 fatty acids from crude or distilled tall oils. The tall oils are supplied to the emulsion producer, who prepares a water solution or "soap" by addition of sodium or potassium hydroxide. The addition is not stoichiometric; soap solutions lie in a range of pH 10.5–12.5. Slow-setting anionic emulsions are prepared with a high dosage of emulsifier (typically 1–2% active material). Nonionic surfactants with very large head groups, for example nonylphenol with 50–100 mol of ethylene oxide, are most commonly used. ζ-Potential measurements show that emulsions formed using these nonionic emulsifiers do have negative charge (Wates and James, 1993). Emulsions meeting the specifications of slow-set anionic emulsion can be prepared at more or less neutral pH using nonionic emulsifiers, but most commonly have a pH around 11 and 12. Stabilizers based on lignin (Schilling, 2002) can be included in the emulsion recipe to provide additional stability, perhaps through a steric effect or through an ability to complex calcium ions. Alkylbetaines are also used as emulsifiers for anionic slow-set emulsions (James, 2006).

Cationic emulsifiers are nitrogen derivatives. These cationic emulsifiers are prepared either by the nitrile process in which fatty acids are reacted with ammonia and then hydrogen, or by direct condensation of fatty acids or oils with polyamines such as aminoethylethanolamine, diethethylene triamine, or dimethylaminopropylamine to form amidoamines and imidazolines (James, 1997). The fatty portion of the emulsifier molecule is usually derived from natural sources such as tallow, palm oil, tall oil, or rapeseed oil and has hydrocarbon chains mainly in the C16–18 range. Further derivatization of the amines by alkoxylation, quaternization, or reaction with acrylonitrile and hydrogen provides a wide range of emulsifier chemistries, often with multiple charged nitrogen centers in the head group. More recently, betaine and amphoteric surfactants, which contain potentially both negative and positive charge centers in one molecule, have been used for both cationic and anionic emulsions (Marcilloux et al., 2008).

www.EngineeringEBooksPdf.com

Cationic rapid-setting (CRS) grades are prepared with low dosage (0.15–0.4%) of C16–18 fatty amine, fatty diamine, or amidoamine surfactants in the form of their hydrochloride salts, or, much less often, as acetate salts. Emulsifiers are supplied to the emulsion producer in insoluble amine form, often as a mixture of several components, and the emulsion producer dissolves them in hot water by the use of acid to form the emulsifier solution. The acid addition is not stoichiometric, and solution pH may vary from 1.5 to 4.5. The pH has subtle effects on the reactivity and physical properties of the emulsion.

Cationic medium-setting (CMS) grades are generally prepared from the same emulsifiers as RS grades, but used at higher dosage 0.4–0.8%.

Cationic quick-setting (CQS) emulsions are a special class, with reactivity intermediate between medium and slow settings, and are used more or less exclusively for microsurfacing and slurry seal. The emulsion recipes are developed to provide the right mixing and setting behavior with aggregates to be used in the field, rather than to a more general emulsion reactivity specification used for the other grades. The most common emulsifiers are the hydrochloride salts of fatty imidazolines and amidoamines derived from tall fatty acids and polyethylene polyamines, or tallowtripropylenetetramine. These products may have four or more cationic charge centers in their head group. Products derived from modified tall oil fatty acids showed improved performance (Birken, 2010; Schilling, 1997; Schilling and Schreuders, 1998). Emulsions with similar reactivity can also be prepared using fatty amidoamines and fatty polyamines, but reacted with phosphoric acid instead of hydrochloric (James, 2008). Amphoteric and betaine emulsifiers have also been used in quick-set emulsions (Lesueur et al., 2006).

Slow-setting cationic emulsion grades use high concentrations (1–2% active material) of emulsifiers with low sensitivity to pH changes, such as nonionic surfactants or quaternary amines that do not lose their charge at higher pH. Lignin amines (Schilling, 2002) may be included to further lower reactivity.

13.3 Surface tension and surfactants (emulsifiers)

13.3.1 Molecular origins of surface and interfacial tensions

There is not a fundamental distinction between the terms surface and interface, although it is customary to describe the boundary between two phases, one of which is gaseous, as a surface, and the boundary between two nongaseous phases as an interface. The surface tension of the liquid arises from the short-range intermolecular attraction at the surface region. For liquid alkanes, this intermolecular attraction is entirely due to London dispersion forces, thus

$$\gamma_o = \gamma_o^d \tag{13.1}$$

where γ_o is the surface tension of the alkane oil, and the superscript d designates the dispersion forces contribution (Fowkes, 1964; Takamura et al., 2012). The surface

www.EngineeringEBooksPdf.com

tension of water is the sum of a dispersion forces contribution, γ_w^d, and a polar (hydrogen-bonding) forces contribution, γ_w^p:

$$\gamma_w = \gamma_w^d + \gamma_w^p \tag{13.2}$$

and γ_w^d and γ_w^p are 21.8 and 51.0 mN/m, respectively, at 20 °C (Fowkes, 1964).

Water molecules in the oil/water interfacial region are attracted toward the interior of the water phase by water–water interactions (dispersion forces and hydrogen bonding) and toward the oil phase by oil–water interactions (dispersion forces only); likewise, oil molecules at the interfacial region are attracted to the oil phase by the oil–oil dispersion forces and to the water phase by oil–water dispersion forces. The interfacial tensions are related to the geometric means of the oil–oil and water–water intermolecular interactions (Girifalco and Good, 1957):

$$\gamma_{wo} = \gamma_w + \gamma_o - 2\sqrt{\gamma_w^d \gamma_o^d} \tag{13.3}$$

The aromatic molecules are more hydrophilic than the saturated hydrocarbons (Fowkes, 1964; Pormerantz et al., 1967), resulting in lower interfacial tensions (e.g., 34.4 and 52.0 mN/m for benzene and *n*-heptane at 20 °C, respectively). Owens and Wendt (1969) have extended Equation (13.3) for the polar molecules:

$$\gamma_{wo} = \gamma_w + \gamma_o - 2\left(\sqrt{\gamma_w^d \gamma_o^d} + \sqrt{\gamma_w^p \gamma_o^p}\right) \tag{13.4}$$

Values of γ_o^d and γ_o^p for toluene are 27.8 and 1.3 mN/m, respectively (Binks and Clint, 2002), and Equation (13.4) predicts $\gamma_{wo} = 36.4$ mN/m. A small value of $\gamma_o^p = 1.3$ mN/m for toluene results in rather substantial reduction in γ_{wo} because of the strong polar forces of water $\left(\gamma_w^p = 51 \text{ mN/m}\right)$ with $\gamma_o = 29.1$ mN/m for toluene. The importance of aromatics at the crude oil/brine interface has been discussed in detail by Takamura et al. (2012).

13.3.2 Physical properties of surfactants (emulsifiers)

13.3.2.1 Surface activity and micelle formation

The surface tension of water ($\gamma_w = 72.8$ mN/m at 20 °C) is significantly higher than that of alkanes of similar molecular mass (e.g., $\gamma_o = 18.4$ mN/m for hexane) due to the strong polar forces contributions, as discussed above. The surface tension of water can be reduced by addition of a small amount of molecules containing both polar and nonpolar parts (amphiphilic), such as the asphalt emulsifiers described above. These molecules are able to locate their hydrophilic head groups in the aqueous phase and allow the lipophilic hydrocarbon chains to escape into the vapor phase (Figure 13.1). The strong adsorption of such materials at the surface in the form of an orientated monomolecular layer is termed *surface activity*, and those molecules possessing

www.EngineeringEBooksPdf.com

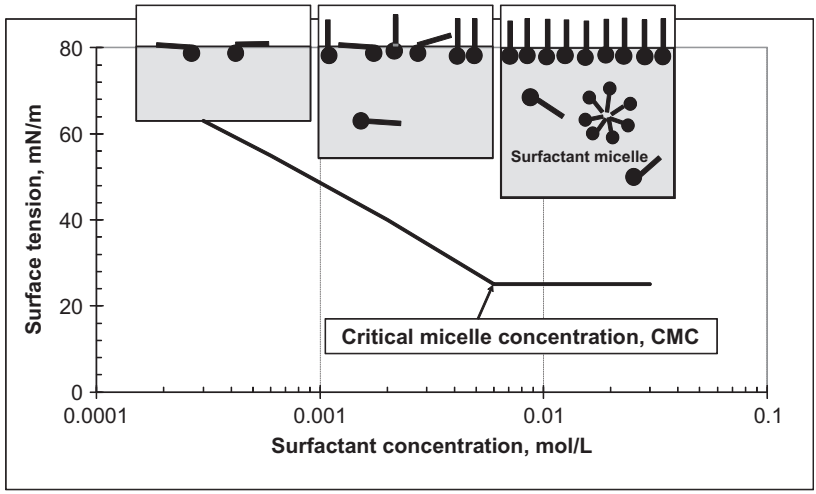


Figure 13.1 Schematic description of the surface coverage of surfactant molecules at the water surface and resulting linear reduction in the surface tension as a function of log of the surfactant concentration.

strong surface activity are called *surface-active agents* or *surfactants* (Schwartz and Perry, 1949). Surfactant molecules would also preferentially adsorb at the water/oil or water/solid interface through the dispersion forces interaction. Surfactants are often named in relationship to their application, hence names such as detergent, wetting agent, emulsifier, and dispersant.

The surface tension of a typical aqueous surfactant solution against its concentration is depicted in Figure 13.1. The surface tension drops linearly against the log of the surfactant concentration as surfactant molecules accumulate at the surface. Once the surface is fully covered, the surfactant molecules aggregate themselves to form micelles in the bulk water phase, in which the lipophilic hydrocarbon chains are oriented toward the interior of the micelle, leaving the hydrophilic groups in contact with the aqueous medium. The concentration above which micelle formation becomes appreciable is termed the critical micelle concentration (CMC). In solutions of surfactant above the CMC, the water phase comprises a solution of individual molecules at approximately the CMC and aggregates of surfactants. The surface tension remains almost constant at surfactant concentrations above the CMC: more micelles are formed, but their size remains relatively constant. The CMC can be identified by observing an abrupt change in the concentration dependence of several physical properties, including osmotic pressure, turbidity, electrical conductance, dye solubility, and surface tension (Hunter, 1986).

Micelle formation of the surfactant is a balance between the association among hydrocarbon tails and coulombic (charge) or steric repulsion among head groups. Therefore, there exists a direct relationship between the chain length of the hydrocarbon tails; the longer the hydrocarbon chain, the lower the CMC. Lower repulsion

www.EngineeringEBooksPdf.com

between the head groups, as with nonionic surfactants or through the effect of electrolyte addition on ionic surfactants, leads to lower CMC and bigger micelles (see Figure 13.2). Length of $(CH_2CH_2O)_n$ of the nonionic surfactant has little effect on CMC, but micelle size increases with increase in "*n*" (Shinoda, 1978). The CMC of the ionic surfactants is sensitive to the electrolyte concentration in the aqueous phase: with electrolyte addition, the CMC is lowered and bigger micelles are formed. In the case of emulsifiers with head groups with weak base or acid character, the CMC and micelle size is also sensitive to pH. Further discussion on the micelle structure has been given by Hoffmann (1990).

13.3.2.2 Solubility of ionic surfactants: Krafft point

The solubility of an ionic surfactant shows a rapid increase above a certain temperature, known as the Krafft point (Krafft and Wiglow, 1895). Below the Krafft temperature, the solubility of the surfactant is below the CMC. If surfactant is added, an insoluble phase of surfactant separates, surface tension is not further reduced, and micelles do not form. As surfactant is added above the Krafft point, surface tension reaches a minimum, micelles start to form, and any further surfactant simply increases the number of micelles. The result is a rapid increase in solubility of the surfactant (Shinoda and Hutchinson, 1962).

The Krafft point of the ionic surfactant is directly related to its hydrocarbon chain length: a higher Krafft point has a longer hydrocarbon chain. The Krafft point increases with the lower ionic nature of the polar group, and thus is very sensitive

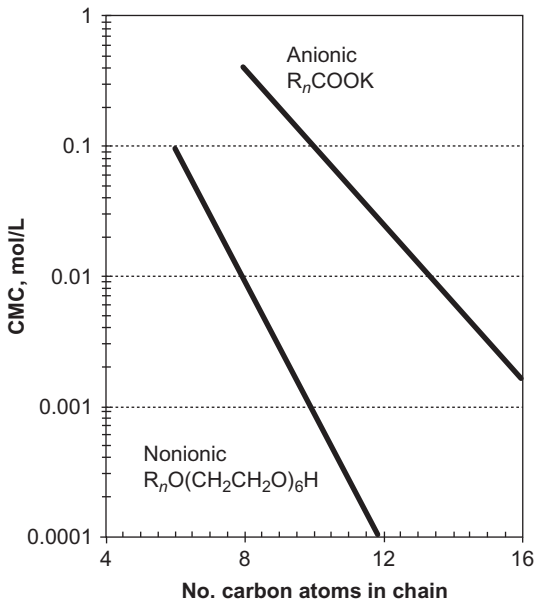


Figure 13.2 Comparison of the critical micelle concentration, CMC of anionic and nonionic surfactants as a function of their carbon chain length.

www.EngineeringEBooksPdf.com

to counterion valency. Anionic surfactants form precipitates with the calcium and magnesium ions contained in hard water. Because of their high Krafft points (50 °C for calcium dodecyl sulfate, compared to 9 °C for the sodium salt), these precipitates are hardly soluble at ambient temperatures (Shinoda and Hirai, 1977).

The Krafft point can effectively be lowered by introducing ethyleneoxide (CH_2CH_2O) groups between the hydrocarbon chain and ionic groups of the ionic surfactant, even in the presence of high valency counterions. In addition, calcium salts of these surfactants have significantly lower CMC than the sodium salt (Shinoda and Hirai, 1977; Shinoda et al., 1986). Zapf et al. (2003) reviewed the current status of calcium salt surfactants, and Laskowski et al. (2007) discussed the Krafft point of cationic surfactants used for mineral flotation.

13.3.2.3 Solubility of nonionic surfactants: cloud point

The nonionic surfactant is water soluble through hydrogen bonds formation of hydrophilic moieties with water. As the temperature is raised, it reaches the point at which large aggregates of the nonionic surfactant separate out into a distinct phase. The temperature at which the phase separation occurs is referred to as the cloud point. The surfactant molecules partition into the oil phase above the cloud point, and a large amount of water is solubilized in the oil phase near this temperature (Shinoda and Ogawa, 1967). Polyoxyethylene $(CH_2CH_2O)_n$ moieties of the nonionic surfactant range from 3 or 4 to 40 or more. The cloud point increases almost linearly with n: the longer the polyoxyethylene chain, the higher the cloud point. Nonionic surfactants used in asphalt emulsion generally have cloud points above the boiling point of water, which is an issue only when emulsifying high softening-point asphalts at high temperatures (James and Logaraj, 2002).

Abrupt changes in application properties occur below the Krafft point of ionic and above the cloud point of nonionic surfactant solutions. For example, asphalt emulsion used for chip seal application is sometimes manufactured using the cationic emulsifier with a Krafft point near 60 °C, and the emulsion should be stored and tested above this temperature to prevent premature breaking.

13.4 The emulsification process and emulsion properties

13.4.1 Hydrodynamic aspects of emulsification

Two-dimensional linear flows can be characterized by the parameter λ, which can vary from -1, pure rotational, to $+1$, pure shear (extensional), as shown in Figure 13.3 (Kao et al., 1977; van de Ven, 1989); and the simple shear flow, $\lambda = 0$, is a combination of rotational and extensional flow. In the simple shear flow, deformation and breakup of an isolated drop depends on the viscosity ratio (dispersed-phase viscosity, μ_D, divided by the continuous-phase viscosity, μ_C) and on the capillary number, Ca, defined as

www.EngineeringEBooksPdf.com

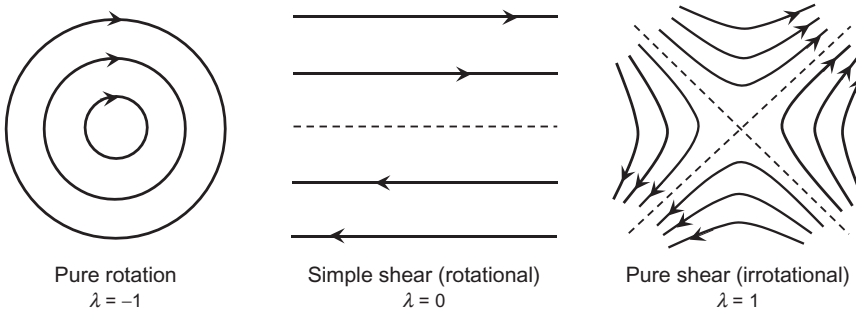


Figure 13.3 General two-dimensional linear flows characterized by the parameter λ which can vary from -1 (pure rotation) to +1 (pure shear).

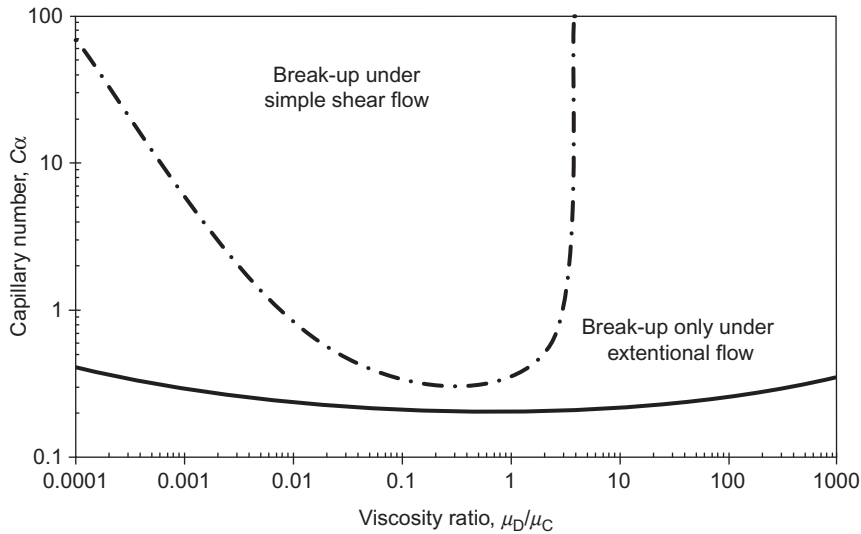


Figure 13.4 Boundaries for break-up of a liquid drop subjected to the simple shear and extensional flow. No droplets break-up occurs when the viscosity of the suspended drop is more than 4× of the suspending medium under the simple shear flow. In contrast, droplets break-up occurs under a wide range of conditions under the extensional flow.

$$Ca = \frac{a\mu_C G}{\gamma_{wo}} \tag{13.5}$$

where a is the droplet radius and G is the shear rate (Briscoe et al., 1999; Janssen et al., 1994). Droplet breakup occurs when the balance between the shearing stress and the retracting interfacial tension becomes higher than a critical value, as shown by the solid line in Figure 13.4 (Grance, 1982; Rallison, 1984). The figure demonstrates that no droplet breakup occurs when $\mu_D > 4\times$ of μ_C under the simple shear flow. This means that the emulsification of asphalt into water would not occur in the simple shear flow.

www.EngineeringEBooksPdf.com

Under the extensional flow, the viscosity ratio plays only a minor role, and droplet breakup occurs under a wide range of conditions once *Ca* is below the critical value, as shown in Figure 13.4 (Chin and Han, 1979, 1980). Here, the droplet is stretched into a thin liquid thread under the pure shear flow without rotation, and breaks into a great number of daughter droplets due to the growth of instabilities on the droplet surface (Khakhar and Ottino, 1987; Rumscheidt and Mason, 1962).

The colloid mill employs a very high-shear extensional flow, and is capable of dispersing a highly viscous fluid at a high-volume fraction into a low-viscosity medium. Here, it is the capillary-force-driven breakup in the mill, and lowering the interfacial tension is not necessarily beneficial for the emulsification (Wieringa et al., 1996). Use of appropriate emulsifiers is, however, essential to achieving desired storage stability and application properties of the emulsions produced.

13.4.2 Emulsion rheology

Table 13.1 represents a typical formulation for preparing 3 kg of a CRS emulsion containing approximately 65% asphalt. The resulting asphalt emulsion has mean particle size of 2–5 μm in diameter with distribution from 0.3 to 20 μm, as illustrated in Figure 13.5 (narrow distribution). The emulsion contains as many as 3×10^{13} asphalt droplets, and their total surface area exceeds 600 m^2. In contrast, the surface area of the bulk asphalt is only 2×10^{-3} m^2 prior to the emulsification. There is no doubt that

Table 13.1 A typical formulation for the CRS asphalt emulsion

Materials	Asphalt	Emulsifier	HCl	Water
Weight	2 kg	4 g	3 g	900 g

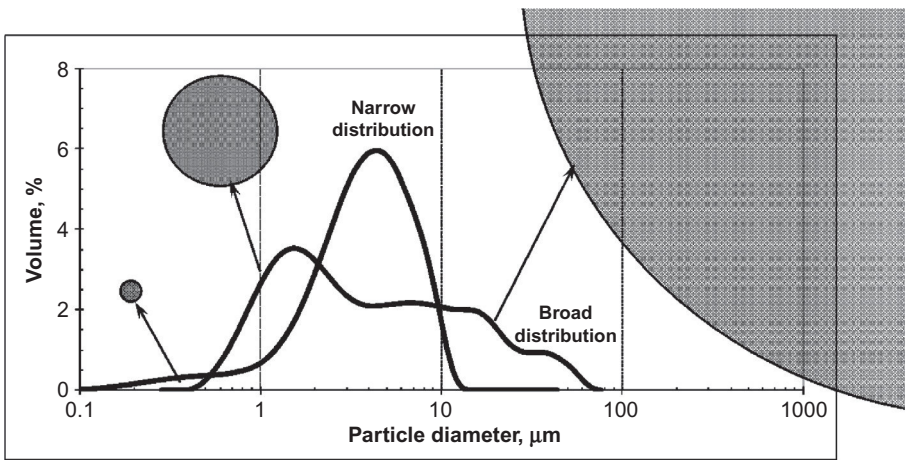


Figure 13.5 Particle size distributions of typical asphalt emulsions having narrow and broad distributions. A 20 μm in diameter particle has the equivalent volume of 8000 fine particles.

www.EngineeringEBooksPdf.com

this large number of particles with enormous surface area must have a significant influence on the rheological and application properties of asphalt emulsions.

The apparent viscosity of a liquid increases with the addition of colloidal particles. Einstein (1906) calculated the increases in viscosity with volume fraction of the colloidal particles, and obtained the result for low-volume fractions $\phi \ll 1$:

$$\mu = \mu_o(1 + 2.5\phi) \tag{13.6}$$

where μ is the apparent viscosity of the dispersion and μ_o is that of the suspending medium. Booth (1950) extended the calculation, including the increase in viscosity due to the presence of an electrical double layer around the colloidal particle:

$$\mu = \mu_o(1 + [\mu]\phi) \tag{13.7}$$

His result for the intrinsic viscosity $[\mu]$ for particles with low ζ-potentials can be written as

$$[\mu] = 2.5 + \overline{b}y^2 Q(\tau) \tag{13.8}$$

Here, $\overline{b}$ is the average dimensionless ion size, related to ion mobility; y is the reduced ζ-potential ($e\zeta/k_BT$, where e is the electron charge, k_B the Boltzmann constant, and T the absolute temperature); and $Q(\tau)$ is the function of the double-layer parameter, $\tau = \kappa a$, $\kappa = \sqrt{2e^2 n_o z^2/\varepsilon k_B T}$, κ being the reciprocal double-layer thickness, n_o and z the number of ions and their valency in the solution, and ε the permittivity of the solution. The function of $Q(\tau)$ approaches infinity as $\tau \to 0$, that is, as the double-layer thickness approaches infinity or, equivalently, as the ion concentration approaches zero. For a neutral sphere and/or $\tau \to \infty$, $[\mu] \to 2.5$.

The contribution to the viscosity of the order of ϕ^2 can be expressed as (Batchelor and Green, 1972; Cox and Brenner, 1971):

$$\mu = \mu_o\left(1 + k_1\phi + k_2\phi^2\right) \tag{13.9}$$

Here, $k_1 (= [\mu])$ and k_2 are the first and second virial coefficients, originating from the energy dissipation (μG^2) due to the disturbance flow around a sphere and around two colliding spheres, respectively. k_2 is a function of the type of flow and Péclet number, $Pe = Ga^2/D$, where D is the diffusion constant, and for the spherical particle, $D = k_BT/6\pi a\mu_o$. For $Pe = \infty$, $k_2 \approx 5.2$ and 7.0 for the simple and extensional flow ($\lambda = 0$ and 1, respectively) in Figure 13.3, respectively (Takamura and van de Ven, 2010).

For dispersions of highly charged colloidal particles, increase in k_2 due to the electric double-layer interactions is usually referred to as the secondary electroviscous effect, and can be approximated as (van de Ven, 1989):

$$k_2 = k_2^o + \frac{3}{40\tau^5}\left[\ln\left(\frac{\alpha}{\ln(\alpha/\ln(\alpha))}\right)\right]^4 \ln\left(\frac{\alpha}{\ln(\alpha)}\right) \tag{13.10}$$

www.EngineeringEBooksPdf.com

where k_2^o is the second virial coefficient in the absence of electrostatic particle interactions, and $\alpha = 4\pi\varepsilon^2 a\tau \exp(2\tau)/k_B T$. At low electrolyte concentrations (small τ), the secondary electroviscous effect is known to be significant.

Van de Ven (1989) extended Equation (13.9) to highly concentrated dispersions using a modified effective-medium theory, and obtained

$$\mu = \mu_o \left[\frac{1-\phi/\phi_m}{1-(k_o\phi_m - 1)\phi/\phi_m}\right]^{-2.5\phi_m/(2-k_o\phi_m)} \tag{13.11}$$

where ϕ_m is the volume fraction at which the viscosity reaches an infinite value ($\phi_m \cong 0.74$ for hexagonal cross-packing of nondeforming monodisperse particles and 0.85 for polydisperse dispersions), and k_o is the particle interaction parameter relative to the hydrodynamic forces.

Equation (13.11) has been successfully applied to examine the shear-thinning behavior of concentrated latex dispersions over a wide range of conditions of $10^{-3} < \mu < 10^2$ Pa s and $10^{-3} < G < 10^4$ s^{-1} (Takamura and van de Ven, 2010). The equation assumes that the shear thinning is a result of the energy dissipation associated with hydrodynamic and colloidal particle interactions, and $k_o \cong 1.7$ at the high-shear limit. The particle trajectories of two colliding spheres in simple shear flow are a strong function of their size ratio (Adler, 1981), and the time these spheres spend within the separation distance where the colloidal forces becomes significant, decreases sharply as one sphere is smaller than the other. Therefore, a lesser degree of energy dissipation is associated with colloidal particle interactions when the particle sizes are different, even at lower shear rates, and the electroviscous effect is weaker.

Equation (13.11) would lead us to a number of new insights for understanding the rheological properties of the asphalt emulsions. Figure 13.6a illustrates the estimated low-shear ($1 < G < 10$ s^{-1}) viscosity versus asphalt content of two emulsions having distinctly different size distribution. The upper curve in this graph represents a typical asphalt emulsion with narrow-size distribution, as shown in Figure 13.5. Only a few percent increase in the (effective) asphalt content would result in significant increase in the emulsion viscosity, as demonstrated by swelling of the water-in-oil-in-water emulsion during storage (James et al., 1999). This type of emulsion also shows strong shear-thinning behavior, as illustrated in Figure 13.6b, due to the secondary electroviscous effect (Johannes and Bahia, 2013; Nuñez et al., 2000). As seen in the figure, the magnitude of the shear-thinning behavior is highly sensitive to the asphalt content.

In contrast, the emulsion depicted by the lower curve in Figure 13.6a (similar to the one with the broad distribution in Figure 13.5) is near the Newtonian fluid. The presence of one 20 μm diameter particle is equivalent to the absence of 8000 fine particles of 1 μm diameter, thus drastically altering particle–particle interactions under the simple shear flow. Equation (13.11) predicts that the concentrated emulsion is the shear-thinning behavior under simple shear flow (Figure 13.3), but shear thickening in extensional flow. This fact should be considered when evaluating the sprayability of CRS emulsions.

www.EngineeringEBooksPdf.com

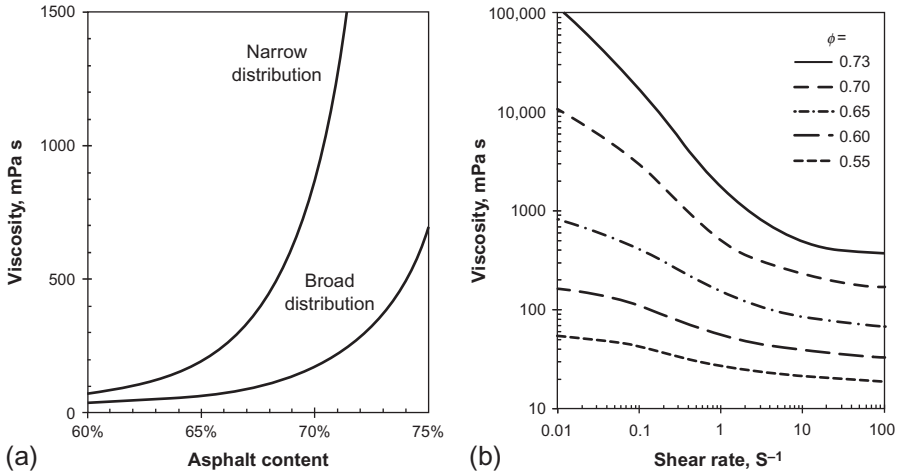


Figure 13.6 (a) Predicted viscosity vs. asphalt content relationship for narrow and broad particles distributions at $1 < G < 10\ s^{-1}$. (b) Shear thinning behavior of the asphalt emulsion with narrow-size distribution at asphalt contents between 0.55 and 0.73.

13.5 Fundamental aspects of dispersion stability of asphalt emulsions

13.5.1 Electric properties of asphalt/water interface

In 1937, Danielli (1937) stated, "The work of Donnan (1899), Jahrisch (1922), Hartridge and Peters (1922) and Peters (1931) has shown that the interfacial tension between solutions of long-chain acids, or amines, and aqueous solutions is much lowered when the pH of the aqueous phases is such that the end group of the acid or amine, which forms the interfacial film between the immiscible solvents, is electrically dissociated. . . . Close inspection of Peter's curves shows, however, that the range of pH over which the interfacial tension change occurs with the fatty acids is about 3 units of pH more alkaline than the range over which dissociation occurs in bulk phases; also that dilution of the buffer solutions, without changing in pH, may cause a rise in interfacial tension. . . . Those results strongly suggest that the pH in the surface layer may not be the same as in the bulk aqueous phase." Zisman (1941) also confirmed Danielli's observation through examining the effects of polar components on the spreading of mineral oil on water.

The dissociation behavior of the ionizable charge groups as a function of both bulk pH and electrolyte concentration can be quantitatively predicted by the ionizable surface-group model (Healy and White, 1978; Takamura and Chow, 1985). For example, let us assume the charge of the bitumen/water interface is derived from the dissociation of carboxyl groups derived from natural acid groups in the bitumen (i.e., heavy crude oil from Athabasca oil sand in Canada):

www.EngineeringEBooksPdf.com

$$\mathrm{RCOOH} \rightleftharpoons \mathrm{RCOO^-} + \mathrm{H^+} \tag{13.12}$$

and

$$K_a = \frac{[\mathrm{RCOO^-}][\mathrm{H^+}]_s}{[\mathrm{RCOOH}]} \tag{13.13}$$

where K_a is the dissociation constant for the surface group and $[\mathrm{H^+}]_s$ is the hydrogen-ion concentration in the vicinity of the $\mathrm{COO^-}$ sites on the surface. We assume $[\mathrm{H^+}]_s$ is related to the bulk hydrogen-ion activity $[\mathrm{H^+}]_b$ by

$$[\mathrm{H^+}]_s = [\mathrm{H^+}]_b \exp(-y_o) \tag{13.14}$$

where y_o is the reduced surface potential:

$$y_o = \frac{e\psi_o}{k_B T} \tag{13.15}$$

Here ψ_o is the surface potential. $[\mathrm{H^+}]_s > [\mathrm{H^+}]_b$, because $\exp(-y_o) > 1$ because of $\psi_o < 0$ for the negatively charged surface. Equation (13.14) implies that hydrogen ions are preferentially accumulated near the negatively charged bitumen surface. Equation (13.14) may be rewritten as

$$\mathrm{pH_s} = -\log\{[\mathrm{H^+}]_s\} = \mathrm{pH_b} + \frac{y_o}{2.303} \tag{13.16}$$

indicating that $\mathrm{pH_s} < \mathrm{pH_b}$ because $y_o < 0$, where $\mathrm{pH_s}$ and $\mathrm{pH_b}$ are the pH in the vicinity of the surface and in the bulk solution, respectively. This derivation assumes that these effects are solely due to the coulombic interaction between positive hydrogen ions and the negatively charged surface.

We have assumed that the surface charge is due to the dissociation of the carboxyl groups on the surface; thus, the surface charge density, σ_o, is given simply by

$$\sigma_o = -e[\mathrm{COO^-}] \tag{13.17}$$

The total surface density of functional groups, N_s, is given by

$$N_s = [\mathrm{COO^-}] + [\mathrm{COOH}] \tag{13.18}$$

Combining Equations (13.13), (13.14), (13.17), and (13.18) results in

$$\sigma_o = \frac{-eN_s}{1 + [[\mathrm{H^+}]_b / K_a] \exp(-y_o)} \tag{13.19}$$

The charge density, σ_d, in the diffused electric double layer may be related to the surface potential by equating the surface charge to the net space charge in the double layer and applying the Gouy–Chapman theory:

www.EngineeringEBooksPdf.com

$$\sigma_d = -\sqrt{8 n_o \varepsilon k_B T} \sinh(z y_o/2) \tag{13.20}$$

By assuming $\sigma_d = -\sigma_o$, the solution of Equations (13.19) and (13.20) provides an explicit relationship between the surface charge density and surface potential in terms of bulk pH, n_o, and N_s:

$$pH_b = -y_o/2.303 + pK_a - \log\left\{\frac{\theta}{\sinh(z y_o/2)} - 1\right\} \tag{13.21}$$

where

$$\theta = \frac{-eN_s}{\sqrt{8 n_o \varepsilon k_B T}} \tag{13.22}$$

In Equation (13.21), both θ and y_o have negative values for the bitumen/water interface. Equations (13.21) and (13.22) allow a direct calculation of the bulk pH required to establish any arbitrary surface potential at given N_s, pK_a, and bulk electrolyte concentration, C, expressed in mol dm^{-3} because $n_o = 10^3 C N_A$, where N_A is Avogadro's number. Once a $\psi_o - pH_b$ relationship has been obtained, the surface charge density, σ_o, can be calculated using Equation (13.20).

Calculated relationships between σ_o and pH_b are shown in Figure 13.7a using values of $pK_a = 4.5$ and $N_s = 2 \times 10^{18}\,m^{-2}$, which correspond to the monolayer coverage of carboxylic acid at the bitumen/water interface, in aqueous NaCl solutions of 10^{-3}, 10^{-2}, and 10^{-1} M. The ionizable surface-group model predicts that 50% dissociation of acid groups occurs at pH_b is 6.4, 7.4, and 8.4 in these three NaCl concentrations, respectively, thus successfully confirming Danielli's observation: "The range of pH over which the interfacial tension change occurs with the fatty acids is about 3 units of pH more alkaline than the range over which dissociation occurs in bulk phases; also that dilution of the buffer solutions, without changing in pH, may cause a rise in interfacial tension." The figure also explains why the anionic asphalt emulsion is produced at a particular pH range of 10.5–12.5, where naturally occurring carboxylic acids in the asphalt are 90–100% dissociated.

The above discussed calculation can be extended to include the specific interaction between Ca^{2+} and $RCOO^-$ on the bitumen surface:

$$RCOO^- + Ca^{2+} \rightleftharpoons RCOOCa^+ \tag{13.23}$$

and the Ca^{2+}-binding constant is defined by

$$K_{Ca} = \frac{[RCOO^-][Ca^{2+}]_s}{[RCOOCa^+]} \tag{13.24}$$

Here again, the subscript "s" refers to the concentration of ions in solution immediately in contact with the bitumen surface. As in Equation (13.14), $[Ca^{2+}]_s$ is related to the bulk calcium ion concentration, $[Ca^{2+}]_b$:

www.EngineeringEBooksPdf.com

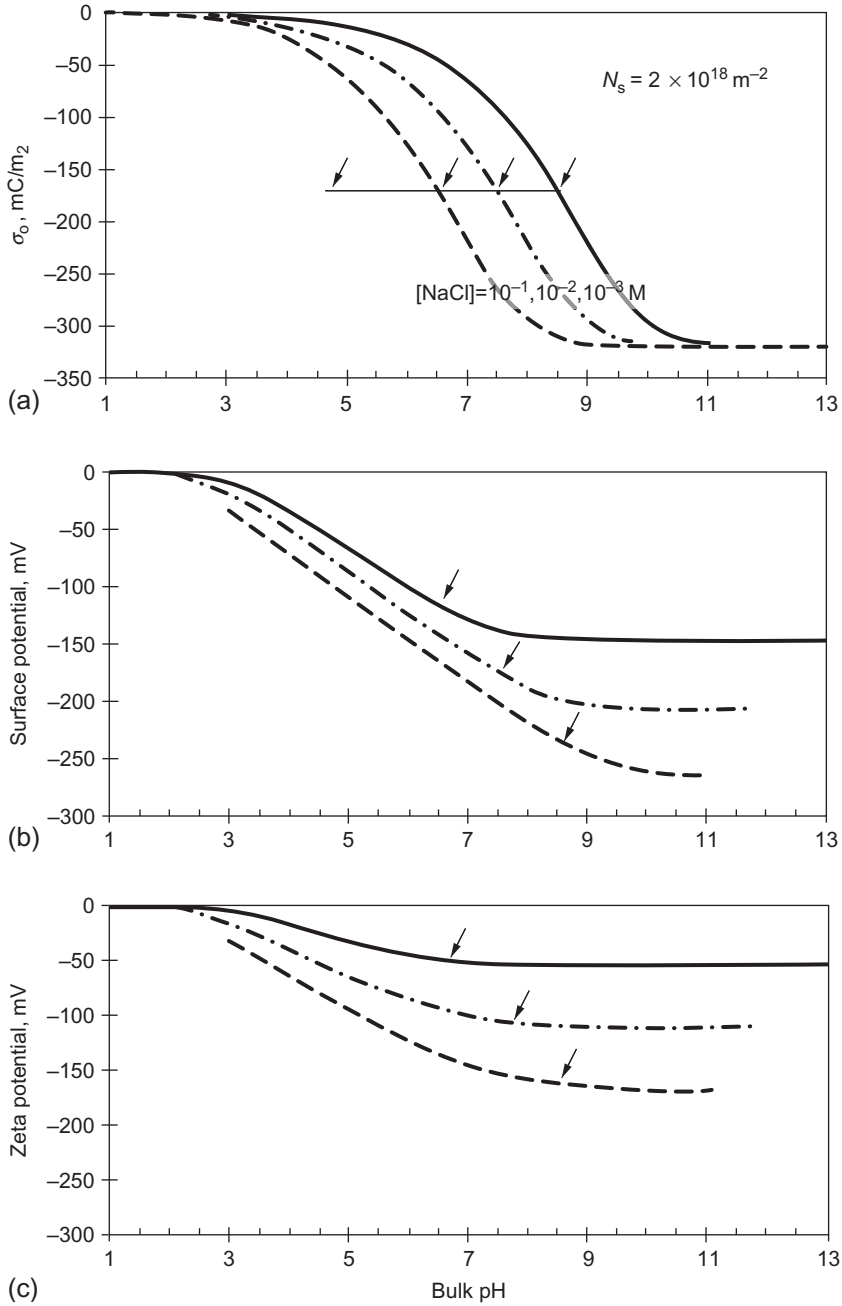


Figure 13.7 Predicted (a) surface charge density, (b) surface potential, and (c) ζ-potential as a function of the bulk pH at three different electrolyte concentrations of 10^{-1}, 10^{-2}, and 10^{-3} M NaCl at 25 °C. Arrows indicate conditions 50% dissociation of carboxyl groups at the bitumen/water interface.

www.EngineeringEBooksPdf.com

$$\left[Ca^{2+}\right]_s = \left[Ca^{2+}\right]_b \exp(-2y_o) \tag{13.25}$$

The surface charge density can now be expressed as

$$\sigma_o = eN_s \times \frac{\left(\left[Ca^{2+}\right]_b/K_{Ca}\right)\exp(-2y_o) - \left(\left[H^+\right]_b/K_a\right)\exp(-y_o)}{1 + \left(\left[Ca^{2+}\right]_b/K_{Ca}\right)\exp(-2y_o) + \left(\left[H^+\right]_b/K_a\right)\exp(-y_o)} \tag{13.26}$$

Now, in the presence of both mono and divalent ions, the equation is expressed as

$$\sigma_d = \left\{2\varepsilon k_B T \sum_i n_i^o [\exp(-z_i y_o) - 1]\right\}^{1/2} \tag{13.27}$$

where n_i^o and z_i are the ion densities in the bulk solution and their valencies, respectively. Equations (13.26) and (13.27) are solved numerically, using $pK_{Ca} = 0.53$ for the acetic acid (Chow and Takamura, 1988).

Similar arguments show that for cationic emulsions, the pH at the surface of the asphalt droplet is higher than the bulk pH, and the extent of protonation of basic amine groups is correspondingly less. Because of naturally occurring carboxylic acids in the asphalt, the surface charge will depend also on the relative amounts of cationic and anionic groups at the interface. This is discussed in more detail in Section 13.5.2.4.

13.5.2 DLVO theory of dispersion stability

13.5.2.1 Stability diagram of bitumen emulsions

The dispersion stability of the bitumen emulsion can be predicted using the DLVO (Derjaguin, Landau, Verwey, and Overbeek) theory of colloid stability (Hunter, 1986) in conjunction with the ionizable surface-group model as a function of pH and electrolyte concentration (Takamura et al., 1987). The total potential energy, $V_{ttl}(h)$, between a pair of bitumen droplets can be calculated as a function of the separation distance, h, between the surfaces using the relation

$$V_{ttl}(h) = V_{rep}(h) + V_{attr}(h) \tag{13.28}$$

where $V_{rep}(h)$ and $V_{attr}(h)$ are the double-layer and van der Waals interactions, respectively. $V_{rep}(h)$ can be calculated using ζ-potential of particles, shown in Figure 13.7c (Gregory, 1975):

$$V_{rep}(h) = \frac{a_1 a_2}{a_1 + a_2} \times \frac{128\pi n_o k_B T}{\kappa^2} Y_1 Y_2 \exp(-\kappa h) \tag{13.29}$$

where $Y_1 = \tanh(ze_1/4k_BT)$, and a_1 and ζ_1 are the radius and ζ-potential of droplet 1, and so on. The retarded van der Waals attraction is expressed (Gregory, 1981).

www.EngineeringEBooksPdf.com

$$V_{attr}(h) = \frac{-A_{bwb}}{6h} \times \frac{a_1 a_2}{a_1 + a_2} \times \left[1 - \frac{5.32h}{v} \ln\left(1 + \frac{v}{5.32h}\right)\right] \quad [13.30]$$

Here, A_{bwb} is the Hamaker constant between bitumen particles in water and v is the London wavelength of roughly 100 nm. An approximate value of A_{bwb} can be estimated from the expression (Hunter, 1986)

$$A_{bwb} = \left(\sqrt{A_{bb}} - \sqrt{A_{ww}}\right)^2 \quad (13.31)$$

where A_{bb} and A_{ww} are the Hamaker constants of bitumen and water in vacuum. Using the values of 6.0×10^{-21} and 3.5×10^{-21} J for A_{bb} and A_{ww}, respectively (Takamura and Chow, 1983), Equation (13.31) yields $A_{bwb} = 5.7 \times 10^{-21}$ J (Takamura and Wallace, 1988).

Figure 13.8a and b represents examples of the calculated $V_{ttl}(h)$ for anionic bitumen emulsions in four different concentrations of NaCl and $CaCl_2$ solutions at pH 6.0. The particle radius was assumed to be 2.0 μm ($a_1 = a_2$ and $\zeta_1 = \zeta_2$). The presence of a deep secondary energy minimum of approximately $-40\ k_B T$ in 3×10^{-1} M NaCl, which is the result of the high ζ-potential of bitumen particles even at such a high NaCl

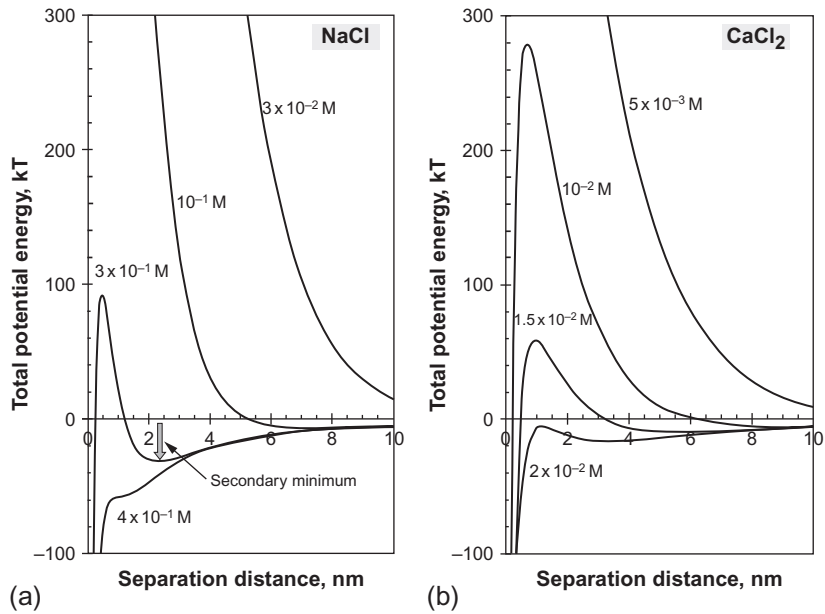


Figure 13.8 Calculated $V_{ttl}(h)$ for bitumen particles in the presence of four different concentration of (a) NaCl and (b) $CaCl_2$ at pH 6. The deep secondary minimum of approximately $-50\ k_B T$ exists in 3×10^{-1} M NaCl, causing flocculation of bitumen emulsions. The presence of as low as 2×10^{-2} M $CaCl_2$ in the emulsion would cause coalescence of bitumen droplets. Ca^{2+} is the bivalent counter ion for negatively bitumen particles.

www.EngineeringEBooksPdf.com

concentration (Figure 13.7c), can be seen in Figure 13.8a. The bitumen droplets will weakly flocculate around this electrolyte concentration.

The stability diagrams for bitumen emulsions were constructed by conducting similar calculations at various pH and electrolyte concentrations, as shown in Figure 13.9a and b for NaCl and $CaCl_2$ solutions, respectively. Vertical lines at 0.43 M NaCl and 0.011 M $CaCl_2$ represent critical coagulation concentrations (ccc) for monovalent and bivalent counterions, above which the emulsion becomes unstable.

In asphalt emulsions stabilized with carboxylic acid emulsifiers, the surface of the droplets may not be fully covered with surfactant, or, on the other hand, the surface may be full and the water phase (serum) of the emulsion may contain excess

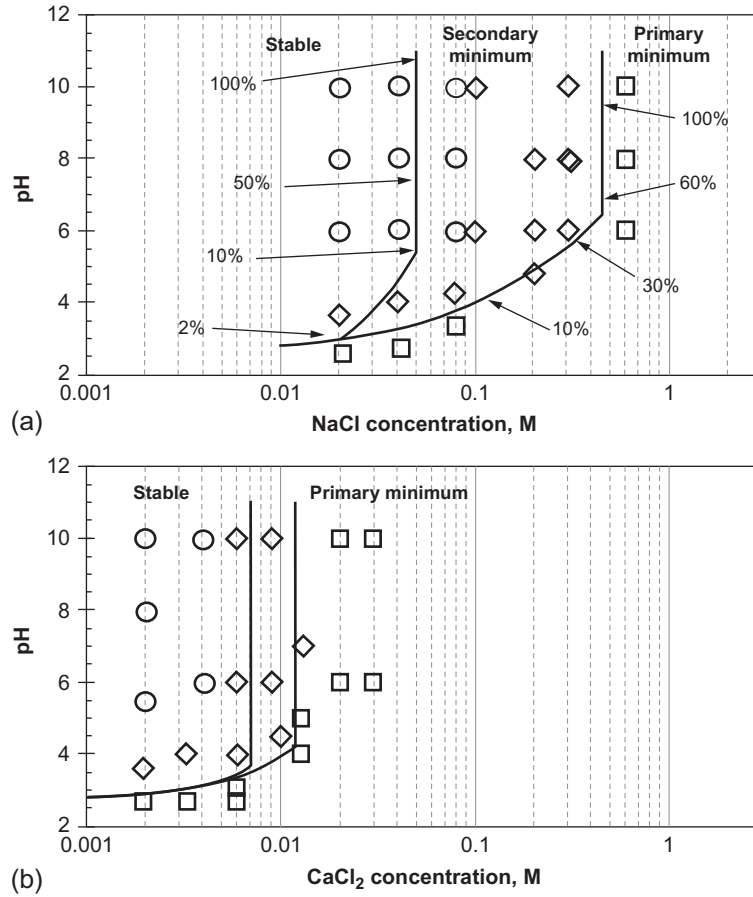


Figure 13.9 Stability diagram of bitumen droplets as a function of pH and electrolyte concentrations: (a) for NaCl and (b) for $CaCl_2$. Estimated % dissociation of the carboxyl acids on the bitumen surface are also indicated in (a). Experimentally determined stability of the bitumen droplets (symbols) agrees well with the prediction.

www.EngineeringEBooksPdf.com

emulsifier. Titration of anionic asphalt emulsion with calcium chloride solution at the natural pH of the emulsion (typically 11–12) is widely used in the industry to estimate reactivity. In the test, known as the demulsibility test, a 0.01 M calcium chloride solution is added to emulsion in a proportion to give an approximately 0.005 M solution when combined with the water phase of the emulsion. If substantial coagulation (>40%) of the emulsion occurs, then the emulsion is classified as RS.

13.5.2.2 Experimental confirmation of the stability diagram

The stability of the bitumen emulsion produced from Athabasca oil sand (high-acid-number heavy crude oil) was studied as a function of NaCl and $CaCl_2$ at various pH (Takamura et al., 1987). Here, a 10 mL aliquot of the bitumen emulsion (4% bitumen) was placed in a test tube, and the pH and electrolyte concentration were adjusted by adding a small amount of NaOH or HCl, and NaCl or $CaCl_2$ solutions. After gently mixing, the sample was left standing for 24 h, and any changes in the emulsion stability (stable, weakly coagulated, or strongly coagulated) were recorded.

The emulsion was stable below 0.08 M NaCl at pH 6. Small-size aggregates started to appear in 0.1 M, and their size and number increased in 0.2 M NaCl. The formation of large-size aggregates was clearly seen in 0.6 M NaCl, and complete coalescence of these aggregates were seen as the emulsion was heated to 70 °C (lowering the bitumen viscosity from 400 to 2 Pa s). Results of the observed coagulation behavior of the emulsion in NaCl and $CaCl_2$ solutions are superimposed on the theoretical stability diagrams in Figure 13.9a and b, respectively. These figures demonstrate that the stability of the bitumen emulsion can be adequately predicted using ζ-potentials calculated from the ionizable surface-group model in conjunction with the DLVO theory, without any experimentally determined variables.

13.5.2.3 Stability test of cationic asphalt emulsions

Figure 13.9a indicates that as little as 10–30% dissociation of carboxyl groups ($\sigma_o \approx 30-90$ mC/m^2, respectively) is enough to maintain the stable dispersion at [NaCl] < 0.3 M. This suggests that the electrostatic interaction alone would not be enough to control the reactivity of the asphalt emulsion, and that it is necessary to use application-specific surfactants that provide desired stability through electrosteric stabilization.

Figure 13.10a and b compares the coagulation behavior of CRS and CQS emulsions in 1 M NaCl and 0.02 M Na_2SO_4 solutions. SO_4^{2-} is the bivalent counterion for the cationic emulsion. Asphalt droplets in the CRS emulsion form small-size coagula in 1 M NaCl, and completely coalesce to become just one blob at the bottom of a vial in the presence of 0.02 M SO_4^{2-}, demonstrating that asphalt droplets in this emulsion are stabilized by the electrostatic interaction alone. In contrast, the CQS emulsion maintains some stability in 1 M NaCl, forming only very fine coagula, and coagulum size remains relatively small even in 0.02 M Na_2SO_4.

As discussed in Section 13.2, the CRS emulsifier is with a small hydrophilic "head" group, which provides the electrostatic interaction to asphalt droplets. Emulsifiers for

www.EngineeringEBooksPdf.com

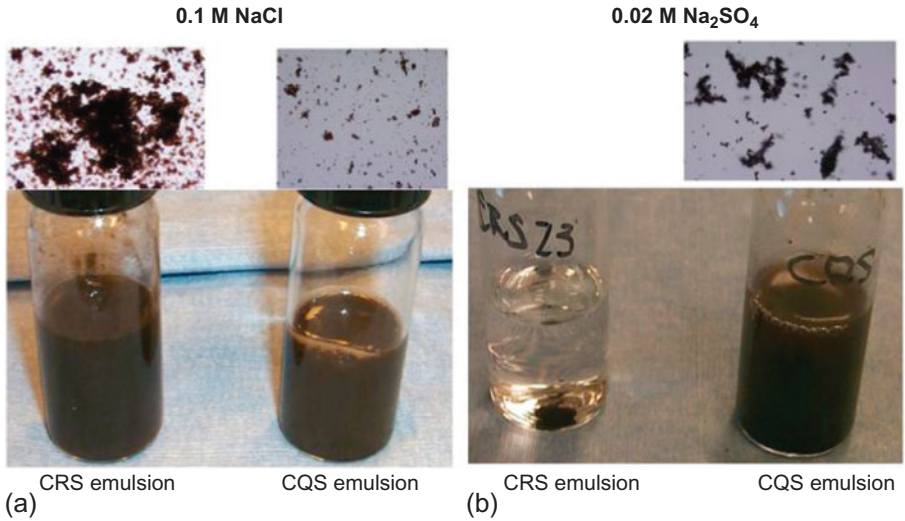


Figure 13.10 Coagulation behaviors of CRS and CQS emulsions in (a) 0.1 M NaCl and (b) 0.02 M Na_2SO_4. SO_4^{2-} is the bivalent counter ion for positively charged CRS and CQS emulsion particles. Results demonstrate the CRS emulsion is stabilized by the electrostatic interaction alone but the CQS emulsion is electrosterically stabilized.

less reactive emulsions are with bigger size "head" groups, which prevent asphalt particles approaching below 0.5–2 nm (steric repulsion), thus weakening or overcoming strong van der Waals attractive forces at $h < 2$ nm. The slower the setting, the bigger the size of "head" groups in the emulsifier molecules.

13.5.2.4 *Mathematical models for asphalt/water and aggregate/water interfaces*

Some crude oils and asphalt contain naturally occurring acid as well as base groups (Salou et al., 1998), and the ionizable surface-group model was extended to take the zwitterionic nature of the interface into account (Buckley et al., 1987; Harding and Healy, 1985):

$$AH \rightleftharpoons A^- + H^+ \tag{13.32}$$

and

$$BH^+ = B + H^+ \tag{13.33}$$

Here, A^- and BH^+ represent acidic and basic groups at the interface, and their dissociation constants are defined by

www.EngineeringEBooksPdf.com

$$K_{a1} = \frac{[A^-][H^+]_s}{[AH]} \tag{13.34}$$

and

$$K_{a2} = \frac{[B][H^+]_s}{[BH^+]} \tag{13.35}$$

Similar to Equations (13.19) and (13.26), σ_o for this type of interface can be written as

$$\sigma_o = eN_{a1} \times \left[\left(\frac{f}{1 + (K_{a2}/[H^+]_b)\exp(y_o)} \right) - \left(\frac{1}{1 + ([H^+]_b/K_{a1})\exp(-y_o)} \right) \right] \tag{13.36}$$

where fractional coverage, f, of the surface by acidic and basic groups is expressed as $f = N_{a2}/N_{a1}$, and N_{a1} and N_{a2} are the total number of acidic and basic sites at the interface, respectively. Fractions of acid and base groups dissociated, $[A^-]$ and $[B^+]$, respectively, are represented in Figure 13.11; together with $[A^-]+[B^+]$ at [NaCl] = 0.01 and 0.1 M using N_{a1} and N_{a2} are 1.0×10^{18} and $N_{a2} = 1.1 \times 10^{18}$ m^{-2}, respectively. The pK_{a1} and pK_{a2} for the acid and base groups are assumed to be 4.5 and 10, respectively. These variables are chosen to represent the CRS asphalt emulsion with a primary amine emulsifier (Castro et al., 1986) and relatively low-acid-number asphalt. Acid values of paving-grade asphalts range up to 4 mg KOH/g (7 mequiv./100 g), which is comparable to the amine value of a rapid-set emulsifier like tallow-diamine, which at 0.2% on emulsion is about 4 mequiv./100 g asphalt.

Dissociation behavior of these charge groups is rather complex, because pH_b is now influenced by both $[A^-]$ and $[B^+]$. The figure indicates that the CRS emulsion

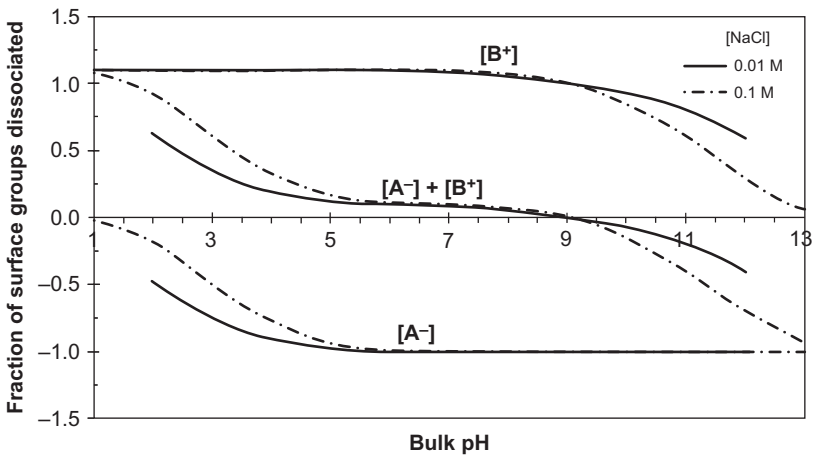


Figure 13.11 Fraction of acid $[A^-]$, base $[B^+]$ and sum of dissociated surface groups for the CRS asphalt emulsion as a function of the bulk pH in 0.01 and 0.1 M NaCl. See the text for detailed conditions.

www.EngineeringEBooksPdf.com

becomes negatively charged at pH > 9 due to excess [$RCOO^-$]. ζ-Potential measurements on diluted cationic asphalt emulsions (with uncontrolled ionic strength) confirm this behavior (Samadijavan, 1994; Wates and James, 1993), with emulsion based on high-acid-value Venezuelan bitumen and 0.2% tallowdiamine hydrochloride having a point of zero charge of pH 8, compared to pH 10.5 for an emulsion of neutral oil.

Similarly, the amphoteric nature of the silica/water interface can be described by (Healy and White, 1978)

$$SiOH_2^+ \rightleftharpoons SiOH + H^+ \tag{13.37}$$

and

$$SiOH \rightleftharpoons SiO^- + H^+ \tag{13.38}$$

Dissociation constants for these reactions are given by

$$K_+ = \frac{[SiOH][H^+]_s}{[SiOH_2^+]} \tag{13.39}$$

and

$$K_- = \frac{[SiO^-][H^+]_s}{[SiOH]} \tag{13.40}$$

An expression for the surface charge density is now given by

$$\sigma_o = eN_m \times \frac{([H^+]_b/K_-)\exp(-y_o) - (K_-/[H^+]_b)\exp(y_o)}{1 + ([H^+]_b/K_+)\exp(-y_o) + (K_-/[H^+]_b)\exp(y_o)} \tag{13.41}$$

Once again, the conditions that satisfy $\sigma_o + \sigma_d = 0$ (Equations 13.19 and 13.41) can be solved numerically to obtain the $\psi_o - pH_b$ relationship. A predicted ζ versus bulk pH relationship for the silica surface is shown in Figure 13.12, using $N_m = 1 \times 10^{18}\ m^{-2}$, and pK_+ and pK_- of 1 and 5, respectively, in aqueous solutions of 0.03 M NaCl. Those variables are chosen to fit measured results by Wiese et al. (1971). The calculation indicates that less than 5% of surface groups are dissociated at $1 < pH < 4$. The figure also includes the same relationships for the CRS asphalt emulsion under the same conditions as Figure 13.11, except [NaCl] = 0.03 M. The CRS emulsion becomes negatively charged at pH > 9 due to excess [$RCOO^-$].

13.6 Setting mechanism of emulsions

13.6.1 Chip seal

Chip seal is referred to as the surface dressing in Europe. In this application, the road is sprayed with a CRS asphalt emulsion and then covered with mineral chippings (aggregates). Tausk et al. (1981) provide one of the most comprehensive discussions on the

www.EngineeringEBooksPdf.com

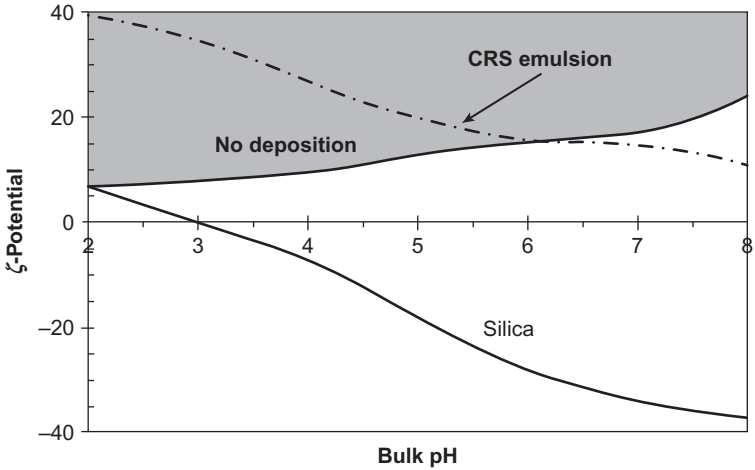


Figure 13.12 ζ-Potential vs. bulk pH relationships for asphalt particles in the CRS emulsion and clean silica surfaces as a function of bulk pH in 0.03 M NaCl. The deposition boundary for the asphalt particle on the silica surface is superimposed. Asphalt particles would not deposit on the silica surface when the ζ-potential of the silica surface fell above the non-deposit boundary line by adsorbing free cationic emulsifier molecules from the CRS emulsion.

curing mechanism of the asphalt emulsion for the chip seal application. They have described the curing of the emulsion as a two-stage process: (i) deposition and consolidation of asphalt droplets around the aggregate surface and (ii) water evaporation from the bulk emulsion surrounding the aggregates.

13.6.1.1 Deposition diagram of asphalt emulsion on the aggregate

The Hamaker constant between the asphalt droplet and aggregate (silica) in water, A_{bws}, can be estimated using the relationship

$$A_{bws} = \left(\sqrt{A_{bb}} - \sqrt{A_{ww}}\right) \times \left(\sqrt{A_{ss}} - \sqrt{A_{ww}}\right) \tag{13.42}$$

and $A_{bws} = 1.0 \times 10^{-20}$ J, using $A_{ss} = 1.7 \times 10^{-20}$ J, where A_{ss} is the Hamaker constant of silica particles in vacuum (Takamura and Wallace, 1988).

Similar to predicting the dispersion stability of the bitumen emulsion, it is now possible to construct a deposition diagram of the CRS asphalt particles on the silica surface using their ζ-potential versus pH relationships, and results are superimposed in Figure 13.12. Here, we have assumed that the emulsion serum contains 0.03 M NaCl, representing a relatively low level of the emulsifier and $2 < pH < 3$ of the CRS emulsion. In this diagram, no deposition of emulsion particles occurs if ζ-potential of the silica surface exceeds the value indicated by the boundary line due to adsorption of free CRS emulsifiers on its surface.

www.EngineeringEBooksPdf.com

13.6.1.2 Deposition and consolidation with nonreactive aggregates

The first stage of the curing of the chip seal can be best visualized with a simple test performed by Rodríguez-Valverde et al. (2008). Here, a drop (8 μL) of CRS emulsion is placed on a polished siliceous aggregate surface. This type of aggregate is classified as acidic and nonreactive against the cationic asphalt emulsion (Tausk et al., 1981), and the asphalt emulsion maintains its original pH ≈ 3 even after contact with the aggregate (Deneuvillers, 1997). A thin water-film, free of asphalt particles, spreads ahead of the bulk emulsion drop immediately after deposition and maintains its near-spherical-shape three-phase (air/emulsion/aggregate) contact line, and the dried emulsion drop exhibits a "volcano" shape deposit with a ring-like outer ridge and a slightly collapsed interior, as seen in Figure 13.13. This is the characteristic shape of a dried emulsion drop from stable dispersion, but a cone-shaped deposit results from unstable dispersion (Erkselius et al., 2008). The water-film continues to spread, even after semisolidification of the outer edge of the droplet. The originally hydrophilic surface of the siliceous aggregate becomes hydrophobic as a result of contact with the water-film (which contains free cationic surfactant molecules) from the asphalt emulsion at the outer perimeter of the dried emulsion (Rodríguez-Valverde et al., 2008).

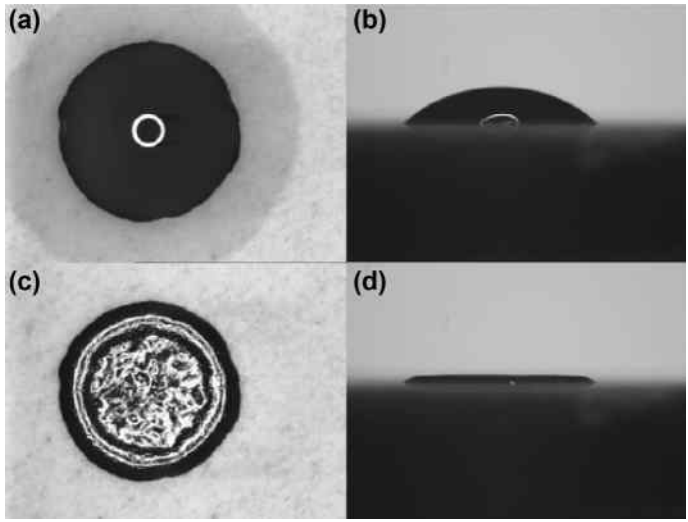


Figure 13.13 Top (a and b) and side (c and d) views of an emulsion drop (8 μL) on a polished siliceous aggregate surface. (a) A fast spreading water, free of asphalt particles, can be seen around the drop contact line. The inner bright ring is the light source reflection. (c) After 10.5 min drying, the drop has collapsed to exhibit a 'volcano' shape deposit with a ring-like outer ridge and a slightly collapsed interior.
After Rodríguez-Valverde et al. (2008).

www.EngineeringEBooksPdf.com

The deposition diagram shown in Figure 13.12 indicates that the ζ-potential of the clean silica is near neutral and in the vicinity of the nondeposition boundary at $2 < pH < 4$, where the asphalt particle possesses a highly positive ζ-potential. Only a limited deposition of asphalt particles is enough to prevent their further deposition on the silica surface. These partially deposited asphalt particles on the silica surface act as a filter to particles, but allow the transport of water from the bulk emulsion toward the spreading thin film. This results in rapid rises in asphalt content near the outer edge of asphalt emulsion on the silica surface.

The buildup of the apparent viscosity during this consolidation process is depicted in Figure 13.14, which extends to 78% asphalt content and also includes the near-low-shear-limit viscosity ($G \approx 0.01\ s^{-1}$). Tausk et al. (1981) reports that the consolidation occurs at around 50–60% loss of water from the emulsion, and this corresponds to an increase in the asphalt content from 62% to ~78%. This would cause a more than 330,000-time increase in the low-shear viscosity, from 0.3 to >100,000 Pa s for the emulsion with narrow-particle-size distribution. In comparison, the low-shear

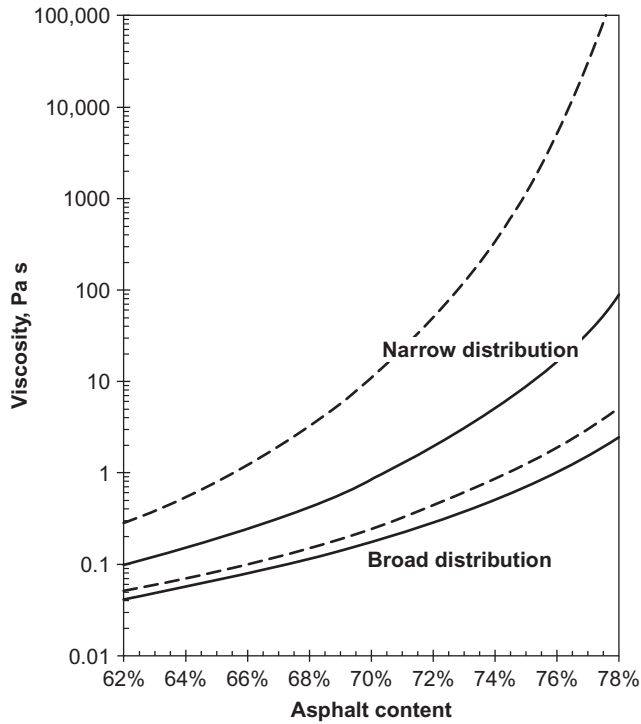


Figure 13.14 Same as Figure 13.6 but extended to 78% asphalt content and plotted against exponent of the emulsion viscosity. Dashed lines are for the estimated low-shear limit ($G \approx 0.01\ s^{-1}$) viscosity. The viscosity of the asphalt emulsion with narrow-particle size distribution sharply increases at higher asphalt content, whereas that with a broad-size distribution shows only minor changes.

www.EngineeringEBooksPdf.com

viscosity of the emulsion with a broad-size distribution increases less than 100 times, from 0.06 to 4 Pa s at the same condition.

The above observation by Rodríguez-Valverde et al. (2008) has been confirmed with chip seal aggregates, as shown in Figure 13.15. The CRS emulsion strongly wets (near-zero contact angle) the aggregate surface, clean water quickly wicks through the aggregate surface, and some of the aggregate surfaces are entirely wetted with water. This increase in the water-wetted surface significantly enhances the water evaporation rate, thus translating to faster curing.

The use of fine emulsion with narrow-size distribution is the most critical parameter for a successful chip seal operation, which provides quick aggregate retention (Deneuvillers, 1999; Tausk et al., 1981). The smaller and narrower the size distribution, the larger the total surface area of the asphalt particles, and the fewer the free emulsifier molecules in the emulsion serum. Therefore, it is possible to maintain the hydrophobic nature of the aggregate surface during the chip seal operation, which promotes strong asphalt adhesion after full curing. The formation of the bilayer emulsifiers makes the aggregate surface hydrophilic (Deneuvillers, 1997).

13.6.1.3 Water evaporation

The rate of water evaporation from the colloidal dispersion is a linear function of the square root of time, and at the early stage of drying is nearly the same rate as pure water under the same conditions of humidity, temperature, and wind speed. A stable dispersion may maintain this linear drying rate until nearly complete water loss (below 5% residual water content), as demonstrated using a concentrated polydimethylsiloxane (PDMS) oil-in-water (o/w) emulsion stabilized with 20 mM sodium dodecylsulfate as an emulsifier (Aranberri et al., 2004). Similar observations were also reported with anionic latex dispersion (Erkselius et al., 2008) and the CRS asphalt emulsion (Banerjee et al., 2012; Lesueur et al., 2001). Particles may become concentrated at the surface, leading eventually to a reduction in drying rate to below that of pure water. Also, as water is lost, the



Figure 13.15 A photograph demonstrating rapid wicking of water on the aggregate surface immediately after placed on the CRS asphalt emulsion.

www.EngineeringEBooksPdf.com

concentration of ions in the serum rises and may exceed the ccc of the dispersed particles. The result of coalescence is that water evaporation slows and stops well before all the water is lost. For the PDMS system, this effect has been demonstrated by the addition of electrolytes (i.e., NaBr) to the PDMS o/w emulsion. The phase inversion of the o/w emulsion also observed above-critical NaBr concentration for a given volume fraction of the dispersed oil. The addition of calcium chloride to the asphalt emulsion was similarly shown to slow the water evaporation (Lesueur et al., 2001).

13.6.1.4 Problems associated with reactive aggregates

The pH of the CRS emulsion rises quickly to near 7 in contact with reactive aggregates, for example, basalt and carbonate (Deneuvillers, 1997; Tausk et al., 1981). The silicate part of these aggregates possesses a high negative ζ-potential, but that of the CRS emulsion particles continuously decreases from near 40 to 10 mV at pH 8. The DLVO theory predicts that the CRS emulsion becomes unstable, and coalescence of asphalt particles would occur at pH > 6.5. This means that the aggregate surface in contact with the CRS emulsion will be completely covered by asphalt particles, and further deposition of asphalt particles continues. This dense deposition of the asphalt on the aggregate surface chokes off the water flow, and the aggregate surface along the three-phase contact line remains dry. A water-impermeable asphalt film forms at the asphalt emulsion/air surface and further retards evaporation of water from the bulk asphalt emulsion. Very slow curing of the CRS emulsion with reactive aggregates is expected. Some water might also be trapped within the "dried" asphalt emulsion and/or under the aggregate, causing potential chip loss during winter months as the trapped water freezes.

13.6.2 Slurry seal and microsurfacing

Slurry seal and microsurfacing are a homogeneous mixture of well-graded fine aggregates, latex-modified asphalt emulsion, water, and mineral fillers applied to old pavement for preventive maintenance. A small amount of Portland cement, hydrated lime, or fly ash aids in setting. The microsurfacing mix has to be fluid enough for 2–3 min (mix time) so that the formulated mix can be spread uniformly on the pavement surface to be treated. The mix should also develop enough strength (cohesion) that the treated pavement can be open to traffic within an hour or so.

The CQS and/or CMS emulsions for this application are prepared with a higher emulsifier level and lower pH (<2) than those of the CRS emulsion, and a high-acid-number asphalt is preferred for quick curing. Electric properties of the asphalt/water interface are simulated in the presence of 0.1 M NaCl in the aqueous phase, representing higher levels of emulsifier and HCl. $pK_{a2} = 13$ represents the chemistry of cationic surfactants for this application. In the low-pH emulsion, the majority of carboxyl groups on the asphalt particles are in protonated form, and amines from the cationic surfactant determine a positive surface charge. In the microsurfacing process, cement reacts with water:

$$CaO + H_2O \rightarrow Ca(OH)_{2\downarrow} \tag{13.43}$$

www.EngineeringEBooksPdf.com

or hydrated lime is used directly and the emulsion pH rises to 11–12, where organic acids are fully dissociated. At the same time, the degree of dissociation of the cationic surfactant decreases, resulting in the net negative charge of asphalt particles (especially those with high-acid-number asphalts), as shown by the ζ-potential versus pH relationship shown in Figure 13.16.

Limited solubility of calcium salt in lime or Portland cement maintains approximately 25 mM Ca^{2+} in water. These Ca^{2+} complex with $RCOO^{-}$ to form $RCOOCa^{+}$ (Equation 13.23), thus maintaining the total charge to be near neutral, which would result in the destabilization of the asphalt emulsion. However, the asphalt emulsion for the slurry seal and microsurfacing is designed to flocculate upon neutralization of the surface charge (Figure 13.10). Flocculated asphalt emulsions with fines in the aggregate cause a sharp increase in the mix viscosity after 2–3 min of mixing time. Cohesion of the mix develops slowly when excess water is expelled from the mix, known as the viscous-sintering phenomenon, described by Bonakdar et al. (2001). Asphalt viscosity drops sharply at higher temperatures; thus, mixing and curing become faster during mid-summer days.

Latex polymers, together with these fine-mineral fillers in the aqueous phase of the slurry seal, transform into a continuous microscopic polymer film surrounding asphalt particles upon curing (Takamura, 2002). The same paper also describes a liquid-based setting aid, taking advantage of

$$2NaOH + CaCl_2 \rightarrow Ca(OH)_{2\downarrow} + 2NaCl \tag{13.44}$$

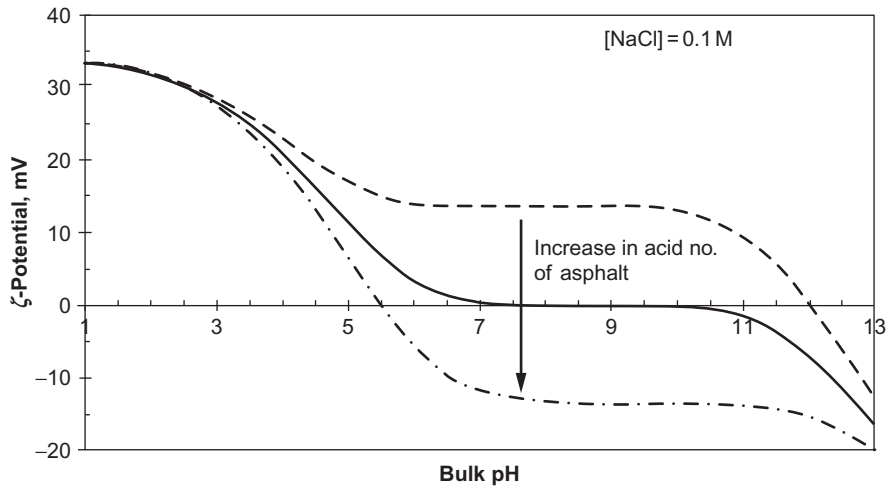


Figure 13.16 Estimated ζ-potential vs. bulk pH relationship for the CQS emulsion in 0.1 M NaCl, assuming $N_{a2} = 2.0 \times 10^{18}$ m^2 and p$K_a = 13$ for the CQS emulsifier. Three different values of N_{a1} of 1.8, 2.0, and 2.2×10^{18} m^2 represent increase in acid number of the asphalt.

www.EngineeringEBooksPdf.com

This new system opens possibilities of independently controlling the mix time and curing behavior of the microsurfacing mix for wide varieties of aggregates and asphalts, without adjusting the bitumen emulsion formulation.

13.7 Characterization of emulsion residues

The residue-recovery procedure should closely simulate the curing behavior of the asphalt emulsion during paving operations. We have demonstrated that excess heat applied to the asphalt emulsion during conventional residue-recovery procedures in the United States and Canada (i.e., evaporation and distillation methods) significantly alters the polymer morphology in the recovered residue and hardens the asphalt binder (Takamura, 2000). The procedure developed for the asphalt emulsion-based warm mix could be adapted for all other emulsion-based paving technologies (Davidson et al., 2007; Takamura, 2008).

In this procedure, the asphalt emulsion is placed into a pressure-aging vessel stainless steel pan to a depth of less than 5 mm, and dried in a forced airflow oven at 80 °C for 20 h. The recovered emulsion residue closely simulates the binder in the pavement after a few days of placement. In comparison, the rolling thin-film oven test aging procedure simulates the binder aging (loss of volatiles) during the mixing and placement of the hot-mix asphalt, and the binder sample is subjected to 163 °C for 85 min. Detailed binder characterization by Davidson et al. (2007) and Takamura (2008) demonstrates that the pavement constructed using the emulsion-based warm mix after 10–15 years of in-service life would be as flexible as freshly placed conventional hot-mix pavement.

Their studies also demonstrate that the polymer network in the modified asphalt binder does not prevent oxidation of the asphalt binder; rather, it reduces the net effects of undesired changes in the rheological properties of the asphalt binder upon aging or oxidative hardening. These observed advantages should be applicable to all emulsion-paved technologies. In addition, Khadivar and Kavussi (2013) provide a detailed comparison of the rheological characteristics of emulsion residues recovered from the styrene–butadiene and natural-rubber latex-modified emulsions.

References

Adler, P.M., 1981. Interaction of unequal spheres: I. Hydrodynamic interaction: colloidal forces. J. Colloid Interface Sci. 84, 461–473.

Aranberri, I., Binks, B.P., Clint, J.H., Fletcher, P.D., 2004. Evaporation rates of water from concentrated oil-in-water emulsions. Langmuir 20, 2069–2074.

Banerjee, A., de Fortier Smit, A., Prozzi, J.A., 2012. Modeling the effect of environmental factors on evaporative water loss in asphalt emulsions for chip seal applications. Constr. Build. Mater. 27, 158–164.

Batchelor, G.K., Green, J.T., 1972. The hydrodynamic interaction of two small freely-moving spheres in a linear flow field. J. Fluid Mech. 56, 375–400.

www.EngineeringEBooksPdf.com

Binks, P.B., Clint, J.H., 2002. Solid wettability from surface energy components: relevance to pickering emulsions. Langmuir 18, 1270–1273.
Birken, I., 2010. New emulsifiers for efficient coating of "highly reactive" aggregates with bitumen emulsion. In: Proceedings of the Seventh ISSA World Congress, Lyon, France.
Bonakdar, L., Philip, J., Bardusco, P., Petkov, J., Potti, J.J., Méléard, P., Leal-Calderon, F., 2001. Rupturing of bitumen-in-water emulsions: experimental evidence for viscous sintering phenomena. Colloids Surf. A Physicochem. Eng. Asp. 176, 185–194.
Booth, F., 1950. The electroviscous effect for suspensions of solid spherical particles. Proc. R. Soc. Lond. Ser. A 203, 511–533.
Briscoe, B.J., Lawrence, C.J., Mietus, W.G.P., 1999. A review of immiscible fluid mixing. Adv. Colloid Interface Sci. 81, 1–17.
Buckley, J.S., Takamura, K., Morrow, N.R., 1987. Influence of electrical surface charges on the wetting properties of crude oil. In: Proceedings of the Society of Petroleum Engineers, Paper No. 16962, pp. 317–327.
Capitão, S.D., Picado-Santos, L.G., Martinho, F., 2012. Pavement engineering materials: review on the use of warm-mix asphalt. Constr. Build. Mater. 36, 1016–1024.
Castro, S.H., Vurdela, R.M., Laskowski, J.S., 1986. The surface association and precipitation surfactant species in alkaline dodecylamine hydrochloride solutions. Colloids Surf. 21, 87–100.
Chin, H.B., Han, C.D., 1979. Studies on droplet deformation and breakup. I. Droplet deformation in extensional flow. J. Rheol. 23, 557–590.
Chin, H.B., Han, C.D., 1980. Studies on droplet deformation and breakup. II. Breakup of droplet in nonuniform shear flow. J. Rheol. 24, 1–37.
Chow, R.S., Takamura, K., 1988. Electrophoretic mobilities of bitumen and conventional crude-in-water emulsions using the Laser Doppler apparatus in the presence of multivalent cations. J. Colloid Interface Sci. 125, 212–225.
Cox, R.G., Brenner, H., 1971. The rheology of a suspension of particles in a Newtonian fluid. Chem. Eng. Sci. 26, 65–93.
Crews, E., 2006. Emulsion-based warm mix asphalt: materials and field performance. In: Fourth World Congress on Emulsion, Lyon France.
Danielli, J.F., 1937. The relations between surface pH, ion concentrations and interfacial tension. Proc. R. Soc. Lond. Ser. B 122, 155–174.
Davidson, J.K., Lubers, C., Takamura, K., 2007. Characterization of unmodified and SBR latex-modified Evotherm warm mix binder. Proc. Can. Tech. Asphalt Assoc. 52, 297–324.
Deneuvillers, C., 1997. Study of interaction between minerals and cationic surfactant. In: Second World Congress on Emulsions, pp. 29–35.
Deneuvillers, C., 1999. Relationship between characteristics and properties of cationic bitumen emulsions. In: Asphalt Emulsion Manufacturers Association Annual Meeting, pp. 104–112.
Dijkink, J.H., Reintjes, R.C., Wilms, K.P., 2000. Steamed asphalt pavement design & construct project service area A15-Rotterdam NL. In: Proceedings of the Second Eurasphalt & Eurobitume Congress. European Asphalt Paving Association, Brussels, Barcelona Paper Proc.0143.uk.
Einstein, A., 1906. Eine neue Bestimmung der Moleküldimensionen. Ann. Phys. 324, 286–306.
Erkselius, S., Wadsö, L., Karlsson, O.J., 2008. Drying rate variations of latex dispersions due to salt induced skin formation. J. Colloid Interface Sci. 317, 83–95.
Fowkes, F.M., 1964. Attractive forces at interfaces. Ind. Eng. Chem. 56, 40–52.
Girifalco, W.D., Good, R.J., 1957. A theory for the estimation of surface and interfacial energies. I. Derivation and application to interfacial tension. J. Phys. Chem. 61, 904–909.

www.EngineeringEBooksPdf.com

Grance, H.P., 1982. Dispersion phenomena in high viscosity immiscible fluid systems and application of static mixers as dispersion devices in such systems. Chem. Eng. Commun. 14, 225–277.
Gregory, J., 1975. Interaction of unequal double layers at constant charge. J. Colloid Interface Sci. 51, 44–51.
Gregory, J., 1981. Approximate expressions for retarded van der Waals interaction. J. Colloid Interface Sci. 83, 138–145.
Harding, I.H., Healy, T.W., 1985. Electrical double layer properties of amphoteric polymer latex colloids. J. Colloid Interface Sci. 107, 382–397.
Healy, T.W., White, L.R., 1978. Ionizable surface group models of aqueous interfaces. Adv. Colloid Interface Sci. 9, 303–345.
Hoffmann, H., 1990. Fascinating phenomena in surfactant chemistry. Adv. Colloid Interface Sci. 32, 123–150.
Hunter, R.J., 1986. Foundations of Colloid Science, vol. 1. Oxford University Press, Oxford, ISBN 0-19-855187-8.
James, A., 1997. In: Gunstone, F.D. (Ed.), Cationic Surfactants, Lipid Technologies and Applications. Marcel Dekker Inc., New York, pp. 609–631 (Chapter 24).
James, A., 2006. Use of surfactants in the construction and maintenance of asphalt roadways. In: 97th Annual Meeting of American Oil Chemists Society, St Louis.
James, A., 2008. Reaction of bitumen emulsions with cement. In: Proceedings of the Fourth International Symposium on Asphalt Emulsion Technology, Arlington, VA.
James, A., Logaraj, S., 2002. Emulsification of high softening point hydrocarbons. In: Proceedings of the Third World Congress on Emulsion, Lyon, France.
James, A., Furlong, S., Kalinowski, E., Thompson, M., 1999. Water enclosed within the droplets of bitumen emulsions and its relation to viscosity changes during the storage. Colloids Surf. A Physicochem. Eng. Asp. 152, 147–153.
Janssen, J.J.M., Boon, A., Agterof, W.G.M., 1994. Droplet break-up in simple shear flow in the presence of emulsifiers. Colloids Surf. A Physicochem. Eng. Asp. 91, 141–148.
Johannes, P.T., Bahia, H.U., 2013. Using viscosity at variable shear rates to evaluate asphalt emulsions sprayability and drain-out characteristics in chip seals. In: Transportation Research Board Annual Meeting, Washington, DC, Paper No. 13-2805.
Kao, S.V., Cox, R.G., Mason, S.G., 1977. Streamlines around single spheres and trajectories of pairs of spheres in two-dimensional creeping flows. Chem. Eng. Sci. 32, 1505–1515.
Khadivar, A., Kavussi, A., 2013. Rheological characteristics of SBR and NR polymer modified bitumen emulsions at average pavement temperatures. Constr. Build. Mater. 47, 1099–1105.
Khakhar, D.V., Ottino, J.M., 1987. Breakup of liquid threads in linear flows. Int. J. Multiphase Flow 13, 71–86.
Krafft, F., Wiglow, H., 1895. Über das Verhalten der fettsauren Alkalien und Seifen in Gegenwart von Wasser. III. Die seifen als krystalloïde. Berichte der deutschen chemischen.
Laskowski, J.S., Pawlik, M., Ansari, A., 2007. Effect of brine concentration on the Krafft point of long chain primary amines. Can. Metall. Q. 46, 295–300.
Le Bouteiller, E., Roffe, J.C., 2011. Bitumen emulsion in 2010: a watershed year. Eur. Roads Rev. (RGRA) (Spring), 42–48.
Lesueur, D., Coupé, C., Ezzarougui, M., 2001. Skin formation during the drying of a bitumen emulsion. Road Mater. Pavement Des. 2 (2), 161–179.
Lesueur, D., Javier, H., Potti, J.J., Monin, D., Martine, J.V., Peña, J.L., 2006. New environmentally friendly amphoteric surfactants for bituminous emulsions: application for microsurfacing. In: Proceedings of the Fourth World Congress on Emulsion, Lyon, France.

www.EngineeringEBooksPdf.com

Mamlouk, M.S., Zaniewski, J.P., 1999. Pavement preventive maintenance: description, effectiveness, and treatments. Symposium on Flexible Pavement Rehabilitation and Maintenance, ASTM STP 1349, 121–135.

Marcilloux, J., Benvegnu, T., Goursaud, F., Plusquellec, D., Antoine, J.P., 2008. Vegetable emulsifier for bitumen emulsion. In: Proceedings of the Fourth Eurasphalt & Eurobitume Congress, Copenhagen, Denmark. European Asphalt Paving Association, Brussels, Paper 405–517.

Newcomb, D., 2007. An Introduction to Warm-Mix Asphalt. National Asphalt Pavement Association (NAPA), Lanham, MD. www.fsl1.hotmix.org/mbc/introduction_to_Warm-mix_Asphalt.pdf.

Nuñez, G.A., Sanchez, G., Gutierrez, X., Silva, F., Dalas, C., Rivas, H., 2000. Rheological behavior of concentrated bitumen in water emulsions. Langmuir 16, 6497–6502.

Owens, D.K., Wendt, R.C., 1969. Estimation of the surface free energy of polymers. J. Appl. Polym. Sci. 18, 1741–1747.

Pormerantz, P., Clinton, W.C., Zisman, W.A., 1967. Spreading pressures and coefficients, interfacial tensions, and adhesion energies of the lower alkanes, alkanes, and alkyl benzenes on water. J. Colloid Interface Sci. 24, 16–28.

Potti, J.J., Peña, J.L., Martínez, M., 2006. Warm bituminous mixes with emulsion. An step forward to ecoeffectiveness. In: Fourth World Congress on Emulsion, Lyon, France.

Rallison, J.M., 1984. The deformation of small viscous drops and bubbles in shear flows. Annu. Rev. Fluid Mech. 16, 45–66.

Roberts, F.L., Kandhal, P.S., Brown, E.R., Lee, D.Y., Kennedy, T.W., 1996. Hot Mix Asphalt Materials, Mixture Design and Construction, second ed. NAPA Research and Education Foundation, Lanham, MD.

Rodríguez-Valverde, M.A., Ramón-Torregrosa, P., Páez-Dueñas, A., Cabrerizo-Vílchez, Hidalgo-Álvarez, R., 2008. Imaging techniques applied to characterize bitumen and bituminous emulsions. Adv. Colloid Interface Sci. 136, 93–108.

Rumscheidt, F.D., Mason, S.G., 1962. Break-up of stationary liquid threads. J. Colloid Sci. 17, 260–269.

Salou, M., Siffert, B., Jada, A., 1998. Interfacial characteristics of petroleum bitumens in contact with acid water. Fuel 77, 343–346.

Samadijavan, A., 1994. Elektrophoretische Untersuchung des Brechverhaltens von Bitumenemulsionen. Bitumen 4, 151–156.

Schilling, P., 1997. Anionic and cationic emulsions prepared with modified tall oil. In: Second World Congress on Emulsion, Bordeaux, France.

Schilling, P., 2002. Slow-set bitumen emulsions for road construction. In: Third World Congress on Emulsion, Lyon, Paper 4E-142.

Schilling, P., Schreuders, H.G., 1998. Improved quick-set slurry seal emulsifiers with tall oil derivatives. Transport. Res. Rec. (1171), 98–107.

Schwartz, A.M., Perry, J.W., 1949. Surface Active Agents, Their Chemistry and Technology, vol. I. Interscience Publishers: A Division of John Wiley & Sons, Inc., New York.

Shinoda, K., 1978. Principles of Solution and Solubility. Marcel Dekker, New York, pp. 157–179.

Shinoda, K., Hirai, T., 1977. Ionic surfactants applicable in the presence of multivalent cations. Physicochemical properties. J. Phys. Chem. 81, 1842–1845.

Shinoda, K., Hutchinson, E., 1962. Pseudo-phase separation model for thermodynamic calculations of micellar solutions. J. Phys. Chem. 66, 577–582.

Shinoda, K., Ogawa, T., 1967. The solubilization of water in nonaqueous solutions of nonionic surfactants. J. Colloid Interface Sci. 25, 56–60.

www.EngineeringEBooksPdf.com

Shinoda, K., Maekawa, M., Shibata, Y., 1986. Ionic surfactant soluble in hard water and in hydrocarbons: behavior of organized surfactant solutions as a function of the hydrophilic–lipophilic balance. J. Phys. Chem. 90, 1228–1230.

Takamura, K., 2000. Comparison of emulsion residue recovered by the forced airflow and RTOT drying. In: AEMA/ISSA Annual Meeting.

Takamura, K., 2002. Portland cement-free microsurfacing. In: International Slurry Seal Association Annual Meeting.

Takamura, K., 2008. Characterization of emulsion based warm mix binder. Road Mater. Pavement Des. 9, 87–102.

Takamura, K., Chow, R.S., 1983. A mechanism for initiation of bitumen displacement from oil sand. J. Can. Petrol. Technol. 22, 1–9.

Takamura, K., Chow, R.S., 1985. The electric properties of the bitumen/water interface: part II. Application of the ionizable surface-group model. Colloids Surf. 15, 35–48.

Takamura, K., van de Ven, T.G.M., 2010. Comparisons of modified effective medium theory with experimental data on shear thinning of concentrated latex dispersions. J. Rheol. 54, 1–26.

Takamura, K., Wallace, D., 1988. The physical chemistry of the hot water process. J. Can. Petrol. Technol. 27, 98–106.

Takamura, K., Chow, R.S., Tse, D.L., 1987. Prediction of electrophoretic mobilities and the coagulation behavior of bitumen-in-water emulsions in aqueous NaCl and $CaCl_2$ solutions using the ionizable surface-group model. In: Attia, Y.A. (Ed.), Flocculation in Biotechnology and Separation Systems. Elsevier Science Publishers, Amsterdam, pp. 565–578.

Takamura, K., Lok, K.P., Wittlinger, R., 2004. Microsurfacing for preventive maintenance: eco-efficient strategy. Proc. Can. Tech. Asphalt Assoc. 49, 64–72.

Takamura, K., Loahardjo, N., Winoto, W., Buckley, J., Morrow, N.R., Kunieda, M., Liang, Y., Matsuoka, T., 2012. Spreading and retraction of spilled crude oil on sea water. In: Younes, M. (Ed.), Crude Oil Exploration in the World. Available from http://www.intechopen.com/books/crude-oil-exploration-in-the-world/spreading-and-retraction-of-spilled-crude-oil-on-sea-water.

Tausk, R.J.M., Scott, J.A.N., Stassen, W.J.M., Wonk, W.C., 1981. Colloid chemical studies on bitumen-in-water emulsions. Part IV. On the setting mechanisms of cationic emulsions in contact with mineral aggregate. Colloids Surf. 3, 13–36.

van de Ven, T.G.M., 1989. Colloidal hydrodynamics. In: Colloid Science: A Series of Monographs. Academic Press, London. ISBN 0-12-710770-3.

Wates, J.M., James, A.D., 1993. Zeta potential measurements on bitumen emulsions and road aggregates. In: Proceedings of the First World Congress on Emulsion, Paper 1-40-089, Paris, France, EDS, Paris.

Wieringa, J.A., van Dieren, F., Janssen, J.J.M., Agterof, W.G.M., 1996. Droplet breakup mechanisms during emulsification in colloid mills at high dispersed phase volume fraction. Trans. Inst. Chem. Eng. 74, 554–562.

Wiese, G.R., James, R.O., Healy, T.W., 1971. Discreteness of charge and salvation effects in cation adsorption at the oxide/water interface. Discuss. Faraday Soc. 52, 302–311.

Zapf, A., Beck, R., Platz, G., Hoffmann, H., 2003. Calcium surfactants: a review. Adv. Colloid Interface Sci. 100–102, 349–380.

Zisman, W.A., 1941. The spreading of oils on water: Part I. Ionized molecules having only one polar group. J. Chem. Phys. 9, 534–551.

www.EngineeringEBooksPdf.com

A new approach for aggregate grading optimization for mixtures

14

F. Olard, S. Pouget
Eiffage Travaux Publics R&D Department, Corbas, France

14.1 Introduction

Roads are a huge public financial asset. For instance, the European road network consists of 5.5 million km, and it represents an estimated value of more than €8 trillion, managed under local, regional, and national responsibility (European Road Federation, 2014). Under those circumstances, and because of the ongoing financial crisis in Europe, different scenarios are currently emerging there in order to maintain the road network quality. These include more and more chip seals and microsurfacing, especially on low-volume roads, on the one hand, and optimization of existing asphalt mix designs in order to "do better with less," on the other hand. The purpose of this chapter is to present a new methodology for optimizing mix design, developed in France in 2010, and from then on widely implemented and generalized in France, Spain, and South Africa. Such an optimization may bring about huge cost savings, and make it possible to develop long-lasting asphalt concretes as well.

Controlling the volumetrics and the compactability of asphalt concretes is the first step of any mix design procedure. Apart from binder-related considerations, because the aggregates represent 94–96% of the weight of asphalt mixes, predicting, and controlling the packing properties of aggregates is of prime importance. Broadly speaking, the aggregate packing characteristics are mainly influenced by the following five parameters (Caquot, 1937; Baron and Sauterey, 1982; De Larrard, 1988; De Larrard et al., 1994; De Larrard and Sedran, 1994, 2002; Corte and Di Benedetto, 2004):

- Gradation (continuously graded, gap-graded, etc.)
- Shape (flat and elongated, cubical, round)
- Surface microtexture (smooth, rough)
- Type and amount of compaction effort (static pressure, impact, or shearing)
- Layer thickness (e.g., Cooper et al., 1985)

This chapter mainly focuses on the first parameter (gradation) by specifically optimizing the combination of fine and coarse fractions. The result is an interactive network of coarse particles in asphalt concrete, indirectly providing the strongest mix resistance (Roque et al., 1997; Kim et al., 2008), and in particular, the highest mix modulus.

Apart from the previous gradation-related considerations, the ability of styrene–butadiene–styrene (SBS) polymers to reduce fatigue cracking and aging is well

Advances in Asphalt Materials. http://dx.doi.org/10.1016/B978-0-08-100269-8.00014-3
© 2015 Elsevier Ltd. All rights reserved.

www.EngineeringEBooksPdf.com

recognized (Baaj et al., 2005; Dreessen et al., 2011), but the high modulus required for perpetual pavement base structures usually calls for hard binders (and thus slightly higher binder content to preserve fatigue resistance), which have viscosity and compatibility issues with conventional SBS. Under those circumstances, at Eiffage Travaux Publics, we set out to combine both optimal aggregate interlock (using aggregate packing methods initially developed in the field of high-performance cement concrete) and the use of SBS polymers, in order to obtain both very stiff and fatigue-resistant polymer-modified base course material in a single formulation.

14.2 Theoretical background on aggregate packing

Many researchers developed empirical methods of relating air void content in mineral aggregates to the gradation, or proposed "ideal" gradations, which aim for maximum solid volume density. These theoretical curves are always continuously graded curves, and they generally have a parabolic form (Nijboer, 1948; Yoder, 1959). They all have a similar shape when placed on the same plot. The most prevalent theoretical "ideal" gradation is based on the following empirical equation:

$$P = 100(d/D)^b \tag{14.1}$$

where P is the percentage of aggregate, by weight, passing a particular sieve; d the size of openings in the particular sieve (mm); D the maximum size of aggregate particles in the gradation (mm); and b the coefficient. Nijboer (1948) and Yoder (1959) found that the maximum density of any continuously graded compacted mix is obtained when b equals 0.45 or 0.5.

Despite Equation (14.1), Lees (1970) emphasized that correct proportions for minimum void content must inevitably be affected by changes of aggregate shape from source to source and from size to size, by the level of compaction effort applied, by the presence of lubricating coatings, and by size and shape of the section in which the material is to be used. In addition, some more general concepts of aggregate packing were first developed by Caquot in 1937, and then by contemporary researchers since the 1970s, especially in the field of cement concrete (De Larrard, 1988; De Larrard et al., 1994; De Larrard and Sedran, 1994, 2002; Andersen and Johansen, 1993). A state-of-the-art of basics has been recently presented by Perraton et al. (2007), Olard and Perraton (2010a,b), and Olard (2012), transposing those concepts into the field of asphalt mix design. The following subsections are partially drawn from these papers.

14.2.1 Basic concepts associated with granular combinations

When filling a container with an aggregate or granular mix, just a fraction of the volume is occupied by the particles, and the remainder is composed of interstices. It is worthwhile to remark that for an infinite medium, the void index (e = volume of air voids/volume of solid particles) of an aggregate mix composed of one-dimensional

www.EngineeringEBooksPdf.com

particles remains, for all practical purposes, independent of particle size (Ben Aïm and Le Goff, 1967; Ben Aïm, 1970; Cumberland and Crawford, 1987).

When studying the porosity of mixes composed of two aggregates with differing yet one-dimensional individual sizes, Caquot first highlighted in 1937 the importance of two types of interparticle interaction on the void index: the wall effect and the interference effect. The latter is also called the loosening effect.

The wall effect is tied to the interaction between particles and any type of wall (pipe, formwork, etc.) placed in contact with the granular mass. The case of a uniform, two-aggregate mix can be considered in order to understand the concept. The two composing fractions only differ by their average particle dimension, that is, one for the coarse aggregate particles and another for the fines. When adding a few coarse particles into an infinite volume of fines, the void index of the blend is reduced. Nevertheless, the coarse particles disturb locally (at the interface) the arrangement of fines whose porosity is increasing (i.e., an increasing void index). This local porosity increase is proportional to the particle surface area of the incorporated coarse aggregate (Caquot, 1937; Chanvillard, 1999). Figures 14.1(left) and 14.2 indicate the wall effect on the void index of a granular combination when raising the coarse fraction at the expense of fine aggregates within a binary mix.

By increasing the fraction of coarse particles within the fines, at a certain point a specific quantity of small particles winds up entrapped in the interstices delimited by the coarse particles. Therefore, outside of the wall effect, the fine aggregate void index increases due to interference: the arrangement of fine particles will depend not only on the surface areas of coarse particle walls (the wall effect), but also on the actual layout of these particles, that is, the shape of their interstices.

The interference (or loosening) notion can be illustrated by focusing on the effect induced by introducing a few fine particles into an infinite volume of coarse particles. As the amount of fines increases, at some point the coarse particles are forced apart by means of loosening, thus modifying their spatial configuration: interference occurs. Figures 14.1(right) and 14.2 also display the interference effect on the void index of a binary granular combination.

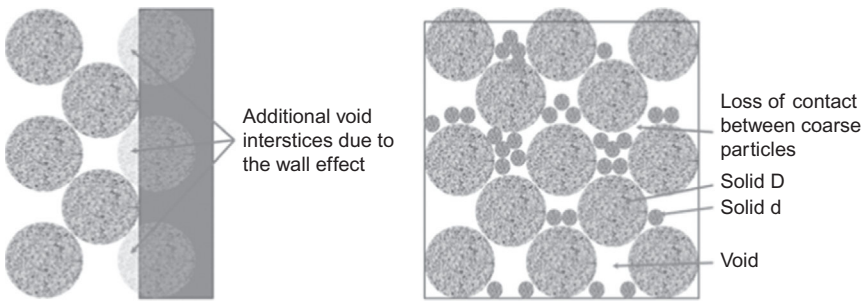


Figure 14.1 (Left) Schematic of the wall effect (case of the contact of fine particles at the surface of a coarse particle). (Right) Loosening effect (loss of stone-to-stone contact due to the all-too-high content of fine particles).

www.EngineeringEBooksPdf.com

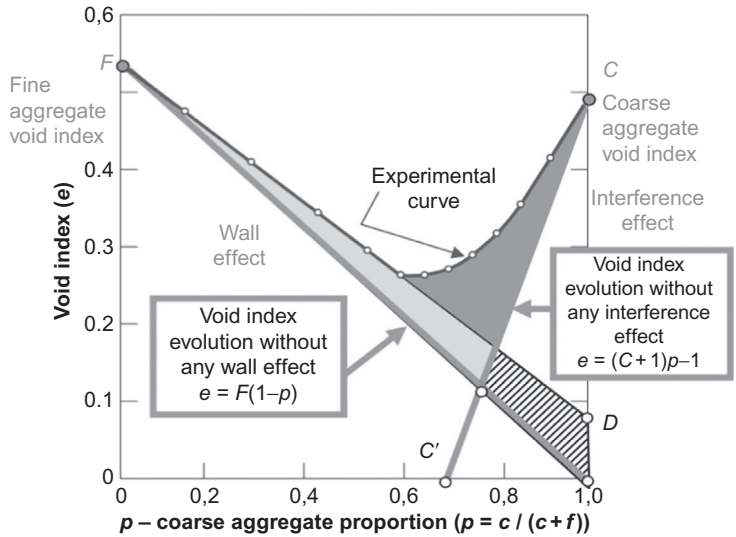


Figure 14.2 Schematic of the wall and interference effects (Powers, 1968). f and c are, respectively, the solid volumes of fine and coarse particles ($f+c=1$); F (resp. C) = void index of fine (resp. coarse) particles.

If the average particle dimension of fines (d_{FINE}) is small enough compared to that of coarse particles (d_{COARSE}) (e.g., when the d_{FINE}/d_{COARSE} ratio is lower than 0.2), the wall effect is linear and satisfies the superposition principle: the effect of two walls amounts to the sum of effects of each wall taken individually (Baron and Sauterey, 1982). In contrast, the interference/loosening effect is never linear, and consequently difficult to frame simplistically (Baron and Sauterey, 1982).

14.2.2 Evolution in aggregate porosity versus average particle dimension

Furnas (1928), Powers (1968), and Oger (1987) showed the dependence of the shift in void index (e) versus coarse aggregate portion in a binary combination on the ratio of average particle sizes. Figure 14.3 reveals that as the ratio of average fine aggregate dimension to average coarse aggregate dimension rises, interaction effects become more significant as well.

In order to reduce interactions of intermediate particles with the coarsest ones in the mix, it is crucial to limit both their size and amount, and fill air voids by a higher fraction of fines instead. In addition, it appears that if the ratio between successive sizes in a gap gradation is chosen so as to give the most drastic reduction in voids, that reduction would be equal to, or possibly greater than, the most drastic reduction in voids for a continuous gradation.

www.EngineeringEBooksPdf.com

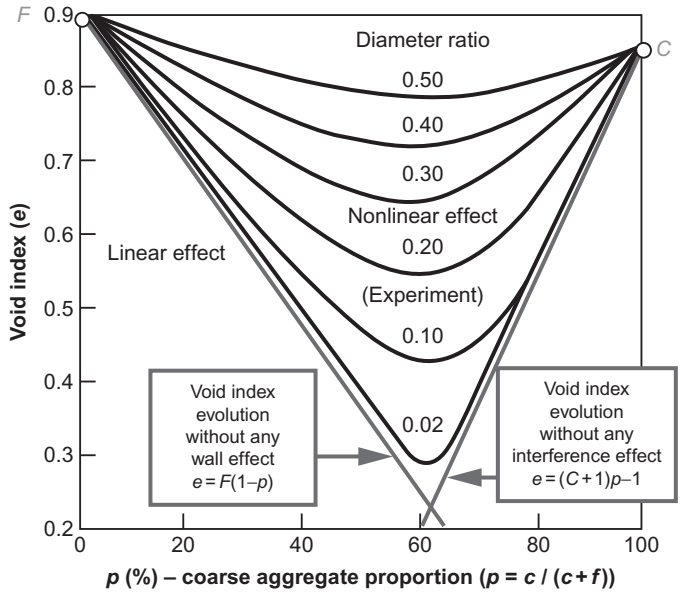


Figure 14.3 Effect of diameter ratio (d_{FINE}/d_{COARSE}) on void index (e) of binary granular blends (Furnas, 1928; Powers, 1968; Oger, 1987).

14.2.3 Ideal case of a mix of an extremely fine aggregate with a coarse aggregate

For a situation in which one aggregate is very fine in comparison with the other ($d_{FINE}/d_{COARSE} \sim 0.008$), Baron and Sauterey (1982) proposed to describe the void index variation of a mix by means of three straight lines (Figure 14.4). Baron defined two thresholds, p_X and p_T, which indicate the critical concentrations that enable the elimination of interference effects. Within a binary mix of coarse and fine particles, threshold p_X corresponds to the maximum coarse aggregate concentration that can be combined with fine aggregate without altering the fine aggregate arrangement, whereas threshold p_T is equal to the maximum fine aggregate concentration $(1 - p_T)$ for combination with coarse aggregate so as not to interfere with the coarse particle layout.

Depending on whether the granular mixture has a high ($p < p_X$), medium ($p_X < p < p_T$), or low ($p > p_T$) content of fine aggregates, void index variation can be defined according to three distinct laws, as shown in Figure 14.4:

– High content of fines in the mix, $p < p_X$:

$$e = F(1 - p) + D_p \tag{14.2}$$

where F is the void index of fines and D a parameter of the wall effect (Figure 14.4).

www.EngineeringEBooksPdf.com

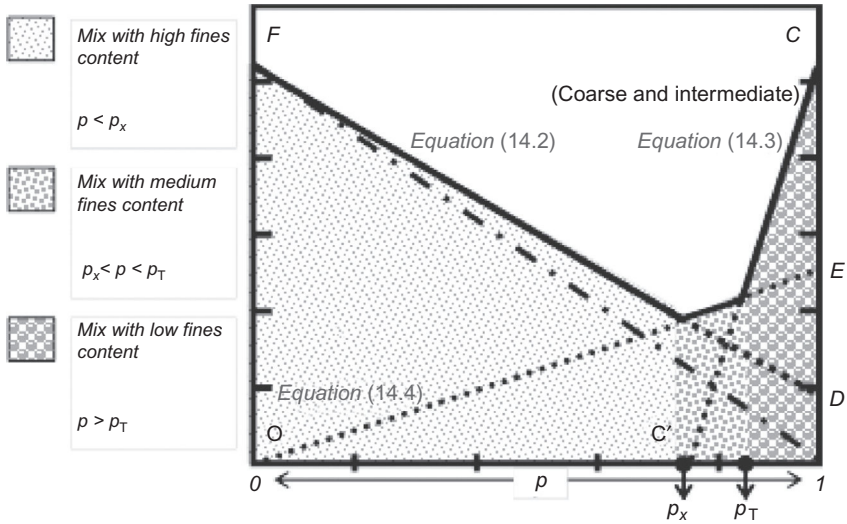


Figure 14.4 Void index variation (e) in the case of a two-aggregate mixture, one of which is very fine compared to the other (Baron and Sauterey, 1982).

– Low content of fines in the mix, $p > p_T$:

$$e = (C + 1)\, p - 1 \tag{14.3}$$

where C is the void index of coarse particles (Figure 14.4).

– Medium content of fines in the mix, $p_X < p < p_T$:

$$e = E_p \tag{14.4}$$

where E is a coefficient without any simple physical significance.

14.2.4 Transposition of Baron's approach to the design of stone mastic asphalts (SMAs) with an optimal coarse aggregate packing, according to Perraton et al. (2007)

By applying the concepts initially developed by Baron for the design of high-performance cement concrete, Perraton and his colleagues from the Ecole de Technologie Supérieure (University of Quebec) recently illustrated that the laboratory performances of some SMA mixes may be substantially enhanced by means of a maximized coarse aggregate packing (Perraton et al., 2007).

The proposed mix design method was then applied to producing SMA-Cpack (SMA with an optimal coarse aggregate packing) mixes with various nominal maximum particle size (NMPS) values using materials available in Montreal. Figure 14.5 shows a schematic diagram of the macrostructure in asphalt mix section cuts obtained

www.EngineeringEBooksPdf.com

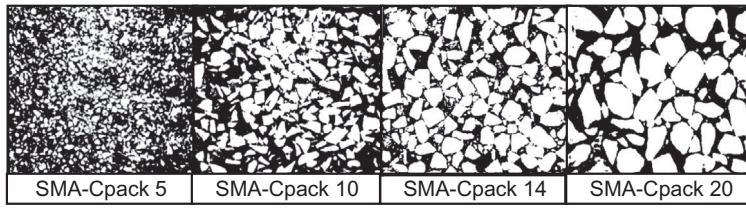


Figure 14.5 Illustration of the coarse aggregate proportion in the SMA-Cpack mixes (Perraton et al., 2007).

using digital imaging. It may be noticed that the coarse particle content is high for each of the SMA-Cpack mixes produced.

First, the initial set of laboratory results suggests a potential binder saving of nearly 15%, because the maximized coarse aggregate packing brings about a reduced void content in the granular skeleton. Second, based on Perraton's results, compactability and resistance to rutting of such mixes are remarkable.

Baron's approach for optimal aggregate packing, developed in the field of high-performance cement concrete in 1982, was transposed and adapted to the field of asphalt concrete. The main goal was to evaluate the relevancy of such an approach in the asphalt field, especially with typical French aggregates. The underlying questions were, can we develop high-performance dense asphalts with multiple-gap grading mainly thanks to aggregate packing optimization? And, likewise, can we use more specific guidelines for aggregate structure selection?

After the publication of the first encouraging results obtained by Perraton et al. (2007) and after some technical exchanges with Perraton and his colleagues, Eiffage Travaux Publics launched a large experimental program at its research center, including the evaluation of moisture resistance, stiffness modulus, and fatigue resistance as well. Laboratory tests consisted of the assessment of compactability using the French GC, moisture resistance using the Duriez test, rutting resistance using the French wheel tracking tester (FWTT) at 60 °C, stiffness modulus at 15 °C, and finally fatigue resistance at 10 °C.

14.3 Proposed method of aggregate packing optimization

To make the simplest possible selection of an optimal granular combination with a maximized coarse fraction, it is herein proposed to separate the granular skeleton into three phases: fine, intermediate, and coarse particles. The latter constitute the granular fraction that provides continuity in handling the force transfer within the mix macrostructure. This phenomenon is commonly referred to as coarse-on-coarse particle contact.

To enhance compactability, this method proposes monitoring the choice of granular combination in order to overcome the loosening effect by the intermediate fraction on the coarse fraction layout. In particular, the intermediate particles' dimension

www.EngineeringEBooksPdf.com

must be held below a certain critical value. With respect to Furnas' work (Figure 14.3), it is advised to limit the ratio of intermediate particle diameter (d_{INT}) to coarse particle diameter (d_{COARSE}) to 20% ($d_{INT} \leq 0.20\ d_{COARSE}$) (see particle dimensions in Table 14.2). Likewise, $d_{FINE} \leq 0.20\ d_{INT}$.

Using the French GC on aggregates only—without any bitumen—the respective void index of coarse, intermediate, and fine aggregate particles is first determined after 20 gyrations. Indeed, after 100 gyrations, attrition, segregation, and abrasion may be observed (Figure 14.6).

Depending on the NMPS of the designed mix and thus on the number of used granular fractions (n), the optimization sequence is performed during $n-1$ steps. For instance, in the case of a three-fraction mix with fine, intermediate, and coarse aggregates, the optimization sequence is performed during two steps:

- Step 1: Granular optimization of the intermediate aggregate–coarse aggregate blend (i.e., determination of the corresponding optimal ratio according to Baron's approach, illustrated in Figure 14.4).
- Step 2: Granular optimization of the blend between the previous optimized aggregate blend and the fine aggregates (same methodology, Figure 14.4).

For each step (i), the only slight difference with Baron's original approach is that a sensitivity study is realized around threshold p_T (Figure 14.7). Two additional points are performed around p_T value ($p_T \pm 3\%$). Moreover, for each step (i), Equation (14.2) is defined by carrying out two GC tests: the first one with $p = 0\%$ and the second one with $p = 40\%$. As illustrated in Figure 14.7, six GC tests are performed for each step (i). In the case of a three-fraction mix with fine, intermediate, and coarse aggregate particles, granular optimization is performed with a series of 12 GC tests on this tertiary configuration.

Eventually, considering the effect of diameter ratio (d_{FINE}/d_{COARSE}) on the void index (e) of binary granular blends (illustrated in Figure 14.3), it has been decided to introduce single or double gaps in granular gradations in order to obtain very dense aggregate packings with great coarse aggregate interlock (maximization of contacts between coarse particles) and without any risk of the loosening effect (related to rutting issues).

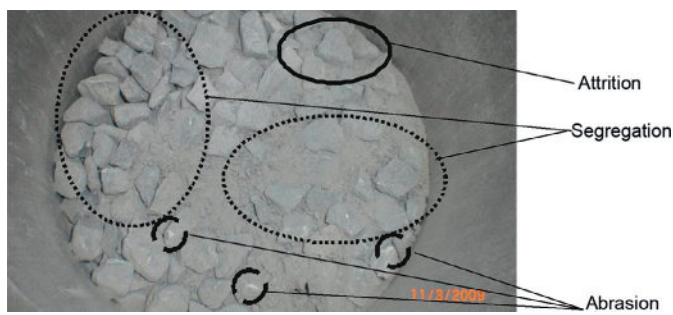


Figure 14.6 Example of attrition, segregation, and abrasion phenomena observed at 100 gyrations using the gyratory shear compactor.

www.EngineeringEBooksPdf.com

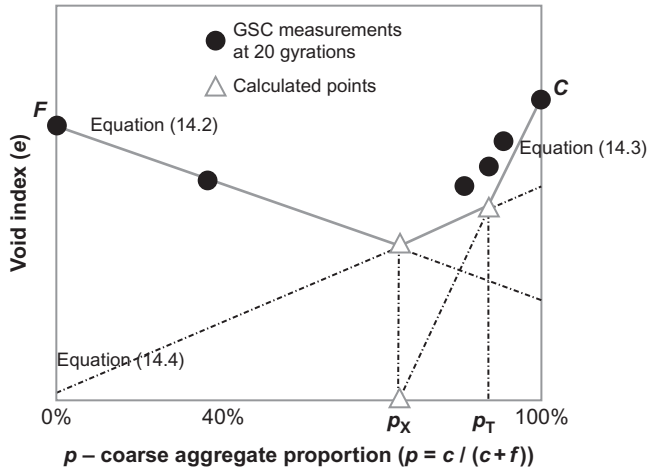


Figure 14.7 Experimental determination of the two thresholds p_X and p_T.

14.4 Examples of aggregate packing optimization

The use of a single-gap or even a double-gap gradation may be very helpful so as to obtain very dense asphalt concretes with an outstanding coarse aggregate packing (far less interaction between intermediate and coarse particles, cf. e.g., Figure 14.3). Thus, such single-gap and double-gap gradations were, respectively, investigated with Noubleau and Obourg aggregates.

14.4.1 Materials

Two pure paraffinic bitumens coming from the same crude and refinery were investigated: a straight run 35/50 and a semiblown 35/45B ("B" stands for "semi-blown") pen-grade bitumen. In addition, two polymer-modified binders (PMBs) made from these two pure bitumens with 2.5% SBS (proprietary cross-linking process) were also investigated. The analysis of the recovered aged binder of two reclaimed asphalt pavement (RAP) aggregates, both of them being studied hereafter, was also realized. Table 14.1 presents the results of conventional tests (penetration at 25 °C, ring-and-ball softening point, and Fraass brittle point) initially performed on these different binders.

Because of the great number of aggregate combinations tested in the framework of this laboratory study, only two typical French aggregate natures are presented here: the diorite-crushed aggregate fractions (0/2, 0/4, and 10/14 mm) coming from La Noubleau quarry and the limestone-crushed aggregate fractions (0/2, 6/10, and 14/20 mm) coming from the Obourg quarry. In both cases, added limestone filler coming from the St. Hilaire quarry in France was considered. Moreover, some RAP aggregates coming from either the Touraine Enrobés asphalt plant (Eiffage TP Centre Ile-de-France) or the MEN asphalt plant (Eiffage TP Nord) were used,

www.EngineeringEBooksPdf.com

Table 14.1 Conventional results on the studied binders

Binder	Pen 25 °C (mm/10) NFEN1426	Softening R&B (°C) NFEN1427	Fraass (°C) NFEN12593
35/50	38	53.5	−15
35/45B	37	62	−15
35/50 + cross-linked 2.5%SBS	38	62.2	−15
35/45B + cross-linked 2.5%SBS	33	71	−15
Aged RAP binder Touraine Enrobés plant	10	71.2	0
Aged RAP binder MEN plant	19	61.4	−5

respectively, with the diorite and the limestone aggregate formulas. Table 14.2 and Figures 14.8 and 14.9 give the gradation curves of each granular fraction.

Apart from the average dimension of added filler being determined by means of a Coulter® particle size analyzer (NF ISO, 13320-1, 2000), the average particle dimension of the other fractions was determined by sieve passing (cf. Table 14.2).

14.4.2 Description of the tests used for characterizing asphalt concretes

Many laboratory tests were conducted on asphalt concretes, including:

- Compactability, measured with the GC, following the requirements of NF EN 12697-31 (2005). This test gives a good idea of the job-site density values, according to course thickness. Conducted ahead of the other mechanical tests, this test is used to make a preliminary selection or screening of mixes, and to optimize the asphalt mix composition (Harman et al., 2002).
- Water resistance, measured from the Duriez test (NF EN 12697-12, 2002), which consists of a direct compression test on two sets of six cylindrical samples, with one set of six samples tested after conditioning in water. If the ratio of average compression strength after and before conditioning is above a certain value, the material is deemed acceptable. This ratio is the French counterpart of the tensile strength ratio value with Marshall samples.
- Resistance to rutting at 60 °C, determined with the FWTT (NF EN 12697-22, 2004). Rectangular samples are subjected to repeated passes at 1 Hz of a wheel fitted with a tire, inducing permanent deformation.
- Complex stiffness modulus measured at 15 °C–10 Hz, in accordance with NF EN 12697-26 (2004) requirements (strain-controlled test on cylindrical specimens). A complex modulus test was also performed for some high-performance asphalt mixes (HPAs) from −30 to 45 °C, with a frequency ranging from 0.01 to 10 Hz.
- Complex stiffness modulus and fatigue resistance at 10 °C–25 Hz, following NF EN 12697-24 (2005): controlled-strain test on trapezoidal specimens with unconfined conditions; see Figure 14.10. The fatigue criterion used in this paper is the classic one, referenced as Nf_{50}.

www.EngineeringEBooksPdf.com

Table 14.2 Passing percentage and average particle size for each granular fraction

Sieve (mm)	Passing (%)								
	Filler	Noubleau aggregates			RAP tours	Obourg aggregates			RAP MEN
		0/2	0/4	10/14		0/2	6/10	14/20	
20								98	
16				100	100			56	
14				93	97			23	100
12.5				77	89		100	7.8	99
10				22	72		89	2.2	91
8				5	63		52	1.7	68
6.3			100	1.7	55		15	1.3	48
4		100	96	0.4	45	100	5	1.1	33
2		97	54	0.3	32	91	3	1	25
1		68	37	0.2	23	57	2	1	20
0.25	100	31	18	0.2	10	25	1	0.9	12
0.125	94	22	13	0.2	10	19	1	0.9	9
0.08	83	17	10	0.2	9	15	1	0.9	8
Average particle dimension, hereafter named d_{50}									
Diameter (mm)	0.025	0.6	1.9	11.5	5	0.85	7.9	15.8	6.5

www.EngineeringEBooksPdf.com

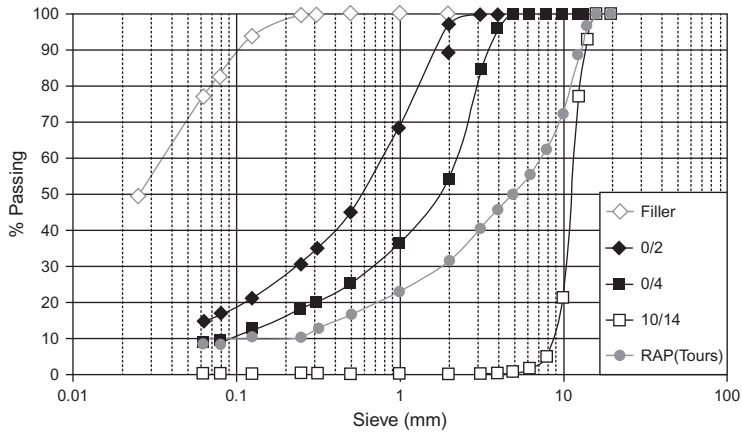


Figure 14.8 Gradation curves for each tested Noubleau granular fraction.

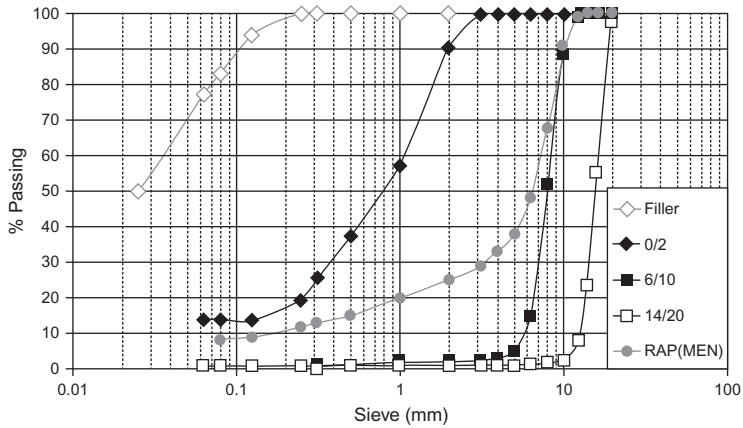


Figure 14.9 Gradation curves for each tested Obourg granular fraction.

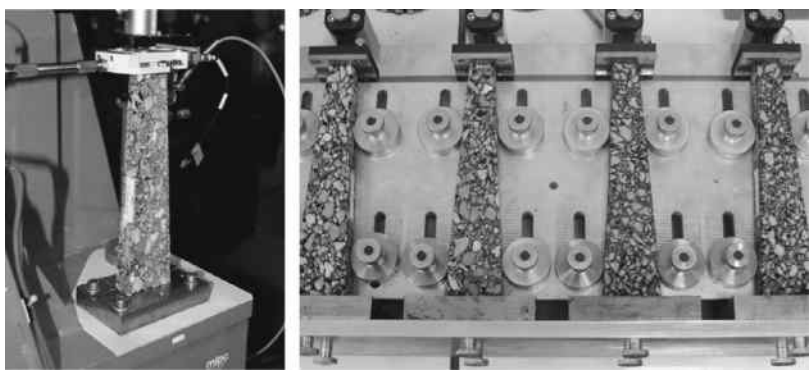


Figure 14.10 Complex modulus test and fatigue test configuration on trapezoidal specimens (NF EN 12697-24, 2005).

www.EngineeringEBooksPdf.com

It corresponds to the number of cycles for which either the complex modulus decreases to 50% of its initial value or a sudden failure occurs (before 50% decrease of modulus). The value of the strain amplitude leading to failure at one million cycles is hereafter called ε_6. This parameter is used in the French design method SETRA-LCPC (1997).

14.4.3 Optimization of single-gap-graded granular curve with Noubleau aggregates

Figure 14.11 illustrates the three-step iterative aggregate packing optimization of a quaternary 10/14–0/4–0/2-filler aggregate combination (4/10 mm gap), using the GC on aggregates only—at ambient temperature and without any bitumen—as previously detailed.

The optimal 10/14–0/4–0/2-filler quaternary blend is the following:

- 10/14 content: 55.3% (=0.865 × 0.64);
- 0/4 content: 13.9% (=0.865 × 0.16);
- 0/2 content: 17.3% (=0.865 × 0.2);
- Added filler content: 13.5% (=1 − 0.865).

At the very last stage of such an optimization, when determining the optimal content of added filler, the three theoretical straight lines described by Baron are clearly validated (Figure 14.4 and Equations (14.2)–(14.4) in the particular case of a binary blend of very fine particles and coarse particles). Nevertheless, even if the addition of 13.5% of filler is quite convenient and relevant in the field of cement concretes where final air voids are close to zero and production is realized on discontinuous batch plants, the added filler content was arbitrarily fixed at 5% in order to avoid overfilled asphalt concretes in the end, and because the production may be realized on continuous drum mix plants. Table 14.3 and Figure 14.12 show gradation curves of each tested asphalt concrete. Figure 14.12 shows in particular that the passing of the different HPA aggregate gradations at the 2-mm sieve is above the SMA window (NF EN, 13108-5, 2006), which is indirectly due to the 4/10 mm gap gradation.

A typical gradation curve of a “grave bitume 2” material (GB2) is also presented, for comparison.

14.4.4 Optimization of double-gap-graded granular curve with Obourg aggregates

The proposed methodology was applied to optimize the double-gap-graded granular curve with the Obourg aggregates. To the extent that four granular fractions were investigated (14/20, 6/10, 0/2 mm, and filler), optimization of aggregate packing was realized in three steps (see Figure 14.13):

- First step: Optimization of the binary blend composed by 14/20 and 6/10 ($p = 60\%$ (i.e., 60% 14/20 and 40% 6/10), cf. Figure 14.13). As $d_{50}(6/10)/d_{50}(14/20) = 0.50$, a true interference occurs in the case of the 14/20–6/10 binary aggregate composition (see Figure 14.3). The optimal content of coarse aggregate 14/20 may be arbitrarily fixed at 60% (leading to the densest binary blend).

www.EngineeringEBooksPdf.com

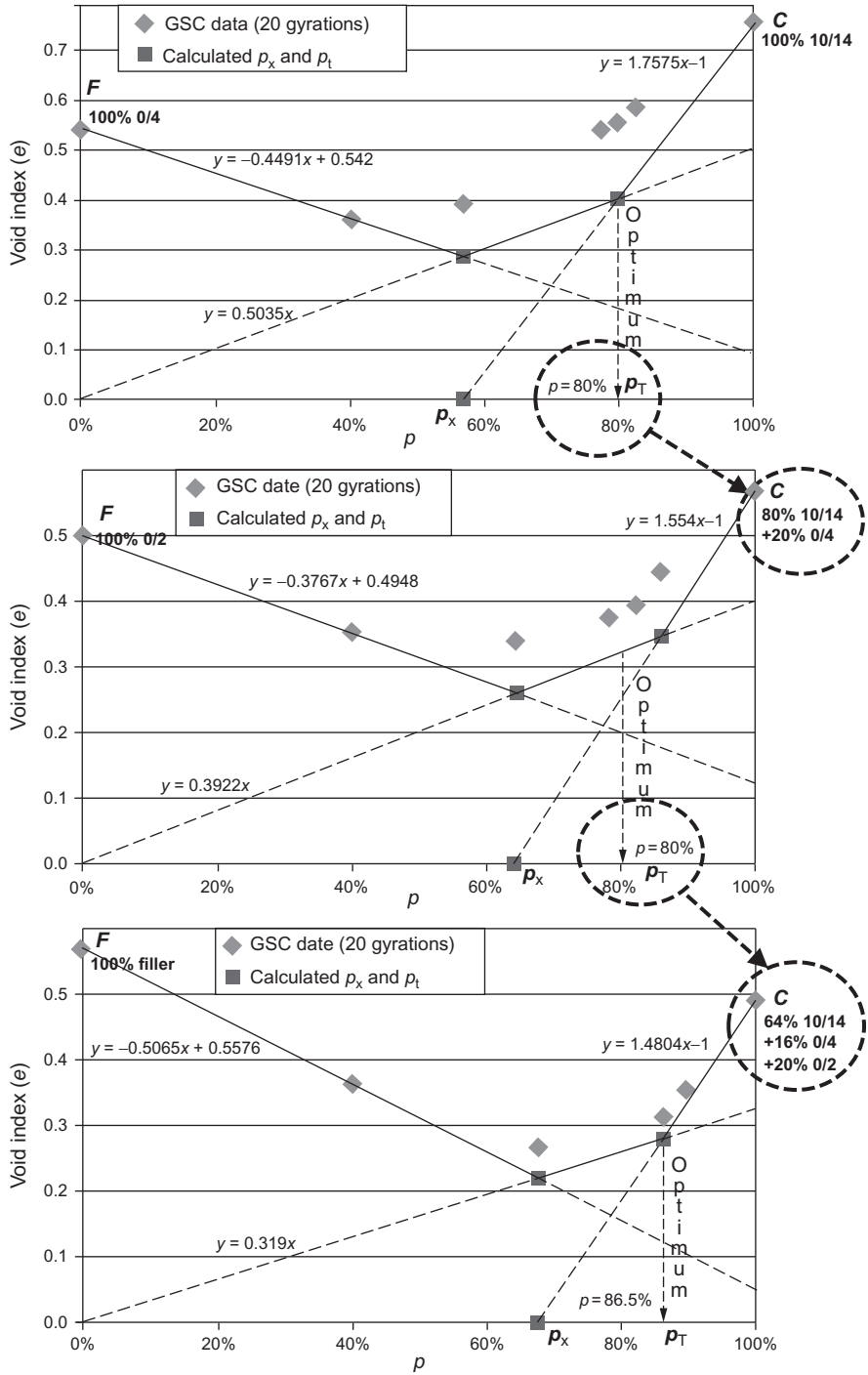


Figure 14.11 Three-step iterative optimization of the 10/14–0/4–0/2-filler blend.

www.EngineeringEBooksPdf.com

Table 14.3 Passing percentage for each tested asphalt mix made from the Noubleau aggregates

Sieve (mm)	Passing (%)		
	Reference grave bitume GB2 0/14	HPA 0/14 with 5% added filler (4/10 gap-graded)	HPA 0/14 with 5% added filler (4/10 gap-graded) +10% RAP
20	100	100	100
16	96	96	96
14	94	92	93
12.5	88	83	84
10	67	51	54
8	57	42	44
6.3	50	40	42
4	42	38	39
2	34	32	32
1	25	24	24
0.25	13	14	14
0.125	9	11	11
0.08	8	9	9

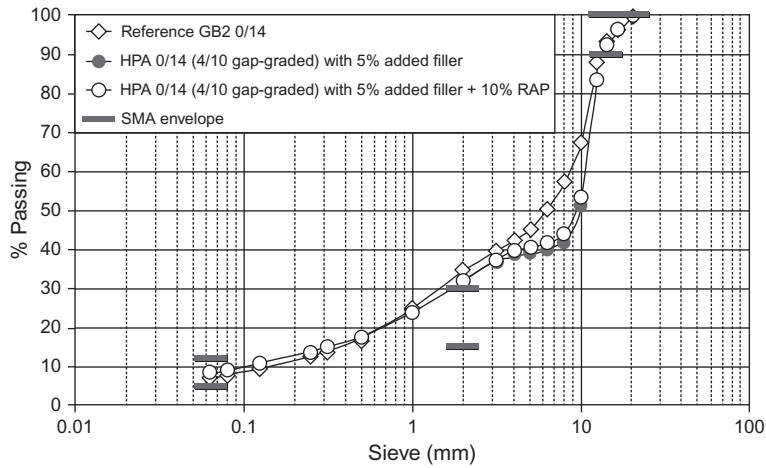


Figure 14.12 Gradation curves for the optimal 10/14–0/4–0/2-filler quaternary Noubleau aggregate blends versus typical gradation curve of the reference GB2.

www.EngineeringEBooksPdf.com

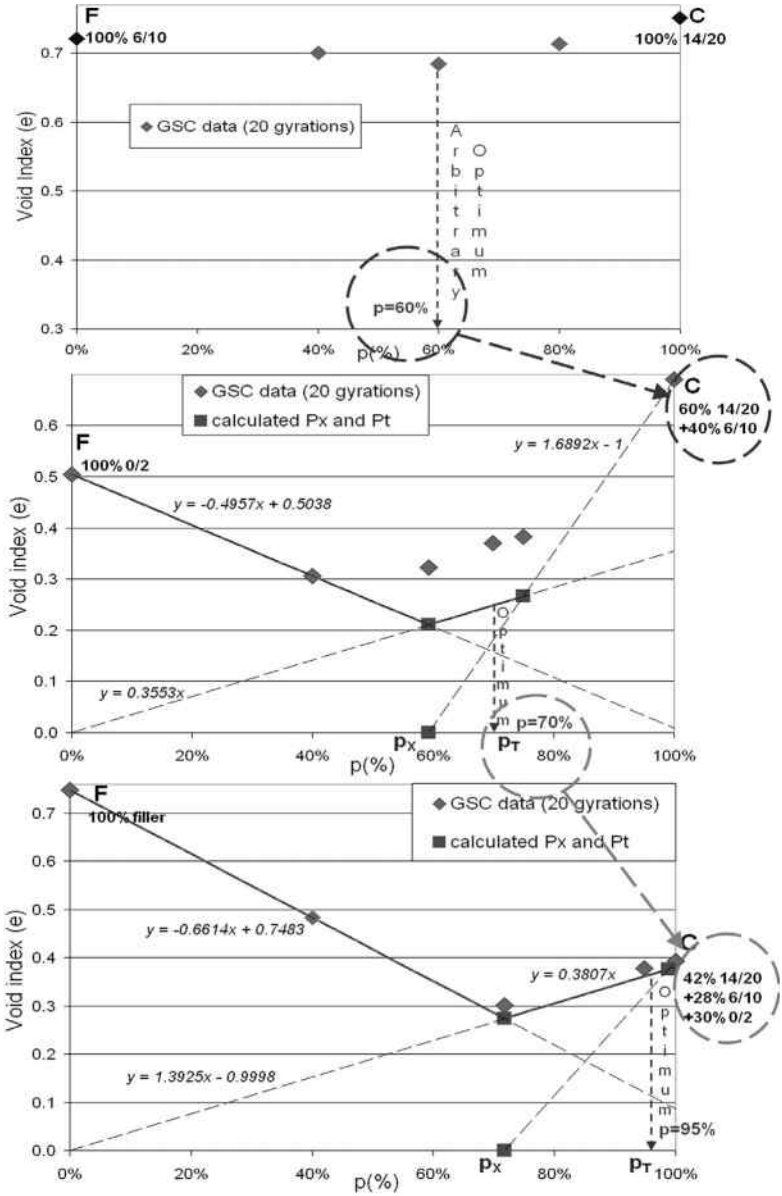


Figure 14.13 Three-step iterative optimization of the 14/20–6/10–0/2-filler blend.

- Second step: The optimal blend obtained at step 1 (60% 14/20–40% 6/10) is considered the "coarse fraction," whereas the 0/2 fraction is considered the "fine fraction." Optimal coarse ratio is $p_T = 70\%$. It is noteworthy that $d_{50}(0/2)/d_{50}(6/10) \approx 0.11$, leading to negligible interference between 0/2 and 6/10 particles (see Figure 14.3).

www.EngineeringEBooksPdf.com

- Third step: The optimal blend obtained at step 2 (42% 14/20–28% 6/10–30% 0/2) is considered the "coarse fraction," whereas the filler is then considered the "fine fraction." Optimal coarse ratio is $p_T = 95\%$. Note that $d_{50}(\text{filler})/d_{50}(0/2) \approx 0.03$, hence next to no interference between filler and 0/2 particles is observed (see Figure 14.3). In addition, the three straight lines from Baron's approach cannot be obtained (Figure 14.4 and Equations (14.2)–(14.4)).

The optimal 14/20–6/10–0/2-filler quaternary blend is the following:

- 14/20 content: 40% ($=0.95 \times 0.42$);
- 6/10 content: 26.5% ($=0.95 \times 0.28$);
- 0/2 content: 28.5% ($=0.95 \times 0.30$);
- Added filler content: 5% ($=1 - 0.95$).

Figure 14.14 and Table 14.4 show in particular that the passing of the different HPA aggregate gradations at the 2-mm sieve is above the SMA window (NF EN 13108-5, 2006), which is indirectly due to the 2/6- and 10/14-gap gradation.

14.5 Mechanical performance and related discussion

In the framework of our study with Noubleau and Obourg mixtures, a 4% binder content by weight of aggregate (10 vol.%) was used. Tables 14.5 and 14.6, respectively, present the performances of HPAs made from Noubleau and Obourg aggregates, compared to the reference continuously graded GB2 material normally used in France.

French specifications for a continuously graded GB2 and EME2 are given as well. The reference EME2 material consists of a continuously graded curve and relies on the use of hard binders (penetration at 25 °C < 30 dmm) at a content of 5.5–6.0% by weight of aggregates to preserve fatigue resistance. EME2 is traditionally used as base course material in Perpetual Pavement design in Europe, and in particular in France.

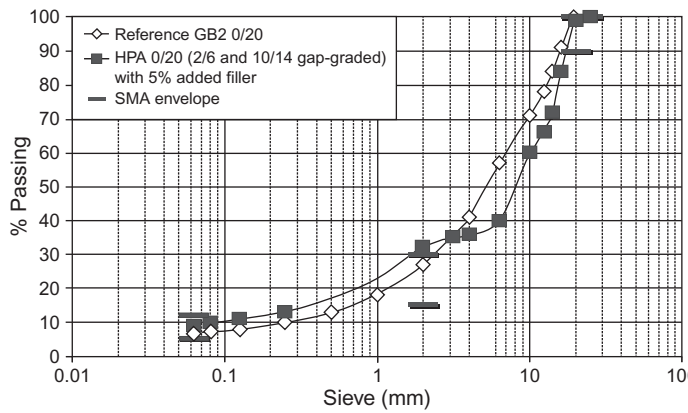


Figure 14.14 Gradation curves for the optimal 14/20–6/10–0/2-filler quaternary Obourg aggregate blends versus typical gradation curve of the reference GB2.

www.EngineeringEBooksPdf.com

Table 14.4 Passing percentage for each tested asphalt mix made from the Obourg aggregates

Sieve (mm)	Passing (%)		
	Reference grave bitume GB2 0/20	HPA 0/20 with 5% added filler (2/6 and 10/14 gap-graded)	HPA 0/20 with 5% added filler (2/6 and 10/14 gap-graded) + 10% RAP
20	100	100	100
16	91	83	83
14	87	70	70
12.5	78	65	66
10	70	59	60
8	64	49	49
6.3	57	38	39
4	41	34	35
2	27	31	31
1	18	22	22
0.25	10	12	12
0.125	8	10	10
0.08	7	8	8

14.5.1 Compactability evaluated from the GC

Compactability, measured from the GC at 100 gyrations, is significantly improved:

- Regarding HPAs made from Noubleau aggregates (with single-gap-graded curve), densities are increased by 2.3% up to 3.8%. Nonetheless, the use of 10% (continuously graded) RAP slightly decreases the compactability of the HPA (7.2% air voids at 100 gyrations, instead of 5.9%), which indicates that nonnegligible interference effects do occur between aggregate particles. Further work with 25% RAP will be set out to confirm or infirm this point.
- Regarding the HPAs made from Obourg aggregates (with twice-gap-graded curve), densities are indeed increased by about 5%. The use of such optimized double-gap-graded granular curves appears the most promising.

It is worthwhile to point out that such an excellent compactability of HPAs made from either Noubleau or Obourg aggregates has been confirmed on site during experimental roadwork near Blois, Tours, and Arras (France) using the same asphalt formulas.

Eventually, even with a somewhat low value of binder content (%vol = 10%), the proposed single- or double-gap-graded curves allow us to obtain very encouraging voids-in-mineral-aggregate (VMA) results (from 13.8% to 15.8%).

www.EngineeringEBooksPdf.com

Table 14.5 Performances of HPAs and reference GB2 material

Formula			GC 100 gyrations		Duriez test		Rut depth (mm) 3×10^4 cycles	E (MPa) 15 °C–10 Hz	ε_6 (10^{-6}) 10 °C–25 Hz
	Binder nature	% RAP	%Air	VMA	R (MPa)	Moist. Res. (%)			
Specifications for "Grave Bitume 2" (GB2)			<10%	–	–	>70%	<10	>9000	>80
Specifications for "Enrobé à Module Elevé 2" (EME2)			<6%	–	–	>70%	<7.5	>14,000	>130
GB2	35/50	0	9.7	19.7	10.1	93	4.1	13,300 at 5.1% air	86
		0	5.9	15.9	11.8	83	5.1	16,500 at 2.7% air	89
		10	7.2	17.2	12.1	91	4.1	16,600 at 2.7% air	90
HPA	35/50 +2.5%SBS	0	5.7	15.7	12.3	93	2.4	15,600 at 3.2% air	115
	35/45B		5.8	15.8	12.7	92	2.5	13,100 at 2.9% air	115
	35/45B +2.5%SBS		5.7	15.7	13.1	91	3.0	13,700 at 2.5% air	130

Noubleau aggregates with a 4% binder content by wt of aggregate (%vol = 10%).

www.EngineeringEBooksPdf.com

Table 14.6 Performance of HPAs and reference GB2 material

Formula		GC 100 gyrations		Duriez test		Rut depth (mm) 3×10^4 cycles	E 15 °C–0.02 s (MPa)	ε_6 10 °C–25 Hz (10^{-6})
Binder nature		%Air	VMA	R (MPa)	Moist. Res. (%)			
Specifications for "Grave Bitume 2" (GB2)		<10%	–	–	>70%	<10	>9000	>80
Specifications for "Enrobé à Module Elevé 2" (EME2)		<6%	–	–	>70%	<7.5	>14,000	>130
GB2	35/50	8.7	18.7	11.8	83	5.1	13,900 at 7.0% air	89
	35/45B	8.9	18.9	11.3	84	3.3	10,800 at 7.2% air	109
HPA	35/45B	3.8	13.8	12.7	85	3.4	13,000 at 3.6% air	114
	35/45B +2.5%SBS	3.8	13.8	12.5	83	2.1	12,800 at 4.3% air	135

Obourg aggregates with a 4% binder content by wt of aggregate (%vol = 10%).

www.EngineeringEBooksPdf.com

14.5.2 Compressive strength and moisture resistance assessed from the Duriez test

Direct compressive strength (determined on the first set of cylindrical samples kept 8 days in the air at 18 °C), measured from the Duriez test, is also improved (an increase from 1.2 to 2.5 MPa is obtained).

In addition, moisture resistance (the Duriez ratio), which is far above the minimum specification value for typical GB2, does not seem to be influenced by the innovative gradations and PMBs used.

14.5.3 Rutting resistance assessed from the FWTT

The HPAs exhibit great resistance to rutting (low values of rut depth at 60 °C after 30,000 cycles ($\leq$5.1%), cf. Tables 14.5 and 14.6) for two main reasons: the first is due to the well-interlocked and dense mixtures obtained from the optimization of aggregate packing, while the second reason lies in the fact that semiblown and polymer-modified bitumens give high resistance to rutting at high temperatures, in particular at 60 °C.

14.5.4 Complex modulus

For a fixed bitumen nature and content, the complex stiffness modulus of such well-interlocked and dense mixtures, measured at 15 °C–10 Hz, is significantly increased (in the range of 20–26%). Further work with different aggregate natures and fractions remains to be done so as to confirm this encouraging result. Indeed, the proposed procedure to optimize the aggregate packing characteristics could be used in the framework of high-modulus mix design with slightly softer grades than usual (penetrability at 25 °C $>$ 30 dmm in contrast with the reference European EME2 mix design), thus enhancing both reclaiming ability and fatigue resistance of asphalt concretes.

In addition, in order to assess the influence of the proposed gap gradation on both glassy and static moduli, complex stiffness modulus tests were also performed for the GB2 reference material and the proposed gap-graded HPA with Noubleau aggregate, with the same binder (35/50) at the same amount (4% binder content by weight of aggregate), from −30 to 45 °C with a frequency ranging from 0.01 to 10 Hz (see Figure 14.15).

Regarding the glassy modulus (asymptotic value of complex modulus in the low-temperature and high-frequency domain), an increase of 20% was obtained, whereas for the static modulus (asymptotic value in the high-temperature and low-frequency domain), a threefold increase was obtained. These first results could make such HPAs interesting for heavy-duty pavements, heavy-duty bridge deck pavements, and so on.

www.EngineeringEBooksPdf.com

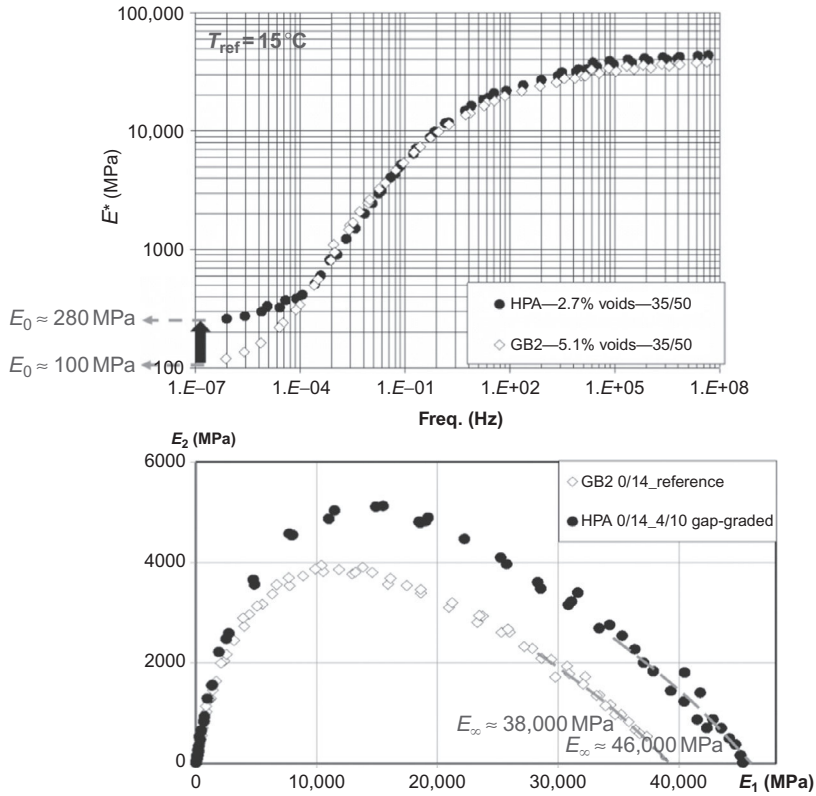


Figure 14.15 Complex modulus of the gap-graded HPA versus that of the reference GB2 (Noubleau aggregate and 4% of 35/50 binder by weight of aggregate): master curves at 15 °C and Cole–Cole diagram.

14.5.5 Fatigue resistance

The very first results of HPA fatigue resistance tests appear comparable to those of the reference GB2 material, for a fixed bitumen nature and content. Fatigue resistance is indeed hardly influenced by the developed aggregate packing optimization. On the contrary, binder nature highly influences fatigue resistance:

- With regard to the HPA with Noubleau aggregates (with single-gap-graded curve), the polymer modification (2.5% cross-linked SBS) of the 35/50 neat bitumen leads to an increase of the ε_6 value by 21 microstrains.
- Regarding the reference "grave bitume" (GB) made from Obourg aggregates (with continuous gradation), moving from the neat 35/50 bitumen to the blown 35/45B bitumen brings about an increase of the ε_6 value by 20 microstrains.
- Regarding the HPA with Obourg aggregates (double-gap-graded curve), the polymer modification (2.5% cross-linked SBS) of the blown 35/45B bitumen increases the value of ε_6 by 21 microstrains, leading to an ε_6 value of 135 microstrains, which is an incredibly high value for an asphalt concrete with only a 4% binder content in France.

www.EngineeringEBooksPdf.com

An attempt was made to adjust the GB2 blends in order to lower VMA values close to those of the optimized blends to see the effect on the stiffness and fatigue performances, yet it was impossible to get the 2.7% air void target.

14.6 Economic and environmental outlook

An alternative to the traditional high-modulus and high-binder content EME2 (for which binder content is about 5.5–6%) may be proposed for long-lasting and cost-effective asphalt mixes. Considering the very encouraging results presented in Tables 14.5 and 14.6 (with only 4% of bitumen by weight of the aggregate), at Eiffage Travaux Publics, we set out to combine both optimal aggregate interlock and the use of semiblown and/or SBS-modified bitumens, in order to obtain both very stiff and fatigue-resistant base/binder course material in a single formulation.

This has been done with many aggregate natures (mainly from France) using either single- or double-gap-graded curves and a tremendous number of polymer-modified and semiblown bitumens. Obtained performances are close to the specifications required for EME2 (stiffness modulus of 14,000 MPa at 15 °C and a fatigue resistance of 130 microstrains at 10 °C), with a significantly lower bitumen content (in the range of 3.9–4.9% by weight of aggregate). Such innovative mix design, which is referred to as GB5®, has been patented.

The following two subsections present a case study with comparative pavement design and environmental impact.

14.6.1 Hypothesis for pavement design and material cost

The French method for pavement design has been used, and calculations presented hereafter rely on the use of ALIZE software. The adjustment factor, k_c, that is used to determine the strain value $\varepsilon_{t,ad}$ considered acceptable at the bottom of the GB5® base course is considered equal to 1.3 (typical value for a French (GB) base layer). Furthermore, the $k_c = 1$ hypothesis is made when considering conventional high-modulus asphalt concretes (referred to as EME2), which use very low-pen-grade bitumens (penetrability at 25 °C in the range of 10–30 dmm). Broadly speaking, this k_c coefficient adjusts the results of the computational model in line with the behavior observed on actual pavements of the same type. For more details, the value of this coefficient for bituminous materials is detailed in the French design manual for pavement structures (SETRA-LCPC, 1997).

In order to compare the costs of road structures with traditional EME2 or innovative GB5® base courses, the following orders of magnitude were taken into account for material costs:

- Cost of 10/20 hard bitumen ≈ 35/50 pen-grade bitumen + 40–60 €/t;
- Cost of 35/45B ≈ 35/50 pen-grade bitumen + 40–60 €/t;
- Cost of 35/50 + 2.5%SBS ≈ 35/50 pen-grade bitumen + 150–170 €/t;
- Cost of 35/45B + 2.5%SBS ≈ 35/50 pen-grade bitumen + 200–220 €/t.

www.EngineeringEBooksPdf.com

The apparent specific gravities (t/m^3) are:

- ρ(BBM): 2.42 t/m^3
- ρ(GB5): 2.47 t/m^3
- ρ(EME2): 2.49 t/m^3

A "béton bitumineux mince" (BBM) is used as a 4-cm thick overlay in France.

14.6.2 Comparative pavement design, corresponding costs, and environmental impacts

Table 14.7 presents a comparative pavement design using the ALIZE software and considering a "TC620" traffic category (cumulative traffic over 20 years in the range between 6.5 and 17.5 million 13-t axles), a 4-cm BBM overlay, and a "PF3" pavement formation class (120 MPa). Materials are the same ones listed in Table 14.5, together with their respective performance results.

Table 14.7 shows that innovative GB5 mixes to have very positive environmental and economical impacts when considering the reduced base-layer thickness and the reduced quantities of binder and aggregate required per square meter.

Table 14.7 Comparative pavement design with Noubleau materials (from Table 14.5), corresponding costs, and related environmental impacts (per square meter)

Thick bituminous pavement structures. "TC620" traffic category 4-cm BBM overlay. "PF3" pavement formation class				
	EME2 solution Binder content = 5.7%	**Innovative GB5® solutions Binder content = 3.9%**		
Binder	**Hard 10/20**	**35/45B**	**35/50 +2.5%SBS**	**35/45B +2.5%SBS**
Overlay	4 cm BBM	4 cm BBM	4 cm BBM	4 cm BBM
Base course	16 cm EME2	14 cm GB5	12 cm GB5	10 cm GB5
Difference in base-layer thickness		−2 cm (−10%)	−4 cm (−20%)	−6 cm (−10%)
Difference in aggregate quantity		−10%	−20%	−30%
Difference in bitumen quantity	Reference	−28%	−39%	−48%
Difference in material cost/m^2		−23%	−27%	−38%
Difference in kg CO_2equiv./m^2		−24%	−17%	−28%

www.EngineeringEBooksPdf.com

Insofar as greenhouse gas emissions (GGEs) are concerned, carbon dioxide (CO_2) quantities (main GGE generated during roadwork) associated to aggregates, pure bitumen, and PMB are, respectively, equal to 10, 285 and 310 $kgCO_2/t$. Therefore, the proposed high-performance GB5® base layers may lead to a reduction in CO_2 emissions by almost 30% in comparison with the traditional EME2-based pavement design (see Table 14.7).

However surprising it may seem, the proposed aggregate packing optimization makes the SBS affordable in base-layer materials (its use was limited to surface courses until recently, for economic reasons).

14.7 *In situ* validation of the GB5® mix design: development and large-scale roadwork of 2010–2014

Ten full-scale suitability tests were carried out on several Eiffage asphalt plants in 2010, before generalizing the technique on each of the 180 Eiffage sites (see Figure 14.16). These preliminary field trials allowed us to validate the technical choices with either the single-gap or double-gap gradations initially studied in the laboratory. In particular, the great compactability of the proposed mixes was confirmed up to that point.

In 2011, the use of the proposed GB5® mix design was generalized on most French Eiffage sites. Several aggregate natures were studied and four main NMPSs were used: 11, 14, 16, and 20 mm. Both single-gap-graded curves and double-gap-graded granular curves were successfully investigated. Semiblown 20/30, 35/50, 50/70, and 70/100 pen-grade binders were used. SBS modification was also carried out (referred to as Biprène® and Orthoprène®, with a proprietary cross-linking procedure) for most



Figure 14.16 Paving GB5® 0/14 mm with Noubleau aggregates and 35/45 bitumen in the Tours area. In-place density: 96.4%; stiffness modulus measured in indirect tension configuration E^* (15 °C–10 Hz): 14,100 MPa.

www.EngineeringEBooksPdf.com

of our full-scale suitability tests up to this point. In PMB compositions, SBS content was in the range of 2.5–7%. The overall binder content (virgin + aged binders) was generally in the range of 4.0–4.6%.

The GB5® mixes were applied by the paver and very easily compacted by double-roll vibrating compactors (Figures 14.17 and 14.18). There was no need for pneumatic tire rollers, with final density in the range between 2% and 6%. Layer thickness was between 5 and 15 cm, thanks to the gap gradations used.

600,000 t of GB5® mixes have been paved so far, corresponding to a savings of about 6000 t of bitumen in comparison with the reference EME2 (high-modulus high-binder content mix) usually used as base course material in Perpetual Pavement design in Europe. On top of that, almost 15,000 t of PMBs have been produced and used so far in base courses, whereas their use had previously been limited to surface courses, for economic reasons.

After several months (trials in 2010–2011), these different sites were revisited in order to assess the condition of the pavement and/or take cores to assess the density and complex or secant modulus in indirect tension mode. This follow-up is very encouraging and confirms the great performance initially obtained in the laboratory.

One initial concern was to check the validity and effectiveness of the proposed approach with mixes containing high RAP content. In 2011, some GB5® mixes were successfully designed and manufactured with 40% RAP: RAP aggregate size was 0/10 mm and the added crushed aggregate size was 14/20 mm, in order to get a single 10/14 mm gap in the 0/20 mm gradation. Further work is planned within the next few years on this issue, using specially fractionated recycled materials. By fractionating RAP and combining high RAP content with unaged SBS-modified binder, the GB5® mix design could produce a longer life pavement with a very interesting economic outlook.



Figure 14.17 GB5® 0/14 mm with Budillon aggregate and SBS-modified binder Biprène® 41 (proprietary composition) and 15% RAP near Chambery. In-place density: 97%; modulus E^* (15 °C–10 Hz): 15,900 MPa.

www.EngineeringEBooksPdf.com



Figure 14.18 12,000-t GB5® 0/14 roadwork on the French A43 toll highway (AREA network, Chignin-Francin section) in the alpine area. Budillon aggregate, 15% RAP, and PMBs Biprène® 41 and Orthoprène® were used.

Last but not least, in the framework of the Road Innovation Charter procedure of SETRA (Service d'Etudes Techniques des Routes et Autoroutes), in France, the innovative GB5® project was awarded in 2010. In 2011, a Road Innovation Charter was signed with SETRA and several general councils and companies in charge of toll highways. From then on, several GB5® projects were undertaken in different climatic zones in France, under very high traffic. A 5-year follow-up by SETRA is planned for validation of this new technique.

14.8 Future trends

Effective particle packing, whatever the NMPS (from 4 or 6 mm up to 14 or 20 mm), enables very different uses. Some examples of high-value roadwork and specific structures, such as harbors, bridge sealings, or surfacings, and ring-abouts, are given in Figure 14.19 (clockwise from top left):

www.EngineeringEBooksPdf.com



Figure 14.19 Examples of high-value roadwork and specific structures.

- 6 cm strongly SBS-modified dense surfacing on the Winston Churchill bridge in Lyon (with bus lane).
- Thick asphalt structure for Honfleur harbor: 10 cm base course + 8 cm surface course.
- SBS-modified dense asphalt 0/14 mm as a 7 cm surface of ring-about in Marcilloles.
- Strongly SBS-modified dense asphalt 0/6 mm as a 3 cm sealing of the Raymond Barre bridge in Lyon.

14.9 Conclusions

Effective particle packing seeks to select proper sizes and proportions of small particle-shaped materials to fill larger voids. These small particles in turn contain smaller voids that are filled with smaller particles, and so on. Such well-interlocked gap-graded mixtures have greater friction angles than the continuously dense-graded mixtures. Starting from such basic concepts associated with granular combinations, aggregate packing methods first developed in the field of high-performance cement concrete were successfully transposed and adapted to the field of asphalt concrete, and enabled the development and design of HPAs. We hereafter refer to the proposed mix design method as the GB5® mix design method in France.

A GB2 continuously graded mixture, traditionally used for base courses in France, was studied, acting as a reference material. The first laboratory assessments of the optimal single- or double-gap-graded mixtures designed in this study were very encouraging:

- Compactability, evaluated through gyratory shear compaction, is remarkably improved. In the framework of this work, for the same compaction energy, density values are approximately 4% higher.
- Moisture susceptibility, assessed using the Duriez test, does not appear to be influenced by the proposed optimal gradations. Further work is planned to confirm this point.

www.EngineeringEBooksPdf.com

- Compressive strength value at 18 °C is increased by about 15%.
- Rutting resistance at 60 °C–1 Hz is hardly influenced by the optimal gradations used, yet the ability of blown bitumens or SBS polymers to reduce susceptibility to rutting is once again evidenced.
- Secant stiffness modulus measured at 15 °C–0.02 s is significantly increased (in the range of 11–20%). The proposed procedure to optimize aggregate packing characteristics could be used in the framework of high-modulus mix design (e.g., French "EME" with slightly softer bitumen grades than usual (penetrability at 25 °C > 30 dmm), thus enhancing both reclaiming ability and fatigue resistance of such asphalt concretes.
- Fatigue resistance of GB5® mixes, evaluated at 10 °C–25 Hz and for a fixed considered bitumen, appears comparable to that of the reference GB2 material. In addition, as the single- or multiple-gap-graded asphalt mixtures really enhanced stiffness moduli, the use of softer bitumen grades, semiblown binders, or PMBs yields great fatigue resistance. Such particular combination of innovative single- or double-gap-graded curves with semiblown and/or SBS-modified bitumens, leading to very stiff and fatigue-resistant polymer-modified base or binder course materials in a single formulation, was recently patented by Eiffage Travaux Publics.

To some extent, such GB5® mixes used for base or binder courses could provide real long-life pavements that do not deteriorate structurally, needing only timely surface maintenance to maintain their overall condition.

Finally, the on-site application of GB5® mixes on experimental roadwork with or without RAP, at either hot (160 °C), warm (125 °C), or even half-warm (90 °C) temperature, was successfully realized: more than 600,000 t of GB5® mixes have already been paved on high-traffic highways and toll motorways, mainly in France, and to a lesser extent in Spain and in South Africa. This rapid development and the numerous large-scale roadwork of GB5® mixes, with SBS in base or binder courses, could be put into practice particularly because of the proposed GB5® mix design relies on a rather low binder content (from 4.0% to 4.6%, generally). Indeed, the optimization of aggregate packing allows one to obtain such low binder content, and thus makes it economically possible to use SBS in base courses, leading to an alternative concept of perpetual pavement.

Acknowledgments

The author gratefully acknowledges the help provided by the staff of the Eiffage road research center in Lyon, in particular P. Huon, F. Desvignes, R. Lictevout, and C. Billet, for the performance of most aggregate packing optimizations and of many mechanical tests on HPAs. The author also thanks S. Dupriet for conducting all the fatigue tests on HPAs at the Eiffage road research center in Ciry-Salsogne.

References

Andersen, P.J., Johansen, V., 1993. A guide to determining the optimal gradation of concrete aggregates. SHRP-C-334 report, Strategic Highway Research Program, National Research Council, Washington, DC.

Baaj, H., Di Benedetto, H., Chaverot, P., 2005. Effect of binder characteristics on fatigue of asphalt pavement using an intrinsic damage approach. Int. J. Road Mater. Pavement Des. 6 (2), 147–174.

www.EngineeringEBooksPdf.com

Baron, J., Sauterey, R., 1982. Le béton hydraulique: Connaissance et pratique. Presses de l'École Nationale des Ponts et Chaussées, Paris, France (in French).
Ben Aïm, R., 1970. Étude de la texture des empilements de grains. Application à la détermination de la perméabilité des mélanges binaires en régime moléculaire, intermédiaire, laminaire. Thèse de la Faculté des Sciences de l'Université de Nancy (in French).
Ben Aïm, R., Le Goff, P., 1967. Effet de paroi dans les empilements désordonnés de sphères et application à la porosité de mélanges binaires. Powder Technol. 1, 281–290 (in French).
Caquot, A., juillet-août, 1937. Le rôle des matériaux dans le béton. Mémoires de la Société des Ingénieurs Civils de France, 562–582 (in French).
Chanvillard, G., 1999. Le matériau béton: Connaissances générales. Editions Aléas, Lyon (in French).
Cooper, K.E., Brown, S.F., Pooley, G.R., 1985. The design of aggregate gradings for asphalt basecourses. Proc. Assoc. Asph. Paving Technol. 54, 324–346.
Corte, J.F., Di Benedetto, H., 2004. Matériaux Routiers Bitumineux 1: description et propriétés des constituants. Lavoisier, Paris, 238 p. (in French).
Cumberland, D.J., Crawford, R.J., 1987. Handbook of Powder Technology, vol. 6. Elsevier Science, Amsterdam (Chapter 4).
De Larrard, F., Mars 1988. Formulation et propriétés des bétons à très hautes performances. Rapport de recherche LPC N149, ISSN 0222-8394 (in French).
De Larrard, F., Sedran, T., 1994. Optimization of ultra high-performance concrete by the use of a packing model. Cement Concrete Res. 24 (6), 997–1009.
De Larrard, F., Sedran, T., 2002. Mixture-proportioning of high-performance concrete. Cement Concrete Res 32 (11), 1699–1704.
De Larrard, F., Sedran, T., Angot, D., 1994. Prévision de la Compacité des Mélanges Granulaires par le Modèle de Suspension Solide I: Fondements Théoriques et Calibration du Modèle (Prediction of the packing density of granular mixtures with the solid suspension model. I: Theoretical basis and calibration). Bull. Liaison Lab. Ponts et Chaussées 194, 59–86 (in French).
Dreessen, S., Ponsardin, M., Planche, J.-P., Dumont, A.-G., Pittet, M., 2011. Durability study: field aging of conventional and cross-linked polymer modified bitumens. In: LJMU (Liverpool John Moores University) Conference.
European Road Federation (ERF), 2014. Road asset management: maintaining and improving a sustainable and efficient road network. Position paper.
Furnas, C.C., 1928. Relations between specific volume, voids and size composition on systems of broken solids of mixed sizes. Report of investigations, 2894, US Bureau of Mines, 1–10.
Harman, T., Bukowski, J.R., Moutier, F., Huber, G., McGennis, R., 2002. The history and future challenges of gyratory compaction 1939 to 2001. In: Annual Meeting of the TRB, Washington, DC.
Kim, S., Guarin, A., Roque, R., Birgisson, B., 2008. Laboratory evaluation for rutting performance based on the DASR porosity of asphalt mixture. Int. J. Road Mater. Pavement Des. 9 (3), 421–440.
Lees, G., 1970. The rational design of aggregate gradings for dense asphaltic compositions. In: Proceedings of the Association of Asphalt Paving Technologists Conference.
NF EN 12697-12 Specification Septembre 2002. Essais statiques sur mélanges hydrocarbonés, essai Duriez sur mélanges hydrocarbonés à chaud.
NF EN 12697-22 Specification Juin 2004. Méthodes d'essai pour mélange hydrocarboné à chaud: essai d'orniérage.
NF EN 12697-24 Specification Mars 2005. Méthode d'essai pour mélange hydrocarboné à chaud: résistance à la fatigue.

www.EngineeringEBooksPdf.com

NF EN 12697-26 Specification Décembre 2004. Méthode d'essai pour mélange hydrocarboné à chaud: module de rigidité.
NF EN 12697-31 Specification Janvier 2005. Méthode d'essai pour mélange hydrocarboné à chaud: confection d'éprouvettes à la presse à cisaillement giratoire.
NF EN 13108-5 Specification December 2006. Bituminous mixtures, material specifications, Part 5: stone mastic, asphalt.
NF ISO 13320-1 Specification September 2000. Analyse granulométrique, Méthodes par diffraction laser, Partie 1: Principes généraux.
Nijboer, L.W., 1948. Plasticity as a Factor in the Design of Dense Bituminous Road Carpets. Elsevier Publishing Company, New York, NY.
Oger, L., 1987. Etude des corrélations structure-propriétés des mélanges granulaires. Thèse d'Etat. Université de Rennes (in French).
Olard, F., 2012. GB5 mix design: high-performance & cost-effective asphalt concretes by use of gap-graded curves & SBS modified bitumens. Road Mater. Pavement Des. 1, 234–259, Special Issue: Papers from the 87th Association of Asphalt Paving Technologists' Annual Meeting, April 1–4.
Olard, F., Perraton, D., 2010a. On the optimization of the aggregate packing characteristics for the design of high-performance asphalt concretes. Int. J. Road Mater. Pavement Des. 11 (Special Issue EATA Parma), Best Scientific Paper Award.
Olard, F., Perraton, D., 2010b. On the optimization of the aggregate packing for the design of self-blocking high-performance asphalts. In: Congress of the International Society for Asphalt Pavements, Nagoya.
Perraton, D., Meunier, M., Carter, A., 2007. Application of granular packing methods to the mix design of stone matrix asphalts (SMA). In: Bulletin de Liaison des Ponts et Chaussées, N° 270–271.
Powers, T.C., 1968. The Properties of Fresh Concrete. John Wiley & Sons, Inc., New York.
Roque, R., Huang, S., Ruth, B.E., 1997. Maximizing shear resistance of asphalt mixtures by proper selection of aggregate gradation. In 8th International Society for Asphalt Pavements, Seattle.
SETRA-LCPC., 1997. Guide Technique. French Design Manual for Pavement Structures. LCPC et SETRA, Paris.
Yoder, E.J., 1959. Principles of Pavement Design. John Wiley & Sons, Inc., New York.

www.EngineeringEBooksPdf.com

Index

Note: Page numbers followed by *b* indicate boxes, *f* indicate figures and *t* indicate tables.

A

Acid-base model, 313
Acoustic wave propagation, 3D LVE, 79–86
Adherence energy
  FD-AFM, 122*t*, 123–124
  fracture, 119
Adhesion
  definition, 309
  failure theories, 309–316
  FD-AFM, 121–122
  testing, 20–21
Adsorption chromatography, 36–38
Aggregate packing, 427
  characterizing concretes, 436–439
  complex modulus, 447
  compressive strength, 447
  economic and environmental outlook, 449–451
  fine and coarse, 431–432
  granular combinations, 428–430
  granular fraction, 437*t*
  high-value roadwork, 454*f*
  interference notion, 429, 430*f*
  loosening effect, 429*f*
  materials, 435–436
  mechanical performance, 443–449
  moisture resistance, 447
  optimization, 433–434
  pavement design and material cost, 449–451
  porosity *vs.* average particle dimension, 430
  rutting resistance, 447
  stone mastic asphalts, 432–433
  theoretical background, 428–433
  void index variation, 432*f*
  wall effect, 429, 430*f*
Aggregate/water interface, 413–415
Aging, 17–20
  effects, 180–181, 192
  energy threshold and damage healing, 151*f*
  oxidative (*see* Oxidative aging)
Aliphatic sulfides, 42
ALIZE software, 449
Alternative binders
  cellulosic biomass, 358
  development, 360–361
  nonindustrialized, 359*t*
  for partial replacement, 358–359
  protein components and vinegar, 357–358
  vegetable oils and wood coproducts, 347–358
Ambient temperature deformation
  modified cross model, 187–192
  power-law model, 182–187
American Association of State Highway and Transportation Officials (AASHTO), 6–7
American Petroleum Institute (API) Project 60, 39, 44–45
American Society for Testing and Materials (ASTM), 6
Amorphous polymers, 173
Anisotropy, 86–92
  asphalt mixtures, 249
  complex modulus, 87–88, 89*t*
  poisson's ratio, 88–92
  viscoelastic properties, 245–248
Arrhenius equation, 184–185
Artificial RA binder, 373–375
Asphalt. *See* Bitumen
Asphalt binders
  bee structure, 98, 102, 105
  construction of pavements, 97
  healing in, 212*f*, 214–219
  oxidation impacts, 286–291
  simulations, 212*t*
  toluene solvent, 111
Asphalt cement, 279–285

www.EngineeringEBooksPdf.com

Asphalt concrete
multiscale perspective behavior, 276–278
viscoelasticity of, 285–286
Asphaltenes
effects, 178*f*, 179*f*, 180*f*
importances, 170–171
properties, 172
Asphalt FAM, 277
Asphalt mastic, 277
diffusion coefficients, 335*t*
Asphalt materials, oxidation effects, 279–286
Asphalt mixture
anisotropic viscoelastic properties, 245–248
axial strain decomposition, 252*f*
digital lateral scanner, 246*f*
energy-based mechanistic approach, 255–257
fatigue coefficients, 140*t*
fracture, 263–268
healing, 208–213, 220–226, 261–263, 264*t*
isotropic viscoelastic properties, 244–245
oxidation impacts, 286–291
parameters in HMA-FM model, 156*t*
permanent deformation, 249–255
properties, 243
pumping action in, 316–319
recovery, 261–263
water flow modeling, 316–319
Asphalt pavements
environmental conditions, 303
saturated, 318*f*
Asphalt/water interface, 413–415
ASTM. *See* American Society for Testing and Materials (ASTM)
Atomic force microscopy (AFM), 313, 315–316. *See also* Force–displacement atomic force microscopy (FD-AFM)
advantages and disadvantages, 104–105
force-mode imaging, 97–98
information sources/advice, 126–128
nanomechanical approaches, 99–100
nanorheological methodologies, 125–126
phase-contrast technique, 98
sample preparation techniques, 116–118
scanning thermal imaging, 126
SHRP asphalts, 98
surface structuring analysis, 105–118
Axial strain, 61
amplitude, 62
on bituminous mixture, 63*f*
Axial stress, 63*f*

B

Baron's approach, 432–433
Bee microstructures, 105, 116
Bending beam rheometer (BBR) test, 14
Béton Bitumineux Semi-Grenu (BBSG) type, 85
Bioflux®, 359–360
Biomasses, oil productivity, 354*f*
Biophalt®, 349*t*, 351
Bitumen
adhesion testing, 20–21
aging and conditioning regimes, 17–20
attributes of specification, 3
binder properties derived from, 7*t*
characteristics, 1–3
elevated service-temperature test methods, 10–13
fatigue testing, 14–16
fundamental/empirical binder testing, 22–24
geographical considerations, 3–4
intermediate service temperature, 16
low service-temperature properties, 13–14
microalgae extracts *vs.*, 355*f*
names of, 1
physical properties, 350*t*
precision of test methods, 21–22
properties, 2–3
regulatory frameworks, 4–9
specification, 2–4
stiffness, 2–3
temperatures, 1–2
temperature sensitivity, 17
test methods, 2–3, 10–21
values, 2–3
Bitumen Test Validation (BiTVal), 9
Bituminous materials
behavior for, 59–60, 60*f*
scanning probe microscopy imaging, 97–99
Borosilicate stone, chemical composition, 376*t*

www.EngineeringEBooksPdf.com

C

Capillary tube, dynamic viscosity using, 11
Carboxylic acids, 43
Catana phase/peri phase, 313
Cationic asphalt emulsions, 395, 412–413
Cationic medium-setting (CMS) grades, 396
Cationic quick-setting (CQS) emulsions, 396
  coagulation behaviors of, 413*f*
Cationic rapid-setting (CRS) emulsion, 396, 402–403, 402*t*
  coagulation behaviors of, 413*f*
  with hydrophilic head group, 412–413
CDC test. *See* Cyclic displacement-controlled (CDC) test
CEN. *See* Comité Européen de Normalisation (CEN)
Chemical bonding theory, 314
Chemical force microscopy (CFM), 101–102
Chip seal, 415–420
Chromatography, 35
  adsorption, 36–38
  affinity, 38–43
  SEC, 43–52
  separation methods, 37–38
Climate change, global warming and, 303
Cloud point, 400
Coalescent phase, of crack growth, 257–259
Cohesion
  definition, 309, 315
  failure theories, 309–316
Colloidal model
  of asphalt structure, 33–34, 44
  molecular structure, 172
  pure bitumens, 171–172
Comité Européen de Normalisation (CEN), 5–6
  data collection program, 23–24
  structure, 6*f*
Compactability, from GC, 444–446
Complex modulus, 60, 61, 447
  anisotropy, 87–88, 89*t*
  strain measurement systems, 62*f*
  test equipment, 61, 61*f*
  test principle, 62–63
  tests, 75–76
Complex Poisson's ratio, 60, 61
  Cole-Cole and Black spaces, 65*f*
  constants, 70
  norm and phase angle, 65*f*
  shift factor, 67*f*
  strain measurement systems, 62*f*
  temperature and frequency, 64
  test equipment, 61, 61*f*
  test principle, 62–63
  and 3D 2S2P1D model, 74*f*
  values of, 70
Complex shear modulus (G*), 16
Complex Young's modulus
  Cole-Cole plot, 65*f*, 76, 76*f*
  normalization, 76*f*
  norm and phase angle, 64*f*
  shift factor, 67, 67*f*
  temperature and frequency, 64
Compression, asphalt mixtures
  anisotropic viscoelastic properties, 245–248
  fracture, 263–268
  permanent deformation, 249–255
Compression axial loading, 62
Compressive strength, 447
Concretes
  characterizing, 436–439
  multiscale perspective behavior, 276–278
  viscoelasticity of, 285–286
Constitutive model, 206–207, 221
  moisture damage, 316–327
Construction Products Regulation (CPR), 4–5
Continuum damage approach
  healing, 220
  mastics and fine aggregate mixtures, 205
  to quantify healing, 220–226
Controlled-strain RDT test, 245, 259
Corbett procedure, for separations, 36–37
Coulter®, 436
CPR. *See* Construction Products Regulation (CPR)
Crack growth, 258*f*
  coalescent phase, 257–259
  formative phase, 257
  law, HMA-FM, 155–158
  unitary phase, 257–259, 259*b*
Cracking pavement
  advanced modeling observations, 145–150, 151
  experimental observations, 139–145, 150–151
  mechanisms, 135–136

www.EngineeringEBooksPdf.com

Cracking pavement (*Continued*)
traditional fatigue cracking, 137–139, 137*f*
types, 136*t*
Crack wetting, 208–210
Creep
constant change with temperature, 185*f*
low-temperature behavior, 194*f*
steady-state behavior, 183*f*, 190*f*
stress tests, 192–193, 193*f*
Creep and steploading recovery (CSR) test, 261, 262
Creep–recovery curve, 13*f*
Critical condition approach
HMA-FM, 151–159
TDC performance model, 159–164
Critical micelle concentration (CMC), 398–399
Crude oils
paraffinic and microcrystalline waxes, 35
refining, 1
Cyclic displacement-controlled (CDC) test, 235–238
Cyclic pore pressure conditioning (CPPC), 159

D

Damage density
definition, 256, 258*b*
healing, 262*b*
unitary phase of crack growth, 259*b*
Damage, pavement cracking
accumulation, 144–145
zones, 147–148, 149*f*
Damage, thermodynamics, 229–233
DBN model, 142
DCF. *See* Distributed continuum fracture (DCF)
Deformation, 10
ambient temperature, 182–192
high-temperature, 174–182
low-temperature, 192–195
permanent, asphalt mixture, 249–255
Deformation-mechanism maps
construction, 195–198
of engineering polymers, 173–174
features, 199
tension, 197*f*, 198*f*
Detachment, moisture damage, 306
Dewetting, 309–310
Differential scanning calorimetry (DSC)
measurements, 170
volume dilatometry, 169–170
Diffusion coefficients, asphalt mastic, 335*t*
Direct-measurement flying-time method, 79, 81–83
Dispersed polar fluid model, 172
Dispersion
of binder, 315
stability, DLVO theory, 409–415
Displacement, moisture damage, 306
Dissipated pseudostrain energy (DPSE), 259
Dissipated strain energy (DSE), 245
Distributed continuum fracture (DCF), 255, 261–262
DLVO theory, dispersion stability, 409–415
Double-gap-graded granular curve, 439–443
DSC. *See* Differential scanning calorimetry (DSC)
Ductile–brittle transition temperature, 123–124
Duriez test, 447
Dynamic shear rheometer (DSR)
aged binders, 374, 375*f*, 376*f*
at high temperature, 76
intrinsic healing, 214–215, 217–219
in oscillatory mode, 11
Dynamic shear tests, 192
Dynamic viscosity, 11

E

Eco-efficient analysis, 394
ED-P model. *See* Extended Drucker–Prager (ED–P) model
Electric properties, emulsions, 405–409
Elevated service-temperature test methods, 10–13
Elution, 36
EME2 material, 449
French specifications, 443
Empirical specifications, 22–24
Emulsions, 393–394
characterization, 422
chemistry, 394–396
deposition diagram, 416
electric properties, 405–409
hydrodynamic aspects of, 400–402

www.EngineeringEBooksPdf.com

Krafft point, 399–400
narrow-size distribution, 419
nonreactive aggregates, 417–419
physical properties, 397–400
reactive aggregates, 420
recipes, 394–396
rheology, 402–404
setting mechanism of, 415–422
slurry seal and microsurfacing, 420–422
stability diagram, 409–415
surface activity and micelle formation, 397–399
surface tension and surfactants, 396–400
viscosity ratio, 402
volcano shape, 417
water evaporation, 419–420
Energy-based mechanistic (EBM) approach, 255–257
Energy-based parameter, 158–159
Energy ratio (ER), 158–159
Engineering polymers, 173–174
ENTPE transformation, 77–78
ETG. *See* Expert task group (ETG)
European road network, 427
European test method, 17
Europe, regulatory frameworks, 4–6
Expert task group (ETG), 12
Explicit modeling, molecular restructuring, 210
Extended Drucker–Prager (ED–P) model, 250, 254, 254*f*
Eyring plasticity model (EPM), 193–195, 196*t*

F

Failure limits, HMA-FM principles, 152–154
Fatigue cracking
asphalt mixture, 140*t*, 255, 257–260, 264*t*
experimental observations, 139–142
reduction in stiffness, 139–142, 141*f*
traditional, 136*t*, 137–139, 137*f*
Fatigue resistance, 448–449
Fatigue testing, 14–16
Federal Highway Administration (FHWA). *See* Strategic Highway Research Program (SHRP)
Fine aggregate matrix (FAM) specimen, 217–219
asphalt, 277
mastic modulus on modulus, 296*f*
oxidative aging, 296
Flame ionization detector (FID), 38
Floraphalte®, 349*t*, 350*t*
penetrability and softening temperature, 351*t*
water resistance test, 350–351
Flying-time method, 81–83
Force–displacement atomic force microscopy (FD-AFM), 118–119
adherence energy, 123–124
ductile–brittle transition temperature, 123–124
methodology, 119–121
theory, 119
work of adhesion, 121–122
Force–displacement curve (FDC), 118–119
Formative phase, of crack growth, 257
Fourier transformation, 83, 83*f*
Fourier transform infrared (FTIR) spectrometer, 206
chemical changes, 383–384
mixture, 383*f*, 387*f*, 389*f*
peak values in, 383*t*, 387*t*
Fraass breaking point, 14
Fracture
adherence energy, 119
asphalt mixtures in compression, 263–268
healing—reversal, 208–211
mechanics-based approach, 217–218
threshold, 144–145
toughness test, 14
Free-volume model, 174–176
French wheel tracking test, 447
Fume emission measurements, 360–361
Functional groups in bitumens, 171

G

Gaestel index, 37
GB2 material
French specifications, 443
performances of, 445*t*, 446*t*
GBs of 5 mm (GB5)
binders extracted from, 379*t*, 380*t*
G* values, 384*f*

www.EngineeringEBooksPdf.com

GBs of 5 mm (GB5) (*Continued*)
mix design, 451–453
mixture, 365–366
precoated, 377
preheated, 378
sieving and separating, 379*f*
surface area ratio, 384–385
total surface area, 382–383
volumetric properties, 376–377
GBs of 8 mm (GB8)
binders extracted from, 379*t*, 380*t*
G* values, 384*f*
mixture, 365–366
sieving and separating, 379*f*
surface area ratio, 384–385
total surface area, 382–383
volumetric properties, 376–377
Gel-permeation chromatography. *See* Size-exclusion chromatography (SEC)
Generalized Drucker–Prager (GD–P) model, 250, 252–254, 253*f*, 254*f*
Glass beads (GBs), 375–377
as artificial aggregates, 364
gradation adjustments, 380*t*
volumetric property, 377*t*
Glass transition, 169–170
Global aging system (GAS) model, 275, 282–283
Global warming, and climate change, 303
Glover model, 274*t*
original-to-RTFO aging prediction, 282*f*
viscosity, 274–275, 283
Gouy-Chapman theory, 406–407
Grade bumping, 8
Granite stone, chemical composition, 376*t*
G*/sinδ (inverse of the loss compliance), 11–12
Gyratory compactor (GC), 444–446

H

Half-warm mix, 393
Hamaker constant, 416
Healing
in asphalt binders, 214–219
asphalt mixture, 261–263, 264*t*
continuum approach to quantify, 220–226
field studies, 207–208
hypothesized mechanism, 208–213
index, 206
laboratory studies, 206–207
material properties and, 210*f*
microdamage (*see* Microdamage healing)
molecular morphology, 211–213
properties of asphalt binders, 205
test protocol, 225*f*
Healing—reversal of fracture process, 208–211
Heat casting techniques, 102–103, 104
Heithaus method, 32–33
High-modulus asphalt concretes, 449
High-performance asphalt mixes (HPAs)
fatigue resistance tests, 448–449
performances of, 445*t*, 446*t*
High-performance liquid chromatographic (HPLC) techniques, 42
High-pressure aging test (HiPAT), 20
High-temperature deformation
on composition, 176–180
effects of aging, 180–181
free-volume model, 174–176
on pressure, 181–182
HMA-FM-based enhanced cracking performance (HMA-FM-E) model
calibration and validation, 160–161
components, 159–160
framework, 159–160
input module, 161–163
predicted results, 163–164
Hot dog test, 246
Hot mix asphalt (HMA)
definition, 363
recycling, 364
Hot mix asphalt-fracture mechanics (HMA-FM), 135–136, 151–152
crack growth law, 155–158
energy ratio, 158–159
failure limits, 152–154
features, 152
material parameters, 155
rate of damage, 154–155
threshold concept, 152
Huet-Sayegh model, 68
Hydraulic scouring, 306–307
Hydrodynamic aspects, of emulsification, 400–402
Hydrophobic fraction, 356*f*
Hydrothermal liquefaction process, 355, 356*f*

www.EngineeringEBooksPdf.com

I

Impact resonance method, 83–84
  experimental device, 84*f*
  recorded signal during, 84*f*
Impact Resonance (IR) test, 79
Indirect tensile test, 353*f*, 354*f*
Intermediate service temperature, 16
International Bitumen Emulsion Federation, 393
Intrinsic healing
  asphalt binders, 214–219
  description, 208–209, 210–211
Inverse of the loss compliance (G*/sinδ), 11–12, 15
Ion-exchange chromatography (IEC), 39–40
  amphoterics, 42–43
  asphalts separation, 39, 40*f*
  compound-type analyses, 43
  isolation of amphoterics, 41*f*
  neutral fractions, 42
  separation method, 39
  solvent strengths, 42–43
Ionic surfactants, solubility of, 399–400
Isotropic viscoelastic properties, asphalt mixture, 244–245

K

Krafft point, 399–400

L

Large molecular size (LMS), SEC chromatograms, 47
Linear amplitude sweep test (LAST), 16
Linear variable differential transformer (LVDT), 236–238
Linear viscoelasticity (LVE), 277–278. *See also* 3D linear viscoelasticity
  behavior, 59
  Orthochape®, 80*f*
  parameters, 75–76
  properties, 283–285
Liquid additives, moisture damage, 338*t*
Log-pen rule, 385, 389, 391
Long-term oven aging (LTOA) procedure, 159, 285, 286
Loss modulus forms, 15
Low service-temperature properties, 13–14
Low-temperature deformation, 192–195

M

Maltenes, 169, 172
Marcusson procedure, for separations, 36–37
Material parameters, HMA-FM principles, 155
MCM. *See* Modified cross model (MCM)
MDR. *See* Moisture damage ratio (MDR)
Mechanical theory, 315
Medium-setting (MS) grades, 394
MEN asphalt plant, 435–436
Metravib tension, 76
Micelle formation, of surfactant, 397–399
Michigan road test, 37
Microalgae, 352–357
Microcrystalline waxes, in crude oils, 35
Microdamage healing, 142–144
  absence of rest period, 226–228
  constitutive relationships, 233–235
  during cyclic loading, 236–238
  effects, 206–207
  microforce balance, 230–231
  reversal of, 208–211
  thermodynamics, 229–233
Micromechanical finite element models, 324–325, 327
Microsurfacing, 420–422
Mineral additives, moisture damage, 338*t*
Modified cross model (MCM)
  ambient temperature deformation behavior, 187–189
  application, 191*f*
  dependence on composition, 189–191
  effects of aging, 192
  parameters, 196*t*
Modified effective-medium theory, 404
Modified Lottman test, 328–332
Modified Paris' law, 257–259, 260, 261*f*, 268*f*
Modified RTFOT (M-RTFOT), 18
Moisture damage, 303, 304–305
  additives for preventing, 338*t*
  mechanisms, 305–309
  modes of failure, 309–316
  parameter, 334–337
  physical-mechanical, 320–327
  pumping action, 316–319
  simulations, 322, 322*f*
  test methods to characterize, 327–334
  water flow modeling, 316–319

www.EngineeringEBooksPdf.com

Moisture damage ratio (MDR)
multiple-parameter, 333*t*
single-parameter performance function, 330*t*
Moisture resistance, 447
Molecular mobility, 211, 212–213
Molecular orientation theory, 314
Molecular weight (MW)
distributions, 47–48
materials, 47
subfraction, 42
M-RTFOT. *See* Modified RTFOT (M-RTFOT)
Multiple stress creep recovery test (MSCRT), 12

N

Nanorheology, 125–126
Needle penetration, 16
n-Heptane, 34
Nonhydrocarbon constituents of asphalts, 33
Nonionic surfactants, solubility of, 400
Nonlinear viscoelastic-viscoplastic model, 323
North Carolina State University artificial neural network (NCSU ANN) model, 289, 290–291
Noubleau aggregates
comparative pavement design, 450*t*
granular fraction, 438*f*
single-gap-graded granular curve with, 439, 441*t*

O

Obourg aggregates, 438*f*
double-gap-graded granular curve with, 439–443
passing percentage, 444*t*
Oléoflux 18®, 359
Orthochape®, 74, 78
definition, 72–74
LVE properties of, 80*f*
Orthoprene®, 78
Oxidative aging, 33
asphalt concrete behavior, 276–278
binder database for, 280*t*
description, 273–276
impacts, 286–291
mixture database, 287*t*
models, 274*t*
at molecular level, 278–279
rheology of asphalt cement, 279–285
sequential multiscale approach, 291–297
viscoelasticity of asphalt concrete, 285–286

P

PANDA. *See* Pavement Analysis using Nonlinear Damage Approach (PANDA)
Paraffinic waxes, in crude oils, 35
Paraforpont®, 72–74
Parameter determination, for modeling moisture damage, 334–337
PAV. *See* Pressure aging vessel (PAV)
PAV85, 20
Pavement Analysis using Nonlinear Damage Approach (PANDA)
CDC test, 236–238
definition, 233
microdamage-healing constitutive relationship, 234–235
Pavement cracking
advanced modeling observations, 145–150, 151
experimental observations, 139–145, 150–151
mechanisms, 135–136
traditional fatigue cracking, 137–139, 137*f*
types, 136*t*
Pavement distress index (PDI), 334
Penetration index (PI), 17
Penetration viscosity number (PVN), 48
Performance-related specifications, 23
Perpetua phase, 313
Petersen model, 172
Petroleum, waxes in, 35
Phase-contrast AFM technique, 98
PI. *See* Penetration index (PI)
PLM. *See* Power-law model (PLM)
PMBs. *See* Polymer-modified binders (PMBs)
Poisson's ratio
complex tests, 60–63
phase angle of, 64

www.EngineeringEBooksPdf.com

Polymer-modified binders (PMBs), 10–11, 19, 435
behavior of, 11, 24
European binder standards, 12
properties of, 25
Pore pressure development process, 307–309
Porous asphalt (PA) mixture, 324
Power-law model (PLM)
definition, 185
dependence on composition, 186–187
parameters, 196*t*
stress dependence, 182–183
temperature dependence, 183–186
Precipitation of asphaltenes, 31–34
Prediction sum of squares (PRESS) method, 161, 162*f*
Pressure aging vessel (PAV)
description, 20
oxidative, 279–282, 292–293
Propane asphaltenes, 34
Pumping action, 309
asphalt binder cracking, 308*f*
in asphalt mixtures, 316–319
definition, 307–309
phenomenon, 317
Purchase specifications, 23
Pure bitumens, 169
compositional models, 171–172
molecular structure, 169–171

R

RA binder. *See* Reclaimed asphalt (RA) binder
Radial strain, 61, 63*f*
Radial tire-contact stresses, 146–147
Rapid-setting (RS) grades, 394
Rate of damage, HMA-FM principles, 154–155
Raveling of asphalt mixes (RoAM), 321
RCAT. *See* Rotating cylinder aging test (RCAT)
RDT test. *See* Repeated direct tension (RDT) test
Receiver sensor signal, 82
Reclaimed asphalt (RA) binder, 363
artificial, 373–375
blending, 391–392
double drum mixer, 363
extraction and recovery method, 367–369
extraction test at two layers, 371–373
glass beads, 375–377
manual washing, 372
material and processes, 366–369
mixture, 365–366, 377–381
properties, 372*t*
research approach, 364
results and analysis, 381–389
stage extraction, 369–373
Reclaimed asphalt pavement (RAP), 370*f*, 435
Recoverable strain energy (RSE), 245
Refractive index (RI), 44–45
Regulatory frameworks
Europe, 4–6
United States, 6–9
Repeated direct tension (RDT) test
controlled-strain, 245, 259
damage density measuresement, 259–260
Residue-recovery procedure, 422
Resins, 39
Rheological evaluation, of aged binders, 374–375
Ring-and-ball softening point (SPt) test, 10–11
Rolling thin-film oven (RTFO) aging, 279–280
viscosity, 280–282, 283
Rolling thin-film oven test (RTFOT), 18–19
Rotating cylinder aging test (RCAT), 19, 364, 373–374, 373*f*, 376*f*
Rutting resistance, 447

S

Saturate-aromatic-resin-asphaltene (SARA) fractions, 273–274, 278
Scanning probe microscopy (SPM)
heat casting techniques, 102–103
imaging investigations, 97–99
nanochemical/nano-adhesive techniques, 101–102
nano-infrared, 126
nanomechanic techniques, 99–101
nanorheological methodologies, 125–126
sample conditioning, 103–104
solvent casting techniques, 102–103
spin casting techniques, 103

www.EngineeringEBooksPdf.com

Scanning thermal probe imaging, 126
Scenedesmus sp., 353–355
Secondary electroviscous effect, 403–404
Separations
  on adsorption chromatography, 36–38
  by affinity chromatography, 38–43
  Corbett procedure, 36–37
  Marcusson procedure, 36–37
  methods of analysis, 37–38
  precipitation, 31–34
  size-exclusion chromatography, 43–52
  solvent precipitation and extraction methods, 34–36
Séquoia®, 349*t*
Sessile drop method, 313–314
Shear tests, dynamic, 192
Shift-Homothety-Shift and time-Shift (SHStS) transformation, 77–78, 79*f*, 80*f*
Short-term oven aged (STOA), 286–288
SHRP. *See* Strategic Highway Research Program (SHRP)
Simulations
  asphalt binders, 212*t*
  moisture damage, 322, 322*f*
  top-down cracking, 161–164
Single-gap-graded granular curve, 439, 441*t*
Sinusoidal tension, 62
Size-exclusion chromatography (SEC), 42
  calibration curves, 45
  chromatograms, 46, 50*f*
  fingerprinting, 44–45
  fraction-I materials, 51, 52
  fraction-II materials, 52
  hydrodynamic volume, 44
  physical properties, 49
  separations, 43–52
Slow-setting cationic emulsion, 396
Slurry seal, 420–422
SMA. *See* Stone mastic asphalt (SMA)
Sol-type asphalts, 32
Solution spreading extraction method (SSEM), 368*f*
  definition, 367
  G* values, 368*f*, 369*t*
Solvent casting techniques, 102–103, 104
Solvent extraction methods, 34–36
Solvent precipitation, 34–36
Specifications
  attributes of, 3
  characteristics, 1–3
  empirical, 22–24
  geographical considerations, 3–4
  performance-related, 23
  properties, 2–3
  purchase, 23
  test methods, 2–3
  values, 2–3
Spin casting techniques, 103
Spontaneous emulsification, moisture damage, 306
SPt test. *See* Ring-and-ball softening point (SPt) test
Stability
  bitumen emulsions, 409–412
  cationic asphalt emulsions, 412–413
  experimental confirmation of, 412
Stage extraction, 369–373
Standard stochastic finite element (SFE) models, 313
Stiffness
  of asphalt mixture, 2–3
  gradients, 148–150
  reduction, 139–142, 141*f*
Stone mastic asphalt (SMA), 324, 355–357, 356*f*, 357*f*, 432–433
Straight-chain alkanes, 35
Strategic Highway Research Program (SHRP), 8–9, 59, 313
  AFM, 98
  fractions, 41
  objective, 39
  oxidative aging, 275, 292–293
  scanning probe microscopy, 97
Stress dependence, 182–183
Superpave, 8–9, 15
Surface activity, 397–399
Surface energy
  approach, 311–312
  measurements, 312
Surface free energy, instantaneous intrinsic healing, 217–219
Surface freezing crystallization, wax, 105–116
Surfactants, 397–398

www.EngineeringEBooksPdf.com

T

Task groups (TGs), 5
TC 336 structure, 6*f*
TDC. *See* Top-down cracking (TDC)
Technical committees (TCs), 5
Temperature dependence, 183–186
Temperature sensitivity, 17
Tensile strength ratio (TSR), 334
  definition, 328–332
  permeability, 334
Tensile tests, 182–183
Tension-compression test, 61, 76, 85, 85*f*, 88, 91
Tetrahydrofuran (THF), 44–45, 47–48
TFOT. *See* Thin-film oven test (TFOT)
Thermal annealing, 104
Thermal behavior, pure bitumens, 170
Thermal chamber, 61
Thermal cracking, 136*t*
Thermodynamic theory
  adhesion, 309–310
  microdamage healing, 229–233
Thermomechanical properties, of bituminous mixtures, 59
Thin film, AFM analysis, 105–118
Thin-film oven test (TFOT), 19
Thixotropic effect, 208
3D linear viscoelasticity, 59–60
  bituminous mixtures, 75–78
  experimental results, 64–67
  parameters, 85–86
  properties, 79–86
  reference temperature, 66*f*, 67*f*
  shift factor, 66
  tridimensional 2S2P1D model, 67–70
3D 2S2P1D model, 67–70
  analogical representation, 68*f*, 69–70
  in Cole-Cole space, 69*f*, 71*f*
  complex modulus measured data, 74*f*
  complex Poisson's ratio and, 74*f*
  equivalent analogical scheme, 68*f*
  high-modulus mixture, 70–71, 72*f*, 73*t*
  modeling for, 70–75
  parameters, 73*t*
Threshold concept, HMA-FM principles, 152
Time–temperature superposition principle (TTSP), 64–66, 85–86
Toluene, 47
Top-down cracking (TDC), 136*t*
  calibration and validation, 160–161
  example simulations, 161–164
  framework, 159–160
Touraine Enrobés asphalt plant, 435–436
TR15352, 23–24
Traditional fatigue cracking, 136*t*, 137–139, 137*f*
Transition temperature, ductile–brittle, 123–124
Transmitter, 82
TSR. *See* Tensile strength ratio (TSR)

U

Ultrasonic (US) wave propagation, 79
Ultraviolet-visible (UV-vis) detectors, 44–45
Unitary phase of crack growth, 257–259, 259*b*
United States, regulatory frameworks, 6–9
U.S. Bureau of Public Roads (BPR) study, 176–177

V

Vapor phase osmometry (VPO), 37–38
VECD theory. *See* Viscoelastic continuum damage (VECD) theory
Vegecol®, 348, 349*t*, 350–351, 350*t*
Vegetable
  binders, physical properties of, 350*t*
  fluxes and surfactants, 359–360
Vegetable oil-rosin binders
  biomasses productivity, 354*f*
  consistency, 348–350
  cracked pavement, 353*f*
  field experience feedback, 351–352
  indirect tensile test, 353*f*, 354*f*
  manufacturing, 350
  mechanical properties, 350–351, 352*t*
  and microalgae, 352–357
Vegetable oils
  alternative binders from, 347–358, 348*f*
  composition of, 349*t*
  price of, 348
Virgin aggregates (VAs), 363
  in recycled mixture, 364
  temperatures, 363
Virgin bitumen (VB), 363
Viscoelastic behavior, dependence on pressure, 181–182

www.EngineeringEBooksPdf.com

Viscoelastic continuum damage (VECD) theory, 142, 147
aforementioned studies, 222–223
definition, 220–221
Viscoelastic damage model, 324
Viscoelasticity, asphalt concrete, 285–286
Viscoelastic-viscoplastic-viscodamage (VE-VP-VD) model, 236–238
Viscosity, asphalt cement, 280–283
Viscosity–temperature susceptibility (VTS), 47, 48–49
Voids-in-mineral-aggregate (VMA), 444
Volume dilatometry, 169–170

W

Warm mix asphalt, 393
Water evaporation, emulsions, 419–420
Water flow modeling, asphalt mixtures, 316–319
Water-induced damage
adhesive and cohesive failure due, 310*f*
deteriorated pavements due to, 304*f*
mechanisms, 309
Wave propagation tests, 87, 87*t*
Wax
in petroleum, 35
surface freezing crystallization, 105–116
Wax-containing asphalts, 105
Waxphaltene Determinator, 35
Williams-Landel-Ferry (WLF) equation, 169–170
applicability, 176*f*
free-volume model, 174, 177, 180–181
power-law model, 184–185, 186
Witczak models, 289, 290–291
Wood coproducts, alternative binders from, 347–358
Working groups (WGs), 5

www.EngineeringEBooksPdf.com